SOCIÉTÉ DES INGÉNIEURS DE L'AUTOMOBILE

BOOK OF PROCEEDINGS

With the support of the French Car industry and the French Association of Oil & Gas industry

PFA FILIÈRE AUTOMOBILE & MOBILITÉS

EVOLEN Energy Made in France

International Conference and Exhibition

SIA POWERTRAIN & ENERGY

The complete propulsion solution within its energy framework for long range passenger cars and commercial vehicles



EXHIBITION :
54 exhibitors

15-16 JUNE 2022

PARC DES EXPOSITIONS, ROUEN – FRANCE

Exclusive Sponsors

A2Mac1 Automotive Benchmarking

SCHAEFFLER

TotalEnergies

Premium Sponsors

HYVIA

Innovation in Motion Miba

PLASTIC OMNIUM

vitesco TECHNOLOGIES

QUARTZ EV FLUID

TotalEnergies in pole position on electric with DS-TECHEETAH



The FIA Formula E is the privileged field of innovation for developing electric mobility.
TotalEnergies is accompanying DS Automobiles and is commercializing the Quartz EV Fluid range which offers performance and efficiency to hybrid and electric vehicles.

TotalEnergies

competition.totalenergies.com/eng

COMITEES

Conference Chairman
Noureddine GUERRASSI, BorgWarner

Steering Committee
Frédéric CHARON, SIA
Philippe CHINA, TotalEnergies
Bernard CLEMENT, Evolen
Adélaïde EVRA, SIA
Emmanuel JEAN, Faurecia
Bertrand LARGY, SIA Experts' Community EVEE
Marc LEJEUNE, Renault Trucks
Jean-Philippe MERCIER, Renault Group
Gaëtan MONNIER, IFP Energies Nouvelles
Jérôme MORTAL, Valeo
Joël OP DE BEECK, Plastic Omnium
Rémy SCHMITT, Robert Bosch

Organising Committee
Nadim ANDRAOS, FEV
Philippe BERNET, SIA
Jean-Marc BOULARD, AVL
Omar HADDED, IAAPS
Pascal LONGUEMARE, IFP School
Dominique MARTINEAU, Vitesco Technologies
Geoffroy MARTIN, NextMove
Martin PIERRELEE, SIA
Sébastien POTTEAU, EMC
Claudine ROCHETTE, Valeo
Ralph SALIBA, IAV

Scientific Committee Session Chairmen
Members' list under finalization

Session 1.
Electrified Thermal Engines
Chairmen - Gaëtan MONNIER, IFPEN & Rémy SCHMITT, Robert Bosch

Session 2.
Electric Machines & Batteries
Chairmen - Bertrand LARGY, SIA & Jean-Philippe MERCIER , Renault Group

Session 3.
Electrified Propulsion Systems including Full Electric & Hybrids
Chairmen - Marc LEJEUNE, Volvo Group & Jérôme MORTAL, Ultima Mobility

Session 4.
Electrified Propulsion Systems based on Hydrogen Combustion & Fuel Cell
Chairmen - Emmanuel JEAN, Forvia & Joël OP DE BEECK, Plastic Omnium

Session 5.
Energy for Sustainable Mobility including Low Carbon Fuels & Electricity
Chairmen - Philippe CHINA, Total & Jean-Philippe LELIEVE, Renault Group

KEYNOTE SPEAKERS & PANELISTS



Sophie BIRE
Sponsor of the congress, VP R&D Fuels and Lubricants, OneTech, TotalEnergies



Marc LEJEUNE
Business Intelligence Director, Renault Trucks



Julien SALESSY
VP Powertrain engineering France, Volvo Group



Nicolas CHAMPETIER
SVP Advanced Engineering for Clean Technologies and French Delegate, Stellantis



Stéphane FREGOSI
President Vitesco Technologies France



Matthias Kratzsch
CEO IAV Group



Ulrich KRAMER
Technical Specialist Fuels - FORD / Chairman FVV Fuels Group



Philippe SCHULZ
VP Advanced Powertrain & EV Technology, Groupe Renault

CONTACT : MARTIN PIERRELÉE // martin.pierrelee@sia.fr // +33 6 76 62 24 87 // **www.sia.fr**



Sustainability isn’t only on our agenda. It’s at the heart of everything we do.

We pioneer motion

If you’re to take sustainability seriously, you have to approach it holistically, which is why we‘ve made it a top priority. As our sustainability report shows, this is true throughout the company: from products and production processes to selecting suppliers and raw materials, and to our corporate culture.
we-pioneer-motion.com

SCHAEFFLER

15 JUNE 2022

FUEL CELL VS HYDROGEN INTERNAL COMBUSTION ENGINE p. 11
Emmanuel JEAN - FORVIA & Cédric LIBERT - RENAULT GROUP

HYBRID VEHICLE ARCHITECTURE p. 39
Andreas BUCHNER - BMW & Sébastien POTTEAU - EMITECH

ELECTRIC MOTOR p. 60
Eric CHEVALIER & Sophie PERSONNAZ - VALEO

POWER ELECTRONICS AND COMPONENTS p. 73
Patrick CREMONA & Olivier PLOIX

ELECTRIC VEHICLE HOLISTIC VIEW p. 87
Jean-Philippe MERCIER - RENAULT GROUP & Paul ARMIROLI

ELECTRIFIED PROPULSION SYSTEMS OVERVIEW p. 108
Marc SENS - IAV & Marc LEJEUNE - RENAULT TRUCKS

HYDROGEN INTERNAL COMBUSTION ENGINES p. 132
Fabrice FOUCHER - ORLEAN UNIVERSITY & Joël OP DE BEEK - PLASTIC OMNIUM

ELECTRIFIED PROPULSION SYSTEMS CONTROL p. 165
Philippe BERNET- RENAULT & Dominique MARTINEAU - VITESCO TECHNOLOGIES

COMBUSTION OF HYDROGEN & SYNTHETIC FUELS p. 185
Rémy SCHMITT - BOSCH & Thomas KÖRFER - FEV

THERMAL ENGINE FOR HYBRID APPLICATIONS p. 213
Gaëtan MONNIER - IFPEN & Daniel ROETTGER - FORD

BATTERY ARCHITECTURE p. 235
Bertrand LARGY - SIA EV&EE Experts Community & Christophe MORIN

ELECTRIFIED PROPULSION SYSTEMS TESTS AND SIMULATIONS p. 256
Pierre GAUDILLAT - AVL & Yannick RAYNAUD - PLASTIC OMNIUM

16 JUNE 2022

ELECTRIC VEHICLE ARCHITECTURE p. 278
Jérôme MORTAL - ULTIMA MOBILITY & Claudine ROCHETTE - VALEO

ENERGY FOR SUSTAINABLE MOBILITY p. 300
Philippe CHINA - TOTAL ENERGIES & Jean-Philippe LELIEVRE - RENAULT

FUEL CELL AND HYDROGEN STORAGE p. 332
Nicolas OBRECHT - TOTAL ENERGIES & Mathias REUM - SCHAEFFLER AUTOMOTIVE

BATTERY THERMAL MANAGEMENT AND SAFETY p. 360
Bertrand LARGY - SIA EV&EE Experts Community & Masato ORIGUCHI

vitesco
TECHNOLOGIES

ELECTRIFYING YOUR FUTURE.

CLEAN, SUSTAINABLE MOBILITY.

Our drive technologies are powering clean mobility.
Whether electric car or hybrid, Vitesco Technologies delivers modern powertrain solutions for clean and efficient vehicles.
A driving force for generations to come – Vitesco Technologies.



WWW.VITESCO-TECHNOLOGIES.COM

210x279mm_VT_AZ_Brunswick_MTZ_03-21_EN_RZ_39L300.indd 1 03.03.21 14:39

AMPERE ROOM
FARADAY ROOM
TESLA ROOM
VOLTA ROOM

PROGRAMME 15 JUNE 2022 MORNING

OPENING PLENARY SESSION

08:30 ›
Welcome introduction
Luc MARBACH - SIA President
Sophie BIRE - VP Research and Development Merketing and Services - TOTAL ENERGIES
Julien SALESSY - VP Powertrain Engineering France, Volvo Group

08:35 ›
Opening address by the conference chairman
Noureddine GUERRASSI - BORGWARNER

08:45 ›
Keynote: Road freight decarbonation
Marc LEJEUNE - Business Intelligence Director, RENAULT TRUCKS

09:15 ›
OPENING PANEL SESSION « Technologies and energy for carbon neutrality for long range »
Philippe DIVINE, VP Advanced Strategy and Business Development LCV, Renault Group
Philippe DIVRY, SVP Group Truck Strategy, Volvo
Renault
Professor Thomas KOCH, Director of the Institut für Kolbenmaschinen, Karlsruher Institut für Technologie
Mathieu SOULAS, VP Strategy & Supply, TotalEnergies
Yann VINCENT, CEO, ACC (Automotive Cells Company)
Moderator : Stephen Marvin - R&D Director - PLATEFORME FILIÈRE AUTOMOBILE ET MOBILITÉS

10:30 › COFFEE BREAK IN THE EXHIBITION // TEST DRIVE

	FUEL CELL VS HYDROGEN INTERNAL COMBUSTION ENGINE Bertrand GATTELIER - IFPEN & Cédric LIBERT - RENAULT GROUP	HYBRID VEHICLE ARCHITECTURE Andreas BUCHNER - BMW & Sébastien POTTEAU - EMITECH	ELECTRIC MOTOR Eric CHEVALIER & Sophie PERSONNAZ - VALEO	POWER ELECTRONICS AND COMPONENTS Patrick CREMONA & Olivier PLOIX
11:30 ›	Heavy-duty trucks: hydrogen fuel cell vs. hydrogen internal combustion engine **Mickaël LOSZKA** - IFPEN	RENAULT E-TECH Hybrid Technology and its last improvement **Nicolas FREMEAU** - RENAULT GROUP	Calibrating Optimal IPMSM Torque Control with Flux-Weakening Using Model-Based Calibration **Kévin ROBLET** - MATHWORKS Inc.	Power GaN FET technology in CCPAK for high power applications like OBC and DCDC **Didier CHOWHRY** - NEXPERIA
12:00 ›	Comparison between different hydrogen fuelled powertrains for urban busses **Luciano ROLANDO** - POLITECNICO DI TORINO	Hybrid transmission for commercial vehicles: architectures and benefits **Benoist AUFFRAY & Loïc VASSIEUX** - VALEO	Wound Field Synchronous Machine **Martin BRUELL** - VITESCO TECHNOLOGIES	CarXield - First EMI Filter to set standards **Muhittin YILDIZ** - TDK
12:30 ›	Evaluation of the impact of different Active Thermal Management System layouts on medium/heavy duty FCEVs performance **Michele BILANCIA** - PUNCH Hydrocells	Dynamic Simulation using ECMS Controller to Optimize the HEV Fuel Economy on a Real-World Commuting Cycle with Battery Thermal Management **Michael ZAGUN** - GAMMA TECHNOLOGIES	Analysis of Reconfigurable Motor Windings for Better Efficiency, Increased Power Density, and Reduced Magnet Usage **Ryan HUGHES** - UNIVERSITY OF BATH	One for All: Functional Integrated Electronics for HV Architectures **Ayman AYAD** - VITESCO TECHNOLOGIES

13:00 › LUNCH BREAK IN THE EXHIBITION // TEST DRIVE

AMPERE ROOM
FARADAY ROOM
TESLA ROOM
VOLTA ROOM

PROGRAMME 15 JUNE 2022 AFTERNOON

	ELECTRIC VEHICLE HOLISTIC VIEW Jean-Philippe MERCIER - RENAULT GROUP & Paul ARMIROLI	ELECTRIFIED PROPULSION SYSTEMS OVERVIEW Marc SENS - IAV & Marc LEJEUNE - RENAULT TRUCKS	HYDROGEN INTERNAL COMBUSTION ENGINES Fabrice FOUCHER - ORLEAN UNIVERSITY & Joël OP DE BEEK - PLASTIC OMNIUM	ELECTRIFIED PROPULSION SYSTEMS CONTROL Philippe BERNET- RENAULT & Dominique MARTINEAU - VITESCO TECHNOLOGIES
14:30 ›	Efficient E-Motors as key for a sustainable future **Jannick HEILCK** - SCHAEFFLER AUTOMOTIVE	The World Automotive Powertrain Outlook - WAPO: a unique forecast toolbox to assess the evolution of the Light Vehicle market and its related impacts **Juan VERA** - BIPE-BDO	Direct injection hydrogen combustion engine - an attractive Zero CO_2 powertrain concept for Light Commercial Vehicles **Thomas KÖRFER** - FEV	Connected strategy for energy-efficient driving of electric vehicle : experimental results **Antonio SCIARRETTA** - IFPEN
15:00 ›	Life Cycle Comparison of the Latest Electrified Propulsion Systems **Hervé DUPONT** -VITESCO TECHNOLOGIES	Electric Mobility 48V. New Value Space Road Map **Paul ARMIROLI** - VALEO	The AVL Hydrogen Engine for CO_2 neutral goods transportation **Bernhard RASER** - AVL List	Efficiency Improvement of Automotive Traction Systems by Dynamic Motor Drive **Zhiqian CHEN** - TULA TECHNOLOGY
15:30 ›	Holistic comparison between Si IGBT and SiC MOSFET for the next generation BEV: materials, devices, systems, supply chains, and cost analysis **Yu YANG** - YOLE	Vehicle to Grid: Towards a cybersecure electric system including vehicle, charging points and batteries **Joseph KAMEL**- ETAS	Hydrogen internal combustion engine lubrication challenges and engine oil requirements **Nicolas OBRECHT** - TOTAL ENERGIES	Optimal control for serial hybrid coach **Antoine DELACOURT** - SIEMENS IND. SOFTWARE
16:00 ›	COFFEE BREAK IN THE EXHIBITION // TEST DRIVE			
	COMBUSTION OF HYDROGEN & SYNTHETIC FUELS Rémy SCHMITT - BOSCH & Thomas KÖRFER - FEV	THERMAL ENGINE FOR HYBRID APPLICATIONS Gaëtan MONNIER - IFPEN & Daniel ROETTGER - FORD	BATTERY ARCHITECTURE Bertrand LARGY - SIA EV&EE Experts Community & Christophe MORIN	ELECTRIFIED PROPULSION SYSTEMS TESTS AND SIMULATIONS Pierre GAUDILLAT - AVL & Yannick RAYNAUD - PLASTIC OMNIUM
17:00 ›	Optimizing a Heavy Duty Hydrogen DI combustion system using experimental and numerical workflow **Vincent GIUFFRIDA** - IFPEN	Future ICE Technologies for High Efficient Hybrid Electric Powertrains **Matthias KRAUSE** - IAV	Boardnet and Powernet improvements through supercapacitor / battery hybridisation **HAUF HARALD** - NAWA TECHNOLOGIES	Real-Time Multi-Physics Simulation of BEV VTM for X-in-the-Loop Control Development **Eduardo GRAZIANO** - PWT
17:30 ›	H2 efficient and near zero emissions operation on a PFI HD single cylinder Diesel ICE **Richard OUNG** - UNIVERSITE D'ORLANS - PRISME	Electrically heated catalyst performance at low ambient temperature **Mathieu CAPIRCHIA** - FAURECIA	Modular and Distributed battery design with integrated multi-level power electronics converter **Jay AL-TAYIE** - RICARDO	Virtual Calibration of a detailed HEV thermal management system **Hanna SANA** - GAMMA TECHNOLOGIES
18:00 ›	Chassis dynamometer and road pollutant emissions assessment on Euro6d Gasoline PHEV vehicles with conventional and synthetic fuels **Christophe CHAILLOU** - ARAMCO	mproving the efficiency of P0 and P1 hybrids by valve deactivation strategies **Frank HIMSEL** - SCHAEFFLER AUTOMOTIVE	High power battery pack for 48V mHEV applications using Sodium-ion chemistry, Ni & Cobalt free. **Franck DHAUSSY** - PLASTIC OMNIUM	Influence of Measurement Uncertainty on the Range and Efficiency Evaluation of Electric Cars **Alexander STOCK** - HOTTINGER BRUEL & KJAER
18:30 ›	COCKTAIL IN THE EXHIBITION // TEST DRIVE			
20:00 ›	GALA DINNER AT THE « PARC DES EXPOSITIONS »			

AMPERE ROOM
FARADAY ROOM
TESLA ROOM
VOLTA ROOM

PROGRAMME 16 JUNE 2022

	ELECTRIC VEHICLE ARCHITECTURE Jérôme MORTAL - ULTIMA MOBILITY & Claudine ROCHETTE - VALEO	ENERGY FOR SUSTAINABLE MOBILITY Philippe CHINA - TOTAL ENERGIES & Jean-Philippe LELIEVRE - RENAULT	FUEL CELL AND HYDROGEN STORAGE Nicolas OBRECHT - TOTAL ENERGIES & Mathias REUM - SCHAEFFLER AUTOMOTIVE	BATTERY THERMAL MANAGEMENT AND SAFETY Bertrand LARGY - SIA EV&EE Experts Community & Masato ORIGUCHI
08:00 ›	Electrification, efficiency and fun to drive – Hyundai Motor Group's E-GMP **Michael WINKLER** - HYUNDAI	eFuels and Biofuels as possible complementary strategy to e-mobility **Johannes ULLRICH** - HYUNDAI	Optimization of PEMFC cold-start strategy using multi-physical real-time capable system simulation **Christoph POETSCH** - AVL LIST	Ascend Polyamide-based solutions for High Voltage EV battery structures and enclosures **Ould Mohammed YAHYA** - ASCEND PERFORMANCE MATERIALS
08:30 ›	48V Electrified Propulsion kit for Cross Car **Gillem ENJALBERT** - VALEO	How the VALEO Smart Ebike system will simplify the last mile delivery? **Benjamin MORLIERE** - VALEO	Development of fuel cell retrofit kit for commercial vehicles and TCO analysis **Joanna RICHART** - RICARDO	Thermal Propagation Prevention Technologies for safe Battery Designs **Uwe FRANKEN** - HENKEL KGAA
09:00 ›	Holistic Development Methodology for Future Powertrains with an efficient Combination of Simulation and Testing Environment **Tobias MINK** - APL GROUP	Combination of advanced emission control technologies and sustainable renewable fuels on a long-haul demonstrator truck **Dirk BOSTEELS** - AECC	Hydrogen High Pressure Storage Systems for Mobile Applications **Sullivan ICARD** - FAURECIA	Smart Thermal Management **Bart VAN MOERGASTEL** - DENSO **François PLANTE** - RENAULT GROUP
09:30 ›	System design of optimized 800V eDrive systems **Joao BONIFACIO** - ZF FRIEDRICHSHAFEN AG	Ammonia powertrain for a carbon free mobility **Clément DUMAND** - STELLANTIS	CO_2 free Hydrogen Mobility for Passenger Cars without compromises **Bjorn CRIEL** - PLASTIC OMNIUM	Battery Thermal Management for EV using Artificial Intelligence (AI) methodologies **Leonardo CANZIO** - HYUNDAI
10:00 ›	COFFEE BREAK IN THE EXHIBITION // TEST DRIVE			
11:00 ›	Keynote: Results of VisionAir and the Hydrogen Mix for 2030-2040 **Jean-Luc BROSSARD** - Program Director PLATEFORME FILIÈRE AUTOMOBILE ET MOBILITÉS			
11:30 ›	**PANEL SESSION « Technology mutations and their impact on the skills and organisations of our groups »** **Nicolas CHAMPETIER** - SVP Advanced Engineering, Stellantis **Alexandre CORJON** - Executive VP Innovation, Plastic Omnium **Stéphane FREGOSI** - President, Vitesco Technologies France **Matthias KRATZSCH** - CEO , IAV Group **Alain RAPOSO,** Executive Vice President / R&D Division, Hyundai **Moderator: Frédéric CHARON - Director, SIA**			
12:45 ›	STUDENT POSTER AWARD			
13:00 ›	LUNCH BREAK IN THE EXHIBITION // TEST DRIVE			
CLOSING PLENARY SESSION **Thomas KOCH - KARLSRUHER INSTITUT FÜR TECHNOLOGIE & Federico MILLO - POLITECNICO DI TORINO**				
14:30 ›	Keynote: Sustainable mobility for long range passenger cars and light duty vehicles **Nicolas CHAMPETIER** - SVP Advanced Engineering - STELLANTIS			
15:00 ›	Keynote: FVV Fuels study IV - Transformation of mobility to the GHG neutral post fossil age **Ulrich KRAMER** - Technical Specialist Fuels - FORD / Chairman FVV Fuels Group			
15:30 ›	Keynote: Powertrain electrification: on the road towards carbon neutral target **Philippe SCHULZ,** VP Advanced Powertrain Engineering, RENAULT GROUP			
16:00 ›	Closing remarks by the conference chairman **Noureddine GUERRASSI** - BORGWARNER			
16:15 ›	END OF THE CONGRESS			

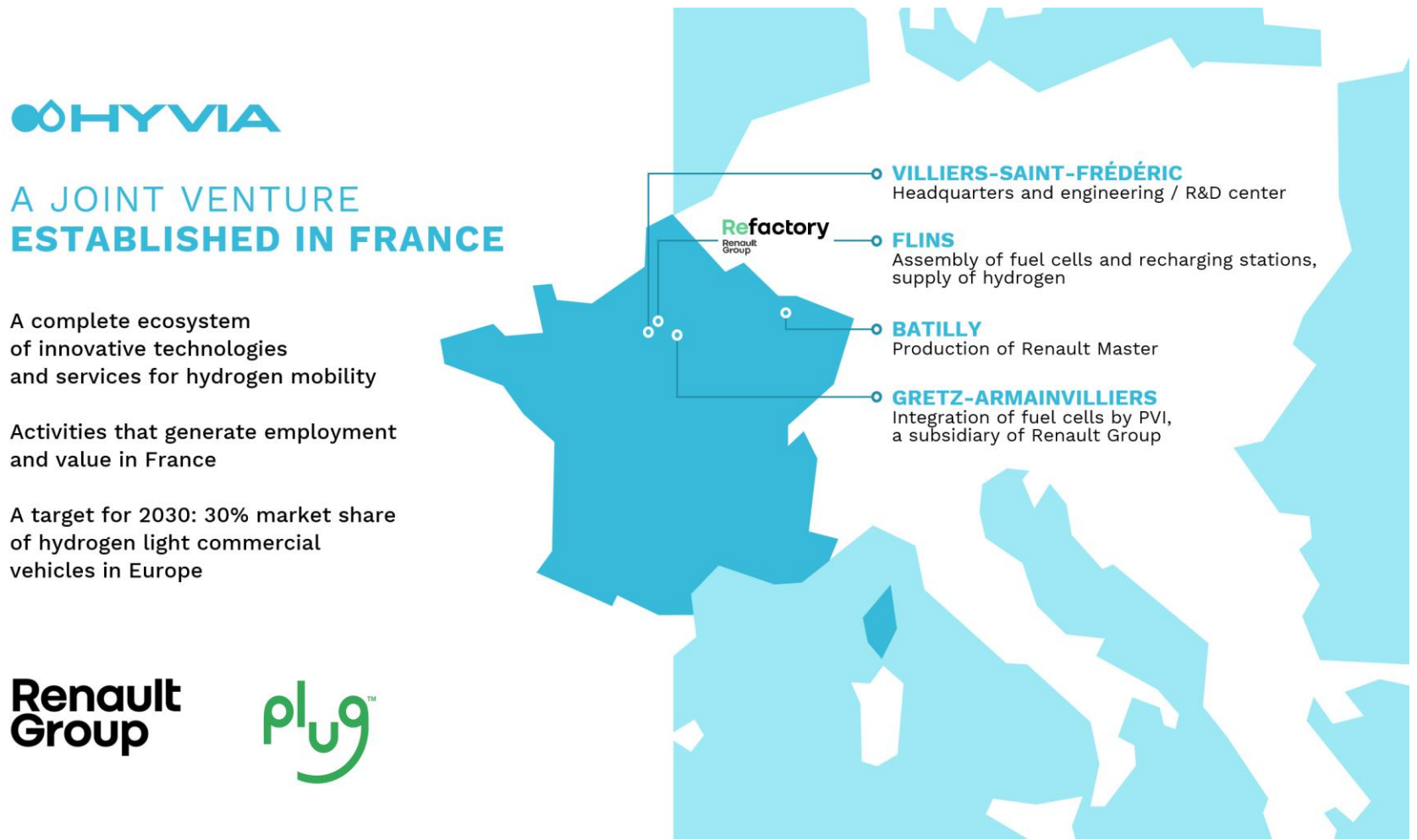
DRIVE WITH HYVIA HYDROGEN ECOSYSTEM



Left to right: Renault Master Chassis Cab H2-TECH, Renault Master City Bus H2-TECH, Renault Master Van H2-TECH.

“HY” for hydrogen, “VIA” for road: HYVIA paves a new way forward for carbon-free mobility, with hydrogen mobility solutions. Created in June 2021, HYVIA is a joint venture equally owned by Renault Group, a dominant player in the automotive industry, and Plug Power, a world leader in turnkey hydrogen and fuel cell solutions.

Based in France, for European markets, HYVIA offers a complete and unique ecosystem that includes **light commercial vehicles** with fuel cells, **hydrogen refueling stations**, supply of carbon-free hydrogen, services for financing and maintenance of fleets.



https://www.hyvia.eu

15 JUNE 2022

FUEL CELL VS HYDROGEN INTERNAL COMBUSTION ENGINE

OBRIST
POWERTRAIN

aFuel®

World's First Global Climate Positive Fuel



aFuel® is eMethanol with cSink, created by collaborative technology.

Visit www.obrist.at for more information.

Long-haul Trucks: Hydrogen Fuel Cell vs. Hydrogen Internal Combustion Engine

M. Loszka[1], R. Martin[1], O. Guyon[1], P. Leduc[1], C. Ternel[1]

1 : IFP Energies nouvelles, 1 et 4 avenue de Bois-Préau, 92852 Rueil-Malmaison, France ; Institut Carnot IFPEN Transports Energie

Abstract: Hydrogen has been lately recognized as a means of decarbonizing several industries, including the transportation sector. Such a carbon-free fuel would indeed help reducing greenhouse gas emissions and tackling global warming. In 2020, heavy-duty trucks accounted for 1532Mt of carbon dioxide emissions, which represents 4.5% of the global emissions [1]. While battery electric vehicles have been identified as key enablers for the reduction of passenger road vehicles emissions [2], the equivalent for road freight vehicles has not been clearly stated. In this context, this paper aims at studying the potential of hydrogen powertrains for long-haul trucks. When considering long-haul trucks, high power as well as high energy content are needed, and hydrogen powertrains, be it with a fuel cell or an internal combustion engine, are serious candidates. First, the sizing of the typical long-haul truck used for the study is detailed. A simulation study using the Simcenter Amesim™ software is then conducted, based on the peer-reviewed duty cycles for heavy trucks of the VECTO tool [3], to compare the fuel economy of powertrains including either a hydrogen fuel cell or a hydrogen internal combustion engine. The fuel economy of the truck is 20 to 30% better in case of the fuel cell powertrain, while a hydrogen internal combustion engine powertrain will have a much lower price tag. The last part of this paper gives an outlook on the total cost of ownership of each configuration along with a lifecycle assessment in an attempt to assess what powertrain would be optimal for long-haul trucks in a hydrogen ecosystem.

Keywords: fuel cell, hydrogen combustion engine, trucks, TCO, LCA

1. Introduction

As BEVs arouse more and more interest to decarbonise the passenger cars sector, heavy-duty transports still lack their clean powertrain solutions. Although BEVs have been and are still in development for specific heavy-duty applications, they have clear disadvantages when it comes to long-haul trucks. These vehicles indeed need a high autonomy, which inevitably leads to large batteries, and therefore long charging time, in a sector where operator sometimes organize drivers switches in order to monetize the high investment needed to buy such a truck.

Hydrogen powertrains have the advantage of combining fast refuelling time with zero tailpipe carbon emissions. Two solutions have emerged and are allegedly opposed: hydrogen fuel cells and hydrogen internal combustion engines. While the transportation sector still lacks industrial maturity and feedback on the performances and ageing of fuel cells (FC), H2 ICEs seduce by their resemblance with common ICEs, even though they cannot rigorously be stamped as zero-emission.

This paper aims at giving an objective comparison of the relevance of fuel cells and H2 ICEs concerning energy consumption, cost and environmental impact. Multiple variants of FCEVs are compared to insist on the impact of the electric powertrain sizing parameters on all these factors.

This article is a revamped excerpt of the full report of a study conducted in partnership with the French ecological transition agency (ADEME). The project codename, *TranpLHyn*, is a redesigned version of the French word for “springboard”.

2. Energy consumption evaluation

The first step to perform a full comparison between all vehicle variants is to assess their energy consumption on relevant duty cycles. The following paragraphs detail the corresponding assumptions and methodology.

2.1 Design assumptions

Vehicle description: In this paper, all truck variants consist of a 4x2 tractor with a single trailer. The maximum power at wheel has been set to about 400kW, to be comparable with existing vehicles. Other specifications have been defined, especially concerning constant speeds at given slope values. All chosen powertrains should maintain a 44t long-haul truck at 90km/h on a flat road as well as at 50km/h at 5% slope and 10km/h at 12% slope. FCEVs should be able to address this last requirement even with an empty battery, which has consequences on the fuel cell sizing.

Vehicle road load and aerodynamic parameters are summarized in Table 1. The hydrogen tank capacity

was set to 50kg for each variant thus vehicle range is an output.

SCx	5,7 m²
Crr	6 kg/t
Vehicle weight (with empty trailer, no powertrain)	13 728 kg
Tires	315/80 R22,5
H2 tank	1900 Wh_{LHV}/kg_{tank} 0,057kg_{H2}/kg_{tank}
Battery	150 Wh/kg_{pack}
Power electronics	10 kW/kg
Internal Combustion Engine	0,45 kW/kg
Electric Motor	2,5 kW/kg
Fuel cell	0,65 kW/kg_{system}

Table 1: Vehicle parameters and mass density hypotheses (from [4])

The same aerodynamic drag as for Diesel trucks was applied to FCEVs. In fact, the higher cooling needs of FCEVs may require a wider radiator grille and a related impairment of the aerodynamic efficiency of these vehicles, but this effect was neglected in this study.

The behaviour of the fuel cell and of the battery was also simplified. Indeed, no impact of ageing or hot and cold ambient temperatures were accounted for in the vehicle simulations.

The mass of each variant was computed using the hypotheses listed in Table 1. The empty vehicle mass of the Diesel reference is about 14 600kg, trailer included. For the H2 ICEV, the mass rises up to about 15 400kg, mainly because of the 700bar hydrogen tank. The H2 FCEV variants have a mass ranging from 15 300kg to 16 200kg depending on the fuel cell and the battery features.

Powertrain sizing: A range of FC systems (FCS) power and battery capacity was considered. A base FC module of 75kW was stacked so as to simulate FCS with power levels between 150kW and 450kW. Four battery capacity levels were chosen, evenly distributed between 25kWh and 100kWh. The same 400kW electric motor was used for each of these variants.

The FCEVs variants are confronted to ICEVs equipped either with a conventional Diesel ICE or with an H2 ICE.

The transmission is the same for all the truck variants and corresponds to a 12-speed gearbox and an axle ratio.

Efficiency assumptions: The peak brake efficiency of the simulated Diesel ICE is 46%. It is two points higher than that of the H2 ICE, which efficiency map is presented in Figure 1. This map is derived from [5].

A variant of this map was also considered, with a peak efficiency of 50%.

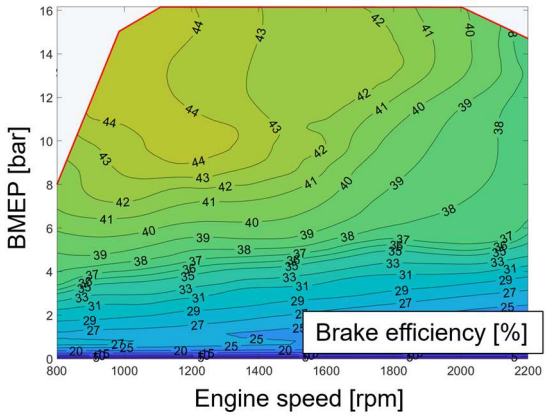


Figure 1: H2 ICE brake efficiency map (derived from [5])

Two fuel cell characteristics were derived from on-vehicle measurements: a first characteristic with 55% peak efficiency and a second one with 65% peak efficiency. These are illustrated in Figure 2, along with the experimental efficiency curves of the Toyota Mirai and of the Hyundai Nexo, derived from [6, 8].

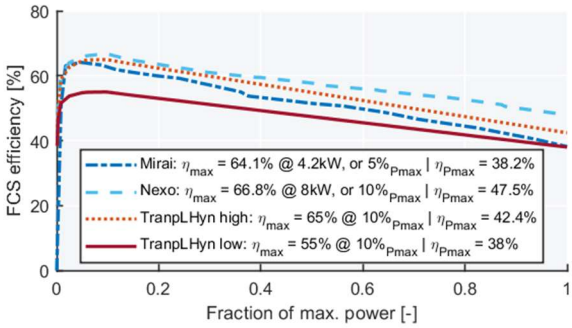


Figure 2: Fuel cell efficiencies considered in this study (derived from [6-8])

2.2 Methodology for consumption calculation

The variants described in the last paragraph were simulated using Simcenter Amesim. The duty cycles used for the consumption evaluation come from VECTO: VECTO Urban Delivery, VECTO Regional Delivery and VECTO Long-haul. Each simulation was run either without cargo payload, or with a 19.3t payload. Then, weighting factors were applied to the 6 simulation results in order to estimate an aggregate score. This score is associated to the weighting given as an example in Table 2, and, using the detailed results published in the full report of this study, the weighting factors can be adjusted to better fit a particular usage.

Without cargo payload			With 19.3t cargo payload			Total
Urban	Regional	Long-haul	Urban	Regional	Long-haul	
2%	3%	24%	4%	7%	60%	100%

Table 2: Example of weighting to calculate a score based on the consumption on VECTO cycles

To validate the sizing and the relevance of the method described above, real trips were also simulated (Paris-Lille, Rennes-Strasbourg, Bordeaux-Strasbourg, Lyon-Milan). Those were generated using a webservice developed and hosted on the Mobicloud platform by IFPEN.

2.3 Results

A summary of the scores of the different simulated plug-in variants is shown in Figure 3. The score of the Diesel reference is 31.8L/100km, which is in line with the mean fuel consumption of French long-haul trucks [9]. The impact of the fuel cell sizing appears clearly, and the consumption difference between a right-sized FC and an oversized FC lies around 1 kgH2/100km. For a given variant, there is also a 1 kgH2/100km gap when comparing fuel cells with different efficiency levels.

The impact of battery capacity is relatively low on vehicle consumption. Therefore, in this context, battery sizing should be done to meet performance needs such as maintaining high speeds at high slope levels, for example.

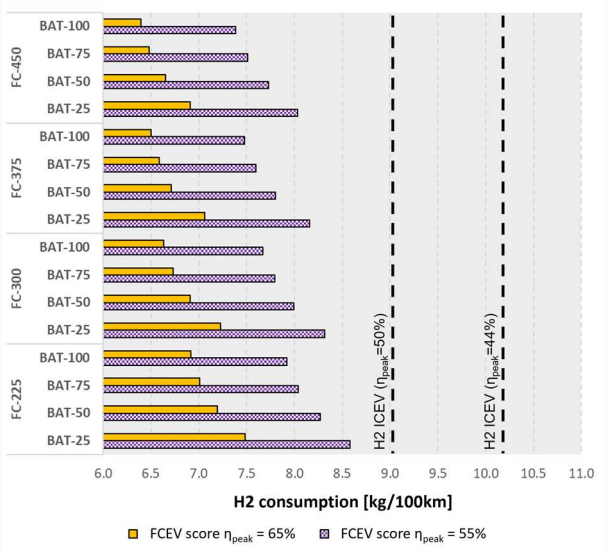


Figure 3: Score of the truck variants simulated in this study (based on the weighting of Table 2)

Table 3 gives a synthetized overview of the simulation results. FCEVs consumption is between 20% and 30% less than that of H2 ICEVs. This difference depends on the chosen weighting factors for the energy consumption on the VECTO cycles. It should be noted that these results are presented for plug-in FCEVs. However, as the battery capacities considered in this study are rather low compared to the trucks' energy consumption, results for non-plug-in vehicles show a fuel consumption approximately 3-4% higher, depending on the battery size.

	Orders of magnitude	
	Energy consumption	Range @ 50kg H_2
ICEV D	31,8 L/100km	-
ICEV H2 - η_{peak} = 44%	10,2 kgH_2/100km	≈500 km
FCEV H2 - η_{peak} = 55%	≈8 ± 0,6 kgH_2/100km and between 3 and 12 kWh_{elec}/100km	≈630 ± 50 km
FCEV H2 - η_{peak} = 65%	≈7 ± 0,6 kgH_2/100km and between 3 and 11 kWhelec/100km	≈730 ± 50 km

Table 3: Orders of magnitude of fuel consumption results for the different architectures of long-haul trucks simulated in this study

As mentioned above, real driving cycles were simulated as a comparison to the score calculated with the weighting of the VECTO cycles. Figure 4 shows a comparison of the results on VECTO cycles with payload and the simulated trips. While the profile of the Paris-Lille trip is rather close to that of the VECTO Long-haul, there are clear discrepancies when comparing the weighted score to other trips. This highlights the fact that the suggested weighting is an example, and that it should be adjusted if needed.

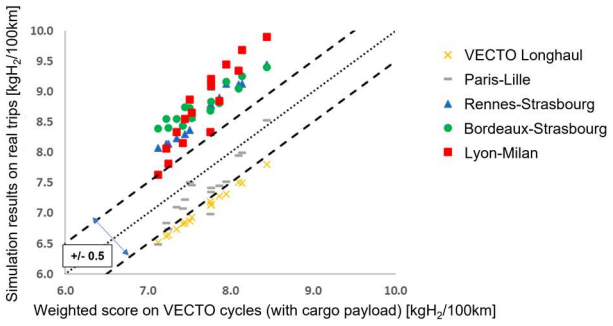


Figure 4: Comparison between the score on VECTO cycles and the consumption simulated on real trips

The Lyon-Milan trip is particularly interesting because of its altitude profile. Figure 5 shows a comparison of the battery SOC for different configurations on this trip. It appears that for such hill-climbs as the one between 220 and 250km, there is a trade-off between FC power and battery capacity in order to maintain vehicle performances: either the FC is not powerful enough and the battery needs to be depleted to avoid decreasing vehicle speed, or the FC is more powerful and the battery depletion is less severe during hill climb. These results could be further elaborated by considering the effect of vehicle speed and cooling fans on truck cooling capacity. This would finally have

an impact on FCS efficiency, especially when considering high ambient temperature situations.

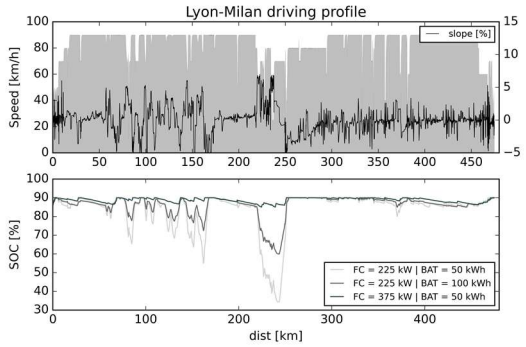


Figure 5: Illustration of the trade-off between fuel cell and battery sizing for hill climbs

3. Total Cost of Ownership

In the first part, vehicle variants have been defined and evaluated on several duty cycles. An aggregate score enables to sort them by energy efficiency. In the next part, the economic aspects of each variant will be investigated.

3.1 Hypotheses

By definition, the Total Cost of Ownership (TCO) aggregates all costs supported by the operator of a vehicle. These costs range from the initial investment to energy expenses and maintenance during the entire lifecycle up to resale or destruction. Resale is not included here due to a lack of trustworthy information, and neither is the driver's salary.

This is summed up in equation [1].

$$TCO[€/km] = \frac{Investments - Incentives + \sum Annual\ costs}{Lifecycle\ mileage} \quad [1]$$

The reference is still the conventional Diesel truck. The costing is based on 2022 assumptions, and cost evolution hypotheses are made for the estimated lifetime of the vehicle, which is 12 years in this study. The annual mileage considered here is 90 000 km/y. The TCO is actualized at the common rate of 5%.

Energy cost: Several assumptions concerning the energy cost over time were made. Those are based on [4, 10, 11].

Hydrogen cost depends on its source. Three cases were considered: local renewable H2, central renewable H2 and fossil H2 (from industrial SMR). Local H2 corresponds to small volumes produced at the refuelling station, while central H2 installations will yield bigger volumes for approximately 75% of local H2 cost. Yet, a hydrogen transportation cost must be accounted for, which is 1.5€/kgH2 in this study. The price evolution for these three types of hydrogen is illustrated in Figure 6. The VAT is not included here.

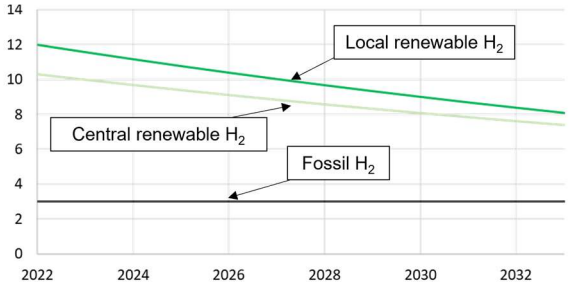


Figure 6: Hydrogen price evolution assumption [€/kg]

The evolution of the price of Diesel fuel and electricity was also taken into account, as pictured in Table 4. The price of Diesel does not account for temporary variations and increases due to a higher taxation.

	2022	2030	2033
Diesel [€/L]	1.00	1.25	1.41
Electricity [€/kWh]	0.130	0.158	0.175

Table 4: Diesel fuel and electricity price evolution over time

CAPEX and OPEX: Powertrain components pricing mainly depends on the power or energy requirement. Although a value of 300€/kW was considered here for the cost of the fuel cell, a sensitivity analysis is suggested in the following paragraphs.

Maintenance and insurance cost assumptions are based on bibliographical references.

The values in Table 5 are derived from [4, 10, 12, 13].

Costs	
ICE	45 €/kW
EM	15 €/kW
Battery	200 €/kWh
FC	300 €/kW
H2 tank	500 €/kg_{H2}
Other elec. comp.	2000 €
Maintenance	
Diesel ICEV	0.07 €/km
FCEV	0.13 €/km
Insurance	
Diesel ICEV	1,5%$_{investment}$
Fuel Cell	2%$_{investment}$

Table 5: Cost hypotheses for long-haul trucks

3.2 Results

Main outcomes: Figure 7 shows TCO results on a handful of chosen variants. The plot corresponds to the case of local renewable H2 and high efficiency fuel cells (peak efficiency: 65%). This representation shows that the TCO of H2-fueled variants is 2 or 3 fold the TCO of the Diesel reference. This is due to the high price of hydrogen compared to Diesel fuel,

especially for less energy-efficient variant like H2 ICEV, but also to higher investments, be it for the purchase of the hydrogen tank, or for that of the fuel cell. An incentive of 50 000€ from the French government was applied for FCEVs. This measure will last at least until the end of year 2022.

It is also interesting to remark that although more powerful fuel cells have higher efficiencies on a given duty cycle, the higher investment compared to less powerful ones is not compensated by the fuel economy. The gap is even more important when considering fuel cell replacement after six years, as is the case in Figure 6.

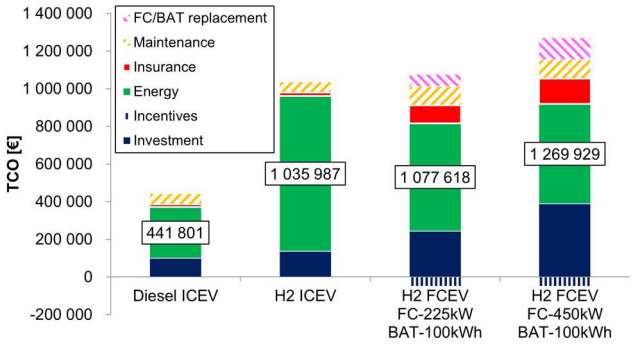


Figure 7: TCO breakdown comparison of some simulated variants of long-haul trucks (high-efficiency fuel cell with 65% peak efficiency)

A sensitivity analysis on the lifetime of the vehicle would show lower TCO values, but the hierarchy between the variants remains unchanged. Even though fuel cell replacement might not be necessary when considering shorter lifetimes, in the range of 4 years for instance, the H2-fueled variants TCO would still be 2 to 3 times higher than that of the Diesel reference.

Sensitivity analysis: In the previous paragraph, some parameters have been set that could be discussed. This paragraph aims at studying the impact of hydrogen origin, annual mileage, fuel cell price and hydrogen price.

Figure 8 shows the impact of hydrogen origin on the TCO of some simulated variants. In either case, the hierarchy between the solutions is the same: the cheaper is always the Diesel reference, then comes the H2 ICEV and the costlier variants are those with the highest-power fuel cells. The impact of central hydrogen production is relatively low on the TCO. However, the use of fossil H2 would bring H2 ICEV almost to the same level as the Diesel reference, while drastically reducing the gap between FCEVs and the Diesel ICEV. The high investment cost for FCEVs remains a limiting factor in reducing the gap between FCEV and ICEV TCOs.

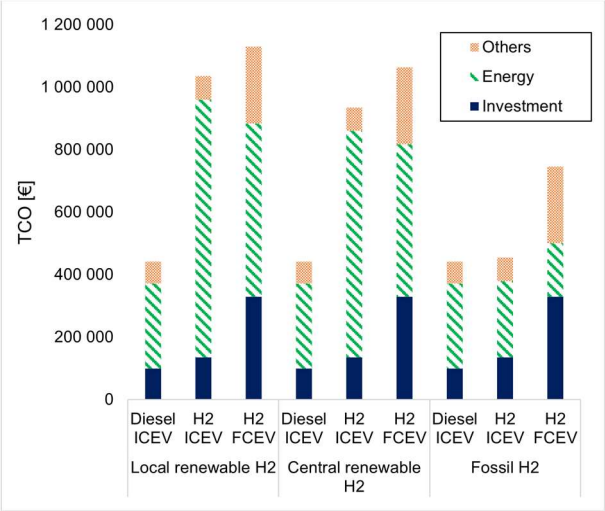


Figure 8: Impact of hydrogen origin on the TCO of long-haul trucks (FCEV variant: FC-300kW, BAT-75kWh)

Figure 9 represents the sensitivity of the TCO to annual mileage. The hierarchy between the solutions is not impacted by this parameter. Higher annual mileage means higher energy consumption over the lifetime of the vehicle, so the TCO of hydrogen-powered variants is greatly increased with this parameter. Above 90 000km/y and for a lifetime of 12 years, a second fuel cell replacement is considered, hence the slope discontinuity on the FCEV curve. Very little feedback is available on the expected lifetime of a hydrogen fuel cell in real long-haul truck operation.

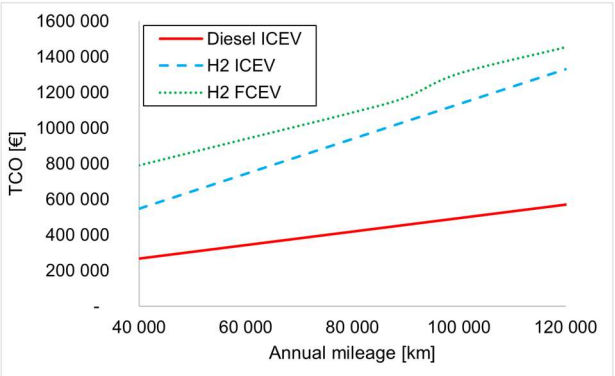


Figure 9: Impact of annual mileage on the TCO of long-haul trucks (FCEV variant: FC-300kW BAT-50kWh)

Figure 10 displays the TCO variation due to a difference in fuel cell price and hydrogen cost, for a given fuel-cell-powered variant. The error bars represent the impact of fuel cell replacement in each case. The horizontal line depicts the TCO of the Diesel reference, while the other line shows the evolution of the TCO of the H2-ICEV with hydrogen price. This plot shows that to be competitive with the Diesel reference, the hydrogen-powered variants

would need a hydrogen price around 2€/kg and a fuel cell price of 100€/kW.

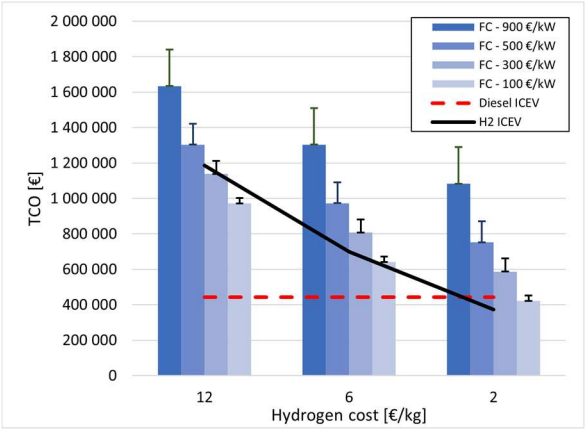


Figure 10: Impact of fuel cell and hydrogen cost on the TCO of long-haul trucks (FCEV variant: FC-300kW, BAT-50kWh)

4. Life Cycle Assessment

Knowing in which range the cost items of each configuration lie, it is important to also get a vision of the impact of each configuration on global warming. In this part, the equivalent CO2 emissions of long-haul trucks variants is investigated. The objective is to analyze the environmental impact of both the vehicle's and the fuel's life cycle, considering three scenarios, each corresponding to a specific means of production of hydrogen.

4.1 Hypotheses

The LCA was done with the SimaPro® software (version 9.2.0.2), and the database Ecoinvent v.3.8 (denoted below as EI 3.8).
Table 6 summarizes the main environmental impacts related to FCEVs and hydrogen-powered vehicles. The battery end-of-life and recycling is considered in this study, which has a positive impact on its environmental impact. Two electrical mixes for hydrogen production are compared: the French, low-carbon electricity mix and the renewable hydrogen mix where electricity comes only from on-shore wind farms.

H2 tank	22.8 kg $CO2_{eq}/kg_{tank}$
Fuel cell	40.9 kg $CO2_{eq}$/kW
Battery production and recycling	96 kg $CO2_{eq}/kWh_{bat}$
French electricity mix	59.9 g $CO2_{eq}/kWh_{elec}$ (→ 3.66 kg $CO2_{eq}/kg_{H2}$)
Electricity from wind farms	15.7 g $CO2_{eq}/kWh_{elec}$ (→ 1.12 kg $CO2_{eq}/kg_{H2}$)
H_2 from SMR	9.5 kg $CO2_{eq}/kg_{H2}$

Table 6: Environmental impacts hypotheses for the LCA of long-haul trucks [14-20]

Figure 11 illustrates the modelling of the hydrogen production from the electrolyser output through compression and transport up to the higher compression and distribution at the gas station.

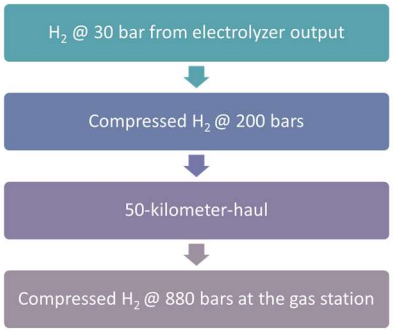


Figure 11: Hydrogen production model

4.2 Results

The first scenario considers hydrogen from electrolysis with the French electricity mix. The results are shown in Figure 12, left. The switch from Diesel to hydrogen enables to halve greenhouse gas (GHG) emissions. It is also clear that hydrogen production is the biggest contribution to GHG emissions for H2 FCEVs and H2 ICEVs. In that case, FC and H2 tank play a minor part in total GHG emissions.

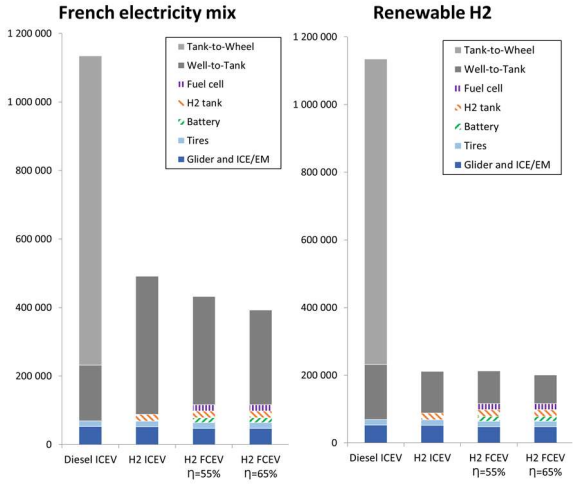


Figure 12: Lifetime GHG emissions [kg CO2eq] (FCEV variant: FC-300kW BAT-75kWh)

When considering electricity from on-shore wind farms, the GHG emissions related to hydrogen-powered variants can be halved again, as depicted in Figure 12, right. At this point, FC and H2 tank contributions become significant parts of the total GHG emissions.

The third scenario enables to show the environmental irrelevance of hydrogen-production from SMR. As shown in Table 6, there is roughly a nine-fold increase in Well-to-Tank GHG emissions compared to

renewable H2. In that case, the H2 ICEV would emit more GHG than the Diesel ICEV over its lifetime. The FCEVs variants would lag close behind, unfortunately reducing the interest of using a carbon-free fuel.

5. Conclusion

This study compared several powertrains for long-haul trucks from the energetic, economic, and environmental point of views.
Considering several FCEV designs and given H2 ICEV, consumption scores on VECTO cycles could be computed and compared to a Diesel ICEV reference. The powertrain performance requirements could be validated on real trips simulations. The simulations showed that FCEVs consume 20-30% less energy than ICEVs, with the weighting considered here.
The TCO comparison showed that there was no economical compensation of higher efficiency, more powerful fuel cell systems. In fact, low H2 price is key to competitivity of H2 vehicles. Plus, low FC stack price and high durability are needed for FCEVs to economically compete with Diesel ICEVs. This study also showed that battery has a very low impact on TCO for the designs studied here. Battery design criteria should be performance-related when it comes to long-haul FCEVs.
Finally, although H2 vehicles are 2 to 3 times costlier than Diesel solutions, they emit less GHG, as shown in the LCA part of this article. H2 from SMR is economically interesting but irrelevant from an environmental point of view. Even when compared to a low-carbon electricity mix like the French one is, renewable hydrogen would enable to cut GHG emissions of H2 vehicles by at least half.
The choice of an optimal powertrain for long-haul trucks therefore depends on the context and the different cost items. To go further, some aspects left aside in this study should be addressed, such as the impact of fuel cell ageing on its control, performance, and efficiency. The impact of cooling and the integration of the whole system and its impact on aerodynamic performances should also be investigated. Yet, this study showed that investment (i.e. CAPEX) is one of the biggest cost item for FCEVs and that fuel consumption reduction alone is no game changer in the actual economical context, unless it is significant.

6. Acknowledgments

The authors acknowledge the contribution of their colleagues to this work, especially Helen Bewi Komesse for her help in the LCA analysis.

This study has been conducted with the financial support of ADEME, the French Agency for the Environment and the Energy transition. The authors would like to thank Denis Benita for his help and assistance during this work.

7. References

[1] IEA (2021), World Energy Outlook 2021, IEA, Paris, https://www.iea.org/reports/world-energy-outlook-2021

[2] IEA (2020), Electric Vehicles, IEA, Paris https://www.iea.org/reports/electric-vehicles-2

[3] Zacharof N; Fontaras G. Report on VECTO Technology Simulation Capabilities and Future Outlook. EUR 28272 EN. Luxembourg (Luxembourg): Publications Office of the European Union; 2016. JRC103864

[4] ADEME, IFPEN, "Etude Energétique, Economique et Environnementale du Transport Routier à Horizon 2040 (E4T 2040)," 2022.

[5] Koch, D., Eßer, E., Kureti, S. et al, "H2-deNOx Catalyst for H2 Combustion Engines," MTZ Worldwide 81, 30-35, 2020, doi:10.1007/s38313-020-0229-3.

[6] Sery, J., Leduc, P., "Fuel cell behavior and energy balance on board a Hyundai Nexo," International Journal of Engine Research, 2021, doi:10.1177/14680874211059046.

[7] Sens, M. et al, "Hydrogen Powertrains in Competition to Fossil Fuel Based Internal Combustion Engines and Battery Electric Powertrains," 42nd International Vienna Motor Symposium, 29-30 April 2021.

[8] Argonne National Laboratory, Energy Systems Division, "Technology Assessment of a Fuel Cell Vehicle: 2017 Toyota Mirai," Report # ANL/ESD-18/12, 2017.

[9] Comité National Routier, "Enquête Longue Distance," 2019.

[10] France Hydrogène Mobilité, "Quelles perspectives pour le poids lourd électrique à hydrogène pour le transport de marchandises ?" 2020.

[11] RTE, Futurs énergétiques 2050, 2021.

[12] Ricardo Energy & Environment, "Improving understanding of technology and costs for CO2 reductions from cars and LCVs in the period to 2030 and development of cost curves," 2014.

[13] DOE, "DOE Advanced Truck Technologies – Subsection of the Electrified Powertrain Roadmap," 2019.

[14] ADEME, "Analyse du cycle de vie relative à l'hydrogène," 2020.

[15] Greet Model. [Online]. https://greet.es.anl.gov/

[16] DOE, "DOE Advanced Truck Technologies – Subsection of the Electrified Powertrain Roadmap," 2019.

[17] Bareiß, K., de la Rua, C., Möckl, M., Hamacher, T., "Life cycle assessment of hydrogen from proton exchange membrane water electrolysis in future energy systems," Applied Energy, vol. 237, pp. 862-872, 2019, doi:10.1016/j.apenergy.2019.01.001.

[18] Zhao, G., Schrøder Pedersen, A., "Life Cycle Assessment of Hydrogen Production and Consumption in an Isolated Territory," Procedia CIRP, vol. 69, pp. 529-533, 2018, doi:10.1016/j.procir.2017.11.100.

[19] FCH JU, "Life Cycle Assessment of Hydrogen and Fuel Cell Technologies," JRC Technical Report, 2020.

[20] JEC, "Well-To-Wheels report v5," JRC Science for Policy Report, 2020.

8. Glossary

BAT: Battery
BEV: Battery Electric Vehicle
CAPEX: CAPital Expenditure
Crr: rolling resistance coefficient
D: Diesel
EM: Electric Motor
FC: Fuel Cell
FCEV: Fuel Cell Electric Vehicle
FCS: Fuel Cell System
GHG: GreenHouse Gases
ICE: Internal Combustion Engine
ICEV: Internal Combustion Engine Vehicle
LCA: Life Cycle Assessment
OPEX: OPerational Expenditure
SCx: frontal area multiplied by aerodynamic drag coefficient
SOC: State Of Charge
SMR: Steam Methane Reforming
TCO: Total Cost of Ownership
VECTO: Vehicle Energy Consumption Calculation Tool
WtT: Well-to-Tank

Comparison Between Different Hydrogen Fuelled Powertrains for Urban Busses

F. Millo[1], L. Rolando[1], A. Piano[1], A. Vinogradov[1], Benedetta Peiretti Paradisi[1]

1: Politecnico di Torino, C.so Duca degli Abruzzi 24, 10129 Turin (ITALY)

Abstract: In the compelling need for the decarbonization of the transport sector, hydrogen could play a crucial role, especially in heavy duty applications where the limited specific energy of chemical batteries can significantly reduce either the payload or the operative range. Moreover, the possibility to use Hydrogen not only within Fuel Cells (FCs) systems but also as a fuel in Internal Combustion Engines (ICEs) makes it even more attractive for future sustainable transport systems. In such a framework, this work aims to compare, through numerical simulation, different hydrogen powertrain configurations designed for an urban bus application. In particular, a series hybrid architecture was chosen as a reference considering three different technologies for its Auxiliary Power Unit: two internal combustion engines fuelled with Diesel and Hydrogen respectively, and a Fuel Cell featuring almost the same power level of the internal combustion engines. The study was carried out in real world driving condition and it showed the benefits of both hydrogen powertrains on the vehicle fuel economy. Finally, in order to provide a more comprehensive overview, an analysis of the Total Cost of Ownership (TCO) was performed demonstrating that the H2-engine could achieve a significant improvement of the powertrain efficiency with investments and operating costs closer to the Diesel configuration.

Keywords: Hydrogen fuelled powertrains; Total Cost of Ownership; Urban bus

1. Introduction

Nowadays the decarbonization of the human activities represents one of the most important topics in the agenda of the European Commission in order to limit the climate changes related to the Green-House-Gas (GHG) effect [1]. Among the other, the transportation sector is particularly under the microscope of the governments since it is currently responsible for about 25% of the total CO_2 emissions and it has shown a constantly increasing trend in the past 25 years [2]. In such a framework, the powertrain electrification may represent one of the most promising solutions not only to decarbonize the transportation sector, but also to improve the air quality in highly congested urban areas. However, it may not be suitable for heavy duty applications whose range requirements may be quite challenging for current state-of-the art electrochemical batteries. As an alternative, new policies, such as the European Green Deal, should also promote the development and the production of sustainable alternative fuels capable to achieve a zero impact in their entire life cycle [3]. Among them, hydrogen has recently become a highly attractive solution, since it could be produced from renewable energy sources [4] and it can be used in both Fuel Cell (FC) Systems and Internal Combustion Engines (ICEs).

Moreover, beside the environmental aspects, from the customer perspective, the next powertrain generation should be comparable in terms of costs with conventional propulsion systems without relying on public subsidies. From this perspective, Battery Electric Vehicles (BEVs) may benefit of low operational costs thanks to their high conversion efficiency and to their low maintenance costs [5]. On the contrary, despite a strong reduction was observed in the last years [6], the still high cost of Li-Ion Batteries may result in a significantly higher initial investment in comparison with other propulsion systems.

In such a framework powertrain hybridization may represent a valuable alternative to limit the cost of the Energy Storage System (ESS), since the presence of an additional power unit allows reducing the size of the battery for the same vehicle range. Moreover, the integration of either a Fuel Cell (FC) or of a H_2-ICE avoids the local production of any GHG emission. Unfortunately, the economical convenience of hydrogen powertrain strongly depends on the fuel cost, which significantly changes according to the production technology, and it is currently significantly higher than Diesel and Gasoline [7].

Focusing on FC technology, the limited production volumes as well as the need of precious materials for some of its components may still result in a quite high capital investment, especially in a short time scenario [8]. Furthermore, the high FC efficiency may be affected by several operating parameters, such as sudden load changes, or frequent switch on/off

events, which can increase the hydrogen consumption.

On the other hand the use of H_2 in ICEs could represent a valuable solution thanks to the limited number of hardware changes required to run an engine with such a fuel and to the availability of well-establish production processes [9,10]. The main drawbacks of a hydrogen engine may be represented by its relatively low energy conversion efficiency compared to FC, corresponding to a higher fuel expenditure, and to the possible generation of criteria pollutant emissions (such as Nitrogen Oxides) which may require tailored aftertreatment devices [11].

In such a framework, the definition of the optimal powertrain solution cannot be unique, but it strongly depends on the specific application [12]. Public transportation is one of the sectors with the higher penetration of Battery & FC propulsion systems, thanks to the peculiarities of its mission profiles (e.g. charging/fuelling infrastructure availability, well-known route) and to the public funding programs which may result in a short-time economic sustainability [13,14]. Recently, a comprehensive analysis of different powertrain solutions for urban busses has shown that electrified powertrains are the most suitable option for the 12m urban bus class [15].

Therefore, the present paper aims to perform, through numerical simulations, a comparison among 5 different propulsion systems suitable for a 12m urban bus. The study will not only consider the vehicle energy consumption of each configuration in real world driving conditions, but it will also analyse its Total Cost of Ownership (TCO). The analysis will cover a wide range of powertrain solutions, ranging from a conventional Diesel ICE, taken as a reference, to a full electric configuration. The intermediate electrification levels feature a series hybrid architecture, in which different technologies for the Auxiliary Power Unit (APU) will be considered. In particular, the benefits of both a Fuel Cell and H_2-ICE will be assessed with respect to a downsized version of the reference Diesel Engine.

The paper will be organized as follows: in Section 2 the case study will be presented with a short overview on the features of the vehicle and of the mission profiles. Afterwards, Section 3 will focus on the methodologies used to create the virtual test rig of the vehicle and to perform the TCO study. Then, in Section 4, the main findings of the study will be presented. First, the energy consumption of each powertrain configuration over different driving cycles will be assessed (Section 4.1). Afterwards, the results of the TCO will be discussed (Section 4.2). Finally, the main conclusions and findings of the research activities will be presented.

2. Case study

In the present paper, a 12m urban bus, the main specification of which are reported in Table 1, was considered as a test case.

Table 1: Main Specifications of the Tested Vehicle

Mass	12 tons
Road Load @ 50 km/h	16 kW
Road Load @ 80 km/h	43 kW
Road Load @ 100 km/h	74 kW

Concerning the powertrain, the configurations listed in Table 2 were taken into account.

Table 2: Powertrain Configurations

Conf. ID	Architecture	APU
1	Conventional	-
2	Series Hybrid	Diesel ICE
3		H2 ICE
4		Fuel Cell
5	Pure Electric	-

The first powertrain configuration, which was taken as a reference for this analysis, is a conventional powertrain equipped with a Heavy-Duty Diesel Engine. Moving to the hybrid configurations, they all feature a series architecture where the main power actuator is a Permanent Magnet Electric Motor capable to deliver a maximum power of 200 [kW], and the reversible EES is a Li-Ion Battery with a total installed energy of about 20 [kWh], whose cell specifications are reported in Table 3

Table 3: Battery Cell Features

Technology	LiFePO	-
Nominal Capacity	33	Ah
Specific Energy	120	Wh/kg
Nominal Voltage	3,6	V
Max Current	500	A
Arrangement	85s2p	-

Focusing on the APU, the reference engine was downsized to a rated power of about 100 kW. As far as the H_2 ICE is concerned, a power unit obtained by modifying the Diesel engine has been considered, choosing the solution that minimizes the cost and the level of complexity [16,17]. It features a PFI (Port Fuel Injection) system, coupled with the original diesel combustion chamber design, featuring a centrally mounted spark plug, replacing the original diesel injector. More details on the whole combustion and fuel injection systems are given in [18].

For the Fuel Cell Electric Vehicle (FCEV) the same power level of both H_2 and Diesel engines has been considered, rescaling a real FC system to obtain a power of about 100 kW. A DC/DC converter was also

integrated to couple the FC with the high voltage board net of the electrified powertrain. The energy consumption of the FC ancillaries (such as the air compressor and the humidifier) were also included in the study in order to achieve the correct Balance of Plant (BOP).

Finally, the pure electric bus uses the same EM of the hybrid powertrains, while the battery was scaled up to achieve the same daily range of the other configurations (about 250 km).

The simulations were carried out on 3 different mission profiles, representative of a typical urban bus operation. Their specifications are listed in Table 4.

Table 4: Main Features of the considered mission profiles.

	Braunschweig	*Gillingham*	*MLTB*
Duration [s]	1740	2875	2281
Distance [km]	10.9	16.6	9.0
Avg. Speed [km/h]	22.5	20.8	14.2
Max Speed [km/h]	58.2	59.9	48.7
Avg. Acc. [m/s^2]	0.2	0.2	0.2
Max Acc. [m/s^2]	2.4	2.3	1.5
Stop Phases [%]	22.4	21.7	26.7
Constant Speed Driving [%]	16.1	12.2	6.4
Acceleration [%]	35.3	33.5	39.2
Deceleration [%]	26.2	32.5	27.7
Spec. Energy Demand [kWh/km]	0.90	1.05	0.94

The Braunschweig is an urban driving cycle, frequently employed in various research projects or equipment certification programs [19]. The MLTB cycle was developed by UK transport authorities in 1996 to verify the compliance of new vehicles with emissions and fuel economy standards [20]. Finally, the Gillingham Uphill, obtained from GPS acquisitions, features high elevation changes, to test also challenging driving conditions [16].

3. Methodology

The virtual test rig of the bus was developed in the GT-Suite environment [21] applying a “quasi-static” approach [22]. The models of the ICEs and of the EM relies on performance maps, experimentally measured under steady-state conditions, or computed from 1D-3D/CFD simulations depending on the considered configuration, while the battery dynamics were reproduced through a Thevenin’s equivalent circuit.

Focusing on the H_2-ICE model, the engine operating maps for the selected combustion system configuration were obtained by means of a synergetic 0/1/3D-CFD approach previously developed by the authors [18]. At first a 3D-CFD numerical setup, based on a detailed chemistry scheme for both hydrogen combustion and NOx emission predictions, was implemented to obtain the reference results for calibrating a predictive combustion model in 1D-CFD environment. Afterwards, the latter simulation platform was used to optimize the main engine operating parameters (such as air/fuel ratio, boost level and spark timing) to maximize its thermal efficiency, achieving a peak of about 41%, while ensuring, at the same time, NOx emission below the current EU6 limit for HD applications. Figure 1 presents the engine efficiency map for the considered combustion system.

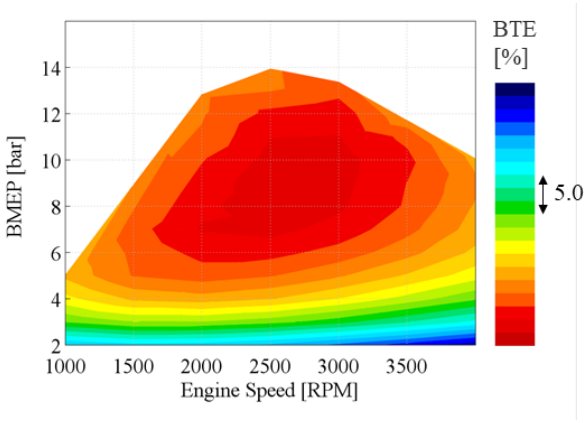


Figure 1: Normalized efficiency map of the H_2-ICE integrated in the APU.

For the Fuel Cell, a 1D CFD model was created and calibrated against a set of steady-state experimental data to properly reproduce the sensitivity of the FC polarization curve to the main operating parameters of the plant. Figure 2 proves the robustness of the developed models showing a more than satisfactory agreement between the simulation results (blue line) and the measurements (black line) in an operating condition not considered during the calibration process.

Finally, all the ancillaries needed to guarantee the FC operation were integrated in the model, considering both the air and the hydrogen supply systems. A compressor was needed to overcome the pressure losses inside the system on the air side and to ensure the correct excess of air at the anode.

Furthermore, a humidifier was needed too, to control the water content and the humidification, avoiding the degradation of the membrane. A recirculation pump was then integrated for the hydrogen, to mix the

humid hydrogen exiting the cathode with the dry one coming from the tank storage and feed the FC anode.

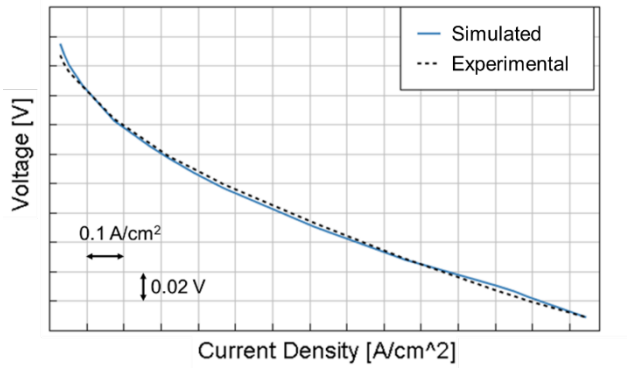


Figure 2: Comparison between the simulated polarization curve and the experimental measurements.

All the hybrid architectures require the definition of a suitable Energy Management System (EMS) [23] capable to split for each instant of time the driver power request among the available actuators. Since the optimization of the EMS is out of the scope of this study, for series hybrid configurations the same rule-based control strategy already designed in [16,24] was selected. Such a powertrain controller can achieve the charge sustaining operations by adjusting the power output of the APU according to the actual status of the vehicle and aims at minimizing the energy consumption of the vehicle keeping the operating conditions of the APU within its highest efficiency region.

3.2 Fuel Cell Efficiency Degradation

Differently from the ICE whose performance do not show any significant degradations with respect to lifetime, several studies [25,26] showed that, for a Fuel Cell, the higher the number of operating hours, the lower the system efficiency. Therefore, such a behaviour may significantly reduce the gap between the energy consumption of FCs and ICEs, and it should be included in the TCO analyses especially in the case of heavy-duty applications which typically features a long operating life.

The degradation of the Fuel Cell performance can be observed in steady state conditions, but it is more relevant in highly dynamic conditions such as for automotive applications, where load changes, Start & Stop (S&S) cycles, and cold starts events are quite frequent.

Since experimental data in aged conditions were not available in this study, a simplified approach for the lifetime prediction of the FC performance is proposed. It relies on the methodology already presented in [26] whose mathematical formulation was modified in order to include the effects of higher load operations on the degradation phenomena observed in [27].

$$\Delta V = \sum_{i}^{ChLvs} \Delta V_{ss,i} \cdot t + \Delta V_{LC} \cdot n_1 + \Delta V_{st} \cdot n_2 \qquad \text{Eq. 1}$$

In Eq. 1 a correction coefficient on the Fuel Cell Voltage ΔV is proposed to model the impact of:

- **Load Levels:** $\boldsymbol{\Delta V_{ss,i} \cdot t}$, where $\Delta V_{ss,i}$ is the voltage decay for each power level [V/h], and t is the corresponding resident time [h];
- **Load Changes:** $\boldsymbol{\Delta V_{LC} \cdot n_1}$, where ΔV_{LC} is the voltage decay for each load change [V] and n_1 is the corresponding load change frequency [1/h];
- **Switching Cycles:** $\boldsymbol{\Delta V_{st} \cdot n_2}$, where ΔV_{st} is the voltage decay per on/off switching cycle [V] and n_2 is the corresponding event frequency [1/h].

The proposed methodology leads to the degradation factors reported in Table 5 for the mission profiles analysed in this study.

Table 5: Degradation Factors on the considered driving cycles

Driving Cycle	*Degradation Factor [µV/h]*
Braunschweig	23.1
Gillingham	21.5
MLTB	13.6

These results are in good agreement with the values already presented in [26] for a similar PEMFC system. Moreover, the MLTB shows significantly lower penalties since the FC is working for long periods at low loads and with few load changes during the cycle.

The degradation factor allows calculating the actual efficiency of the Fuel Cell (see Eq. 2) which can be considered proportional to the voltage as follows:

$$\eta_{FC} = \frac{V_{cell} - \Delta V}{V_{th}} \qquad \text{Eq. 2}$$

where:

- η_{FC} is the actual Fuel Cell efficiency;
- V_{cell} is the nominal FC voltage;
- ΔV is the degradation factor;
- V_{th} is theoretical FC voltage.

The V_{th} is almost constant, since it only shows a light dependence on both operating temperature and pressure. Given a certain voltage decay and an expected lifetime of the system, the new efficiency can then be easily calculated.

Finally, the Fuel Cell system efficiency can be estimated through Eq. 3:

$$\eta_{FCS} = \eta_{FC} \cdot \eta_{aux} \cdot \eta_{DC/DC} \qquad \text{Eq. 3}$$

where $\eta_{DC/DC}$ is the efficiency of the DC/DC converter and η_{aux} the ratio between the power of the auxiliaries

and the FC output power. This ratio is assumed to increase over time during the lifetime of the Fuel Cell: as a matter of fact, for a constant power request, the degradation of the FC voltage requires an increase of the current, which results in a higher mass flow rate for both hydrogen and oxygen. A constant rate of 0.5% for 1000 [h] was empirically assumed in this study.

With this simplified approach, the degradation of the Fuel Cell performance leads to an efficiency decrease of about 15% and 25% at 200'000 km and 350'000 km respectively, as shown in Figure 3.

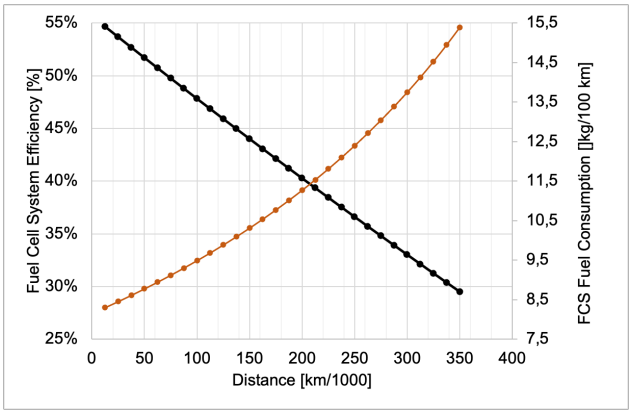


Figure 3: Reduction of the FC efficiency and increase of fuel consumption as a function of the travelled distance.

Finally, based on the actual system efficiency η_{FCS}, the actual hydrogen consumption $H_{2,FC}$ was calculated through Eq. 4 as a function of the nominal hydrogen consumption $H_{2,FC,0}$ and of the nominal system efficiency $\eta_{FCS,0}$.

$$H_{2,FC} = \frac{H_{2,FC,0}\eta_{FCS,0}}{\eta_{FCS}} \qquad \text{Eq. 4}$$

3.3 Total Cost of Ownership (TCO)

Before analyzing all the contributions included in the TCO, it is worth mentioning the main assumptions of the study.

Foremost, based on data reported in literature [16], an expected travelled distance of about 700'000 km was considered for the 12m bus. Such a distance was reached through repetitions of the considered elementary driving cycles. Moreover, when the target distance is reached, the residual value of the vehicle is assumed to be zero.

From the time-perspective, a horizon of about 10 years was chosen, considering cost forecasts for year 2030.

Moving toward the cost assessment, two main contributions can be identified. The former, which includes the investments for the glider, for the powertrain and for the storage, is the CAPital EXpenditure (CAPEX). The latter is the OPerational EXpenditures (OPEX) which accounts for fuel, repair, and maintenance costs.

CAPEX

The vehicle glider is shared among the proposed architecture and its cost was derived from a previous work of the authors [16], which also provide values for the Internal Combustion Engine. An additional penalty was also introduced for the Hydrogen conversion [28].

On the contrary, for the electric drive, values derived from an extensive literature review were assumed [6].

Similar approaches were used for the hydrogen pressurized tank, for which several studies set a cost ranging between 500-700 [€/kg] [8,28] and for the chemical battery. As already mentioned in the paper introduction, for this subsystem a significantly cost reduction was observed in the last years [6] and, according to literature [29], a value of about 100 [€/kWh] seems to be reasonable for 2030. Furthermore, a swap of the battery pack can be expected after about 1800 operating cycles [8]. Indeed, an urban bas may represent a quite demanding application for Li-Ion batteries because of the high number of depth discharge cycles which can shorten the battery life.

Finally, the cost of the Fuel Cell seems to be one of the most critical to estimate since, depending on the future market penetration, it could oscillate in a very wide range [7]. Thus, similarly to, a base scenario featuring a niche market penetration was considered, assuming a production of 2500 units per OEM per year. In addition, the significant degradation of the FC performance (see Figure 3) will force a swap of the stack at about 350'000 km when the efficiency drops below 30%. The assumptions regarding the powertrain are summarized in Table 6.

Table 6: Summary of the CAPEX costs assumed for the Reference scenario.

	Cost	*Reference*
Diesel ICE	30	[28]
H_2-ICE	40	-
Fuel Cell System [€/kW]	280	[8]
Electric Drives [€/kW]	8	[28]
Power Electronics [€/kW]	10	-
Battery [€/kWh]	100	[29]
700 bar Hydrogen Tank [€/kg]	500	[8] [28]

OPEX

Fuel Cost

A reliable forecast of the H_2 cost can also be quite difficult. Several sources indicate that in 2023 the prize of green hydrogen will range between 3-7 €/kg. A mean value of 5 €/kg was chosen for the reference scenario, but additional sensitivity analyses will be performed on this parameter.

For BEVs the recharging cost may significantly change depending on the evolution of the energy market [30], especially when fast charge is considered. Values between 0.15 and 0.6 €/kWh were observed in [30,31], but significant variations may occur thanks to either the higher share of renewable energy sources or to the increase of the demands. Therefore, for this parameter a value of 0.26 €/kWh was considered.

Finally, for the Diesel, the cost was set to about 1.6 €/l, because of the increase expected in the upcoming years.

A summary of the OPEX contributions is reported in Table 7.

Table 7: Summary of the OPEX Costs assumed for the Reference Scenario.

	Cost	*Reference*
H_2 Cost [€/kg]	5	[8]
Diesel Cost [€/L]	1.6	-
Electricity [€/kWh]	0.26	[8]

Repair and Maintenance

When considering Internal Combustion Engines, the maintenance cost was considered independent on powertrain architecture. The complexity of hybrid architecture may introduce additional contributions, but, at the same time, could reduce the wear of other components (e.g.: friction brakes).

4. Results and Discussion

4.1 Assessment of the Energy Consumption

The virtual test rig developed for the 12m bus was used to assess the energy consumption of each powertrain configuration on the selected mission profiles.

A preliminary analysis was performed among the hybrid architectures in order to prove their capability to achieve the charge sustaining conditions which is necessary to perform a fair comparison with the other powertrain configurations. The results collected on the Braunschweig driving cycle and reported in Figure 4 prove the capability of the powertrain control strategy to achieve the battery charge balance with all the different APU technologies.

Moving to the analysis of the energy consumption, Figure 5 shows the results collected for each powertrain configuration. As expected, the conventional Diesel Engine features the highest energy consumption for all the considered driving cycles (black bars), while the powertrain hybridization (green bars) introduces an improvement of about 8%, on average. Nevertheless, the benefit is significantly lower (about 4%) on the Ghillingam driving cycle, since the high load request allows even the conventional powertrain to keep the engine within its highest efficiency region without the need of exploiting the powertrain hybridization.

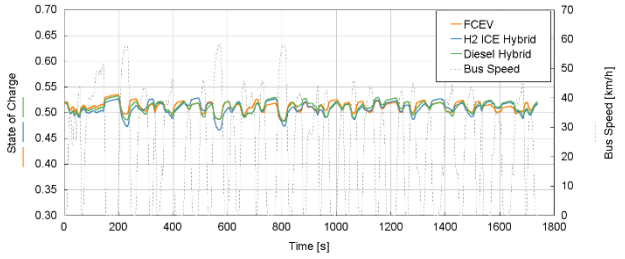


Figure 4: Comparison of the SOC trajectory of the hybrid powertrain configurations on the Braunschweig driving cycle.

The comparison between the Diesel (green bars) and the Hydrogen APUs (blue bars) highlighted that both engine technologies are able to achieve similar efficiency levels. The use of a Fuel Cell (orange bars), on the contrary, enables a huge step forward resulting in an average -30% of the energy consumption.

Nevertheless, from the Tank-to-Wheel (T2W) perspective, the best solution is a pure electric powertrain (yellow bars) which is able to achieve the minimum energy consumption in all the analysed driving scenarios.

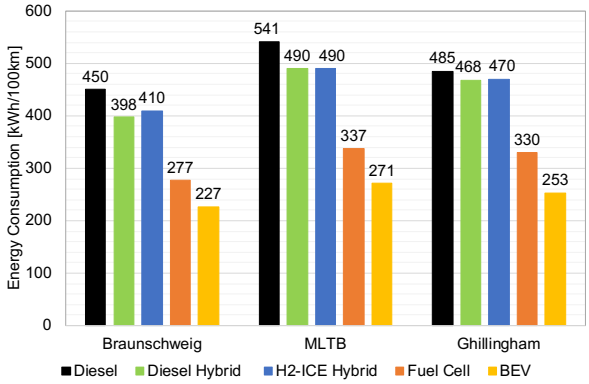


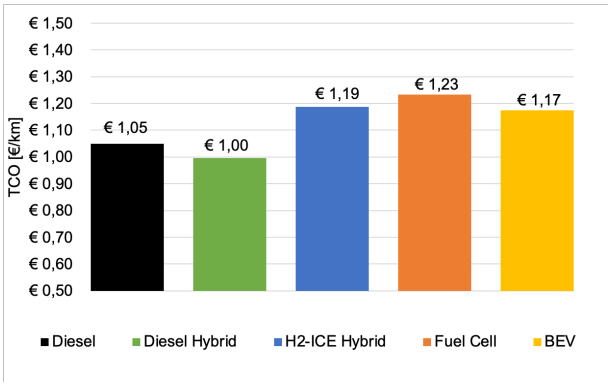
Figure 5: Comparison of the energy consumption of the proposed powertrain configurations on the considered driving cycles.

4.2 TCO Results

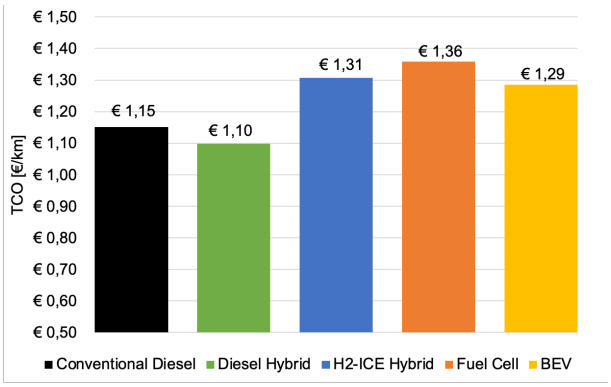
In the following section the TCO of the proposed powertrain architectures will be presented over the three driving cycles. The comparison will be performed with the reference cost scenario described in the previous section of the paper. Finally, two sensitivity analyses will be performed on the FC and on the hydrogen costs.

Base Scenario

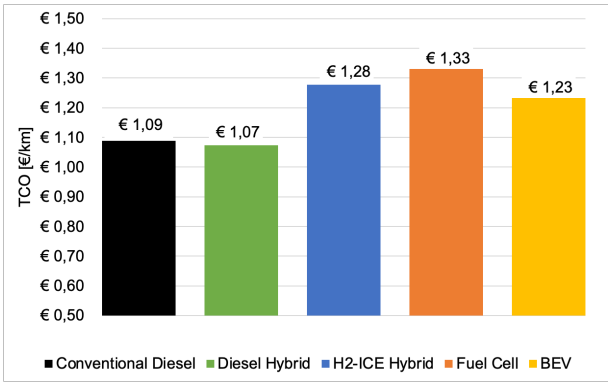
The analysis of Figure 6 where the TCO is reported for all the considered driving scenarios shows that the Diesel Hybrid Electric Vehicle (HEV) represents the most convenient solution, achieving a specific cost about 0.04 €/km lower, on average, than the reference conventional powertrain.



(a)



(b)



(c)

Figure 6: TCO of the proposed powertrain architectures over different driving cycles. (a): Braunscheweig - (b): MLTB - (c): Ghillingham.

The higher fuel economy and the lower cost of the downsized engine, indeed, allow overcompensating the investment for the powertrain hybridization which, in this case, is quite limited, thanks to the small battery size (about 20 kWh). Among the different tail-pipe carbon-free architectures, the BEV achieves the lower TCO thanks to its significantly higher efficiency and to its lower maintenance cost. The H_2-ICE, on the contrary, despite a competitive CAPEX, suffers of higher fuel consumption and higher fuel cost. Finally, as far as the Fuel Cell system is concerned, Figure 6 highlights a further increase of the TCO caused by the higher investment for the APU.

These trends seem to be quite homogeneous among the driving cycles, as demonstrated by the comparison of Figure 6.a,b and c.

Sensitivity Analyses

In Section 3.3 both the Fuel Cell and the Hydrogen costs were identified as one of the most difficult parameters to forecast since they can be affected by many factors such as market penetration or production technology. Therefore, two sensitivity analyses were performed on these parameters in order to assess their impact on the TCO of the proposed powertrain architectures. This study was performed on the Braunschweig driving cycle.

Fuel Cell Cost

Similarly to other new technologies, the cost of a Fuel Cell can be strongly influenced by market penetration as demonstrated by Roland Berger [8] which forecasted a huge variability of the system cost moving from niche to mass market applications (see Table 8)

Table 8: Evolution of the Fuel Cell Cost depending on the market penetration [8]

	€/kW
Niche (Base Scenario 2500 p. OEM)	280
Rather Niche (5000 p. OEM)	155
Rather Mass (25000 p. OEM)	100
Mass Market (75000 p. OEM)	55

Figure 7, where the results of the sensitivity analyses are reported, shows that a huge drop in TCO could be achieved with a *rather niche* market penetration, since the system cost would be half of the value predicted for the reference (*niche*) scenario. This almost completely closes the gap with respect to H_2-ICE, while a further increase to *rather mass production* would allow reaching the TCO of the Battery Electric Vehicle.

The achievement of the mass production, on the contrary, would not produce a significant benefit on the TCO since the hydrogen cost would become the dominant parameter.

To limit the impact of the fuel, it is much more important to limit the degradation of the Fuel Cell performance, which strongly affects the energy consumption over the whole vehicle lifetime.

According to the degradation model used, besides the improvements of both the membrane and catalyst technologies, a powertrain control strategy capable to include the degradation phenomena could significantly reduce the FC fuel economy.

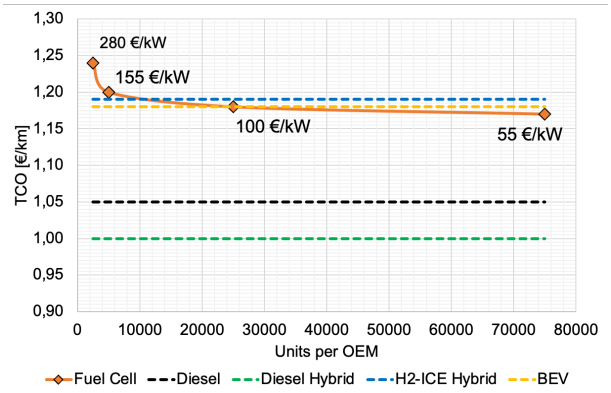


Figure 7: TCO sensitivity analysis on the Fuel Cell cost.

Hydrogen Price Sensitivity

The World Energy Council predicts that, starting from the actual average value of 5 €/kg, the hydrogen price may drop down to 3 €/kg in the upcoming years. From the TCO perspective such a reduction could be very beneficial, allowing the hydrogen powertrains to achieve the cost levels of the Diesel ones. Moreover, if a rather-niche market penetration is considered (see Figure8.b), with a hydrogen price of 3 €/kg the Fuel Cell becomes economically convenient with respect to H_2-ICE

Nevertheless, such a low fuel price would require a very low cost of the electricity, whose achievement could be quite difficult, even with a strong exploitation of renewable energy sources. As an example, considering an efficiency of 80% for the electrolysis process, the electricity cost should be lower than 0.07 €/kg, even if the costs of the electrolyzer, of the water and of the compression power is neglected.

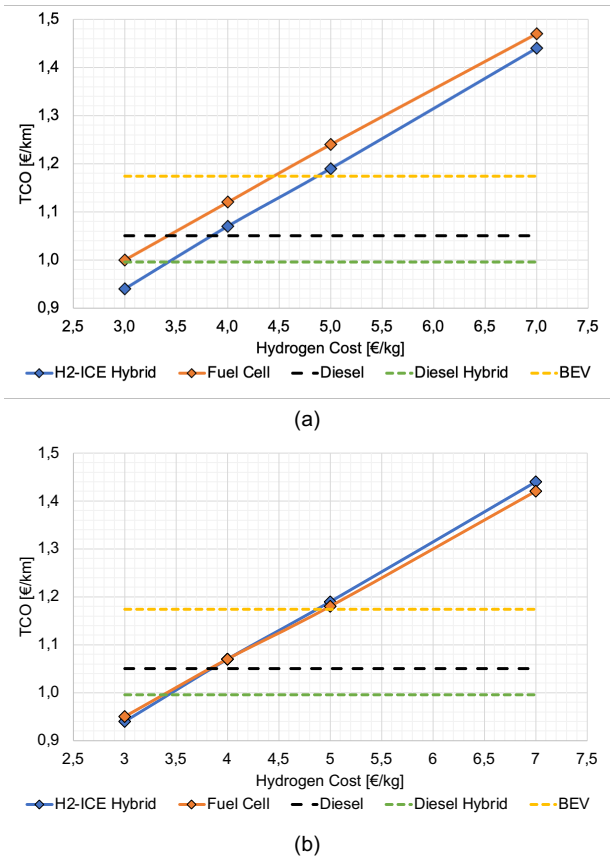


Figure 8: TCO sensitivity analysis on the hydrogen cost. (a): Fuel Cell Cost: 280 [€/kW] – (b): Fuel Cell Cost: 100 [€/kW]

5. Conclusions

In the present paper a comparison among different powertrain solutions for a 12m urban bus was performed. The study analyzed, through numerical simulations, both the energy consumption and the Total Cost of Ownership of each architecture in different driving scenarios. A virtual test rig for each powertrain configuration was developed and a simplified methodology for the degradation of the fuel cell performance was introduced to consider the H_2 consumption penalty during the lifetime. Finally, two sensitivity analyses on the cost of the Fuel Cell system and on the hydrogen prize cost were performed, since they represent the most difficult parameters to be forecasted.

The numerical simulations highlighted the minimum energy consumption for the BEV but the minimum TCO for the Diesel HEV thanks to the lower fuel cost. As a matter of fact, the H_2 could achieve almost the same efficiency, but with a significantly more expensive fuel. Among the hydrogen solutions, the Fuel Cell achieved the best energy consumption, thanks to its higher efficiency, but not the lowest TCO which was obtained with the H_2-ICE. The FC system would require a cost of 155-100 €/kW to be competitive with the H_2-ICE and BEV, respectively.

Hydrogen as fuel could be economically competitive if its price could reach a value of about 3.5 €/kg, which would require very low electricity price and a huge exploitation of renewable energy sources.

5. Acknowledgement

This research activity was financially supported by the Italian Minister of the University and Research (MUR), through the PRIN 2020 CALL, *H2ICE: development of a hydrogen fueled hybrid powertrain for urban buses* project.

7. References

1. European Commission, “The European Green Deal,” Brussels, 2019.

2. Korn, T., “The Most Efficient Way for CO2 Reduction: the New Generation of Hydrogen Internal Combustion Engines,” *41st International Vienna Motor Symposium*, 2020.

3. Dilara, P., “The future of clean cars in Europe: EU Green Deal and EURO 7,” *4th Sino-EU workshop on New Emissions Standards and Regulations for Motor Vehicles*, 2021.

4. European Commission, “European Clean Hydrogen Alliance,” 2020.

5. Burnham, A., Gohlke, D., Rush, L., Stephens, T., Zhou, Y., Delucchi, M.A., Birky, A., Hunter, C., Lin, Z., Ou, S., Xie, F., Proctor, C., Wiryadinata, S., Liu, N., and Boloor, M., “Comprehensive Total Cost of Ownership Quantification for Vehicles with Different Size Classes and Powertrains,” 107–115, 2021.

6. International Energy Agency, “Energy Technology Perspectives - Special Report on Clean Energy Innovation,” 2000.

7. World Energy Council, “Hydrogen Demand And Cost Dynamics,” *Work. Pap.* 13, 2021.

8. Ruf, Y., Baum, M., Zorn, T., Menzel, A., and Rehberger, J., “Fuel Cells Hydrogen Trucks - Roland Berger,” 2020.

9. White, C.M., Steeper, R.R., and Lutz, A.E., “The hydrogen-fueled internal combustion engine: a technical review,” *Int. J. Hydrogen Energy* 31(10):1292–1305, 2006, doi:10.1016/j.ijhydene.2005.12.001.

10. Stępień, Z., “A comprehensive overview of hydrogen-fueled internal combustion engines: Achievements and future challenges,” *Energies* 14(20), 2021, doi:10.3390/en14206504.

11. Desantes, J.M., Molina, S., Novella, R., and Lopez-Juarez, M., “Comparative global warming impact and NOX emissions of conventional and hydrogen automotive propulsion systems,” *Energy Convers. Manag.* 221(X):113137, 2020, doi:10.1016/j.enconman.2020.113137.

12. Sens, M., Danzer, D., Essen, C., Brauer, M. Von, Wascheck, R., Seebode, J., and Kratzsch, M., “Hydrogen Powertrains in Competition to Fossil Fuel Based Internal Combustion Engines and Battery Electric Powertrains,” *42 International Vienna Motor Symposium*, Wiem, 2021.

13. Lozanovski, A., Whitehouse, N., Ko, N., and Whitehouse, S., “Sustainability assessment of fuel cell buses in public transport,” *Sustain.* 10(5), 2018, doi:10.3390/su10051480.

14. Quarles, N., Kockelman, K.M., and Mohamed, M., “Costs and benefits of electrifying and automating bus transit fleets,” *Sustain.* 12(10), 2020, doi:10.3390/SU12103977.

15. Depré C. and Guida U., “ZeEUS eBus Report #2 - An Updated Overview of Electric Buses in Europe,” Brussels, 2017.

16. Golisano R., Scalabrini S., Arpaia, A., Pesce, F.C., Vassallo, A., Borgia, L.., Cubito, C., Biasin, V., Kniche, T., Millo, F., Piano, A., and Rolando, L., “PUNCH Hydrogen Internal Combustion Engine & KERS: an Appealing Value-Proposition for Green Power Pack,” *42 International Vienna Motor Symposium*, Wien, 2021.

17. Vassallo, A., Pesce, F., Arpaia, A., Millo, F., Rolando, L., Piano, A., and Bianco, A., “Ultra-lean Combustion System Optimization for H 2-fuelled ICEs via Synergistic Application of 1D-and 3D-CFD,” in: Société des Ingénieurs de l’Automobile, ed., *SIA Powertrain & Power Electronics*, Rouen: 1–9, 2021.

18. Millo, F., Piano, A., Rolando, L., Accurso, F., Gullino, F., Roggio, S., Bianco, A., Pesce, F., Vassallo, A., and Rossi, R., “Synergetic Application of Zero-, One-, and Three-Dimensional Computational Fluid Dynamics Approaches for Hydrogen-Fuelled Spark Ignition Engine Simulation,” *SAE Int. J. Engines* 15(4):3–15, 2021, doi:10.4271/03-15-04-0030.

19. Kivekäs, K., Lajunen, A., Vepsäläinen, J., and Tammi, K., “City bus powertrain comparison: Driving cycle variation and passenger load sensitivity analysis,” *Energies* 11(7), 2018, doi:10.3390/en11071755.

20. Leach, F.C.P., Peckham, M.S., and Hammond, M.J., “Identifying NOx hotspots in transient urban driving of two diesel buses and a diesel car,” *Atmosphere (Basel).* 11(4), 2020, doi:10.3390/atmos11040355.

21. Gamma Technologies, GT SUITE User Manual, 2020.

22. Millo, F., Rolando, L., Fuso, R., and Zhao, J., “Development of a new hybrid bus for urban public transportation,” *Appl. Energy* 157:583–594, 2015, doi:10.1016/j.apenergy.2015.03.131.

23. Onori S., Serrao L., and Rizzoni G., “Hybrid Electric Vehicles Energy Management Strategies,” 1st ed., Springer, ISBN 978-1-4471-6781-5, 2016, doi:10.1007/978-1-4471-6781-5.

24. Millo, F., Rolando, L., Piano, A., Peiretti Paradisi, B., and Vinogradov, A., “Hydrogen Powertrains: A Comparison Between Different Solutions for an Urban Bus,” *22. Internationales Stuttgarter Symposium.* , Springer Vieweg, Wiesbaden, ISBN 978-3-658-37009-1: 259–271, 2022, doi:10.1007/978-3-658-37009-1_18.

25. Wu, J., Yuan, X.Z., Martin, J.J., Wang, H., Zhang, J., Shen, J., Wu, S., and Merida, W., “A review of PEM fuel cell durability: Degradation mechanisms and mitigation strategies,” *J. Power Sources* 184(1):104–119, 2008, doi:10.1016/j.jpowsour.2008.06.006.

26. Chen, H., Pei, P., and Song, M., “Lifetime prediction and the economic lifetime of proton exchange membrane fuel cells,” *Appl. Energy* 142:154–163, 2015, doi:10.1016/j.apenergy.2014.12.062.

27. Cleghorn, S.J.C., Mayfield, D.K., Moore, D.A., Moore, J.C., Rusch, G., Sherman, T.W., Sisofo, N.T., and Beuscher, U., “A polymer electrolyte fuel cell life test: 3 years of continuous operation,” *J. Power Sources* 158(1):446–454, 2006, doi:10.1016/j.jpowsour.2005.09.062.

28. Handwerker, M., Wellnitz, J., and Marzbani, H., “Comparison of Hydrogen Powertrains with the Battery Powered Electric Vehicle and Investigation of Small-Scale Local Hydrogen Production Using Renewable Energy,” *Hydrogen* 2(1):76–100, 2021, doi:10.3390/hydrogen2010005.

29. Bloomberg, “Battery Pack Prices Fall to an Average of $132/kWh, But Rising Commodity Prices Start to Bite,” https://about.bnef.com/blog/battery-pack-prices-fall-to-an-average-of-132-kwh-but-rising-commodity-prices-start-to-bite/, 2021.

30. Schlaak T., Franke H., and Brod K., “Power Market Study 2030 A new outlook for the energy industry,” Hamburd, 2018.

31. European Commission, “EU energy trends to 2030 : update 2009,” Publ. Office of the European Union, ISBN 9789279161919, 2010, doi:10.2833/21664.

8. Glossary

APU	Auxiliary Power Unit
BEV	Battery Electric Vehicle
BOP	Balance Of Plant
BSFC	Brake Specific Fuel Consumption
CAPEX	Capital Expenditure
CFD	Computational Fluid Dynamic
DC	Direct Current
EM	Electric Motor
ESS	Energy Storage System
FC	Fuel Cell
GHG	Green House Gases
HEV	Hybrid Electric Vehicle
ICE	Internal Combustion Engine
NOx	Nitrogen Oxides
OPEX	Operational Expenditure
PEMFC	Proton Exchange Membrane Fuel Cell
PFI	Port Fuel Injection
SOC	State Of Charge
T2W	Tank to Wheel
TCO	Total Cost of Ownership
WOT	Wide Open Throttle

Evaluation of the impact of different Active Thermal Management System layouts on medium/heavy duty FCEVs performance

A. Almondo[1], M. Bilancia[1], M. Pini[2]

1: Punch Hydrocells, Corso Castelfidardo 36, Torino, Italy
2: Punch Torino, Corso Castelfidardo 36, Torino, Italy

Abstract: H2 FCEVs are considered a potential enabler for the future decarbonization of the transportation sector, in particular in the medium and heavy-duty sectors. In present days FCEV technology is still characterized by a quite high cost of both hardware systems and of the H2 fuel. Active Thermal Management systems (ATM) in FCEVs must be considered as one of the main actors that can contribute to the improvement in the fuel efficiency that participates to the reduction of the pay-back period of the FCEVs. This aspect is much more important when complex thermal architectures must be considered for medium and heavy-duty vehicles such as Busses, Trains, and Refrigerated Trucks, in which a great role is played by the thermal requirements of the HVAC system.

Purpose of this paper is to show how an Active Thermal Management strategy can be implemented in order not only to reach the goal of an optimal thermal conditioning of all the components of a fuel cell propulsion system, but also to properly manage the heat flows among different circuits to achieve the target of a higher energy efficiency of the vehicle. The study is based on a detailed thermal model of the system (plant model) used to analyse which can be the best solutions for an overall optimal efficiency of the FCEV.

As a result of this work, a quite considerable H2 consumption reduction (in the range of 9%) is calculated using a dedicated plant model simulating a 12m urban bus application.

Keywords: Active Thermal Management, Fuel Cell, Simulation, Consumption reduction

1. Introduction

The more and more evident effects of climate changes in the last years, caused by greenhouse gases emissions, underline the need to progressively move away from the usage of fossil fuels.
European Union has set the goal of carbon neutrality by 2050, that for the mobility sector implies a strong shift towards electrification, that means hybrids, as a solution for transition, and electric vehicles (BEV).

Compared to the traditional internal combustion engine technology (ICE), BEVs have some drawbacks, mainly related to long recharging time and higher weight, due to lower energy density of batteries compared with fuel tanks.

For heavy duty vehicles, whose mission profile requires higher amounts of energy (e.g., goods transport or long-haul buses) the battery solutions present some challenges related to the low energy storage density, leading to increase in vehicle weight and reduction of the available payload.

For this reason, in the last years an increasing attention is growing for hydrogen propelled vehicles due to the advantages provided in comparison with BEVs and ICEs. Hydrogen vehicles in fact have zero CO2 emissions and hydrogen as a fuel presents a high gravimetric energy density, giving an interesting solution for applications requiring a high energy storage, such as heavy-duty applications like buses and trucks. This is valid also considering the extra weight given by the storage tanks used for carrying the pressurized hydrogen.

Hydrogen propulsion systems (PS) can be based on a hydrogen fuelled ICE or on a fuel cell module combined with one or more electric motors. Fuel cells present some advantages compared to ICEs, given by higher efficiency and absence of pollutants emissions. On the other side, fuel cell power module to reach their life goals need to be managed with lower load gradients during transients.

To overcome this problem, a high voltage (HV) battery (or other devices such as supercapacitors) is also included in the PS, this allows both to recover braking energy from the electric motor and to respond quickly to load variations. Power electronic components such as DC/DC converters, DC/AC inverters and power distribution units need also to be included in the propulsion system, in order to allow proper energy conversions.

The different components (fuel cell, high voltage battery, electric motors, and power electronics) have their optimal operative condition at different working temperatures, so that the baseline FCEV cooling system is composed of three independent circuits: high temperature (HT), mid (MT) and low temperature (LT). Moreover, in general the cabin compartment HVAC system is an additional independent component, powered by the HV circuit. This baseline cooling circuits layout is aimed to guarantee to not exceed the working temperatures of the different components and to permit fast and independent warm-up of the FC and of the HV battery.

In the solution implementing independent circuits, the thermal energy, that has to be dissipated by one sub-system of the PS, is wasted because this layout

does not allow heat flows between different heat sources and heat sinks. For this reason, this is not an optimal choice from the energetic perspective.

Several papers, e.g. [1] [3] [5] [7], define how an optimal Thermal Management may be used to guarantee ideal working conditions of the different components of a FCEV architecture. In [2] and [9] additional work has been done to define how a proper Thermal Management strategy may help during cold start conditions. Detailed control strategies are presented in references [6]-[10], capable to set multiple temperature levels over the FCEV cooling circuit. Reference [11] shows how detailed Thermal Management needs to be performed at the FC Stack level on a FCEV. Studies [4]-[8] show how a detailed mathematical model-based plant may be beneficial to develop FCEVs Thermal Management architectures.

This publication presents the following two main topics:

- Detailed thermal model of a complex vehicle architecture, capable to evaluate the effect on fuel consumption of the different ATM architectures and control strategies
- Comparison of ATM architectures to evaluate H2 consumption reduction and cabin conditioning performances of the selected systems

2. Description of the Fuel Cell Propulsion System and Cooling Circuits

Similarly to a BEV vehicle, in a FCEV the mechanical torque for propulsion is generated by one or more electric motors. In the case of FCEV architectures, whose schematic is shown in Figure 1, the electric energy needed by EMs is supplied by a combination of a fuel cell module and of high voltage battery, that works as an energy buffer for the system.

The electric power management is obtained through a system of high voltage cables and components. The common voltage level (DC link voltage) can vary depending on the application, with a trend towards 800V for heavy duty applications. Higher voltage values in fact allow to manage higher power flows with a reduction of components sizing, with an impact on cost and weight.

The voltage supplied by the Fuel cell Module is adapted to DC link voltage by a DCDC converter. Depending on the architecture design, the high voltage battery may be directly connected to the DC link or an intermediate additional DCDC converter may be added, in this second case further degrees of freedom are made available in design and calibration of the propulsion system.

The AC voltage supply and control for each electric motor is provided by dedicated inverters, connected to the DC link.

The hydrogen supply to the fuel cell power module is guaranteed by pressurized storage tanks, equipped with dedicated regulation and safety valves.

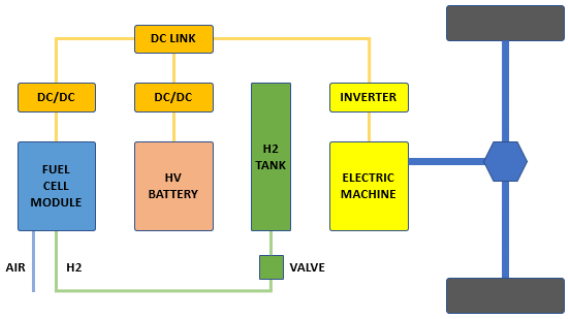


Figure 1 – high level schematic of a fuel cell propulsion system

The FCEV propulsion system components need to be thermally conditioned, i.e. cooled or heated, based on their optimal temperature level and on their working conditions. Since different components have different optimal target temperature levels, normally they are organized in three different cooling circuits:

- High Temperature (HT) circuit (coolant temperature around 60-90°C) that serves mostly the FC stack. This component needs to be cooled at its ideal temperature (to maximize efficiency and durability) during standard operation, but during warm-up phases, a specific heat procedure needs to be applied through a FC Electrical Heater. In some cases, depending on design solution, this circuit can also include the FC Balance of Plant components, implementing a single cooling circuit for the FC Module. In this last case, the working temperature of the HT circuit may be lower, if compared to what described before.
  Moreover, the FC stack cooling requires the usage of a dielectric coolant. For this reason, the HT cooling loop has to be hydraulically separated from other loops in the vehicle.
- Medium temperature (MT) circuit (coolant temperature around 45-55°C) that serves mostly the power electronic of the FCEV (electric drive with inverter and DC/DC converters). Normally, these electrical components require to be cooled and keeping an optimal temperature level helps to improve overall system efficiency. When the FC module is equipped with dual cooling circuit, the MT loop can also incorporate the FC cathode air cooler, the compressor, and the FC power electronic
- Low Temperature (LT) circuit (coolant temperature around 35-45°C) that serves mostly the high voltage battery. This component needs to be cooled at its ideal temperature (to maximize efficiency and durability) in standard operation

and needs to be warmed-up when starting from cold condition. The proper warm up of the battery is critical for guaranteeing durability and performance of the component. In this phase the battery is self-heated by internal power losses and by the usage of a Battery Electrical Heater.

Another system that is heavily involved on the thermal behaviour of the FCEV is the HVAC system aimed at controlling the passenger compartment temperature level. This is normally equipped with an electrical heat pump or by an electric heater, both driven by the HV Battery but that, using some specific solutions, may use some heat embedded in the HT/MT/LT circuits.

Figure 2 represents a basic FCEV thermal layout in which it is considered to have heat flows between each thermal loop (HT/MT/LT loop and HVAC) and the ambient, and also heat flows inside each loop (both heat flows required to satisfy thermal inertias and heat flows associated with the activation of the electric heaters, if present). In standard high-performance applications HT and MT circuits are equipped with liquid-to-air heat exchangers, while the LT is cooled using a Heat Pump integrated in the HVAC system.

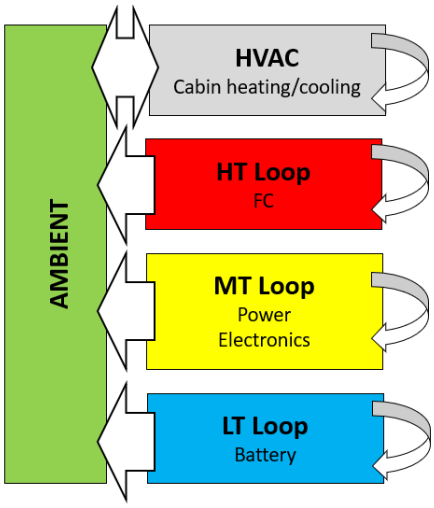


Figure 2 - Heat flows for standard FCEVs ATM architecture

This paper presents a study that is developed for a typical 2 axles 12 meters urban bus application (19000 kg GVW). The Table 1 reports high level dimensioning information of the considered bus.
The bus architecture described before is virtually tested on a real reference bus driving cycle (representative of urban and extra-urban driving), with an ambient temperature of 0°C. This ambient temperature has been chosen because it is representative of a warm-up that may happen frequently in winter European conditions, and

Table 1 - 12m Urban Bus Specifications

FCEV Urban Bus Specifications	
Electric motor	250 kW
HV Battery	40 kWh
Fuel Cell	100 kW
H2 Tanks	30 kg, 700 Bar

because it is a condition that shows higher possible benefits for ATM strategies.
The speed/slope traces over time of the selected real driving cycle are reported in the following figure 3.

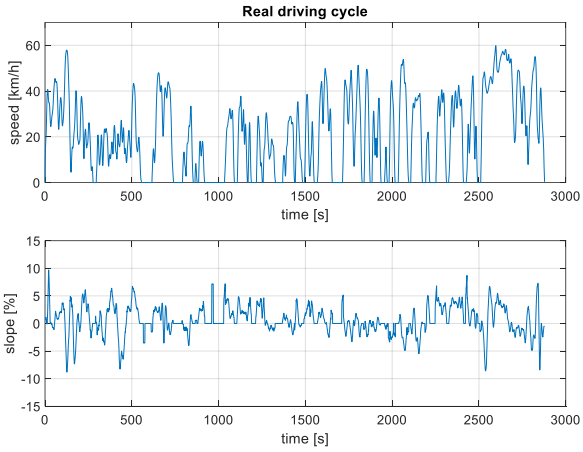


Figure 3 - Speed and Slope traces over time of the real driving cycle selected to simulate the energy consumption

3. Simulation model description

This paper is developed on a detailed GT-Suite System-level model of the described FCEV bus architecture. There are two main portions of the model that interact together to evaluate the effect of the ATM architecture on the energy consumption of the vehicle:

- Performance model of the vehicle:
  Every component of the FCEV propulsion system is simulated in GT-Suite based on the behaviours of typical components available in the market. Every component has its own sub-model and has “performance” characteristics function of its thermal level. Also, the vehicle itself is simulated to evaluate the required road-load, to be fulfilled by the powertrain. The power management control is performed using a Rule Based logic that manages the power-split between FC and battery so to turn on FC to maintain a constant battery SOC.

The performance model is capable to calculate the H2 consumption and the HV Battery consumption over the testing cycle.

- Thermal model of the vehicle:
  The thermal model can be considered as a subsystem of the overall vehicle model; the cooling system includes vehicle and powertrain components thermal masses, heat exchangers for heat released to ambient and a detailed plumbing with dissipation model. Flow distribution is managed through electric water pumps, whose performance and efficiency maps are included in the model, and temperature dependent ATM control valves.
  The model includes the vehicle cabin and its air conditioning system as well, to simulate warm up of the cabin in case of low ambient temperature.
  There is a constant interaction between performance and thermal model, the first one defines the heat losses at different working points, that become an input for the second one that calculates the new component temperature and consequently the efficiency.
  As baseline architecture, battery and power electronic components have two separated cooling systems working at two different operating temperature. One more cooling loop for fuel cell has been included; in this way the ATM control allows the optimal heat balance among the different cooling system. For example, we can take advantage of the heat from fuel cell to warm up the cabin reducing PTC heater usage.

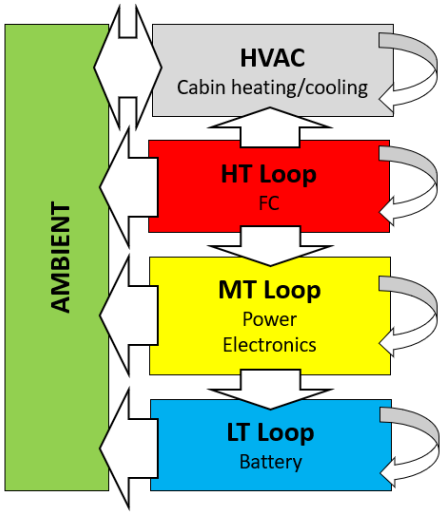


Figure 4 - Schematic of allowed heat flows between the different ATM thermal loops

As mentioned before, the interaction among the cooling loops is managed by ATM, that allows the optimal heat balance across all cooling systems.
An equivalent H2 consumption is calculated on the testing cycle of interest, to compare different ATM strategies. This equivalent consumption considers the effective FC consumption over the testing cycle, plus the H2 consumption required to get the same SOC at the end of every tested configuration.

4. Evaluation of the influence of the thermal architecture

The 1D thermal model described below is used in the paper to evaluate the effect of different heat-reutilization concepts.
The main heat source of the FCEV ATM system is the FC. This component delivers heat with a certain rate during normal operation (around the same amount of energy of the electrical production). During warm-up this is heat is kept inside the FC itself because it is required to achieve the FC stack optimal working temperature (effect on deliverable power-out and efficiency). In this phase, it is often used an electrical HV PTC heater to have faster warm-up time. After the warm-up, the FC delivers heat that needs to be removed from the HT loop to avoid overheating.
Another heat-source available in the system is the portion of power electronics. These components deliver most of the heat that needs to be removed from the MT loop to guarantee safe operations of the architecture. Also, these components require a thermal conditioning to deliver an optimal behaviour in terms of efficiency and durability.
Also the battery, once warmed-up, is an additional heat source in the FCEV system. But, due to its high efficiency and its high mass, it is characterized by a quite long warm-up phase, and it is equipped with a dedicated HV PTC heater to accelerate this phase. Also, during cold ambient operations, the battery, if operating at quite low power, may tend to release a lot of thermal energy directly to the external ambient elongating the warm-up temperature and increasing the HV PTC Heater utilization time.
The analysis proposed in this paper is focused in finding a good strategy to define energy flows between the different components of the circuit, so that if any energy source has heat available in excess, this heat may be used by any heat sink that needs it to enable faster warm up (and eventually lower utilization of the HV PTC heaters) and better optimal temperature level control (to optimize efficiency of the system). To perform this analysis, three high level thermal energy reutilization features have been identified:

1. Utilization of HT loop heat to warm-up cabin volume

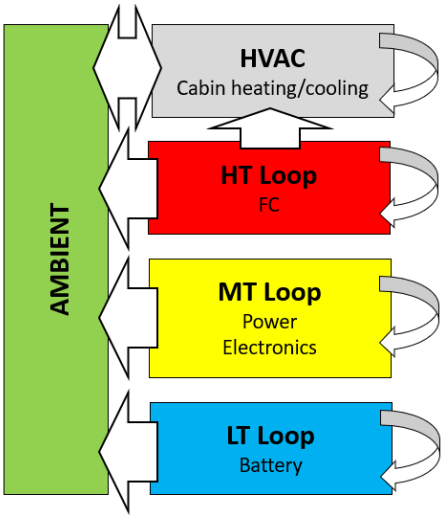


Figure 5 - Heat flows using HT loop heat to warm HVAC

This feature has a clear pro on reducing the usage of the HVAC to warm the cabin, while has a drawback lowering the FC working temperature (and possibly increasing the usage of the FC PTC heater)

2. Utilization of HT loop heat to warm-up MT loop

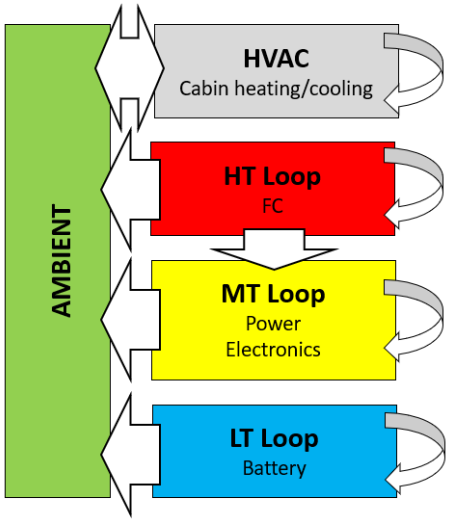


Figure 6 - Heat flows using HT loop heat to warm MT loop

This feature has a pro on faster MT loop components warm-up, while has a drawback lowering the FC working temperature (and possibly increasing the usage of the FC PTC heater)

3. Utilization of MT loop heat to warm-up LT loop

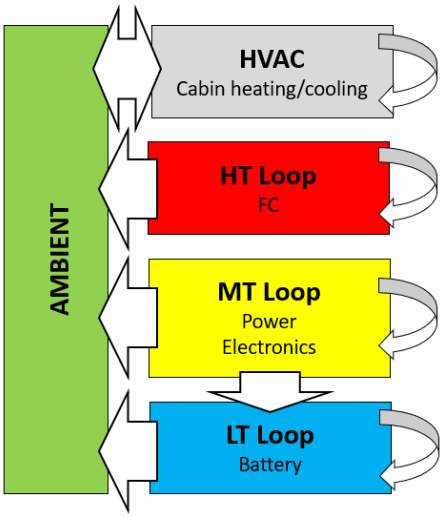


Figure 7 - Heat flows using MT loop heat to warm LT loop

This feature has a pro on reducing the usage of Battery PTC heater to warm-up the battery and to keep it warm in low ambient temperature and low battery load, while has a drawback lowering the MT Loop working temperature.

The three thermal features described before may be combined to generate the following three thermal architectures:

- Architecture 1: Use heat from HT loop to help HVAC heating, use heat from MT loop to help HV Battery heating
- Architecture 2: Use heat from HT loop to help both MT loop and Battery heating, keeping HVAC independent
- Architecture 3: Use heat from HT loop to help HVAC, MT loop and Battery heating

Table 2 reports the H2 consumption (calculated by the combined thermal and vehicle performance model) obtained by the three Thermal Architectures comparing them with the baseline solution (Figure 2). The lowest H2 consumption is obtained with Thermal Architecture 1, that reports a considerable reduction if compared to the baseline solution.
In the following portion of the paragraph, the authors explain which is the physical behaviour that causes the equivalent H2 consumption reduction of the three architectures, if compared to the baseline solution. The benefit comes mostly from the lower utilization of electric HVAC heater.

Table 2: H2 consumption reduction related to the considered thermal architectures

Thermal Architecture #	Thermal features	H2 Consumption reduction [%]
Baseline	Independent circuits	NA
1	HT->HVAC | MT->LT	9.3
2	HT->MT->LT | HVAC	0.9
3	HT-> HVAC | HT->MT->LT	7

Figure 8 shows that Architecture 1 requires a substantially lower activation time of the HVAC electric heater if compared to baseline and to the other two architectures (having lower usage of battery electric energy and consequently lower H2 consumption from the FC that tries to recover for lower battery SOC). In this case, even if the thermal energy extracted from the HT cooling loop tends to cooldown the FC (with consequent lower FC working efficiency), the benefit on the HVAC tends to recover the effects of the lower FC working temperature.

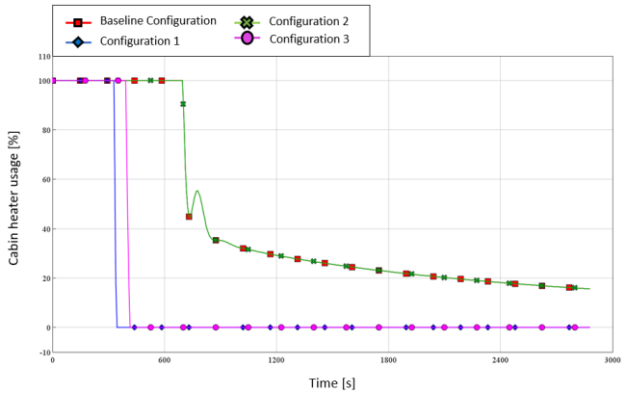


Figure 8 - Comparison of HVAC electric heater routine between baseline solution and the three proposed Thermal Architectures

Also interesting is the comparison between the three Architectures and baseline solution on the temperature level in the cabin volume. Figure 9 shows how Architecture 1 not only guarantees a better H2 consumption, but also guarantees a better comfort in the cabin, requiring lower time to reach the HVAC target temperature.
Similarly to what has been discussed for the HVAC electric heater, Figure 10 shows how, comparing baseline solution to the three proposed Architectures, it is possible to notice that it is considerably anticipated the first time that the Battery PTC heater is shut-off.

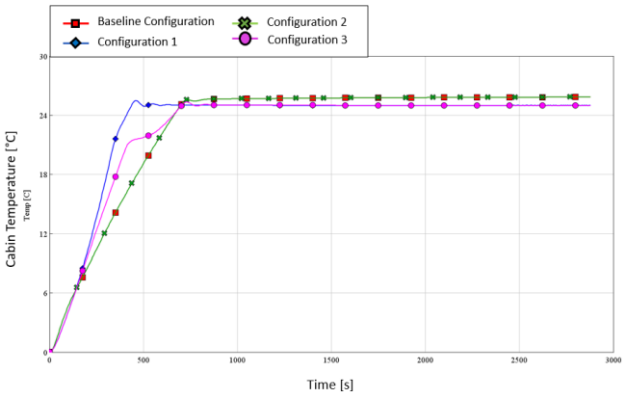


Figure 9 - Comparison of internal cabin temperature between baseline solution and Thermal Architecture 1

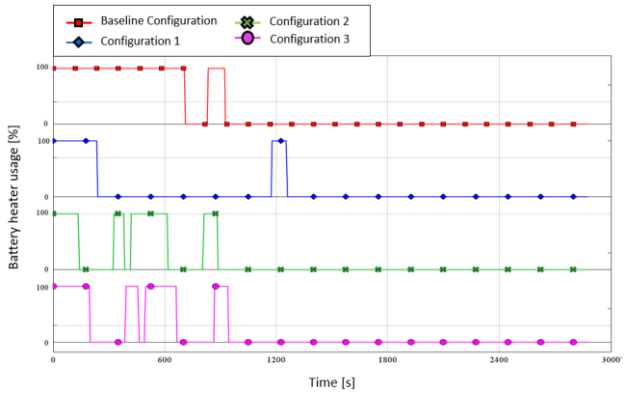


Figure 10 - Comparison of Battery electric heater routine between Experiment 1 and 10

But it has also to be noticed that Architectures 2 and 3 lead to a fast re-activation of the Battery PTC heater, due to the fact that, using HT loop heat to warm-up the battery trough MT and LT circuits, leads to reach in a really short time high temperature in the MT. As a result, the selected control strategy stops coolant flow between MT and LT circuits (for battery temperature protection). At this point the only way to re-enable battery heating is through the Battery PTC heater, increasing the H2 consumption. Instead, in Architecture 1 this phenomenon does not happen and heat from MT to LT may be used for a long period (reducing considerably the Battery PTC heater activation time), causing higher H2 consumption reduction.
This behaviour is well evident in picture 11 where it's possible to notice that the coolant temperature in the MT circuit for Architectures 2 and 3 is really fast to go up, reaching in very short period the conditions to separate LT from MT.

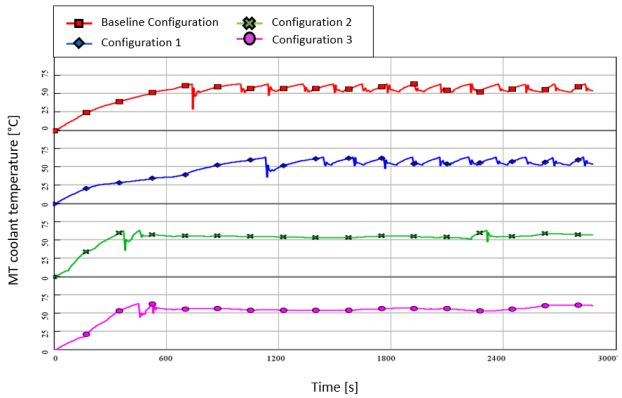


Figure 11 - Comparison of MT coolant temperature between baseline solution and Thermal Architecture 1

In a similar way, figure 12 shows the coolant temperature behavior in the LT, highlighting again how fast the temperature rises-up for Architectures 2 and 3 till the MT/LT splitting conditions, while in Architecture 1 the temperature build-up is slower than Architectures 2 and 3, but considerably higher than the baseline solution.

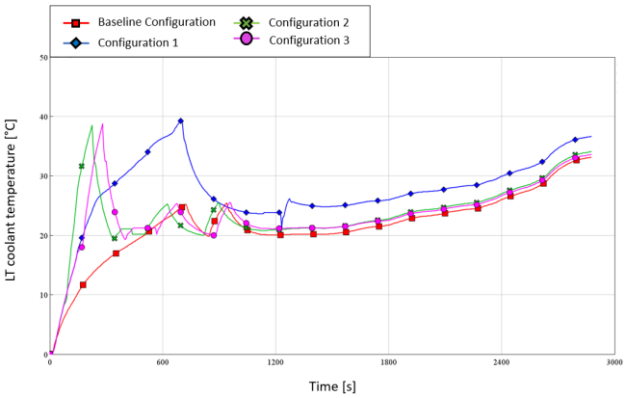


Figure 12 - Comparison of LT coolant temperature between baseline solution and Thermal Architecture 1

This implies that the ATM heat flows schematic defined in figure 4 may be further modified to get better results in terms of H2 consumption, enabling a better utilization of the HT heat for Battery warming purposes.

5. Conclusion

This paper analyses the effect of multiple ATM strategies on a FCEV 12 meters urban bus architecture, showing the effect of different ATM architectures on the energy consumption at a full-vehicle level. The mentioned architectures are simulated in GT-Suite, with a detailed 1D thermal model that couples vehicle and thermal simulations of the powertrain, with the addition of simulating the vehicle HVAC system. Tests are performed on a typical transient bus testing cycle at low ambient temperature (0°C).

Three Thermal architectures have been simulated to assess which are the most advantageous thermal features to be utilized.

The best active thermal management solution allows to achieve both a 9.3% equivalent hydrogen fuel consumption reduction and, at the same time, the targets of thermal conditioning of each subsystem.

This paper represents the first comparison activity that tries to combine different ATM features. Additional development steps are now ongoing to further optimize the hardware configuration and the control strategy defining a more optimized thermal architecture (both from the cooling circuit layout and the control strategy) so to allow additional H2 consumption reduction.

6. References

1. Christian M. Moeser, Wolfgang Dillig, Raik Heyne, Emmanuel Simon, Thomas Traudt, “Thermal Management of Fuel Cells for Medium and Heavy-Duty Architectures”, SIA POWERTRAIN & POWER ELECTRONICS Congress - Digital Edition 2021 - 9 & 10 June 2021
2. J.Y. Berard, J. Lefebvre, G. Morin, S. Ruby, N. Stekelorom, S. Parpais, “Optimum Thermal-Management Strategies for low Ambient Temperatures”, SIA Powertrain Congress - Versailles 2015, 27-28 May 2015
3. Yiping Wang, Jing Li, Qi Tao, Mohamed H. S. Bargal, Mengting Yu, Xiaohong Yuan, Chuqi Su, “Thermal Management System Modelling and Simulation of a Full-Powered Fuel Cell Vehicle”, J. Energy Resour. Technol. Jun 2020, 142(6): 061304
4. Liren Yang, Amey Karnik, Benjamin Pence, Md Tawhid Bin Waez, Necmiye Oza, “Fuel Cell Thermal Management: Modeling, Specifications and Correct-by-Construction Control Synthesis”, Electrical Energy and Computer Science department (EECS), University of Michigan
5. Mounir Nasr, Dave Dickinson, “Thermal Management of Fuel Cell-driven Vehicles using HT-PEM and Hydrogen Storage”, 2014 Ninth International Conference on Ecological Vehicles and Renewable Energies (EVER),
6. Philipp Rehlaender, Philipp Kemper, Andreas Schwung, Ulf Witkowski, “Control of a fuel cell vehicle thermal management system”, 2018 IEEE International Energy Conference (ENERGYCON), 3-7 June 2018

7. V. Hovland, “Integrated Cabin and Fuel Cell System Thermal Management with a Metal Hydride Heat Pump”, Eighth International Symposium on Metal-Hydrogen Systems (MH2002), Annecy, France, September 2–6, 2002
8. Jiamin Xu, Caizhi Zhang, Ruiji Fan, Huanhuan Bao, Yi Wang, Shulong Huang, Cheng Siong Chin, Congxin Li, “Modelling and control of vehicle integrated thermal management system of PEM fuel cell vehicle”, Energy volume 199, 15 May 2020
9. Hongliang Jiang, Liangfei Xu, Jian qiu Li, Zunyan Hu, Minggao Ouyang, “Design and Control of Thermal Management System for the Fuel Cell Vehicle in Low-Temperature Environment”, WCX SAE World Congress Experience, SAE Technical Paper 2020-01-0851
10. C Venkatesh Chandrasekar, “A Novel Thermal Management Simulation Model Analysis for The Fuel Cell Electric Truck Systems”, Symposium on International Automotive Technology, SAE Technical Paper 2021-09-22
11. Ho-Seong Lee, Choong-Won Cho, Jae-Hyeong Seo, Moo-Yeon Lee, “Cooling Performance Characteristics of the Stack Thermal Management System for Fuel Cell Electric Vehicles under Actual Driving Conditions”, Energies 2020, 9, 320

7. Glossary

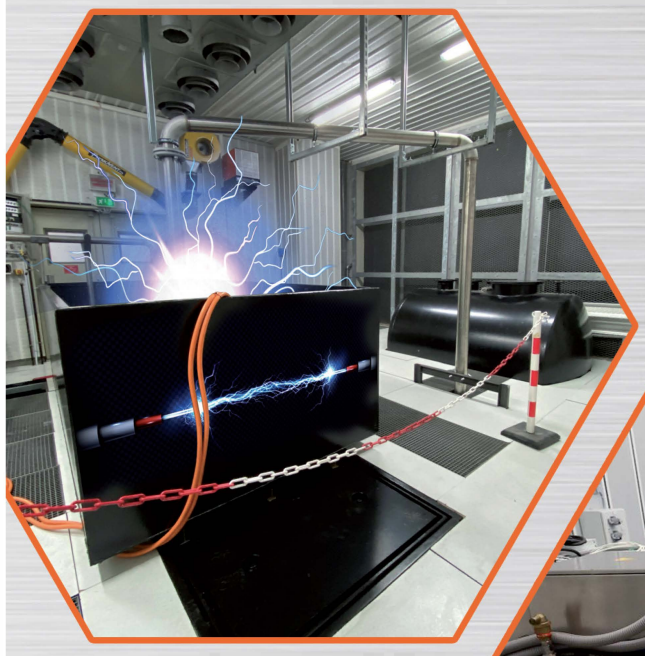
ATM – Active Thermal Management
Bar – Pressure measurement unit
BEV – Battery Electric Vehicle
BoP – Balance of Plant
DFSS – Design for Six Sigma
DOE – Design of Experiment
FC – Fuel Cell
FCEV – Fuel Cell Electric Vehicle
GVW – Gross Vehicle Weight
H2 – Hydrogen
HT – High temperature cooling loop
HV – High Voltage
HVAC – Vehicle conditioning system
kg – kilogram
kW – kilowatt
kWh – kilowatt hour
LT – Low temperature cooling loop
MT – Medium temperature cooling loop
PEM – Proton Exchange Membrane
PTC – Electric Heater
SOC – State of Charge

15 JUNE 2022

HYBRID VEHICLE ARCHITECTURE

CRITTM2A

Independent Testing Center









ELECTRICAL ABUSE TEST BENCH

- Short circuit
- Overcharge
- Over discharge
- ECE R100 Homologation
- IEC 62620, IEC 62928
- ISO 16750...



4WD POWERTRAIN BENCH

- Robot driver (pedal, gearbox)
- Battery Simulators up to 500kW
- Performance :
  500kW and 2500Nm/dyno(wheel)

9 PACK TEST CHANNELS
UP TO 1800A, 750kW, 1200V

9 MODULE TEST CHANNELS
UP TO 1200A, 64kW, 100V

96 CELL TEST CHANNELS
UP TO 1000A, 8kW, 8V

INVERTER TEST BENCH

- Battery simulator
  Current : 800A
  Power : 320kW
  Voltage : 1000V
- E-motor emulator
  Current : 400A
  Power : 320kW
  Voltage : 735V

www.crittm2a.com

Renault E-tech Hybrid New software and hardware Improvement.

N. Fremau[1], A. Ketfi-Cherif[1], P. Le Roy[1], R. Delcloy[2]

1: Renault SA Technocentre Guyancourt
2: Renault SA Centre technique de Lardy

Abstract:

E-tech hybrid is now on market for more than two Years. We will present the basis of this clutch-less hybrid technology. In a second part we will explain an important tuning improvement to get the best of this system. Thanks to this work, ETECH efficiency increases, and all Renault HEV were re-homologated and gain more than 3 g/km with only tunning. As a conclusion we will shortly introduce "ETECH Medium"; an Upscale of today ETECH that will be a unique offer CO2 and power for new C-SUV Renault Audace.

Keywords: ***ETECH, Hybrid, Tunning, HEV, PHEV.***

1. Introduction

Despite the complex pandemic context ETECH HEV and PHEV start of sales is clearly a commercial success. For example, HEV represented more than 50% of the "Arkana" market share (much more than expected in the most optimistic projection). This new and innovative technology was also awarded in several countries and is now a serious player in HEV / PHEV market.



FIG1
Renault Hybrid Line-up

For start of production we decided a to go on robust and state of art tunning. we chose to delay many High-end optimizations that were patented and tested during advanced phases; This was clearly time to market oriented.

ETECH hydrid will last for 8 to 10 years (Renault and Dacia and other OEM). It is important to get top tunning level during the first years of production because it will be carried over in all the coming ETECH line up.

2. ETECHBasis

2.1 Product Target and DNA:

From Renault point of view Hydrid is the perfect bridge to fill gap from ICE to EV. This transient era will last about 15 years in Europe and maybe 20 to 25 years in other markets. To face this challenge, we chose to develop a DHT (Dedicated Hybrid Transmission) that can fit to both HEV and PHEV and can be easily upscaled and extended to a large line-up.

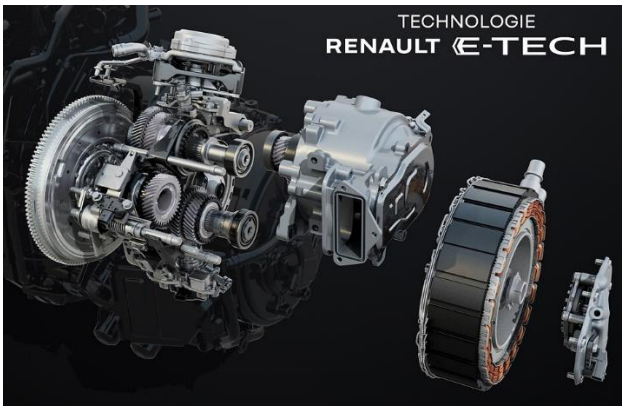


FIG 2
ETECHStep1 Powertrain

To achieve a cost optimized powertrain with real customer value, a whole transmission was completely re-designed and electric components are replacing certain functionality of a "conventional ICE vehicle".

Instead of just adding e-motor capacity to an average powertrain, we must reconsider the whole powertrain performance. The ICE can be right-sized to provide steady state performance, and e-motor must be designed to ensure vehicle acceleration and full electric driving. With this principle, high performance can be achieved with a right sized 69kW engine (Lambda one) and a 35kw-50kW e-motor

Confidential C

(depending on battery voltage). These values depend on the exact vehicle (HEV / PHEV)

2.1 No clutch:

e-motor is the best way to take-off a vehicle, avoiding vibration and ICE overshoot. Using E-motor there is no energy losses in clutch friction, and inefficient ICE set point during takeoff. Thus, we chose to remove the clutch and reallocate space for a powerful electric motor. This point is also key for packaging. As a result, ETECH powertrain can fit easily in a B/C segment for both low and high drive vehicles. Its length is similar to a manual transmission powertrain.



FIG3
E-tech a clutchless Hybrid

2.2 A no synchromesh technology:

For a classical hybrid E-motor is mostly considered as an additional torque generator. In E-tech technology we decided to use additionally E-motor as an accurate torque actuator. A four-year control study permits to replace mechanical synchromesh by an accurate control algorithm that make the gearshift quick and seamless.

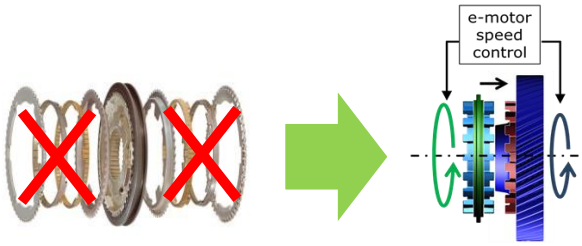


FIG4
E-tech : E-synchronisation

Next figure 5 describes E-synchronization versus manual gearbox mechanical gearshift.

<u>For conventional gearshift:</u> During synchronization of two rotary elements, a synchromesh applies a friction torque thanks to a normal load on synchromesh devICE that reduce differential speed.
<u>For ETECH :</u> we use “smart synchronization”:speed gap between elements is evaluated by the speed sensor, and a dynamic torque is applied by the e-motor in order to reduce this rotational gap.

We understand that sensor and their redundancy are a key Item to keep gearshift quality at top level for a long time. This technology is robust because e-synchronization in not sensitive to mechanical wear and much more stable than synchromesh.

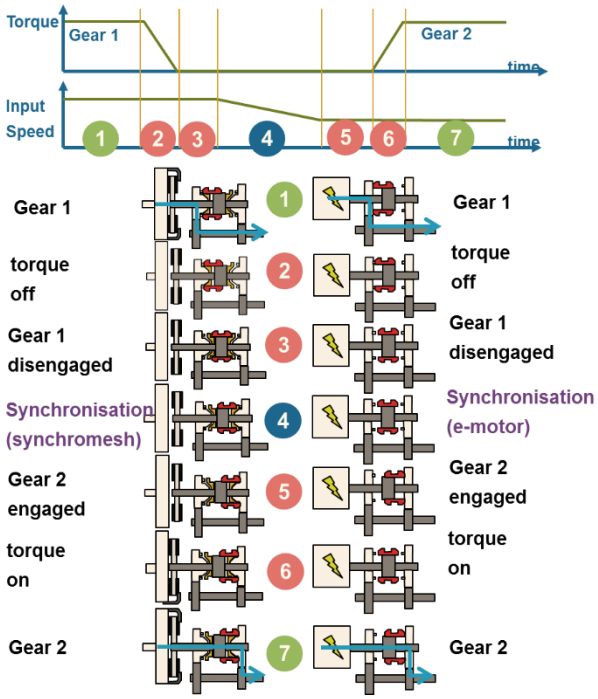


FIG5
Step by step gearshift for Etech
Versus manual Gearbox.

2.3 a multimode transmission:

To offer the best CO2 and drivability performance ETECH structure needs a specific design. It includes two “half gearboxes” that can work independently or together. With this drawing we can connect the minimum component to the wheels and minimize friction to get best fuel economy.

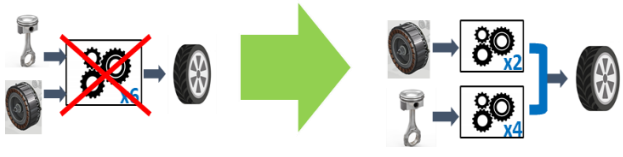


FIG6

Confidential C

The first half gearbox: is a two speeds EV gearbox to insure the full Ev driving. Twin ratio permit to combine Electric vehicle torque level at start and High speed EV capability when needed.

Second half gearbox is a 4 speeds gearbox connected to ICE and a downsized starter generator. This part of the transmission allows to power the car with ICE and to adjust its set point to “alpha-line” without using main motor. (An additional 5th ratio is available but not used in initial tuning -evB+ICE 3’- in fig7).

For High power request the two gearboxes can move the vehicle simultaneously combining: ICE torque + Main E-motor torque + Generator torque used in traction. This torque addition can be made with the best ratio selection for each vehicle speed. (15 modes can be obtained FIG7)

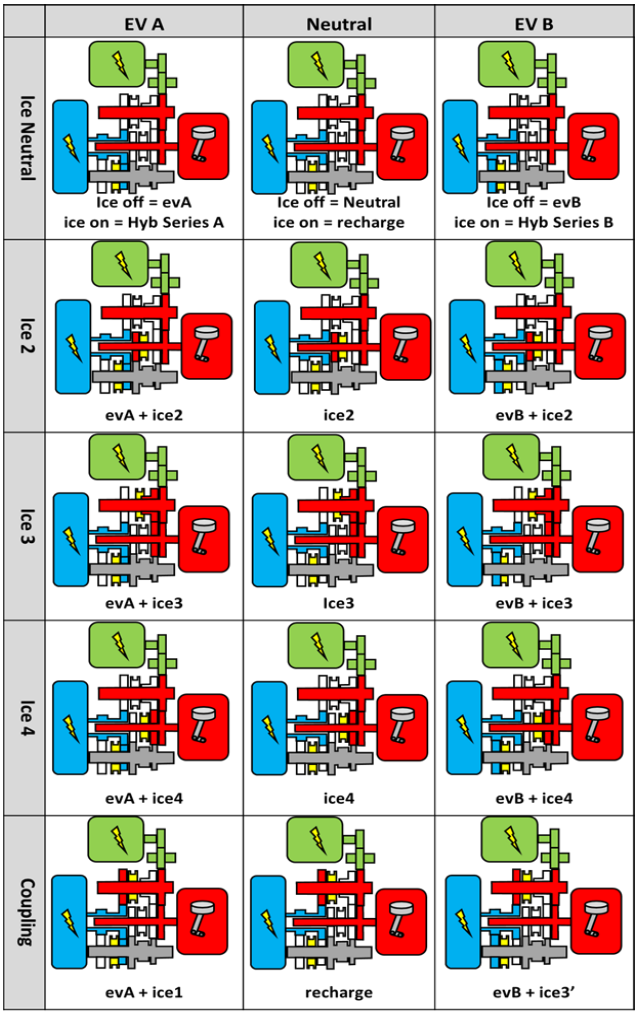


Figure 7: Possible driving mode
HYB – XY: X = A,B is the ratio connected to E motor and Y = 1,2,3,4 to ICE Motor

2.4 E-Tech structure for gearshift:

Basically E-Tech gearbox can be described as a dual-clutch transmission but without a clutch! To understand this paradigm let’s describe a gear shift sequence for example from 2nd ICE gear to 3rd ICE gear.

The basic principle is torque compensation during gearshifts. The global gearbox is divided in 2 “half gearboxes”; One half gearbox can continue to provide torque to the wheels during the shifting process of the other half gearbox. The following figure illustrates torque compensation during the transition of HybA2 => HybA3 (ICE gear is changing from 2nd => 3rd , and e-motor compensation on ratio A).

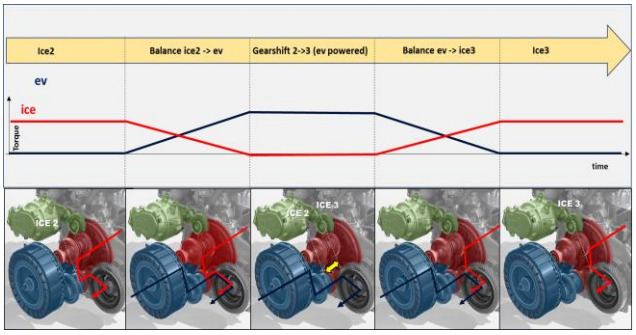


Figure 8 : Hyb A2 -> Hyb A3
3 steps of gearshift: torque compensation, Gearshift, final applied torque

2.5 direct feeling:

Figure 9 shows another positive aspect of ETECH techno. The step ratio approach gives a natural and already well-known behavior for European customers. When ICE is started, we come back to the familiar DCT or step-AT feeling. But we keep the responsive acceleration from EV. To make it simple no “ruber-band” effect !

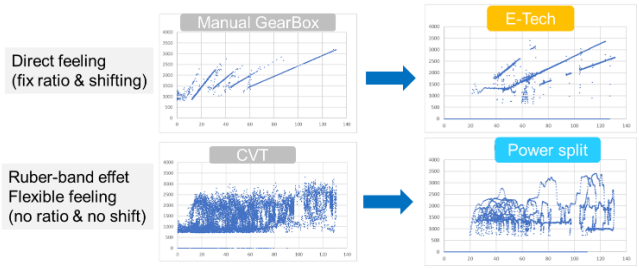


Figure 9 ETECHdirect feeling

Confidential C

2.6 E-tech on WLTP cycle:

E-tech analysis on WLTP cycle brings a lot of information on real driving behavior. We must keep in mind that WLTP load and speed are very close to an average client driving: urban driving (beginning of wltp to 600s) suburban and road (600s to 1450s) and highway (1450s to the end).

At first, we can compare ICE power to vehicle power request during the cycle. Basically, we can see on figure 10 that ICE is ON only 1/3 of the total duration of the cycle. When ICE is turned ON, most of the time (except the catalyst warmup) its load stays close to “alpha-line” (ie best consumption area). We can also see that ICE is started around 15 times during the cycle with long period of pure electric driving specially in urban phase (ICE OFF more than 80% of time).

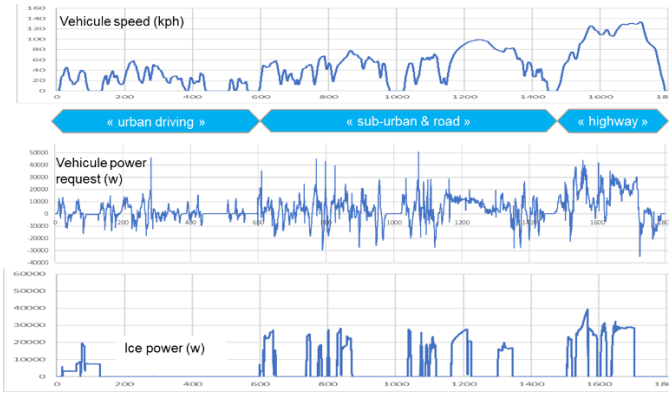


Figure 10: WLTP ICE behavior

In ETECH Powertrain ICE shows an almost constant load. This means that E-motor insures most of the transient part of vehicle power request with direct CO_2 benefits since real BSFC in transient is known to be 8% higher than steady state.

To go further on the analysis, we can have a look on, figure 11. It shows the way E-motor, ICE, and Generator interacts. We can see that except the 3 “doted area” only one of the two half gearbox is selected; near 2/3 on the cycle is in full EV (blue half transmission) and the other 1/3 is “ICE + generator” selection. We can understand that ICE or E-motor is mostly disconnected to avoid drag when they are not needed. During ICE driving phase a right sized small generator insures the ICE setpoint (and so main e-motor disconnection).

ICE needs to be warmed at the beginning of the cycle. This is a specific phase to insure the catalyst warmup. During this event ICE set point is at low load and E-tech is working in series hybrid mode with the generator. The traction is insured with main E-motor. It allows to have clean ICE start. The warm-up is also maintained to ensure water heating to secure an ICE “hot” restart around 300 seconds after the end of the warmup.

.

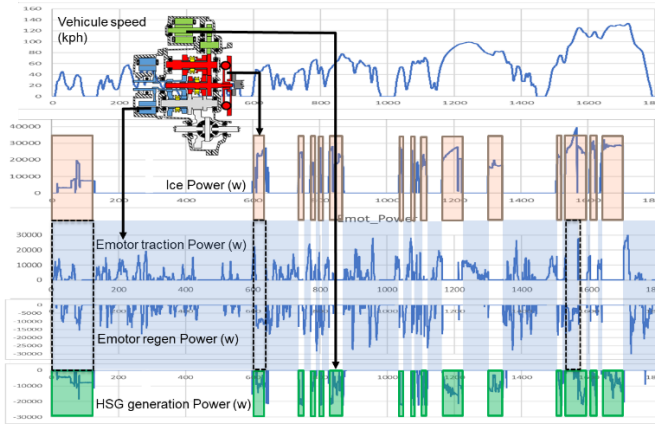


Figure 11: Most of the time only on part of transmission is use to reduce friction *(both are used together for high power request)*

In the last figure we can check ICE efficiency in WLTP (average customer driving). Most of the points are around alpha-line from 1600 to 2800 rpm. The two red circles show the behavior during warm-up. Until correct catalyst temperature is reached pollutant constraint imposes a low load. All other points are transient during gear shift or ICE stops and starts.

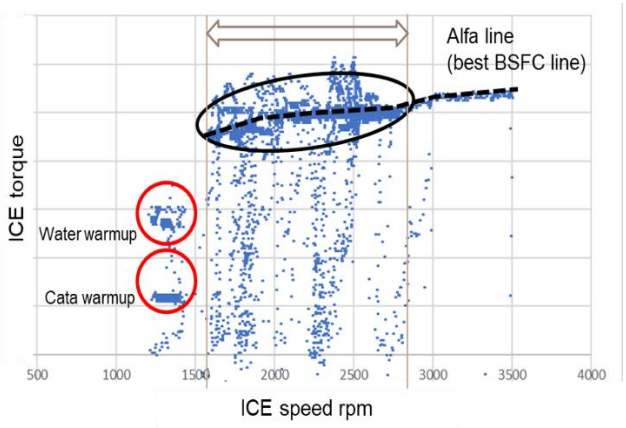


Figure 11 : ICE set point WLTP

Confidential C

3. An optimized tuning:

3.1 New tuning opportunity:

We decide to re-tune ETECH to include best level techno bricks and go on re-homologation on HEV to offer an optimized CO_2. And as result more than 3g benefit on HEV line up (Captur/Clio/Arkana).

Improvement can be divided in 2 main ideas:

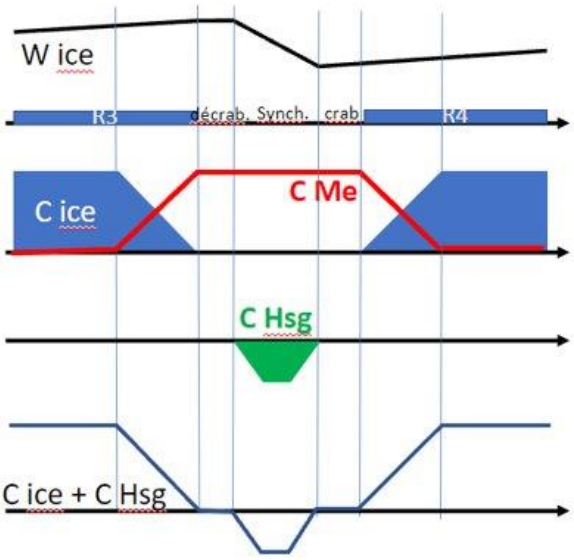
1) Increase the load of ICE
2) Limiting powertrain 12V volt electric consumption.

3.1 Increasing ICE load: gearshift example:

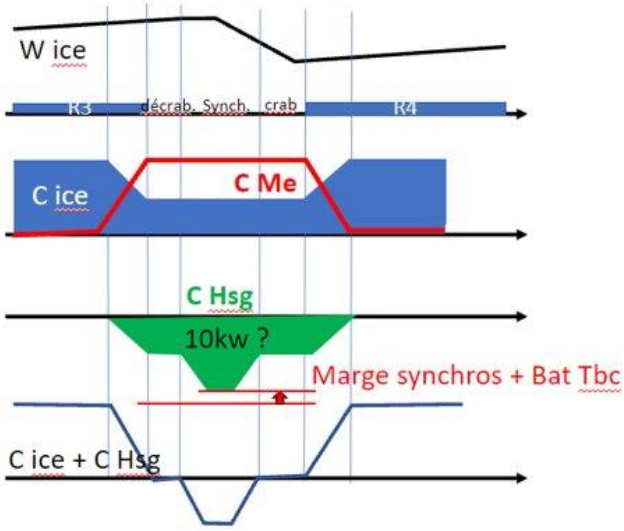
As we have seen previously when ICE is on it is set on alpha-line load except during ICE restarts and gearshifts. Basically, technical analysis shows that we have more than 50 seconds on transient (start and gearshift) over the 600 seconds ICE is ON. There is a real opportunity to increase the global ICE load and so increase ICE efficiency.

To do so a specific ETECH patent *(Ahmed Ketfi-Cherif and Ludovic Merienne)* is applied to manage: “series Hybrid” during restart ramp-up and gearshift. With 18kw secondary motor it possible to keep around 12kw to do series hybrid which is far better than ICE rotation with no torque. (6 last kW can achieve speed control).

Figure 12 show the initial process and the new process.



Initial gearshift: with zero ICE torque (in plain blue)



Initial gearshift: with zero ICE torque (notICE the 12kw torque in plein blue compensate by increasing HSG torque in plain green)

Figure 12 (new gear shift process)

Another positive impact of this modification is the gearshift time reduction (due to shorter ICE torque transient). The result can be appreciated in the final measurement and give also an even better fluidity to ETECH Powertrain (Figure 13).

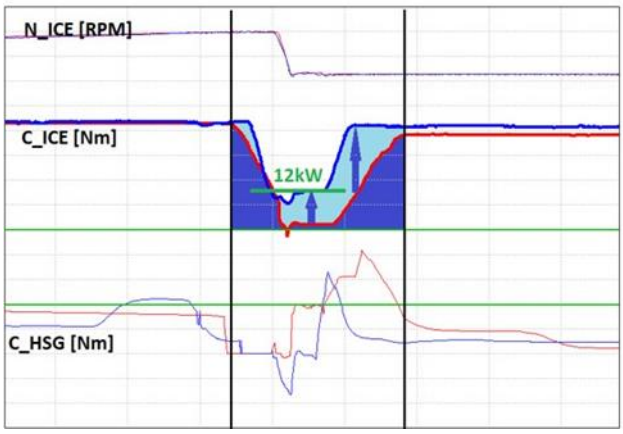


FIGURE13: Final tuning result of loaded ICE gear shift *(shifting time gain 1sec and 12kw load during gear shift)*

Restart optimisation optimization was done on the same principles. Figure 14 shows the global ICE load improvement and faster ETECH responses.

Confidential C

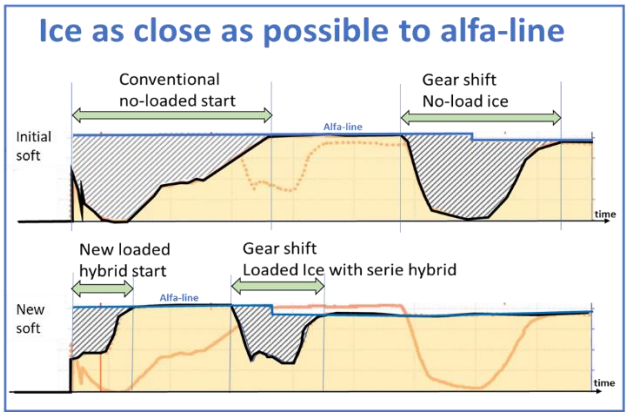


Figure 14 global improvement on ICE load with new tuning (start and gearshift)

3.2 Optimising powertrain 12V energy consumption.

For HEV all vehicle energy is coming from fuel. As Electric energy is balances for a WLTP cycle and in real life driving, it is important to minimise 12V electric consumption. For ETECH we re-studied the global powertrain consumption, and we listed several 12V electric powertrain consumption:

-gearbox actuators (almost zero consumption!)

-gearbox small lubrication pump

-ICE oil e-pump

-e-motors / power electronics water pump

-Electric braking system

We focused on two items:

-gearbox pump

-e-motor pump

Let's take the example of gearbox pumps. In initial tuning we set two power levels on the pump:

- low flow when the gearbox is at stop

- high flow when the vehicle moves.

With additional technical studies it was possible to check that low flow was suitable for electric driving and High flow only requested when ICE on.

A similar work was carried out on E-motor water pump to adjust water flow to optimal level.

All Theses modification permit to gain 25% of 12V fuel consumption with the optimized strategy.

4.1 conclusion and next steps:

ETECH now reaches a good Maturity level and will be an important player in the strategy to efficiently shift to full Electric vehicle and will continue to be improved.

End of 2022 Renault Austral will be on the market as the second generation of ETECH.Hybrid Powertrain.

Austral (figure 15) will be available with "ETECH gen2": this package includes:

- New gearbox (more torque capability, Optimized efficiency, and thermo management).

- New HR12turbo Miller engine with an outstanding peak efficiency at 41,5% and a wide sweet spot area.

For WLPT hot condition the new ETECH will achieve 40% ICE average efficiency on cycle. This C-suv should be homologated around 105g and should be best in class for CO_2 with top dynamic performance.



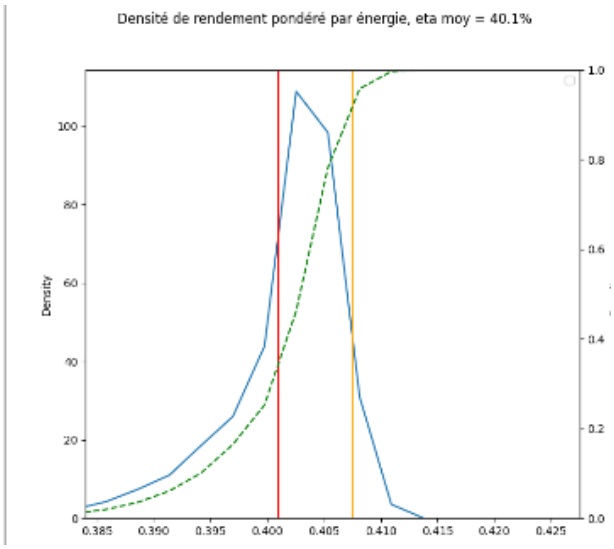


Figure 15 : New Renault Austral

And ICE efficiency measurement on WLTP

Midterm improvements are also on-going to extend the line-up :

- new ETECH system with a rear electric powertrain.

- a new optimized B/C system with top level ICE and a new axial flux e-motor.

Confidential C

5. Acknowledgement:

The authors acknowledge AVL LMM teams for their contribution in the optimization process.

6. References:

[1] FREMAU, KETFI-CHERIF, CAILLETON, MUKUNDAN

SIA 2019

Renault New dedicated hybrid transmission for B and C segment

[2] FREMAU/KETFI-CHERIF/VIGNON:

SIA 2017

2L/100km Eolab to global PHEV-HEV project solution

[3] FREMAU/KETFI/ONOYAMA/VIGNON

CTI Shanghai 2016

Alliance Renault/Nissan high performance and low cost PHEV transmission for EOLAB and some others vehicles

[4] MIRO-PADOVANI/COLIN/KETFI/COLLIN /CHAMAILLARD

PUBLICATION 2015

Implementation of an Energy Management Strategy for Hybrid with Drivability Constraint

[5] KETFI-CHERIF

THESE DOCTORAT 1999

Modélisation mathématique d'organes de véhicule automobiles à basse consommation. Applications en simulation, estimation et commande

8. Glossary

EV: electric vehicle

ICE: Internal combustion engine

HEV: Hybrid Electric Vehicle

P-HEV: Plug-in Hybrid Electric Vehicle

Confidential C

Valeo hybrid solutions for Commercial Vehicle

Benoist AUFFRAY[1], Loïc VASSIEUX[1], Arame DIOP[1]

1: VALEO Transmissions Centre Technique, Z.I. Nord. Rue de Poulainville, BP 926, Cedex 1

Abstract: To cope with regulation demands on CO_2 reduction for Commercial Vehicles, Valeo develops plug and play electrical modules for transmission hybridization from base technical bricks to a fully integrated system.

The presentation illustrates two optimized architectures for hybrid truck: 48V and High Voltage. The target is to recover free energy for higher board network demand and increase drivetrain efficiency. Moreover High Voltage allows zero emission driving for last miles delivery. These two solutions bring CO_2 reduction while matching TCO target.

VALEO expertise on transmission and electrical machines cope with compatible architectures on all truck makers platforms.

Improvements in efficiency and resulting range increase on the VECTO cycle are shown in detail.

Keywords: Hybrid, Commercial Vehicle, 48-Volt, High Voltage, Gearbox.

1. Introduction

The Valeo hybrid systems from 48-Volt up to 800-Volt can bring the contribution to fuel savings and CO_2 reduction to cope with future environmental requirements by 2025 (-15%) and 2030 (-30%) [1]. Valeo hybrid solutions are easy to connect to the standard AMT gearbox (Automated Manual Transmission) and bring progressive improvement with adaptive functions.

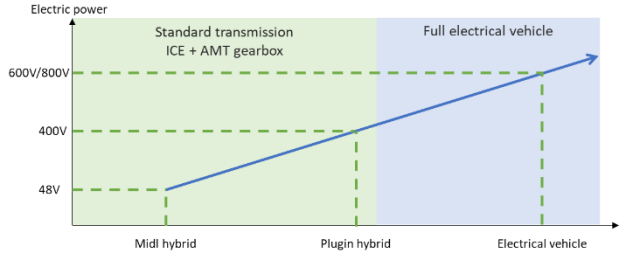


Figure 1: Electrification roadmap for commercial vehicle

First level is the 48-Volt P2.5 concept (Figure 2) with one 48V e-motor (electrical motor) and two speeds gearbox connected with PTO AMT gearbox (Power Take Off). It brings power for the future need in 48-Volt network, like electrical steering, brake compressor, engine cooling, heater catalyst, etc… And it has the capacity to turn off the ICE in coasting phase (Eco-Roll).

Second level is the High Voltage P2.5 & P3 (Figure 2) concept with two e-motors and one gearbox connected to the AMT gearbox countershaft or output shaft. It increases the hybridization for the truck, with more functions and emissions gain. The Valeo High Voltage module runs in Zero Emission Area up to 45kph to combine long range and last delivery mileage.

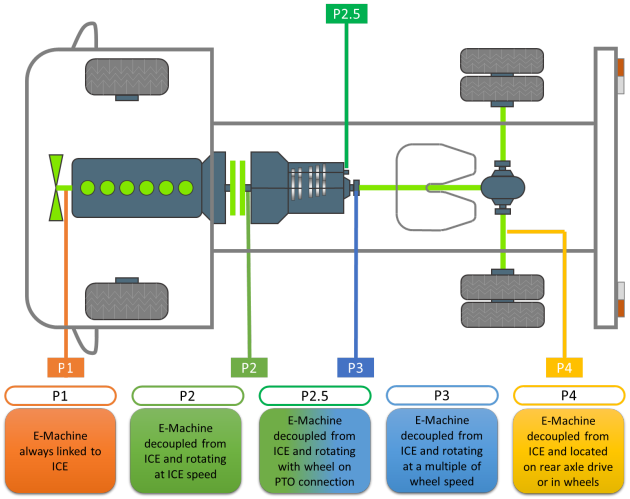


Figure 2: Hybrid architectures for Commercial

2. Valeo 48-Volt solutions

2.1. Valeo architecture solution

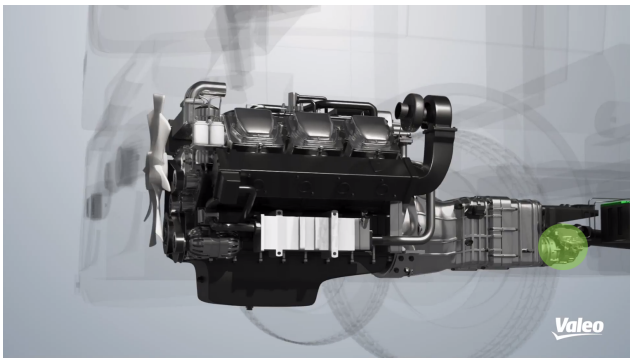


Figure 3: Driveline integration

The module (Figure 3) combines :

- A two speed gearbox developed in two architecture types: epicyclic gear set for compact or layshaft gear set for affordable solution (Figure 4). One speed is dedicated to shifting management and recovery energy and the second is for the ICE start.

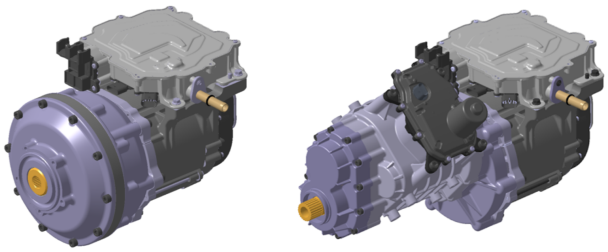


Figure 4: Epicyclic gear (2 speeds) and layshaft gearbox (2 speeds)

- A Valeo 25kW e-motor (Figure 5) permanent magnet with maximum speed 20 000 rpm. It is designed with an integrated inverter. See below the characteristics of e-motor.

Valeo 48V motor & inverter	
Motor type	DMG 25 KW 48V
Inverter type	IPM, integrated inverter
Winding type	2x3 phases / 4 Upin
Cooling	Water cooling
Length	77mm
Stator external diameter	Ø 161mm
Weight	21.7 kg
Power @ 48V 70°C	25 kW
Max speed	20 000 rpm

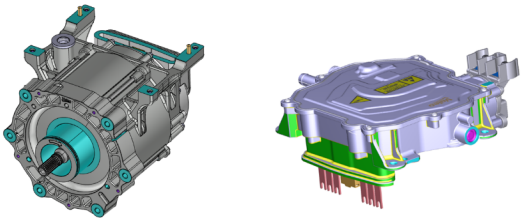


Figure 5: Motor and inverter 48V

- A wet clutch brake (Figure 6). The clutch allows to optimize the connection of the 48V module, reducing the operating time of the electrical engine from 30 000 hr to 8 000 hr. This allows to use passenger car electrical engine, to the benefit of cost. The brake is used for safety condition when the battery is full.

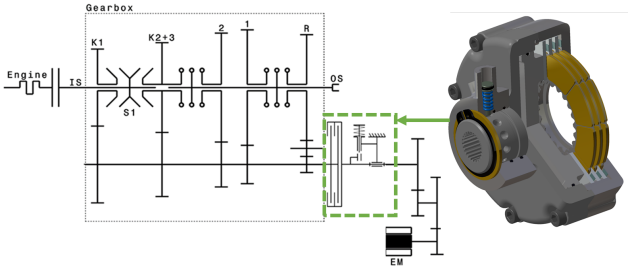


Figure 6: Wet clutch brake

2.2. Valeo 48-Volt architecture option

In addition to the 48-Volt module, the multi wet clutches are developed to maintain the PTO connection (Figure 7). Consequently, different peripherals can be connected to the PTO output.

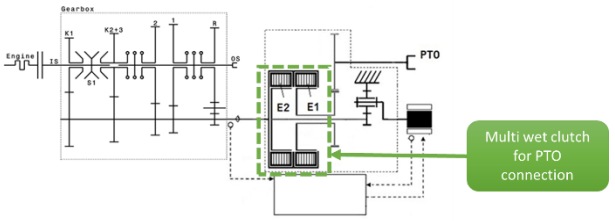


Figure 7: Multi wet clutches for PTO connection

2.3. Technical benefits

The first video (episode I) from Valeo explains all the functions for the 48-Volt module:

- The strategic P2.5 position optimizes the gear shifting speed management. For the upshift, the 48-Volt module replaces the layshaft brake. For the downshift, it accelerates the AMT countershaft to allow a fast and efficient synchronization of dog clutch. No more double declutching is necessary. The shifting time is reduced by up to 35%.
- Regenerative mode recharges the battery with free energy, during downhill or deceleration phase.
- Generation mode can be used at any time to recharge the battery with ICE power.
- Torque assist mode optimizes ICE: to generate downspeeding at low ICE speed, or downsizing on the ICE operated speed range.
- Stop and start mode in start up or coasting phase (Ecoroll), allows to remove the standard starter.

2.4. Benefit performance with VECTO profile

In this chapter, simulation results will be presented and explained. In the first step, the procedure used for simulation is presented (simulation tools, truck application target and speed profiles). In a second time, simulation results for conventional truck and 48-Volt hybrid truck are presented and analyzed. Finally, a battery sensitive analysis will be studied to show sub components constraints on CO_2 emissions values.

In order to assess CO_2 emissions benefit using this 48-Volt module, several simulations are run. Using VECTO (Vehicle Energy Consumption calculation TOol), a baseline application is chosen to assess the

CO_2 emissions for a conventional heavy duty 44T truck [2]. VECTO is a simulation tool developed by the European Commision and is used to assess CO_2 emissions and fuel consumption of heavy duty vehicles.

For this 44 Tons vehicle category, two speed profiles are identified: the long haul speed profile and the regional speed profile (Figure 8). Long haul speed profile is used to simulate vehicles on highway. During almost all the time, the vehicle is at its maximum speed (85 kph). The average speed is 80 kph. Regional delivery is used to simulate a mixed road profile with more restarts of the vehicle. Its average speed is 60 kph.

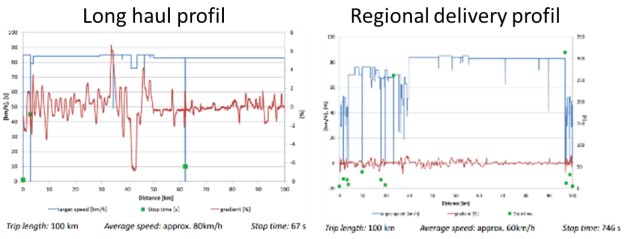


Figure 8: VECTO mission profiles

With these two speed profiles, the conventional heavy duty truck is simulated using the VECTO tool. Since VECTO cannot simulate a hybrid vehicle, an internal simulation tool is used for this purpose. To assess the CO_2 emissions benefit according to the conventional (the baseline), both configurations (hybrid & baseline) are calculated with Valeo internal simulation tool. A first step of correlation between VECTO results and Valeo simulation results is necessary. This allows to have emissions benefits based on similar VECTO results using one single simulation tool.

The second step of this study is then to assess CO_2 emissions of the hybrid module. Valeo simulation tool is developed for vehicle (conventional, hybrid & electric) energy consumption and performance studies. The objective is to minimize the fuel consumption over a driving cycle taking into account the component constraints and the regulations applied to hybrid vehicles. One of the most important regulations is the battery SoC (State of Charge) balance for hybrid vehicles. It implies that the battery SoC value at the beginning of the driving cycle must be the same at the end of the driving cycle. Hybrid modes which are simulated are:

- Regenerative mode : when decelerating and slope descending
- Generation mode : when ICE is used to propel the vehicle and to recharge the battery at the same time
- Torque assist mode : when both ICE and EM are used to propel the vehicle
- Start and stop mode

In this part, two CO_2 emissions results will be presented: one with the long haul speed profile and another with the regional speed profile (Figure 9). The following figure shows the CO_2 emissions benefit for 44T trucks for each speed profile.

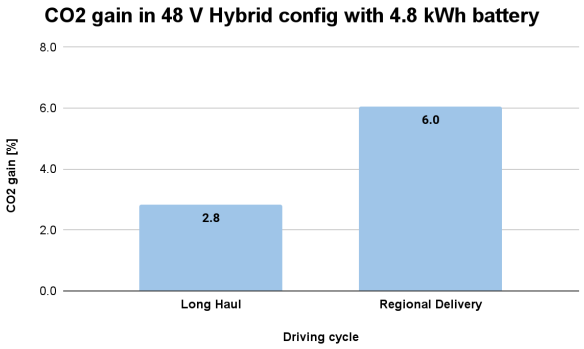


Figure 9: 48-Volt hybrid CO_2 emissions gain

In the long haul profile, the max vehicle speed is quasi maintained during the whole cycle. Consequently, few restarts and braking modes are available. It can be seen in the following figure 10 which shows where the hybrid modes are used during the driving cycle. Most of the time, the vehicle is in generation mode and the few regenerative modes available are used to recharge the battery.

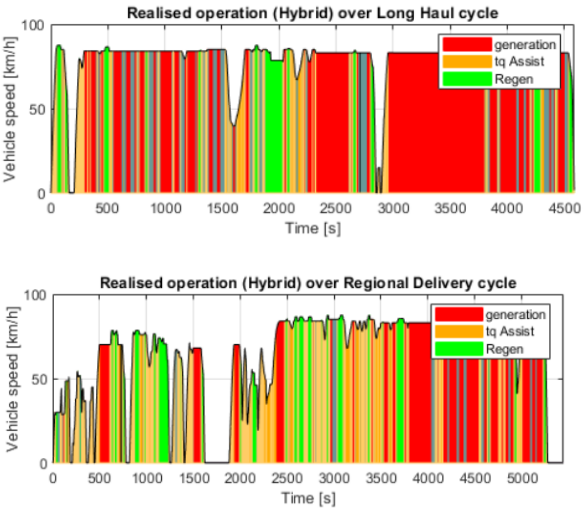


Figure 10: 48-Volt hybrid modes on speed profile

However, more benefit is reached in the regional delivery, which is more dynamic with more speed variations. Consequently, more regenerative braking is possible in this driving cycle, which leads to more CO_2 emissions benefit.

Working points on electric machines can also be shown with the associated modes.

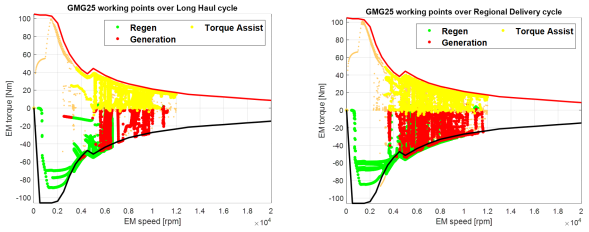


Figure 11: 48-Volt hybrid modes on electric machine

Additionally, a battery capacity study is done in order to assess the best compromise between CO_2 emissions benefit and battery energies (between 1.5 kWh and 9.5 kWh). The following figure 12 shows the CO_2 emissions gain according to the baseline for each battery energy. The study is done for the long haul and the regional driving cycle. The graphs can be split in two parts. From 1.5 kWh to near 4 kWh, it can be seen that the gain increases with the battery capacity.

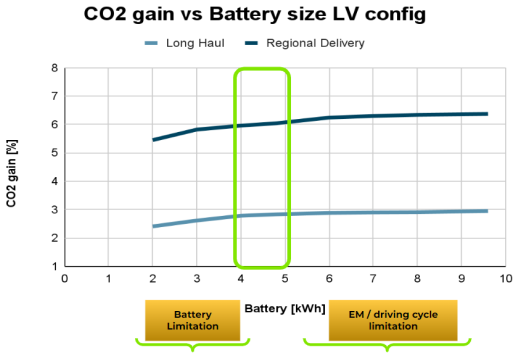


Figure 12: 48-Volt battery sensitive analysis

Above 5kWh the gain slightly increases with higher battery energy. This is due to the fact that the electric machine is already used at its maximum capacity (maximum torque used in several working points in figure 11). The driving cycle could also be part of the causes (especially for the long haul driving cycle).

In conclusion, it can be said that for 44 Tons application with this 48-Volt hybrid module, battery usable capacity between 4 kWh - 5 kWh is a good compromise to get the CO_2 emissions benefit (2.8% in long haul and 6% in regional delivery).

In addition to this result, higher gain can be reached with the 48-Volt hybrid modules with a more dynamic driving cycle.

Note that in this study, shifting management using the 48-volt module is not taken into account.

3. Valeo High Voltage solutions

3.1. Valeo architecture solution

To increase the CO_2 emission gain, it is necessary to extend the functionality and the capacity of energy regeneration. In these conditions, the Valeo High Voltage hybrid module uses high voltage e-motors (400-Volt - 800-Volt) with a connection on the AMT gearbox output shaft (P3), in addition of countershaft connection (P2.5).

The patented HV module (Figure 13) combined :

- A two speed gearbox with dog clutch. One speed for the connection to the countershaft (P2.5) and the second speed for the output shaft (P3).
- Two Valeo e-motors and inverters for heavy duty truck based on passenger car design : 300kW peak and 120kW continuous power. For medium duty trucks, only one e-motor and inverter is required.

The Valeo hybrid module is a plug-in solution with the capacity to drive in zero emission until 45kph.

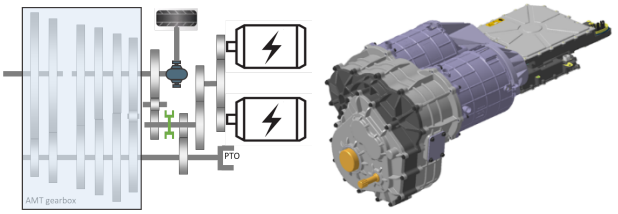


Figure 13: Valeo high voltage hybrid module

3.2. Technical benefits

Valeo hybrid module is explained and detailed in the video episode II.

The output shaft connection (P3) achieved two mains functions :

- Regenerative mode for retarder function. The two e-motors brake the output shaft during the vehicle slowdown. This regen phase recharges the battery with free energy. In standard transmission this free energy is lost and dissipated in the form of heat on the hydraulic retarder.
- Powershifting mode is a torque assist during AMT gear shifting. This solution avoids vehicle deceleration.

The countershaft connection (P2.5) achieves five functions:

- Zero emission driving mode (ZEV: Zero Emission Vehicle) up to 45kph in the urban zone where the regulation bans ICE vehicles. The truck must be a plug-in vehicle to recharge the battery during the trailer load or unload and to increase the capacity of Zero emission driving distance. The module uses the ratio of AMT gearbox with the clutch open. It is possible to switch from electrical mode to ICE mode or vice versa in driving condition.

- Generation mode can be used at any time to recharge the battery. Without plug-in facilities, it is possible to recharge the battery before driving in a low emission area.
- e-PTO mode: e-motors supply power to the PTO shaft (Power Take Off). All conventional peripheral pumps are usable.
- The Boost mode allows to optimize the ICE performance with the downspeeding or the downsizing of ICE.
- Stop and start mode stays possible, and allows to remove the standard starter.

3.3. Benefit performance with VECTO profile

In this part, the same simulation procedure as for 48-Volt simulation is used. Simulations do not take into account the plug-in function. The hybrid modes simulated are:

- Regenerative mode: retarder
- ZEV mode: the vehicle is propelled by the electric machine
- Torque assist mode
- Generation mode
- Start and stop mode

Figure 14 shows the CO_2 emissions benefit for the HV module over the long haul and regional speed profile.

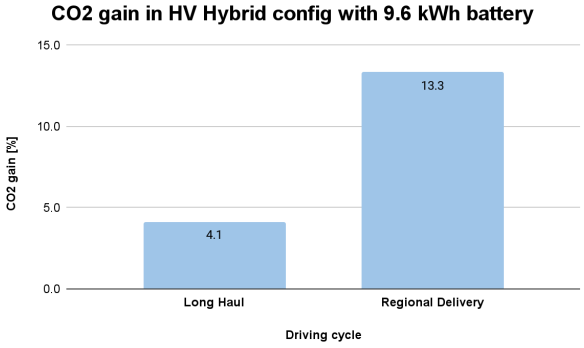


Figure 14: HV hybrid CO_2 emission benefit

While in the long haul profile, the CO_2 emissions benefit is close to the 48-Volt one, the regional speed profile one is higher. This is due to the fact that in the regional delivery driving cycle, there are more speed dynamics (acceleration, braking, restart phases) which allow different hybrid modes according to the situation. This can be more visible in the figure 15 and 16

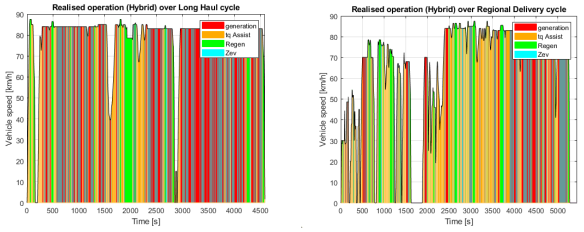


Figure 15: HV hybrid modes on speed profiles

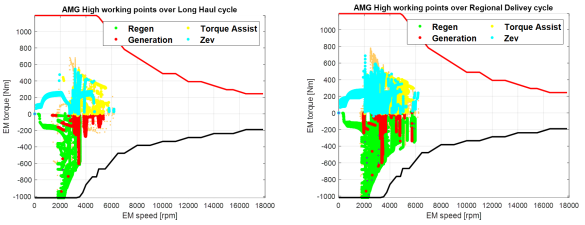


Figure 16: HV hybrid modes on electric machines

In fact, it can be seen that there are more regen and ZEV possibilities on the regional driving cycle. Consequently, these modes will generate less CO_2 emissions than conventional.

Like for 48-Volt study, a battery capacity study is also done in order to assess the evolution of CO_2 emissions. The results are shown in Figure 17. The graphs describe the CO_2 emissions benefit evolution over the increase of HV battery energy for the long haul and the regional driving cycle. In the long haul driving cycle, the emissions gain cannot exceed 6%. It can be deduced that the limit is reached given the driving cycle profile. In the regional driving cycle, from 10kWh, the increase of the battery energy provides just a little increase of the CO_2 emissions benefit. Once again, it can be said that the limit of the regional driving cycle has been reached. A good compromise between energy battery and CO_2 benefit could be between 10 and 12 kWh for the regional delivery.

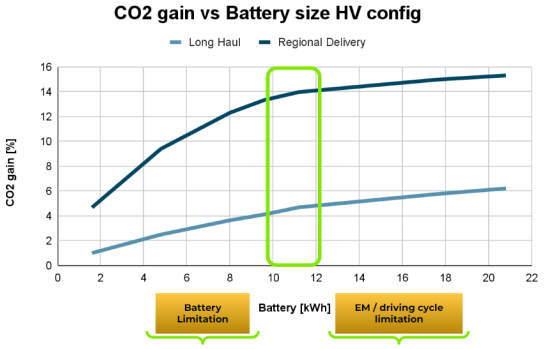


Figure 17: HV battery sensitive analysis

These CO_2 emissions gains are obtained without taking into account the plug-in function in this HV module. In addition to the technical benefits explained above, more benefits could be reached with the e-PTO function. The powershift mode, which

is not taken into account during simulations, allows to have more shifting comfort, increasing the vehicle performance.

4. Conclusion

Valeo is developing compact and flexible solutions for 48-Volt and for high voltage to cope with future regulations. These modules are easy to connect to the standard AMT gearbox.

For the 48-Volt, Valeo module includes one 25kW e-motor with two speed gearbox and a wet clutch brake connected to the countershaft, keeping the PTO and retarder connection available. CO_2 emission reduction is at least : 2.8% for long haulage and 6% for regional delivery based on the official VECTO profile. Regen free energy, generator, Torque assist, Stop&start functions are taken into account. The CO_2 reduction can increase with gear shifting management, and mission profiles with more decelerations, brakings and slopes. Additionally, this module answers to the increase of electricity on board: switch from 24-Volt to 48-Volt network.

To further increase energy efficiency and reduce CO_2 emissions, Valeo develops the high voltage plug-in module: two HV e-motors with a two speeds gearbox (One speed for the output shaft and one for the countershaft of the standard AMT gearbox). CO_2 emission reduction is at least: 4% for long haulage and 13% for regional delivery based on the official VECTO profile. Regen free energy, Zero emission driving, generator, torque assist, Stop&start functions are taken into account. The CO_2 reduction can increase with powershifting, plug-in recharge, e-PTO, and mission profiles with more decelerations, brakings and slopes.

Valeo has developed all technical bricks and systems for smart hybrid trucks.

5. References

[1] Sources: The European Union - PE_60_2019_REV_1 - REGULATION OF THE EUROPEAN PARLIAMENT AND OF THE COUNCIL SETTING CO2 EMISSION PERFORMANCE STANDARDS FOR NEW HEAVY-DUTY VEHICLES AND AMENDING REGULATIONS (EC) No 595/2009 AND (EU) 2018/956 OF THE EUROPEAN PARLIAMENT AND OF THE COUNCIL AND COUNCIL DIRECTIVE 96/53/EC - https://data.consilium.europa.eu/doc/document/PE-60-2019-REV-1/EN/pdf

[2] Sources: VECTO - Vehicle Energy Consumption tool - European commission: https://ec.europa.eu/clima/system/files/2018-12/201811_overview_en.pdf

6. Glossary

PTO:	Power Take Off
AMT:	Automated Manual Transmission
ICE:	Internal Combustion Engine
e-motor:	Electrical motor
LV:	Low Voltage
HV:	High Voltage
ZEV:	Zero Emission Vehicle

Dynamic Simulation using ECMS Controller with Integrated Vehicle Thermal Management to Optimize the HEV Fuel Economy on a Real-Driving Cycle

M. Zagun[1], D. Lodaya[2], M. Okarmus[2], J. Zeman[2], S. Vankayala[3], P. De Araujo[4]

1: Gamma Technologies GmbH, Danneckerstraße 37, 701782 Stuttgart, Germany
2: Gamma Technologies, LLC., 601 Oakmont Lane, Suite 220, Westmont, IL 60559, USA
3: Garrett Motion Engineering Solutions Private Limited, 4c, RMZ Ecoworld Rd, Adarsh Palm Retreat, Bellandur, Bengaluru, Karnataka 560103, India
4: Garrett Motion France, Z.I. Inova 3000, 2 rue de l'Avenir, Thaon-les-Vosges, 88155, France

Abstract: Fleet electrification requires to effectively manage the onboard energy sources of hybrid vehicles. Battery-electric hybrid powertrains allow multiple operating modes, which are crucial to fuel economy and emissions. The concept of optimal controls offers insights into improving the present state-of-the-art supervisory control strategies, whether as benchmarking or even as an integral part. On-line adaptation of the supervisory control strategy to cover all possible driving manoeuvres with the goal of minimizing energy consumption while sustaining the electric battery charge is a fundamental requirement.

In this paper, a novel model-based on-line Equivalent Consumption Minimization Strategy (ECMS) controller is implemented on a dynamic forward-facing simulation model of a P2 hybrid vehicle. The model integrates a high-fidelity vehicle thermal management ('VTM') and aftertreatment ('AT') system, which offers realistic response dynamics and thermal effects. The novel approach dispenses the need of a priori calculated optimal control inputs, and thus, offers a significant workflow improvement. The resulting control policies, subjected to standard regulatory as well as real-world driving cycles are compared against control policies obtained from an off-line ECMS and Dynamic Programming ('DP') algorithms.

It is shown that real-world driving offers additional leverages in terms of projected vehicle routes, driver behaviour and traffic information to improve the energy management strategy. The results give insights into how real-world driving and on-line adaptive supervisory controls affect the fuel economy compared against standard regulatory cycles.

Keywords: Hybrid Powertrain, Optimal Controls, ECMS, Dynamic Programming, Fuel Economy

3. Introduction

This paper focuses on the energy management task and its integration with the VTM task for a plug-in hybrid electric vehicle ('PHEV'). The supervisory control concept is based on ECMS, which means the selection of a locally optimal operating mode based on the variation of admissible control input and the evaluation of an associated cost function. The cost function relates the battery energy consumption and the engine fuel consumption, by means of the efficiency chain of the hybrid drivetrain.

The integration of the VTM task with the supervisory control concept ECMS is applied to an integrated modelling and solution approach of the hybrid drivetrain system, the VTM system, the AT system, the supervisory controls and the component-level controls using the system simulation software GT-SUITE from Gamma Technologies, LLC.

The model structure of the integrated ECMS controller and the features of the solution algorithm are oriented on the concepts from literature [1] and which is illustrated in Figure 1.

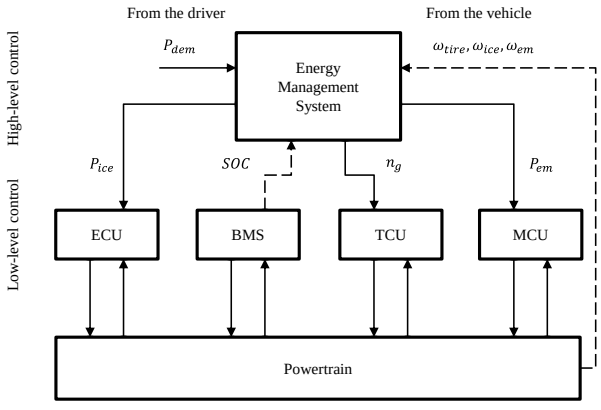


Figure 1: Two-layer control structure in a hybrid vehicle

2. Vehicle Model

The dynamic simulation model represents a P2 PHEV topology with an integrated VTM and AT model. The energy storage, the energy transformers, the drivetrain and the vehicle are represented by phenomenological, data based, mechanically rigid component models. The VTM model consists of multiple thermal circuits, which components are

represented by phenomenological, data-based and physical component models. Figure 2 shows the basic subassembly structure of the vehicle simulation model. The thermal losses from the hybrid drivetrain are imposed onto the VTM model. In return all major electric power consumers are considered as battery terminal load.

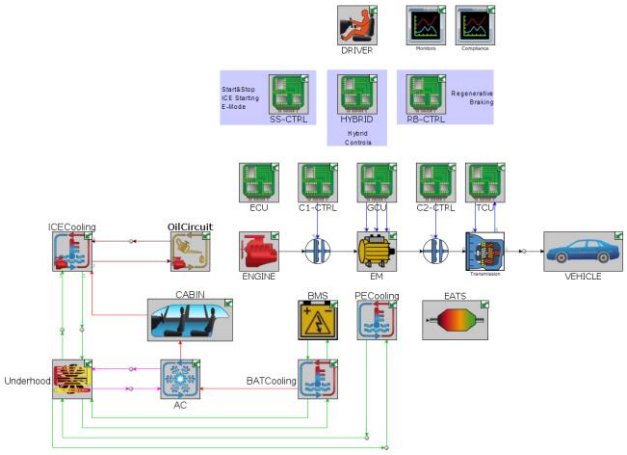


Figure 2: Simulation model of the P2 hybrid drivetrain topology with an integrated thermal management system model.

The vehicle model controls consist of the driver model, the supervisory controls and the subordinate component-level controllers for the internal combustion engine ('ICE'), the transmission, the clutches and the mechanical brakes.

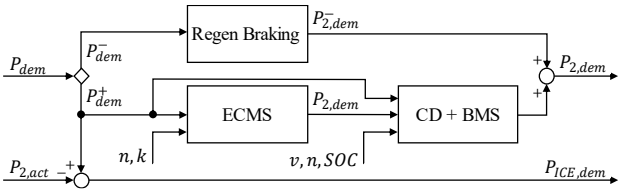


Figure 3: Supervisory Controls with integrated ECMS controller.

Figure 3 shows the supervisory controls including the ECMS controller for the purpose of hybrid power split and additional rule-based controls, for the purpose of enabling electric drive (CD mode), regenerative braking, ensuring battery state of charge stays within desired range and gear number selection. During the first period of this project and for comparability to the previous off-line ECMS approach, the structure of the supervisory controls is retained.

The novel model-based ECMS controller replaces the concept of off-line ECMS and power split maps, which need to be evaluated a priori based on stationary operating conditions and control inputs and which are invoked by means of multidimensional lookup and interpolation methods. Following a previous proof of concept [2] the novel model-based ECMS controller utilizes a surrogate model of the underlying dynamic hybrid drivetrain, which is illustrated in Figure 4.

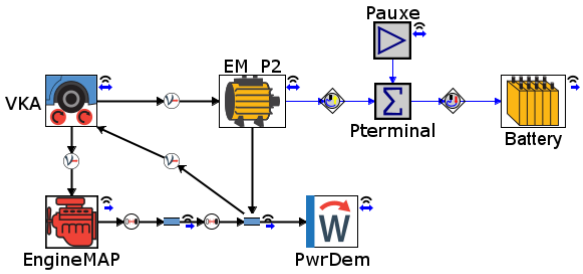


Figure 4: Model-based ECMS Controller: Surrogate model of the P2 hybrid drivetrain topology.

The surrogate model evaluates the efficiency chain and the energy consumptions based on a backward-facing kinematic solution approach at every update interval. The execution of the ECMS controller makes use of a co-simulation approach between the dynamic forward-facing vehicle model and the backward-facing kinematic surrogate model. Each update interval comprises a sequence of steps, which are the reinitialization of the backward-facing kinematic surrogate model, the solution of the ECMS algorithm for a single time step and the return of optimal controls to the dynamic forward-facing vehicle model. The reinitialization approach ensures a tight alignment of the surrogate model operating conditions and consequently the relevance of the returned optimal controls. The backward-facing kinematic solution considers all relevant inertias within the drivetrain with the target to account for the exact power demand during the acceleration of the system and all electrical auxiliary loads to account for the optimal power split.

This approach is proposed as a robust alternative to creating multi-dimensional lookup maps which may need to be retuned for each unique drivetrain specification.

3. Problem Statement

3.1 Equivalent Consumption Minimization Strategy

The Equivalent Consumption Minimization Strategy, which goes back to the work of Paganelli [3], [4] constitutes a local minimization problem. It considers the current system state x and the cost J, which is associated with the control input u.

$$\int_0^{t_f} \min_{u(t)} J(x(t), u(t), t)\, dt \qquad [1]$$

Following the notion that for a charge sustaining ('CS') operating strategy the net sum of electrical power consumed from and replenished to the electrical energy storage is zero, and that finally all replenished electrical energy originates from the conversion of

onboard fuel and the recuperation of kinetic energy, the internal battery power P_{bat} is transformed to an 'electrical' fuel consumption by means of the equivalence factor k. Consequently, the cost function is defined from these two objectives, the fuel consumption $\dot{m}_f$ and the internal battery power and represents an equivalent fuel consumption $\dot{m}_{eqv}$. [1]

$$J(x(t), u(t), t) = \dot{m}_{eqv}(x(t), u(t), t) = \dot{m}_f(u(t), t) + k(t) \cdot P_{bat}(x(t), u(t), t) \quad [2]$$

The control input is discretized and considers the system constraints. For each given time instance, all control input combinations are evaluated to calculate the resulting cost. The admissible control input combination with the least cost is deemed the local optimal control policy. In the context of the energy management task in a modern hybrid vehicle the power split between the ICE and the electric machine ('EM') represents the control input and the battery state of charge ('SOC') represents the system state.

With the target to sustain the battery SOC within a desired range and any driving condition, the equivalence factor k must be dynamically adapted. One approach to do so, consists in adapting k using an auto regressive moving average concept at a discrete update interval Δt, as depicted in [6].

$$k(t) = \frac{k(t - \Delta t) + k(t - 2 \cdot \Delta t)}{2} + C_p \cdot \left(SOC_{target} - SOC(t)\right) \quad [3]$$

The novel ECMS controller is expected to offer additional functionalities and will allow to migrate switching between electric and hybrid drive, gear number selection and regenerative braking from the existing supervisory control. Therefore, the ECMS Controller offers the application of additional control inputs, switching frequency and change rate constraints, penalties on control inputs and constraints on dependent variables but also the utilization of a custom cost function.

3.2 Dynamic Programming

DP as a global optimization strategy goes back to the work of Richard Bellman and constitutes a numerical method for the solution of a multi-stage decision making problem [5]. It considers the dynamic nature of the underlying system and derives the global optimal control policy for an a priori known manoeuvre by operating backwards in time according to Belman's principle of optimality. The states of the system x and the control inputs u are discretized and are subjected to the system constraints. The implementation of DP optimization algorithm in GT-SUITE can be summarized into three steps. In the first step, the discrete transitional costs of advancing the plant model from time t_i to t_{i+1} over the entire time horizon are computed for each combination of specified system states and admissible control inputs. In the second step, all control policy variants are evaluated considering the cost J of the state they are originating from and the change of state they are causing to arrive at the Optimal Cost-to-Go. Finally, in the third step, the control policy corresponding to the lowest cumulative cost is calculated and deemed the global optimal control policy. For the detailed description of the optimal control problem and for the holistic overview of the deterministic DP algorithm, the interested reader is referred to [7].

In the context of the energy management task in a modern hybrid vehicle the battery state of charge and the gear number represent the system states x and the power split between the combustion engine and the electric machine and the gear number represent the control inputs u.

The DP solution states a well-recognized control policy benchmark due to delivering superior fuel consumption savings. It conducts a huge computational effort and requires the a priori knowledge of the manoeuvre.

4. Results

4.1 Dynamic Programming

The DP solution is applied to the regulatory (WLTC (Class 3)) and a selected real driving emissions ('RDE') drive cycle with the purpose to derive a global optimal control policy under the premise of ensuring battery charge sustainance ('CS'). The cost function coefficients and their values are listed in Table 1.

The DP solution is segregated from the solution of VTM system and the electrically heated AT system. Consequently, the according electrical auxiliary loads are unknown and disregarded in the initial step. As such, the estimated fuel economy and emissions may be considered as too optimistic. The impact of the according auxiliary loads on the DP solution will require an iterative solution sequence of DP and VTM, but which is not part of this project.

Table 1. Coefficients for DP solution

Coefficient	Condition
SOC_{target}	0.2 ± 0.1
SOC state resolution	2%
Penalty Function Exponent α	2
$Penalty\ Function\ Weight\ \lambda$	4
$Terminal\ State\ Penalty\ Exponent\ \beta$	2
$Terminal\ State\ Penalty\ Weight\ \gamma$	600,000

Figure 5 and Figure 6 show the time series of the control input and the main result variables for the two drive cycles WLTC and RDE.

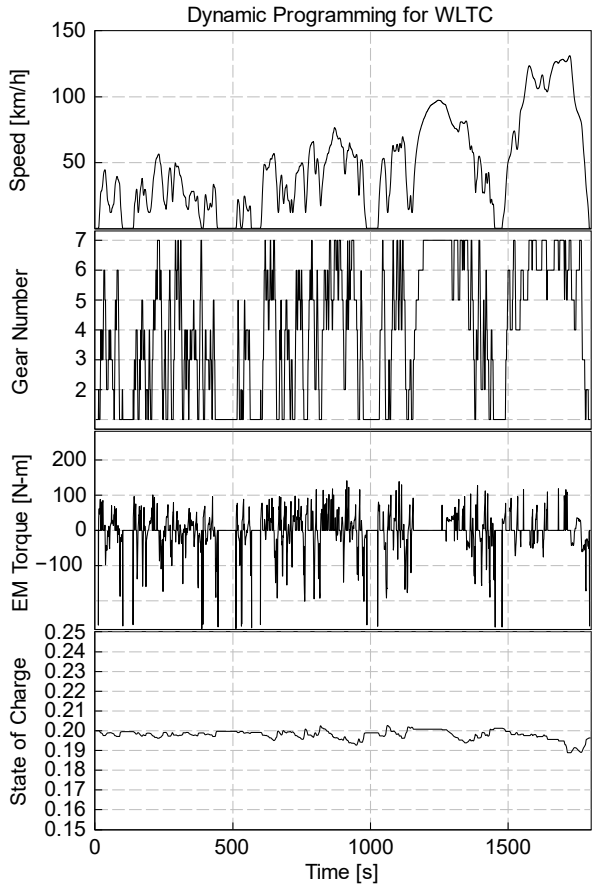


Figure 5: Control policy derived from DP solution for the WLTC drive cycle.

The fuel economy and CO_2 emissions are summarized in Table 2**Erreur ! Source du renvoi introuvable.**.

Table 2: Fuel economy and CO_2 emissions

Cycle	Fuel consumption*	CO2* (fuel eq.)
WLTC	5.9 l/100km	134 g/km
RDE	7.0 l/100km	159 g/km

* disregarding energy consumption from auxiliaries

4.2 ECMS Controller

Finally, the ECMS Controller solution is applied to the same regulatory and RDE drive cycle with the purpose to derive a local optimal control policy under the premise of CS. The cost function coefficients and their values are listed in Table 3. In contrast to the DP solution the gear shifting strategy is still rule-based and not part of the ECMS solution. In addition, the integrated VTM and AT control strategies lead to an overall mean electrical load of 3.2 kW (WLTC) and 2.9 kW (RDE), which roughly accounts for 2.6 l/100km (WLTC) and 2.2 l/100 km (RDE) higher fuel consumption.

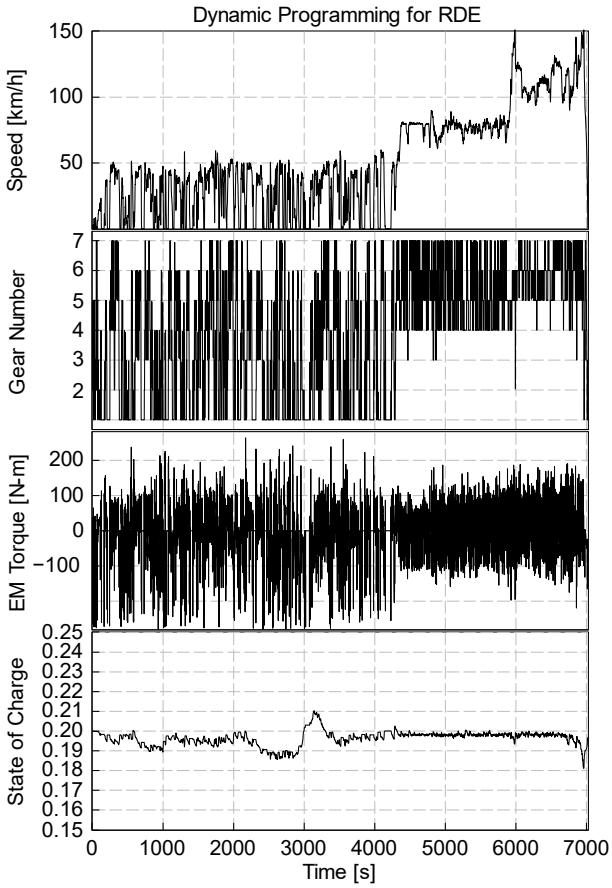


Figure 6: Control policy derived from DP solution for a selected RDE drive cycle.

Table 3: Coefficients for ECMS Controller solution

Coefficient	Condition
Initial equivalence factor k	232 g/kWh
Proportional constant c_p	450 g/kWh
Update Interval Δt	30 s

Figure 7 and Figure 8 show the time series of the control input and the main result variables for the two drive cycles WLTC and RDE. The fuel economy and the tail pipe emissions are corrected with respect to SOC deviation and summarized in Table 4**Erreur ! Source du renvoi introuvable.**.

Table 4: Fuel economy and tailpipe emissions

Cycle	Fuel consumption	CO2	NOx
WLTC	8.8 l/100km	188 g/km	192 mg/km

RDE	8.8 l/100km	189 g/km	204 mg/km

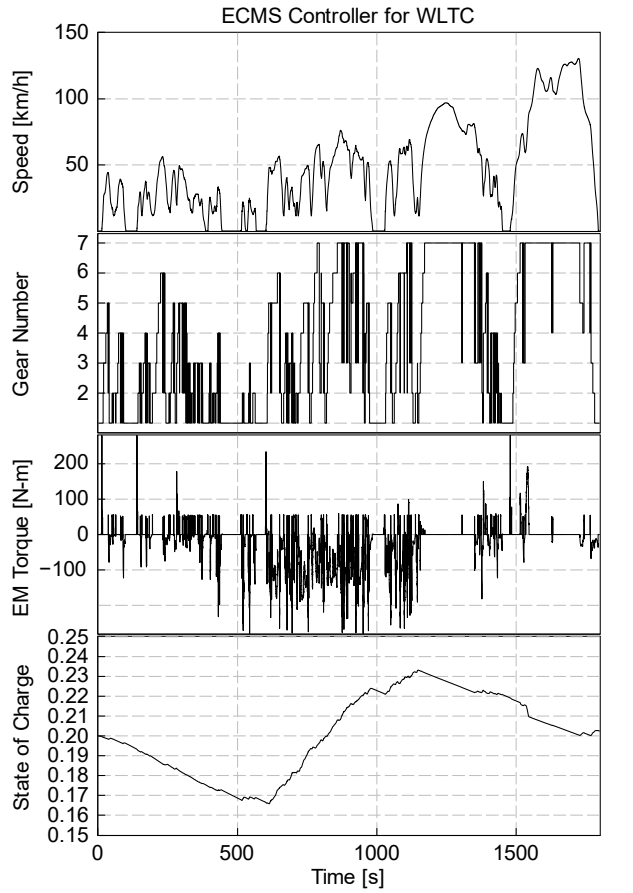


Figure 7: Control policy derived from ECMS Controller for the WLTC drive cycle.

In addition, the local optimal control policy, which is derived from the novel model-based ECMS Controller is compared to the output of the reference off-line ECMS power split maps.
The correlation plots in Figure 9 show a close correlation in a wide range of operating conditions. Minor deviations are expected from the consideration of inertial effects and the electrical auxiliary loads within the solution approach of the novel model-based ECMS controller.

5. Conclusion

A supervisory control concept based on the Equivalent Consumption Minimization Strategy is successfully realized by means of an integrated ECMS controller in the system simulation software GT-SUITE. The introduced approach integrates the VTM task with the supervisory control concept of ECMS, which results in a holistic and integrated modeling and solution approach of the hybrid drivetrain system, the VTM system, the AT system, the supervisory controls and the component-level controls of the PHEV.

The novel model-based concept of the ECMS Controller leverages the integration of the on-line

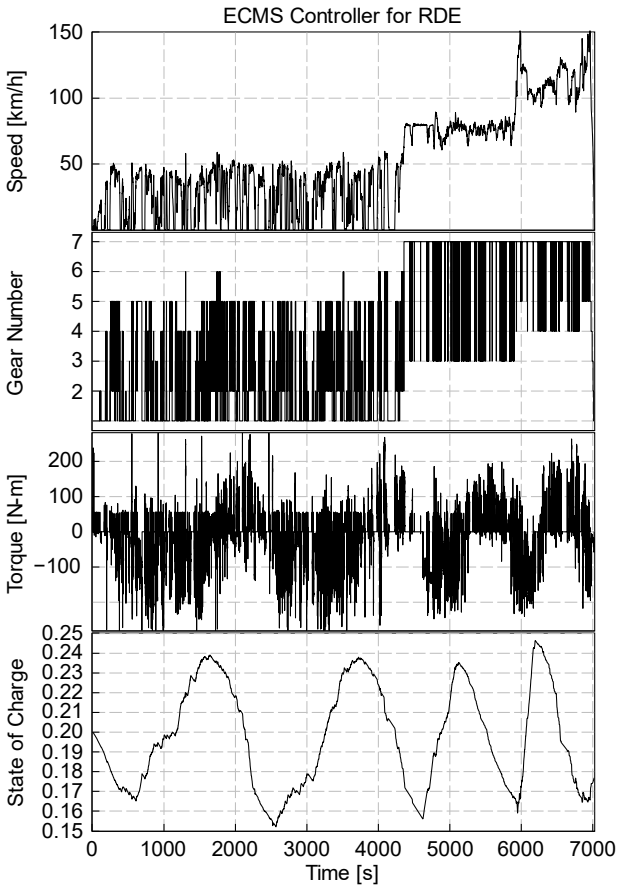


Figure 8: Control policy derived from ECMS Controller for a selected RDE drive cycle.

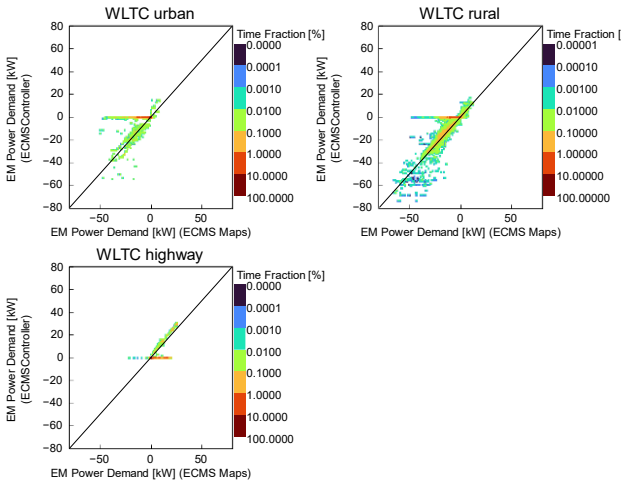


Figure 9: Correlation Plot for control policy based on ECMS Controller.

ECMS control strategy into the forward-facing multi-physics dynamic vehicle simulation by dispensing the effort required for the setup of the off-line ECMS approach. This improves the overall workflow and the

predictiveness of the solution approach during the supervisory controls design phase.
During this period of the project and for the task of on-line hybrid power split the novel model-based ECMS Controller correlates well. In addition, it allows to account for drivetrain inertias and all electrical consumers with the target to evaluate the local optimal power split.

6. Outlook

The novel model-based concept of the ECMS Controller will allow to include a more complex supervisory control definition during the further progress of this project, including local optimal switching between electric and hybrid drive, gear number selection and regenerative braking. Further, it is anticipated to investigate how the model-based ECMS Controller solution can leverage the optimal control policy with respect to battery thermal management and exhaust aftertreatment specific objectives.

7. Acknowledgement

The author likes to thank all contributors to this project for their consent. Especially, to the development departments from Gamma Technologies, which were involved in the implementation of the novel co-simulation-based ECMS Controller solution. Last but not least, a special thanks to the R&D departments at Garrett Motion for providing a well-defined and detailed vehicle system model.

8. References

[1] S.Onori, L.Serrao, G.Rizzoni: "*Hybrid Electric Vehicles*", Chapter. 3.2, page 32, Springer, 2016.

[2] M.Zagun: "*Holistic Optimization of Energy Consumption of a Hybrid Powertrain with an "Equivalent Fuel Consumption Minimization Strategy" Algorithm*", Proceedings of the 21. International Stuttgart Symposium, Volume 2, Springer, 2021.

[3] G. Paganelli, T. M. Guerra, S. Delprat, J.-J. Santin, M. Delhom and E. Combes: *"Simulation and Assessment of Power Control Strategies for a Parallel Hybrid Car"*, SAGE Proceedings of the Institution of Mechanical Engineers, Part D: Journal of Automobile Engineering, pp. 705-717, 2000

[4] G. Paganelli, M. Tateno, A. Brahma, G. Rizzoni and Y. Guezennec: *"Control Development for a Hybrid-electric Sport-Utility Vehicle: Strategy, Implementation and Field Test Results",* IEEE Proceedings of the 2001 American Control Conference, pp. 968-973, 2001

[5] R. Bellman, *"Dynamic Programming"*, New York: Princeton University Press, 1957

[6] S. Onori, L. Serrao, G. Rizzoni, *"Adaptive Equivalent Consumption Minimization Strategy for Hybrid Electric Vehicles"*, Proceedings of the ASME DSCC, 2010

[7] Lodaya, D., Zeman, J., Okarmus, M., Mohon, S. et al., *"Optimization of Fuel Economy Using Optimal Controls on Regulatory and Real-World Driving Cycles"*, *SAE Int. J. Adv. & Curr. Prac. in Mobility* 2(3):1705-1716, 2020

9. Glossary

AT: Exhaust aftertreatment
CD: Charge depleting
CS: Charge sustaining
DP: Dynamic Programming
ECMS: Equivalent Consumption Minimization Strategy
EM: Electric machine
ICE: Internal combustion engine
PHEV: Plug-in hybrid vehicle
RDE: Real-driving emissions
SOC: State of charge
VTM: Vehicle thermal management
WLTC: Worldwide Harmonized Light Vehicles Test Cycle

15 JUNE 2022

ELECTRIC MOTOR



INNOVATION
THAT MOVES US

RICARDO ENABLES OUR CUSTOMERS TO SOLVE THE MOST COMPLEX CHALLENGES TO ACHIEVE A SAFE AND SUSTAINABLE WORLD

Our strategic and technical experts define future technologies to ensure sustainable, scalable solutions for our global customers. We tailor bespoke solutions that help to address the world's energy and mobility challenges, accelerating your journey from concept to implementation and beyond.

Together, we innovate what moves us.

CONTACT RICARDO TO LEARN MORE
INFO@RICARDO.COM | +44 (0)1273 455611 | RICARDO.COM

Calibrating Optimal PMSM Torque Control with Field-Weakening Using Model-Based Calibration

Dakai Hu and Kevin Roblet
The MathWorks Inc

Abstract: Permanent magnet synchronous motor (PMSM) calibration is an indispensable step in the design of high-performance electric traction drive controls. Traditionally, the calibration process involves extensive hardware dynamometer (dyno) testing and data processing, and its accuracy depends largely on the expertise of the calibration engineer. Model-based calibration standardizes the PMSM calibration process, reduces unnecessary testing, and generates consistent results. It is an industry-proven, automated workflow that uses statistical modeling and numeric optimization to optimally calibrate complex nonlinear systems. It can be used in a wide range of applications and is well known for being adopted in internal combustion engine control calibration. When applied to e-motor control calibration, the model-based calibration workflow can help motor control engineers achieve optimal torque and field-weakening control for PMSMs.

Keywords: PMSM, traction drives, dynamometer testing, field-weakening control, model-based calibration.

1. Introduction

PMSMs stand out from other types of e-motors because of their high efficiency and torque density. This is because the permanent magnets inside the machine can generate substantial air gap magnetic flux without external excitation. This special trait makes PMSM an excellent candidate for both traction and non-traction motor drive applications.

Most non-traction PMSM applications only require the machine to operate in the constant torque region, where its control scheme is relatively straightforward. Traction PMSM control, in addition to fast dynamic response, also requires accurate torque output and wide constant power-speed range (CPSR) operation. To achieve these control goals, particularly in an electric or hybrid electric vehicle, the traction PMSM must be able to operate in the field-weakening region, where tradeoffs need to be made between torque, speed, and efficiency.

A huge part of designing a high-performance field-weakening control algorithm is calibrating the field-weakening control lookup tables. Before generating the table data, PMSM characterization tests often need to be performed either using a dyno setup or through an FEA tool like ANSYS Maxwell or JSOL JMAG. After PMSM characterization testing, flux linkage tables and measured torque at different current and speed operating points can be obtained. Here we need to distinguish PMSM characterization from calibration. PMSM characterization involves performing a series of tests either on a dyno or using an FEA tool, with the goal of extracting important machine information, such as flux linkage and torque. PMSM control calibration involves calculating controller lookup tables that will generate maximum torque or optimal efficiency at different operating points. The control calibration process usually happens after PMSM characterization. Both processes are required for high-performance PMSM control design.

2. The Model-Based Calibration Workflow

The Model-Based Calibration workflow is designed to optimally calibrate the control of complex nonlinear systems using statistical modeling and numeric optimization. It can be used in a wide range of applications and is well-known for its adoption in internal combustion engine control calibration. When applied to PMSM control calibration, the model-based calibration workflow usually involves four steps (Fig. 1):

1. Design the experiment for characterization.
2. Preprocess the PMSM characterization dataset.
3. Fit PMSM characterization models.
4. Optimize PMSM controller lookup table data.

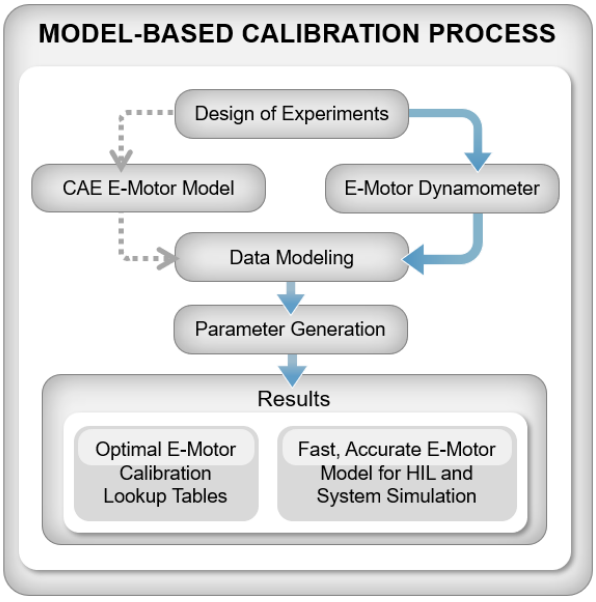


Fig.1. Model-Based Calibration workflow for PMSM control calibration

2.1 Designing the Experiment for Characterization

Full factorial characterization on a physical dyno is wasteful because it increases experiment time, cost, and maintenance. In model-based calibration, statistically spaced operating points are proposed as characterization testing points (Fig. 2). Whether the experiment is carried out on a physical dyno or in an FEA environment, the generated testing points of current id and iq will be given as control commands and the PMSM speed will be regulated by the dyno machine or set in the FEA tool. Using a virtual dyno requires a detailed PMSM FEA model. However, once the model is created, it can be tested over a more comprehensive set of operating points without incurring additional cost overhead.

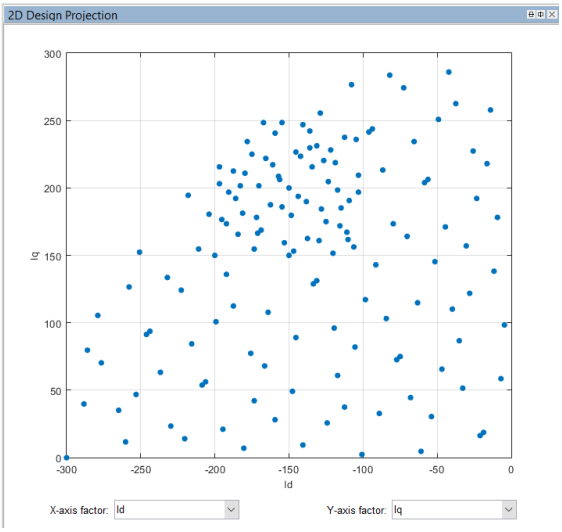


Fig. 2. Example of proposed operating points for characterization testing

2.2 Preprocessing PMSM Characterization Dataset

During PMSM characterization, torque and dq-axis flux linkage data is either directly measured on a dyno or derived from an FEA tool for each operating point of id, iq, and speed. After characterization, the dataset is rearranged by torque contours and speed steps, and each variable (for example, torque) is stored in a single-column format, which is then imported into Model-Based Calibration Toolbox™ (Fig. 3). If necessary, additional analysis can be performed to remove outlying data. Outliers are common during physical testing due to noise and measurement error.

2.3 Fitting PMSM Characterization Models

Model fitting is a crucial part of the model-based calibration workflow. (Note that the models referred to in this article are not electric motor or its controller models; they are statistical models in which functions such as Gaussian process regression or radial basis function represent the relationship between variables in the imported dataset.) Specifically, two sets of models are created: iq as a function of id and torque, and voltage margin as a function of id and torque. Each is modeled at a common set of motor speeds. These speed points are used as breakpoints for final controller

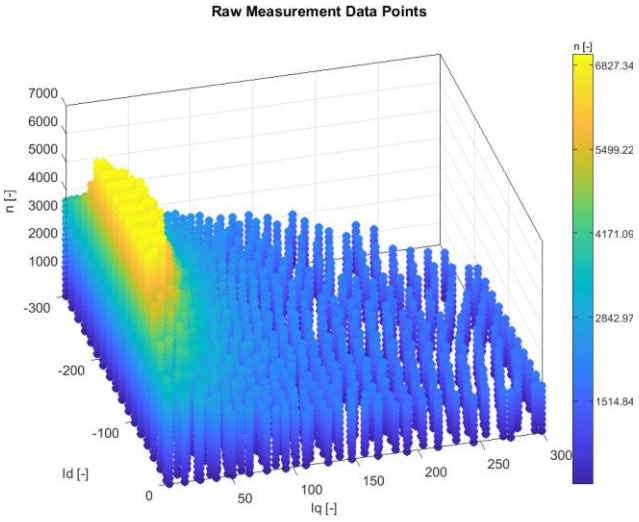


Fig. 3. Dataset of operating points imported into Model-Based Calibration Toolbox

lookup tables. Fig. 4-7 are the fitted models grouped by two speed operating points:1000 rpm and 5000 rpm.

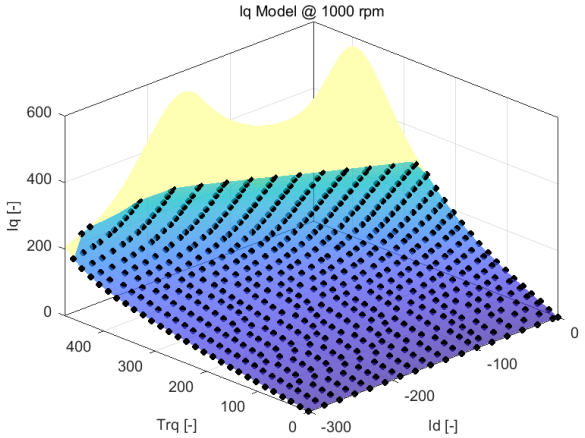


Fig. 4. Iq model at 1000 rpm operating point

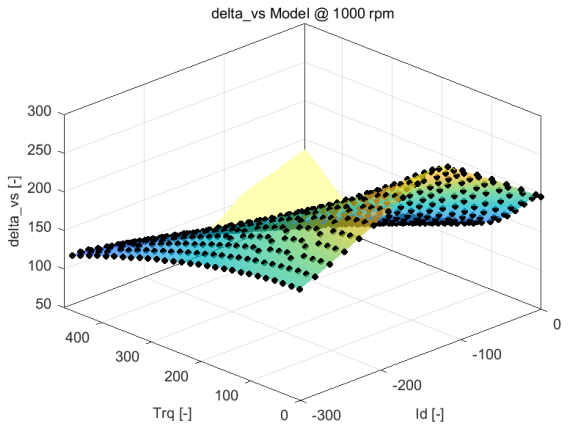


Fig. 5. Voltage margin model at 1000 rpm operating point

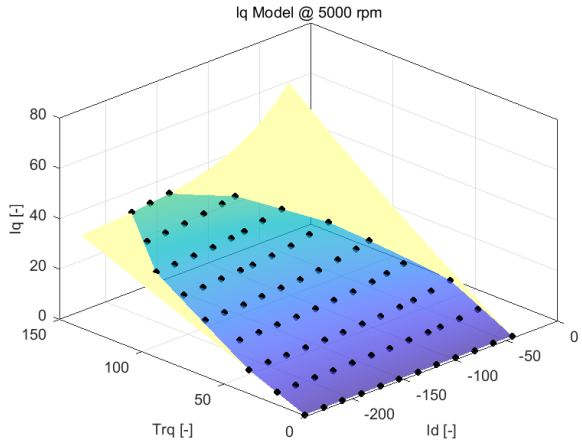


Fig. 6. Iq model at 5000 rpm operating point

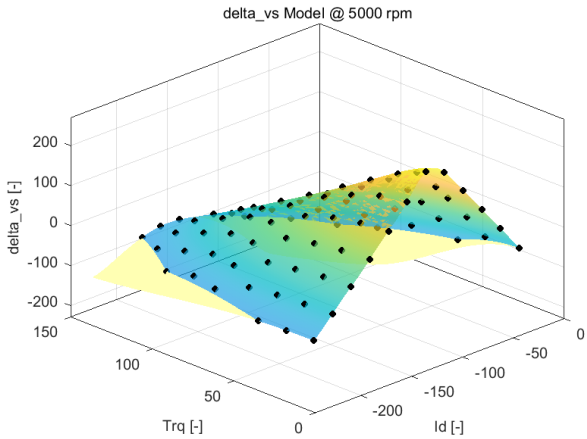


Fig. 7. Voltage margin model at 5000 rpm operating point

Both iq and voltage margin models vary based on speed operating points, as speed can directly affect the boundary of operation. It is impossible to exactly represent the operation boundary from a finite number of characterized data points. The actual operation boundaries for the PMSM under calibration are often imposed by external limiting factors such as the thermal limit of the drive system and the DC bus voltage level of the inverter.

In model-based calibration, the operation boundaries of fitted models are approximated by the convex hulls enclosing the dataset, as depicted by the edges of colored surfaces in Fig. 4-7. These boundaries are important for step 4 of the calibration workflow, since they are used as constraints for the optimization problem.

2.4 Optimizing PMSM Controller Lookup Table Data

In model-based calibration, the process of running optimization routines and generating the final calibration lookup tables is performed using CAGE, the calibration generation tool in Model-Based Calibration Toolbox. In CAGE, the models from step 3 are used either for objective function models or as constraints. For example, the voltage margin models are used as voltage constraints at different speeds to guarantee that the overall modulation voltage does not exceed the maximum imposed by the DC bus voltage. In addition to constraints, single or multiple objectives can also be set up based on these fitted models.

A common objective for optimized field-weakening control is to maximize the PMSM's efficiency while reaching the required torque. This is achieved by setting up torque-per-ampere (TPA) as the target to maximize and simultaneously enforce current and voltage constraints. The result is an optimized operation region that covers maximum torque per ampere (MTPA), maximum torque per volt (MPTV), and operation points in between.

Fig. 8 shows how an optimized operation point in the lookup table is obtained through the CAGE process. The light blue and yellow shaded areas represent the corresponding current and flux (or voltage) constraints at a specific speed operating point, with the green area being the viable region satisfying both constraints. The torque contour in the plot represents a specific torque requirement. To achieve maximum efficiency control for the PMSM, the optimizer in CAGE searches along the torque contour inside the viable region to find a point that maximizes the TPA target. As a result, in the example shown in Fig. 8, point A will be chosen as the optimum. The other optimized lookup table points in Fig. 8 are calculated by the same routine in CAGE.

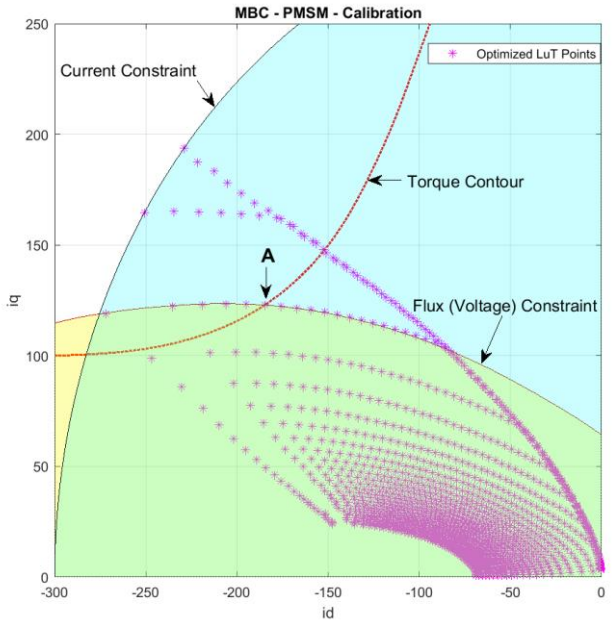


Fig. 8. TPA optimization under flux and current constraints

3. Calibration Results

Engineers can take advantage of MathWorks Parallel Computing Toolbox when fitting models and running the optimization routine described above. With parallel computing enabled, the entire workflow converges in under 10 minutes on a typical four-core PC.

After running the optimization routine, final calibration lookup tables can be filled by the optimization results through various filling methods, such as interpolation or clipping. In theory, engineers can choose any torque and speed

breakpoints for the lookup table, but a common choice of breakpoints for torque is the percentage of maximum torque. Choosing torque percentage of maximum achievable torque rather than absolute torque values ensures that the entire lookup table can be filled with valid optimization results. Fig. 9(a)(b) below provide an example of the final id and iq calibration tables.

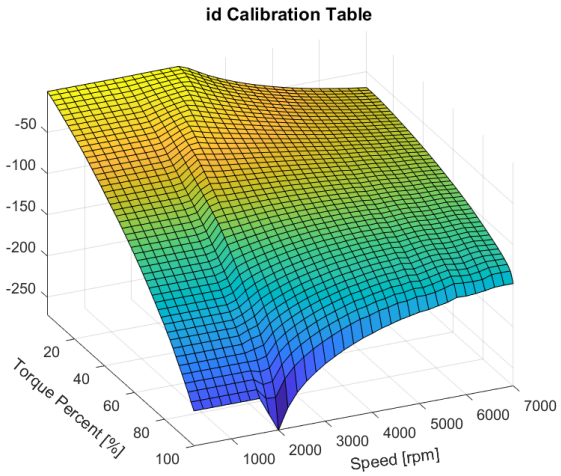


Fig. 9(a) Optimized id calibration table

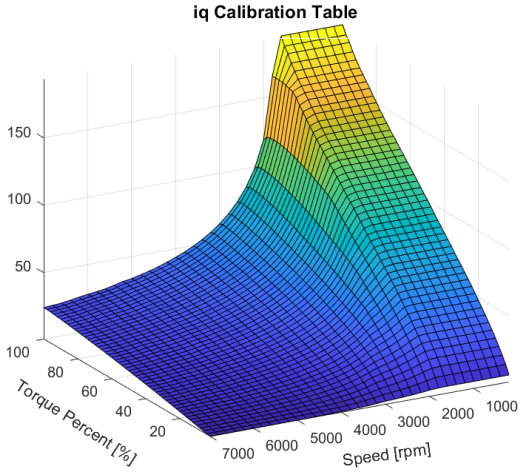


Fig. 9(b) Optimized iq calibration table

4. Conclusion

This article covered the basic model-based calibration workflow for the generation of optimal PMSM torque control lookup tables with field-weakening. The example described in the article is based on field-weakening control tables where torque command, speed, and possibly DC bus voltage are inputs.

For an algorithm that uses torque command and maximum flux linkage as inputs to its lookup tables, the workflow is the same, only with slightly different setup of models and breakpoints. In addition, if your application requires a more accurate and refined calibration, you can consider more variables, such as inverter voltage drop, core loss, AC resistance, and windage or friction, during the model fitting and CAGE process.

5. References

[1] “Model-Based Calibration Toolbox”, https://www.mathworks.com/products/mbc.html

Analysis of an Electric Motor with Reconfigurable Motor Windings when Accounting for Switching Mechanism Volume

R. Hughes[1], X. Pei[2], C. Vagg[3]

1: University of Bath, AAPS CDT, Claverton Down, Bath, United Kingdom
2: University of Bath, IAAPS, Claverton Down, Bath, United Kingdom
3: University of Bath, IAAPS, Claverton Down, Bath, United Kingdom

Abstract: This study analyses a permanent magnet synchronous motor with reconfigurable windings to improve its performance. Building on existing literature, this work accounts for the size of a switching mechanism to determine whether the reduction in active volume is worth the benefits provided. The results show that through minor rotor redesign, the downsized motor can be operated at an increased maximum speed without excessive rotor stresses. This allows the motor to be regeared and deliver a similar torque profile throughout the speed range. However, the reconfigurable motor produces more power at high speeds, has an increased peak efficiency island, and reduces the total quantity of rare earth magnets required.

Keywords: Electric motor, Reconfigurable windings, Performance, Efficiency, Automotive

1. Introduction

Globally, there are increasing pressures to decarbonise sectors contributing to climate change, illustrated by the widely adopted Paris agreement of 2015 [1]. Within the subsequent governmental policies, the transportation sector has regularly been at the forefront [2] [3]. A common theme within these policies is the shift towards transport electrification, which has been shown to substantially reduce the lifetime carbon emission of passenger vehicles in most of the developed world [4] [5]. However, the environmental impacts of electric vehicles (EV) can be further improved, most notably by reducing the dependency on rare earth elements, found within the powertrain, which are currently associated with toxic pollution and price instability [6].

This paper specifically focuses on the electric motor in the powertrain. Due to their high efficiency and power density, permanent magnet synchronous motors (PMSM) have become a widely used choice for automotive applications [7]. However, the permanent magnets (PM) used within these motors are made from rare earth elements and therefore efforts must be made to reduce their usage. One possible solution is through the downsizing of current motors by utilizing methods to improve their performance and operational range.

Commercial electric vehicles such as the Porsche Taycan have implemented two-speed transmissions [8]. This increases the torque applied to the wheels at low speeds in first gear, while enabling a high maximum speed in second gear. However, multi-speed mechanical transmissions add undesirable cost and complexity to the EV drivetrain. Additionally, the increased size conflicts with packaging requirements. Therefore, this paper proposes a solution using reconfigurable motor windings, whereby the motor windings are switched between a parallel and series configuration to alter the performance characteristics. This paper also recognises that such a system will require a switching mechanism to operate. Therefore, this will be considered to ensure the overall size of the proposed motor system does not exceed the baseline motor. The design of this switching mechanism is not discussed in detail as it is to be developed and presented in future work.

2. Background

Nipp [9] [10] was among the first to demonstrate a reconfigurable winding scheme on a PMSM. In these works, the PMSM was reconfigurable between series or parallel windings and star or delta connection schemes. However, Nipp focused on the use of reconfigurable windings to reduce the reliance on field weakening. This is possible as a motor's speed may be increased due to the lower back-emf present in different configurations, illustrated in Figure 1. This contrasts with systems from the last 10 years, which seek to also incorporate field-weakening control [11] [12] [13].

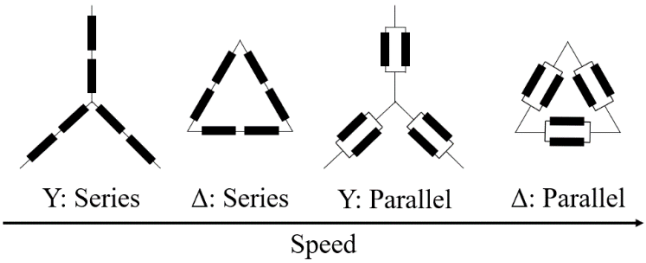


Figure 1: Illustration of each possible motor winding configuration

Work by Hsu [11] and Tang [12] investigated the reconfigurable windings in combination with field-weakening, maximising the operational window of the motor. In each case, only wye (star) connections

schemes were considered. The purpose of this was to reduce the complexity and cost of the system, hence making it applicable to commercial applications. This trend can be seen more widely within the literature as research is conducted to simplify the systems which reconfigure the windings [14]. Despite this work, the effect on motor performance when the volume of the complete system is kept constant, including the switching system, is not well understood. Hence, this is the novel contribution of this work.

The different motor characteristics for each winding configuration are firstly explained by the changes in current flow through the motor phases. In parallel each set of coils experiences half the current to a series configuration, this halves the total ampere-turns, hence halving the maximum torque of the motor. Secondly, as the sets of coils are reconfigured from series to parallel, the voltage induced within them are no longer summed together to create the back-emf. Therefore, the back-emf of the motor is halved in the parallel configuration, enabling the motor to spin at approximately double the speed before field weakening is employed. Finally, it is also possible for the reduced back-emf to result in a higher maximum power output by enabling the maximum phase current and phase voltage happen simultaneously while operating in the high efficiency section of the power curve.

As the general working principle of the reconfigurable motor windings are well understood within the literature, the winding switching system has become the primary area of research. As previously mentioned, the cost and complexity are the main barriers for commercial implementation, with numerous designs aiming to reduce these factors by minimising the use of expensive thyristors [14] [15]. Additionally, due to fast switching times the thyristors minimise the torque interrupt time when switching between each configuration. However, as highlighted by Nipp [9], mechanical contactors may also be used, offering low losses, low complexity, high overload capability, and no additional cooling. As the design of mechanical contactors is out of scope for this work, calculations will assume the size of the switching mechanism is no bigger than can be achieved using currently available transistors.

3. Methodology

3.1 Model Overview

The overall aim of the modelling in this paper is to understand whether the benefits of reconfigurable motor windings outweigh the drawbacks of axially reducing the motor's size, in relation to power and efficiency. For this, the axial reduction was reduced by the estimated size of a switching mechanism.

During this study, the performance of a baseline PMSM and the downsized reconfigurable motor are first obtained using 2D FEA and a D-Q model. Then, a 0D vehicle model is used to analyse how each of these systems compare when driven under standard drive cycles.

3.2 Motor Configurations

For this study, the baseline motor was a 50 kW 8-pole permanent magnet motor with interior magnets from the 2004 Toyota Prius. Parameters for this motor are shown in Table 1, with a diagram of the geometry in Figure 2.

Table 1: High-level baseline motor specifications [16]

Specifications	Value
Rated Power	50 kW
Maximum Speed	6000 rpm
Stator Outer Diameter	269.2 mm
Rotor Outer Diameter	162 mm
Lamination Length	83.6 mm
Number of Slots	48
Number of Poles	8
Max Phase Current (RMS)	216 A
Max Phase Voltage (RMS)	170 V

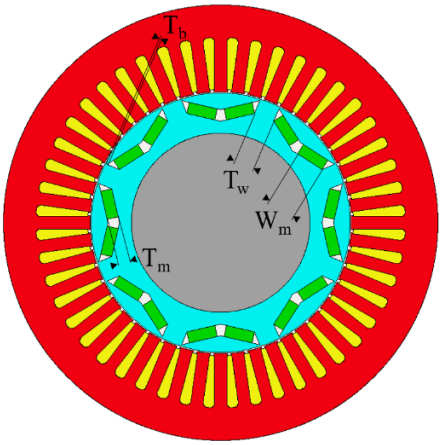


Figure 2: 2D CAD drawing of baseline motor

The next phase of the modelling process was to determine the specifications of the downsized reconfigurable motor. This was achieved by firstly determining the size of the switching system so the motor could be sufficiently downsized. A mechanical contactor system may prove more compact, however since this is yet to be designed in future work, it is assumed it must be no bigger than the alternative of using thyristors. Therefore, a worst-case scenario has been chosen which represents the same volume required to use 5 anti-parallel thyristor modules, as demonstrated by Tang *et al. [14].* This occupies a 20 mm section of the motor using MTC110-1600 thyristors [17].

Therefore, when accounting for the size of the switching mechanism, the lamination length in Table 1 was reduced to 63.6 mm, illustrated in Figure 3. Next, appropriate alterations to the RMS phase current and voltage were made. This was achieved using the simplified PMSM scaling laws by Stipetic *et al.* [18]. The scaling laws used are shown in Equations 1 and 2.

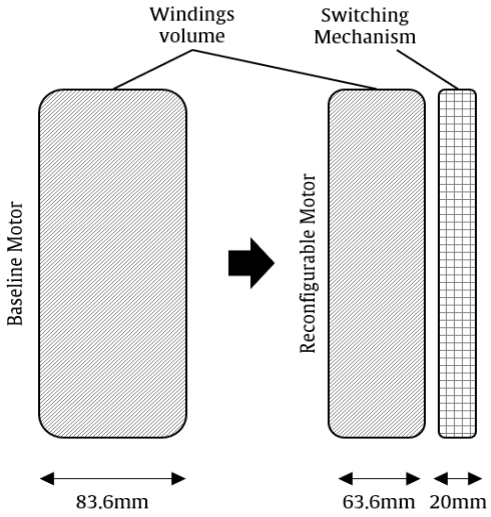


Figure 3: Illustration of how the motor geometry changes with the switching mechanism

$$I_s = \frac{1}{K_w} I_o \quad (1)$$

Where I_S is the scaled current, K_W is the rewinding factor, and I_O is the original current.

$$V_s = K_W K_R K_A V_o \quad (2)$$

Where V_S is the scaled voltage, K_R is the radial scaling factor, K_A is the axial scaling factor, and V_O is the original voltage.

For the scaling laws, the radial scaling factor was 1 and the axial scaling factor was 0.76. To maintain the voltage at the same level, a rewinding factor of 1.32 was used, hence dropping the maximum phase current to 164 A_{RMS}. This related to an increase from 9 turns per coil to 12 turns per coil in the downsized motor, reducing the cross sectional area and increasing the length of the conductor. Finally, the downsized motor windings were switched between one and two parrallel paths to represent the reconfiguration.

3.3 Motor Modelling

Modelling of the motor was done using the software package ANSYS Motor-CAD. The two-dimensional finite element E-Magnetic suite was used for inputting and designing the machine geometry. Subsequently, the Motor-CAD Lab module was used for generating efficiency maps and the Mechanical module was used for stress analysis. After generating efficiency maps for the downsized motor with series and parallel windings, the results were combined in MATLAB by taking the maximum efficiency values at all possible operating points of each configuration.

3.4 Vehicle Modelling

To compare the baseline and reconfigurable motor, a 0D vehicle model was used. This enabled the motor losses to be measured over different drive cycles, and for vehicle level performance to be compared. Due to the relatively low power output of the motor, a small lightweight vehicle was simulated. Parameters for this are presented in Table 2.

Table 2: Vehicle parameters for 0D model

Parameter	Value
Mass	880 kg
Rolling resistance	0.02
Air density	1.23 kg/m^3
Gravity	9.8 m/s^2
Frontal Area	2.05 m^2
Drag coefficient	0.38
Drivetrain efficiency	95%
Gear Ratio	1:4.5
Tyre Radius	0.286 m

The 0D model was constructed using Equation 12, which totals the forces acting upon the vehicle to find the power required for a given speed. All terms relating to the incline have been neglected as the road profile was assumed to be flat.

$$P_w(t) = \left(ma(t) + mg.C_r + \frac{1}{2}\rho A_f C_d V^2(t)\right).V(t) \quad (12)$$

Where P_w is power at the wheel, m is vehicle mass, a is acceleration, g is gravity, C_r is rolling resistance, ρ is air density, A_f is frontal area, C_d is drag coefficient, V is vehicle velocity, and t is time.

To relate the power at the wheel to the power from the motor, drive train losses must be accounted for, shown in Equation 14.

$$P_m(t) = {\mu_d}^{-1} P_w(t) \quad (14)$$

Where P_m is power at the motor, and μ_d is drivetrain efficiency.

Finally, the torque and speed of the motor were required to correlate a given driving state to a position on the motor efficiency map. Hence, these were found using Equations 15 and 16.

$$\mathrm{T}_m(t) = \frac{P_m(t) \times r_t}{V(t) \times K_g} \quad (15)$$

$$\omega_m(t) = \frac{V(t) \times K_g \times 60}{2\pi r_t} \quad (16)$$

Where T_m is torque at the motor, r_t is the tyre radius, and K_g is the gear ratio, and ω_m is the mechanical speed of the motor.

4. Results

4.1 Motor Geometry

Due to a reduction in the axial length of the motor, the maximum torque dropped proportionally. To ensure a like-for-like comparison of the baseline and reconfigurable motors, the driveline gear ratio was adjusted to provide equal maximum torque at the driveshaft. As a result, the maximum speed of the driveshaft would have been reduced in the case of the downsized reconfigurable motor. To mitigate this, it was allowed to spin to 7600 rpm, ensuring the maximum driveshaft speed was equal.

Higher motor speeds lead to increased centrifugal forces acting on the magnets in the rotor. Therefore, to ensure the rotor could safely operate at 7600 rpm, the Von Mises stresses were calculated to confirm the safety factor in the rotor remained above 2, which is generally seen as a minimum value for rotating machinery. To meet this aim, redesigns to the rotor geometry were investigated using a grid-search methodology. This resulted in the new geometry shown in Figure 4b for the downsized and higher speed motor. Table 3 provides an overview of the changes to the rotor geometry.

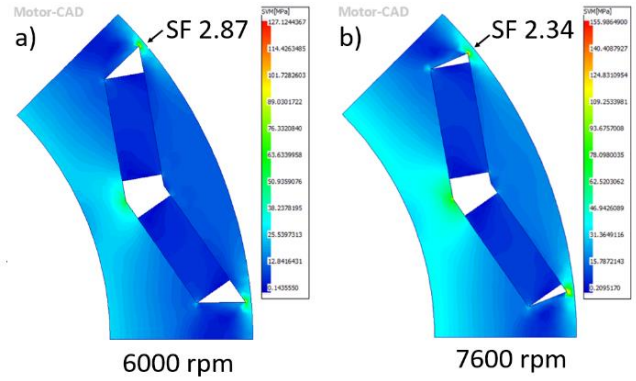


Figure 4: a) Baseline rotor stresses at 6000 rpm
b) Redesigned rotor stresses at 7600rpm

Table 3: Comparison of baseline and redesigned rotor parameters

Parameter	Baseline	Redesigned
Bridge Thickness (T_b)	1 mm	1.3 mm
Magnet Width (W_m)	18 mm	19.5 mm
Magnet Thickness (T_m)	7 mm	7 mm
Web Thickness (T_w)	13 mm	16 mm

When accounting for the 24% reduction in axial length and slight increase in magnet width for the downsized reconfigurable motor, the overall reduction in magnet useage is 17.6%.

4.2 Motor Efficiency Maps

Following the rotor modifications, the gear ratio for the reconfigurable motor was increased to 1:5.7. This provides efficiency maps for each motor configuration that can be compared as like-for-like systems. The results for these are presented in Figure 5 and 6.

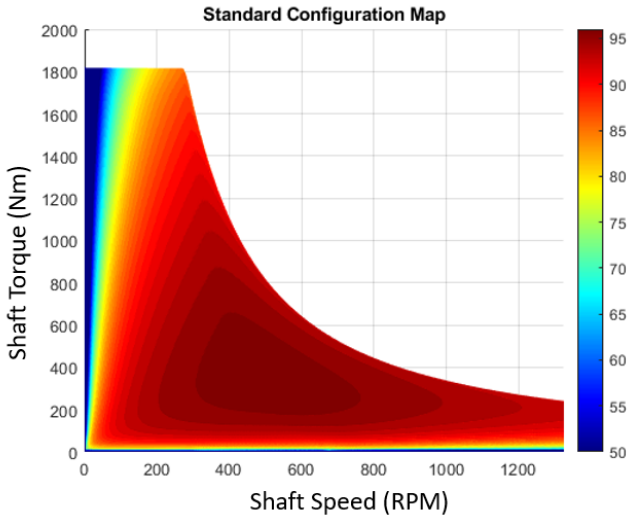


Figure 5: Baseline motor efficiency map

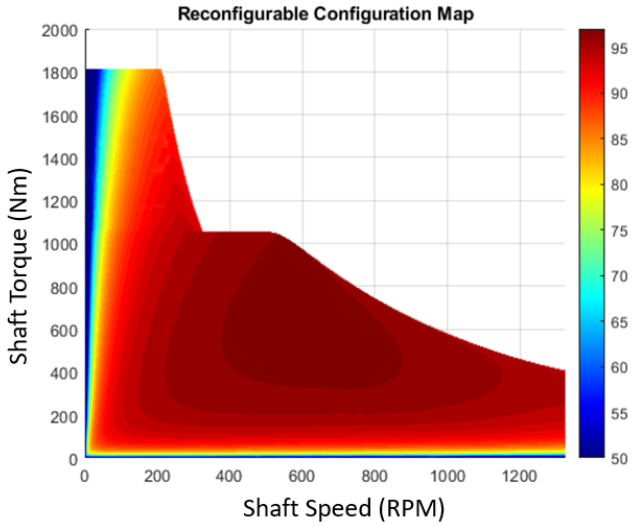


Figure 6: Reconfigurable motor efficiency map

The first comparison that can be made between the baseline motor in Figure 5 and the reconfigurable system in Figure 6 is the reduction in corner speed. This drops from 270 rpm to 210 rpm, respectively. Secondly, as the reconfigurable motor shifts to parallel windings the lower back-emf enables it to spin much faster before the torque curtails. Comparitively,

due to the effects of field-weaking in the baseline motor, the torque continues to drop rapidly at elevated speeds. As a result, the reconfigurable motor can deliver higher shaft torques than the baseline motor past 420 rpm. Hence, the reconfigurable motor is also able to deliver more power at these higher speeds. This is discussed further in Section 4.3.

The efficiency islands in each motor are notably different, with the reconfigurable motor peaking at 96%, instead of 95%. The reconfigurable motor shows significantly improved efficiencies at elevated speeds. However, during low torque mid-speed operation the baseline motor is marginally more efficient. The effects of this are discussed further in Section 4.4.

4.3 Motor Power Curves

Figure 7 provides a comparison of the power delivered to the vehicle shaft by each of the considered motors.

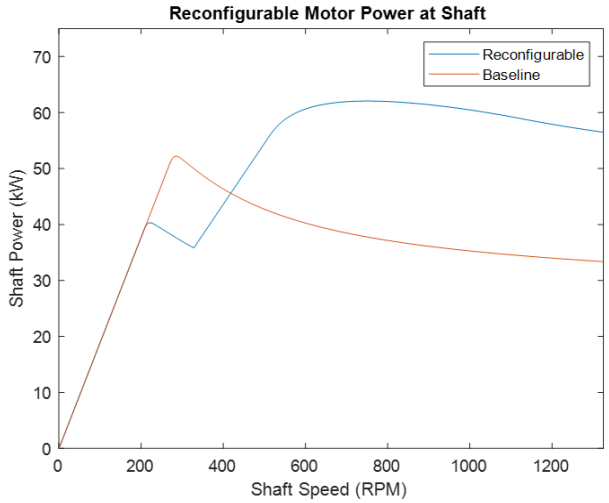


Figure 7: Comparison of power delivery to the shaft by each motor

The observed power curves show that the baseline motor is only able to deliver higher power in a short window between 210 and 420 rpm. The high back-emf constant of the baseline machine causes a sharp drop in power beyond the corner speed, resulting in higher power outputs above 420 rpm from the reconfigurable motor whilst in parallel configuration.

4.4 Motor Losses

To accurately quantify the differences in efficiency between the two motors, the vehicle model outlined in Section 3.4 was used to measure the cumulative motor losses in two different use cases. The use cases analysed are for the standard US06 and WLTP drive cycles, presented in Figure 8 and Figure 9, with Figure 10 and Figure 11 comparing the cumulative losses for each motor during these use cases.

Figure 10 shows a significant 9% reduction in total losses throughout the US06 drive cycle for the reconfigurable motor. The improvements are primarily seen after 200 seconds, where the majority of highspeed driving occurs.

In Figure 11, the distinction between the baseline and reconfigurable motor is less obvious. At very low speeds before 600 seconds there is negligible difference in losses. From 600 to 1400 seconds, the baseline motor performs slightly better as the speed and torque slightly increase. However, after 1400 seconds, the high-speed section of the drive cycle favours the reconfigurable motor, resulting in a reduction in total losses of 1% compared to the baseline system.

The results in these graphs are consistent with what would be expected when viewing the efficiency maps of the two systems in Section 4.2.

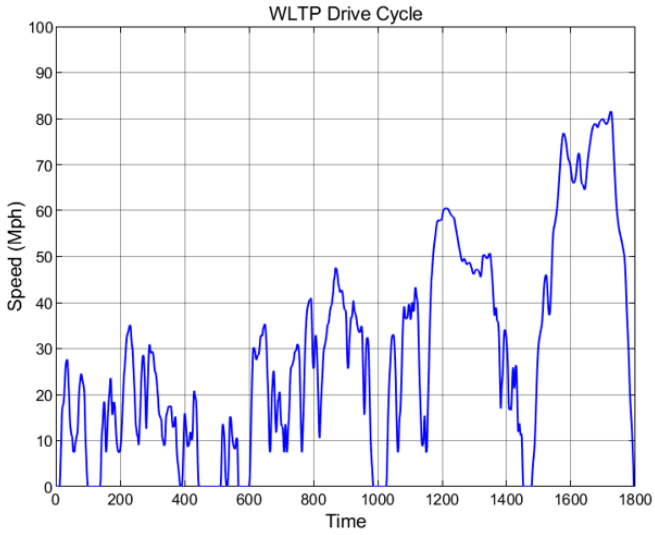


Figure 8: Velocity profile of the WLTP drive cycle

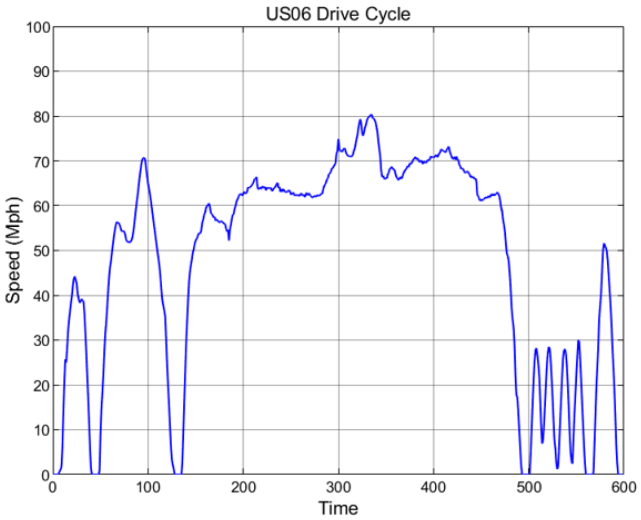


Figure 9: Velocity profile of the US06 drive cycle

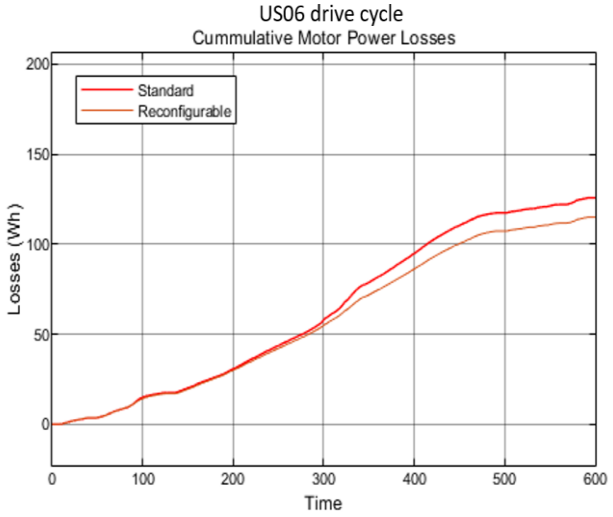


Figure 10: Comparison of cumulative motor losses for the US06 drive cycle

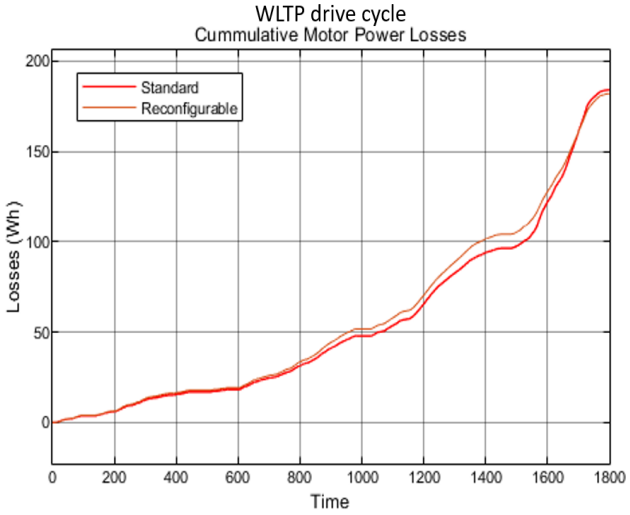


Figure 11: Comparison of cumulative motor losses for the WLTP drive cycle

5. Discussion

5.1 Interpretation

The results within this study indicate there are significant benefits to be realised from reconfigurable motor windings, despite the active motor volume that is sacrificed. In contradiction to what may be expected, the downsized motor was able to output a higher peak power when in parallel configuration than the baseline motor. This effect may be exaggerated due to the design of the baseline motor prioritising low speed power. Hence, this trend may differ when other motor topologies are studied.

Notably, the motor analysed already had a low volume, and crucially was very compact in the axial direction. As a result, the size of the switching mechanism was quite large in relation to the lamination stack length. This caused a total reduction in axial length of 24%, which is unlikely to be the optimal amount to downsize the motor by.

Findings within this work broadly agree with those of Tang *et al.* [12], who developed a reconfigurable motor that reduced the use of rare earth magnets in a PMSM. The power curve of the reconfigurable motor by Tang *et al.* is closely resembled in this study. Additionally, they also found the best improvements in efficiency to be achieved during aggressive driving.

When considering the proposed reconfigurable motor, the use case must be thought through. If the requirements for the motor are primarily at medium loads and speeds, the reduced efficiency may be a burden, whilst the increased power would not be utilised. However, if operating at high loads and high speeds, the benefits would be significant.

5.2 Implications

The presented simulations provide new insights into the effect of accounting for the size of switching mechanisms. This has direct implications for manufacturers as reconfigurable motors are viewed as an alternative to two speed transmissions [19], which are generally not suitable for low cost and compact applications.

Implications to the wider powertrain may be caused by the 24% reduction in maximum current for axially scaled motors. This could enable smaller and cheaper components to be used within the power electronics. The downsized reconfigurable motor in this study could have assumed the same maximum phase current as the baseline motor, thereby recouping the lost torque, though consideration would also have to be made for the thermal management system, as similar losses in the motor would result in higher temperatures due to the reduced volume. As a result, advanced cooling systems may be required in some applications, such as direct stator liquid cooling [20]. The design methodology for benchmarking reconfigurable motors needs further research, as there are so many parameters which can be traded off depending on the design objective.

6. Conclusion

In this paper a 50 kW rated interior permanent magnet synchronous motor was simulated in a standard and reconfigurable configuration. When reconfigurable motor windings were used, the axial length of the motor was reduced by 24% to account for a switching mechanism. The two motor designs were then simulated in a 0D vehicle model so system level effects could be understood.

The rotor of the downsized reconfigurable motor was modified to allow the motor to spin faster without damage. After regearing the motor, this enabled the maximum speed and torque to be consistent at the vehicle shaft, enabling a like-for-like comparison of

the systems. Despite reducing the maximum phase current by 24%, from 216 A to 164 A, the reconfigurable motor provided a higher peak power of 60 kW at a shaft speed of 700 rpm, compared to 53.5 kW at 270 rpm for the baseline motor. At shaft speeds above 420 rpm, the reconfigurable motor delivered significantly higher power than the baseline motor.

The efficiency of the reconfigurable motor was found to be significantly higher during the US06 drive cycle, resulting in 9% lower losses. This is predominantly due to the reconfigurable motor having a noticeably larger maximum efficiency island in the high-speed range. The peak efficiency is also increased to 96%, versus 95% for the baseline motor. However, during medium speed operations the baseline motor had slightly lower losses due to higher slow to medium speed efficiencies.

From this study, it is clear a reduction in the axial length of the rotor to enable reconfigurable windings can be a worthwhile trade off. Efficiency and performance benefits are apparent for high speed and high-power applications, whilst reductions in magnet usage are beneficial in all cases. In future, similar studies should be conducted on various motor topologies used in automotive applications, with considerations for thermal management.

7. Acknowledgement

R.H. is supported by a scholarship from the EPSRC Centre for Doctoral Training in Advanced Automotive Propulsion Systems (AAPS), under the project EP/S023364/1.

8. References

[1] U. Nations, “Paris Agreement,” Paris, 2015.
[2] U. D. f. Transport, “The Road to Zero,” HM Government, London, 2018.
[3] Executive Department State of California, “Executive Order N-79-20,” California, 2020.
[4] Ricardo Energy & Environment, “Determining the environmental impacts of conventional and alternatively fuelled vehicles through LCA,” European Commission, Brussels, 2020.
[5] G. Bieker, “A Global Comparison of The Life-Cycle Greenhouse Gas Emissions of Combustion Engine and Electric Passenger Cars,” The International Council on Clean Transportation, Berlin, 2021.
[6] G. Charalampides, K. Vatalis, V. Karayannis and A. Baklavaridis, “Environmental Defects And Economic Impact On Global Market Of Rare Earth Metals,” IOP Conference Series: Materials Science and Engineering, vol. 161, 2016.
[7] J. Santiago, H. Bernhoff, B. Ekergard, S. Eriksson, S. Ferhatovic, R. Waters and M. Leijon, “Electrical Motor Drivelines in Commercial All-Electric Vehicles: A Review,” IEEE Transactions on Vehicular Technology, vol. 61, no. 2, pp. 475-484, 2012.
[8] Porsche, “The technology behind the new Porsche Taycan,” Press Kit Workshop, Stuttgart, 2020.
[9] E. Nipp, “Alternative to Field- Weakening of Surface-Mounted Permanent-Magnet Motors for Variable-Speed Drives,” IEEE Industry Applications Society Annual Meeting, vol. 1, pp. 191-198, 1995.
[10] E. Nipp, Permanent Magnet Motor Drives with Switched Stator Windings, Stockholm: PhD Thesis, 1999.
[11] J. Hsu, “Electronically Commutated Seral-Parallel, Switching for Motor Windings”. United States of America Patent 2011/0234139 A1, 29 September 2011.
[12] L. Tang, “Electric Motor Performance Improvement Techniques,” Oak Ridge National Laboratory, Oak Ridge, 2016.
[13] S. Sin, M. Ayub and A. Kwon, “Operation Method of Non-Salient Permanent Magnet Synchronous Machine for Extended Speed Range,” IEEE Access, vol. 8, pp. 105922-105935, 2020.
[14] L. Tang, T. Burress and J. Pries, “A Reconfigurable-Winding System for Electric Vehicle Drive Applications,” in IEEE Transportation Electrification Conference and Expo (ITEC), Chicago, 2017.
[15] M. Kreiger, “Electric motor having windings operable in parallel and/or series, and related methods”. United States of America Patent US20120086380, 12 April 2012.
[16] V. Kuptsov, P. Fajri, A. Trzynadlowski, G. Zhang and S. Magdaleno-Adame, “Electromagnetic Analysis and Design Methodology for Permanent Magnet Motors Using MotorAnalysis-PM Software,” MPDI Machines, vol. 7, no. 75, 2019.
[17] PDKJ, “MTC110-1600 Datasheet”, Shenzhen: Shenzhen piandian Technology Co.,ltd, Date N/A.
[18] S. Stipetic, D. Zarko and M. Popescu, “Ultra-fast axial and radial scaling of synchronous permanent magnet machines,” IET Electric Power Applications, vol. 10, no. 7, pp. 658-666, 2016.
[19] L. Shao, A. Karci, A. Taverini, A. Sorniotti and M. Cheng, “Design Approaches and Control Strategiesfor Energy-Efficient Electric Machinesfor Electric Vehicles - A Review,” IEEE Access, vol. 8, pp. 116900-116913, 2020.
[20] P. Lindh, A. Gronman, M. Martinez-Iturralde, M. Satrustegui and J. Pyrhonen, “Direct Liquid Cooling Method Verified with an Axial-Flux Permanent-Magnet Traction Machine Prototype,” IEEE Transactions on Industrial Electronics, vol. 64, no. 8, pp. 6086-6095, 2017.

9. Glossary

FEA: Finite Element Analysis

PMSM: Permanent Magnet Synchronous Machine

RMS: Root Mean Squared

WLTP: Worldwide Harmonised Light Vehicle Test Procedure

15 JUNE 2022

POWER ELECTRONICS AND COMPONENTS



Superior Solutions for E-Mobility

TDK offers a uniquely broad product range for all types of electric vehicles (xEV). Among the most important components, which are characterized by high reliability and a long service life, are DC link capacitors in their fi lm, ceramic and aluminum electrolytic capacitor versions. Protective components and solutions for EMC protection play an equally important role.

In addition, there are power inductors and transformers for converters between different voltage levels. But long-term stable NTC temperature sensors for thermal monitoring of the charging process of HV batteries are also indispensable components.



Learn more about our
E-Mobility Applications

www.tdk-electronics.tdk.com

CarXield™ – The first standard EMI filter for EV

Muhittin Yildiz[1], Vladimir Ostapenko[2], Fabian Beck[3]

1: TDK Electronics AG, Rosenheimer Strasse 116b, 81669 Munich
2: TDK Electronics AG, In den Seewiesen 26, 89520 Heidenheim
3: TDK Electronics AG, In den Seewiesen 26, 89520 Heidenheim

Abstract: Inverters are used in electrically powered vehicles to convert energy from Direct Current (DC) to Alternating Current (AC) and thus to run the vehicle. This inversion creates electromagnetic disturbances which propagate through the whole system and may cause interferences anywhere. Such problem can be prevented using Electro-Magnetic Interference (EMI) filters like the CarXield™ developed by TDK Electronics AG.

Keywords: EV, EMI Filter, EMC Problem, Standard Solution

1. Introduction

TDK Electronics AG (formerly known as EPCOS AG) develops, manufactures, and sells electronic components and systems under the product brands TDK and EPCOS. The customers are from the industrial, consumer electronics, telecommunications but also from the technologically sophisticated automotive sector. The wide range of TDK Electronics products includes capacitors, ferrites and inductors, piezo and protective components as well as sensors. Beyond the offer of standard products, the R&D departments of TDK are globally very well positioned so that a collaboration and finding the right solutions for its customers can easily be guaranteed. To achieve this, TDK Electronics employs 23,600 people in around 20 development and production sites and uses its close meshed sales network.

The EMI filters of the TDK Corporation have been solving the electromagnetic problems in industrial applications for decades and impress with their quality and reliability. The trend towards electromobility and the need of Electro-Magnetic Compatibility (EMC) solutions in electrically powered vehicles was recognized in an early stage and know-how in this area was expanded. For more than half a decade, customized EMC solutions have been developed and offered in numerous projects for customers.

There are several sectors such as research, private designers, or industries with low volume. A common development project is usually not profitable for such sectors. However, companies with larger quantities also need cost-intensive prototypes or pre-development statuses for an initial estimate or for preliminary investigations. It usually takes a certain amount of time from the initiation to the use of such prototypes. To avoid such problems and among other things to serve customers with smaller quantities, TDK has now developed the first standard EMI filter platform for automotive applications and creates a cost-effective and efficient solution for EMC problems with the CarXield. Thanks to its fully validated design, these filters are available quickly and at any time.

2. EMI Basics

2.1 Electromagnetic Interferences

Each electronic device functions simultaneously as a disturbance source by emitting signals and as disturbed equipment during their receipt. As the frequency increases, disturbances propagate due to parasitic effects. Depending on the frequencies these disturbances are following different EMC paths.

You can divide in three types of effects. While usually in the lower frequencies up to some 100 kHz, you have dominating conductive emission on the lines, above this frequency range coupling of electric and magnetic fields begin to play a more important role. At frequencies above about 30MHz the structures become large enough for radiation of electro-magnetic fields (far field). For these three kinds of disturbance propagation there are different kind of remedies like reactors, EMC filters, grounding, proper PCB design or shields (see Figure 1)

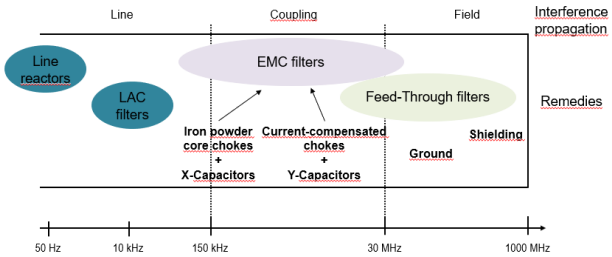


Figure 1: Interference propagation and Remedies illustrated depending on frequency

There are two kind of disturbances which occur in the frequency range of the conducted disturbances. There are kinds of interference modes of conducted disturbances: Differential Mode (DM) and Common Mode (CM) interferences. A floating disturbance source primarily emits only DM disturbance which is propagated along the connected lines, see Figure 2. The disturbance current will flow towards the disturbed equipment on one line and on the other line back, just as the line current does. DM disturbances occur typically at low frequencies (up to several hundred kHz).

Parasitic capacitances in disturbance sources, disturbed equipment or intended earth connections however also produce a disturbance current in the earth circuit. This Common-Mode interference current flows towards the disturbed equipment along both the connecting lines and returns to the disturbance source through earth. Since the parasitic capacitances will tend to form a short-circuit with increasing frequencies and the undesired coupling effects on the connecting cables and the equipment itself will increase correspondingly, common-mode disturbances become dominant above several MHz.

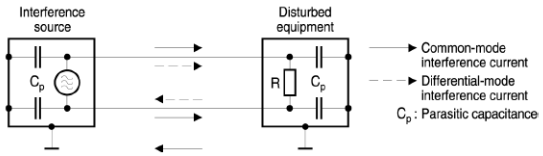


Figure 2 CM and DM interferences

While in some literature Differential Mode disturbances are also called symmetrical disturbances, the Common Mode disturbances are described as asymmetrical disturbances.

2.2 EMI filter and components

The term EMC filter is used in the same way for various components. Generally spoken EMC filters are an electrical circuit comprising inductors, capacitors, and resistors, which limit electrical interferences in power networks. They act predominantly in the frequency area of the conducted interference.

The filter type is virtually always a low-pass filter,

which feeds through the usable frequencies generally unaffected, disturbance frequencies are however weakened. The key components of an EMC filter are typically:

- X capacitors (C_X)
- Chokes (L)
- Y capacitors (C_Y)
- Current-compensated chokes (L_1/L_2)
- Discharge resistors (R)

Depending on the type of network or application, EMC filters are implemented with a different number of lines. 2-line filters are used for DC (like the CarXield) or single-phase AC applications. The structure of a 2-line filter is shown as an equivalent circuit diagram in Figure 3. By “LINE” in this figure the HV DC battery side is meant and by “LOAD” the side connected with the inverter is meant.

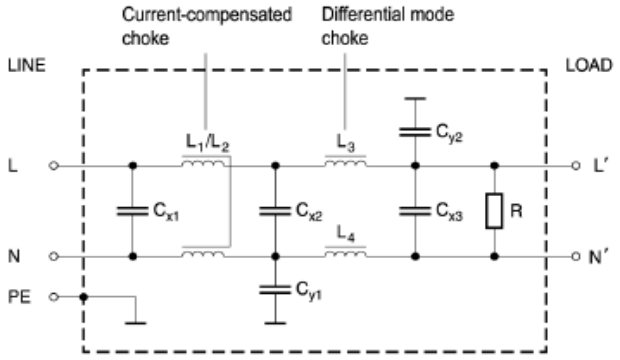


Figure 3: Equivalent circuit diagram for a 2-line EMI filter

While chokes and “X-capacitors” influence the DM disturbances, the current-compensated chokes and “Y-capacitors” primary are filtering the CM disturbances.

2.3 Regulations

Electromagnetic compatibility is a very important indicator for quality of product manufacturers and even if non-safety relevant products may be introduced to the market without a type approval, a conformity must be documented by the OEM in a later step. The proof of the conformity is required by regulations like the ECE-R10 and must be documented. Test procedures like a noise immunity (ISO 11452) or interference emission (CISPR 25) are standard that can be followed.

The Quality Management System of TDK Electronics forms the basis for certification according to ISO 9001 and IATF 16949, in which all TDK Electronics plants and sales organizations are included, and all certificates can be found on the TDK websites. The production plants that serve the automotive industry apply the IATF 16949 standard. The IATF certificates confirm compliance with the requirements of a quality management system that reflects the requirements of the automotive industry.

Figure 5: Use of CarXield means avoiding complex shielding of the cables

3. Standard Solution for e-Mobility application

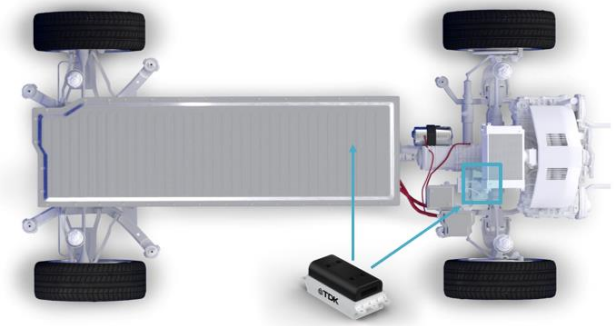
3.1 Inverter application

At the core of the term e-mobility are electrically powered trains, streetcars, buses, trucks, motorcycles, and electric bikes in addition to cars. Electromobility is considered as the key technology when it comes to future-proofing the transport system. One basic feature of electromobility is that the drive of the vehicles is partially or fully electrically powered. Batterie electrical vehicles (BEV) seem to force through and establish as the new way of transportation system.

The frequency converter used in the drive system represents a source of high-frequency disturbances, due to the fast-switching edges, which can be distributed via the motor leads and high-voltage supply lines in the vehicle. The frequency converter is often located directly at the motor housing due to the integration density in the vehicle. In such cases, the motor leads are guided by the housing. Alternatively, shielded lines are used as motor cables.

To minimise interaction with other vehicle supplies, such as the low voltage on board supply or communication lines, the HV DC supply lines between the loads, e.g., the frequency converter and the HV battery may have a shielded design. However, the use of high-quality, shielded cables and connectors is a very expensive approach.

Furthermore, the cables and plug connectors only have a finite shielding attenuation, which may worsen considerably throughout the service life due to corrosion. Should repair work be required, i.e., when replacing a cable, the shielding quality of the restored connection can only be inferred to a limited extent, apart from the horror of investigation, where the source of a now an then arising EMC problem is exactly located to take the right measures. A cost-optimised and reliability solution is on the other hand offered using EMC filters in the HV bus system (see Figure 5).



3.2 The CarXield platform - 500V

After the power and energy density of batteries was high enough, and the first BEV for the mass market had started being introduced, it was fast recognized that the high amount of switching frequencies of the used inverters played a role. Also shielding was not the best and cost-efficient solution. After a short market analyse the idea of an automotive compliant standard EMI Filter was born.

TDKs innovative filter solution CarXield™ is a new standard design for most electric vehicle inverter platforms. The first design was for a rated Voltage of 500V DC and a rated current of 200A @85°C. With the CarXield there are no extra R&D and production expenses, which saves a lot of costs on the customer side. The customer can easily adjust the amount of the needed filters to its production capacity. And finally, the customer can purchase a variant without copper bars. This pushes the costs of the filter even further down.

Derived from this initial filter several adaptations were created (see Figure 6).



Figure 6: CarXield variants in the small housing

While the initial filter can handle a rated current of 200A, 360A for 1min and 600A for 10sec, increasing the bus bar cross section from 42mm² to 96mm² and adjusting some small details, this derived type can handle a rated current of 400A, 640A for 1min and 1000A for 10sec. The last derivation in Figure 6 has a L-bus bar shape, which makes it possible to connect the filter on the line side with cable lugs of the vehicle

system (Figure 7). The energy potential of the 500V DC filter variants is less equal to 0.05 J

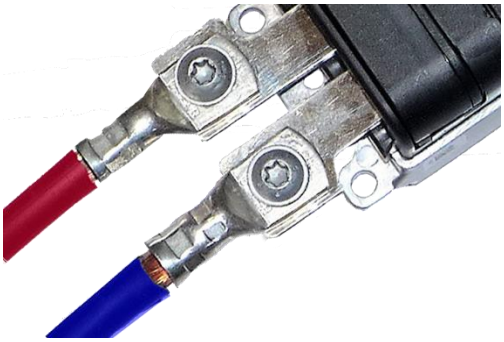


Figure 7: CarXield connection with cable lugs

This compact filter has a length of 140mm, width of 59mm and a height of 50mm. The straight busbar has a length of 155mm. In Figure 8 you can see the mechanical drawing of this type and can find it also in our data sheet.

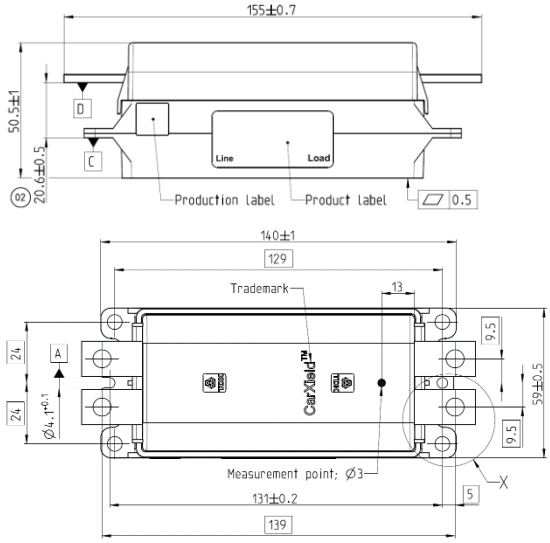


Figure 8: 500V Type mechanical dimensions

Its insertion loss thus the performance is very high. In Figure 9 you can find the measured insertion loss under the conditions Z = 50 Ohm, 0dBm and 23°C ± 5°C and in various applications a CISPR 25 HV Class 5 could be reached easily.

Frequency [MHz]	Symmetrical Min. attenuation [dB]	Asymmetrical Min attenuation [dB]
0.1	28	20
1	65	65
10	38	50
80	20	40

Figure 9: Insertion loss of 500V, typical values at Z = 50 Ohm

3.3 The CarXield platform - 900V

The market was analysed and the increasing demand for more power and the increase of the voltage of the Batteries from 400V to 800VDC was recognized very fast. For that reason, TDK developed a 900V version of the CarXield.

Within this voltage class it is the same as in the 500V platform, there are several variants. The rated currents vary from 250A and 400A. The maximum currents correlate for the 250A version up to 600A for 10 seconds or for the 400 A up to 1000A for 10sec. A version with an L - shape busbar is here also available (Figure 10).



Figure 10: CarXield variants in the big housing

This big housing has a length of 232mm, a width of 103 and a height of 54mm. The straight busbar has a length of 253mm. The insertion loss of these bigger types thus their performance is higher than the compact variants. In Figure 11 you can find the measured insertion loss with the conditions Z = 50 Ohm, 0dBm and 23°C ± 5°C.

Frequency [MHz]	Symmetrical Min. attenuation [dB]	Asymmetrical Min attenuation [dB]
0.1	35	35
1	52	57
10	52	60
80	40	50

Figure 11: Insertion loss of 900V, typical values at Z = 50 Ohm

The size of the housing is specified by its very high performance and the height of the voltage thus the needed creepage distances. In contrast with construction, agriculture or common vehicle

manufacturers, a lot of personal car applications may have even more challenging size requirements.

Thanks to the knowledge and experience of many years within the EMI field, our developers finally could fit a 900V EMI Filter in a compact housing with the outer dimensions from Figure 8! In Figure 12 you can see this 900V compact type!



Figure 12: 900V Filter in small housing

3.4 Application EMC Zone Concept

To reduce most disturbances and achieve the best results, TDK suggests using the CarXield and suggests working with the so called “4 zone concept”. For the appropriate application of the EMC filter a basic EMC understanding, an appropriate grounding and shielding concept are necessary and the importance of the zone concept increases with the switching frequency of the inverter.

For the application of the 4 zone concept your inverter system must be thought in 4 EMC zones (Z0 to Z3) like presented in Figure 13.

On the battery side of the inverter, which is described as zone Z3, the CarXield will be located within a shielded EMC enclosure.

Zone Z2 contains the storage capacitor. It is recommended that this zone incorporates at least a capacitor value of C_{Gi} = 68nF between Inverter-line and the Ground or even less and correlates with parasitic capacitances of the electric drive. In combination with a damping resistor R_{Gi}, the losses of the resistor shall be considered.

Z1 contains the inverter bridge zone. The pulse width modulation frequency (PWM) shall be chosen by the customer not to exceed the limitation of the specified value in the respective datasheet. Commonly spoken this limit is approximately a Common Mode Current of I_{CM} = 1 A peak at 10kHz, for not active cooled inverter, the DVDT voltage transient on the filter from Line L to GND shall be less or equal to 900V/µs with a metal mounting surface temperature of ≤ 85°C.

On the other side of the inverter, in Z0, a Common Mode Choke over the 3 motor phase busbars is recommended, to reduce the asymmetrical or CM current.

Any further communication or control cable, which penetrates one of those above-mentioned zones, needs to be EMC treated.

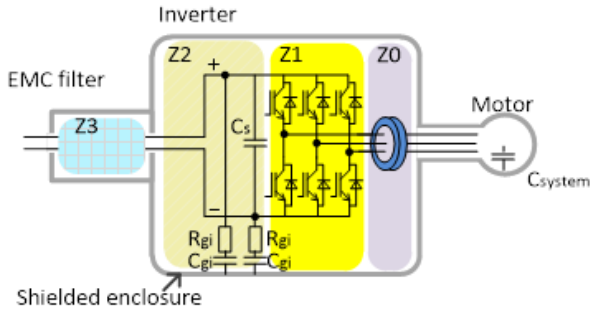


Figure 13: 4 - zone concept

4. Conclusion

Because the basic product design is already running in production or like with some variants where the production process is approved, the customer can plan its production in advance and the needed budget can be predictable and be flexible adjusted. Besides reliability and flexibility, the customer has the advantages of cost-saving thanks to a reduced development time, to an already finished product validation and the not required custom specific production line investment.

By developing such a standardized filter TDK wants to afford its customers also a huge flexibility, why there are different kind of variants in the power class, in the size and in the type of the connection to the customer system.

If this flexibility is not enough for the customer, TDK can also offer more adaptation based on the CarXield. Besides the CarXield there is also the possibility of starting custom specific EMI solutions. To meet the targets of the customer requirements, the own TDK facilities like its accredited EMC laboratory (Accreditation: ISO IEC 17025, D-PL-12167-01-00 and Certifications: IATF 16949 and the ISO 9001) offer the best conditions. Within its semi-anechoic chamber and shielded cabins, radiated emission as also conducted emission and the immunity of automotive components or vehicles can be tested by the TDK EMC experts.

Besides measurements based on customer demands there is also the opportunity to take advantage of a Full EMC support, where TDK supports the customer

through the whole EMC process starting from pre-compliance to final declaration of conformity.

5. References

[1] TDK Electronics AG: “EMV-Filter und Drosseln für die Leistungselektronik”, Edition 2021

[2] Website https://www.tdk-electronics.tdk.com/

6. Glossary

AC: Alternating Current
BEV: Battery Electrical Vehicle
C_{Gi}*:* Capacitance Ground - Inverter
CM: Common Mode
CMC: Common Mode Choke
C_X*:* X-Capacitor, here capacitor between lines
C_Y*:* Y-Capacitor, here capacitor between line & ground
DC: Direct Current
DM: Differential Mode
DVDT: Voltage Transient
EV: Electric Vehicle
EMI: Electro Magnetic Interference
EMC: Elector Magnetic Compatibility
GND: Ground
HV: High Voltage
I_{CM}*:* Common Mode Current
L: Line
PWM: pulse width modulation
R_{Gi}: Resistance Ground - Inverter

One for All: Functional Integrated Electronics for HV Architectures

Philip Brockerhoff, Ayman Ayad

Vitesco Technologies, Siemensstraße 12, 93055 Regensburg, Germany

Abstract: We present a high voltage (HV) converter capable to replace all galvanic connected functions. It provides DC boosting, bidirectional AC charging, traction inverter and external power supply for electrical consumers.
The converter uses silicon carbide (SiC) MOSFETs built up on a low-inductance power stage. It operates with switching frequencies of up to 500 kHz to dynamically control the output capacitor as generic voltage source for bidirectional energy flow. It boosts or bucks the vehicles battery voltage with true sinusoidal output voltage. The control of the system is performed by latest control software.

Keywords: converter, efficiency, electric drive, charging

1. Introduction

Challenges for electric vehicles (EV) include short driving distance, long battery charging time, low energy conversion efficiency and high vehicle price. We believe that electronic products having higher efficiency, smaller size, and lighter weight will provide car manufactures with more freedom in designing electric vehicles and offer users a more comfortable car life. As one of the approaches to extend the driving distance, car manufactures are trying to reduce the driving resistance by improving the vehicle aerodynamic performance, i.e. by reducing the frontal projected area of the vehicle body, as well as by increasing the efficiency of the power electronics. In addition, to provide a comfortable driving environment, the cabin space must be secured and in recent years many car manufactures are developing a powertrain system with a skateboard-type platform that integrates HV products on the floor of the car. In other words, the space allowed for those products is becoming smaller and smaller and the trend is towards downsizing, weight reduction, and high integration, not only for HV system components but also for other products. Furthermore, car manufactures need to prepare several variations of HV products such as on-board chargers (OBC) according to the target market demand and power conditions for each country, that increases the product cost. In addition, to improve battery charging efficiency during cold temperatures, traction battery conditioning systems are adopted in recent years to heat up the battery to its optimum temperature. That must be designed while minimizing the negative side-effect on the battery energy consumption and the battery itself. We believe that this newly developed approach could be one of the solutions in order to manage these challenges already published in [6].

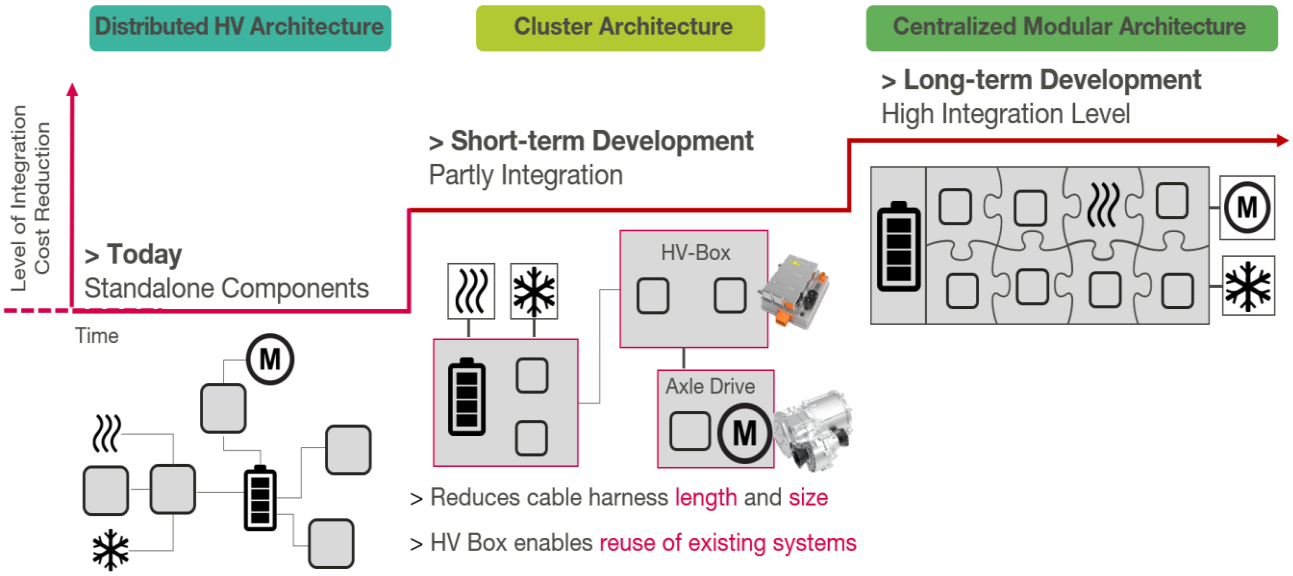


Figure 1: Evolution of HV architecture

2. Challenge: Cost, Volume, and Efficiency Improvement for EV's Power Electronics

HV architecture is changing from past distributed, one box per function, to today's cluster architecture with battery, HV box, and axle drive as main components as shown in Figure 1 [1]. Integration will continue to reduce cost and volume to a centralized modular architecture either in the battery or engine compartment. For this centralized electronic the paper proposes an "one-for-all" multifunctional power supply converter.

3. Multifunctional Power Supply Converter Description

A functional overview of the multifunctional power supply is depicted in Figure 2. The converter combines the following functions:

- Inverter with inherent boost function
- Bidirectional charger for AC and DC including DC boost
- External power take-off (ePTO)

All the functions are galvanically connected. Key feature is a true sinusoidal or DC output voltage, like a voltage source with minimum voltage ripple, that can be freely configured. Also any other voltage signal shape can be created.

Basically, the multifunctional converter approach improves the story of the previous AllCharge [2] [3] design, which originally used the machine inductance as grid filter and introduced a high power DCDC converter in addition to the inverter.

The same functions are now addressed without the necessity of the machine inductance in one integrated, multifunctional component. Using the

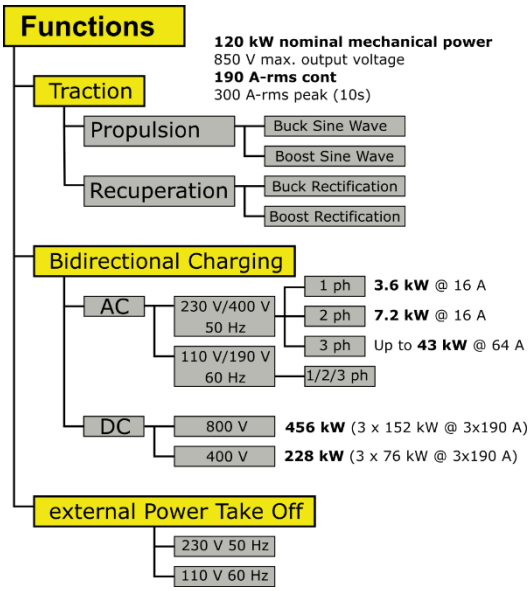


Figure 2: Functional overview

converter as an inverter with inherent boost function, it is capable to drive a permanent magnet synchronous machine (PMSM) with 120 kW nominal mechanical power. By the functionality of a DCDC boost converter the 800 V battery can be charged via a 400 V DC charging station with more than 220 kW or 76 kW per phase (190 A). The converter enables three-phase AC charging at a 230 V/400 V, 50 Hz grid with up to 43 kW (64 A).

One- or two-phase charging is also possible. The external power take-off is limited by the domestic socket capability of 3.6 kW (230 V/16 A) which can also be used during three-phase and one-phase charging mode.

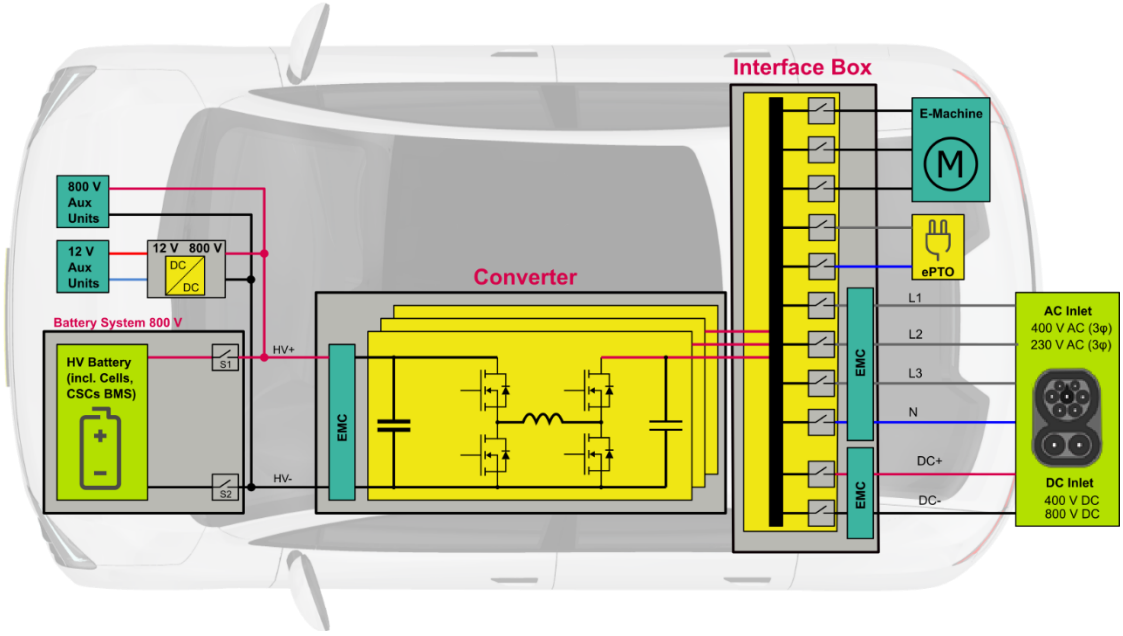


Figure 3: Multifunctional converter system overview

4. Technical Idea and Hardware Design

Figure 3 shows a detailed overview of the HV system architecture: Three identical phase modules of the converter are multiplexed via relays to the different functions described in chapter 3. The relays are integrated in an interface box, also visible in Figure 3. Auxiliary functions like heater, AC compressor or HV to LV DCDC are directly connected to the battery.
The widespread 400 V and the novel 800 V charging stations are fully supported. For the 400 V charging stations the converter will boost the input voltage up to the necessary voltage level of the approx. 800 V battery system. In traction mode, as visible in the current and voltage waveforms shown in Figure 4, the converter is providing phase voltages to the electrical motor independent of the state of charge of the HV battery. The inherent boost function in the converter will boost the phase voltages in case the battery voltage is lower than its required amplitude.

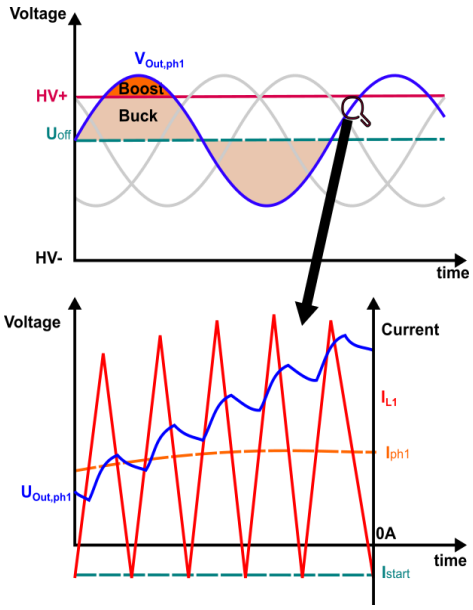


Figure 4: Current and voltage waveform in traction mode

The simplified schematic of the converter in Figure 3 depicts the technical approach: two half bridges connected via an inductor are used with SiC MOSFETs up to 500 kHz switching frequency to dynamically modulate the analog voltage of the output capacitor. The load is driven by the voltage difference of at least two output capacitors. This approach has been introduced as Y-inverter [4] [5] for high speed drives for single digit kW applications and is new for multifunctional approaches in the above 100 kW range.
To reduce the well-known high-switching losses inside the 1200 V SiC MOSFETs, a soft switching control was implemented. The parasitic effects in the circuit were reduced by a power module PCB design with very low impedance.
The high frequencies switching enabled a design for this high-power class compared to other designs with very small capacitors and a relatively compact inductor. In Figure 4 there is the current waveform of the inductor depicted, which is operated at high currents (up to 190 A rms / 300 A peak) and high frequencies at the same time. Therefore, it is a critical component, which is sensitive in terms of saturation, cooling, stray fields, and mechanic integration.
The current design of the converter section illustrated in Figure 3 is based on a modular design including, amongst other components, the semiconductors, the input and output capacitors, the current measurement shunt, all the gate drivers and the error-logic circuits. Furthermore, it is also designed for measuring the input and output voltages, the coil current and all drain-source voltages for the zero-voltage switching (ZVS) control and integrates the auxiliary driver supplies as well.

5. Control System

Due to the high-switching frequencies of up to 500 kHz, one challenge in controlling the multifunctional converter is the short closed-loop controlling times. This makes it necessary to use field-programmable gate array (FPGA) technology. Combining this with one of the project's control system requirements of consistent model-based development (MBD) plus subsequent automatic code generation and synthesis, additionally a performance real-time machine has been chosen as controller platform. It comprises a CPU, as well as a FPGA equipped with fast I/O modules. This makes it possible to deploy behavioral logic and slower tasks like torque and speed control on CPU; whereas fast tasks, like inductor current control or Pulse Width Modulation (PWM) actuation are implemented on the FPGA. As controller technique a cascaded motor speed/torque-phase current controller is employed like proposed in [5]. In Figure 5 the implemented controller structure is shown. It is used for both, driving and AC charging. It starts with mode selection for pure torque control, charge power demand or speed control followed by a well-known field-oriented current control (FOC). Controller inputs are machine speed ωM, angle φM and phase currents ii, i ∈ a,b,c, as well as grid voltage angle φG and frequency ωG for AC charging. This part with sample times down to 100 µs is located on the CPU. Its output phase voltage references of the electric machine u_i^*, i ∈ a,b,c, added up with an offset voltage u_{off}^* for getting strictly positive output voltages are fed into the cascaded voltage and inductor current control system.
The output voltage control is used to ensure true sinusoidal output phase voltages given by the references from FOC followed by inductor current controller yielding inductor voltages u_{Li}^*, i ∈ a,b,c, as input for the Buck-Boost modulator. It also utilizes the

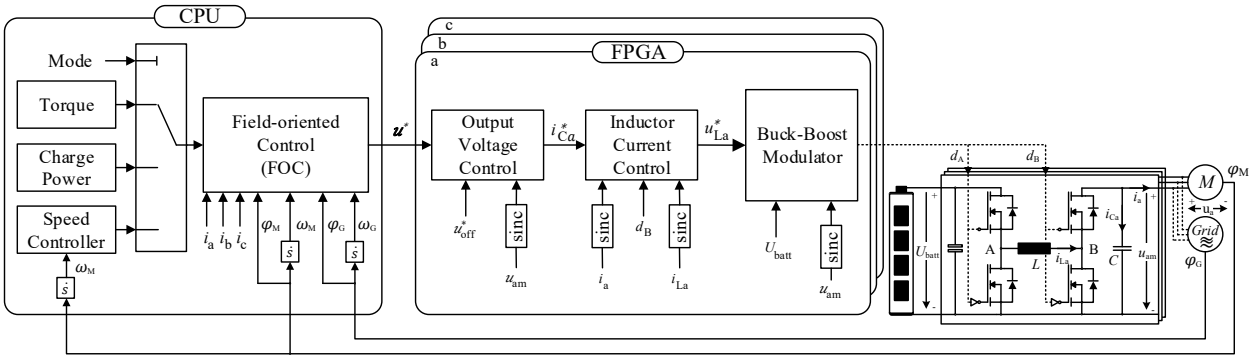


Figure 6: Cascaded control structure based on [5]

"democratic" approach like in [5] by calculating duty cycles for both half bridges of all three phases equally shared with regards to the appropriate buck and boost demands. Because of needed closed-loop sample times above 500 kHz, up to some MHz, the calculation therefore is done on the FPGA.

These high switching frequencies and hence fast controlling times also require a very accurate analog-to-digital signal conversion at a rapid pace being able to read in the control variables, such as output voltages u_{im}, inductor currents i_{Li} and load currents i_i, $i \in a,b,c$, in appropriate quality. Furthermore, there are intense electromagnetic interference sources coming from steep voltage and current gradients what makes it necessary to measure the signal over a whole periode improving the signal-to-noise ratio (SNR). That challenges are tackled by using sigma-delta converters in combination with digital sinc filters which are located on the FPGA as well.

6. Simulation Results

In order to prove the concept and to support the design phase, dynamic and losses simulations were carried out. The system parameters for the dynamic simulation are chosen as follows:

- Battery voltage = 800 V
- Maximum output voltage = 850 V
- Input and output capacitance = 5 µF
- Converter inductance = 5 µH
- Switching frequency = 300-450 kHz

To optimize the converter losses, a variable switching frequency strategy is used. Figure 6 shows the desired sinusoidal output voltage of 600 V and its corresponding three phase currents with an RL load for a switching frequency of 450 kHz and a fundamental frequency of 1 kHz. As can be seen in Figure 6, the output phase voltages are pure sinusoidal waveforms. This in turn results in approximately zero harmonics and very low noise in the electric machine.

To check the losses of the new converter in both modes of operation, a simulation model was built based on different SiC technologies. In the simulation

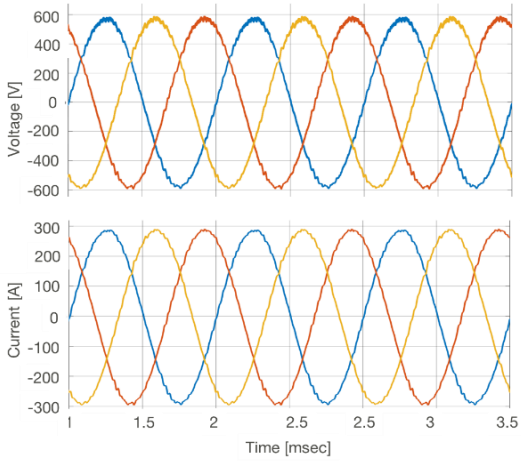


Figure 5: Output phase voltages and currents of the new converter

model four SiC chips per switch are considered, that can achieve phase current of 300 A rms and a maximum DC-link voltage of 950 V. In addition, the ZVS technique was used to eliminate the turn-on losses of the switches.

In driving simulation, WLTC with a C-segment battery electric vehicle of 1700 kg weight and a cW-coefficient of 0.28 was considered. Figure 7 highlights the switching, conduction, and coil losses of the converter.

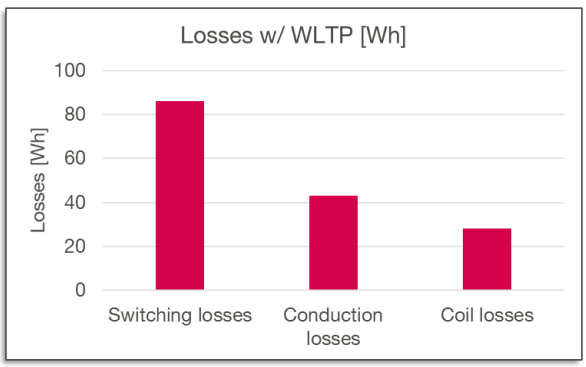


Figure 7: Losses with WLTC cycle

The total WLTC cycle losses are 157 Wh and distribute in 86 Wh switching losses, 43 Wh conduction losses and 28 Wh coil losses. This results in an average cycle efficiency of ~95 %. Optimization analyses are ongoing to further decrease the switching losses and optimize the efficiency over the whole operating range of the electric machine.
Besides driving and recuperation modes, DC and AC charging are main functionalities of the new converter. For DC charging, active power ranges from 50 kW to approx. 500 kW were examined. The charging efficiencies vary between 97.2 % and 98.1 %. For this type of charging, efficiency decreases with increasing charging currents due to the increase of the conduction losses. With 11 kW AC charging, the efficiency of the new converter was compared with the standard 2-stage OBC over the voltage range of an 800 V battery (see Figure 8). From Figure 8 it can be concluded that the new converter outperforms the standard OBC over the whole battery operating voltage level. This makes the new converter very attractive for charging use cases.

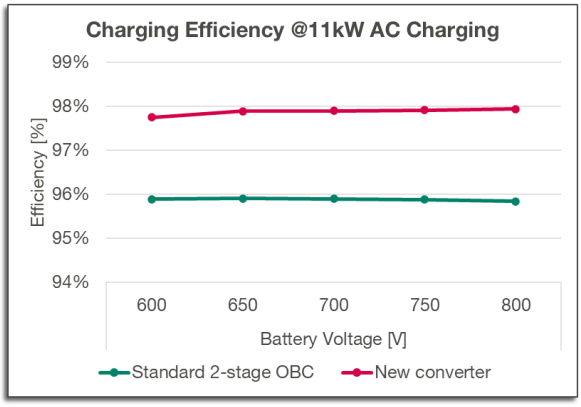


Figure 9: Comparison of charging efficiencies

7. Benefits

Figure 9 highlights a competitive architecture comparison for a typical baseline based on company internal cost evaluation data (NBE: non-binding estimation) versus estimated component geometric volumes.:

- Battery electric vehicle with 120 kW traction power
- 11 kW OBC and 400 V charging compatibility (for 800 V cars)
- SOP 2025

Main comparison architectures are 800V architectures in silicon (Si) and silicon carbide (SiC), especially with focus on the inverter. Bubble size highlights uncertainty of the evaluation.
It can be seen that the potential of the new approach is superior in cost and volume at the same time offering also additional functionality, by its free configuration feature.

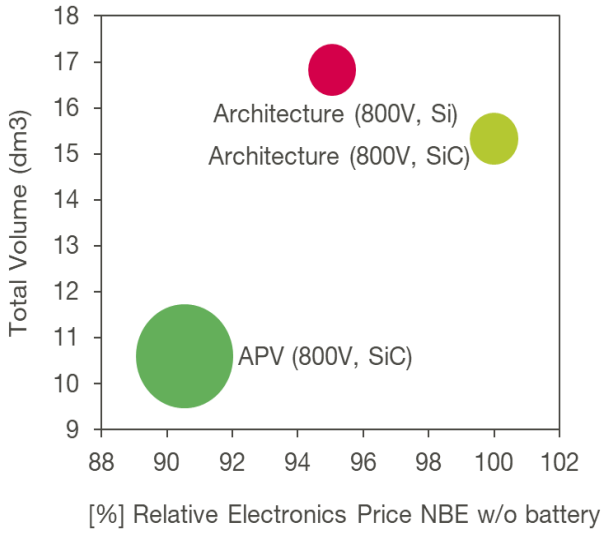


Figure 8: Converter comparison in terms of cost and volume

8. Conclusion

The paper contains the current status of the newly developed highly integrated multifunctional power electronics for 800 V battery electric vehicles. The key feature of the component is a highly integrated device capable of providing the functionality of a bidirectional on-board charging system, DC booster as well as traction inverter, all combined.
The component itself can produce freely adjustable output voltage signals with bidirectional signal flow and signal conversion capabilities. The maximum voltage levels are set suitable for today's 800 V power net applications. This characteristic enables the conversion of high-power DC signals for DC boosting as well as rectification of AC input signals for HV battery charging as well as inverting of the passenger car power net voltage to drive an electric machine.
The ability to create this highly integrated features is given by the usage of modern wide bandgap semiconductors, complex control algorithms and optimized electrical interfaces as well as a very low-inductive design.
Remaining important challenges are the HV safety for galvanic connected charging and the complexity of the power stage.

8. Acknowledgement

The work has been previously published during [6].

9. References

[1] P. Brockerhoff and A. Ayad: "*SiC/GaN drives the high voltage architecture evolution for future 400 V and 800 V platforms*", CTI US 2021.

[2] M. Bruell, P. Brockerhoff, F. Pfeilschifter, H.-P. Feustel, and W. Hackmann: "*Bidirectional Charge-*

and Traction-System", EVS29 Symposium, Montréal, Québec, Canada, 2016.

[3] M. Bruell and P. Brockerhoff: "*Avoid the DC charging trap"*, Electric Vehicle Symposium EVS30, Stuttgart, Germany, 2017.

[4] M, Antivachis, D. Bortis, D. Menzi, and J.W. Kolar: "*Comparative Evaluation of Y-Inverter against Three-Phase Two-Stage Buck-Boost DC-AC Converter Systems",* 2018 International Power Electronics Conference (IPEC-Niigata 2018-ECCE Asia), pp. 181-189.

[5] M. Antivachis, D. Bortis, L. Schrittwieser, and J.W. Kolar: "*Three-phase buck-boost Y-inverter with wide DC input voltage range"*, 2018 IEEE Applied Power Electronics Conference and Exposition (APEC), 2018, pp. 1492-1499, doi: 10.1109/APEC.2018. 8341214.

[6] P. Brockerhoff, C. Bottke, T. Kühner, W. Heimann, A. Ayad, P. Schmusch, M. Ehrmann, and T. Mimori: "*Functional Integrated Electronics for HV Architectures -From today's dedicated electronics to multifunctional power supplies in electric vehicles-"*, JSAE Spring Congress, Yokohama, Japan, 2022.

10. Glossary

AC: alternating current

CPU: central processing unit

DC: direct current

WLTC: Worldwide harmonized Light Duty Test Cycle

15 JUNE 2022

ELECTRIC VEHICLE HOLISTIC VIEW

One-stop shop IAV: **Catalyst for smart automotive tech**

Digitization, automation and new business models are upsetting the automotive space. Besides an obsession with tech, thinking outside the box is what it takes to harness that change. As Tech Solution Provider, we offer far more than classic development services. No matter whether it's about turnkey solutions for e-traction, battery technology or hydrogen fuel cells or even powertrain software: We raise the bar and take on more responsibility to shape the mobility of tomorrow. Because the future of vehicle propulsion holds more than one answer and mastering complexity is part of our DNA.

iav.com

Efficient E-Motors as key for a sustainable future

Jannick Heilck

Schaeffler Automotive Buehl GmbH & Co. KG, Bühl (Baden)

Abstract:

Sustainability is an important driver of mobility transformation. With this in mind electric drive systems are commonly identified as leading technical solution. A big impact to this is the optimization of an E-Motor regarding its sustainability footprint in different fields like development & production.

Looking more detailed on the early lifetime phase of an E-Motor, higher power density and increased efficiency lead to a reduced demand for materials of the motor itself as well as the whole electric drivetrain. Results of this are highly integrated dedicated hybrid transmissions but also e-axle traction motors with optimized cooling. In this talk this optimization is explained using an example recently developed which is considering motor design driven sustainability effects as well as the complete system sustainability affected by the E-Motor layout.

Taking this product example to the next step of series production, well optimized production processes are needed to further reduce material consumption, achieved by efficient material use avoiding only process relevant product features. In addition to that the whole production line concept should be designed for a minimized carbon emission & energy use.

To sum up, the development & production of efficient e-motor concepts optimized regarding their sustainability over the whole lifecycle will be deepened & discussed in this talk.

Keywords: Sustainability, Carbon Footprint, E-Motor

1. Introduction – Motivation for sustainable E-Motors

Climate change and material shortage are nowadays challenges affecting companies & their products. Sustainability is one solution to reach alleviation of the consequences and take social responsibility [1].

Sustainability itself can be defined as a three pillars conception carried by social, economic and environmental criteria [2]. This is taken further by the definition of the United Nations sustainable development goals defined in 2012 [3]. These goals will be the basis for the analysis taken in this paper.

An example for a sustainability management structure consists of 4 subcategories analyzed (see Figure 1).



Figure 1: Sustainability Management focus areas affecting the e-motor sustainability analysis taken from [3]

Three of these are affecting the technical product electric motor (e-motor) will be further discussed in this talk: “Customer and Products” is directly contributing to chosen E-Motor concept CO2 footprint, whereas “Environment and Energy” affect the way of E-Motor production with the focus of CO2 neutral production and resource efficiency. The last item of E-Motor Materials analyzed here belongs to the topic “Suppliers & Materials”. Broken down the sustainability management to e-motor product level this results in a pyramid of e-motor sustainability consisting of E-Motor Concepts on top level, E-Motor Production and E-Motor Materials on foundation level (see Figure 2).

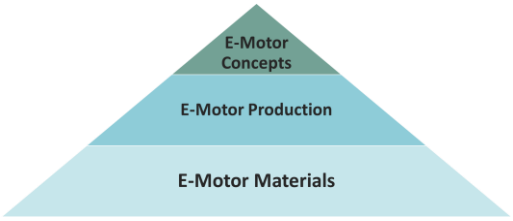


Figure 2: Pyramid of E-Motor Sustainability

The pyramid broadens over the production of subassemblies, where dedicated optimizations on

CONFIDENTIAL

production level are necessary, e.g. for rotor & stator assembly. To further detail this analysis, the assembly can be broken down to multiple components to reach the E-Motor material level.

In this case, a sustainability management example considering all these three topics from concept to material will be shown. The next chapter will start with an e-motor concept comparison for a 3-in-1 e-Axle used in a medium class Battery electric vehicle (BEV).

2. E-Motor Concept Level – Carbon Footprint for different EM Concepts

The sustainability management area "customer & products" introduced in the previous chapter can be applied to electric motor concept level.

The first step is to define the application for this example where the E-Motor shall be applied to. In this example the E-Motor shall be the implemented in a 3-in-1 electric axle main drive for an exemplary C-segment BEV (see boundaries in Table 1). This requires then a high driving cycle efficiency (WLTC in this case) to maximize the range of the vehicle in relation to its battery capacity. Two different gear ratios will be compared.

Table 1 – E-Motor Concept Boundaries

	Unit	Slow Concept	Fast Concept
Nominal Voltage	VDC	650	
Maximum Peak Current	Arms	300	
Peak Power	kW	150	
EM Active Part OD	mm	220	
Gear Ratio	-	8.2	12
Peak Torque	Nm	445	300
Max. Speed	rpm	12500	18500

The second step is to choose the electric motor type for the example application, which is strongly depending on the design focus parameters. Due to the main drive purpose and the optimization target towards sustainability efficiency and material weight are identified as the focus parameters. A separately excited synchronous (EESM) & permanent magnet synchronous motor (PSM) are the suitable motor topologies to fulfil these goals (see Figure 3). The induction motor is not likely and beneficial for main drive applications with lower power density and efficiency.

The EESM is seen as most beneficial with respect to efficiency and no use of rare earth magnets whereas a lower material consumption in total can be achieved with a PSM.

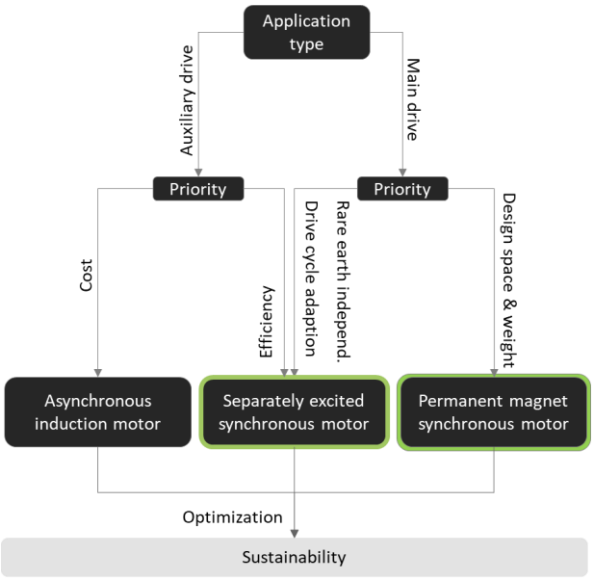


Figure 3 - Example of a high-level e-motor technology selection adapted from [5]

The overall EM concept chosen is affecting mostly the rotor layout, leaving the stator technology open. This evaluation will focus on distributed winding stator technology with rectangular wires. To achieve such a configuration a wave winding or hairpin stator can be used for PSM as well as EESM. Leaving the electromagnetic design identical, the differences for a sustainability analysis between hairpin and wave winding are a result of a higher copper winding head mass in the hairpin stator.

For this concept comparison 4 different E-Motor concepts and their material carbon footprint will be compared. A slow spinning hairpin PSM is the baseline for this analysis. Another slow speed concept with wave winding stator shows the influence of a different winding head mass (see Table 2). The other two examples keep the wave winding stator technology but having an increased gear ratio. One of them is an EESM and the other PSM.

CONFIDENTIAL

Table 2 – Overview about slow speed E-Motor concepts with gear ratio of 8.2

	Unit	Hairpin PSM	Wave Winding PSM
Total Length (incl. winding head)	mm	174	165
WLTC Efficiency	%	95.87	95.93
Copper Use	kg	5.0	4.7
Magnet Mass	kg	1.5	

The EESM concept is only shown for the higher gear ratio due to its better efficiency at higher speeds. This was experienced in an internal optimization process. The benefit of the EESM is the absence of rare earth magnets coming along with the drawback of an increased copper mass due to the rotor winding (see Table 3).

Table 3 – Overview about high speed E-Motor concepts with gear ratio of 12

	Unit	Wave Winding EESM	Wave Winding PSM
Total Length (incl. winding head)	mm	154	154
WLTC Efficiency	%	95.9	96.0
Copper Use	kg	6.9	4.1
Magnet Mass	kg	0	1.1

For a deeper analysis the carbon footprint will be calculated out of the individual concept characteristics. The biggest CO2 reduction compared to the low-speed baseline scenario can be achieved with a higher speed wave winding PSM. The achieved CO2 emission reduction only by optimizing the concept is 21% (see Table 4).

Table 4 – Raw Material CO2 Footprint Calculation for the 4 different E-Motor concepts

Gear Ratio	Topology	Relative Material CO2 Reduction
8.2	PSM Hairpin	0% (Reference)
	PSM Wave W.	-1 %
12	EESM Wave W.	-20%
	PSM Wave W.	-21%

The shown raw material CO2 footprint calculation doesn't include further material processing like magnet insertion or stamping. This comparison is still valid for the whole E-Motor because the production is already CO2 neutral and only the material supply chain emits CO2. Due to its big CO2 emission reduction potential the high speed wave winding PSM will be taken for the further analysis within the next chapters

3. E-Motor Production Level - Green production with material saving processes

Sustainable E-Motor production needs to be thought out from building infrastructure itself over the production processes.

The sustainability of building infrastructure can be evaluated with standards like the one for sustainable buildings from the German Sustainable Building Council (DGNB). The E-Motor plant in Hungary (see Figure 4) used for the CO2 footprint calculation is certified with the DGNB Gold standard and reaches CO2 neutrality with measures like a photovoltaic system for electricity production, heat recovery and separated rain-/wastewater treatment.



Figure 4 – CO2 neutral certified E-Motor plant in Hungary used for this sustainability analysis

Combining the concept analysis from the previous chapter with the described plant specific properties, a dedicated carbon footprint can be created. This is done for the e-motor active parts of the high speed wave winding PSM concept, which consists of the stator assembly with winding and the rotor assembly including transfer molded magnets and shaft (see Figure 5).

CONFIDENTIAL

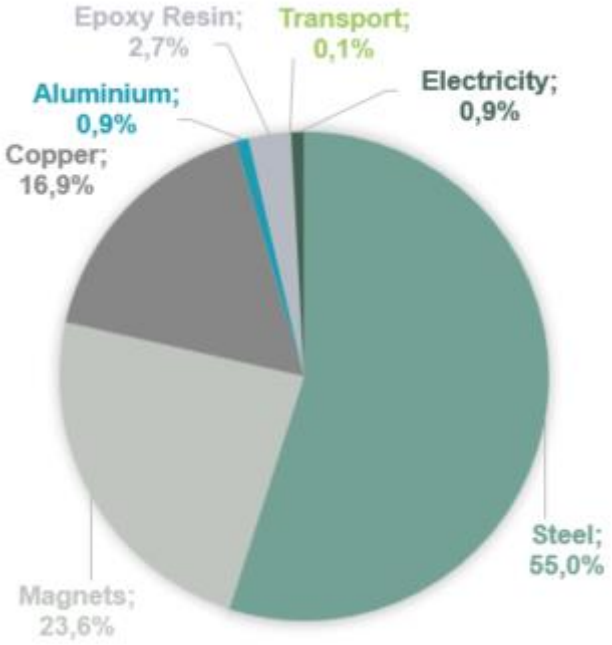


Figure 5 – Carbon footprint distribution for a high speed wave winding PSM

With the sustainable plant concept applied, there are two large remaining contributors to the carbon footprint. The biggest contributor is the electrical sheet for stator and rotor lamination, followed by the permanent magnets.

To further reduce the carbon footprint in comparison to the reference low speed hairpin PSM design, the material supply chain needs to be optimized. In the next chapter this is done for the permanent magnet.

4. E-Motor Material Level - Material Supply Chain optimized towards sustainability

The E-Motor example shown here has already been optimized towards a lower carbon footprint and sustainability on concept and production level. For further optimization, the material level gets involved.

In this case the sustainability optimization is exemplary performed for the permanent magnets. For the best result the whole supply chain needs to be optimized. This is ranging from mining to production of the final magnets as assembled in the rotor assembly process (see Figure 6).

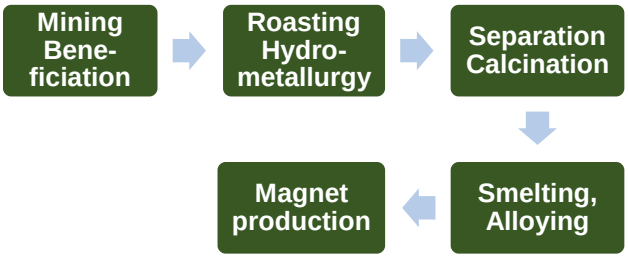


Figure 6 – Magnet supply chain process

For this EM example an optimized european/canadian magnet supply chain [5] was taken into account compared to the state-of-the-art supply chain with magnets where every process from mining to magnet production is done in China.

With this optimized supply chain the carbon footprint can be reduced about 42% (see Figure 7). This is mainly achieved by use of renewable energies for electricity and will be further optimized.

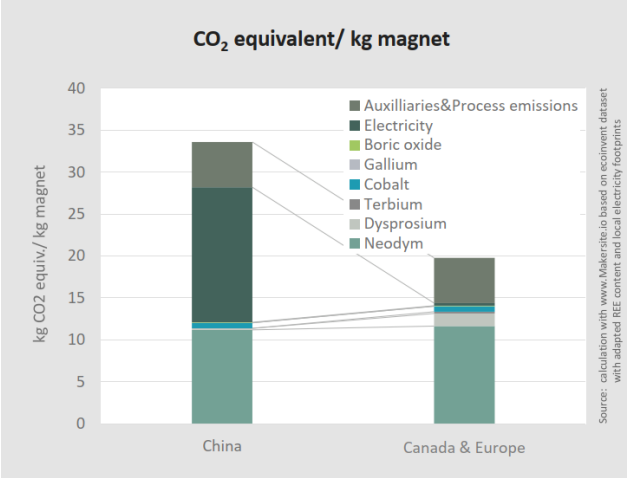


Figure 7 – Carbon footprint of permanent magnet used for exemplary high speed wave winding PSM

Taking this reduction into account and summing up with the optimization achieved on concept level, an overall carbon footprint reduction of 30% can be achieved. 9% are related to the optimized European/Canadian magnet supply chain with a large use of electricity from renewable sources (see Figure 8).

CONFIDENTIAL

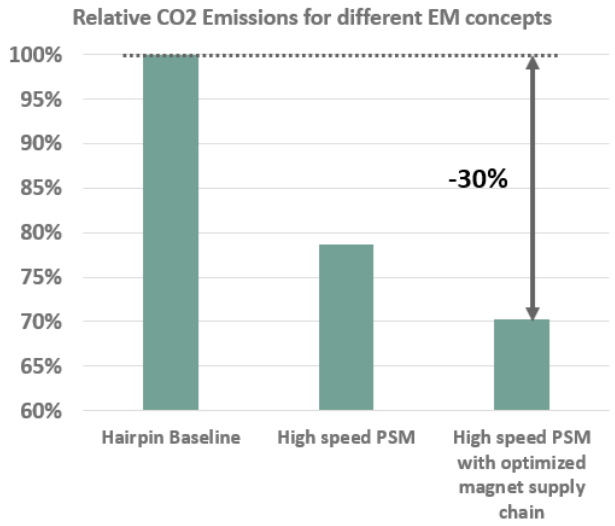


Figure 8 – Achieved carbon footprint reduction combining optimizations on concept & material level

5. Conclusion & Outlook

This paper has shown the possibilities to improve the sustainability of an e-motor by reducing its carbon footprint on concept, production and material level.

As a first step an overall carbon footprint reduction of 30% was achieved. Baseline was a hairpin E-Motor with already CO2 neutral production. It was optimized towards a higher speed system concept with a wave winding stator and optimized magnet supply chain.

As a second step in the future the sustainability of electrical sheet and copper supply chain will be investigated and optimized to come closer to the target of a CO2 neutral e-motor.

With more and more EVs in the market, e-motor recycling as a third point becomes more evident to achieve higher sustainability. Then the e-motor sustainability optimization needs to be extended: besides concept, production & material level, efficient recycling processes need to be evaluated.

6. Acknowledgement

I would like to thank Peter Schwanemann for his ingenious thoughts and ideas regarding sustainable e-motors. I'd also like to extend my gratitude to Luc Muller for his thoughts when it comes to e-motor-optimization. In addition, many thanks to all my colleagues from the Schaeffler Business Unit E-Motors who contributed to this work, especially to our R&D and purchasing teams.

7. References

[1] Schaeffler AG: "*Sustainability Report 2021*", Introduction, Schaeffler AG, 2022.

[2] Purvis, B., Mao, Y. & Robinson, D. *"Three pillars of sustainability: in search of conceptual origins."* Sustain Sci 14, 681–695, 2019

[3] UN: "*The future we want*. - *Outcome document of the United Nations Conference on Sustainable Development*", Chapter IV B, 63-64, United Nations, 2012

[4] Schaeffler AG "*Schaeffler zeigt nachhaltige Mobilität*", Press release, 06.09.2021, Herzogenaurach Source: https://www.schaeffler.com/de/news_media/press_releases/press_releases_detail.jsp?id=87723395.

[5] P. Schwanemann: *"Market driven E-Motor designs from Schaeffler"*, Dritev – Drivetrain for Vehicles 2020, Aachen, 2020

[6] Schaeffler AG: *"Schaeffler strengthens sustainable supply chain for electric motors"*, Press release, 19.04.2022. Herzogenaurach/Oslo

9. Glossary

BEV: Battery Electric Vehicle
CO2: Carbon Dioxide
EESM: Externally Excited Synchronous Motor
EM: Electric Motor
e-motor Electric Motor
PSM: Permanent Magnet Synchronous Motor

CONFIDENTIAL

Life Cycle Comparison of the Latest Electrified Propulsion Systems

Hervé Dupont[1], Paul Boucharel[1], Dr. Florian Uhrig[2]

[1]Vitesco Technologies, 44, Av. du Général de Croutte, 31100 Toulouse, France
[2]Vitesco Technologies, Siemensstraße 12, 93055 Regensburg, Germany

Abstract: Sustainability is the greatest challenge for the future of humanity. For the automotive industry, one consequence is the electrification of propulsion systems.

In this paper, the contributions to the energy consumed in the use phase of a BEV are analysed for different cycles. The benefits of the latest improvements to powertrain components are quantified and the impact on the reduction of greenhouse gas emissions over the entire life cycle is assessed. This shows that significant benefits can be obtained when optimising the powertrain system. However, it confirms that acting on the powertrain only is not sufficient. Improving the driving resistance of the car is a must for a drastic reduction of greenhouse gas emissions. This will trigger a virtuous cycle for the design of the whole vehicle with a right-sizing powertrain system. The current trend for BEVs is rather to target performances similar to ICEV, including the range, which is not compatible with a low environmental footprint.

Thanks to its know-how, Vitesco Technologies has the capabilities to develop efficient components corresponding to the daily usage of the car and helping to reach the required energy sobriety. This is mandatory to get closer from the Paris Agreement's goals.

Keywords: Life Cycle Analysis (LCA), Battery Electric Vehicle (BEV), Propulsion system, Electric machine

1 Introduction / Remaining carbon budget

The greenhouse gas emissions continue to grow year after year and are not in line with the trajectory defined in Paris Agreement to limit global warming "well below" 2°C above pre-industrial levels. The Figure 1 shows the evolution of these emissions between 1990 and 2019 with the contribution of the different sectors. In 2019, 59 Gt of CO_2 equivalent have been emitted and transport sector represents 15 % of them.

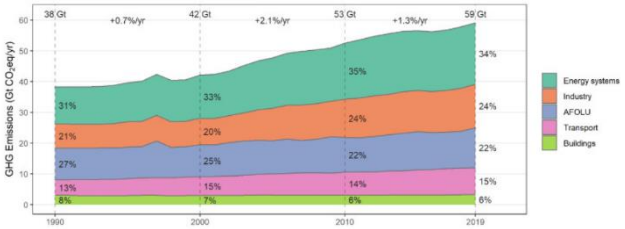


Figure 1: Sector-based GHG emissions between 1990-2019 (Source: Carbon Brief)

The part of emissions due to transport is mainly linked to road mode with 69 % in 2019 (Figure 2).

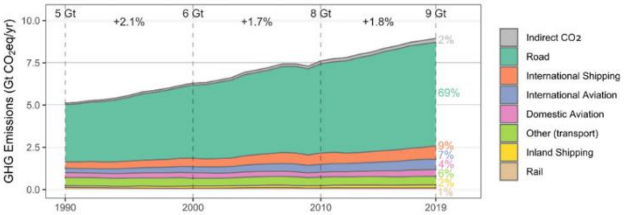


Figure 2: Evolution of transport emissions over 1990-2019 as a global average (Source: Carbon Brief)

Almost all regions around the world show increasing emissions. Asia presents the highest growth, surpassing now Europe (*Figure 3*).

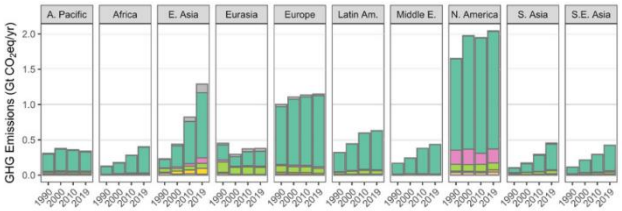


Figure 3: Evolution of transport emissions over 1990-2019 by continent (Source: Carbon Brief)

These figures from "Carbon Brief" [1], are based on the 6th Assessment Report released by the IPCC (Intergovernmental Panel on Climate Change) in April 2022 [2]. One of the main conclusions is concerning the remaining carbon budget to limit the temperature increase at a given level. To limit it to 1.5 °C with a likelihood superior to 50 %, the remaining carbon budget amounts to 500 Gt CO_2 equivalent, this means less than 10 years at current rate (Figure 4).

Global Warming Between 1850–1900 and 2010–2019 (°C)		Historical Cumulative CO_2 Emissions from 1850 to 2019 ($GtCO_2$)				
1.07 (0.8–1.3; likely range)		2390 (± 240; likely range)				
Approximate global warming relative to 1850–1900 until temperature limit (°C)[a]	Additional global warming relative to 2010–2019 until temperature limit (°C)	Estimated remaining carbon budgets from the beginning of 2020 ($GtCO_2$) *Likelihood of limiting global warming to temperature limit*[c]				Variations in reductions in non-CO_2 emissions[c]
		17%	*33%*	*50%*	*67%*	*83%*	
1.5	0.43	900	650	500	400	300	Higher or lower reductions in accompanying non-CO_2 emissions can increase or decrease the values on the left by 220 $GtCO_2$ or more
1.7	0.63	1450	1050	850	700	550	
2.0	0.93	2300	1700	1350	1150	900	

Figure 4: Estimates of historical carbon dioxide emissions and remaining carbon budgets. (Source: IPCC)

Following the Paris Agreement, the European Commission has launched the Green Deal with the target to reach an overall carbon neutrality by 2050 [3]. For automotive industry, the target is to reach zero emission from new cars in their use phase by 2035. Car makers are then moving towards pure electric vehicles (Battery Electric Vehicle). Several OEMs have announced the end of vehicles with internal combustion engine (ICEV) in Europe by 2030. Moreover, some of them aim to become carbon-neutral by 2040 [4], [5].

These targets are ambitious but no more in line with conclusions from the last IPCC report.

The purpose of this paper is to identify the contributors to greenhouse gas emissions of a typical BEV today and to assess possible improvements to reduce them.

2 Energy consumption of a BEV

Several studies have shown that a BEV has similar or lower greenhouse gas emissions than an equivalent ICEV over its entire life cycle [6], [7], [8], [9]. The main difference is the distribution between the emissions in car production and use phase. For an ICEV, around 80 % of emissions are generated in the use phase, versus 50 % approximately for a BEV (with the current European energy mix for electricity production). Even if this is significantly less, the improvement of a BEV to reduce this part is relevant.

In this chapter, the emissions of a BEV in its use phase will be quantified. The first step consists in computing the energy required at the wheel for a given cycle. This is done by integrating the resistive forces F_{res} seen by the vehicle over the considered cycle according to the formula:

$$F_{res} = F_0 + F_1.V + F_2.V^2$$

where F_0, F_1 & F_2 are the coefficients of a second order polynomial fit of these forces and V the vehicle speed. These coefficients are determined from the vehicle during deceleration phase and are used on chassis dynamometer for the certification test.

In our case, the computation is done using a model of the vehicle that include the chassis body, the powertrain and a driver. The same coefficients are applied in the model to simulate the vehicle. The reliability of the model has been assessed correlating several measurements. The energy consumption is predicted with a deviation lower than 3 %.

With characteristics of most recent BEVs extracted from the EPA database [10], the driving energy demands vary between 8 and 16 kWh/100 km on WLTC (Figure 5). The results show a wide dispersion for a given segment that can be linked to the inertia of the vehicle. This is especially the case for large SUVs (J2 segment).

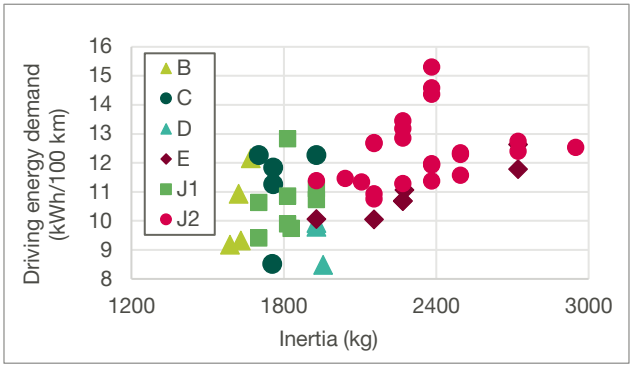


Figure 5: Comparison of driving energy demand per vehicle segment displayed as a function of vehicle inertia on WLTC

In a second step, the total energy consumed on the cycle is computed. For getting a realistic value, one specific vehicle representing J1-segment has been selected. The table 1 summarizes the main characteristics of this vehicle.

Parameters	value
Mass [kg]	1814
Tire dynamic radius [m]	0.324
Coast down coefficient F_0 [N]	115.9
Coast down coefficient F_1 [N/(km/h)]	-0.17
Coast down coefficient F_2 [N/(km/h)²]	0.040

Table 1: J1-Segment vehicle characteristics

Then a representative powertrain system is defined, and the model parametrized accordingly:

- Electric machine: Permanent Synchronous Machine 150 kW / 250 Nm
- Battery: Lithium Ion 50 kWh, 400 V
- Transmission: single ratio reducer

For the selected vehicle, the Figure 6 presents a waterfall diagram starting from the energy required at the wheel to the total energy consumed on WLTC at 23 °C. In this case this leads to an energy required at the wheel of 10 kWh/100 km. It is not possible to go below this value without changing the vehicle characteristics. This is due to the weight of the car and its aerodynamic and rolling resistances. Moreover, it

is assumed that the available kinetic energy is fully recovered.

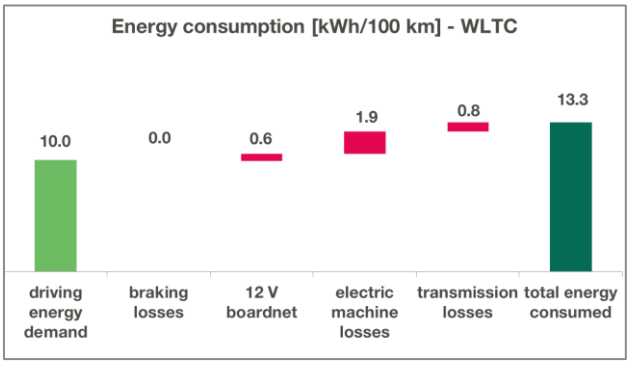


Figure 6: Waterfall diagram of a BEV from driving energy demand to total energy consumed - J1-Segment on WLTC

This would be the achievable energy consumption on WLTC with a perfect powertrain without any losses. The reality differs and several items must be added to reach the total energy consumed on the cycle:

- Energy dissipated in mechanical braking: in this case the powertrain system is able to decelerate the vehicle by itself, without using the mechanical brakes.
- Energy to supply the 12 V board net: it includes an average consumption of 250 W and the losses of the DCDC.
- Losses of electric machine (including inverter and motor losses)
- Losses of the transmission

For this vehicle, all together, this leads to a total energy consumed of 13.3 kWh/100 km.

Note that the energy spent to recharge the battery is not included.

The electric machine losses represent the highest item cumulating losses in motor mode and generator mode when recovering kinetic energy. These losses would be lower without recuperation, but the total energy consumed would then increase.

To assess the impact, this configuration, where no recuperation is achieved, has been simulated. In this case a significant part of the energy is dissipated by the mechanical brakes (Figure 7). The losses from electric machine are reduced as expected, like transmission losses. But the total energy consumed is significantly increased reaching 17.7 kWh/100 km (i.e. + 33 %). At the end, it is of course not favourable to prevent recuperation.

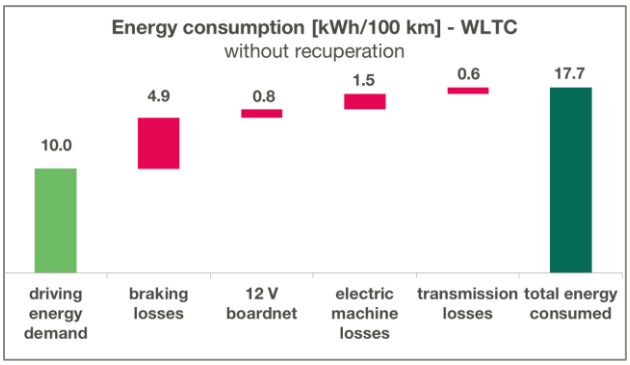


Figure 7: Waterfall diagram of a BEV without recuperation of kinetic energy - J1-Segment on WLTC

Dividing the driving energy demand by the total energy consumed allows computing the overall “vehicle efficiency”. With 13.3 kWh/100 km, it rises to 74.8 %. In comparison, a typical ICEV will be around 20 to 30 %.

The representativeness of the cycle is of first importance for assessing the use phase emissions for the Life Cycle Analysis. Several other cycles have been simulated to get a better understanding of the variability: three Real Driving Emissions profiles, the Chinese certification cycle (CLTC) and the urban part of WLTC (until 590 s). The real driving cycles are compliant with RDE definition (i.e. with right proportions of urban, road and motorway). They also contain variations of altitude, making them more realistic.

The simulation results are presented in Figure 8. In all cases, the powertrain was able to decelerate the vehicle without using mechanical brake.

The three RDE cycles behave similarly to WLTC in terms of energy distribution.

The Chinese cycle, however, presents significant differences. First the driving energy demand is much lower (reduced by 35 % compared to WLTC) and the distribution of powertrain losses reveals electric machine losses increased by 10 %. The total energy consumed is reduced by 22 %. This leads to a vehicle efficiency of 63 %, much smaller compared to WLTC.

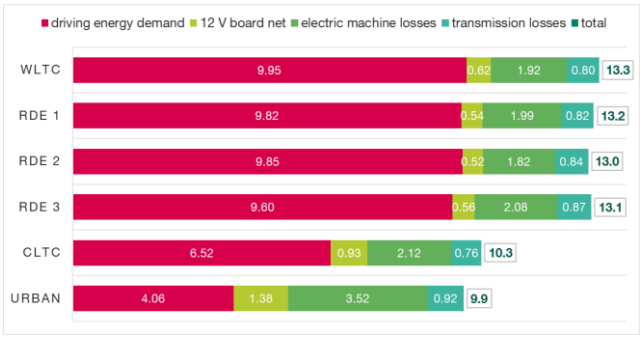


Figure 8: Distribution of total energy consumed for J1-Segment on different driving cycles

As there is no difference in the vehicle definition (same powertrain, same load road characteristics), the origins of the deviation are only linked to the driving profiles (Figure 9).

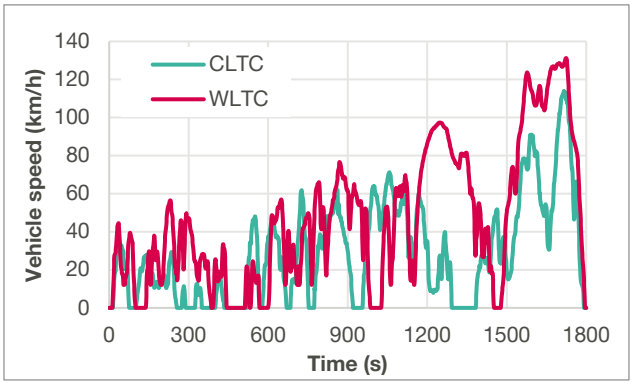


Figure 9: Comparison of driving cycle profiles CLTC & WLTC

The table 2 gives a comparison of the main characteristics of WLTC & CLTC. The CLTC has the same duration but a higher proportion of standstill and a lower average speed.

Characteristic	unit	WLTC	CLTC
Duration	s	1800	1800
Distance	km	23.3	14.5
Average Speed	km/h	46.5	29
Max. speed	km/h	131	114
Max. acceleration	m/s²	1.67	1.47
Max. deceleration	m/s²	-1.50	-1.47
Mean acceleration	m/s²	0.41	0.45
Mean deceleration ratio	m/s²	-0.45	-0.49
Acceleration ratio	%	44	29
Deceleration ratio	%	40	26
Standtill ratio	%	13	22

Table 2: Comparison of main characteristics of CLTC & WLTC driving cycles

The higher proportion of standstill degrades the efficiency as the board net is still supplied in these periods. But the main reason for the lower vehicle efficiency is counterintuitive: it is due to the higher proportion of kinetic energy recoverable on CLTC. That represents 55 % of the total energy consumed versus 36 % on WLTC. This amount of kinetic energy reduces the driving energy demand and, in parallel increases the total energy consumed. As it is fully recovered in both cases, this generates proportionally more losses on CLTC. Both effects lead to a lower vehicle efficiency on CLTC.

At the end, it can be concluded that the vehicle efficiency is strongly linked to the driving profile and the comparison of the values between cycles is not relevant. But from LCA point of view, the mission profile representing the use phase is determinant. On CLTC, despite a lower vehicle efficiency, equivalent CO_2 emissions will be reduced by 22 % compared to WLTC, as seen from energy consumption. And thus, all powertrain improvements will allow larger benefits.

Considering only the urban part of WLTC is also interesting. The energy consumption is reduced by 26 % but with much higher losses from the electric machine. This is due to the generator mode that is strongly used in urban part.

From these values, the greenhouse gas emitted in the use phase of the vehicle for the Life Cycle Analysis (LCA) can be computed. To proceed with this computation, some assumptions are required:

- The mileage: 200,000 km have been considered
- The emission factor in gCO_2 equivalent per kWh of electricity: several values have been used.
- The losses of the charger are not considered.

The emission factor is changing significantly from a country to another and from a year to another.

The Figure 10 shows the values compiled by European Environment Agency from 2015 to 2020 for different countries [11]. Between highest emitters (Estonia, Poland) and lowest one (Sweden), there is a factor of 80. The trend is globally to reduce the emissions year after year. Average value for European countries is 231 gCO_2 eq/kWh in 2020.

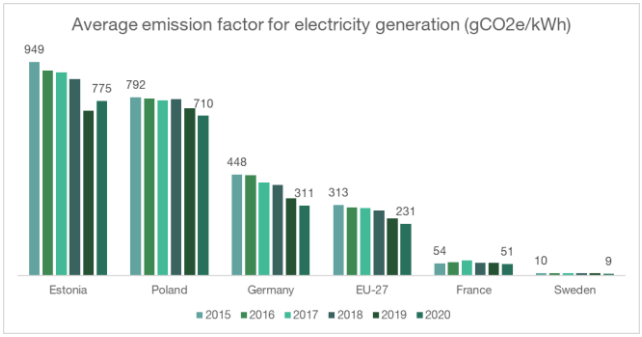


Figure 10: Emission factor for electricity generation for several countries in Europe and EU-27

The European Green Deal aims to reach carbon neutrality by 2050. In these conditions, emission factors of 400, 300, 200 and 100 gCO_2 eq/kWh have been considered. This leads to the following values displayed in Figure 11. For 300 gCO_2 eq/kWh around 8 tons of CO_2 eq. are emitted on RDE or WLTC versus 6 tons on CLTC or urban part of WLTC.

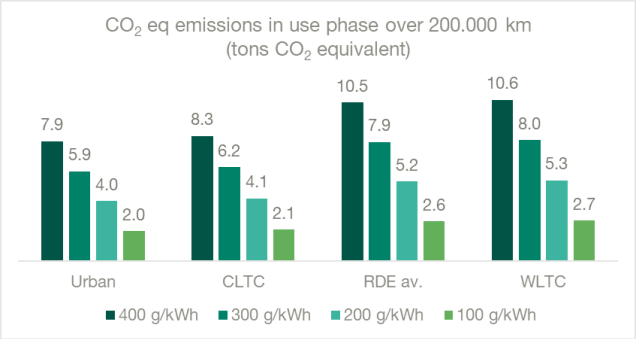


Figure 11: CO_2 equivalent emissions over 200,000 km according to the cycle for J1-Segment vehicle

This confirms the importance of the reference for the LCA.

Note: as indicated previously, these emissions do not include the losses for charging the battery or the additional consumption due to the conditioning of the cabin. All simulations are performed with an ambient temperature of 23 °C.

3 Reduction of energy consumption

In the previous chapter, the contributors to the energy consumed have been identified. The aim is now to assess different ways for reducing these contributions.

For this, a sensitivity analysis has been performed by simulations, applying an improvement on each of the contributors individually. The benefits computed versus the reference are shown in the Figure 12 for WLTC with successively a reduction of:

- 100 kg of the vehicle inertia
- 10 % of rolling resistance
- 10 % of aerodynamic resistance
- 10 % of electric load on 12 V board net
- 10 % of transmission losses
- 10 % of electric machine losses

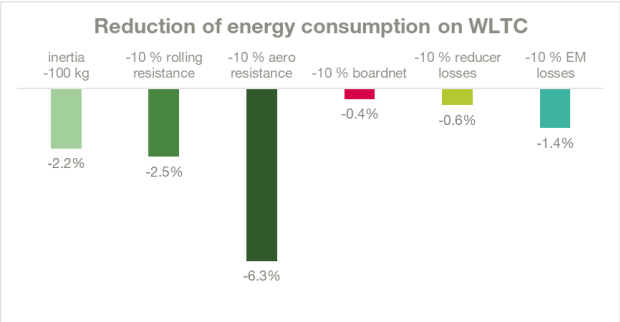


Figure 12: Sensitivity analysis on reduction of energy consumption - J1-segment on WLTC

This analysis does not consider the difficulty for achieving the respective improvements. The purpose is only to quantify the benefits and to compare the impact between the cycles.

As the average speed of the vehicle is higher on WLTC, the same reduction of aerodynamic resistance brings a higher benefit on this cycle. At the opposite, the reduction of vehicle inertia or rolling resistance is more beneficial on CLTC (Figure 13). On the powertrain side, a 10 % reduction of the losses leads to a bigger impact for the electric machine. This reflects the respective contributions identified in the previous part.

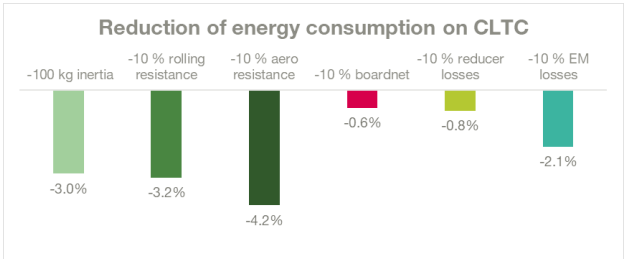


Figure 13: Sensitivity analysis on reduction of energy consumption - J1-segment on CLTC

Again, the benefit is higher on CLTC. The reason is the same as mentioned previously for the vehicle efficiency: on CLTC, there is a higher proportion of energy to be recovered and then the electric machine is more used in generator mode compared to WLTC.

The results for RDE cycle are very similar to WLTC.

A perfect powertrain means a total reduction of 25 % on WLTC and almost 60 % on CLTC.

This analysis shows that improving the powertrain of a BEV is relevant to reduce its overall energy consumption.

A first lever, with limited change on the design of the powertrain, consists in changing the reducer ratio. This offers the possibility to improve the total energy consumed but highly impacts the performances of the vehicle as shown in the Figure 14.

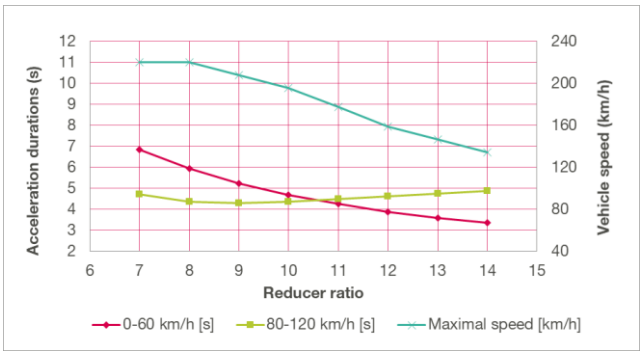


Figure 14: Impact of reducer ratio on performances - J1-segment

The acceleration capabilities from 0 to 60 km/h are much better when increasing the ratio. However, the maximal vehicle speed will be drastically reduced from 230 to less than 140 km/h on the range simulated.

The energy consumption is much less impacted (Figure 15). On RDE and WLTC, the variations between min and max values are in a range of 2 to 4 %. It reaches 6 % on CLTC and exceeds 16% on urban part of WLTC.

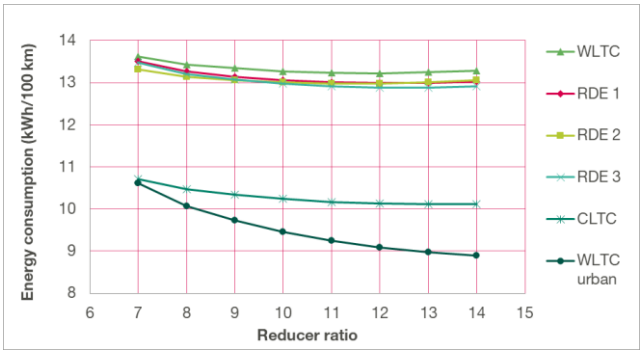


Figure 15: Impact of reducer ratio on energy consumption - J1-segment – different cycles

Therefore, for an urban usage, an interesting trade-off can be found with higher ratio values. The limitation of the maximal speed of the car is not a main drawback and accelerations are improved. For example, using a ratio of 12 instead of 8 makes it possible to reduce the energy consumption by almost 10 % on the urban part of WLTC versus 1.5 % on full WLTC. At the same time, acceleration duration from 0 to 60 km/h is improved by 35 %.

The reduction of energy consumed on urban part of WLTC is due to the reduction of electric machine losses as shown in the Figure 16.



Figure 16: Distribution of total energy consumed for J1-Segment on urban part of WLTC for different reducer ratios

For the same energy demand, the energy to supply the 12 V board net increases slightly with the reducer ratio, like the transmission losses. But this is largely compensated by the reduction of electric machine losses, linked to operating conditions in better efficiency area (Figure 17).

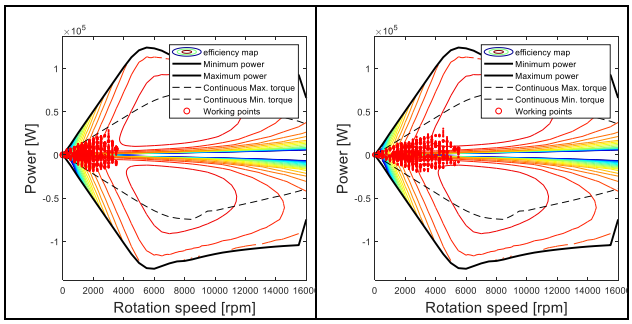


Figure 17: Distribution of operating points of electric machine on urban part of WLTC with ratio of 8 at left and 12 at right - J1-segment

From this picture, it can be noticed that, for such a small SUV, quite common in urban areas nowadays, the electric machine is used in a very small part of its capabilities. This reminds the situation of internal combustion engines that leads to the downsizing trend for operating them in a lower fuel consumption area. High CO_2 benefits are achieved today on millions of cars by this means [12].

However, downsizing the electric machine (100 kW instead of 150 kW) shows a limited benefit (around 1 to 2 %). The reason is the high efficiency level of the electric machine on a wide part of its map at the opposite of an ICE. And then, the repositioning of the operating points is much less sensitive. At the end, this is not the most efficient way for BEVs considering in parallel the strong impact on the performances. But this is an enabler with the reduction of the weight and packaging. We will come back to this later.

As the adaption of reducer ratio offers limited benefits especially on WLTC, going further requires reducing the losses of the powertrain components.

Vitesco Technologies works on several axes to develop optimised components, enhancing weight, packaging, efficiency, and cost.

Electric axle drives, such as the EMR4 (Electronics Motor Reducer 4th generation) is 25 % lighter and 5 % more efficient than 3rd generation [13]. An additional step has been achieved with the introduction of Silicon Carbide (SiC) technology for the inverter enabling a drop of losses of more than 50 % for this component [14]. Lastly Gallium Nitride (GaN) semiconductor technology used in on-board charger and DC/DC converters leads to significant additional savings [15].

Further investigations are on-going using electric machines without permanent magnets. An Externally Excited Synchronous Machine (EESM) generates its magnetic field with an electromagnet consuming some energy. This reduces its efficiency especially at low speed compared to a PSM. On the other hand, at high speed, the EESM does not need to compensate the high magnetic field of permanent magnets which is an advantage compared to PSM. In the production

phase, the EESM offers a better balance with no rare earth magnets. At the end, the global warming potential depends on the emission factor, mileage and mission profile [16].

Applying on our use case the different improvements identified previously for the electric axle drive, the inverter using SiC and the DC/DC using GaN leads to significant benefits on the total energy consumed (Figure 18).

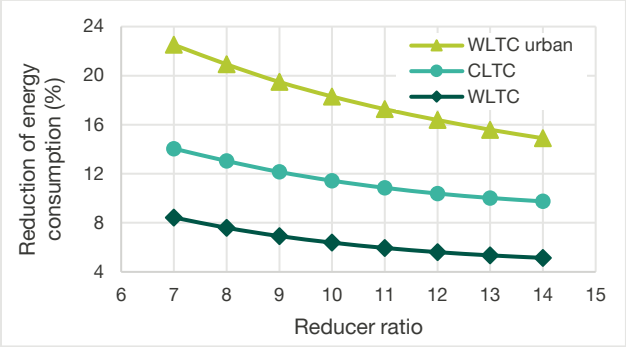


Figure 18: Reduction of the total energy consumed function of reducer ratio - J1-segment

The ranges depend on the ratio and the cycle: 16 % on WLTC urban for a ratio of 12, versus 10.4 % on CLTC and only 5.6 % on WLTC.

Such improvements trigger a snowball effect: it offers the possibility to diminish the size of the battery keeping the same range for the car. And thus, the inertia of the car can be reduced, enabling a new improvement of the efficiency which allows using a higher reducer ratio, etc.

The benefits will be on the use phase, production, and end-of-life, impacting GHG emissions and the overall footprint of the BEV.

Based again on the car considered in this study, an optimised powertrain system is defined compiling all measures. It is achieved thanks to an internal simulation tool chain that embraces a multi-criteria approach combining performances and efficiency.

The results are displayed in the Table 3. The total energy consumed is reduced by 9 % on WLTC keeping similar performances and same range. Cumulating the different phases of LCA, this enables a reduction of the GHG emissions over the lifetime of the vehicle between 5.5 and 7 % (depending on assumptions for battery production). The values are higher for CLTC & urban WLTC.

Benefits (%)	Use phase	Entire life cycle
WLTC	9 %	5.5 to 7 %
CLTC	18 %	11 to 13 %
WLTC urban	28 %	16 to 20 %

Table 2: Reduction of GHG emissions in the use phase and over the entire life of a BEV

Note: it has been considered here that SiC and GaN technologies have a neutral impact on the LCA compared to the current technology. This is an important assumption to be confirmed. Limited data are currently available.

This example demonstrates the need to address the challenge of reducing GHG emissions in its entirety. This is underway within Vitesco Technologies through the implementation of an extended simulation landscape covering the main relevant aspects as shown in the Figure 19, and resorting to design space exploration, artificial intelligence and optimal methods.

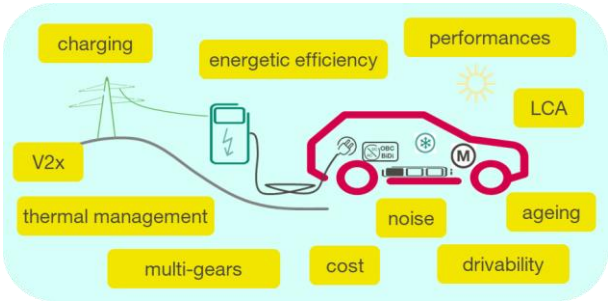


Figure 19: Overview of the landscape for a right design of the powertrain components

4 Conclusions

For a BEV belonging to the J1-segment, the combination of latest improvements for electric axle drive, inverter and DCDC enables to reduce the energy used on WLTC by 9 % and the GHG emissions up to 7 % over its entire life cycle while maintaining the same performances. Considering CLTC, these values are significantly higher (resp. 18 % and 13 %).

It demonstrates that optimising the powertrain components offers valuable benefits. However, these benefits are not sufficient in the context of climate change. Improving the driving resistance of the car is a must for a drastic reduction of GHG emissions. This will trigger a virtuous cycle for the design of the whole vehicle with a right-sizing powertrain system. The current trend for BEVs is rather to target performances similar to ICEV, including the range, which is not compatible with a low environmental footprint.

Thanks to its know-how, Vitesco Technologies has the capabilities to develop efficient components corresponding to the daily usage of the car and helping to reach the required energy sobriety. This is mandatory to get closer from the Paris Agreement's goals.

5 References

[1] Carbon Brief. In-depth Q&A: The IPCC's sixth assessment on how to tackle climate change. (04/2022)
https://www.carbonbrief.org/in-depth-qa-the-ipccs-sixth-assessment-on-how-to-tackle-climate-change/
(downloaded on 15th of April 2022)

[2] P.R. Shukla, J. Skea, R. Slade, A. Al Khourdajie, R. van Diemen, D. McCollum, M. Pathak, S. Some, P. Vyas, R. Fradera, M. Belkacemi, A. Hasija, G. Lisboa, S. Luz, J. Malley, (eds.)
IPCC, Climate Change 2022: Mitigation of Climate Change. Contribution of Working Group III to the Sixth Assessment Report of the Intergovernmental Panel on Climate Change
Cambridge University Press
doi: 10.1017/9781009157926

[3] European Commission, Green Deal
https://ec.europa.eu/info/strategy/priorities-2019-2024/european-green-deal/energy-and-green-deal_en
(downloaded on 5th of April 2022)

[4] Renault Group, Climate Report (04/2021)
https://cdn.group.renault.com/ren/at/renaultat/elektromobilitaet/climate-report-renault-group.pdf
(downloaded on 18th of April 2022)

[5] Volvo Cars reveals ambitious new climate plan (published in November 2019)
https://www.volvocars.com/au/about/australia/i-roll-enewsletter/2019/november/volvo-cars-reveals-ambitious-new-climate-plan
(downloaded on 18th of April 2022)

[6] R. Palm, A. Egeskog, K. Hagdahl, C. Krewer, I. Rade, L. Bolin und L. Dahllöf
The Carbon Footprint of Volvo XC40 BEV and ICE – Presented with Transparency
30th Aachen Colloquium Sustainable Mobility, Aachen, 2021.

[7] E. Pipitone, S. Caltabellotta, L. Occhipinti
A Life Cycle Environmental Impact Comparison between Traditional, Hybrid, and Electric Vehicles in the European Context
Sustainability 2021, 13, 10992.

[8] Ademe, projet E4T (04/2018). Bilan transversal de l'impact de l'électrification par segment
https://librairie.ademe.fr/mobilite-et-transport/1267-bilan-transversal-de-l-impact-de-l-electrification-par-segment.html#/44-type_de_produit-format_electronique
(downloaded on 19th of April 2022)

[9] FVV, Efficient use of the global CO_2 budget in the mobility sector. Four theories based on a meta-study on life-cycle analyses (06/2020)
https://www.fvv-net.de/fileadmin/user_upload/medien/materialien/FVV_LCA_Life-cycle_analysis_Briefing_paper_2020-06_EN.pdf
(downloaded on 18th of April 2022)

[10] EPA database, Certified Vehicle Test Results Report Data (11/2021)
https://www.epa.gov/compliance-and-fuel-economy-data/annual-certification-data-vehicles-engines-and-equipment
(downloaded on 26th of January 2022)

[11] European Environment Agency
Greenhouse gas emission intensity of electricity generation by country (11/2021)
https://www.eea.europa.eu/ims/greenhouse-gas-emission-intensity-of-1
(downloaded on 5th of April 2022)

[12] P. Leduc, B. Dubar, A. Ranini and G. Monnier
Downsizing of Gasoline Engine: an Efficient Way to Reduce CO_2 Emissions
Oil & Gas Science and Technology - Rev. IFP, vol. 58 (2003), No. 1, pp. 115-127

[13] Vitesco Technologies, World premiere: Vitesco Technologies reveals next generation electric axle drives (07/2021)
https://www.vitesco-technologies.com/en-us/press/21-07-08
(downloaded on 18th of April 2022)

[14] Dr Gerd Rösel; Simon Baensch; Nico Oaun; Fabian Meyer; Petra Moenius; Alexander Reich; Matthias Toens; Rainer Weber
400 V Power electronic for Highest Efficiency Demands
Aachen Colloquium Sustainable Mobility, 2021

[15] Dr.-Ing. G. Rösel, M. Hackelsperger, R. Knorr, J. Popov, Dr. rer. nat. C. Preis, A. Reich
Achieving Benchmark in Power Density and Sustainability for Power Net, Power Supply and Onboard Chargers by a New Generation of DC/DC Converters and OBCs With Gallium Nitride Semiconductors
International Vienna Motor Symposium, 2022

[16] Dr. Florian Uhrig, Dr. Paul Boucharel
Comparative Life Cycle Assessment for Permanent and Externally Excited Drive Systems
EVS35 Symposium, Oslo 2022

Holistic comparison between Si IGBT and SiC MOSFET for BEV: materials, devices, systems, supply chains, and cost analysis

Yu YANG

Yole Développement, 75 Cours Emile Zola, 69100 Villeurbanne, France

Abstract: In the pursue of vehicle electrification, which is fueled by regulations, OEM focus shifting, and increasing end customer acceptance, power electronic devices are one of the key enabling components. For automotive OEMs and Tier 1 suppliers, one key question to be answered in planning of their next generation BEV products is the selection between Si IGBT and SiC MOSFET. This is especially critical for traction motor inverters.

Yole Développement reviews both the technical and commercial aspects of the power electronics value chain. Comparing the material properties, and semiconductor device physics of Si IGBT and SiC MOSFET, with a focus on passenger vehicles.

Another focus is the supply chains down to material growth, device design and manufacturing, device packaging, and system topology. Besides the established supply chains, a close look at the rapid development in China is included.

A holistic evaluation of the aforementioned factors is increasingly important for OEMs and Tier 1s to make the optimal strategic choice in power electronics, as a critical part in electrification.

Keywords: Si IGBT, SiC MOSFET, inverters for traction motors, battery electric vehicles

1. Introduction

With no doubt, the electrification of passenger and light commercial vehicles is taking off. It is a global trend accelerating in all major automotive markets, namely China, Europe, and the US. The rest of the world is following up although with few years of delay in development. We grouped the intertwined market driving forces in 5 long-term and 2 short-term factors:

- Long-term 1: global decarbonization trend, converted to regulations, incentives, and other policies on ownership benefits.
- Long-term 2: legacy OEMs shifting focus from ICE to BEV first, or even BEV only.
- Long-term 3: increasing end customer acceptance to BEVs
- Long-term 4: earlier price parity between BEV and ICE than previously anticipated
- Long-term 5: improving public charging infrastructure in major markets
- Short-term 1: 'Tesla Effect' inspiring multiple start-ups mainly in the US and China.
- Short-term 2: supply chain disruption, first linked to COVID-19 pandemic, but expanding to other parts more than Si chips.

More importantly, the market adoption to electrification, first driven by financial incentives, and then pushed by CO_2 emission regulations or plug-in electric vehicle (including PHEV, BEV, and FCEV) mandates, has gone through the early incubation stage. Now, while the aforementioned factors are still valid, there is more and more demands from end customers. The market growth is more 'organic' and sustainable.

We take 10% of market penetration in new passenger sales as a milestone, meaning the technology is no longer in niche market. Europe, or European Union membership countries, plus the UK, and EFTA countries (Switzerland, Norway, Iceland, and Liechtenstein) has reached that milestone back to 2020 with 11% plug-in vehicles in new car registration [1]. The biggest automobile market, China, followed closely in the year after [2]. This means that in two out of three major automobile markets, vehicle electrification is a reality.

From the discussion above, it is clear that all the long-term factors will be either lasting for decades, or will improve over time.

In the past, BEVs have proved to have lower TCO (total cost of ownership) than ICEs, thanks to their lower energy cost and maintenance requirements. However, the initial purchasing costs are absolutely critical for end customers to switch from ICEs to BEVs. Norway has reached nearly full electrification by taxation leverage, exempting import tax of plug-in vehicles and increasing CO_2 emission tax of ICE cars. In China, the push is less extreme, but the sales champions, for example the top three best sellers in 2021, Wuling Hongugang Mini EV from SGMW, Model 3 and Model Y both from Tesla, were actually cheaper than their ICE counterparts in the same segments. Therefore, the cost parity between BEV and ICE is a decisive factor in EV adoption.

Figure 1 illustrates the process. The BOM costs of BEVs are decreasing fast, thanks to the quick capacity expansion of battery production and BEV production. The ICEs have a 'standard' cost down path as the industry has been through in the past

decades. However, other regulatory elements play a key role in the final formula. Additional governmental incentives, seen in China, the US, and various European countries, bring down the actual costs of BEVs than their catalogue prices. For ICEs, the leverage is on the opposite direction: foreseen emission standard upgrading (most stringent ones will be EURO 7 and China 7) results in additional costs for emission upgrading. The contrary trends twisted by regulations will bring forward the price parity point years ahead of its 'natural' cross. OEMs and the supply chain should be fully aware of this trend and calibrate internal plannings accordingly. It is hard to pinpoint the exact date of such a parity point. Volkswagen group estimated it to be in 2025, and Stellantis group set the date in 2026. It is safe to say that the price parity will not take a decade to happen.

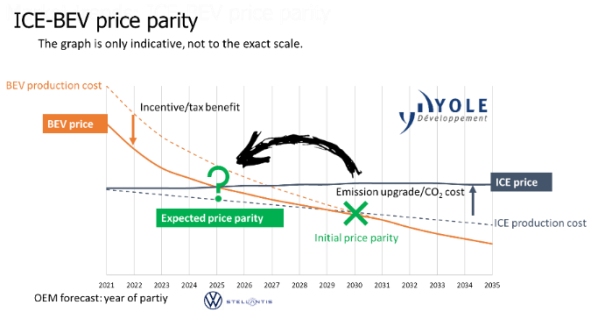


Figure 1: ICE-BEV price parity is moving forward

On the way of this fundamental powertrain transformation, new drivetrain systems, especially inverters, e-motors, and batteries, are the key to success. In this paper, a focus on the full supply chain of inverters and upstream power devices would help all players in the highly dynamic value chain to have a clear view and in-depth understanding with both Si IGBT and SiC MOSFET.

2. Market forecast

2.1 Global passenger vehicle market

We forecast the global xEV market, including MHEV, HEV, PHEV, BEV, and FCEV, to reach 50 million by 2027, representing more than half of the total passenger and light commercial vehicle market already since 2026. The CAGR of global xEV market, in 2021 and 2027 period, is 21%. The forecast is shown in Figure 2.

BEVs will enjoy a slightly higher growth of 22% CAGR, with contribution from China, Europe, and the US.

We also have a strong belief in hybrid technologies in the forecast period. With the existing infrastructure, BEVs can hardly be the only solution to all situations, while PHEVs can be a complimentary technology still with plug-in functions. Of course, it is worth of mentioning that PHEV is highly dependent on regulations. The current forecast is based the current global regulatory frameworks in major markets.

HEVs are historically a segment dominated by Japanese OEMs, with some touches from Koreans. There has been a rising interest from Chinese OEMs in the past two years. The majority focuses on DHT + DHE, which can be configurated to both PHEVs and HEVs. As more models from Chinese OEMs rolling out, the HEV technology is gaining new momentum. Especially for vehicles in lower segments, PHEV is too costly, and HEV, if nicely implemented, would provide an effective solution.

Although MHEV has been highly expected in the past years, it is losing attraction as the fuel saving has much shrink when switching to WLTP cycles. Still, it is an important technology in the next years to reach OEMs' fleet emission targets, particularly for European OEMs. We forecast the peak of MHEV will move forward to 2026/2027, and then start declining. Basically, only OEMs have models in development would continue with MHEV, mostly European and American OEMs. Others are not likely to launch MHEV models.

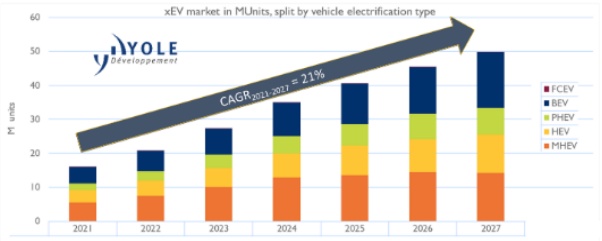


Figure 2: 2021-2027 global xEV market forecast, by powertrain

2.2 Power converter market for xEVs

The total market will grow rapidly to reach almost $23B by 2027. The main inverters for traction e-motors, with much higher power level, have more than 60% of the total converter market. The forecast is shown in Figure 3.

OBC and DC/DC also increase almost in proportion with the market. There is an increasing trend of integrating OBC and DC/DC, which will drive the cost down in faster pace, especially in the co-design case, where active components would be shared by the two sub-systems.

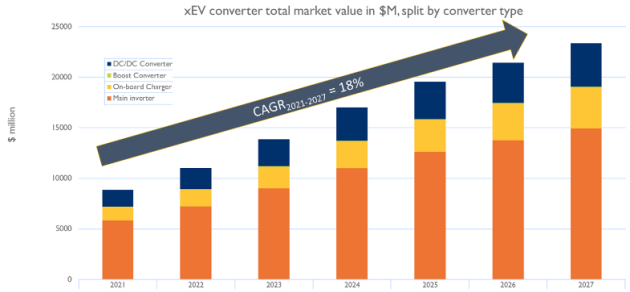


Figure 3: 2021-2027 power converter market for xEV forecast, by system type

2.3 Power electronic device market for xEVs

As the key components in power converter sub-systems, the power electronic device market will boom in the forecast period. The forecast is shown in Figure 4.

The semiconductor power device market will be strongly pushed by the rapid growth of SiC module strongly linked to 800V applications. In this forecast, we have a rather bullish scenario for SiC adoption. We are also aware that, as more announced SiC capacity expansion rolls out in the coming years, it is likely that the price erosion of SiC devices is more rapid than the current scenario, resulting in more in unit however less in absolute market value in $M.

It is always arguable whether SiC will replace Si IGBT as power devices. Although the forecast is in favour of SiC, we still believe Si IGBT will play a substantial role in the electrified future. The comparison between these two devices will be dis-cussed in detail in the next chapter.

GaN, another well discussed wide band gap material, will penetrate from low power applications, such as DC/DC, in the next years. It will still take time for this technology to be mature enough to step into higher power level markets.

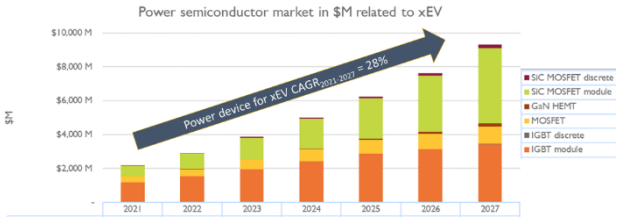


Figure 4: 2021-2027 power semiconductor market for xEV forecast, by device type

3. Comparison between Si IGBT and SiC MOSFET

The main function of an inverter is to convert DC current from batteries to AC current to driving electric motors.

In short, the power devices work like a water tap: by turning on and off a water tap, water flows or stops, converting a constant water supply (like DC) to alternating water supply (like AC). Both Si IGBT and SiC MOSFET function the same way.

3.1 Material properties

The reason of this current modulation is the special properties of semiconductor materials. The conductivity is a variable and can be modulated by external electric potential. This is very different compared to conductors, such as metals, and insulators, such as ceramics and polymers. Silicon and Germanium are the most known semiconductor materials. Other elements in the neighbourhood of those elements, would also demonstrate semiconductor properties, and are generally called as compound semiconductors.

A group of compound semiconductor is referred to as direct band gap materials, such as GaAs and InP, can be used for optical devices (for example, laser).

SiC and GaN are known as wide band gap materials, which feature with wider band gap compared to Silicon, making them suitable for high power applications.

Table 1 [3][4] summaries the major properties of both materials. The most distinguish difference is that the band gap of SiC is three times of that of Si, and the breakdown voltage is 10 times. This difference makes SiC an ideal candidate for high voltage applications.

SiC also has much higher thermal conductivity, which is also highly preferred in power applications, where a critical issue is much higher heat dissipation requirements.

Another striking difference lies in the much higher electron saturation velocity with SiC. This allows higher switching frequency with SiC devices. This is also the case in GaN.

It is clear that SiC is much for suitable for high power, high voltage applications, while the barrier is cost and supply chain, which will be discussed in later sections.

Table 1: Comparion of Si and SiC properties

	Si	SiC-4H
Band gap (eV)	1.12	3.26
Breakdown field strength (MV/cm)	0.3	3.5
Electron mobility (cm2/Vs)	1400	800
Electron saturation velocity (107cm/s)	1.0	2.0

Thermal conductivity (W/cmK)	1.5	3.0-3.8
Therotical maximum working temperature (°C)	175	600
Dielectric constant (C2/NM2)	11.9	9.7
Suppliers	Many	A few established suppliers, but rapidly growing number of suppliers
Cost	Low	Very high
Applications	IC, MOSFET, IGBT, diode	Power MOSFET, diode

3.2 Device features

Based on the material properties, different devices are proposed for high power applications. MOSFET is an ideal device type for switches as its high input impedance and high switching frequency. However, for Si based devices, the MOSFET is limited in source-drain current. Therefore, IGBT device is designed to combine the controllability of MOSFET and driving capability of BJT.

Table 2 [5] summarizes the major characteristics of both devices. Clearly, SiC MOSFET has multiple advantages.

- Lower switching loss and higher switching frequency due to SiC MOSFET is a unipolar device.
- Higher voltage/higher power applications due to breakdown voltage is higher, linked to intrinsic material properties.
- Lower conductance loss, ideal for high power applications, as it means higher transmission efficiency and less heat to be dissipated.
- Higher thermal conductivity, ideal for reliability and helpful in lowering system costs.

On the other hand, the limiting factors are the immaturity of SiC devices, which lack specific standards, and the supply chain is still at early stage.

Table 2: comparion of Si IGBT and SiC MOSFET properties

	Si IGBT	SiC MOSFET
Device type	Bipolar	Unipolar
Breakdown Voltage	400V to about 12 kV	600V to several kV
Current density	High	Very high
Rdson	Medium	Low
High-speed switching characteristics	Low	High
Cost	Medium	High
Thermal conductivity	Low	High
Operation Temp capability	125°C	175-200°C
Suppliers	Many	A few established suppliers, but rapidly growing number of suppliers
Reliability standards	Yes	No (Si standards used, SiC standard is under construction)
Technology maturity level	High	Medium

3.3 System topologies for inverters

In principle, the system topologies for inverters, no matter using which type of devices, are similar, as the devices are used as power switches in modulating currents.

Higher operational frequency, enabled by SiC MOSFET (a unipolar device), would require smaller passive components in the sub-system. This results in higher compactness of an inverter. Toyota compared inverters built with both Si IGBTs and SiC MOSFETs for its HEV powertrains, and found that by using SiC MOSFETs, the volume of the inverter can be decreased by 80% [6].

3.4 Cost analysis

For the moment, the main barrier of large scale SiC implementation is cost.

The positive aspect is that both materials are using abundant elements: Silicon and Carbon. At least there is no long-term limitation of both materials.

Si IGBTs need some special processing when manufacturing Si wafer into devices. Additional investments are needed to adapt from existing foundries. Also as discussed in the forecast section, Si IGBT is mainly using mature technologies, and will expand with both 8-inch and 12-inch wafers. This requires less CAPEX.

In semiconductor manufacturing, larger wafers require similar processing flow, thus cost, to make the final devices. But larger wafers would have many more devices compared to smaller wafers, as the device number is in proportion to area, which is a square of diameter. So from 8-inch to 12-inch, wafer diameter increases by 50%, but the area increases by 125%, which also translates to almost double number

of devices from a 12-inch wafer (area waster due to round wafers and yield lose). This means by slightly increasing costs, the output can be doubled, so as the device cost.

The same principle applies to SiC MOSFETs. However, there are two key difference in SiC compared to Si. The first, and most challenging one, is the cost of SiC wafers. Although no special materials need, the crystal growth of SiC is much more costly and slow. It only happens at fully vaporized environment, requiring much higher action chamber temperature, and leading to much slower crystal growth rate. The defect density in SiC wafers is also much higher than Si wafers. This results in smaller wafers, lower device yield, higher wafer lose in processing, etc. All translate to higher device cost.

We see the two difficulties are being solved, at least partially. Multiple players are investing heavily to SiC wafer production and epitaxy. If all the announced capacity is realized in the next years, SiC wafer cost is expected to be drop, although is will still be much more expensive than Si as crystal growth more costly. SiC device manufacturing has huge room to improve, and is likely to reach lower manufacturing cost and higher device yield.

On top of device cost, packaging cost in power devices is also essential, which is much more expensive due to the requirements in high current, high thermal dissipation, and high reliability (especially for automotive applications). This also applies to both Si IGBTs and SiC MOSFETs, although SiC MOSFETs have less stringent requirements than Si IGBTs at the same power level. So far SiC MOSFETs mainly leverage the packaging solutions from Si IGBTs. More specific packaging solutions for SiC MOSFETs will likely further decrease the module costs.

All in all, we see still relatively high cost with SiC MOSFET modules for the moment. But it definitely erodes faster than Si IGBT modules as multiple factors will contribute to this trend. For power modules at the same power level, the averaging price ratio between SiC MOSFETs and Si IGBT will decrease from 2.5 to 2.0 or less by the end of forecast period. Of course, this is highly dynamic and it is rather dependent on the rolling of the planned capacity and yield improvement.

Sub-system designers (Tier 1s) and OEMs however, will evaluate with a more holistic approach, including peripheral components, thermal requirements, battery costs, and even marketing value for vehicle models.

3.5 Supply chain of Si IGBT

We believe that excellence in power electronics and batteries are the only guarantee of success in the future.

Si IGBT has a relatively mature supply chain, growing from classical Si value chain. As power devices for automotive applications, the supply chain is more split into semiconductor and automotive parts, with only few exceptions.

There is an increasing trend of OEM expansion with Si IGBT or inverter supply chain. As a key element in vehicle electrification, OEMs are entering to sub-systems, in this case, inverters. One move is to create strategic relationship or joint ventures, with Tier 1 and even Tier 2 suppliers. For example, PSA, now part of Stellantis group, formed a joint venture with Nidec to manufacture e-axles (including inverters). SAIC in China built a joint venture with Infineon, covering power module packaging. More cases are in the second move, OEMs are building inverters in-house. There are already examples like Tesla, XPeng, Hyundai-Kia group, and Geely. And other OEMs are reportedly in the launching of such a move. More extreme cases are full integration down to semiconductor manufacturing, as in the cases of BYD and Toyota group (through subsidiaries). In the past months, due to the supply chain disruption, and rapid growth of BEV needs, the higher integration supply chain model turns to be much more resilient.

This trend brings extra pressure to the conventional Tier 1 suppliers, especially for those still with heavy ICE heritage. Transformation to electrification and severe competition, even from previously non-automotive players, requires Tier 1s to carefully examine and implement their strategies, and to come with appropriate value propositions. Excellence in the following aspects, such as supply chain assurance, cost competition, technology advance, flexibility both in products and business conditions, are keys to the future success.

3.6 Supply chain of SiC MOSFET

SiC is ramping up quickly from initial stage. One unique feature of SiC is the material production, including ingot growth, wafering, and epitaxy. SiC grows much slower, and the process is still not standardized. Most manufacturers are developing their recipes together with in-house adapted furnishes. Also the material itself is rather hard, making the wafer sawing, grinding, and polishing processes both slower and more costly. An additional high quality epitaxy layer, depositing extra thin materials on top of wafer surfaces, is necessary before device manufacturing. As explained it is not standardized Si processing, which resulted in limited foundry capacity.

The whole eco system is new, especially when talking about mass production, there are multiple start-up companies, unlike in the case of Si IGBT, having more mature players. Then there are enormous improvements needed to bring up the maturity. At this stage, more vertical integration shows more

advantages to meet the speed of innovation and the quality supply. This is perfectly demonstrated by large number of M&As in the past years, as we have the examples of STMicroeletronics acquired SiC wafer manufacturer Norstel AB, OnSemi acquired SiC wafer manufacturer GT Advanced Technologies, and Rohm acquired SiC wafer manufacturer SiCrystal.

Companies without in-house capability of SiC wafer manufacturing and processing are going through alternative ways to guarantee quality supply. One way is to have strategic relationship directly with suppliers, such as GM and Wolfspeed cooperation, Stellantis Group and STMicroelectronics cooperation, Geely and Rohm cooperation, etc. Another way is to invest directly into SiC start-ups, which is more popular in China. Huawei, as a new Tier 1 in automotive, has made investments in TYSiC and TankeBlue in SiC wafering, EpiWorld in SiC epitaxy. Xiaomi, as a new OEM in BEVs, has made investments in InventChip in SiC module. Geely invested in AccoPower as SiC IDM. GWM invested in Synlight Crystal.

It is also worth of mentioning that there are some other innovative technologies are being developed to solve the high cost issue of SiC substates. Soitec from France is working on a special wafer transferring method, which also has a potential to dramatically lowering SiC wafer cost.

For the moment, the SiC foundry capability is still limited. IDM will still be the mainstream in the next years for SiC.

4. Conclusion

- Vehicle electrification is accelerating and reaching half of the global new car market by 2026, with a CAGR of 21% in 2021 to 2027 period.
- The global market of power device, a key component in electrification, will grow to $9B in a bullish scenario with SiC. The main growth is from both SiC MOSFET and Si IGBT modules for main inverters.
- Si IGBT and SiC MOSFET are both important power devices in vehicle electrification. We believe they will co-exist in the next decade, with the price ratio decreasing from 2.5 to 2.0.
- A thorough comparison between these two devices shows the advantages of SiC MOSFET in high power applications. However, the barrier is cost and immaturity, with improvements on the way.
- The supply chain management of both devices are critical in OEMs' success. For Si IGBT, OEMs are expanding to upstream with various measures, requiring conventional Tier 1s moving to better value proposition. For SiC MOSFET, the security to quality supply is important. Vertical integrated IDMs are favoured. Downstream OEMs/T1s are trying to lock up with key suppliers.

6. References

[1] ACEA: "*Fuel types of new passenger cars in the EU*", https://www.acea.auto/figure/fuel-types-of-new-passenger-cars-in-eu/, 2021.

[2] CAAM: "*Statistics of the Automobile Industry in China: 2021 December*", http://www.caam.org.cn/chn/1/cate_148/con_5235337.html, 2022.

[3] A. Agarwal, R. Singh, S. Ryu, J. Richmond, C. Capell, S. Schwab, B. Moore, and J. Palmour, "*600 V, 1- 40 A, Schottky diodes in SiC and their applications*," CREE Power Appl. Notes, 2005.

[4] Y. F. Wu, A. Saxler, M. Moore, R. P. Smith, S. Sheppard, P. M. Chavarkar, T. Wisleder, U. K. Mishra, P. Parikh, "*30-W/mm GaN HEMTs by field plate optimization*" IEEE Electron Device Lett., vol.25, no.3, pp. 117- 119, 2004.

[5] R. Erikson, D. Maksimovic, "Technology Advances in Power Electronics via WBG Converter Circuits", ARPA-E Workshop on Novel Power Electronic Systems Enabled by Wide Bandgap Semiconductors, 2016.

[6] F. SHANG, A.P. ARRIBAS, M. KRISHNAMURTHY, "*A comprehensive evaluation of SiC devices in traction applications*". Transportation Electrification Conference and Expo (ITEC), 2014 IEEE, 2014.

7. Glossary

IGBT: Insulated Gate Bipolar Transistor

MOSFET: Metal Oxide Semiconductor Field Effect Transistor

BEV: Battery Electric Vehicle

OEM: Original Equipment Manufacturer

ICE: Internal Combustion Engine (thermal motor)

PHEV: Plug-in Hybrid Electric Vehicle

TCO: Total Cost of Ownership

BOM: Bill Of materials

MHEV: Portable Document Format

HEV: Hybrid Electric Vehicle (or full hybrid)

FCEV: Fuel-Cell Electric Vehicle

CAGR: Compound Annual Growth Rate

DHE: Dedicated Hybrid Engine

DHT: Dedicated Hybrid Transmission

WLTP: Worldwide Harmonized Light Duty Vehicles Test Procedure

OBC: On-Board Charger

BJT: Bipolar Junction Transistor

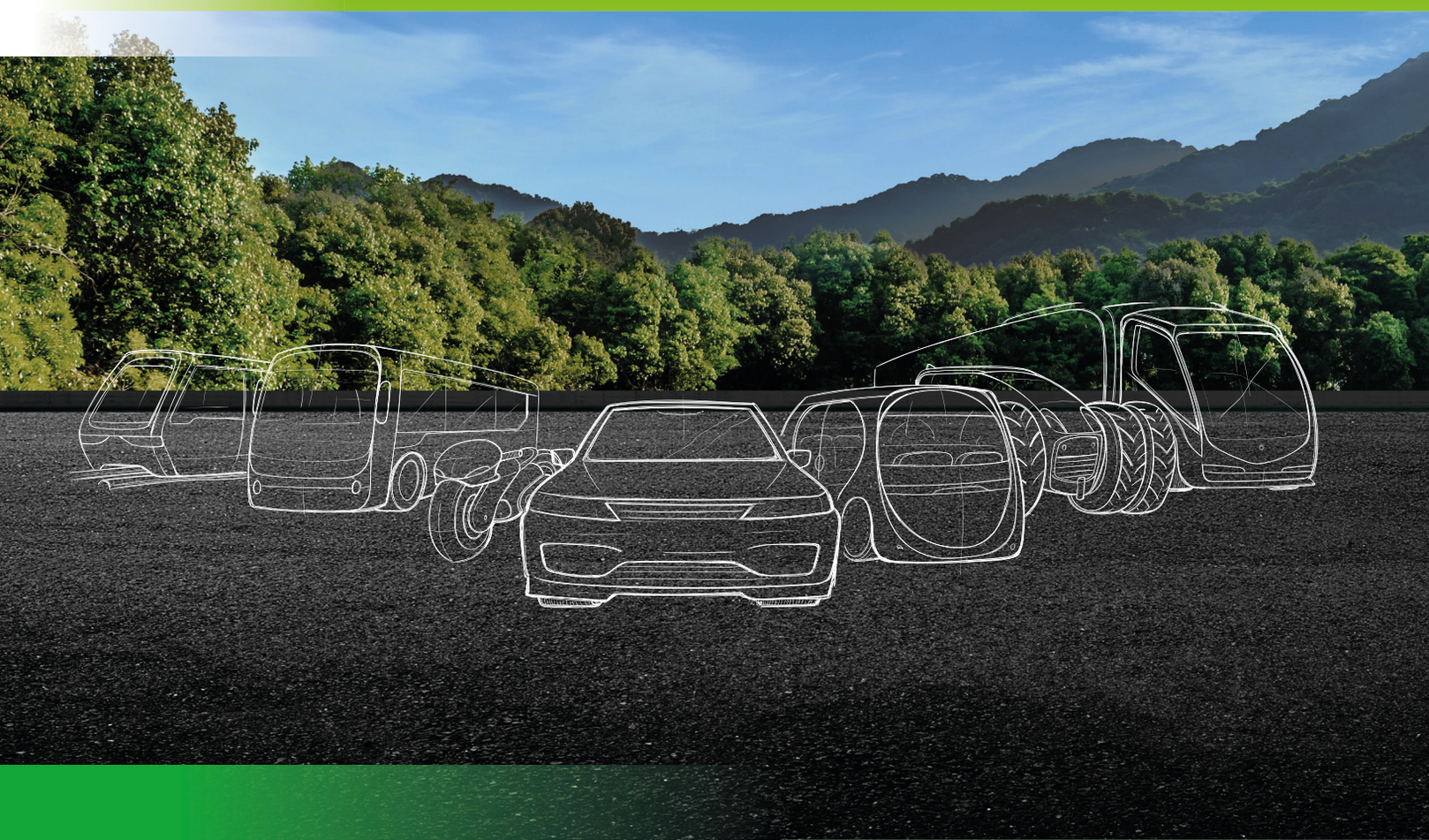
CAPEX: CAPital EXpenditures

IDM: Integrated Device Manufacturer

15 JUNE 2022

ELECTRIFIED PROPULSION SYSTEMS OVERVIEW

AVL



Reimagining Motion

For a greener, safer, better world of mobility.

We are driven by a passion to examine the science, mechanics and philosophy of movement. To help create a world that is carbon neutral and one that makes safe, comfortable, green mobility a reality for everyone on this planet.

Some will call it a distant dream.
We call it ***Reimagining Motion.***

www.avl.com

The World Automotive Powertrain Outlook - WAPO

A novel forecast toolbox to assess the evolution of the Light Vehicle market and its related impacts

J. VERA[1], J. CHOLIN[2], J-L. BROSSARD[3], J. GUEZET[4]

1: BIPE – BDO Advisory 43-47 Avenue de la Grande Armée, 75116 PARIS
2: BIPE – BDO Advisory https://www.bdo.fr/fr-fr/bipe/accueil
3: Stellantis & ***PFA***
4: Renault

Abstract:

The WAPO model primarily provides long-term sales forecasts up until 2040, with year-by-year evolution of the Light Vehicles powertrain mix, supported by a fine granularity (segmentations, architectures, usages, etc.).

Using a set of detailed costs (components, energy), the TCO-based approach enables the selection of the most suitable vehicle configuration for the targeted usage. Combined with scenarios of possible futures (environmental regulations, macro-economy factors), the projected results give relevant food for thought.

Applied to the impact assessment of the newly proposed Fit For 55 policy package in Europe, the 2021 results, in particular:

- show compliance to the updated 2030 CAFE targets, thanks to consumption modelling combined with the forecasted powertrain market shares
- allow comparisons of the impact of various levels of policy stringency on technology

This all-in-one forecast tool also provides bottom-up estimations of the contribution of the Light Vehicles in use to the CO2 emissions, using consolidated fleet data, as illustrated in this paper.

Keywords: Powertrain market forecast, Total Cost of Ownership TCO, CO2 emissions, Battery demand

1. Introduction & Context

All around the world, countries and organizations are setting new objectives and updating their targets to slow down global warming and reduce impacts of all kinds of climate change. The Automotive industry has been actively taking part in tackling this difficult challenge by deploying technological innovations over the last decade, both with regards ICE fuel economy and through increasing electrification of powertrain architectures.

Since 2009, the Association of the French Automotive Industry ***PFA*** has been appointing BIPE - BDO Advisory to develop and enhance the WAPO model, providing independent, rational long-term forecasts for Light Vehicle sales and fleets in use, by segment and powertrain.

Using a TCO selection approach, the mathematical modeling is fed with a rather large set of input data, built collectively, and reviewed yearly with the ***PFA*** members. The WAPO is therefore a powerful tool, for steering purpose as well as strategic planning.

2. Technology selection & deployment

2.1 Structuring principles of the model

In this section, we introduce a brief overview of the structure for our proposed model. Regarding the matters enumerated in introduction, the objective of WAPO model is to select the most affordable vehicle configuration for the targeted application / end-user, and it is performed by using a set of costs (components, energy) according to the TCO-based approach [1]. This selection noticeably depends on different possible futures, framed via 4 built-in scenarios using various environmental regulations and macro-economy factors.

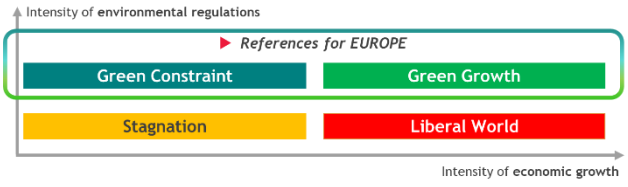


Figure 1: WAPO Built-in Scenarios (simplified view)

In terms of precision, the WAPO model goes deep into refined levels of market segmentations, a kind of unique implementation compared to similar studies [2] in the field that enables to get detailed results on different aspects, such as:

- *Time horizon:* the model covers the short, medium and long terms (2020-2040)
- *Geographic scope:* the geographic division is done by continental area and then by country as well as a territorial aspect, which means that urban areas of large cities are treated differently than rural areas or medium or small cities
- *Vehicle (sub)categories:* this model focuses on Passenger Car (PC) – mostly used for individual mobility – and Light Commercial Vehicle (LCV) – used exclusively for business/work activities
- *Vehicle segments:* different types are defined based on size (usable cabin area), purpose (city, cruising, off-road…) and performances
- *Type of user:* vehicle users have various motives for mobility, differentiated between individuals, corporate fleets, commercial fleets, etc.
- *Usage habits:* they refer to a matrix that defines the most probable usage from daily vs. annual usage which considers the heterogeneity of real use cases
- *Technological offer (market coverage):* going beyond the standard division between ICE, electric, hybrid, and hydrogen powertrains, the model includes the possible variants/solutions within these families of architectures, and their (in)availability at a given time and zone

Using such a deep level of granularity raises different challenges, such as a lack of input availability or excessive computation time, so an extensive review of relevant studies ([3],[4],[5]) was performed to gather all the information; a lot of interviews were also carried out with different OEMs and Tier-1s to complete the data collection. From this granularity, we can focus on the impacts of public policies (incentives, taxes, etc.), consumer behavior, international heterogeneities, technological development on cost reduction, or compatibility of autonomy with usage.

Therefore, the results of our model can provide valuable, explicit data and help answering the main questions that were leading the research and developments of the WAPO model, such as: which powertrain evolutions are to come in the medium and long terms? How will the energy transition in the automotive sector impact CO2 emissions? Which trajectory should the automotive sector follow to meet ambitious climate objectives? Related information about the infrastructure needs is also made available at a fine scale, to better anticipate the deployment of charging stations and service stations for new fuels (gas and hydrogen).

For strategic planning a reliable forecasting tool is essential given the recent accelerating efforts to support the ecological transition (e.g., the Fit For 55 package in Europe [6]), or the potential breaking-out crises (COVID, chip shortage…) which directly and indirectly affect economic and industrial prospects.

This is precisely the major strength of the WAPO model, built on a validated backbone that has been improved for years, and flexible to include such short-term and/or sudden changes and concerns.

The framework of the model is defined as follows: the WAPO covers 33 countries on 8 geographical plates (Europe, China, NAFTA, South America, Asia OECD, Middle East, Rest of Asia, Russia), 11 vehicle segments (7 in PC, 4 in LCV) and 17 powertrains. Powertrains included are defined as follows: pure Gasoline and Diesel ICE, all Hybridization combinations (Mild and Low, full hybrid/HEV, PHEV), Zero-Emission Vehicles (Electric and Fuel Cell) and gas ICE (CNG, LPG).

The model goes through three phases to generate forecasts:

- *Fleet projection:* in this phase, our model projects the volume of the vehicles in use for the 2020-2040 period, by considering the historical data to calibrate the most recent market state and based on sets of macroeconomic parameters such as GDP, populations, etc.
- *Sales projections:* the total sales volumes are calculated through the fleet renewal process, defined by a scrappage law
- *Sales mix by powertrain:* finally, the mix of powertrain is forecasted by using our TCO approach

Keynote: It is noteworthy to highlight that one main assumption in our model is that there is no limitation nor constraint on powertrain choice with regards to the lack of charging/refueling infrastructure of any kind: to be clear, that means no limitation in the powertrain mix selection process due to the related infrastructure.

2.2 Detailed insight of the TCO-based selection process

As previously mentioned, our TCO method is applied (see figure 1) to define the mix of powertrain. The TCO represents the overall cost of a vehicle throughout its life cycle, via two main components:

- *Fixed Cost:* fixed or purchased cost including all the costs that should be paid by the user to buy the vehicle; it is composed of various elements considering the technology of each

powertrain such as Engine Price, Vehicle Price (without engine), Battery Price (Energy Battery, Power Battery, Fuel cell Battery), Taxes/Margin/Subsidies.

- *Usage Cost:* usage-based costs or costs of operations are the sets of expenses that should be considered by owners when using their vehicle, such as Cost of Energy Consumption which depends on Average Annual Mileage, Energy Prices, Average Fuel Consumption, and Taxation per use.

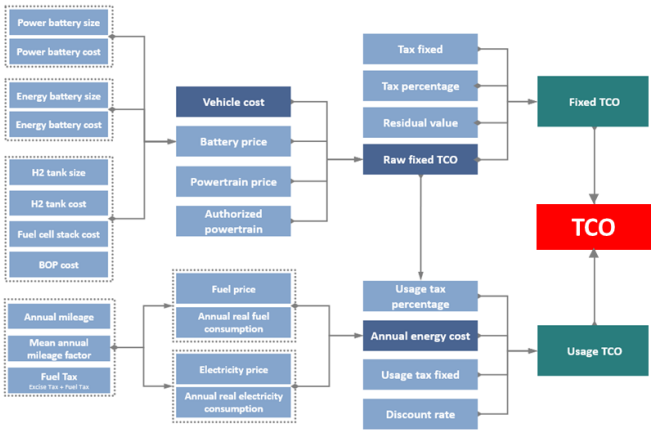


Figure 2: TCO function modelling

After TCO calculations are done for the various segments and powertrains, the selection of powertrain is carried out by a method based on a logistic function, within the technological options offered by the market coverage, as illustrated in the diagram below for the entire approach:

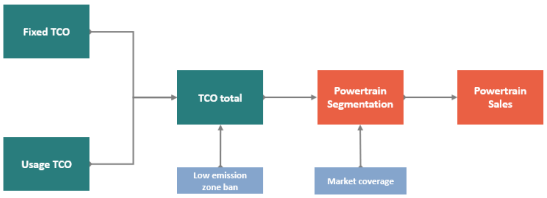


Figure 3: Powertrain selection process by TCO

As mentioned before, our model also considers territorial aspects, because of restriction criteria set for some urban areas – big cities, downtowns – to help "decarbonizing" [7] them, called Low Emission Zones (LEZ). To do so, a specific constraint on the technological offer is assumed, prohibiting traffic of polluting ICE-based vehicles in these zones.

3. Use case 2021: a focus on Europe's forecasts

To illustrate the performances and applicability of our model, the various possible outputs will be displayed for Europe, with a dedicated analysis of the extracted information.

2021 saw some breakthrough announcements from the European Commission, via the release of their Fit For 55 package proposal: this updated framework was therefore used as the reference for this year's forecast (which will be detailed as we go, when relevant for the understanding).

3.1 Sales volume

The first output provided are the sales volumes by scenario. Using macro-economic and demographic data, the model assesses their evolution, capitalizing on the real historical sales records. As explained in the previous sections, all 4 scenarios have been designed according to the macro-economic trends and the environmental regulations.

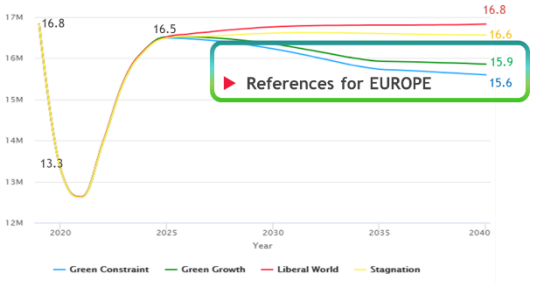


Figure 4: Sales volumes in Millions of units, per year

It is worth noting that for Europe, we only focus on the 2 Green scenarios – Green Growth and Green Constraint – as the most plausible ones for the area.

Looking at the sales trends in the short term, the Covid-19 pandemic caused a sharp drop in volumes that should reach its lowest in 2021, before the recovery starts; a full recovery back to 2019 level should only be seen around 2025.

In both Green scenarios for Europe, the noticeable trend is the steady decrease from 2025 onwards. In fact, due to the slowdown in demand, there will be a gradual reduction in sales volumes, to reach 15.9Mu for Green Growth and 15.6Mu for Green Constraint: the model suggests the market scaling back around 1Mu in the next two decades.

3.2 Powertrain mix

The second output is the powertrain mix evolution. The changes in powertrain shares over the years is displayed next for the 2 Green scenarios and as suggested by the charts, great changes will indeed take place between 2020 and 2040.

Here, the main impact of FF55 is evidently the strict ICE ban proposed from 2035 onwards, when sales become 100% ZEV.

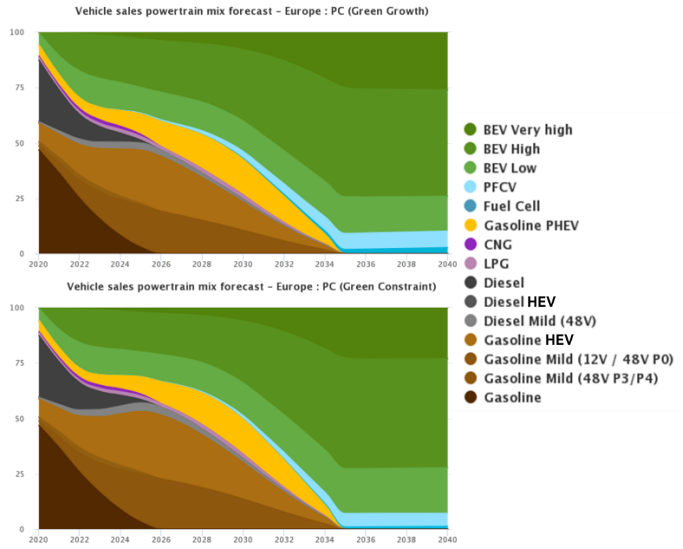


Figure 5: Powertrain mix evolution
(sales shares %, GC/GG, 2020-2040)

Today's market is essentially dominated by gasoline and diesel ICE, while BEV, combined with PHEV, only make a 10% share. In general, powertrains are quite diversified over the next decade and different technologies can be found. However, with the implementation of EURO7 coming up and then of the FF55 policy in 2035, an acceleration of electrification will be observed as early as 2030. In 2040, 89.8% (Green Growth) / 92.8% (Green Constraint) of PC will be BEV and Fuel Cell powertrains will make for the rest of the market.

Both scenarios show quite similar trends, as the FF55 limits the technological offer so much that other parameters are less constraining.

However, their focuses are slightly different. For instance, within the Green Growth scenario, thanks to the great reduction of powertrain component costs and fuel cost, fuel cell cars will reach a 10.2% share in 2040, compared to only 7% in Green Constraint.

With regards PHEV, it should be noted that their market share peaks in 2029, at around 15%.

Keynote: In the Green Growth scenario, the BEV dynamics showcased can only be made possible by major cost reductions, requiring efforts from all stakeholders, in the favorable context foreseen. The model does not consider endogenous learning effects or economies of scale.

3.3 Vehicle segment mix

The fine granularity embedded in the WAPO model allows for a detailed grasp of the vehicle size distribution of the sales. The next figure compares the current segment shares in 2020 with the forecasts in 2040.

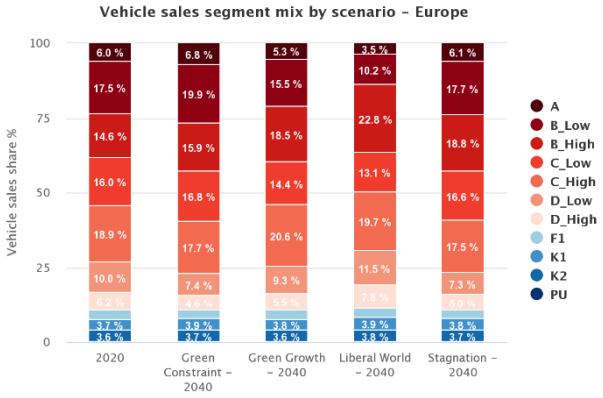


Figure 6: Segment mix evolution
(sales shares %, all scenarios in 2040)

Comparing the 2 green scenarios, by 2040 the B_High segment (Peugeot 2008, Renault Capture) will continue to increase its market share, while the A segment (Twingo) and the B_Low segment (208, Clio), already 100% BEV, will only see slightly higher market shares in the relatively low-growth scenario that is Green Constraint, as consumers will look for less expensive configurations.

4. Impact assessment of upcoming policies

Another strategical aspect that our model treats is the practical understanding of what the forecast means in terms of policy compliance or top-down policies, in a very intuitive manner.

4.1 Compliance to the CAFE targets

The energy consumption modelling embedded in WAPO enables a direct check of the expected CO2 emissions of new vehicle sales, at any milestone.

The chart below shows a different view of the Green Growth powertrain mix evolution, this time as 5-year step bars and including the WLTP CAFE figures.

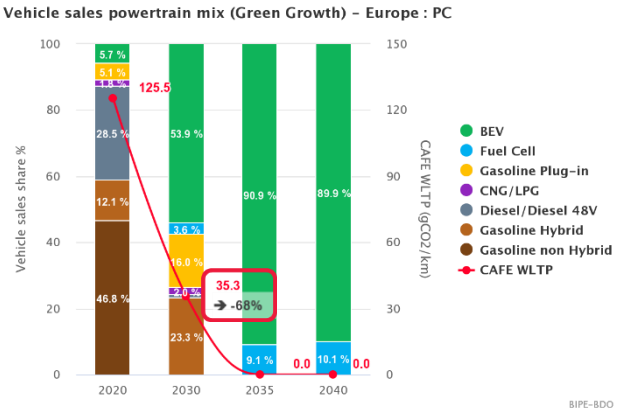


Figure 7: Powertrain mix & CAFE evolution
(sales shares % & gCO2/km WLTP, GG, 2020-2040)

The updated CAFE target for PC in the FF55 package is now 49gCO2/km in 2030 (from -37,5% vs 2021 previously to -55%): in the Green Growth context, the calculation directly shows it should be achieved with a decent margin.

This is valuable, easy-to-read information extracted from the very refined projections provided by our tool.

4.2 Sensitivity run on technology availability

Here is another very interesting feature that can be showcased in the FF55 context: the sensitivity run.

As presented previously, the new FF55 requirements could soon very strongly restrict the powertrain offer for the European market, mainly by banning all ICE Light Vehicles from 2035 onwards. However, in practice, current ZEVs cannot meet the needs for all usages, particularly regarding Light Commercial Vehicles and the associated mileage profiles.

As an alternative future, adjustments were proposed for the market coverage, defining a different technological offer between 2035 and 2040:

- PHEV still allowed
- *for LCV only*: 48V hybridization also extended

Based on the Green Growth scenario, this sensitivity study – referred to as ICE BAN 2040 – provides a complementary understanding of the market dynamics to come in play.

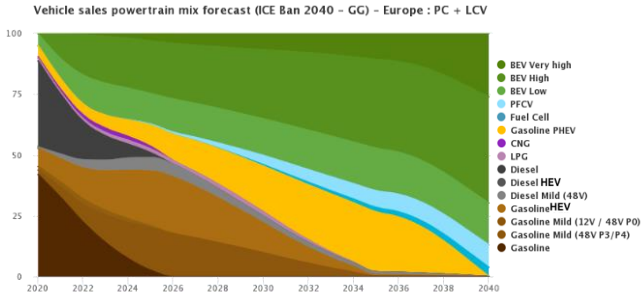


Figure 8: Powertrain mix evolution
(sales shares %, ICE BAN 2040, 2020-2040)

As expected, PHEVs keep deploying beyond 2029, reaching their sales peak in 2035 with a 24.6% share of the LV market. Focusing on LCVs only, all hybrids still account for 21.5% of the market that same year.

The forecast clearly shows different trends compared to the reference case (Green Growth with ICE BAN in 2035).

The value of such sensitivity approach is to look at the global changes triggered by the specific adjustments.

For that matter, the WAPO toolbox also includes a module dedicated to estimating the battery needs of the powertrain sales mix forecasted. As shown next, the dynamic is noticeably different for the ICE BAN 2040 run.

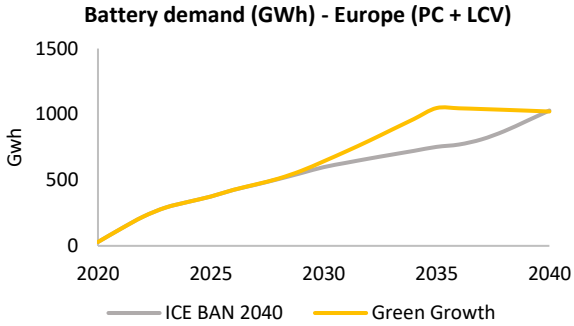


Figure 9: Battery demand for LVs
(Green Growth vs ICE BAN 2040, 2020-2040)

Up until 2030, a dramatic increase in battery demand is observed in Europe. Driven by very favorable financial incentives for electrified vehicles for the next 3 years in many European countries and strong limitations in pure ICE vehicles from 2026 onwards, a first ramp-up phase takes place.

Interestingly, a second phase is clearly visible between 2030 and 2040: in general, thanks to the development of battery-related technologies, the price of electrified vehicles will continue to drop, to a point where its cost will be very comparable to other types of powertrains. However, we can see here the impact of technology (in)availability:
When no more ICE are allowed beyond 2035 (Green Growth), the demand features another strong ramp-up between 2030 (643 GWh) and the peak in 2035 (1048 GWh), followed by a slight decrease as fuel cell vehicles deploy (1021 GWh in 2040).
With loosen constrains on strongly hybridized powertrains (ICE BAN 2040), the demand is much more progressive and regular: 599 GWh in 2030, 753 GWh in 2035 and finally 1029 GWh in 2040.

Keynote: These are key data when analyzing the impacts to come on the mobility battery industry. Considering the critical topic of supply chain associated with the product, the capability to deliver the required volumes of GWh at the right time and allow the expected vehicle electrification is key in the global approach/dynamic of reducing CO2 emissions.

4.3 Contribution of the LVs in use to the CO2 emissions

As made explicit in section §2.1, the WAPO toolbox also provides the yearly evolution of the vehicles in use – also with fine granularity with regards vehicles, segments, and powertrains – which is critical in properly understanding the various impacts of Light Vehicles.

As a main focus of the European Green Deal, CO2 tailpipe emissions can then be directly estimated by

the model, providing once again an efficient means to monitor the trends versus the expected goals.

$$Emissions\ CO_2 = Nb_{Vi} \times Km_{Ai} \times Cc \times F_{TtW} \qquad [Eq]$$

The given formula [Eq] is used in the model to estimate the CO2 emissions, with:

Nb_V	*Number of vehicles*	Km_A	*Mileage/year (in km)*
Cc	*Fuel consumption/km*	F_{TtW}	*TtW emission factor*
i	*Sale year of vehicle*		

1. The data set of LV fleet (Nb_V) is obtained by consolidating the projected fleet data, categorized by segment, powertrain, and vehicle age.
2. A segmented mileage distribution is then applied to the fleet in use, to get the corresponding value (Km_A).
   The mileage defined for a new vehicle is used as the starting point of this segmented distribution, and then it decreases according to the vehicle age (half-Gaussian-like).
3. The fuel consumption (*Cc*) varies according to the segment, powertrain, and age of the vehicle (all displayed in equivalent TWh).

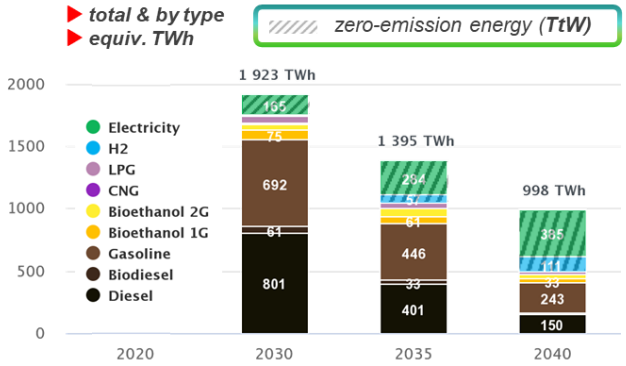


Figure 10: Energy demand of the fleet in use (sc. GG)

Finally, specific Tank-to-Wheel emission factors (F_{TtW}) are applied to convert the energy demand (fuel cons.) into the corresponding CO2 tailpipe emissions (below in Mt, compared to 519 Mt in reference year 1990 [8]).

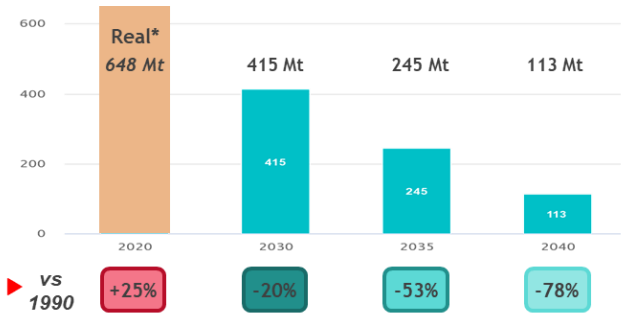


Figure 11: CO2 emissions for the fleet in use (sc. GG)

The two previous charts (Fig. 10 & 11) illustrate the strong changes in energy demand and related CO2 emissions up until 2040.

A first big reduction step will be achieved by 2030, leading to 415 Mt of CO2 emissions. In 2040, the progresses are even more significant vs 2030, as the energy demand is down another 48% for a 73% reduction of the corresponding CO2 emissions. The main drivers for these successive improvements are:

1. The powertrain mix of the fleet in use is, logically, more and more composed of the more recent – and less polluting – variants: much higher ZEV shares, combined with more efficient and frugal ICE-based vehicles.
2. The annual mileage gradually decreasing according to the vehicle age, the most polluting vehicles drive less and less of the total amount of kms.

Keynote 1: As highlighted, reducing CO2 emissions require to work on both drivers simultaneously, as the demand for mobility will remain high and need to be met.

Keynote 2: With the European Green Deal's GHG targets in mind (-55% emissions in 2030 vs the 519 Mt baseline in 1990 [8], Net-Zero in 2050), this reference forecast shows promising reductions of the CO2 emissions of the fleet in use, providing meaningful figures and a practical understanding of the reduction dynamics to come, all backed up by clear data.

4.4 EVSE requirements & sizing

As explained before in section §2, infrastructures are not set as a restriction factor to the sales increase and deployment of New Energy Vehicles.

Therefore, to support the upcoming, increasing demand for electricity supply for mobility – also built on a low/fast charging segmentation – the model outputs the needs for charging points at the various time milestones, to assess roll-out plans.

Capitalizing once again on the projected fleet data up until 2040, an auxiliary module was developed to estimate how many public charging infrastructures should be deployed to meet the projected EV & PHEV volumes' needs.

Three kinds of input and information are required to calculate the number of charging points:

1. The numbers of daily charging (such as commuting) and exceptional charging (such as voyage) were estimated by using the following data – all "average" (segment x powertrain):
   - daily/commuting mileage
   - exceptional mileage
   - operating range

- electricity consumption
- battery size

2. Two types of charging point have been considered: fast charging (50kVA > 150kVA) and normal charging (7kVA > 22kVA), with increasing charging powers over time to adjust for new equipment. The share of each type depends on its installation (at home, at the office, on the road, etc.) and is estimated from bibliographic research.
3. Three different scenarios of availability rate of a public charging station were implemented, linked with the dedicated sources:
   - High availability, i.e., more vehicles served by 1 single charging point
   - Medium availability
   - Low availability, i.e., fewer vehicles served by 1 single charging point

By combining them all – including the availability scenarios – the obtained range of ratio varies from 6.8 to 13.1, aligned with the relevant values from the selected references [9] & [10] (see Table below). The corresponding number of charging points for Europe reaches between 5.8 and 11.2Mu (Green Growth sc.).

EVSE requirements / Europe 2030

Source	*ACEA*	*EC*	WAPO
Fleet of BEV & PHEV (in Mu)	48.1	48.1	76,3
Estimated number of charging points required (in Mu)	7	3.9	5.8 to 11.2
Vehicle/charging point ratio	6.87	12.3	6.8 to 13.1

Figure 12: EVSE requirements table, incl. WAPO

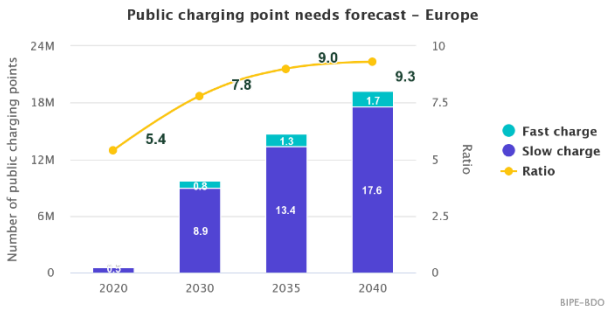


Figure 13: Public charging point prediction

From a different point of view, the chart above looks at the reference results with medium availability, from 2030 to 2040, with details on the charging segmentation and the evolution of the ratio at interest.

Keynote: In practice, the availability of charging stations plays a critical role in persuading customers to purchase EVs (and PHEVs to some extent). Indeed, there is no more doubt that if the EVSE is not deployed at the minimum required level, the market shares of such powertrains will remain low, or even close to non-existent.

7. Conclusion

The WAPO model provides calculated trends of the deployment of Electrified Propulsion Systems in the Light Vehicle market, in Europe and worldwide.

Leveraging its interconnected modules enables the reliable assessment of various impacts of such deployment, directly related to the critical issues at stake right now in Europe: the capacity of this industry to meets its needs in terms of electrification components, as well as the update of the CO2 emissions reductions targets and milestones.

Therefore, the WAPO continues to be a reference forecast toolbox, improved with and primarily used by the 6 global ***PFA*** members (2 OEMs and 4 Tier-1).

6. Acknowledgement

The authors acknowledge the contribution of their colleagues to this work:

S. CHENG M. LEZY

F. NIAKAN M-L. BASTIMENT

*All members of **PFA**'s WAPO working group*

7. References

[1] B. Al-Alawi and T. H. Bradley, "*Total cost of ownership, payback, and consumer preference modelling of plug-in hybrid electric vehicles*", Applied Energy, ISSN 0306-2619, 103(2013), 488–506

[2] J. Roosen, W. Marneffe and L. Vereeck*., A review of comparative vehicle cost analysis*, Transport Reviews,ISSN 0144-1647, 35(2015), 720–748

[3] Roland Berger, "*Powertrain market outlook 2030*, Technical paper, Roland Berger, 2021

[4] IEA, "*Global EV Outlook 2020"*, Technology report, International Energy Agency, June 2020.

[5] GEFI, "*Vehicle Efficiency and Electrification: A Global Status Report*, Global Fuel Economy Initiative, 2020

[6] Council of the European Union, "*The EU's plan for a green transition*", Proposal for a Regulation of The European Parliament and of The Council, March 2020

[7] ICCT, "*Vision 2050, A Strategy to Decarbonize the Global Transport Sector by mid-century"*, Technical paper, International Council on Clean Transportation, 2020

[8] European Environment Agency (europa.eu), *"National emissions reported to the UNFCCC and to the EU Greenhouse Gas Monitoring Mechanism",* Data and maps, Inventory, 2021

[9] ACEA, "Proposal for the Alternative Fuels Infrastructure Regulation (AFIR)*"*, ACEA Position paper, 2021

[10] European Commission, *"Proposal of a Regulation of the European Parliament and of the Council on the deployment of alternative fuels infrastructure"*, 2021

8. Glossary

ACEA	European Automobile Manufacturers' Association
BEV	Battery Electric Vehicle
CAFE	Corporate Average Fuel Economy
EC	European Commission
EV	Electric Vehicle
EVSE	Electric Vehicle Supply Equipment
FCEV	Fuel Cell Electric Vehicle (full power) *also simply referred to as "Fuel Cell" in charts*
FF55	Fit For 55 (package/framework)
GC	Green Constraint (scenario)
GDP	Gross Domestic Product
GG	Green Growth (scenario)
GHG	Green-House Gases
HEV	Hybrid Electric Vehicle
ICE	Internal Combustion Engine
LCV	Light Commercial Vehicle
LEZ	Low Emission Zones
LV	Light Vehicle
MHEV	Mild Hybrid Electric Vehicle
Mt	Megatons (Millions of tons)
Mu	Millions of units
NEV	New Energy Vehicle
OEM	Original Equipment Manufacturer
PC	Passenger Car
PFA	"Plateforme Filière Automobile & Mobilité"
PFCV	Plug-in Hybrid Fuel Cell Vehicle
PHEV	Plug-in Hybrid Electric Vehicle
TCO	Total Cost of Ownership
TtW	Tank to wheel
WAPO	World Automotive Powertrain Outlook
WLTP	Worldwide Harmonized L.V. Test Procedure
ZEV	Zero-Emission Vehicles

Electric Mobility 48V: New Value Space Road Map

Amal John, Robin Vincent, Paul Armiroli, Pierre Faverolle , Erwan Nicot

1: Valeo India Private limited 600130 Chennai, Tamil Nadu
2: Valeo Powertrain Electrical System. Creteil 2 rue Boulle 94000 Creteil
3

Abstract: The automotive industry moves towards powertrain electrification or pure electric drive.This presentation is focused on new electric Mobility based on 48V Systems (Machine +Inverter). The Road Map started with a Belt Driven machine for entry range with start of production in 2021 and followed by a complete range of products developed for Asia Market (India and China), but also for city driving in all countries. The main project targets were to propose easy packaged solutions, low cost, air cooled, less intrusive for 2,3,4 wheelers. Power will be adapted to vehicle weight and performances requests. The main technical challenges will be described. The machine and Inverter assembly is designed to be produced in every Valeo site worldwide. Valeo will complete this presentation with a full 48V Road Map.

Keywords: eMobility, 48V , eDrive.

1. Introduction

The Small Mobility segment includes a wide range of products starting from eBikes to small 4 Wheelers. Electrification of the small mobility segment has seen a considerable interest in recent years mainly driven by government incentives to promote green technologies and reduce crude oil consumption. Small electric vehicle gives a good value proposition for the customer in terms of total cost of ownership of the vehicle due to lower running cost and maintenance. With the improvement in charging infrastructure and government incentives, electric vehicles sales are expected to grow exponentially.

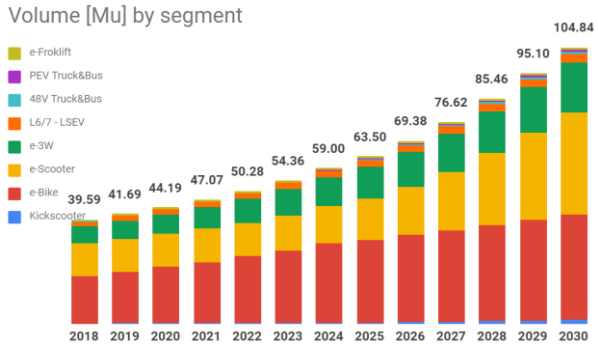


Figure 1- Small mobility segment volume growth

This technical paper describes the development of an electric drives system for the Small mobility vehicles.

The main challenge coming from this market segment is the product cost.
The Small Mobility Motor Generator system consists of a permanent magnet electric machine and an integrated electronics consisting of inverter and Vehicle Control Unit called Small Mobility Control Unit .
This paper also describes a 25kW Electric Drive system as a solution for small 4 Wheel electric vehicles and its benefits compared to HV systems.
This paper covers the typical vehicle application, vehicle architecture, mission profile, and main specification and design challenges.

2. Small Mobility Motor Generator System

The system is intended for the vehicles categorised under L- Category as per UN ECE RE3. Within the L Category, It focuses on two and three wheeler applications. It caters to the market currently covered by the segment of 100-150cc ICE engine vehicles in the 2 and 3 wheeler vehicle segment. .

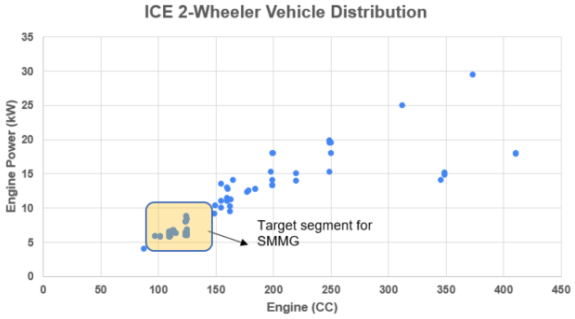


Figure 2 - 2 Wheeler product distribution

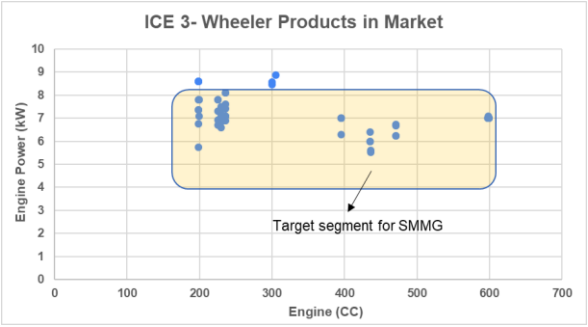


Figure 3 - 3 Wheeler product distribution

2.1. Usage profile

The Usage profile of the small mobility segment is as varied as its application. It involves fleet operation and small distance personal travel. Two wheelers belong to the personal vehicle category and used as an economical and convenient means for daily commute. Three wheeler segment is mainly for fleet application and taxi segment.

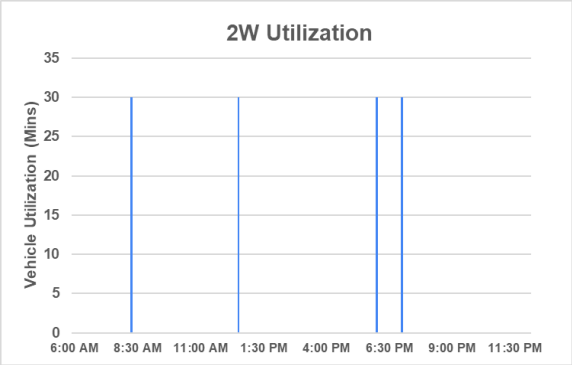


Figure 4 - 2 Wheeler user profile

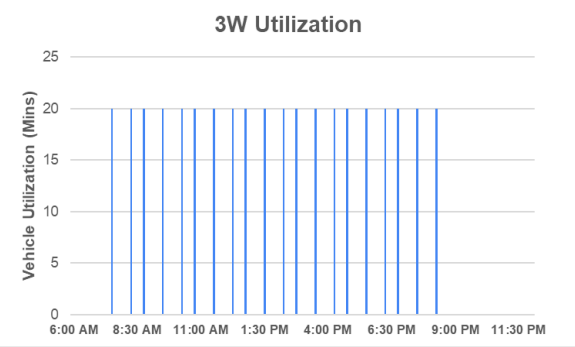


Figure 5 - 3 Wheeler user profile

2.2. Drive profile

Drive profile is important to ensure that the components are rightly sized and to evaluate the thermal and lifetime. It is important that the drive cycles are representative of current scenarios to which the vehicle will be exposed. The World Motorcycle Test Cycle (WMTC) is used as the preferred drive profile for the development.

To validate that the selected drive profile is representative, a real world trial was done with a two wheeler in Chennai, India. The collected drive profile shown in Figure 7 was analysed and compared with standard WMTC cycle. The result is shown in Table 1.

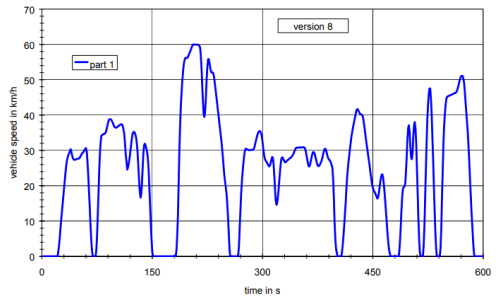


Figure 6 – 2W WMTC Drive profile

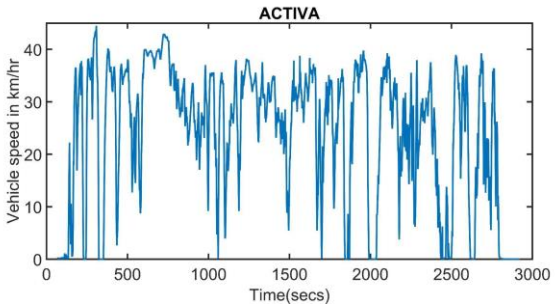


Figure 7 – 2W Drive realworld city drive profile

Parameter	RW City Drive	WMTC
Max speed km/h	45	60
Max acceleration m/s²	2.2	2.5
Max deceleration m/s²	-2	-2.0
Average speed km/h	24	24.5
Average moving speed km/h	29	30

Table 1 – Comparison of Drive profiles

2.3 Mechanical Integration

The vehicle architecture consists of an electric drive system connected to the vehicle rear wheel through a belt or gear mechanism. To reach a vehicle maximum speed, corresponding to the electric machine maximum speed the gear ratio could vary between 6 to 8 depending on the wheel dimension. In 3 Wheelers the gear ratio varies between 12-14.

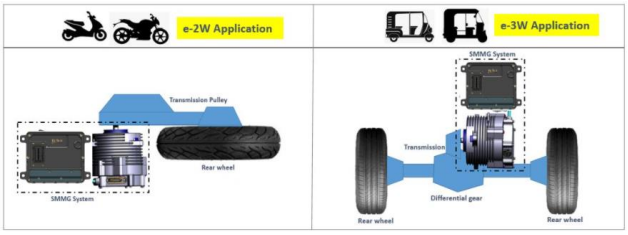


Figure 8: Arrangement of the system in the powertrain

Machine and inverter are both forced air cooled. Forced air could be easily achieved in the 2 or 3 wheeler during the vehicle movement though in some cases an external electric fan would be required. The electric drive system mentioned here is designed to provide its maximum performance for a minimum air flow speed of 1.75m/s. The fins' direction of the machine and inverter are aligned along the direction of motion of the vehicle. Typical location of the machine and inverter in a two-wheeler vehicle is shown in the **Figure 9** below.

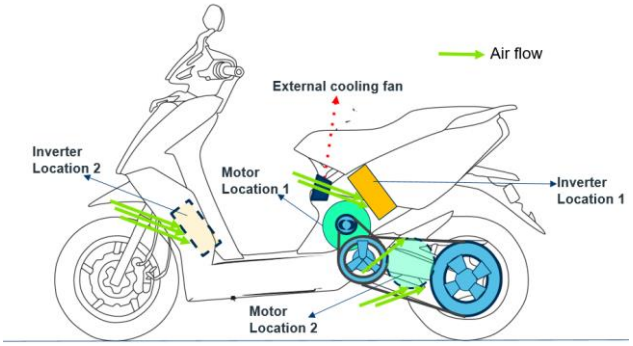


Figure 9: Position of the system & components in vehicle

The motor for this kind of application is located close to the ground plane to implement an easier mechanism for connection to wheels. Due to this reason it is required to meet stringent ingress protection (IP) requirements of IP67 to enable the component to be operational in a fully immersed condition. Fully enclosed motor brings in challenges related to cooling thus affecting the performance of the component. A fully enclosed design reduces the power level of a motor by 50% for the same size.
Meeting water ingress protection on the phase terminal connector imposes challenges in terms of cost of IP protected connectors. The motor's integrated cable design ensures that the complete motor is IP67 protected and operational in an immersed state.

2.4 Electrical & Control Architecture

The system works on a 48V-12V architecture. The control signal of the system operates on 12V while the power circuit operates at 48V following ISO 21780 [1]. The inverter has an isolated hardware architecture for better EMC/EMI performance and addresses failure mode of loss of power cable.

The System control unit integrates the Vehicle Control Unit functionality as well in its architecture. Therefore the system acts as a master controller in a vehicle which interfaces with the driver input like throttle signals and provides the requested torque. It also provides the necessary information to the customer through the display unit.

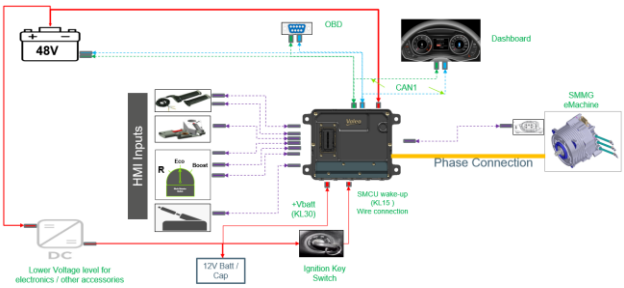


Figure 10: Electrical Architecture

The electronix box reads the driver input like the drive mode, throttle signal, brake signal and estimates the required torque to propel the vehicle. The torque request is sent to the Motor control software through the internal software interface. The electric motor control software then drives the inverter to deliver the requested torque at the motor shaft. The system also performs functions to control the charging functions, control the 12V load, command, monitor the battery states, and manage the cooling control through the external fan.

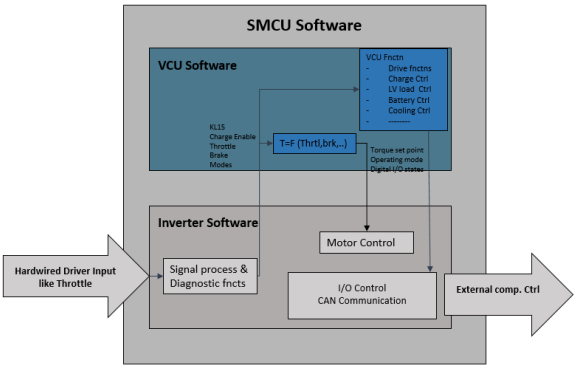


Figure 11: Software Architecture

2.5 Performance

The system is derived to meet the vehicle level performance requirement in terms of the acceleration and max speed. As seen in Figure 10 the system peak torque meets the best in class acceleration values in the vehicle. The peak and continuous power are designed to provide a continuous max speed of 85 mph and short time max speed of 105 mph.

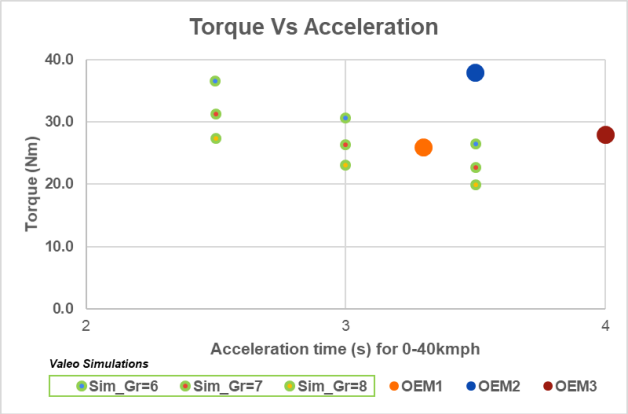


Figure 12: Acceleration performance Simulated and benchmark vehicle spec

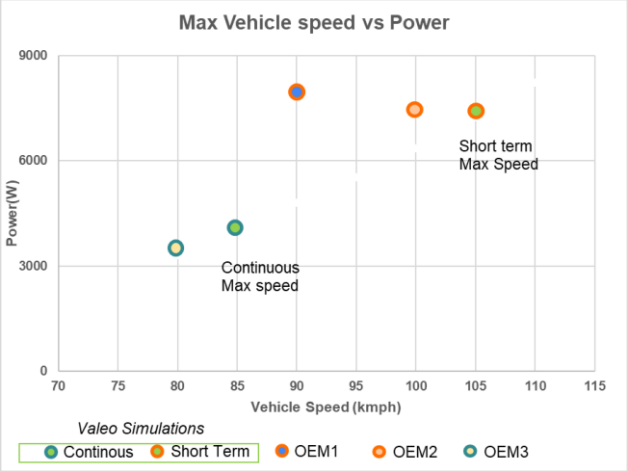


Figure 13: Max speed performance of Vehicle

The system supports a max speed of 12500 rpm. The higher speed capability of the system enhances its applicability in 3 wheeler vehicles where the gear ratios are in the range of 12-14. The overall performance of the system is summarised below

Power (Peak/Cont.)	8kW/4kW
Torque (Peak/Cont.)	35 Nm/ 17 Nm
Max Speed	12500 rpm
Weight	12kg
Position estimation	Hall effect sensors + target bearing
Thermal protection	NTC sensor
Functional Safety	MSILC
IP class	IP67, IP66K

Table 2: System characteristics

2.6 Safety

Though functional safety as ISO 26262 has become a global standard for passenger cars and commercial vehicles, the practice is not yet fully adopted in the L category segment. This is due to the high development effort and cost involved. As we progress toward electric vehicles functional safety development becomes more relevant due to the many controllers , their software and interactions. Valeo has employed its expertise in functional safety of 4 wheeler in 2-3 wheeler applications as well. The system is developed to meet MSILC for unintended torque events and MSIL B for undervoltage and overvoltage events.

The system is designed to be fully protected against hazardous thermal events. The busbar routing and critical components placement are designed to avoid formation of localised hot spots and sparking. The full metal casing of the system ensures avoidance of propagation of thermal event.

2.7 48V Roadmap

Valeo is a pioneer in 48V technology with its integrated Belt Starter Generator leading the market and in mass production for various hybrid and electric vehicle applications. Valeo 48V technology covers electric drive products up to 25kW. 48V smal lmobility system gives a good proposition in terms of benefit to cost because the cost and complexities of High Voltage can be avoided and the performance and efficiency fully available in a compact package.



Figure 14: Valeo's 48V product roadmap

3. 48V BEV

With the increased pressure for ICE ban in cities, the need for small and cheap BEV is growing fast.

These vehicles require a much smaller battery because of the lower daily distance covered during urban commute. This in turn, makes them less expensive, lighter, and allows for a less powerful powertrain.

Valeo Gearbox Motor Generator 25kW solution is thus an excellent solution for these mostly urban BEV.

The eDrive system is a combination of a 25kW permanent magnet synchronous machine, its inverter and a mechanical reduction and differential.

In this part, this eDrive is compared to a high voltage electric machine, with 33kW peak power in a sub-A segment vehicle.

The base vehicle is 970 kg for a 27kWh battery. Two other battery capacities (15 and 20kWh) will also be tested to have different vehicle masses (887 and 922kg).

The base vehicle develops approximately 940 Nm of torque at wheel level. The 48V vehicle will be tested with 940 Nm (reducer of 8.5), 1800 Nm (reducer of 18.5) for better performances.

All these parameters are summed up in the table below

Electric Machine	HV BEV 33kW 240V	48V BEV GMG25	
Reduction	7.5	8.5	18.2
Take off torque	940 Nm	940 Nm	1800 Nm
Battery size vehicle mass	27kWh - 970kg	27kWh - 970kg 20kWh - 922kg 15kWh - 887kg	

Table 3: BEV 48V vs HV configurations

3.1 48V vs High voltage

In terms of performances, the BEV 48V is better compared to the BEV HV up to 50km/h when using the high ratio (18.2). In that case, the lower power is compensated by a higher low end torque that makes the vehicle more performant at low speed.

The gap is bigger at higher speeds, for it takes 3 additional seconds to reach 80 km/h for the BEV 48V with the r18.2 and the 20kWh battery.

	Speed init [km/h]		0	0	0
	Speed final [km/h]		30	50	80
Type	Reducer	Battery			
HV	940Nm	BEV 240V	3.4	5.6	11.2
48V	r8.5	27kWh	3.5	7.2	16.2
		20kWh	3.3	6.8	15.4
		15kWh	3.2	6.6	14.8
	r18.2	27kWh	2.7	5.8	15.1
		20kWh	2.6	5.5	14.4
		15kWh	2.5	5.4	13.9

Table 4: BEV 48V vs HV performances comparison

On the energy efficiency side, we used the WLTC city cycle to simulate the energy consumption at battery level for the different configurations.

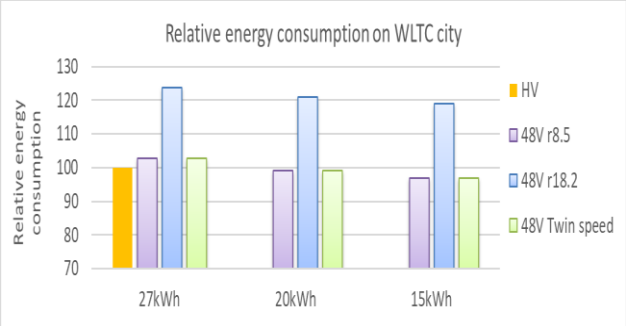


Figure 15: BEV 48V vs HV WLTC city energy consumption

This 1st part shows that a 48V BEV system can be competitive with a high voltage one, up to 50km/h in terms of performance . Only a twin- speed with 2 ratios also show same urban driving efficiency. Details in the following parts.

3.2 Twin speed eDrive

Valeo has developed a twin speed eDrive solution, that enables high low speed performances while maintaining a good system efficiency at higher speeds

This system reuses many existing components, and is compatible with both 48V and high voltage electric machines.

It also includes two key components developed by Valeo PAS (Product Actuation Systems): an Electromechanical Gear Shift with a response time under 50ms and an inductive Position Sensor Unit.

This twin speed eDrive gives an important edge to the 48V eMachine :

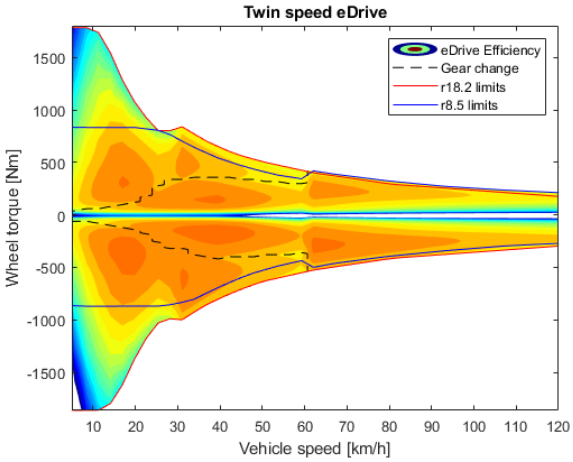


Figure 16 : Twin speed eDrive system efficiency

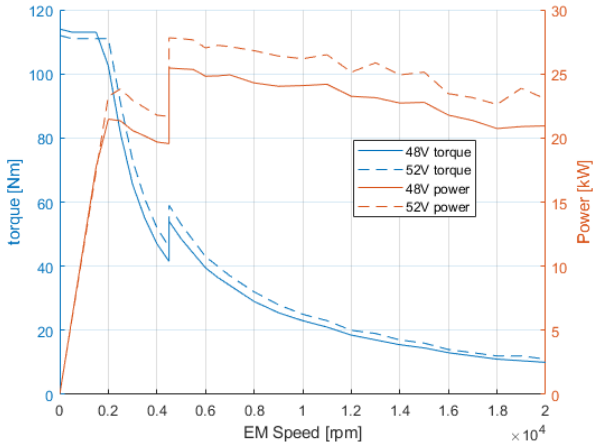


Figure 17 : Twin speed eDrive system efficiency

On the figure 16, we can see the advantage given by the twin speed eDrive. The max wheel torque is the same as with the ratio 18.2, which enable the 48V BEV to be as performant as the HV BEV up to 50km/h

The dotted line represents the limit between 1st and 2nd gear. It shows that the 2nd gear is selected from 30km/h for low to medium power, and always above 60km/h.

It makes this system as performant as the most performant single speed reducer and as efficient as the other single speed reducer.

3.3 52V Supply voltage

One limitation of 48V eMachines is the input DC voltage that must be low enough to prevent any overvoltage that could be harmful, or permanently damage other electrical components.

In that regard, Valeo is working on a way of allowing an increase of the DC voltage at inverter level while complying with all the safety requirements.

The figure below shows the impact of a DC voltage increase from 48V to 52V at the eMachine :

In Figure 17, one can see the effect of the increased voltage. The full lines represent the 48V supply, while the dotted ones the 52V.

If the max torque does not change, the power is increased by 10% on most of the speed range. It leads to better acceleration time, especially at higher speed, as displayed in **figure 18**

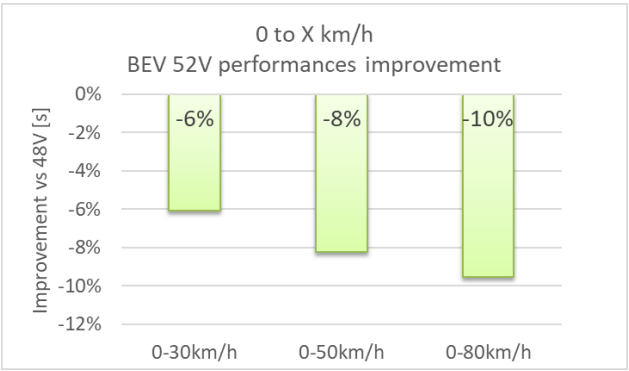


Figure 18 : Acceleration duration variation between 48V and 52V power supply

4. Conclusion

The Small Mobility segment involves a wide range of applications and electrification in this segment is growing rapidly. Electric drive system with 4kWc/8kWp meets the acceleration and maximum speed requirements of 2W and 3W vehicle segments. Water ingress protection is a need of the market and is a major challenge for air cooled motors. Smart packaging of the components in the vehicle with sufficient airflow is essential. Air cooled systems with integrated VCU reduce the complexity and cost of the system.

Electric drives with 25kW are also an interesting solution in higher segments, such as the sub-A. The performances of these BEV make them punchy in urban driving conditions, while the overall energy efficiency is good. Combined with a twin speed gearbox, such a BEV is extremely competitive against high voltage solutions. Future performances can be even better with an increased voltage supply.

5. Acknowledgement

The authors acknowledge the contribution of their colleagues Ramasubramanian Ramakrishnan, Muthukumaran Venugopal and Rajalakshmi Anbalagan for their inputs to complete the paper.

7. References

[1] *Road vehicles — Supply voltage of 48 V — Electrical requirements and tests,* ISO 21780, 2020-08

[2] CTI Berlin 18/11/2021. 48V Road Map from Mild Hybrid to City Electric Mobility .Paul Armiroli

[3] IQPC Berlin Feb 22th 2022. 48V RoadMap from Hybrid to City BEV mobility .Paul Armiroli

[4] Vienna symposium April 29 th 2022. Gearbox Motor Generator 15 kW 48V for DCT Transmission Hybridization .Paul Armirolii

8. Glossary

SMMG: Small Mobility Motor Generator
VCU: Vehicle Control Unit
SMCU: Small Mobility Control Unit
WMTC: World Motorcycle Test Cycle
WLTC: Worldwide harmonized Light vehicles Test Cycles
BEV: Battery Electric Vehicle
MSIL: Motorcycle Safety Integrity Level
iBSG: Integration of Belt Starter Generator
EGS: Embedded Power Electronics
iPSU : Position Sensor Unit

Vehicle to Grid: Towards a cybersecure electric system including vehicle, charging points and batteries.

F. HAIDAR[1]

1: ETAS, 32 Avenue Michelet, 93400 Saint-Ouen, France

Abstract: Vehicle to Grid (V2G) is an ongoing technology that promises many advantages in energy and grid efficiency. The V2G system consists of Electrical Vehicle (EV) communicates with the Charging Point (CP) in order to charge or discharge its battery. The ISO 15118 [1] standard introduces new functionality for electric vehicles, such as Plug and Charge (PnC). The PnC enables an EV to automatically identify and authorize itself to the CP on behalf of the driver, and thus to charge/discharge its battery. That means that with PnC the driver does not need a RFID or credit card information for charging/discharging. Despite the benefits of V2G, the openness of the system to new functionalities may create potential vulnerabilities and risks that must be taken into account. The ISO 15118 proposes new PKI dedicated to V2G. In this paper, we will focus on the V2G PnC use case, the V2G functional requirements and risk assessment. We will also perform an analysis on the cybersecurity risks on multiple level in order to sensibilize on the criticality of the cybersecurity activity to be taken into account.

Keywords: V2G, Cybersecurity, Electric Vehicles, Public Key Infrastructure.

1. Introduction

Vehicle-to-Grid (V2G) describes a system in which an Electrical Vehicle Communication Controller (EVCC) communicates with the power grid to demand services by either charging or discharging their batteries.

V2G helps mitigate the climate change by allowing our energy system to prioritize the renewable energy (wind, solar, etc). The main objectives of the V2G are [2]:

- Decarbonisation: it refers to the deployment of renewable energy sources. Energy produced by the renewable sources should be either used where it's produced or stored somewhere for later usage. Therefore, the growth of renewables inevitably makes our energy system more volatile, requiring new ways to balance and store energy to be used.
- Energy efficiency: in December 2020, the UK grid declined 21.5 GWh of wind energy in 12 hours, because they had no way of using it. This wasted energy could have been used to power daily mileage of nearly 3.5 million electric cars. Here is a concrete example of the importance of energy efficiency in V2G. In V2G system, the vehicle energy can be pushed back to the power grid from the battery of an electric car. With vehicle-to-grid technology, a car battery can be charged and discharged based on different signals.
- Electrification: it refers to the reducing of greenhouse gas emissions.

2. V2G System Description

The V2G system is a complex system with multiple stakeholders and end entities. In such system, Electrical Vehicles (EV), called also EV communication Controller (EVCC), communicates with the Charging Point (CP), called also Supply Equipment Communication Controller (SECC), in order to charge or discharge its battery. The SECC provide services to the EVCC and can also communicate with the backend system depending on the use case.
The V2G system, depicted in Figure 1, is composed of multiple entities and actors.
The vehicle in V2G system can communicate directly with the SECC and indirectly with the backend via the SECC.

- Electric Vehicle Communication Controller (EVCC): embedded system, within the vehicle, that implements the communication between the vehicle and the SECC.
- Supply Equipment Communication Controller (SECC): entity which implements the communication to one or multiple EVCCs and which may be able to interact with the backend. The SECC is located inside the Charging Point (CP) called also Charging Station (CS).
- Mobility Operator (MO): The organisation to which a customer has a contract for providing EV charging services.
- Service Operator: secondary actor responsible for the installation and operation of a charging

infrastructure (including charging sites) and the management of electricity to provide the requested energy transfer services.

- Power generator: is the generator of the power energy.

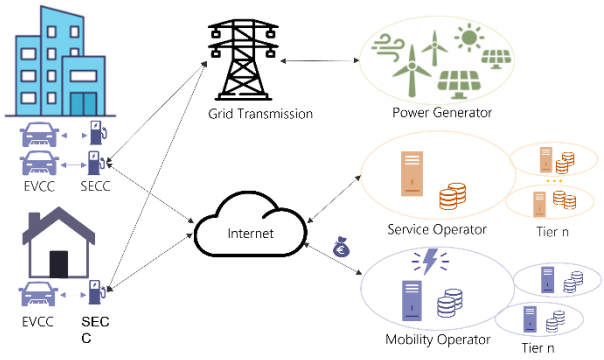


Figure 1: V2G System Overview

The term secondary actor (SA) is used in the ISO 15118 to design any entity other than the EVCC and the SECC.

3. ISO 15118 Standards Documents Family

ISO 15 118 document family is composed of 7 documents, the aim of each document is explained below [3]:

- ISO 15 118-1: Road vehicles - Vehicle to grid communication interface - Part 1: General information and use-case definition is a cross document that specifies terms and definitions, general requirements and use cases for conductive and wireless communication between the EVCC and the SECC. This document provides a general overview and a common understanding of aspects influencing identification, association, charge or discharge control and optimisation, payment, load levelling, cybersecurity and privacy. It offers an interoperable EV-EV supply equipment interface to all e-mobility actors beyond SECC.
- ISO 15 118-2: Road vehicles - Vehicle-to-grid communication Interface - Part 2: Network and application protocol requirements document specifies the communication between EVCC and the EVSE. The application layer message set defined in this part of ISO 15118 is designed to support the energy transfer from an EVSE to an EVCC. This document covers the network, transport, session, presentation and application layer of the OSI model [3].
- ISO 15 118-20 [1]: Road vehicles — Vehicle to grid communication interface - Part 20: Network and application protocol requirements document is an updated version of the ISO 15 118- 2 that correct some issues in the last version and also include requirements in regard to wireless power transfer.
- ISO 15 118-3: Road vehicles – Vehicle to grid Communication interface – Part 3: Physical and data link layer requirements document defines requirements applicable to Data link and physical layer, including V2G standardized service primitive interface.
- ISO 15 118-5: Road vehicles – Vehicle to grid communication interface – Part 5: Physical layer and data link layer conformance test document specifies a set of test cases that are required in order to verify conformance of implementations of ISO 15 118-3.
- ISO 15 118-8: Road vehicles – Vehicle to grid communication interface – Part 8: Physical layer and data link layer requirements for wireless communication document specifies the requirements of the physical and data link layer of a wireless High-Level Communication (HLC) between Electric Vehicles (EV) and the Electric Vehicle Supply Equipment (EVSE).
- ISO 15 118-9: Road vehicles – Vehicle to grid communication interface – Part 9: Physical layer and data link layer requirements for wireless communication conformance test document specifies a set of test cases that are required in order to verify conformance of implementations of ISO 15 118-8.

The ISO 15118 Documents FamilyFigure 2 presented the documents family mapped to the OSI layer.

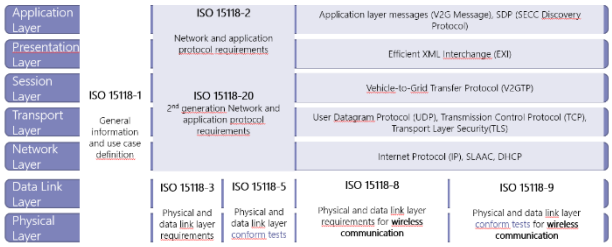


Figure 2: ISO 15118 Documents Family

The ISO 15118-20 is the first standard that tackle the cybersecurity for V2G. In the rest of this paper, we will focus on the ISO 15118-20 with its last published version in 2022.

4. V2G Public Key Infrastructure (PKI)

The PKI is a set of entities that create, manage and distribute digital certificates. The digital certificates are the proof of identity of the users. The PKI is used in the traditional IT that we use every day.
The traditional PKI is not suitable for every type of system. The ISO 15118 standard proposes a PKI

specific for the V2G system. It is important to mention that the ISO 15118 does not provide any mandatory PKI for implementations, it only defines a minimum required certificate structure that should be followed ensuring that the system as a whole is functioning
The PKI entities are presented in the ISO 15118 standard [3] and described below:

- V2G Root CA: the V2G Root is the root of trust for the whole PKI, it issues certificates for sub-CAs.
- Charging Point Operator (CPO) Sub-CA1: it is responsible for delivering certificates to the CPO Sub CA2.
- Charging Point Operator (CPO) Sub CA2: it is responsible for delivering SECC certificate.
- Supply Equipment Communication Controller (SECC) Certificate: it is used to authenticate the SECC while initiating a TLS session with the EVCC.
- Provisioning Services Sub CA1 (Prov Sub CA1): it is responsible for delivering certificates to the Prov Sub CA2.
- Provisioning Services Sub CA2 (Prov Sub CA2): it is responsible for delivering CPS leaf certificate.
- Certificate Provisioning Service (CPS) certificate: it is used to authenticate the entity responsible for certificate provisioning. It could be different than the OEM.
- eMobility service provider (eMSP) Root CA: the eMSP is the entity with which the customer has a contract for all services related to the EV energy transfer. The eMSP Root CA is the root of trust of the eMSP.
- eMobility service provider (eMSP) Sub CA1): it is responsible for delivering certificates to the eMSP Sub CA2.
- eMobility service provider (eMSP) Sub CA2: it is responsible for delivering contract certificates to the EVCC.
- Contract Certificate: it is issued for the EVCC by an eMSP sub-CA, which is used in XML signatures on application layer so that the SECC or secondary actor can verify the signature created by the EVCC with the contract certificate issued for that EV.
- Original Equipment Manufacturer (OEM) Root CA: it is the producer who manufactures products or components that are purchased by a company and retailed under that purchasing company's brand name. In the ISO 15118 it is referring to the car manufacturer.
- Vehicle Sub CA1: it is responsible for delivering certificates to the Vehicle Sub CA2.
- Vehicle Sub CA2: it is responsible for delivering vehicle certificates to the Vehicle.
- Vehicle Certificate: it is the proof of identity delivered by the Vehicle Sub CA2.
- OEM Sub CA1: it is responsible for delivering certificates to the OEM Sub CA2.
- OEM Sub CA2: it is responsible for delivering the OEM provisioning certificate.
- OEM Prov certificate: It is used to authenticate the vehicle for the delivery of the contract certificate before starting the PnC process.
- Private Environment (PE) Root: it is used in the context of private environment; the Root is the trust entity.
- Private Environment (PE) Sub CA1: it is responsible for delivering certificates to the private environment Sub CA2.
- Private Environment (PE) Sub CA2:it delivers the PE certificates for the wall box used to charge in the PE. The PE could be at home for example.

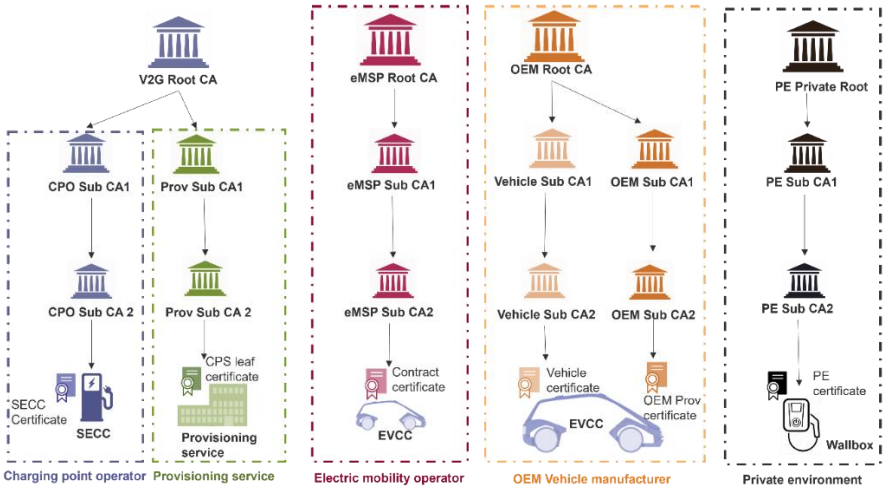


Figure 3: ISO 15118 proposed V2G PKI

5. Use Case: Plug and Charge (PnC)

The Plug & Charge feature proposed in the ISO 15118 enables an electric vehicle to automatically identify and authorize itself to a charging station on behalf of the driver, to receive energy for recharging or discharging its battery. The driver needs only to plug the charging cable into the EV. The car and the charger identify themselves to each other by exchanging certificates to allow payment.

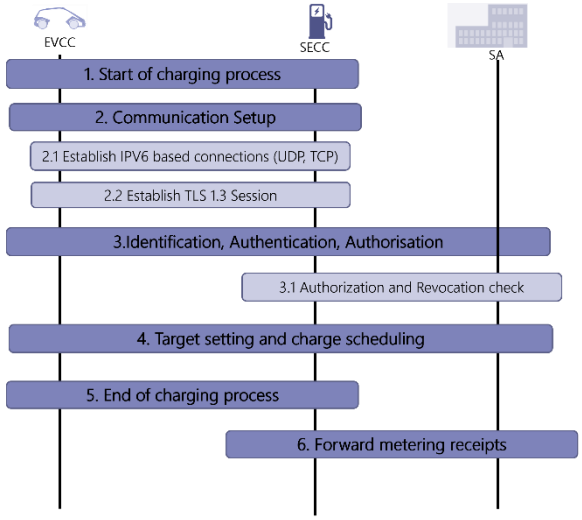


Figure 4: Plug and Charge (PnC) use case steps

As presented in Figure 4, The PnC consists of 6 main steps:

1. Start of charging process:

It is the first step to start the charging process for the PnC.

2. Communication setup:

In this step, the EVCC establish an IP based communication, and then it uses the SupportedAppProtocolReq/Res messages to agree on supported application layer protocols. The EVCC and the SECC use SessionSetupReq/Res messages to establish a V2G communication session. At the end of this step a unique SessionID is agreed to be used for the rest of the PnC process.

3. Identification, Authentication, Authorisation:

This step of PnC consists of multiple sub-steps presented below:

The ServiceDiscoveryReq/Res messages aim at enabling the EVCC to find all the services provided by by the SECC. Services may be the list of payment options an SECC offers to the EVCC indicating what method could be chosen to pay for the services. The EVCC can only select one payment method for all services used by the EVCC.

There might be some other services that should be filtered based on the ServiceDiscoveryReq message scope.

The ServiceDetailReq/Res messages provide specific additional information about services offered by the EVSE.

The paymentServiceSelectionReq/Res, based on the provided services and the corresponding payment options by the SECC this message pair allows the transmission of the selected PaymentOption, SelectedServices and related ParameterSets. Depending on the selected payment additional messages (PaymentDetails message pair) are exchanged.

After all these exchanged messages, the EV may have already connected to a SECC and thus it has an installed contract certificate. In this case the EVCC does not request a new contract certificate. On the other hand, if the EVCC does not have any contract certificate installed, it should send the CertificateIntsallationRequest to the SECC that shall forward the request to the Secondary Actor (SA) or the Mobility Operator (MO).

The SA should verify the signature of the CertificateInstallationReq using the OEM provisioning certificate present in the request. In other words, the SA can verify the authenticity of the EVCC using the OEM provisioning certificate.

If the EV has a ContractCertificate that will expire soon, the EV shall also use the CertificateUpdateReq/Res in order to update the existing contract certificate.

4.Target setting and charge scheduling

After being authorized for charging at the EVSE (SECC) the EVCC and the SECC negotiate the charging parameters with the ChargeParameterDiscoveryReq/Res message pair.

The EVCC provides its charging parameters to the SECC. This message provides status information about the EV and additional charging parameters, like estimated energy amounts for recharging the vehicle, capabilities of the EV charging system and the point in time the vehicle operator intends to leave the EVSE.

The Charging Status message pair provides sanity checks on the meter readings provided by the SECC. On the basis of the iteratively exchanged Charging Status messages the EV has means to check and validate the power drawn from the EVSE. Also, it allows the SECC requesting the EVCC to sign the meter info record included in the ChargingStatusRes message by using the meter receipt message pair.

Usage of this signed meter information for billing purpose may be subject of regulation in certain countries. In addition the request message is used to keep a communication session alive

5.End of charging process

SessionStopReq/Res message pair is used to terminate the current AC/DC session.

6.Forward metering receipts

Forward metering receipts for the SA.

6. Risk Assessment on PnC Use Case

As specified in ISO 21434 [4], a risk assessment shall be performed on every system. Below we propose to perform risk assessment on V2G system, the risks may exist on multiple level as presented below:

- Risks on the vehicle embedded equipment (EVCC)
- Risks on the charging point equipment (SECC)
- Risks on the communication between the EVCC and SECC
- Risks on the communication between the SECC and the secondary Actor (SA)
- Risks on the SA (eMSP, OEM, provisioning services, and private environment)

In the following section we will list some risks that shall be taken into account during the risk assessment.

6.1 Risks on the vehicle embedded equipment (EVCC)

Many existing works has proved that all the embedded equipment inside the vehicle have to be secured.

We propose to perform a risk assessment on hardware and software level. The standard does not propose any solution to secure the EVCC, it is up to the car manufacturer to protect their embedded equipment.

The car manufacturer shall define the scope of the analysis, the internal and external interfaces, the assumptions of their trusted/ non trusted part of the system

Many risks may be present such as:

1. Manipulation of EVCC software: the attacker can have access on open/vulnerable interface such as JTAG/XCP in order to manipulate the existing software. This will impact on the launching of the software, on the charging/discharging, on the billing process.
2. Manipulation of EVCC cryptographic data (keys, certificates): if the cryptographic keys are not protected inside an HSM (Hardware security module), the OEM shall find a way to protect them. Otherwise, an attacker can have access on the keys and use them for billing that could impact on the system reliability.
3. Manipulation of EVCC log data: when the vehicle brokes down (in the field), the user takes it to the workshop/ garage. Log data are used by the OEM to determine in the workshop what is the reason of the problem. If the reason is an attack already done on the vehicle system, and if the attacker can modify these data, then the attacker can hide his malicious acts. Log data shall be protected inside the vehicle.
4. Identity theft: the attacker can have access on the EVCC to steal the keys and certificates of the vehicle user. This could impact on the billing process, the attacker can charge another vehicle by using the victim's credentials, so the bill will be on the name of the victim user.
5. Privacy: some data sent during the the PnC can be related to private information. A risk assessment on privacy shall be done.

6.2 Risks on the charging point equipment (SECC)

Multiple risks might be also possible on the SECC side, especially in a public environment (at the mall, at public road area, etc…)

1. Denial of service (DoS) of SECC: an attacker with a simulated EVCC can send continuously a large number of requests to connect to the SECC, which will impact on the availability of the SECC to receive new request from another genuine vehicle.
2. Manipulation of SECC software
3. Manipulation of SECC cryptographic data (keys, certificates)
4. Manipulation of SECC log data: same as manipulation of log data for the EVCC

6.3 Risks on the communication between the EVCC and SECC

- V2G injector: it consists of injecting data into the power line. The main idea is that the power line messages/ packets are broadcasted in the power line as presented in Figure 5, which means if we have multiple homes connected to the same Power Line (PL), so anyone can eavesdrop on the PL, if we send a packet on one side of the PL, we can listen from the other side. The EV uses a protocol called SLAC (Signal Level Attenuation Characterization) in order to detect which EV is connected to which SE. In [5], the authors present how they used the SLAC protocol to inject messages in the power line.
- Contract Certificate provisioning theft: In the ISO15118 it is specified that the SA generates the key pair (private and public key) for the certificate,

it uses the key pair to generate the vehicle certificate and it distributes the certificate and the private key to the EVCC. The main problem is that the private key of the vehicle is generated outside the vehicle, which is usually a source of vulnerability. The attacker could use the private key of the user for a personal use and thus use the billing service of the genuine user.

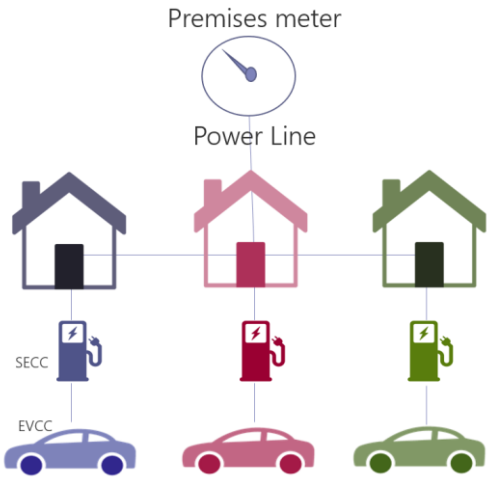


Figure 5: V2G power line connexion

- Dos of wireless channel: The attacker can send a large number of messages on the wireless interface of the SECC in order to block any new request from EVCC. This attack impacts on the availability of the SECC and thus on the charging services.

6.4 Risks on the communication between the SECC and the secondary Actor (SA)

In the ISO 15118, the SECC and the EVCC communicates using a TLS 1.3 connexion, which is considered trusted according to NIST guidelines [6].

On the other hand, in the older version of the standard, in ISO 15118-2 TLS was mandatory only for some use case scenarios, not all scenarios [1].

6.5 Risks on the SA

Privacy violation: the SA might be responsible of users billing information and personal information. The first question to answer is how the SA is protecting these sensible data?

For the eMSP, an attacker can gain access to sensitive data such as users credit cards/ bank account numbers, contracts, personal information, etc…

For the OEM: as presented in Figure 3 the OEM is responsible of management of two types of certificates (vehicle certificate + OEM prov certificate). These certificates are considered as proof of identity of the vehicle for the OEM specific update in the workshop or for PnC use case charging/discharging.

4. Conclusion

This paper provides an introduction to the V2G system, and to the PnC use case introduced by the ISO15118 standard. We describe the V2G PKI. Our contribution consists of highlighting the main risks on V2G system on multiple levels (in the EVCC, SECC, on communication and in the SA cloud).
Many topics still open and needs further investigation, such as the privacy protection on the V2G system.

5. Acknowledgement

This work is done in the context of V2G project at ESCRYPT- ETAS in France.

With the new requirements for OEMs and type approval, the UNECE UN R155 regulation and the ISO 21434 shall also be taken into account.

7. References

[1] “Road vehicles – Vehicle-to-Grid Communication Interface - Part 2: Network and application protocol requirements (ISO 15118-2:2014);,” 2014.

[2] global, Virta, “Vehicle to grid (V2G),” *https://www.virta.global/vehicle-to-grid-v2g*, 2020.

[3] ISO, International Organization for Standardization, “ Road vehicles - Vehicle to grid communication interface.,” 2014.

[4] ISO/SAE DIS 21434, “Road vehicles — Cybersecurity engineering,” 2020.

[5] J.-C. D. V. F. Sébastien Dudek, “V2G Injector: Whispering to cars and charging units through the Power-Line,” Juin 2019.

[6] NIST Special Publication 800-52 Revision 2, “Guidelines for the Selection, Configuration, and Use of Transport, Layer Security (TLS) Implementations,” 2019.

8. Glossary

V2G: Vehicle to Grid
EV: Electric Vehicle
CP: Charging Point
CS: Charging Station
SE: Supply Equipment

PnC: Plug and Charge
SA: Secondary Actor
RFID: Radio Frequency Identification
PKI: Public Key Infrastructure
SECC: Supply Equipment Communication Controller
EVCC: Electric Vehicle Communication Controller
EVSE: Electric vehicle Supply Equipment
OEM: Original Equipment Manufacturer
OSI: Open Systems Interconnection
CPO: Charging Point Operator
Prov: Provisioning
eMSP: electric Mobility Service Provider
XML: eXtensible Markup Language
PE: Private Environment
CA: Certificate Authority
JTAG : Joint Test Action Group
XCP : Universal Measurement and Calibration Protocol
PL: Power Line
Dos: Denial of Service

15 JUNE 2022

HYDROGEN INTERNAL COMBUSTION ENGINES

KST.

TESTING POWERTRAINS TO MOVE THE FUTURE

As an innovative and certified test facility with long-standing tradition we offer our global customer pool from the automotive, heavy duty and non road mobil machinery sectors highly dynamic test benches for combustion engines (up to 4MW), hybrid drive trains and full electric drive trains.

We invite you to try out and test our services and capabilities. Convince yourself of our competence! We will actively support you and address your specific needs!



INNOVATIONS

- Hydrogen engine Development
- Fuel cell Testing
- Inverter Tests
- Electrical Tests (LV 123, LV 124, LV 148)

Your contact:
Nicolas Weyland
Phone +49 6322 799-126
vertrieb@
kst-motorenversuch.de

Representative in France:
Jean-Thierry Schüler
Phone +33 6 07 45 72 00
jean-thierry.schueler@
kst-motorenversuch.de

www.kst-motorenversuch.de

Direct injection Hydrogen Combustion Engine - an attractive Zero CO_2 Powertrain concept for Light Commercial Vehicles

Körfer, Thomas[1]; Busch, Hartwig[1], Durand, Thomas[2]; Huth, Verena[2]; Virnich, Lukas[2]; Dhongde, Avnish[2]; Kerros, Eric[3]

1: FEV Group GmbH, D-52078 Aachen, Neuenhofstrasse 181, Germany
2: FEV Europe GmbH, D-52078 Aachen, Neuenhofstrasse 181, Germany
3: FEV France, F-78190 Trappes, 11 rue Denis Papin, France

Abstract: With its legislative package “Fit for 55”, the European Commission has proposed a significant revision of the CO_2 emission standards for cars and light commercial vehicles (LCV). It is foreseen that without major changes to the current policy framework and legislation, the Paris climate agreement cannot be met and only 60% of emission reductions would be achieved by 2050. Thus, the overall targets become much more ambitious to accelerate the progress towards near carbon-neutral road mobility. In comparison to the emission limits enacted in 2021 for LCV (147g CO_2/km), the emissions of new LCV would have to be lowered by 50% in 2030. To achieve these CO2 targets, not only the technical challenges are significant, also the associated development and product cost increases will play a considerable role in maintaining profitability for all stakeholders, containing manufacturers as well as end users. Therefore, solutions that keep the powertrain changes to a minimal level have the best prospects. In this context, Internal combustion engines (ICE), fuelled with green hydrogen, represents a cost-effective approach to realize CO_2-free transport with a long service life using proven and mature technology. Having no carbon in its composition, H_2 combustion creates no by-product such as CO_2, CO or HC. The NOx emissions remain the only critical factor in hydrogen combustion with regards to pollutant emissions but can be reduced to extremely low levels by precise air/fuel-ratio control. Direct injection (DI) in combination with a suitable boosting system represents a solution to achieve necessary high air/fuel ratios in the entire engine map and to realize attractive engine-out NOx emissions. Applied to LCV with high load factors and nearly 24h usage, DI H2-ICE characterizes an attractive solution for CO_2-neutral transport. It offers good drivability with proper transient response and lower raw NOx emission with even increased lean engine operation compared to a port fuel injection system. Besides, it gives a perspective as well for diesel like power density, which is a key element for the relatively compact engine bay of LCVs for high goods carriage demands. This paper is focusing on FEV’s technical approach of H_2 DI technology to convert an existing diesel-based LCV to hydrogen operation, under given constraints of hardware integration and vehicle performances. Thanks to FEV’s dedicated H_2 simulation tool chain, combustion system is improved to achieve a high degree of mixture homogeneity, knock free operation, high BMEP level and competitive engine efficiency. Moreover, combining the right exhaust aftertreatment layout with advanced engine control algorithm reduces NOx raw emissions and delivers high NOx conversion efficiency to satisfy upcoming zero-impact emission standards.

Keywords: Carbon-neutral mobility, near zero emissions, high efficiency, Hydrogen combustion

1. Introduction

The transportation sector is facing significant challenges due to massively tightened legislative requirements from two sides. On one hand ultra-strict emission standards under massively enlarged real-world conditions are mandated and in parallel the pressure to offer rapidly carbon-neutral options is rising. Both targets could be achieved with battery-electric vehicles, even for heavier applications, if the corresponding impacts and consequences would be quickly solved and substantially enabled in an attractive and affordable way. But, for the time being and also expected for the next decades, the impacts on multiple applications with regard to typical, every-day use cases are multi-facial and partially extremely crucial for the end-user. Facing these challenges, the market is encouraging the OEM to investigate alternative solutions, safeguarding the overall business in terms of usage, TCO and fulfilment of upcoming legal demands.

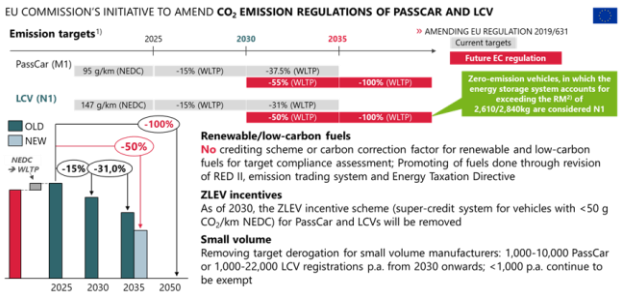


Fig. 1: GHG (CO2) Regulation under the initiated “Fit for 55” Program of the EU Commission

With the recently initiated “Fit for 55” legislative package, a substantial pressure is directed to the mitigation of GHG emissions, mainly CO2 but other species as well. Due to the current “Tank-to-Wheel”-based legislation, CO2-neutral fuels –the easiest and most powerful option to shrink the CO2 emissions for new as well as in-service vehicles out of the transportation segment, are not able to support the fulfilment of the legal targets. As remaining alternatives, only Hydrogen (H2) or Ammonia (NH3) have the potential to meet the requested carbon-neutral operation of the legal rule makers. Based on today’s technical assessment, NH3 is foreseen to preferably power large and largest ICE- applications, like ships and vessels. Hydrogen appears to become more and more interesting for all kinds of mobile On- and Off-Highway installations. Deriving from higher displacement applications like big NRMM and large trucks, the conversion of smaller engine types in the Passenger Car and LCV’s segment becomes more and more attractive in order to offer the end customer possible solutions for specific needs and demands, besides BEV and FC-powered vehicle types. Especially in the LCV sector, ranging from 2,8to up to 7to GVW, the conversion of Diesel engines to H2 operation is intensively evaluated and thoroughly analysed, based on two main attributes, which appear highly relevant for future H2-ICE’s, namely the existing rigid engine architecture with high Peak Firing Pressure (PFP) capabilities and the often already available twin-turbo boosting system, supporting extremely lean combustion regimes with high thermal efficiency and simultaneously low engine-out NOx emissions.

EU7 / VII EMISSION TARGETS: EXPECTATIONS BASED ON LATEST CLOVE SCENARIOS

Light Duty Certification						Heavy Duty Certification			
Passenger Car			Light Commercial Vehicle (< 35 kw/to. → max. 122,5 kW)						
Pollutant	Limit	Unit	Pollutant	Limit	Unit	Pollutant	Cold start	Warm operation	Unit
NO_x	30	[mg/km]	NO_x	**45**	[mg/km]	NO_x	150	90	mg/kWh
PN	$1x10^{11}$	[1/km]	PN	$1x10^{11}$	[1/km]	PN	$3x10^{11}$	$2x10^{11}$	1/kWh
PM	2	[mg/km]	PM	2	[mg/km]	Not defined, yet			
CO	400	[mg/km]	CO	**600**	[mg/km]	CO	2,500	300	mg/kWh
NH_3	10	[mg/km]	NH_3	10	[mg/km]	NH_3	70	70	mg/kWh
CH_4	20	[mg/km]	CH_4	20	[mg/km]	CH_4	450	350	mg/kWh
N_2O	20	[mg/km]	N_2O	**30**	[mg/km]	N_2O	200	60	mg/kWh
NMOG	45	[mg/km]	NMOG	45	[mg/km]	NMOG	70	40	mg/kWh
HCHO	5	[mg/km]	HCHO	**10**	[mg/km]	Not defined, yet			

+50% target on most values

Fig. 2: Prognosed Limits for the upcoming EU7 Emission Standards (acc. to CLOVE/EUCommission)

Realization of high thermal efficiencies around 42% BTE in the best point in combination with appropriately dimensioned H2 storage capacity typically ensures, even for a fully loaded use cases, a driving distance of 450+ km including the quick refill option. In parallel to the mid-term GHG regulation, already around 2026, the next, most likely final pollutant emission legislation will be engaged with the ultra-strict EU-7 standards, which would then as well be relevant for upcoming H2-ICE powertrains. Fig. 2 displays the latest announcements from the CLOVE consortium, supporting the EU commission to define the new emission norms.

According to the properties of the H2 fuel, mainly the nitrogen-based emission species characterize the most challenging demands, as all carbon-related emission components are assumed to be close to zero, as only the engine lubricant can cause any kind of carbon-consisting emissions. Therefore, optimized mechanical layout and specification, minimizing oil consumption (piston liner compound, piston ring tension, …) and oil leakage (Turbocharger) characterize an important prerequisite of H2 engines to support the achievement of the tight future requirements. However, it is supposed that a particulate trap will be mandatory due to public expectations. In terms of nitrogen related pollutant emissions, some aftertreatment measures are mandatory to safeguard the fulfilment of the ultra-low requirements under extended real-world boundaries.

From market perspective, a higher demand for ICE powertrains is expected from the more commercially used applications, rather than from the passenger car segment including SUVs. The quite large bandwidth of market requirements for commercial use cases, covers:

- High daily mileage
- Short stops/downtimes
- 24/7 operation
- Flexibility and easy, unrestricted use
- Versatile Usage
- High payload

All these attributes are crucial for profitable use of commercial applications and are not ensured by battery electric propulsion in the foreseen time frame, especially for some use case classes, as depicted in the Fig. 3.



Fig. 3: Overview of use cases for LCV/LDT Applications in Europe, incl. sectors with probable market demand for H2 propulsion systems

According to this analysis and ranking, an H2-fueled ICE represents an attractive option to cover this range of vehicle applications, as it features the advantage as well, that the value chain remains higher at the

OEM side and existing engine production lines can be used for a longer time. The attractiveness and merits of H2-powered engine is as well showcased in Fig. 4 in comparison to fully electric vehicles (BEV) and fuel cell motored vehicles (FC/BEV).

2. Key Features and Characteristics of H2-fueled ICE

Carbon-neutral Mobility: Hydrogen as enabler

With its “Fit for 55” package, the European Commission has introduced a strict revision of the CO2 emission standards for Light Duty Vehicles (LDV). In contrast to the original CO2 emission standards, enacted from 2021 onwards, emissions from newly registered Passenger cars in the EU, must be lowered by 55 % and the output from new LCV’s by 50 % in 2030 [1]. Furthermore, a new and ambitious target was declared at the end of 2021 for all new passenger cars and LCVs to aim for Zero CO2 emissions by 2035.

Hydrogen (H2) as a carbon-free fuel represents a very promising candidate for environmental-friendly and climate-neutral ICE usage. All possible other carbon-containing pollutant emissions, such as carbon monoxide (CO) and hydrocarbons (HC), can only derive from the combustion of lubricants and are on an extremely low level. The same applies as well to soot particulates, which cannot be formed by the combustion of the gaseous fuel, but only by the oil trapped and burned in the combustion chamber.

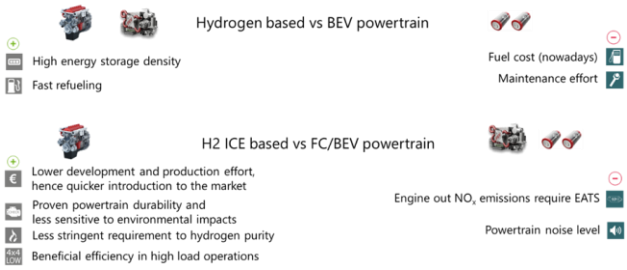


Fig. 4: Pros and cons of H2 fueled engine compared to FC and BEV

Due to the combustion process with environmental air (containing N2 and O2) and high temperature gradients, NOx (nitrous oxide) emissions will be formed on a level, which will request some post-processing to meet upcoming strict, ultra-low emissions norms. With a tailored exhaust gas aftertreatment system and an optimized calibration, the tailpipe NOx emissions can be mitigated to near zero levels, while ensuring all others carbon-based emissions at negligible levels. Secondary emissions such as N2O and NH3, eventually formed in the aftertreatment system, need to stay at near-zero level, below the legal requirements. Thus, the optimal matching of engine-out emissions, balanced against highest thermal efficiency, with a dedicated exhaust aftertreatment configuration, characterizes the H2-ICE as a future-oriented propulsion system for the mid-term transportation sector.

The computational and experimental investigations focus on the effects of relative air/fuel ratio, boosting grade, charge motion, compression ratio, exhaust gas temperature, exhaust mass flow rate on NOx concentration. The aim is to demonstrate a zero-impact emission propulsion system through comprehensive alignment of the base engine definition and the aftertreatment system with a tailored engine calibration.

Thermal Efficiency, Energy Consumption and Power Output

The characteristic of hydrogen offers some significant advantages, but also new challenges compared to classical internal combustion engines using conventional, crude-oil derived fuels. Hydrogen has unique features and characteristics impacting the combustion control such as low quenching distance, low minimum ignition energy, high flame speed, and high auto-ignition temperature. These properties define the main boundary conditions when developing a high-efficiency H2 internal combustion engine.

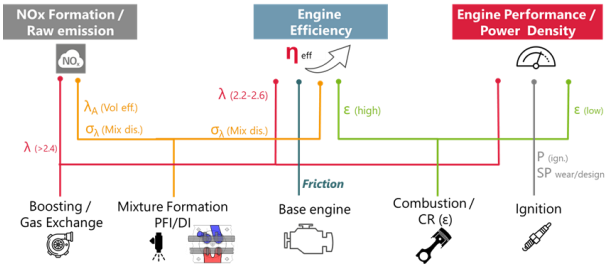


Fig. 5 Key Engine systems that affect performance and emissions

The schematic shown in Figure 5 illustrates the central design parameters to be optimized to resolve the conflicting objectives of efficiency, performance and emissions.

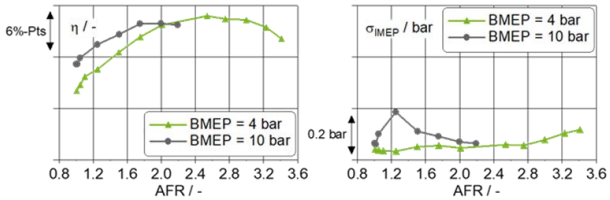


Fig. 6 Engine efficiency and combustion stability as a function of the relative air/fuel ratio

The boosting system must be able to provide enough fresh air to support very lean combustion across the entire engine map, in steady state as well especially in transient conditions. Mixture homogeneity and optimized in-cylinder charge motion must be provided

by adapted designs with proper H2 injectors positioning, and updated combustion chamber (piston bowl geometry and compression ratio). As in a conventional engine, the base engine hardware influences the friction losses and thus impacts overall engine efficiency and engine performance. The ignition system is also a key component , as it must guaranty accurate control of spark timing to avoid pre-ignition and ensure knock-free engine operation.

If highest thermal efficiency is targeted, Diesel-like settings would be preferred, but the compression ratio is limited to appr. 13:1 by occurrence of knocking resp. abnormal combustion, depending on the level of charge motion and mixture formation. Lean and ultra-lean combustion is supported by advanced boosting systems (e.g., advanced VGT or two stage turbo).

H_2 INJECTION SYSTEMS FOR DIESEL BASE ENGINE CONCEPTS

	External mixture preparation		Space requirement cylinder head	
	Low pressure PFI	**Low pressure DI**	**Mid pressure DI**	**High pressure DI**
Fuel Injection	Port fuel injection ~ 5-10 bar	Direct injection ~ 15-30 bar	Direct injection ~ 40-60 bar	Direct injection ~ 300 bar
Specific Power (HD) engine	< 25 kW/l	> 25 kW/l	> 25 kW/l	~ 30 kW/l
Peak BMEP (HD) engine	< 20 bar	> 20 bar	> 20 bar	> 25 bar
Combustion	Stoich/Lean Spark ignited	Lean Spark ignited	Lean Spark ignited	Lean Spark ignited -- Diffusive
Knock tendency	↓	0	0	↑(SI) -- Not existing (DI[1])
Boost pressure demand	↑↑	0	0	0
Transient load response	↓↓	0	0	↑
Main benefit	• Easy to integrate, • Hardware available • Low failure risk	• Robust against back-fire • Power density • Transient response	• Same as LP DI • Smaller packaging compared to low pressure • Potentially better mixture preparation	• Same as MP DI • Diffusive combustion possible
Main challenges	• Boosting • Safety (Backfire)	• Integration DI Injector • Uniform mixture preparation	• Integration DI Injector • Range	• Integration DI Injector • High pressure generation • For Diffusive combustion high NOx raw emissions

Fig. 7 H2 Fuel Introduction – a key sub-system for best functional performance

Both Diesel and gasoline base engines can be principally used for conversion towards hydrogen operation. For example, a state-of-the-art gasoline passenger car engine, featuring pent roof-shaped cylinder head layouts with comparably large valve dimensions, modified for H2 operation with direct injection is capable to achieve gasoline-like power density with mixture enrichment up to stoichiometric operation. Another attractive possible approach is to use a Diesel base engine but converted towards spark ignition and a hydrogen injection system, to achieve diesel-like efficiency with constant lean-burn operation due to favourable boosting grades and high peak firing pressure capabilities.

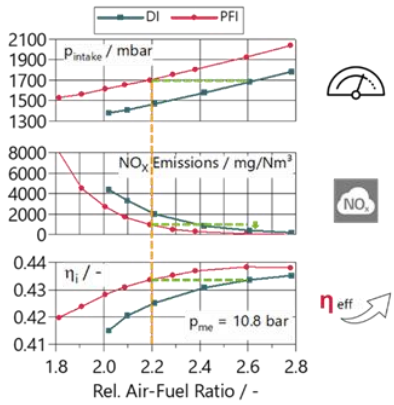


Fig. 8 Boosting performance as enabler of ultra-lean operation for lowest engine-out NOx emissions and high thermal efficiency

The representative results for relative air/fuel ratio (AFR) sweeps, displayed in Figure 6, were performed on a hydrogen-fuelled, turbocharged, SI engine, featuring a direct hydrogen injection. A standard 3-cylinder gasoline engine served as the basis for this engine conversion. The power unit is currently in an advanced prototype stage and is not yet fully optimized. For both part load points with 4 bar and 10 bar BMEP (brake mean effective pressure), it can be observed, that combustion stability – indicated by the low value of the standard deviation of the IMEP (indicated mean effective pressure) – is given at lean operation with λ values up to 3.4. It can also be seen that a significant efficiency gain is achieved by leaning the mixture compared with λ=1 operation.

Limitations of the current boosting system are also evident. Already at 10 bar BMEP, ultra-lean combustion starts to be limited due to lack of air. A more powerful boosting system is required if higher loads are also to be run in a very lean combustion environment.

To support an efficiency-enhanced, lean combustion principle, the fuel introduction system represents an additional key sub-system for achievement. Fig. 7 provides a general comparison of possible fuel injection technologies to realize H2 combustion. In general, it can be separated as for all SI combustion systems between indirect and direct fuel injection. Following the DI route, several pressure stages for H2 injection are feasible, but all demand integration effort for the H2 DI injectors in the existing cylinder head design, concluding in multiple engineering efforts, as port geometry, cooling circuits, cylinder head stiffness and other functionalities might be impacted.

Aiming for an optimized engine performance and efficiency, a combined usage of stoichiometric/lean concept is beneficial. Air/hydrogen charges have ignition limits of 0.15 < AFR < 10.5, which are much wider than those of conventional fuels such as gasoline or diesel. Operation principles of ultra-lean, lean and stochiometric are therefore enabled.

Obviously, a high boosting grade drives the capability of ultra-lean operation for both types of H2 injection, indirect as well as direct injection, which enables the substantial lowering of engine-out NOx emissions. Furthermore, at identical boost pressure levels, DI combustion principles achieve lower engine-out NOx emission concentrations at comparable efficiency levels.

Raw emission characteristics

The tailpipe emissions of a hydrogen internal combustion engine mainly depend on the raw

emissions and the efficiency of the exhaust gas aftertreatment system. As illustrated in Figure 9 [2], the engine-out NOx emissions are strongly influenced by the air/fuel-ratio, while the most important factors defining the aftertreatment system efficiency are exhaust gas temperature, space velocity and mass flow rate as well as exhaust gas composition.

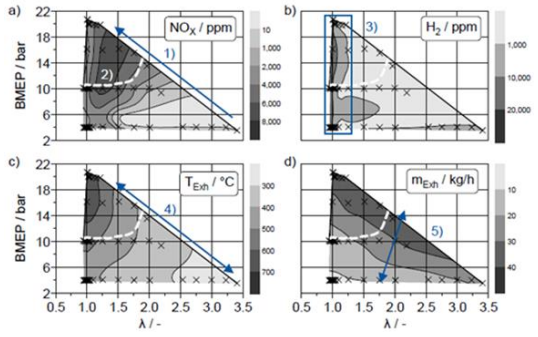
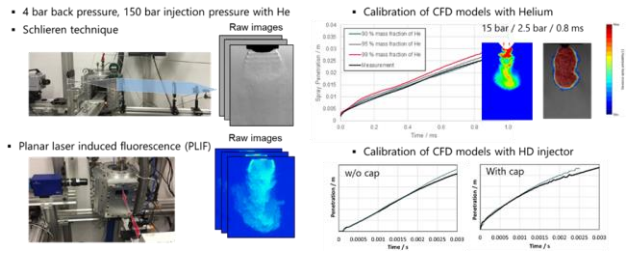


Fig. 9 Engine-out exhaust gas conditions as function of relative air/fuel ratio λ: (a) NOx emissions, (b) H2 exhaust share (c) Exh. gas temperature, (d) Exh. mass flow

The graphs in Figure 9 displays a fair load range according to the given in-cylinder combustion conditions. The achievable torque level reaches stoichiometric conditions at higher loads. An additional important influencing parameter is indicated by the white dashed line. It outlines the area capable of operating at ab efficiency optimized 50% point of mass fraction burned (MFB50). At higher engine loads, the ignition timing needs to be retarded for the given combustion system to avoid knocking combustion. In Figure 9a, the NOx emissions are shown as a function of the relative air/fuel ratio and the load. Starting at stoichiometric conditions, a minor enleaning leads to increased NOx emissions, as known from gasoline engines. With higher oxygen content during the combustion, the NOx formation tendency increases for a certain range. After reaching a maximum around λ= 1.3, the NOx emissions decrease significantly below the level of stoichiometric conditions. This is a consequence of the decreasing temperature, as shown in Figure 9c. As a result, lean operation is extremely beneficial in terms of NOx emissions only at low loads in this case. Looking at the unburned fraction of hydrogen in Figure 9b, significant H2 emissions are detected around stoichiometric operation. One reason for incomplete combustion could be the design of the combustion chamber of the prototype engine, which has not been optimized for hydrogen combustion. Improvements could be achieved here by further optimizing the mixture formation. In addition, the indicated efficiency would also be positively impacted.



Additional important parameters for the exhaust gas aftertreatment system are temperature and mass flow of the exhaust gas. The exhaust gas temperature (Figure 9c) highly depends on the air/fuel ratio and varies in a wide range from below 300°C to higher than 600°C. Looking at the exhaust mass flow isolines distribution in Figure 9, it is seen that several combinations of temperatures and mass flows are possible.

For optimal definition of a future-oriented combustion system for H2-fueled ICE's a certain number of key parameters are crucial and highly relevant, besides general engine parameters like cylinder displacement, stroke-to-bore ratio and engine speed band, as good mixture composition and combustion behaviour must be ensured for a large variety of operational conditions.

For detailed and knowledge-based layout of H2 combustion systems, the extended usage of validated and experimentally verified CAE methods provide a major advantage and safeguard the process effectiveness in terms of compressed development budgets.

The subsequent Fig. 10 delivers the corresponding overview over the entire tool chain developed and tailored in-house to optimize the virtual development process under state-of-the-art boundaries.

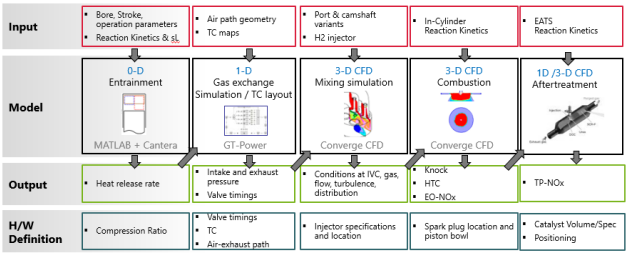


Fig. 10 Validated 0D to 3D simulation tool chain to optimize key parameters

An important element for optimal achievements is seen in the depiction and characterization of the H2 jet penetration and propagation under various boundary conditions, containing the precise, time-based recording of the injector behaviour as well during the fuel introduction phase, depending on the utilized injector type and specification. For best validated 3D CFD detailed, deep knowledge of spray formation is gained thanks to low pressure chamber investigation. Fig. 11 Development toolchain for detailed knowledge of spray formation

Figure 12 displays an exemplarily comparison between different CAE-based combustion system characteristics on the base of different hardware specifications in terms of injector positioning and charge motion characteristics for an identical injector type and a common combustion bowl with fixed compression ratio for a flat cylinder head configuration with 4 valves per cylinder.



Fig. 12 Key parameters and influencing factor of optimal H2 combustion system development For comprehensive analysis and interpretation of observations detailed chemistry is mandatory to model the combustion process and the emission formation accurately and with high definition in order to support decision-making of optimization steps.

For thorough analysis of heat release a dedicated signal filtering methodology is required to identify knocking and abnormal combustion behaviour in an appropriate way. Fig. 13 provides a representative case for a medium load point with the corresponding depiction of in-cylinder occurrences and cylinder pressure data, following two different filtering and post-processing methodologies.

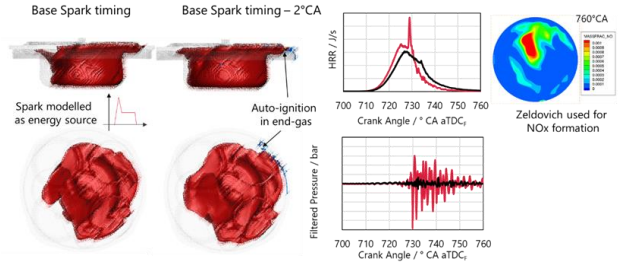


Fig. 13 Comparison of measured and simulated combustion characteristics

Exhaust gas aftertreatment - Solutions for high-efficiency H2-ICE

With the wide range of possible combustion system layouts comes a rather high number of potential combinations for the exhaust gas aftertreatment systems. For selected H2-ICE applications, specific advantages, and challenges result from the right combination of the combustion concept and the exhaust gas aftertreatment system, but also from the boosting system, or a powertrain hybridization, if applicable.

For light commercial vehicles, where high load capacity and relatively high mileage are needed, there is a broader field of possible solutions a H2-ICE can offer. A base diesel engine with a displacement of 2 to 3 litre converted to H2 brings most benefits. Low/medium pressure direct injection in combination with lean full-load and ultra-lean part-load operations appears most favourable regarding durability and driving range. With this lean-burn concept, the use of a diesel-like aftertreatment system with SCR (selective catalytic reduction) and a particulate filter system would be preferable.

	2,5L Diesel	2,5L H2
Engine arrangement [-]	I-4	←
Displacement [mm]	2,49	←
Bore x Stroke [mm]	90 x 98,2	←
Power [kW]	165 @ 3800 rpm	150 kW @ 3500 rpm
Max. Torque [Nm]	550 @ 1500 rpm	440 @ 1500 rpm
Cyl. Block	CGI	←
Max. Cyl. Pressure	205	←
Cyl. Head	4-valve DOHC / VVA protected	←
Crankshaft	Forged Steel / 5-bearing support / 4 counterweights	←
Camshaft	Assembled design	←
Valvetrain	Conventional / (VVA protected)	←
Piston/CR	ST / 18,5 [±0,5]	ST /13:1
FIE System (Pressure / Injectors)	2500 / Sol. 9-hole	30 bar / outwards opening
Boosting System / Charge Cooling	VTG / WCAC	Twin Turbo
EGR-System	cLP + cHP EGR	none
Combustion System	Low swirl high efficiency	Increased In-Cylinder Charge motion
Timing Drive	Chain	←
FEAD/Anciliaries	Var. oil / var. water pump	←
Aftretreatment	DOC + SDPF +SCR + CUC	DOC + SDPF(+ CUC)



Base 2,5L Diesel Variant

Fig.14 Specifications and Features of Base LCV/LDT Diesel Engine and H2 converted Figures

For Passenger cars, equipped with an engine family size of approximately 2 litre, fast refuelling is a key for long distance traveling or “street parking” customers. Both, SI as well as Diesel-derived H2-variants, are in principle possible for these vehicle applications. In such a case, a combustion concept with stoichiometric combustion at higher loads and lean or ultra-lean combustion for part load can be selected. Extreme lean operation in the part load map area offers several advantages for the engine itself. At higher load, a combined stoichiometric concept can be used to improve the specific power output.

In the following, it will be demonstrated that for each combustion concept a specific EATS (exhaust aftertreatment system) layout is required.

Matching of Engine-out NOx Emissions with EATS configuration

The observed results of the thermodynamic investigations from Fig9. depict very different exhaust gas characteristics that can be experienced with H2 combustion. In Fig15. investigations are also performed to capture property of exhaust gas on a MD engine at steady-state operating point (1400 rpm, 8bar BMEP). Relative AFR and centre of combustion directly impact the NOx raw emission, the exhaust temperature and the engine efficiency. It becomes clear that the thermodynamic engine definition and the vehicle calibration have to be engineered in parallel with the exhaust gas aftertreatment system.

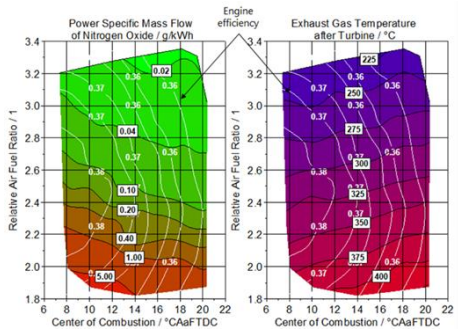


Fig. 15 Key parameters for determination of EATS specifications for a H2-ICE

As mentioned earlier, if the combustion is lean, adopting a diesel-like solution for the exhaust gas aftertreatment is a sensible option. Ultra-lean operation enables very low NOx raw emissions down to levels where emission analysers reach their detection limit. However, very lean combustion conditions come along as well with very low exhaust gas temperatures that are underneath of typical light-off temperatures of catalytic converters. A combination of a NSC (NOx storage catalyst) with a urea-based SCR system can tackle this challenge. NSC can reduce NOx emissions after a cold start by adsorbing NOx at low and desorbing it at higher temperatures. Using a NSC can also in-crease the NO2/NOx ratio for better SCR efficiency. With such a configuration, the NSC coating needs optimization to enable full or nearly passive operation, based on the temperature window only. A solution with active purging is also being studied but the complexity of the combustion control increases. However, with view on the anticipated N2O limits under upcoming EU-7 standards, a refined NSC specification and upgraded control logics are required to ensure compliance.

The coupling of H2-SCR & urea-SCR supports a superior conversion efficiency at temperature levels.

H2-SCR could be fed directly from the H2 slip in the exhaust gases of the engine. However, H2-SCR is a new technology, and its development is still underway and not yet ready for series production. In addition, initial investigations show high N2O production.

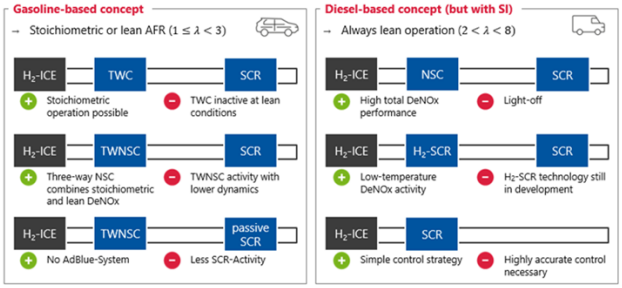


Fig. 16 EATS layout for a H2-ICE based on systems for gasoline or diesel base engines

Using only a single urea-SCR system offers pros and cons that need to be balanced when selecting an EATS layout. Urea-SCR itself can achieve high efficiencies in a wide temperature range. Having no other aftertreatment component located upstream in the exhaust line, the SCR system is heated up quickly and can reach good NOx conversion efficiency. On the other hand, with the absence of an upstream catalyst, exothermic reactions across a catalyst cannot be used to support a rapid heat up of the SCR system. DeNOx is supported by a urea-SCR only which needs to work with low NO2/NOx ratios in the raw exhaust gas from the engine [3].

Under stoichiometric conditions, conventional DeNOx systems such as an SCR or a NOx storage catalyst are not applicable. Instead, a three-way catalyst (TWC) is necessary for exhaust gas aftertreatment. When switching between stoichiometric and lean operation, TWC performance under lean conditions is another issue. Even under lean conditions, a TWC still has a catalytic effect. This enables the TWC to replace an oxidation catalyst and provide NO2 to a downstream SCR system. With a favourable NO2/NOx ratio, improved SCR efficiency can be achieved.

Accordingly, the aftertreatment concept for lean conditions could include a TWC and a urea-SCR system. At that temperature level, a urea-SCR system is more sensible than a H2-SCR. The urea-SCR might even operate as passive concept fed by secondary ammonia emissions formed across the TWC.

Another option for the exhaust gas aftertreatment is the three-way NOx storage catalyst (TWNSC). It is capable of NOx conversion under stoichiometric conditions but has a significantly increased NOx storage capacity. With this, the TWNSC is also applicable for lean operation, where it stores the NOx. For the regeneration, cyclic rich operation is required. However, to define such an aftertreatment concept, more investigations are necessary. In order to bring engine raw emissions, as well as exhaust gas temperature ranges, in line with aftertreatment performance, known after-treatment technologies can be further developed for hydrogen use. In addition, the functions and calibration of the engine and aftertreatment controls must be matched to ensure high engine performance and superior efficiency with near-zero pollutant emissions.

In summary, for a H2-ICE that is operated stoichiometrically, the EATS concepts derived from gasoline application displays the primary solution. Due to the stoichiometric operation, the introduction of a TWC or TWNSC is mandatory. For lean-burn und ultra-lean operation, it must be supported by an additional, highly capable DeNOx system, which is here identified by an SCR-based post treatment.

The focus is clearly given on DeNOx measures, but particulate emissions – mass and numbers - are also intensively investigated, as PM/PN is judged as extremely harmful from the legal rule makers for the upcoming emission norms. Therefore, a particulate trap is seen as mandatory to achieve compliance with upcoming ultra-low emission regulations as well as market acceptance.

According to the approach to operate the H2 engine for efficiency as well as emission aspects mainly under lean combustion conditions, the major issue in terms of NOx tailpipe emissions is found in the highly transient mode, as here typically enrichment is necessary to allow substantial load steps. As appropriate torque built up requires strong enrichment, raw NOx emissions will peak as well for the transitional period. Fig. 17 shows exemplarily the effect of two main calibration parameters on the emission performance during a WHTC exercise. By increasing the targeted min λ-value and the accompanying adjustment of the ignition timing during the transient operation, significant reduction grades are obtained, offering finally a NOx reduction of more than 80% versus the standard steady-state conditions. In this context, it has to be mentioned, that any other assistant measure for dynamic operation, like e.g. electrically assisted boosting systems (e-Charger or e-TC) or a 48V BSG, would substantially simplify the transient boundaries and would improve the fuel efficiency of the application.

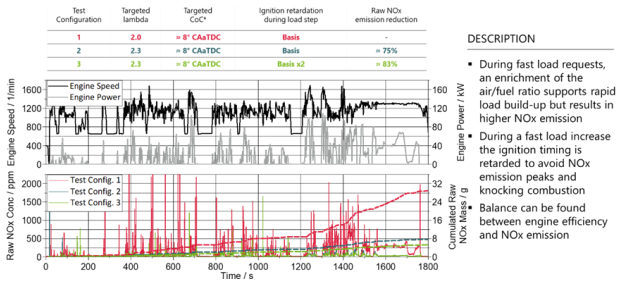


Fig. 17 NOx emission reduction during transient operation by synchronized adjustment

Following the optimized engine calibration process and applying an appropriate exhaust aftertreatment configuration to the H2 engine, best boundaries are arranged to realize a highly efficient, zero CO2 operation with ultra-low tailpipe emissions, according to the expected, very stringent EU-7 emission standards, as depicted in Fig. 18.

Using established technologies while maintaining minimal changes to existing, in-production base engine hardware offers a reliable and cost-effective solution for the conversion and implementation of hydrogen combustion engines into upcoming vehicle applications. The impact of calibration is crucial, and the development of the hydrogen internal combustion engine as near-zero emission powertrain concept requires a well-matched engineering process with alignment of engine definition and exhaust aftertreatment system specifications at all stages of development, i.e. during concept and system design, catalyst selection and calibration.

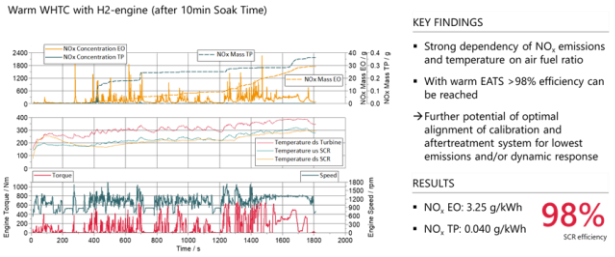


Fig. 18 Tailpipe Emission Results for Transient Cycle

As well during operation, the engine and aftertreatment control needs to be optimized to achieve near-zero emissions under different ambient conditions and operating scenarios. Fig. 19 summarizes the key technology areas for highly efficient H2 engines for LD applications.

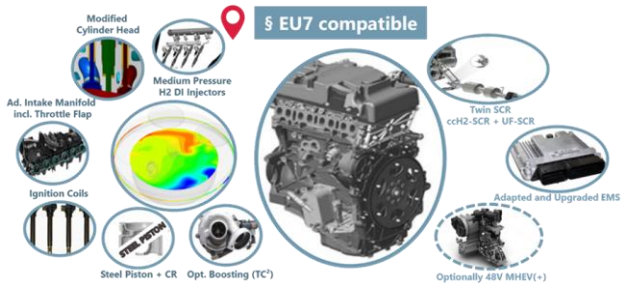


Fig. 19 Main technologies and sub-systems for high-efficiency H2 powertrain

5. Acknowledgement

The authors acknowledge the engaged and continuous assistance and contribution of all involved colleagues to this work.

7. References

[1] European Parliament, https://www.europarl.europa.eu/legislative-train/theme-a-european-green-deal/package-fit-for-55.

[2] Stefan Sterlepper, Marcus Fischer, Johannes Claßen, Verena Huth, Stefan Pischinger. "Concepts for hydrogen internal combustion engines and their implications on the exhaust Gas Aftertreatment System". Energies 2021, 14, 8166. https://doi.org/10.3390/en14238166.

[3] Verena Huth, Lukas Virnich, André Pfortje, Stefan Pischinger, Stefan Sterlepper.

"The hydrogen combustion engine as zero impact emission powertrain concept". 30th Aachen Colloquium Sustainable Mobility 2021.

[4] Thomas Körfer, Hartwig Busch, Christoph Menne, Patrick Recker.
"Future modular Diesel engine portfolio for heavy Light-duty applications to meet all market demands under tightened legal requirements", MTZ 04/2022

[5] Virnich, Lukas; Lindemann, Bernd, Müther, Martin; Schaub, Joschka; Robb, Lynzi; Geiger, José.
"How to improve transient engine performance of HD hydrogen engines while maintaining lowest NOx emissions", Vienna Symposium 04/2021

[6] Huth, Verena, Virnich, Lukas; Balasz, Andreas, Uhlmann, Tolga; van der Put, Dieter, Thewes, Matthias;
"Exhaust Aftertreatment of Hydrogen combustion engines – Zero impact or even zero emission powertrains ?; 9th Intl. Engine Congress 2022

[7] Verena Huth, Lukas Virnich, André Pfortje, Stefan Pischinger, Stefan Sterlepper.
"The hydrogen combustion engine as zero impact emission powertrain concept". 30th Aachen Colloquium Sustainable Mobility 2021.

8. Glossary

AFR	Air Fuel Ratio
BMEP	Brake Mean Effective Pressure
BSG	Belt Starter Generator
CAE	Computational assisted engineering
CLOVE	Consortium for ultra-low vehicle emissions
CO_2	Carbon Dioxide
DeNOx	NOx Reduction System
EATS	Exhaust Aftertreatment System
EU-7	(assumed) EU-7 emission norms
ICE	Internal Combustion Engine
IMEP	Indicated Mean Effective pressure
LCV	Light Commercial Vehicle
LD(T)	Light Duty (Truck)
GHG	Greenhouse Gas
GVW	Gross Vehicle Weight
H2	Hydrogen
λ	Lambda (rel. Air/Fuel ratio)
MFB(50)	Mass Fraction Burned (50%)
NOx	Nitrogen Oxides
OEM	Original Equipment Manufacturer
PFP	Peak Firing Pressure
PM	Particulate Matter
PN	Particulate Number
SCR	Selective Catalytic Reduction
(e)-TC	(electric) Turbocharger
TWC	Three-Way catalyst
TWNSC	Three-Way NOx storage catalyst
WHTC	World Harmonized Transient Cycle

High Efficiency Hydrogen Internal Combustion Engine – Carbon Free Powertrain for Passenger Car Hybrids and Commercial Vehicles

DI (FH) DI Bernhard Raser[1], Dr. Paul Kapus[1], Dr. Peter Grabner[2], DI Anton Arnberger[1], Dr. Renè Heindl[1], DI Michael Egert[1], Neil Kunder MSc[1], Dr. Günter Fraidl[1], DI Michael Weißbäck[1]

1: AVL List GmbH, Hans-List-Platz 1, 8020 Graz
2: Graz University of Technology, Institute of Thermodynamics and Sustainable Propulsion Systems, Inffeldgasse 19, 8010 Graz

Abstract: Europe is leading the race for reducing CO_2 emissions. The contribution of traffic plays a major role in that race. Governments and industry set a focus on Battery Electric Vehicles (BEV).

A possible alternative to BEVs are hydrogen-fueled internal combustion engines. Also, these powertrains can be operated CO_2-free. By using optimized combustion and exhaust aftertreatment, such engines can also be operated close to zero emissions ("zero impact").

Up to now, adaptions to hydrogen typically started with conventional approaches – for passenger cars from boosted direct injection engines, for commercial applications from swirl-based gas- or Diesel engines.

In the future, powertrain systems with highest efficiency are needed – on the one hand to keep the energy requirement for hydrogen production on the lowest possible level, on the other hand to increase the range of the hydrogen-fueled vehicle. Especially for passenger cars the future powertrain will be electrified. This allows a specific layout of the hydrogen engine towards a dedicated hybrid engine.

This publication deals with the layout of hydrogen engines for commercial applications and passenger cars focusing in this segment on hybridized powertrains with a dedicated solution with highest efficiency powertrains. By combining high compression ratio, Miller combustion system, direct hydrogen injection, lean operation and boosting, efficiencies comparable to the ones currently achieved by the best dedicated hybrid engines, which are currently under development, are feasible.

Keywords: Hydrogen engine, hydrogen combustion, hydrogen ICE

1. Introduction

The prerequisite for sustainable use of hydrogen in the transport sector is its production using energy from renewable sources. This requires significant growth rates in renewable energy production itself. Unfortunately, the regions of the world where renewable energy – based on wind or solar – is available are not those where the energy is finally needed, see Figure 1.

As examples, solar energy is available in Africa on a large scale and wind power is available in South America. The Energy produced from those renewable sources will finally be needed in regions with high population density, such as Europe, Japan etc. This discrepancy leads to the need for energy transport. Chemical energy carriers can offer access to energy sources that would not be accessible by direct transmission of the electricity that is produced out of primary energy sources such as solar or wind.

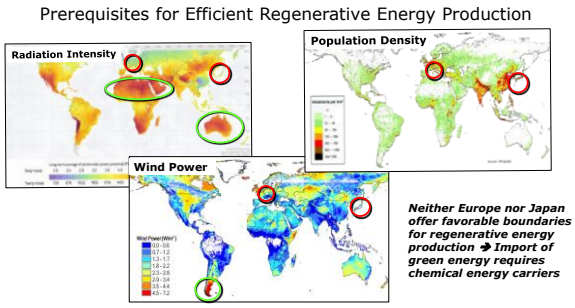


Figure 1: Comparison between supply of renewable energy and transportation demand [i]

The simplest available chemical energy carrier that can quite easily be produced based on electric current is hydrogen, Figure 1. Produced from renewable electric power via electrolysis of water, hydrogen can be stored and transported to where the energy is finally needed. To use this chemically bound energy in a BEV, an upfront reconversion to electric power would be required. On the other hand, this energy could also be utilized directly in hydrogen-powered vehicles, based not only on fuel cell propulsion systems, but also on internal combustion engines.

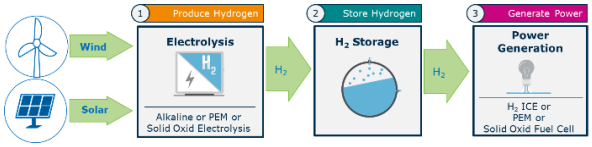


Figure 2: Renewable Energy transformation chain

The usage of hydrogen as energy carrier for internal combustion engines dates back to 1860 and therefore to the early developments of Internal Combustion Engines (ICEs) [ii]. Between 1999 and 2009, several hydrogen passenger car engines were developed [iii,iv] and the City of Berlin, for instance, operated 14 hydrogen internal combustion engine powered buses during the 2000s [v].

All these concepts were not pursued further after their initial presentation. The main reasons were lack of fueling infrastructure, moderate power levels due to backfire and moderate efficiency levels mainly due to high wall heat losses with hydrogen combustion [vi]. However, the introduction of challenging CO_2 reduction targets for heavy-duty vehicles in the European Union and the potential acceptance as zero-emission heavy-duty vehicles [vii] have led to a resurgence in the interest in hydrogen combustion engine technology for different applications.

After MAN presented their H4576LF engine as new member of the D38 engine family [viii], DAF also introduced an operating prototype of the new XF vehicle generation with a hydrogen internal combustion engine. These developments clearly address the requirements of On-Road heavy-duty applications.

Even if there is not yet a mandatory CO_2 roadmap for Non-Road Mobile Machinery (NRMM), several manufacturers have already taken first steps and started the development of hydrogen ICEs. For example, JCB has presented a backhoe loader prototype powered by a hydrogen internal combustion engine [ix] and DEUTZ has announced the series production of the TCG 7.8 H_2 engine in 2024 [x].

Toyota, a manufacturer that already has a second-generation fuel-cell passenger car in production, started in the 24-hour race of Fuji with a special Corolla vehicle powered by a hydrogen internal combustion engine. Even if the required safety procedure and the number of refueling stops has led to a significantly lower number of completed race laps compared to the remaining field, the vehicle has successfully completed the 24 hour race distance [xi].

Latest publications in the passenger car field have demonstrated acceptable levels of performance and efficiency reaching up to 24 bar Brake Mean Effective Pressure (BMEP) and 80kW/l with direct injection of hydrogen [xii].

However, performance levels required for high performance applications or efficiency levels required for Dedicated Hybrid Engines (DHEs) have not yet been achieved.

2. Applications for Hydrogen Internal Combustion Engines as CO_2 Free Power Sources

For the conversion of a hydrogen internal combustion engine different target attributes of the application as such as well as the used base engines have to be considered. Table 1 gives an initial overview of the resulting technology approaches. More detailed explanations of the application specific boundaries and solutions is given in the subsequent chapters.

	Mobile Commercial: HD & MD		Light Commercial	Passenger Car
Base engine	**13l (15-16l)** Diesel Engine (swirl based) GIV/GIL cylinder head SOHC or DOHC	**7-8l** Diesel Engine (swirl based) GIL cylinder head SOHC or DOHC	**2-2.5l** Diesel Engine (swirl based) same engine concept as baseline no dedicated H2 base engine	**1.5 - 2l** Gasoline (Tumble Pentroof) Al cylinder head DOHC, 2 VVT
Top 3 Priorities	1. Efficiency 2. Durability (B10: 1.2mkm) 3. Reliability	1. Cost 2. Reliability 3. Efficiency	1. Cost & Modularity (power limitations OK) 2. Reliability 3. Efficiency	1. CO_2 free powertrain 2. Efficiency 3. Performance
Performance Demands	350kW (~27kW/l) 2200Nm (~22bar)	230kW (~30kW/l) 1200Nm (~20bar)	75kW/300Nm (37kW/L) @ low cost & low production impact	105 - 169kW (70 - 80kW/l) 200 - 380Nm (17 - 24bar BMEP)
Powertrain Concept & Electrification	Conventional / 48V	Conventional / 48V with P0 Mild Hybrid	Conventional / 48V with P0 Mild Hybrid	Conventional or dedicated hybrid (high voltage)
H2 Gas Admission & Ignition	LP-DI, SI (mid term) HP-DI, CI (long term)	LP-PFI, SI (mid term) MP-DI, SI (optionally long term)	LP-PFI, SI (mid term) → cost focus, low power	LP DI Spark ignited
Mixture Formation Combustion Concept	FL: Lean burn PL: Ultra lean burn	←	←	Part load ultra lean burn plus cooled EGR Full load Lambda=1 with water injection / EGR
EGR	HP EGR	←	←	LP EGR
H2 Charging concept	1 or 2-stage TC pref. VGT @ HP stage	←	←	Single stage, SC-TC (2 stage compressor); WG and VTG
H2 Aftertreatment System Euro VII / US Ultra Low NOx	Oxi Cat Va-SCR (1 or 2 stage)	←	←	TWC plus passive SCR
Challenges / Risks	- DI: Mixture formation vs NOx - Transient performance vs NOx - High altitude reserve (1 stage TC) - Combustion irregularity deterioration (durability)	- PFI: pre-igniton / backfire + deterioration - Transient performance vs NOx - High altitude reserve (1 stage TC)	←	

Table 1: Application overview of hydrogen internal combustion engines

3. Hydrogen as Fuel for Internal Combustion Engines

For a part load point, Figure *3* shows the generic dependency of raw Nitrogen Oxide (NO_x) emissions, Brake Thermal Efficiency (BTE), knock behavior and combustion stability vs. charge dilution rate for two different dilution concepts. Solid lines represent dilution with pure air (i.e., increase of excess air ratio: λ), while dashed lines represent dilution by external residual gas in an otherwise stoichiometric combustion concept. For the pure air dilution case, the maximum raw NO_x emissions are reached at λ = 1.2–1.3, while for the λ=1 + external Exhaust Gas Recirculation (EGR) case, they occur at zero external EGR rate as expected.

Mixture formation quality, engine load, combustion timing, and charging rate impact the characteristics of NO_x emissions, especially in the area with high excess air ratio. Almost NO_x-free combustion is reached between an excess air ratio (λ) of 2.0 to 2.8, depending on given boundaries. Alternatively, a stoichiometric combustion with approximately 30% EGR (dilution rate of ≈1.4) can lead to almost NO_x-free combustion. Very high dilution rates can lead to good efficiency. Typically, higher dilution

rates can be achieved with the pure lean combustion concept compared to the λ=1 + external EGR approach. In terms of knock mitigation, lean dilution as well as dilution by EGR can be used. The lower dilution rate requirement for knock mitigation via EGR can be advantageous at high loads in order to limit boost pressure requirements compared to the pure lean combustion approach. Combustion stability is not an issue (in Figure *3*) at high dilution rates neither with air nor with EGR.

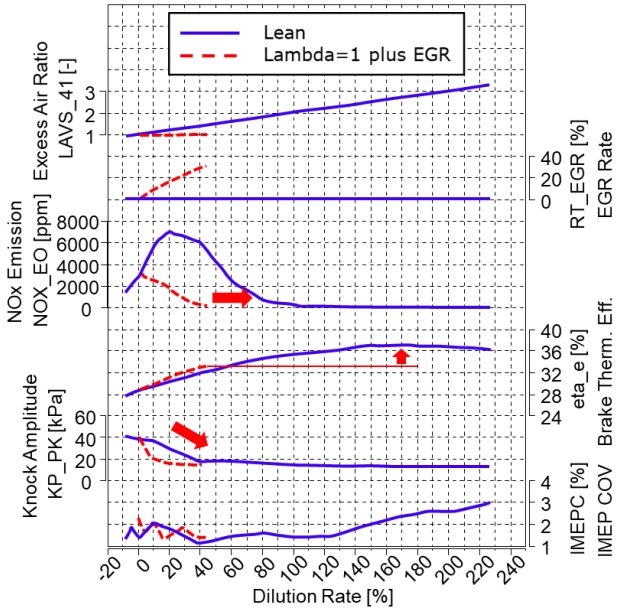


Figure 3: Hydrogen ICE NO_x characteristics, efficiency, knock tendency & combustion stability; lean vs. stoichiometric & EGR

4. Mixture Formation and Combustion System Concepts

Next to the possibility to apply homogeneous mixture with spark ignition also aided compression ignition is possible. Compression ignition can be initiated by a liquid ignition promoter or a local carbon neutral ignition source. Figure 4 gives an initial overview of these possible combustion concepts while in the subsequent chapters dedicated solutions will be presented for commercial vehicles, light duty vehicles and passenger car applications.

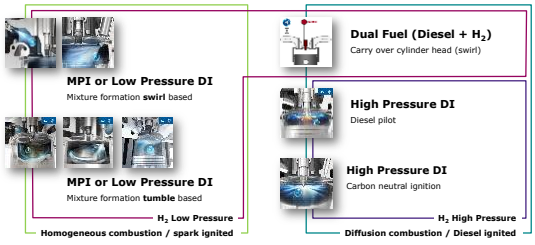


Figure 4: Hydrogen combustion concepts

5. Commercial HD and MD Application

For heavy commercial vehicles, the hydrogen combustion engine is currently favored over the fuel cell due to its more mature basic technology, the established production processes, and the resulting lower costs [xiii] in short and medium term. To utilize all these benefits, the main engine components and powertrain configuration are carried over from the parent Diesel, which causes particular development challenges.

5.1 Combustion Concepts for Commercial Applications

5.1.1 MPI, spark ignited

Multi Point Injection (MPI) represents the most cost-effective solution. In practice, the good mixture formation and hence low raw NOx emissions partly compensate the disadvantage of higher boost pressure demand.



Figure 5: Hydrogen multi point injection

5.1.2 LP-DI, spark ignited

DI mitigates the risk of backfire & utilizes potential for high BMEP due to the high mixture calorific value. This potential can only be utilized when ensuring a proper mixture formation. The Low-Pressure Direct Injection (LP-DI) concept is in the main focus of current commercial engine hydrogen research and development projects.



Figure 6: Hydrogen low pressure direct injection

5.1.3 HP-DI, ignition promoter



Figure 7: Hydrogen high pressure direct injection

Non-premixed (diffusion) combustion of hydrogen offers significant benefits compared to Spark Ignition (SI) concepts (no knocking, high compression ratio, no strong trade-off between excess air ratio and NOx emission, Diesel-like efficiency). As ignition enabler, either a glow plug, a spark plug, or a liquid ignition promoter can be foreseen. The high injection pressure (≥250bar) is a significant disadvantage. AVL is currently preparing a 13-liter class engine demonstrator considering hydrogen High Pressure Direct Injection (HP-DI).

5.2 Current Development Status of the AVL Hydrogen Engine



Figure 8: The AVL Hydrogen Engine

Figure 8 shows the AVL Hydrogen Engine, a 12.8l heavy duty technology demonstrator. The current state of development with external mixture formation is shown in Figure 9. At 1000 rpm, 2200 Nm of torque, and between 1600 and 1800 rpm, a power output of slightly below 280 kW could be achieved in the configuration under investigation. The brake thermal efficiency achieved can be seen in the right half of the picture. Peak efficiency is above 42 %. Efficiency is distinctly very flat in the main driving range of a commercial vehicle [xiv].

In the configuration examined, the achievable full load was limited by combustion anomalies (such as backfiring into the intake air system and pre-ignition significantly before ignition timing), which can be caused, for example, by hot residual gas, hot surfaces and particles or residual discharges of the ignition system. The aim of future investigations is to eliminate these anomalies by measures on the ignition system, the mixture formation and the turbo charging system, compare indication in grey in Figure 9 and Figure 10. Another important measure for raising the load range is the use of reliable direct injection valves with the possibility of selectively influencing mixture formation in the combustion chamber (injection jet orientation, injection time, injection pressure).

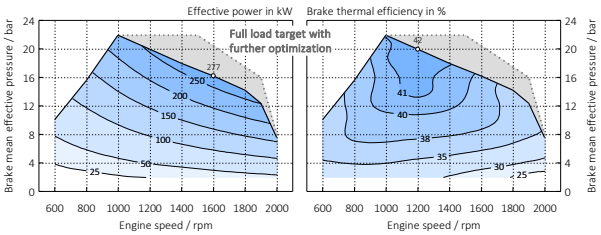


Figure 9: Effective power (left) and brake thermal efficiency (right) in MPI operation

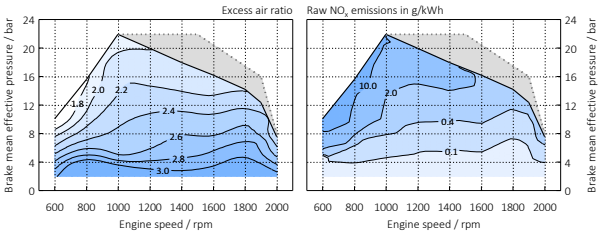


Figure 10: Excess air ratio (left) and raw NO_x emissions (right) in MPI operation

To realize adequate raw NO_x emissions, the engine is operated very lean over the entire operating range. Only in the field of low speeds, excess air ratios below 2 are required to achieve the mean effective pressures shown (see Figure 10 left). The raw NO_x emissions resulting from this operation are shown in Figure 10 (right). The homogenization of the cylinder charge is slightly more difficult with the Diesel engine basis used (swirl instead of tumble, flat cylinder head instead of the pent-roof combustion chamber), which also leads to slightly higher raw NO_x emissions in the very lean range ($\lambda > 2.5$) compared to investigations on a passenger car engine [xv].

In any case, a modified turbocharging system and direct injection (with better cylinder filling) can still achieve significant improvements in raw NO_x emissions.

Figure 8 shows an initial comparison of NO_x emissions for MPI and LP-DI at constant load over excess air ratio. Particularly at lean operation very low NO_x values are realized due to the good homogenization with external mixture formation. The aim is now to be able to achieve these low values with internal mixture formation as well. To achieve this, improvements must be made in mixture formation in particular, i.e. through

optimized injector nozzle geometry and orientation in interaction with the charge motion. The positioning of the DI valve in the combustion chamber also plays an important role. When using a Diesel base cylinder head, however, the freedoms are limited; these could only be fully exploited by redesigning the cylinder head.

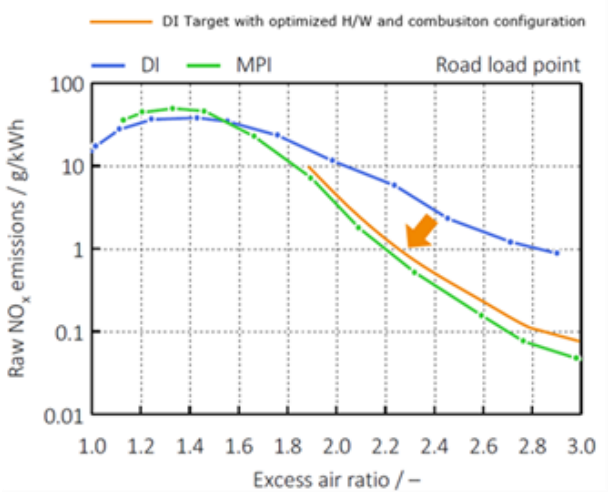


Figure 11: Raw NO_x emissions as a function of excess air ratio at constant load point (road load point, 1200 rpm, 800 Nm)

6. Next Development Steps of the AVL Hydrogen Engine

A further extension of the full load curve requires particular measures on engine and ignition system. First of all, ignition coils, tailored for the demands of a hydrogen engine, will avoid residual loads causing discharges during the intake stroke. Especially for the MPI solution this measure eliminates combustion irregularities in partial load.

To ensure stable combustion at high BMEP (22 bar), late pre-ignition will be avoided mainly by cooling optimization. For this purpose, the spark plug sleeve design was improved and a fire deck machining, enabled by the lower cylinder pressures compared to Diesel, was done. In combination with AVL Top-Down Cooling and a spark plug with low heat value and increased thread length, the component temperatures around the fire deck can be further reduced. In order to avoid spontaneous pre-ignition, potentially caused by hot residual gases and particulates, the gas exchange cycle was optimized by use of a new turbocharger layout.

For direct injection new injector samples from Bosch will be used. Up to 30 bar injection pressure shall ensure proper mixture formation at full load conditions. Still slightly higher raw NO_x emissions compared to MPI are expected, however the lower the NO_x on DI becomes, the more the thermodynamic benefit of higher volumetric efficiency can be utilized, either to increase load or high-altitude margin. As DI mitigates the risk of backfire over long useful life it is of special interest for heavy duty applications. A new approach for controlling engine torque was chosen on the AVL H_2 Rapid Prototype Engine Management System (RPEMS) in order to improve the transient behavior, especially during MPI operation.

7. Light Duty Engines

In the segment of Light Commercial Vehicles (LCV), namely the category N1/III-certified LCVs with a total mass of <3.5t, the predominant engine in the European market is a Diesel engine with a swept volume ranging from 2.0 to 2.2l.

It shares a common base with engines also used for powering heavier passenger cars and Sport Utility Vehicles (SUVs) and is adapted in view of calibration and some external components to cope with the diverging usage-profiles and consequent durability requirements of the LCV.

The typical vehicles in this category serve different end-customers with a huge variety of usage profiles and resulting application requirements. Power ratings vary between around 75 kW up to approximately 140 kW featuring single and two stage boosting systems.

Converting such a 2l-class LCV engine to H_2 combustion will enable potential applications requesting CO_2-neutral propulsion and operating in an environment offering the required refueling infrastructure, e.g., larger local delivery service fleets in city proximity. Moreover, the usability and lifetime of the production facilities of the Diesel base engine can be extended.

Therefore, the focus was to investigate a cost-effective approach, which allows the use of the base engine with minimal changes. This led to applying an MPI combustion system maintaining the (low- to medium-) swirl intake ports which are a common standard in this engine class and, thus, carrying over the main concept features developed for the larger medium-duty H_2-applications – see also Figure 4 and below.

Focusing on the described target niche for this application and the resulting technology approach, it is accepted that the highest levels of specific power output achieved with the current diesel engine shall not be targeted for the H_2-conversion. An engine power of 75 kW and a maximum torque of 300 Nm was targeted for by means of 1-D gas exchange simulation showing the potential of maintaining single stage turbocharging. The simplification of the EGR system from the typically used combined Low- and High-Pressure (LP+HP) EGR system to only cooled HP-EGR contributes to the focus of cost efficiency.

Figure 12 provides an overview on achievable full load performance and raw emission level over the engine map. At full load operation, a sufficiently high excess air ratio can be achieved at lower engine speeds to safeguard NO_x emissions that can be handled by the aftertreatment system carried over from the Diesel engine. At higher speeds, increased EGR rates keep the dilution on a level that enables excellent NO_x performance.

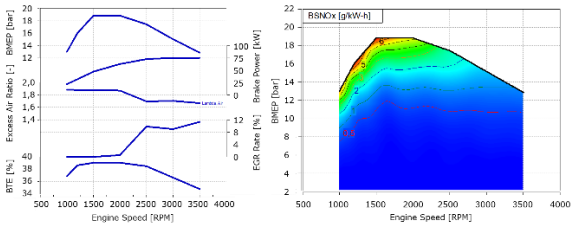


Figure 12: LCV H_2-ICE: Main Parameters Full Load Characteristic and Full Map NO_x Performance

Focusing on a modular solution that considers boundaries of existing production lines, the H_2 engine with port fuel injection can be an attractive option for the LCV segment, combining environmental aspects as well as customer demand on a competitive cost level.

8. Passenger Car Engines

8.1 Combustion Concepts for Passenger Car Applications

The LP-DI concept is in the main focus of current passenger car hydrogen research and development projects due to its favorable tank utilization compared to high pressure injection.



Figure 13: Direct injection hydrogen engine for passenger cars

Benefiting from the strongly increasing interest generated in the last few years for the heavy-duty applications, the H_2-ICE in the passenger car field also started to regain growing interest. Despite recent achievements of performance levels of up to ~24 bar BMEP and ~80 kW/l [xvi], performance levels necessary for high performance applications and efficiency levels required for dedicated hybrid engines have not yet been achieved. Development directions for a potential use of the H_2-ICE in passenger car applications, thus, need to be on the one hand targeted towards higher performance levels for somewhat niche applications in the high-power segments, and on the other hand – as a main driver – efforts need to be focused on increasing efficiency levels for use in hybrid powertrains.

With hydrogen as fuel, several ICE combustion concepts are possible due to the excellent and unique dilution tolerance of hydrogen combustion, Figure 14. Pure lean operation without NO_x-aftertreatment requires excess air ratio values of approx. λ≥2.5 to achieve tailpipe NO_x emissions suitable for passenger car applications conforming to the anticipated EU7 emission standards. This leads to very high boost pressure requirements and subsequently base engines that are needed to be resilient to high Peak Firing Pressure (PFP). Currently most gasoline base engines cannot fulfil this requirement. Additionally, a highly capable and costly turbo machinery (i.e., 2-stage compressor concepts) is needed. It has to provide both sufficient air mass flow and boost pressure at low exhaust gas enthalpy levels. Alternatively, considerable restrictions in engine output capability resulting in very moderate torque and power levels need to be accepted (Figure 14, box I). A relief of requirements for boost pressure can be achieved by combining dilution with both air and external EGR (Figure 14, box II). Pure stoichiometric operation without a combustion moderator (EGR and/or water injection) will lead to irregular combustion (Figure 14, box III). A combination of stoichiometric operation and combustion moderator (EGR and/or water injection) can be a viable option especially for applications with higher power requirements (Figure 14, box IV).

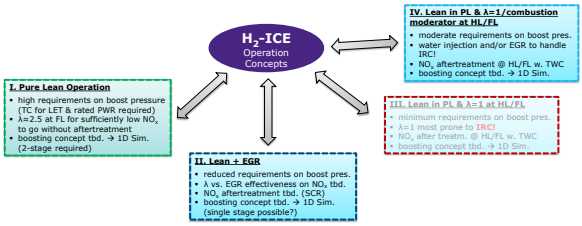


Figure 14: Combustion concepts for hydrogen passenger car engines

For a typical passenger car application, these basic options can lead to a beneficial combination of operation modes for different areas of the engine map. At lower engine loads (up to approximately 10-12 bar BMEP where excess air ratio (λ) drops below 2.5), pure lean operation or a combination of lean and EGR leads to excellent efficiency. At higher loads, the combination of λ=1 and water injection allow stable operation with very low tailpipe NO_x emissions similar to a standard gasoline λ=1 engine [xvi]. A λ-jump-function to

switch between lean and stoichiometric operation, without loss of efficiency, as developed by AVL [xvii] will be required.

In a simulation study, AVL investigated these two aspects of hydrogen engines to achieve highest performance and efficiency levels. The simulation was aligned with previously performed measurements and experiences.

Figure 15 shows the simulation results of achievable efficiency levels for a 2l direct injection H_2 engine at its maximum efficiency point in the map. The simulation also considers measured effects and dependencies of the hydrogen combustion. Highest efficiency can be achieved at excess air ratio values between $1.75 \leq \lambda \leq 2.5$ in pure lean operation. In combination with cooled external EGR, best possible efficiency can already be reached at an even lower excess air ratio. Compression ratios and EGR rates similar to those of the latest gasoline dedicated hybrid engines have to be used. These high excess air ratio values and EGR rates require very high boost pressure levels. In this case, these boost pressure levels were achieved with the help of a highly capable Series Compressor (SC) Variable Turbine Geometry (VTG) turbo charger – a two stage compressor with interstage cooling between the compressors, that is coupled to a single stage VTG [xviii].

To achieve engine-out NO_x levels low enough so that a NO_x aftertreatment is not required (assumed achievable at 0.1 g/kWh raw NO_x as a target value), an excess air ratio of at least $\lambda=2.5$ is required in the pure lean case. Highest efficiency of around 42% can be kept up to these lean excess air ratio values. By combining lean operation with external EGR, an excess air ratio of approximately $\lambda \approx 1.7$ is required to achieve lowest engine-out NO_x. Efficiency levels are only slightly lower compared to the pure lean case.

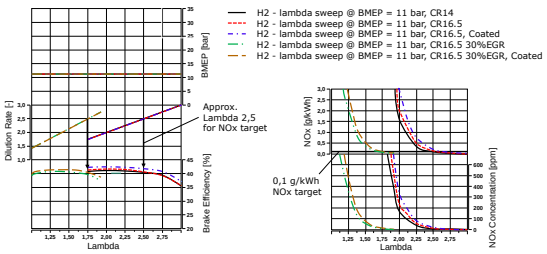


Figure 15: Efficiency of H_2 DI engine at 2500 rpm/11 bar BMEP, simulation result

A further important aspect of future hydrogen engines are the achievable torque and power levels. Figure 16 shows simulation results for full load curves that can be achieved with various technologies. The baseline for these investigations was a high-performance gasoline DI engine equipped with a large single stage turbocharger, solid line in Figure 16. Very high excess air ratio of $\lambda=2$ only allows for limited performance, dashed line. Moderate excess air ratios of $\lambda \approx 1.5$ already show potential reasonable performance levels comparable to those shown in previous publications [xvi] at the expense of high NO_x emissions, dash-dotted line. A combination of operation at stoichiometric conditions and using water injection as combustion moderator to avoid irregular combustion, allows for reaching highest performance levels also with hydrogen – especially when high peak cylinder pressures are protected by the engine concept.

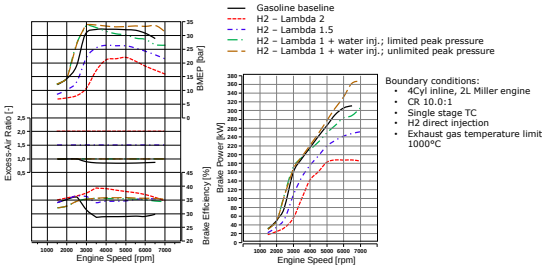


Figure 16: Full load of H_2 DI engine achievable with different technologies, simulation result

Water injection has proven to be an efficient measure to cope with combustion irregularities in high performance engines. Ideally, the water used for water injection can be condensed from the exhaust gas, Figure 17. In gasoline engines, this requires large condensation devices. In hydrogen engines, with their high-water content in the exhaust gas – especially when additional water injection is used – the condensation of water from the exhaust gas is easier. Specific heat exchanger design can help minimize the required cooling power.

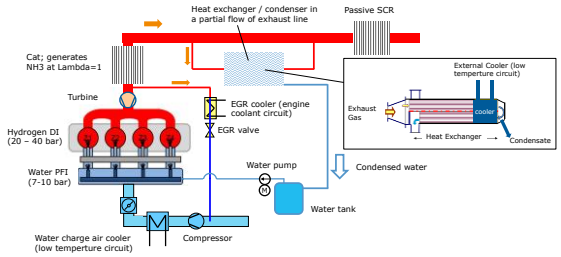


Figure 17: Exhaust system of a H_2 DI engine with a water condenser and a passive EGR system

As hydrogen engines emit NO_x, a specific aftertreatment system is required. A close coupled three-way catalyst can convert NO_x in $\lambda=1$ operation (actually, in slightly rich condition), but creates ammonia (NH_3) as secondary emission. A passive Selective Catalytic Reduction (SCR) system, like the one planned for future EU7 gasoline applications located underbody can convert NH_3 and residual NO_x [xix].

9. Exhaust Aftertreatment Systems for Hydrogen Engines

Independent of application segment, the main pollutant component for H_2-ICE exhaust gas is nitrogen oxides. The operation strategy of the hydrogen engine determines how much raw NO_x emission is to be expected and which NO_x aftertreatment system needs to be considered. The absence of carbon in the fuel does not necessarily mean total absence of carbon-based emissions – traces of CO, CO_2, HC and particulates are to be expected from ambient air, the lubricant as well as urea injection in case a SCR catalyst is used. Depending on (also future) emission legislation, specific aftertreatment systems may need to be considered despite their small amounts. Additionally, secondary emissions, such as NH_3 & N_2O – at barely detectable levels in the raw exhaust gas – are being created in the aftertreatment system itself and might need to be assessed separately too.

Although aftertreatment components & systems from applications using conventional fuels, such as Three-Way-Catalyst (TWC), active & passive SCR and NO_x adsorbers, are likely to work for hydrogen engine exhaust gas, they would most probably need to be not only specifically tailored towards hydrogen exhaust gas components and temperatures – but also towards sufficient long-term reliability. It is, thus, expected that material composition, precious metal loading, etc., will need to be adapted specifically for different H_2-ICE applications.

9.1 Exhaust Aftertreatment System for Heavy-Duty and LCV

To check the feasibility of achieving current and future legislation limits for tailpipe emissions, transient simulations were performed with AVL CRUISE™ M simulation software. The Exhaust Aftertreatment System (EAS) layout used was as shown in Figure 18 and comprises of an Oxidation Catalyst (OC) followed by a single-stage SCR catalyst and an Ammonia Slip Catalyst (ASC). urea dosing is controlled with SCR NH_3 storage-based dosing control. The simulation model was calibrated to synthesis gas measurements [xx].

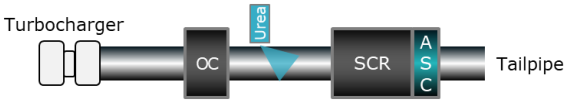


Figure 18: AVL Hydrogen Engine EAS Layout for Euro VI

The raw NO_x level of the hydrogen engine in the cold/hot WHTC is ~6 g/kWh while operating with the minimum excess air ratio limited to ~1.7 for acceptable transient performance and power density using conventional turbocharger technology. The results of the cold and hot WHTC simulations are illustrated in Figure 19.

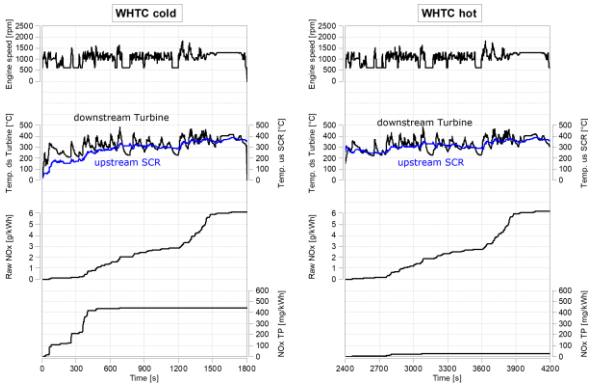


Figure 20: EAS Simulation results in cold/hot WHTC

The results indicate that with a Tail-Pipe (TP) NO_x emission level ~450 mg/kWh in the cold WHTC and ~30 mg/kWh in the hot WHTC, <100 mg/kWh tailpipe NO_x is feasible in the combined WHTC. This is well below the Euro VI limit of 460 mg/kWh, considering sufficient margin to deal with production tolerances.

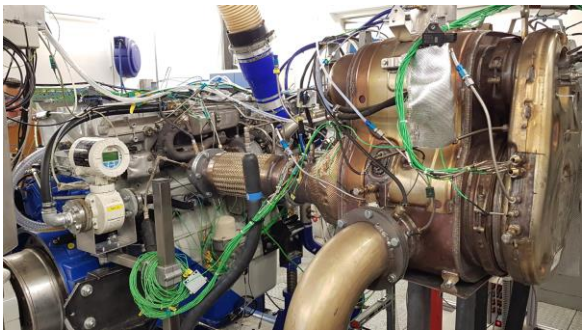


Figure 21: AVL Hydrogen Engine testbed setup @ TU Graz with Euro VI EAS installed

These initial simulation results indicate the possibility of going to even lower excess air ratio limitations and thereby higher raw NO_x emission levels, while not exceeding tailpipe NO_x targets. The real-world optimization is part of the ongoing testbed investigation, as depicted in Figure 21. The upfront performed simulation work ensures effective testbed development.

9.2 Exhaust Aftertreatment Solutions for Passenger Cars

With its theoretical capabilities for excessive lean burn, an H_2-ICE could be operated lean enough ($\lambda \geq 2.5$ also in the local scales), so that negligible NO_x is formed and a specific aftertreatment is not necessary. Practical restrictions such as requirement for highly capable and costly boosting systems, strongly PFP resistant base engine concepts (especially an issue with gasoline engine-

based H_2-ICE concepts compared to their Diesel or CNG-based siblings in the heavy-duty field) and disadvantages in transient operation limit such an approach.

Stoichiometric hydrogen combustion needs a combustion moderator that helps mitigate irregular combustion tendency. Such moderators may be either external EGR or water injection, or both since they support raw NO_x emission reduction. The remaining NO_x can be treated by a conventional close coupled three-way catalyst – the required reduction agent is unburnt hydrogen from slightly rich operation. The downside of such a concept is the generation of ammonia (NH_3) directly in the TWC as a secondary pollutant, that needs to be taken care of. A passive (without active urea dosing) SCR system, similar to the ones targeted for use for future EU7 legislation, located underbody, downstream the TWC, can be an option to convert the remaining NO_x and NH_3 to nitrogen and water, Figure 22 top image.

In case of lean H_2-ICE operation conditions, within the NO_x formation window at excess air ratios of approximately $1.7<\lambda<2.5$ or richer with additional external EGR, a conventional active (with active urea dosing) SCR system can be used to convert nitrogen oxide emissions, Figure 22, bottom image.

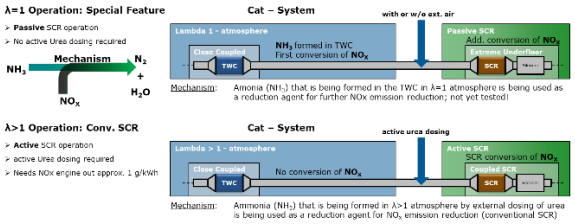


Figure 22: Passenger car H_2 DI engine aftertreatment system concepts

10. Summary and Conclusion

The prerequisite for sustainable use of hydrogen in the transport sector is its production based on renewable energy sources. This requires a global approach to bridge the locations of high demand and the promising areas for harvesting renewable energy with lowest losses. This can be achieved by using hydrogen as the simplest form of a chemical, long-distance carrier for renewable energy.

Whilst the initial focus of the hydrogen combustion engines was both, on- and offroad commercial applications the interest also increased on classical passenger car applications.

Different combustion systems are used for commercial and for passenger car applications. For commercial and light duty engines often Diesel derived swirl-based systems serve as basis. For light commercial engines MPI injection is preferred for cost reasons. Heavy duty applications also consider direct injection. Future applications will also use non-premixed combustion systems in order to utilize the maximum efficiency potential. Passenger car applications use gasoline derived tumble systems.

AVL developed a 12,8l hydrogen engine capable to run on both MPI as well as LP-DI injection systems. Peak efficiency of more than 42% and BMEP levels up to 22,5 bar were achieved so far.

A good mixture homogeneity is a prerequisite for all homogeneous combustion systems.

Simulations show that efficiency levels >42% and performance levels of up to >150kW/l can be achieved on hydrogen engines derived from their passenger car siblings. A viable option is the combination of lean operation at part load and stoichiometric operation with EGR / water injection at high load. The water needed for water injection can be condensed from exhaust gas.

A reasonable aftertreatment system uses an oxidation or three-way catalyst plus a passive or active SCR system.

11. Acknowledgement

The authors of this paper would like to thank all external partners and supporters, but especially the employees of the Institute of Thermodynamics and Sustainable Propulsion Systems at the Graz University of Technology, Robert Bosch GmbH, Garret Motion and Ventrex Automotive GmbH as well as all colleagues at AVL List GmbH who contributed to this publication.

12. References

[i] G. Fraidl et. al.: "Passenger Car Powertrains and Future Energy Scenarios: From Technical Facts towards Political Reality", 42nd International Vienna Motor Symposium, 2021.

[ii] Émile Bourdelin: *La machine Lenoir*. In: Charles Yriarte (Hrsg.) Le Monde illustrè (16. Juni 1860), S. 394–395.

[iii] BMW press release: Das Wasserstoffzeitalter hat begonnen. BMW 750HL: Erstes Wasserstoff-Serienauto der Welt [The hydrogen-age has begun. BMW 750HL: Worlds first hydrogen-production car], https://bmw-grouparchiv.de/research/detail/index.xhtml?id=3418645, Download: 04.01.2021.

[iv] MAZDA press release: "Environmental Technology – Hydrogen vehicle", https://www.mazda.com/en/innovation/technology/env/hre, Download: 04.01.2021.

[v] MAN SE press release: "Erste Wasserstoffbusse für Berlin von MAN" [First Hydrogen-Busses for City of Berlin], https://www.pressebox.de/inaktiv/man-se/Erste-Wasserstoffbusse-fuer-Berlin-von-MAN/boxid/64521, Download: 04.01.2022.

[vi] Eichlseder H., Leitner D., Skalla Ch.: „Concepts, Potentials and Challenges for S.I.-Engines with Hydrogen and Hydrogen-enriched Gases", SAE-Symposium, Torino 2009.

[vii] Commission Regulation (EU) 2019/1242 of the European Parliament and of the Council of 20 June 2019 setting CO_2 emission performance standards for new heavy-duty vehicles and amending Regulations (EC) No 595/2009 and (EU) 2018/956 of the European Parliament and of the Council and Council Directive 96/53/EC.

[viii] Walter L., Sommermann A., Hyna D., Malischewski T., Leistner M., Hinrichsen F., Wöhner P., Schmitt J., McMackin M.: „The H_2 Combustion Engine – the forerunner of a zero emission future", 42nd Int. Vienna Motorsymposium 2021.

[ix] Article about JCB's 4.8L H_2-engine, https://www.dieselprogress.com/news/jcb-develops-hydrogen-fuelled-engine/8012602.article, Download: 05.10.2021.

[x] Press release of the market introduction of the TCG 7.8 H_2-engine, https://www.deutz.com/media/pressemitteilungen/der-wasserstoffmotor-von-deutz-ist-reif-fuer-den-markt, Download: 05.10.2021.

[xi] TOYOTA press release about the H_2-engine used in the 24-hours-race of Fuji in 2021, https://global.toyota/en/newsroom/corporate/36074055.html, Download: 05.10.2021.

[xii] Pauer, T.; Weller, H.; Schünemann, E.; Eichlseder, H.; Grabner, P.; Schaffer, K.: „H_2 ICE for Future Passenger Cars and Light Commercial Vehicles", 41. Int. Vienna Motorsymposium 2020.

[xiii] Mayr, K.; et al.: „Systemvergleich zwischen Wasserstoffverbrennungsmotor und Brennstoffzelle im schweren Nutzfahrzeug – Eine technische und ökonomische Analyse zweier Antriebskonzepte", E-mobil BW – Landesagentur für neue Mobilitätslösungen, 2021.

[xiv] Arnberger A., Grabner P., Eder M., Raser B.: "Hydrogen Combustion Engines for CO_2 neutral Commercial Vehicles", ATZ Heavy Duty 14, 36-41 (2021).

[xv] Seboldt, D., Mansbart, M., Grabner, P., Eichlseder, H.: Wasserstoffmotoren für zukünftige Pkw und leichte Nutzfahrzeuge. MTZ Motortech Z 82, 46–51 (2021). https://doi.org/10.1007/s35146-020-0614-0.

[xvi] Port injection of water into a DI-Hydrogen engine (SAE: 2015-01-0861).

[xvii] AVL patent application WO 2005/088099.

[xviii] Bontemps, N.; Francois, D.; Sierra, J.C.; Davies, P.; Lazzarini Monaco, L.; Fuerhapter, A.: "SC-VNTTM a route toward high efficiency for Gasoline Engines", 25. Supercharging Conference, Dresden 2020.

[xx] Dreisbach, R., Eichlseder, H., Arnberger, A., Zukancic, A., Wieser, M., Kunder, N., Plettenberg, M., Raser, B.: „The Heavy-Duty Hydrogen Engine and its Realization until 2025", 42. Int. Vienna Motorsymposium 2021.

Hydrogen internal combustion engine lubrication challenges and engine oil requirements

N. Obrecht[1], B. Griffaton[1]

[1]: TotalEnergies, Centre de recherche de Solaize 69360, France

Abstract: The transportation industry has set important objectives to reduce green-house gas emissions. Among alternative energy sources, hydrogen produced from low carbon pathways has been intensively studied within the industry and supported by public policies. Although fuel cell powertrains are concentrating most of the attention, hydrogen fueled internal combustion engines can represent an interesting and complementary solution to power transportation equipment and accelerate the transition towards hydrogen mobility.
On the one hand, hydrogen combustion properties offer the possibility to adjust internal combustion performance and meet technical and regulatory requirements expected by the market. On the other hand, the same combustion properties are raising important questions on the lubrication system requirements to ensure a reliable and efficient operation of hydrogen fueled internal combustion engines in the field.
This paper investigates the challenges associated with hydrogen internal combustion engine lubricant with regards to specific calibration features and application targets. Specific focus is given on the impact of hydrogen combustion on engine lubricant performance as well as impact of the lubricant features on engine performance. Experimental tests results are discussed to emphasize the importance of engine oil requirements for hydrogen internal combustion engines.

Keywords: Hydrogen engine, oil, particle emissions, pre-ignition, NOx

1. Introduction

The transportation sector which accounted for 27% of global CO_2 emissions in 2019 with 8.5 $GtCO_2$ is working on massively reducing its contribution to Global Warming [1]. Public policies and regulations in Europe have set CO_2 emission targets for road transportation. Passenger cars are expected to reduce their CO_2 emissions by 37.5% by 2030 compared to a 2021 reference [2], whereas heavy-duty trucks target 30% reduction by 2030 compared to a 2019-2020 reference [3]. The shift from fossil fuel energy to a low carbon emission paradigm brings many constrains to the transportation industry and especially in the heavy-duty vehicle sector that explores different powertrain technologies. Among the various solutions meeting regulatory constraints, battery electric vehicles (BEV) and fuel cell vehicles (FCEV) have been strongly studied and discussed in the past years [4]. However, hydrogen internal combustion engines have been raising more and more interest recently, stimulated by benefits in terms of technology maturity, shorter time-to-market, and competitive total cost of ownership [5], [6].

Manufacturers and research groups are focusing on key challenges related to hydrogen combustion engines such as efficiency, engine performance, emissions control, or abnormal combustion [6]. Engine lubricant plays a major role in reliability and efficiency of modern internal combustion engines, but it is also likely responsible from carbon-based emissions at the exhaust of these engines such as particles and CO_2 as reported by Miller et al. [7]. Furthermore, engine oil has been suggested as a potential source of abnormal combustion in hydrogen engines by previous studies [6], [8].

The role of engine oil on particle emissions has been suggested by several research publications that observed oil contributions to particle number (PN) in the nuclei mode with particle diameters around 10nmn [9], [14]. Reduction of oil consumption through engine hardware modifications has demonstrated significant reductions in PN measurements [15]. Driving cycle profiles also impact particle emissions, and transient cycles with high dynamics such as WHTC are more severe on that criterion [9], [12], [16], [17], [18]. Multiple studies have shown that during idling conditions, oil accumulates in the piston top land and then burns in the following transient phases at high load with higher cylinder temperature, leading to particle emissions peaks [19], [20]. The role of engine lubricant parameters on particle emissions at the exhaust has been studied by many research papers. Although, engine oil viscosity does not seem to have a significant impact on particle emissions [18], engine oil composition has demonstrated a stronger sensitivity. Several studies have reported a decrease in particle numbers while reducing the ash content of the lubricant [10], [11], [12], [21], [22]. Likewise, viscosity modifiers and base oil compositions demonstrated a significant impact on these emissions as well [11], [23].

Additionally, the phenomenon of preignition in gasoline direct injection spark ignited engines, often called “Low Speed Pre-Ignition” (LSPI), has been thoroughly studied, including the role of engine lubricant. Calcium from detergent additives in the lubricating oil has clearly been identified as a promoter of pre-ignition and several studies observed a decrease in pre-ignition frequency when reducing calcium content [24], [25], [26]. Additionally, base oil composition also showed a significant impact on pre-ignition occurrence in gasoline fuelled engines [24], [27]. whereas viscosity modifier chemistry didn’t seem to influence that phenomenon [24].

This paper discusses the possibility for engine lubricants to alleviate some of the challenges that hydrogen fuelled engines are facing with regards to CO_2 emissions, particle emissions or pre-ignition. Previous studies exploring the impact of engine oil parameters on these performances were generated on engines fuelled with gasoline, Diesel or natural gas, but no study has been done on hydrogen fuelled engine to our knowledge. Additionally, observations on oil degradation due to the presence of hydrogen or hydrogen combustion products are reported to explore potential lubricant requirements for hydrogen fuelled engines.

2. Impact of lubricant formulation on hydrogen engine performances

2.1 Engine test setup

On-road heavy-duty vehicles and off-road machinery were identified at an early stage as relevant applications for hydrogen combustion engines. The investigations described hereafter were performed on a 6-cylinders medium duty engine representative of those use cases. A natural gas spark ignited engine has been retrofitted to run on hydrogen fuel. Some parts such as new camshafts or pistons with reduced compression ratio were implemented to fit the requirements of hydrogen combustion. The final engine characteristics are reported in Table 1.
Hydrogen combustion properties allow for engine operation over a wide range of equivalence ratios. Experiments carried out by Das have shown that engine operations with equivalent ratio lower than 0.6 lead to very low NOx emissions [28]. The air management system configuration of the engine used in the present study authorizes ultra-lean mixture at equivalent ratio 0.4 - 0.5 to achieve NOx emissions at engine-out conditions close to the Euro VI emission limits. Advanced Engine calibration allowed for robust transient operations, which was critical for our investigation, especially for particle emissions assessment as commented previously.

Engine type	6 cylinders in line
Displ. Volume	7698 cm3
Bore	110 mm
Stroke	135 mm
Valves per cylinder	4
H_2 injection	Single point injection
Charging system	Dual stage turbocharger
Rated torque	1000Nm @ 1300rpm
Rated power	155kW @ 1600rpm

Table 1: Engine characteristics

The engine was installed in a dedicated dynamic test cell equipped with hydrogen fuel supply and upgraded with appropriate safety equipment (detection, fuel line flushing, ventilation). The engine was coupled with a fast response dynamometer allowing for fast transient cycles such as World Harmonized Transient Cycle (WHTC) to be used in the test procedure. No aftertreatment system was used in this study. The engine crankcase ventilation system (CCV) was modified in this prototype engine and crankcase gas were disconnected from the engine intake manifold to reduce risks of uncontrolled combustion and backfire. Finally, an active system is installed to blow air in the crankcase to keep hydrogen concentration below its explosive limit.

<u>CO_2 and particle emissions measurement</u>

Considering that the CO_2 concentration at the exhaust of a hydrogen combustion engine is significantly lower than that measured while using fossil fuels, the precision of the measuring equipment is paramount to study the influence of lubricant formulations and compare prototype oils. Moreover, given the low concentration levels at the exhaust, the CO_2 concentration of the intake air has a major influence on the result. Consequently, CO_2 concentrations were simultaneously measured at the exhaust and at the intake of the engine using Non-Dispersive Infra-Red sensors (NDIR). Both sensors were carefully calibrated in the concentration range 0 to 5000ppm using certified gas. The difference between the two measurements was reported to quantify the CO_2 emissions related to the combustion/oxidation of the lubricant in the engine.

Particle emissions were measured using an AVL APC+ particle counter commonly used for certification activities. The sampled exhaust gas was conditioned upstream of the Condensation Particle Counter (CPC) through a two-stage dilution process combined with a vaporization phase to remove volatile fractions from the particles and improve measurement

accuracy. This device was selected for its capability to count particles with diameters down to 10nm at 10Hz frequency, to anticipate the future Euro VII emission standard and better account for oil contribution as described previously. Figure 1 provides a description of the engine test setup used in this study.

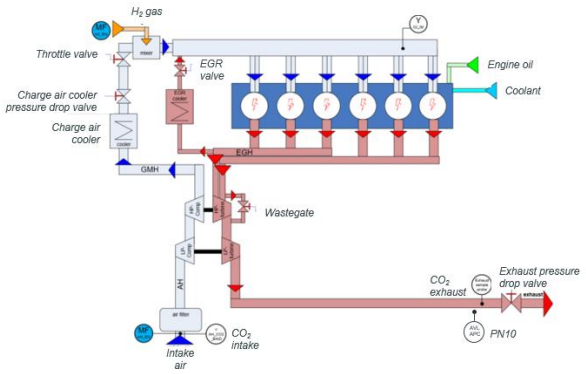


Figure 1: Engine test setup

For each lubricant considered in this campaign, CO_2 and particles emissions were measured during WHTC cycles as well as steady state operating conditions as described in table 2. Due to the complex nature of the oil transport phenomenon into the combustion chamber, the engine test protocol was defined carefully to maximize precision of the results. Each operating point and each WHTC test cycle were repeated at least 6 times to record sufficient data and provide statistical robustness to the results. Oil and coolant temperatures were both controlled at 90°C during the entire study. A reference lubricant (Oil 1) was evaluated at the beginning and at the end of the lubricant campaign to identify any potential drift of the test equipment over time.

Operating point	Engine speed (rpm)	Brake Mean Effective Pressure (bar)
1	1100	5
2	1200	16
3	1600	7
4	2000	10

Table 2: Steady-state operating conditions for emissions measurements

Pre-ignition test protocol

Hydrogen / air mixtures are particularly sensitive to pre-ignition due to their very low minimum ignition energy compared to other fuels [29]. These abnormal combustion events often lead to high cylinder pressure levels that can ultimately result in the destruction of hardware components and engine failure.

In the present study, pre-ignition events are monitored on each cylinder by high-temperature high-sensitivity piezoelectric cylinder pressure sensors installed in each combustion chamber of the six-cylinder engine. Pre-ignition events were detected using two different criteria based on heat release:

- Cycle heat release exceeds 2% after single minimum burn delay time (τ) after ignition timing
- Cycle heat release exceeds 3.5% after double minimum burn delay time (τ) after ignition timing

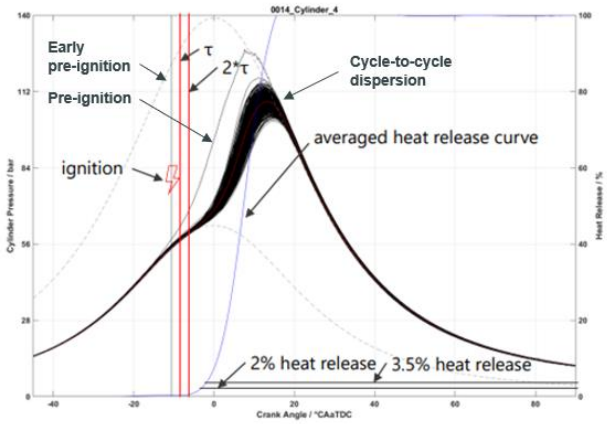


Figure 3: Criteria for pre-ignition events rating

Both criteria are defined empirically and allow to distinguish late pre-ignition events occurring few crank angle degrees before ignition timing (2% - τ criteria), from uncontrolled ignitions occurring earlier in the compression phase (3,5% - 2 τ criteria).

Engine pre-ignition sensitivity was studied on steady state operating points through three different engine stages. For each engine stage, one engine parameter was swept at a time as detailed in table 3. To build a statistical assessment of pre-ignition occurrence, events were recorded for each engine condition on each cylinder and on each steady state points during six segments of 500 engine cycles. Pre-ignition frequency is defined as the average events per 100 cycles (#/100 cycles).

Engine stage	Engine speed (rpm)	BMEP (bar)	Parameter sweep
1	1200	13	ignition timing from -22 to -5 CAD aTDC
2	1400	15	ignition timing from -22 to -10 CAD aTDC
3	1200		BMEP from 5 to 16bar

Table 3: Engine test procedure for pre-ignition investigation

2.2 Engine oil candidates

Based on literature data analysis, six engine oil compositions were proposed for the engine test campaign and summarized in table 4. Considering that viscosity level variation didn't show significant or consistent results on particle emissions or pre-ignition in previous studies, all lubricants in this campaign are formulated around the same viscosity level as illustrated by kinematic viscosity measurements at 100°C (KV100). Oil 1 is an SAE 10W-30 commercially available engine lubricant for medium and heavy-duty applications claiming performance levels ACEA E9 and API CK-4. Oils 2 to 6 are all prototype lubricants derived from reference Oil 1 changing only one parameter. Oil 2 contains only thirty percent of the additive concentration of Oil 1 thereby significantly reducing ash and calcium content. Oil 3 and Oil 4 were designed to explore the impact of alternative viscosity modifiers, whereas Oil 5 and Oil 6 are formulated with alternative base oils compared to reference Oil 1.

Oil candidates	Oil 1	Oil 2	Oil 3	Oil 4	Oil 5	Oil 6
Rel. Additive content	100	30	100	100	100	100
Viscosity modifier	VM-1	VM-1	VM-2	VM-3	VM-1	VM-1
Base oil	BO-1	BO-1	BO-1	BO-1	BO-2	BO-3
KV100 (mm^2/s)	11,6	12,2	11,8	11,9	11,7	11,4
Ash content (%)	1	0,3	1	1	1	1
Ca content (%)	0,251	0,075	0,251	0,251	0,251	0,251

Table 4: candidate oils characteristics

Each lubricant was run in the engine procedures described in the previous section to evaluate its impact on CO_2 emissions, particle emissions and pre-ignition sensitivity. Lubricants were tested in the following sequence: Oil 1 > Oil 2 > Oil 3 > Oil 4 > Oil 5 > Oil 6 > Oil 1. Oil 1 is tested at the beginning and at the end of the campaign to monitor potential drift of the test equipment as described previously. A specific flushing procedure was applied between each lubricant to ensure that one candidate oil was not polluted with the previous candidate in the engine.

2.3 Engine test results

<u>Particle emissions results</u>

Figure 4 shows all the results for specific particle emissions measurements (PN10) on the WHTC cycles for Oil 1 (11 cycles at the beginning of the campaign, 7 cycles at the end of the campaign). These results illustrate the dispersion on the particle measurements, that are likely linked to the stochasticity of the oil transport phenomenon from the lubricating circuit to the combustion chamber. Among all the cycles carried out with Oil 1, cycles #3 and #8 of the first series (at start of the test campaign) were compared. These cycles show similar cumulated PN10 results on their respective WHTC cycles and close to the average value across all cycles ran for Oil 1. However, it is interesting to notice that clear discrepancies are observed on the instantaneous PN10 concentration traces along both WHTC cycles as illustrated on figure 5. Although emission peaks are well phased between the cycles #3 and #8 because they are mainly linked to the cycle speed and load transients, the amplitude of these peaks varies significantly from a cycle to another. These variations tend to show that the quantity of oil droplets transported into the combustion chamber during transient phases is fluctuant due to complex underlying mechanisms.

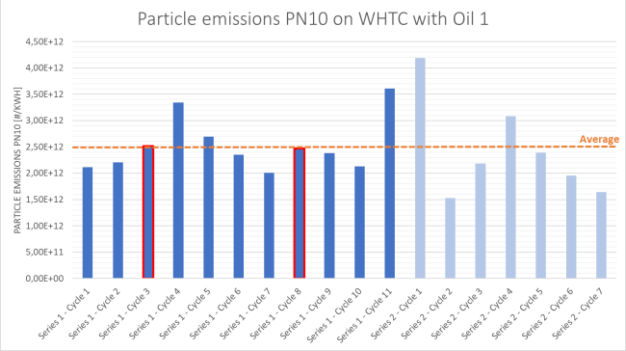


Figure 4: Specific particle emissions (PN10) on all WHTC cycles ran with Oil 1

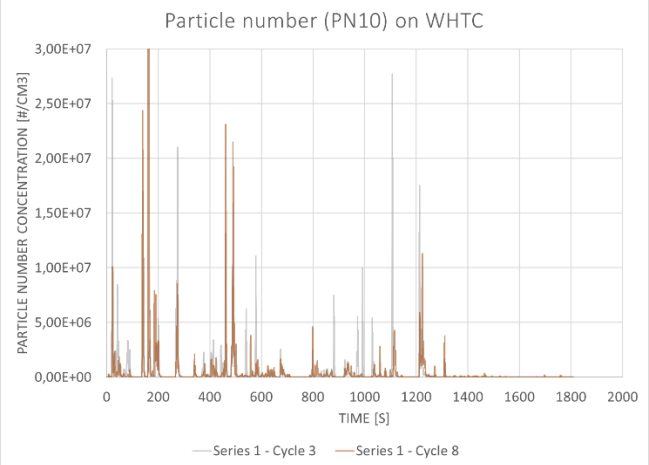


Figure 5: Instantaneous particle concentration on 2 WHTC cycles with Oil 1

It is pointed out that the average PN10 value for all WHTC cycles ran with Oil 1 reaches $2.5x10^{12}$ #/kWh which is significantly higher than the Euro VI limit set

at 6x10^{11} #/kWh. Keeping in mind that Euro VI only accounts for particle diameters above 23nm (PN23), this result shows that engine lubricants strongly contribute to particle emissions at the exhaust of a hydrogen fueled medium duty engine on WHTC cycle. Therefore, it highlights the need for specific lubricants able to mitigate engine-out emissions for these applications.

Figure 6 provides the results of PN10 particle emissions averaged over at least 6 WHTC cycles for each oil. The standard deviation is calculated based on the 2 series of tests for Oil 1.

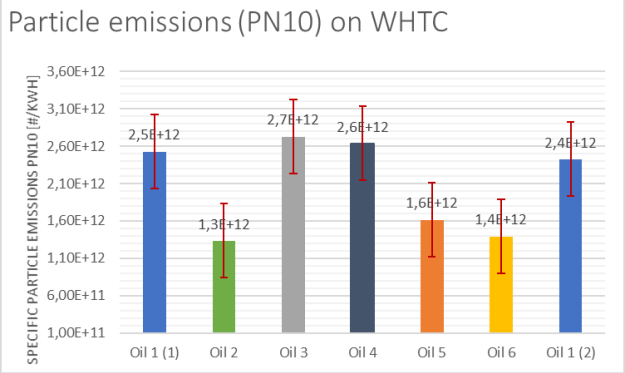


Figure 6: Average specific PN10 emissions on WHTC cycle for each engine oil test

The comparison of the average PN10 values for both tests with Oil 1 are very similar, thereby indicating that the test procedure was stable overtime and that the results are robust. Despite the dispersion of the particle measurements linked to inherent oil transport mechanism, the uncertainty remains manageable thanks to a statistical approach and the repetitions carried out for each oil. Consequently, we can draw clear conclusions on the performance of the different oils tested. Oil 3 and Oil 4 show substantially similar results compared to Oil 1, indicating that the proposed viscosity modifier modifications didn't affect particle emissions. However, Oil 2, Oil 5, and Oil 6 provided significant benefits with PN10 reduction rates around 35 to 45% on the WHTC cycle compared to the average value of Oil 1. Oil 2 results confirm the positive impact of reducing ash content as reported by previous studies but on non-hydrogen engines. Alternatively, base oil selection seems to be an interesting parameter to mitigate particle emissions in these engines.

CO_2 emissions results

Figure 7 shows the specific CO_2 emissions originated from oil consumption on the WHTC cycle by measuring CO_2 concentration at the intake and the exhaust of the engine as described previously.

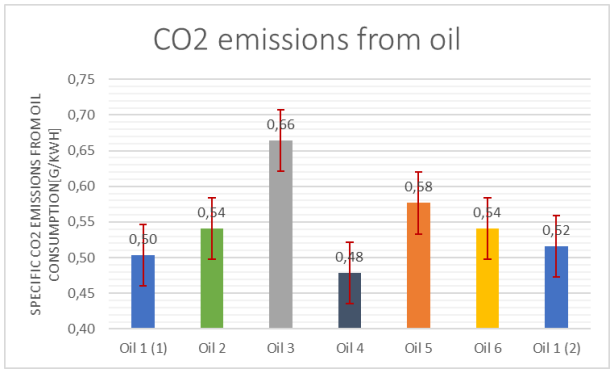


Figure 7: Specific CO_2 emissions from oil consumption, on WHTC cycles

As observed on the particle emission results, CO_2 values for both Oil 1 test series are very similar, confirming the stability of the test procedure. Given the precision of the measurement, Oil 2, Oil 4, Oil 5 and Oil 6 do not show any significant differences in terms of CO_2 emissions compared to Oil 1. Oil 3 has a significant negative impact on CO_2 emissions which increased by approximately 30% compared to Oil 1. It is pointed out that all results reported are below 1gCO_2/kWh.

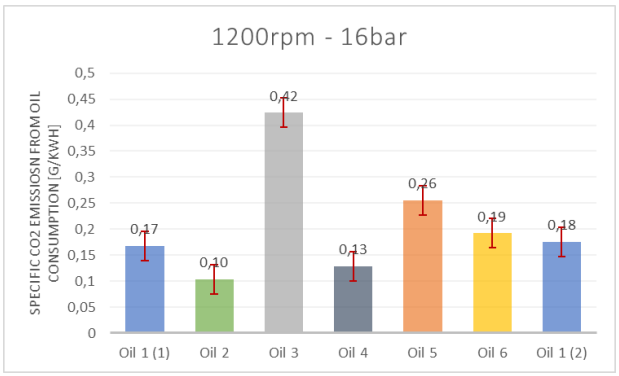


Figure 8a: Specific CO_2 emissions at 1200rpm – 16bar BMEP

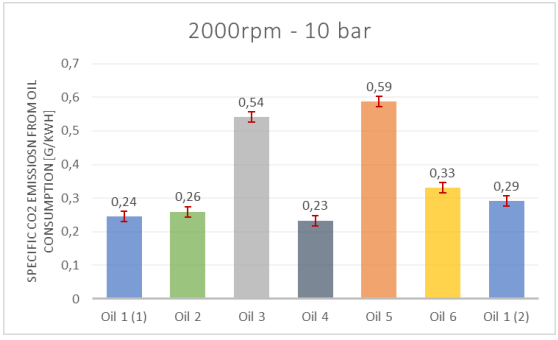


Figure 8b: Specific CO_2 emissions at 2000rpm – 10bar BMEP

Measurements were also performed on 5 different steady state operating points. Figures 8a and 8b illustrate CO_2 emissions result for the operating points

of higher BMEP displaying satisfactory discrimination among lubricants. These results confirm the previous conclusions on WHTC: Oil 3 shows a significant penalty on CO_2 emissions in comparison with Oil 1. Oil 5 also leads to an increase in CO_2 emissions, which varies greatly depending on the operating point. Oil 2, Oil 4 and Oil 6 show small variations in CO_2 emissions compared to Oil 1.

Pre-ignition results

Lubricant induced pre-ignition is a stochastic phenomenon and care should be taken when developing an engine test methodology to quantify the phenomenon. A large quantity of data was generated during the engine test campaign and only a general summary is presented in this paper for clarity reasons. Among the 3 operating points selected, only the point at 1200rpm – 13 bar of PME combined a good distribution of the pre-ignition events and a good repeatability observed on both tests with Oil 1 (figure 9).

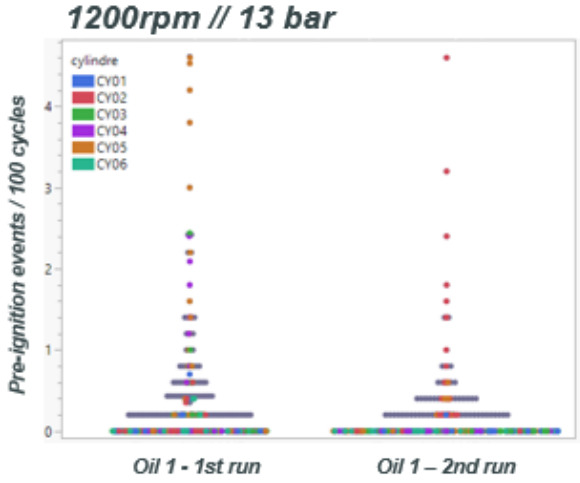


Figure 9: Pre-ignition distribution at 1200rpm – 13bar BMEP

Pre-ignition events are identified by analyzing the cylinder pressures measured on all 6 engine cylinders. Data analysis shows that some cylinders are more sensitive to pre-ignition than others. Figure 10 provides, for the operating point of 1200rpm – 13 bar BMEP, the pre-ignition frequency on each cylinder. A large discrepancy is observed and cylinder 5 generates significantly more pre-ignition events than other cylinders. It appears that the criterion at 3,5% heat release provides a better discrimination among the cylinders. This criterion is used for the rest of the study. Figure 11 presents the cumulative pre-ignition frequency across all 6 cylinders of the engine averaged over the 6 segments of 500 cycles each.

Results on Oil 3 and Oil 6 indicate similar pre-ignition sensitivities compared to Oil 1. Alternative viscosity modifier and base oil used in these prototypes didn't seem to impact pre-ignition phenomenon.

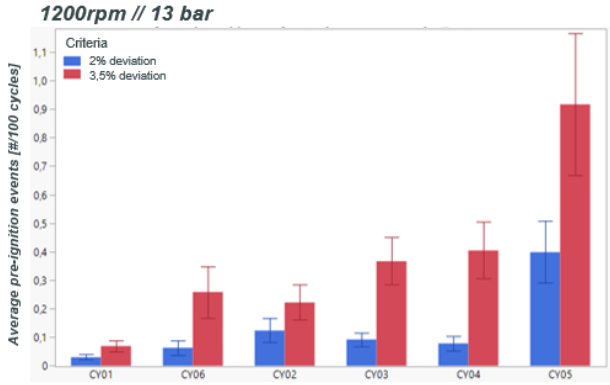


Figure 10: Average pre-ignition events considering the 2 criteria, at 1200rpm 13bar BMEP

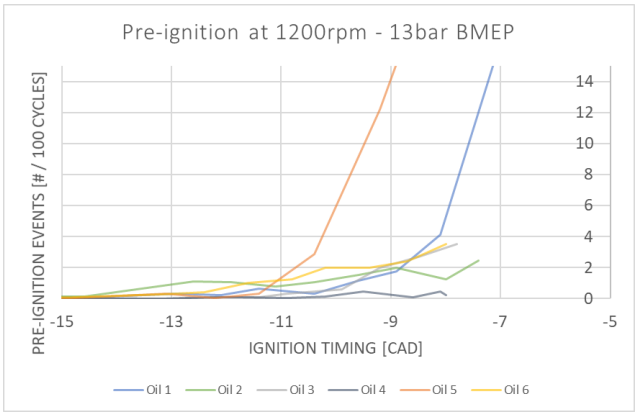


Figure 11: pre-ignition occurrence at 1200rpm – 13 bar BMEP

However, the strong reduction in ash content of Oil 2 significantly reduced pre-ignition sensitivity especially for late ignition timing (later than 9 CAD bTDC). This performance provides the possibility to extend the calibration space for the engine on that operating point. Likewise, Oil 4 lead to very low pre-ignition sensitivity with almost no pre-ignition events recorded, even at late ignition timing compared to the other oil compositions. On the other hand, Oil 5 results show a different trend with a strong increase in pre-ignition frequency at earlier ignition timing. Consequently, the engine would have to operate with a less optimum calibration to avoid abnormal combustion and durability issues. These results demonstrate the significant impact of engine oil composition and the possibility to improve pre-ignition control with specific oil compositions.

2.4 Discussion

Present results emphasize that particle emissions are not negligible in hydrogen combustion engines, especially if we account for particles down to 10nm as considered by future emission standards Euro 7 and Euro VII. Specific engine parameters combining different technical solutions (piston design, ring tension) can help to improve the situation by reducing oil consumption [14]. However, although commercially available lubricant technologies can generate fine particle emissions beyond the normative limit, we have demonstrated that specific engine lubricant formulations can strongly alleviate this phenomenon. Therefore, it appears that collaborations between engine manufacturers and the oil industry can provide relevant synergies to massively reduce particle emissions from future hydrogen combustion engines.

Surprisingly, the sensitivity of particle emissions, CO_2 emissions and pre-ignition frequency to engine oil composition don't follow the same trend. Results have shown that some oil formulations can significantly improve one of these performances without improving others and vice et versa. Consequently, we can assume that mechanisms behind those phenomena differ and require trade-offs (e.g., Oil 5) or ideally, synergistic lubricant solutions (e.g., Oil 2).

CO_2 emissions are likely to be linked to overall oil consumption in the engine if we assume that oil transported into the combustion chamber will burn/oxidize and produce CO_2. However, for a given oil consumption level, oil transport in the combustion chamber can happen through different mechanisms such as oil film evaporation or droplet throw-off [18], [30]. Consequently, based on engine operating points or oil composition these mechanisms can be affected with different intensities. As an example, a change in oil formulation could reduce evaporation mechanism while increasing throw-off mechanism therefore not impacting significantly overall oil consumption, hence CO_2 emissions. Alternatively, for similar oil consumption performance, two engine oil formulations could generate different droplet size distribution patterns which could presumably lead to different particle number measurements at the exhaust. Kittelson reported that particles from the nuclei mode contributes massively to particle numbers but very little to particle mass [31]. Considering that particles originating from the engine oil affect particularly the nuclei mode, one can assume that particle number can vary without affecting overall CO_2 emissions. Access to Particle Size Distribution Functions (PSDF) during the test campaign could have helped to verify that hypothesis for Oil 2, 5 and 6 and to understand the origin of their performances as illustrated on figure 6.

Additionally, Pavaleev et al. theorized that oil droplet ignition delay time in spark ignited engines varies with droplet size in a non-monotonic function and reaches a minimum for droplet diameters around 60µm [25]. This hypothesis could explain the results of Oil 3 where an increase of the average droplet size distribution compared to Oil 1 could lead to a reduction of PN10 while reducing ignition delay time of the droplets. The study lacks evidence to support the physical mechanism and PSDF information could help to challenge this proposition.

Oil 2, characterized by reduced ash content, demonstrated a reduction in particle emissions and in pre-ignition frequency. This observation is consistent with previous results in the literature and reaffirms the role of the lubricant composition on the droplet reactivity, either to produce a particle during the combustion process, or to initiate a flame propagation during the compression stroke. However, one can notice that despite a massive reduction of ash and calcium content, Oil 2 hasn't completely succeeded in eliminating pre-ignition whereas previous studies on LSPI have demonstrated that low calcium containing oils almost eliminate pre-ignition in gasoline engines. This observation can lead to two hypotheses. Either pre-ignition sources in hydrogen combustion engines are not mostly caused by lubricants as observed on gasoline engines, or hydrogen / air mixture are so easy to ignite that even very low calcium content are not sufficient anymore to prevent pre-ignition. Chen et al. reported the role of lubricant in natural gas/hydrogen fueled engine using visualization techniques [8]. Similar approaches in hydrogen fueled engines could help to evaluate the importance of hot spot pre-ignition (ghost spark, made deposits, valve) in comparison with random ignition locations that could be attributed to lubricant droplets or deposits.

Interestingly, Oil 4 didn't impact particle emissions compared to Oil 1 but succeeded to strongly reduce pre-ignition despite conserving high ash content. This result demonstrates that different formulation levers exist to mitigate pre-ignition and that engine oil can be part of the solution to improve hydrogen engine performance and reliability. Further work is required to study trade-offs among the different lubricant functions and identify satisfactory performance balance. Finally, it should be highlighted that due to the stochastic nature of pre-ignition induced by oil droplets, specific test procedures with robust statistical approaches should be explored to properly quantify the impact of lubricant formulation.

Based on the different assumptions discussed in this section, we propose a conceptual diagram to illustrate the role of engine oil in particle emissions and pre-ignition phenomenon (figure 12).

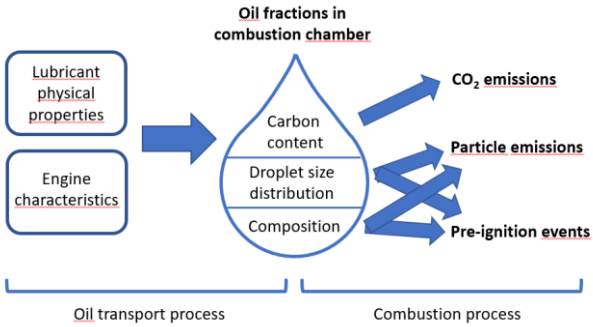


Figure 12: Conceptual diagram of the role of engine oil on emissions et pre-ignition of H_2 engines

Oil transport phenomenon brings lubricant into the combustion chamber from different sources (ring / piston area, valve stems, crankcase ventilation system, turbocharger leaks). This phenomenon is strongly linked to engine characteristics as well as engine oil properties that govern oil consumption. Oil fractions introduced into the combustion chamber can be defined by three main attributes: carbon content, droplet size distribution and composition. During the combustion process these attributes will impact the different engine performances discussed in this paper. On the one hand, carbon content is directly linked to CO_2 emissions through combustion / oxidation process of the oil fraction. On the other hand, particle formation and pre-ignition are linked to droplet size distribution and composition of the oil fractions in the combustion chamber as reported in this study. Underlying mechanisms leading to particle formation or pre-ignition still requires further investigations from the research community.

3. Impact of hydrogen engine operations on lubricant performance

3.1 Engine oil hydrogenation

Due to its small atomic size, hydrogen diffuse easily through materials and can sometimes cause structural alterations leading to detrimental phenomenon such as hydrogen embrittlement in hydrogen rich environments [32], [33]. Consequently, this observation raises the concern on the diffusion of hydrogen in the oil film and the possible impact on engine oil properties and performances.

Previous studies have reported the interactions between hydrogen and lubricant on wear protection and friction performances [34], [35], [36]. These studies were performed in tribological contacts with high mechanical stress, more representative of roller bearing systems that undergo much higher contact pressure that what can be observed in most internal combustion engine lubricated contacts. This assumption could be supported by Beauregard's work who reported endurance tests performed on several full-size pickup trucks over a period of three years and didn't observe any excessive wear in lubricated contacts [38]. However, it is likely that the oil used in this study contained Zinc DialkylDithioPhosphate additive (ZDDP) that performs well in the presence of hydrogen as reported in the literature [33], [35].

The present study proposes to take a more general outlook at oil / hydrogen interaction with regards to lubricant chemical structure or performance. In a hydrogenation reactor, 800g of engine oil was heated at 80°C and subjected to a 2mL/min flow rate of hydrogen under 20 bars for 35 hours. Mechanical stirring was applied in the reactor during the entire procedure to ensure homogeneous contact between hydrogen and the oil. The selected engine oil is a commercially available heavy-duty engine lubricant that fulfills ACEA E7 and API CI-4 specifications (=Oil A). The oil was sampled at the end of the procedure for analysis. Table 5 compares the analyses results of fresh and "hydrogenated" oil. No significant change was observed on viscosity properties or total base number value (TBN) after hydrogen diffusion in the reactor. Oxidation control performance was evaluated using the pressure differential scanning calorimetry (PDSC) protocol described by the CEC standards [38] and specified in ACEA Heavy Duty Oil sequences [39]. No significant difference was observed between fresh and hydrogenated lubricants and both values remain within ACEA specification limits (i.e. > 65 min). Deposit control performance was evaluated using the Micro Coking Test (MCT) as described in the GFC standards [40]. Despite a slight improvement on varnish merit rating for the hydrogenated oil, both results remain within the reproducibility threshold of the method.

Characteristics	Units	Standard	Oil A	Oil A "hydrogenated"
KV100	mm²/s	ISO 3104	15.17	15.10
KV40	mm²/s	ISO 3104	114.9	113.9
VI	-	ASTM D2270	138	138
TBN	mgKOH/g	ASTM D2896	10.7	10.6
Oxidation control - PDSC test		CEC L-85-T-99		
Oxid. induction t	min		159	153
Deposit control - MCT test		GFC Lu-27-A-13		
Varnish merit	/10		6.5	7.3
Varnish temp.	°C		237	233

Table 5: Comparison of laboratory results between fresh and hydrogenated oil

Additionally, a structural analysis of the sample was performed to confirm that hydrogen diffusion didn't significantly modify the oil composition. A Nicolet infrared spectrometer, model IS50 with a 0.1mm wide KBr test cell and a 2cm^{-1} resolution was used to compare transmittance signals from fresh and hydrogenated samples to detect any modifications in chemical functions within the oil compositions. Again, no significant difference was observed between both

samples as illustrated in figure 13. Finally, mass spectrometry experiments were carried out on both oil samples using a hybrid quadrupole-ion mobility-time-of-flight mass spectrometer (Synapt G2Si, Waters, Manchester, UK) equipped with an Atmospheric Solids Analysis Probe (ASAP). The ASAP source was operated in the positive and negative ionization mode. Experiments were accomplished in the V resolution mode in the 50−2000 m/z range. Data acquisition and data treatment were performed using the MassLynx (version 4.1) software. The comparison of both mobility charts confirms that the hydrogen diffusion in the oil film didn't cause any structural modification on the engine lubricant that was selected (figure 14). All these test results show that the selected commercial lubricant was not affected by the diffusion of hydrogen.

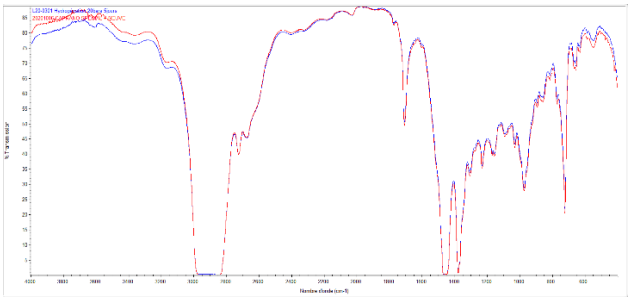


Figure 13: Infrared spectrometer signal comparison between fresh and hydrogenated oil.

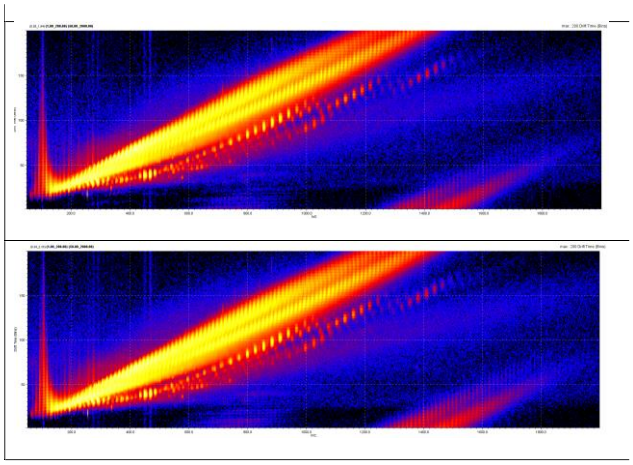


Figure 14: Mobility charts comparison between fresh and hydrogenated oil.

Similar procedure was performed on oil A by adding 100ppm Fe and 50 ppm Cu metal catalyst into the reactor to simulate the presence of wear metals in hydrogen engine lubricant. No impact of the metal catalyst was observed on hydrogen resistance performance of the lubricant. Finally, additional tests were performed without catalyst on other high performance engine lubricants from high quality product range and didn't show signs of alteration due to hydrogen diffusion.

3.2 Impact of hydrogen combustion products on engine oil

Hydrogen wide flammability range in air allows for lean or ultra-lean burn operation modes in internal combustion engines. On the one hand, this characteristic is heavily leveraged by the engine calibration community to minimize engine-out NOx emissions while maintaining good combustion stability. [6], [28]. On the other hand, engine dynamics and torque response requirements tend to increase the equivalence ratio in engine calibration setups. Consequently, depending on the vehicle application, performance targets or operating points, the equivalence ratio can vary greatly thereby leading to large differences in NOx concentrations in the burnt gas. The presence of NOx in the blow-by gas will accelerate the degradation of engine oil via the phenomenon of nitro-oxidation [41], [42], [43] [44], [45]. and thus, require specific lubricant composition adjustment.

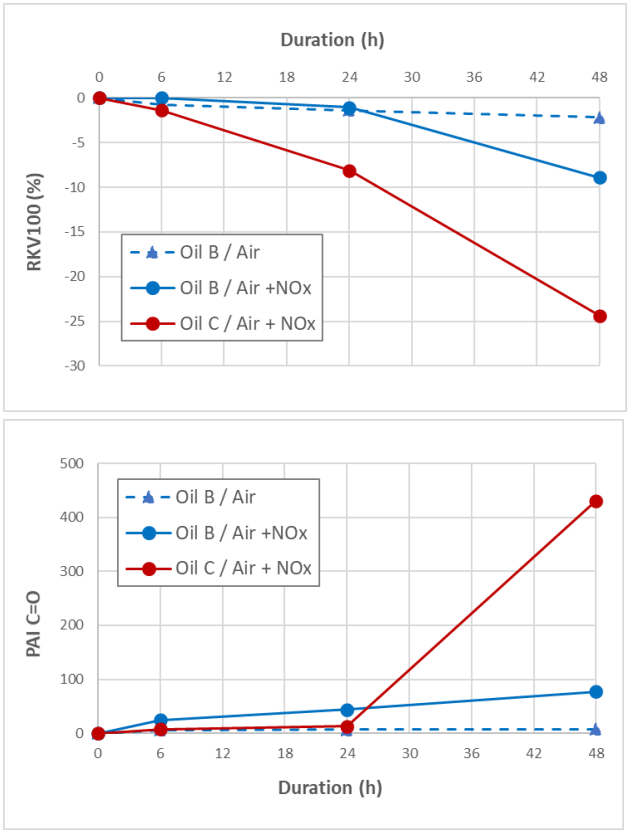


Figure 15: Impact of NOx concentration and oil composition on oil degradation

A glassware nitro-oxidation test was developed to study the impact of NOx on engine oil degradation

and identify relevant oil compositions to cope with nitro-oxidation phenomenon. A 150mL test oil was introduced in a glass tube and heated at 135°C during 48h using a silicon oil bath. A nozzle provided a continuous bubbling in the test sample at a constant flow rate of 10L/min. Samples were taken at 6, 24, 48h and analysed to evaluate their degradation level. Two criteria were considered: Kinematic viscosity evolution relative to that of the fresh oil (RKV100) using ISO 3104 standard and Peak Area Increase (PAI) looking at the difference between the infra-red spectrum of the fresh and used oil between 1820 and 1710 cm^{-1}. Three tests were performed in parallel to study the sensitivity of oil degradation with NOx concentration and oil composition. A 15W-40 API CK-4 commercial engine oil (= Oil B) was tested in tube 1 with air bubbling and in tube 2 with air + 2000ppm NOx. A 15W-40 prototype engine oil with alternative composition (=Oil C) was tested in tube 3 in the same conditions as in tube 2.

Figure 15 illustrates the increase of oil B degradation when NOx concentration increases from 0 to 2000ppm in the bubbling gas. Viscosity drop in this test is indicative of the oxidation phenomenon causing the degradation of the viscosity modifier polymer. PAI C=O results confirms the simultaneous development of carbonyl functions in the oil, characteristic of the oxidation products. Additionally, comparison between oil B and Oil C demonstrate the strong sensitivity of nitro-oxidation to lubricant composition. Consequently, oxidation and nitro-oxidation control should be considered when developing engine lubricant for hydrogen engines operating under higher equivalence ratio.

4. Conclusion

This study discusses the challenges related to hydrogen internal combustion engine lubrication and opportunities to alleviate them in order to improve engine reliability and mitigate pollutant emissions. An experimental hydrogen engine test campaign was designed to explore the impact of engine oil composition on particle emissions (PN10) during WHTC cycles as well as pre-ignition sensitivity on steady state operating points. Hydrogen and NOx impact on engine oil ageing has been studied using specific laboratory apparatus. The following conclusions can be drawn from this study:

- Hydrogen combustion engine without specific lubrication system design can emit particle numbers above Euro VI specification limits on a PN10 basis. These emissions mainly originate from engine oil consumption and could be mitigated by several approaches including hardware design.

- Engine oil composition can strongly impact particle emissions in hydrogen combustion engines. Results on lubricant prototypes have shown up to 45% reduction on PN10 emissions compared to those of a commercial reference oil.

- Engine oil composition seems to play a major role in hydrogen combustion engine pre-ignition phenomenon. Solutions have been identified to significantly reduce pre-ignition frequency compared to a commercial refence oil. However lubricant solutions identified previously for LSPI phenomenon in gasoline spark ignited engines doesn't seem as efficient in hydrogen fuelled engines, thereby suggesting the study of novel lubricant solutions for these applications.

- CO_2 emissions from engine oil consumption has been measured below 1gCO_2/kWh on WHTC cycle when subtracting CO_2 concentration from intake air. No correlation was found between CO_2 emissions, particle emissions and pre-ignition when changing engine oil composition, thereby suggesting different impacting factors. A conceptual mechanism was proposed to describe influencing parameters on these performance criteria.

- Hydrogen diffusion in a heavy-duty commercial engine oil didn't seem to impact its molecular structure or its performances for oxidation control and deposit control. NOx concentration in blow-by gas can significantly impact oil ageing and specific engine oil performances could be required depending on hydrogen calibration targets.

Finally, it was demonstrated that engine lubricant can help to improve hydrogen engine performances and reliability. Whereas this study focuses on some key criteria, many other oil performance requirements remain important items for future hydrogen engine deployment in the field such as water compatibility, deposit control, wear protection, friction reduction, …etc. To maximize synergies between future hydrogen engine technologies and oil formulation, deeper collaborations between engine manufacturers and oil industry are recommended.

5. Acknowledgements

The authors acknowledge the contribution of Mr. S. Faure from TotalEnergies, Mr. C. Biwer, Mr. X. Ritter, Mr. P Simm and Mr. M. Torkler and co-workers from FEV Europe.

6. References

[1] IEA website: https://www.iea.org/reports/greenhouse-gas-emissions-from-energy-overview/emissions-by-sector

[2] European Union Regulation 2019/631, Article 1

[3] European Union Regulation 2019/1242, Article 1

[4] Transport & Environment, Comparison of hydrogen and battery electric trucks, June 2020

[5] Sens M., Danzer C., von Essen C., Brauer M., Wascheck R., Seebode J., Kratzsch M., *"Hydrogen Powertrains in Competition to Fossil Fuel based Internal Combustion Engines and Battery Electric Powertrains,"* 42nd International Vienna Motor Symposium, 2021

[6] Duffour F., Walter B ., Gatellier B., Rouleau L., Kumar R., Maio G., Ternel C., Maisonnier G., *"Potential and challenges of the H2 internal combustion engine from experimental and numerical investigation,"* SIA Powertrain & Power Electronics 2021

[7] Arthur L. Miller A., Stipe C., Habjan M., Ahlstrand G., *"Role of Lubrication Oil in Particulate Emissions from a Hydrogen-Powered Internal Combustion Engine,"* Environmental Science & Technology 2007 41 (19), 6828-6835, DOI: 10.1021/es070999r

[8] Chen L., Zhang X., Zhang R., Li J., Pan J., Wei H., *"Cycle-resolved visualization of lubricant-induced abnormal combustion in an optical natural gas/hydrogen engine,"* Fuel, Volume 321, 2022, 124053, https://doi.org/10.1016/j.fuel.2022.124053

[9] Guido C., *"Emissive Behavior of a Heavy-Duty SI Gas Engine During WHTC"*, SAE Technical Paper 2019-24-0121, doi: 10.4271/2019-24-0121.

[10] Corbin J., Peng W., Yang J., Sommer D., *"Characterization of particulate matter emitted by a marine engine operated with liquefied natural gas and diesel fuel"*, Atmospheric Environment 220 (2020) 117030, doi.org/10.1016/j.atmosenv.2019.117030

[11] Tabata K., *"Studies on Characteristics of Nanoparticles Generated in a Gasoline Direct-Injection Engine"*, JSAE 20199132, SAE Technical paper 2019-01-2328, 2019, doi:10.4271/2019-01-2328

[12] Pirjola L., *"Effects of Fresh Lubricant Oils on Particle Emissions Emitted by a Modern Gasoline Direct Injection Passenger Car,"* Environ. Sci. Technol., Vol 49, p3644-3652, 2015, doi:10.1021/es505109u

[13] Mayer A., *"Metal Oxide Particle Emissions from Diesel and Petrol Engines"*, SAE Technical Paper 2012-01-0841, doi: 10.4271/2012-01-0841

[14] Lehtoranta, K., Murtonen, T., Vesala, H., Koponen, P., Piimäkorpi, P., Isotalo, M., Alanen, J., Kuittinen, N., Rönkkö, T., & Saarikoski, S. (2019). *"New technologies for gas combustion emissions: Final report."* VTT Technical Research Centre of Finland. VTT Research Report No. VTT-R-00482-19.

[15] Tonegawa Y., *"Evaluation of Regulated Materials and Ultra Fine Particle Emission from Trial Production of Heavy-Duty CNG Engine"*, SAE Technical Paper 2006-01-3397, doi: 10.4271/2006-01-3397

[16] Khalek I., *"Solid Particle Number and Ash Emissions from Heav-Duty Natural Gas and Diesel w/SCRF Engines"*, SAE Technical Paper 2018-01-0362, doi:10.4271/2018-01-0362.

[17] Napolitano P., *"Particle and gaseous emissions from a heavy-duty SI gas engine over WHTC driving cycles"*, SAE Technical Paper 2019-01-222, 2019, doi:10.4271/2019-01-2222.

[18] Lensch-Franzen C., Gohl M., Scholl P., Paoloni F., *"Impact of Engine Lubricant Volatility on Oil and Particle Emissions"*, MTZ worldwide 09/2019, pages 44-53

[19] Froelund K., Menezes L., Johnson H., Rein W., *"Real-time transient and steady state measurement of oil consumption for several production SI-engines"*. In: SAE Technical Paper 2001-01-1902; 2001. https://doi.org/10.4271/2001-01-1902

[20] Guido C., Napolitano P., Alfuso S., Corsetti C., Beatrice C., *"How engine design improvement impacts on particle emissions from an HD SI natural gas engine"*, 2021, https://doi.org/10.1016/j.energy.2021.120748

[21] Andersson J., *"Lubricant Composition Impact on the Emissions from a European Heavy Duty Diesel Engine Equipped with a Diesel Particulate Filter"*, SAE Technical Paper 2004-01-3012, doi:10.4271/2004-01-3012.

[22] Ovaska T., *"Role of Lubricating Oil Properties in Exhaust Particle Emissions of an Off-Road Diesel Engine"*, SAE Technical Paper 2020-01-0386, doi:10.4271/2020-01-0386

[23] Kytö M., *"Effect of Lubricant on Particulate Emissions of Heavy Duty Diesel Engines"*, SAE Technical Paper 2002-01-2770, doi:10.4271/2002-01-2770

[24] Takeuchi, K., Fujimoto, K., Hirano, S. and Yamashita, M., *"Investigation of Engine Oil Effect on Abnormal Combustion in Turbocharged Direct Injection - Spark Ignition Engines,"* SAE Int. J. Fuels Lubr. 5(3):2012, doi:10.4271/2012-01-1615.

[25] Palaveev, S., Magar, M., Kubach, H., Schiessl, R. et al., *"Premature Flame Initiation in a Turbocharged DISI Engine - Numerical and Experimental Investigations,"* SAE Int. J. Engines 6(1):2013, doi:10.4271/2013-01-0252.

[26] Fletcher, K., Dingwell, L., Yang, K., Lam, W. et al., *"Engine Oil Additive Impacts on Low Speed Pre-Ignition,"* SAE Int. J. Fuels Lubr. 9(3):2016, doi:10.4271/2016-01-2277.

[27] Zadeh A., Rothenberger P., Nguyen W., Anbarasu M., Schmuck-Soldan S., Schaefer J., Goebel T., *"Fundamental Approach to Investigate Pre-Ignition in Boosted SI Engines,"* SAE paper 2011-01-0340, doi:10.4271/2011-01-0340

[28] Das L.M., *"Exhaust emission characterization of hydrogen-operated engine system: Nature of pollutants and their control techniques"*, International Journal of Hydrogen Energy, Volume 16, Issue 11,

1991, Pages 765-775, ISSN 0360-3199, https://doi.org/10.1016/0360-3199(91)90075-T

[29] Kumamoto A., Iseki H., Ono R., Oda T., *"Measurement of minimum ignition energy in hydrogen-oxygen-nitrogen premixed gas by spark discharge"*, J. Phys.: Conf. Ser. 301 012039, 2011

[30] Yilmaz E., *"Sources and Characteristics of Oil Consumption in a Spark-Ignition Engine"*, MIT PhD thesis, 2003

[31] Kittelson D., *"Engines and Nanoparticles: A Review,"* J. Aerosol Sci., Vol 29, No 5/6, p575-588, 1998

[32] Chen L., Zhang X., Zhang R., Li J., Pan J., Wei H., *"Cycle-resolved visualization of lubricant-induced abnormal combustion in an optical natural gas/hydrogen engine"*, Fuel 321 (2022) 124053, doi:10.1016/j.fuel.2022.124053

[33] J. A. Ciruna, H. J. Szieleit, *"The effect of hydrogen on the rolling contact fatigue life of AISI 52100 and 440C steel balls"*, Wear, 24, 1973, pages 107-118

[34] Tanaka, H., Niste, V., Abe, Y. & Sugimura, J. *"The effect of lubricant additives on hydrogen permeation under rolling contact"*, Tribol. Lett., 65–94 (2017),

[35] Ratoi, M., Tanaka, H., Mellor, B.G. et al. *"Hydrocarbon Lubricants Can Control Hydrogen Embrittlement"*. Sci Rep 10, 1361 (2020). https://doi.org/10.1038/s41598-020-58294-y

[36] G. Liskiewicz, P. Kula, A. Neville, R. Pietrasik, A. Morina, T. Liskiewicz, *"Hydrogen influence on material interaction with ZDDP and MoDTC lubricant additives"*, Wear, Volume 297, Issues 1–2, 2013, Pages 966-971, ISSN 0043-1648, https://doi.org/10.1016/j.wear.2012.11.005

[37] Ellina Lunarska, Danuta Samatowicz, *"The hydrogen-induced modification of the properties of the metal surface coated with oil and lubricant"*, Tribology International, Volume 33, Issue 7, 2000, Pages 491-499, ISSN 0301-679X, https://doi.org/10.1016/S0301-679X(00)00090-6.

[38] Beauregard, Garrett. *"Findings of Hydrogen Internal Combustion Engine Durability"*. United States: N. p., 2010. Web. doi:10.2172/1031548.

[39] CEC, Pressure Differential Scanning Calorimetry (PDSC) Test, CEC SG-L-085

[40] Essai de microcokage sur auget de lubrifiants automobiles (MCT), GFC Lu-27-A-13 Version 3, 2017

[41] Iwakata, K., Onodera, Y., Mihara, K., and Ohkawa, S., *"Nitro-Oxidation of Lubricating Oil in Heavy-Duty Diesel Engine,"* SAE Technical Paper 932839, 1993, https://doi.org/10.4271/932839

[42] Coultas, D.R., *"The Role of NOx in Engine Lubricant Oxidation,"* SAE Int. J. Advances & Curr. Prac. in Mobility 2(5):3009-3016, 2020, doi:10.4271/2020-01-1427

[43] Johnson, M.D., Korcek, S., *"Effects of NOx on liquid phase oxidation and inhibition at elevated temperatures"*, Lubrication Science 3, 1991, 95-118

[44] Davydov, E.Y., Korcek, S., Jensen, R.K., Zaikov, G.E., *"Kinetics and mechanism of liquid-phase nitration of 2,4,6-tri-t-butylphenol"*, International Journal of Polymeric Materials 37, 1997, 201-216.

[45] Pochopien, B.A., *"Interactions of antioxidants with NOx at elevated temperatures"*. PhD thesis, 2012, University of York, United-Kingdom

7. Glossary

ACEA:	*European Automobile Manufacturers Association*
ASAP:	Atmospheric Solids Analysis Probe
BEV:	*Battery Electric Vehicle*
BMEP:	*Brake Mean Effective Pressure*
bTDC:	*before Top Dead Center*
CAD:	*Crank Angle Degree*
CEC:	*Coordination European Council*
CPC:	*Condensation Particle Counter*
FCEV:	*Fuel Cell Electric Vehicle*
KV100	Kinematic Viscosity at 100°C
LSPI:	Low Speed Pre-Ignition
MCT:	*Micro Coking Test*
NDIR :	*Non-Dispersive Infra-Red sensor*
PAI:	*Peak Area Increase*
PDSC:	*Pressure Differential Scanning Calorimetry*
PN10:	*Number of particles with size above 10nm*
PN23:	*Number of particles with size above 23nm*
PSDF:	*Particle Size Distribution Function*
RKV100:	*Relative Kinematic Viscosity increase at 100°C*
TBN:	*Total Base Number*
WHTC:	World Harmonized Transient Cycle
ZDDP:	Zinc DialkylDithioPhosphate

15 JUNE 2022

ELECTRIFIED PROPULSION SYSTEMS CONTROL

SCHRADER PACIFIC
Advanced Valves

VALVES FOR ELECTRIC CARS AND H2 VEHICLES

EV THERMAL MANAGEMENT VALVES:

. AC Systems & Heat Pumps
. Cooling Circuits

HYDROGEN VALVES:

. HP Storage
. Fuel Cell



www.schrader-pacific.fr

Connected strategy for energy-efficient driving of electric vehicle

C. Ngo[1], F. De Smet[2], O. Lemaire[1], M. Espig[2], G. De Nunzio[1], A. Sciarretta[1]

1: IFP Energies Nouvelles, 1-4 avenue de Bois Préau, Rueil-Malmaison, France
2: FORD Research & Innovation Center, Süsterfeldstr. 200, D-52072 Aachen, Germany

Abstract: This paper presents the potential benefits of connected strategies for energy-efficient driving for electric vehicles achieved during the H2020 EU project CEVOLVER.

Two strategies are presented. First solution optimizes the route and the recharge planning such as minimizing the battery energy consumption within a suitable trip time (eco-charging). Second solution, coupled with the first, provide the optimal speed profile using predictive information from the eco-charging and topology and infrastructure data from third party webservices (eco-driving).

The benefits provided by the developed connected strategies are evaluated in simulation. Gains obtained by the eco-driving are validated experimentally with a mixed urban and extra-urban route, showing a significant energy consumption reduction.

Keywords: Connected strategy, electric vehicle

1. Introduction

In the past decade, electric vehicles (EVs) made significant progress in term of range, while charging stations network has been expended all over Europe. EV sales have recently increased showing customers' interest in emission or fuel dependency reduction. However, EVs have still not attained the level of user acceptance needed to support a broader mainstream market uptake. Long charging times and uncertainties in range prediction are still the main obstacles to overcome for a further widespread use.

Connectivity of EV represents a promising way to overcome the range anxiety. Connection to cloud webservices exploiting geographic information system (GIS) and traffic data offers the opportunity to predict the driving range accurately and to minimize the energy consumption. To ensure long trip, crowd-sourced data of existing DC fast-charging stations are useful as well for optimal charge planning. As a result, with the optimization of energy range and fast charging, battery can be right-sized, making EVs affordable.

Within this context, the H2020 European project CEVOLVER [1] aims to develop battery electric vehicles (BEV) that improve user experience over long trips. Project's demonstrator vehicles are designed to take advantage of future improvements of the fast-charging infrastructure, whilst the installed battery is dimensioned for affordability. They also integrate improvements to reduce energy consumption, leveraging connectivity for further optimization of components and system design (right-sizing), as well as vehicle controls (battery pre-conditioning for fast charging, cabin thermal management, powertrain energy management), and driving strategies (eco-charging and eco-driving). The final objective of CEVOLVER is to demonstrate on open road that long-trips are achievable by EVs with limited extra time with respect to conventional vehicles.

The eco-charging algorithm solves the problem of finding a time- and energy-optimal route for an EV requiring multiple battery charging events to complete a long-distance trip. The proposed routing strategy also provides the optimal sequence of charging events, as well as the optimal average speed for each road segment to reduce charging needs and thus save trip time. The route and charging sequence optimizations are based on a predictive model of the Ford Transit. In [2], study shows eco-charging can support trips achieved with small battery capacity and long-distance trips. The eco-driving algorithm provides the driver with instantaneous speed recommendations to minimize energy consumption. The developed real-time strategy bases its calculation on: (1) route topology and infrastructure data from GIS, (2) the predictions made by the eco-charging strategy, in particular the average speed, and (3) the real-time ADAS measurements, if available, to anticipate the surrounding traffic disturbances. For more details about the eco-charging and eco-driving strategies developed during the project, developments have been published in [3] and [4,5] respectively.

Few experimental validations on connected strategy for energy-efficient driving of EVs exist. In [6], predictive eco-driving strategy considering real-world traffic flow has been validated under real-world traffic environment. In [7], the developed eco-driving algorithm has been validated using a driving simulator.

This paper focuses on the potential energy gains provided by the connected eco-charging and eco-driving strategies on a Ford Transit van with a battery

electric propulsion system, obtained in simulation and on open road.

The paper is organized as follows. In Section 2, the energy reduction performance provided by the eco-charging and the eco-driving is evaluated in simulation. Simulation of long trip use case with different average speed will confirm the large impact of the average speed on the trip time for the Ford demonstrator vehicle, enforcing the results obtained with the presented connected functions. In Section 3, experimental test results of eco-driving in real traffic conditions on a representative use case are presented and analysed.

2. Potential energy gain from connected strategies

This section presents the simulation results of eco-charging and eco-driving. First, simulations of a long trip with the Ford demonstrator, with different average speed values shows the impact of the speed on energy consumption. This result is then confirmed by simulations of the complete eco-charging strategy, where both the route choice and average speed are optimized. The saved battery energy reduces the charging needs and thus the trip duration. Then, simulations of the eco-driving strategy on repeated trips in Cologne show how optimizing the instantaneous speed profile can further reduce the energy consumption.

2.1 Average speed variation impact on the Ford demonstrator

For the Ford demonstrator, the main benefit of optimal average speed advice is expected for highway traffic where the travel speed can be adapted largely without constraints. In terms of urban applications, it is expected that on the one hand the observance of the speed advice is more disturbed by interactions with the surrounding traffic and on the other hand, dynamic changes of the recommended target speed are more difficult to be considered by the driver. Thus, the focus of the benefit analyses for the demonstrator was placed on the benefits during long distance trips.

For that purpose, the energy demand for a 350 km trip was considered for different vehicle speeds between 70 and 130 km/h assuming for simplicity that the whole trip is driven at constant speed. In addition, the total trip time was evaluated based on the time demand for driving and the time demand for battery charging with 20 to 150 kW just to the state of charge that is required to reach the target destination. The resulting graphs that show the interdependency between available charging power, energy demand and trip time are shown in Figure 1.

It is obvious that the energy demand is increasing strongly with increasing vehicle speed which is due to the huge frontal area of the BEV demonstrator and the resulting air resistance. Comparing the vehicle speed with the total trip time, the graphs indicate that depending on the available charging power an increase of vehicle speed is not always beneficial in terms of trip time. For an average charging power of 20 kW, the trip time demand at 80 km/h is by far less than for 130 km/h. The reason for that is the difference in driving energy demand and the related amount of charging energy that results in heavily increased time demand for charging. This effect is mitigated with the availability of higher charging power but even for 100 kW average the time savings for travelling at 130 km/h instead of 100 km/h are negligible whereas the increase in energy demand is significant.

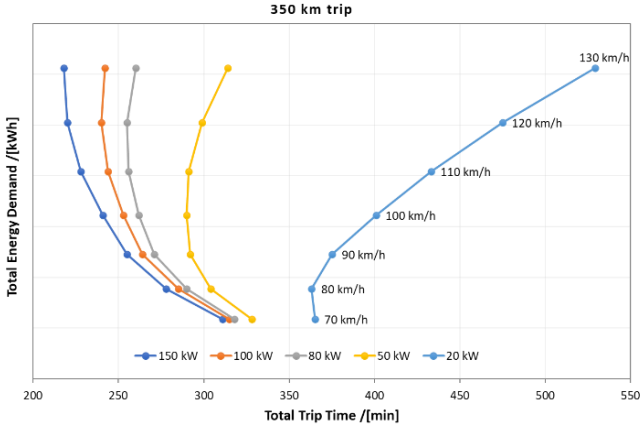


Figure 1: Dependency between available charging power, energy demand and trip time for a long distance trip

2.2 Eco-charging

The performance of the eco-charging strategy is evaluated on a trip between Aachen (Germany) to Deauville (France) of 545 km. Figure 2 shows the trip planned by the eco-charging algorithm with the stop locations. The table 1 shows a comparison of the solutions given by the eco-charging algorithm with the average speed added as a decision variable in the optimization, where “no speed” indicates that average speed is not a decision variable. The indication “with speed” refers to the optimization with average speed v as decision variable with speed varying within a range of $[v-30, v]$ in km/h.

Using travelling speed as decision variable benefits both on the energy consumption and the recharged energy, with a reduction of 3.9 and 11.1% respectively. Eco-charging changes the charging planning according to the adjusted speed profile, avoiding an additional charging stop leading to reduce the overall trip time.

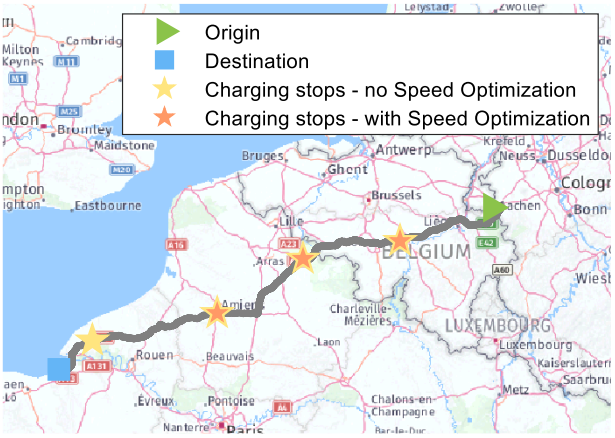


Figure 2: Mission profile between Aachen (Germany) and Deauville (France) (© 2022 HERE)

Table 1: Eco-charging performance with average speed as a decision variable

	No speed	With average speed
Trip time difference	7h38	6h54
Number of charging stops	4	3
Energy consumption [kWh]	/	-3.9 %
Recharged energy [kWh]	/	-11.1 %

2.3 Eco-driving

The potential energy gain from the eco-driving strategy is evaluated on a 19 km trip repeated 24 times in Cologne near Ford's facilities at off-peak hours.

The mission profile is divided into three parts: (1) the highway part for routes with $v_{max} \geq 70\ km/h$, (2) the extra-urban part with $50 < v_{max} < 70\ km/h$, and (3) the urban part where $v_{max} \leq 50\ km/h$. The split is detailed in Figure 3.

The eco-speed is computed using information about the average traffic speed and predictive data from eco-charging about the route segment's end speed. The speed optimization only takes into account the route topology, the legal speed limits constraints and the traffic prediction, although the developed approach is able to consider the surrounding traffic in real-time as described in [4].

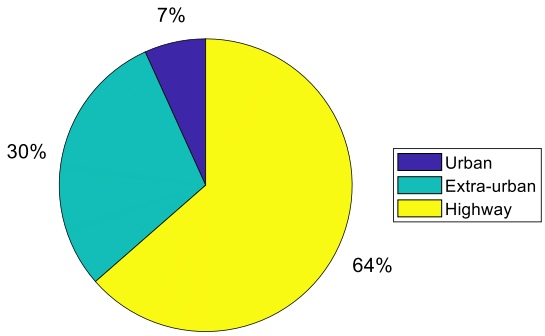


Figure 3: Speed limits split within the trip

The driven and the computed eco speed profiles are represented in Figure 4. The real speed profiles show that the test drives are relatively repeatable but surrounding traffic influences strongly the speed profile, in particular in urban area.

The eco-driving algorithm smooths and adapts the speed to avoid unnecessary acceleration and deceleration between route segments. Deceleration anticipation as segment end approach is possible thanks to the eco-charging predictions. One can notice that predictive information from the eco-charging about the segment ends speed is quite accurate as closed to the real speed transition.

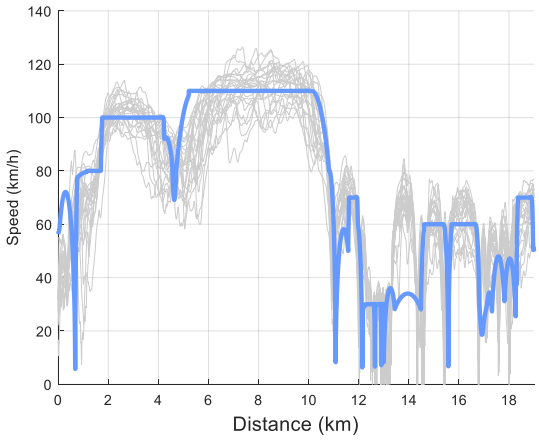


Figure 4: Driven (gray) and eco (blue) speed profile

In Figure 5, the normalized battery energy consumptions against the total trip time for each drives and the computed eco-speed are shown. The impact of the speed profile optimization on the travel time is limited as the strategy takes as a constraint the travel time accordingly to the traffic data obtained from the GIS providers (HERE webservice is used). About the energy gains, eco-driving could reduce the energy consumption of 3.5% in average and up to 13% on the whole trip (Figure 6).

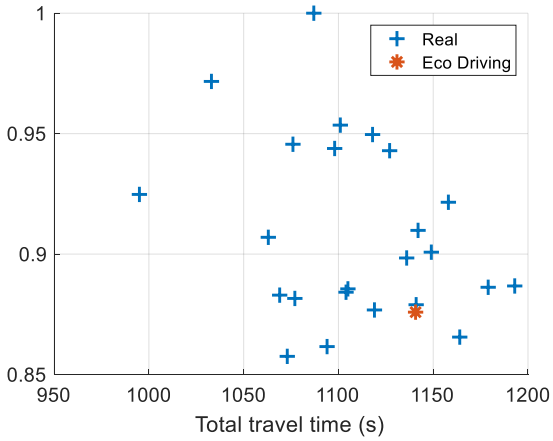


Figure 5: Normalized battery energy consumption according to the total travel time

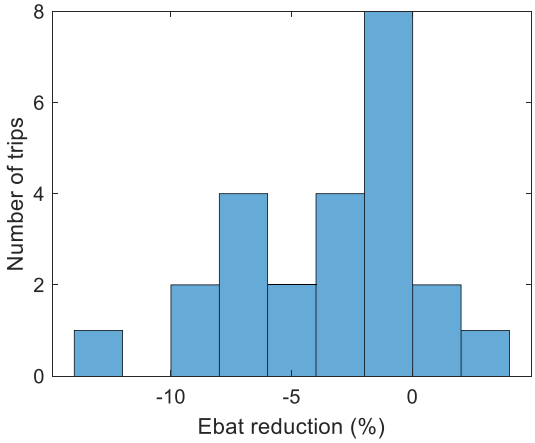


Figure 6: Energy consumption reduction distribution for the whole trip

Focusing on the two main parts of the trip, namely the highway and the extra-urban parts, the energy consumption reduction distribution in Figure 7 shows that reduction will be possible especially in extra-urban parts.

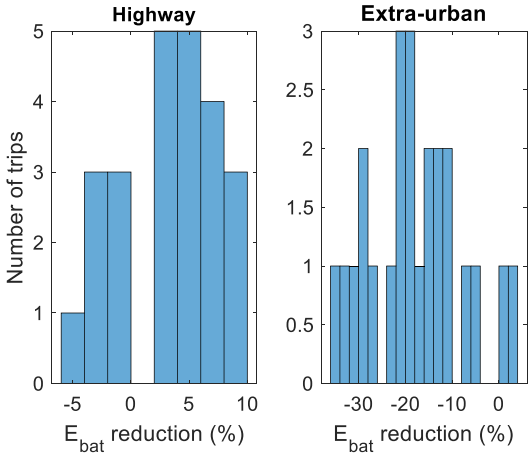


Figure 7: Battery energy reduction distribution according to route type

3. Experimental result of eco-driving on open road

The eco-driving was evaluated on open road in Aachen (Germany) with the Ford BEV demonstrator.

3.1 Demonstrator vehicle

The Ford BEV demonstrator for the CEVOLVER project is a commercial vehicle from the 2T Transit range. The variant used in this project has a short wheelbase and a medium roof. The vehicle's powertrain specification is based on the e-Transit that recently went into production [8]. The battery has a usable capacity of 67 kWh. The vehicle contains an 11.3 kW onboard AC charger. It also supports DC-fast-charging up to 115 kW. The motor-inverter is mounted at the back, behind the battery, where it transmits its forces to the rear wheels. The vehicle's electric motor has a peak output power of 269 hp and delivers 430 Nm of torque. The vehicle is shown in Figure 8.



Figure 8: Ford Transit BEV demonstration vehicle

3.2 On-board implementation of the connected strategies

The implementation of the eco-charging and the eco-driving strategies rely on the connected architecture which is composed of a Brand Independent (BI) cloud and dedicated components hosted on a connected device.

The Figure 9 presents the implementation and dependencies between the components.

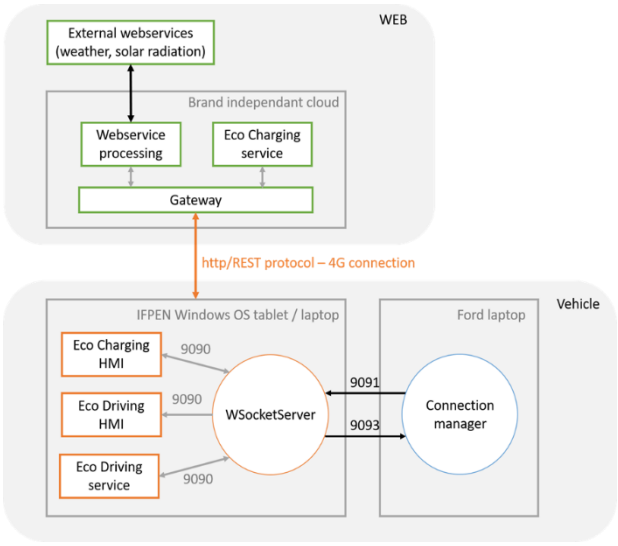


Figure 9: Implementation architecture

The BI cloud serves as a gateway to third party webservices for the connected functions developed during the project (namely eco-charging, powertrain and thermal cabin conditioning optimization, smart fast charging) and hosts the eco-charging webservice. The communication between the connected device and the BI cloud services uses the *http/REST* protocol.

The connected device hosts the eco-driving strategy and serve as HMI for the eco-charging and eco-driving. The device is connected to the BI cloud by 4G connection. on the laptop. A local server, denoted "WSocketServer", handles the *WebSocket* messages between all the implemented components (HMI / Eco-driving / BI Cloud / Ford RCP SW tool) and triggers the eco-driving and eco-charging services.

3.3 Experimental results

The evaluation of the eco-driving strategy on the Ford demo vehicle was performed around the Ford Research Centre in Aachen (Germany). Two routes were selected which represent typical rural and urban routes. The share of the speed limits for the four trips is shown in Figure 10.

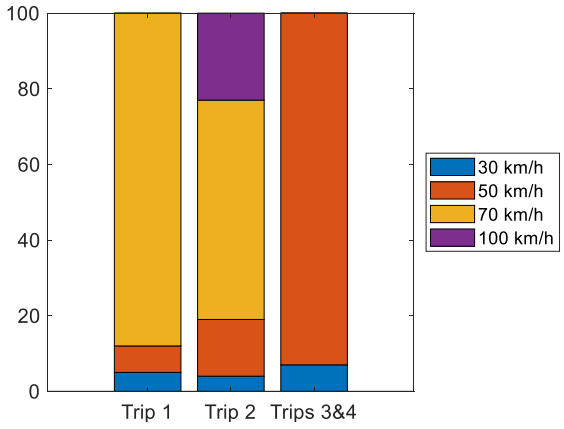


Figure 10: Speed limit share for the two directions of the Ford ECO-driving evaluation route

The rural route is a connection between two urban zones. It has a few stop lights and a rather smooth traffic. The urban route is the main road through a suburb of Aachen. It has more stop lights and crossings. At the time the routes were driven the traffic was moderate, with large shares of the trajectory with no vehicle in front. One could imagine such a route being driven by van drivers, for example from delivery vehicles or craftsmen. The route with the more rural speed profile was driven in both directions, called trip 1 and 2 in the following. The length of the trajectory is 4,25 km for trip 1 and 4,75 km for trip 2. The route starts for less than 100m in a 50 km/h street followed by a ring road where 70 km/h is allowed. At the end, the trajectory turns into a village with a 50 km/h speed limit, to finally find its endpoint in a 30 km/h shopping park zone. On the way back, the ring road contains a share with a speed limit of 100 km/h. After the exit of the ring road, the last part is a 50 km/h street. This part is about 400m longer than in the other direction. The fact that the exit from the ring road is 400m further away from the start point than the entrance explains most of the difference in length for both directions. Further, a second route with a more urban speed profile was added to the evaluation tests. This route was driven in both directions as well which will be called trip 3 and trip 4. The length for both trajectories is 2,97 km. This route has a 50 km/h speed limit, apart from the last part where it ends also in the shopping park zone.

All the trips have been driven repeatedly, whereby the target was three times for each case. The number of drives per case is shown in Figure 11. The repetition of the routes is needed for plausibility of the results, also because the traffic lights influence strongly the speed profile.

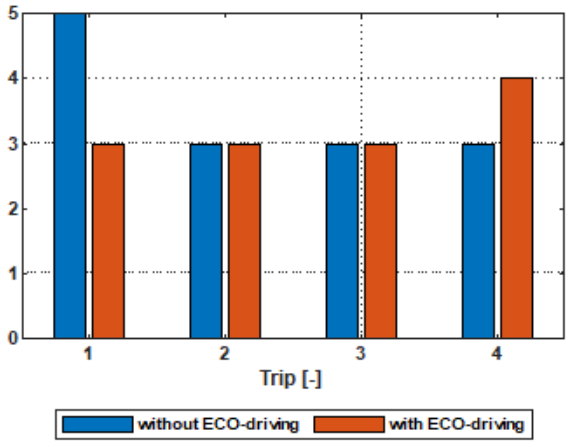


Figure 11: Number of drive repetition with and without ECO-driving

With the advisory function on, the driver attempts to follow the speed advice. No data about the real-time

surrounding traffic was available yet as the radar was not active on demonstrator vehicle. A comparison of two randomly selected traces from the urban route is shown in Figure 12.

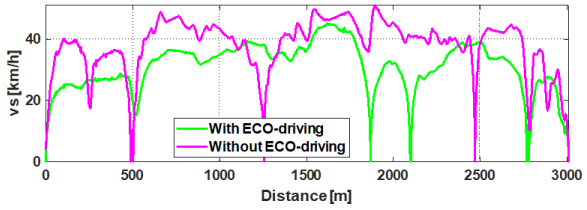


Figure 12: Urban route with and without ECO-driving

In general, the average speed advised is lower than the average speed that would be driven without using the advisory function. One other difference that has been noticed is that the ECO-driving function defines a more economic acceleration profile. A zoom on the speed profile from the mixed rural-urban drive as shown in Figure 13 illustrates this. The acceleration between 70 and 500s, when entering the ring road, is much slower with the ECO-driving speed advice.

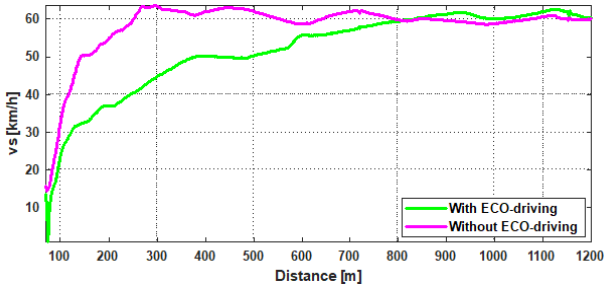


Figure 13: Zoom on an acceleration with and without ECO-driving

The energy savings have been quantified based on the total battery energy consumption over the trip. The Figure 14 compares the averages for the different cases. The Figure 15 reports the average time duration. For all the trips, the average time loss ranges from 65 to 79s. On the other hand, the battery energy consumption is always lower with ECO-driving actively used. The gain is lower for an urban profile (9-10%) than for a more rural type of trip (13-15%). This is also expected, as the urban profile is typically a more dynamic driving profile. The pre-knowledge of the route allows the advisory function to explore opportunities to anticipate stops or, for example, inclinations in the road.

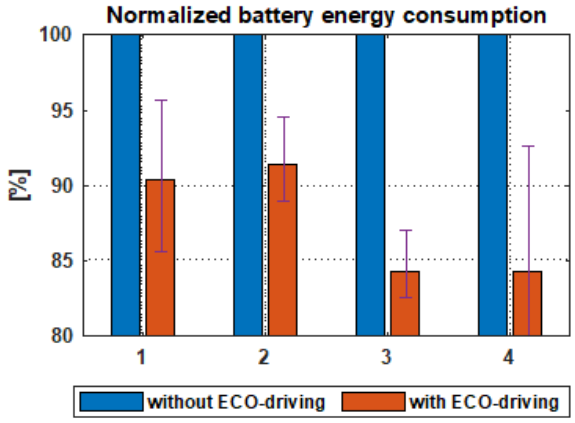


Figure 14: Battery energy consumption with and without ECO-driving for the two directions of the trip

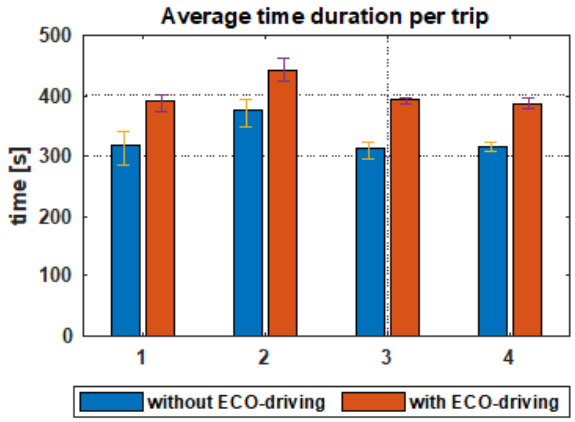


Figure 15: Trip duration with and without ECO-driving for the two directions of the trip

5. Conclusion

This paper has presented a connected strategy for an efficient-energy management of EVs, in particular for the Ford Transit BEV. A comprehensive strategy which optimizes the route, the charge plan and the driven speed provides gains in energy and travel time, thus helps to reduce the range anxiety expressed by EVs users.

Simulation results have shown promising energy gains by optimizing the speed profile. Eco-charging, by both optimizing the charge plan and the average speed, could provide gains up to 5%. Eco-driving by optimizing the instantaneous speed profile could reduce the energy consumption by 3.5% in average up to 13%.

Experimental validation of the developed connected strategy, enhancing the eco-driving feature, shows promising results with average gains of 10% and

demonstrate the technical feasibility of the proposed approach.

6. Acknowledgement

This work has received funding from the European Union's Horizon 2020 research and innovation program under grant agreement No. 824295, CEVOLVER (Connected Electric Vehicle Optimized for Life, Value, Efficiency and Range).

7. References

[1] CEVOLVER H2020 project website, https://cevolver.eu/

[2] H. Brandes, G. De Nunzio, V. Döge, I. Faye, V. Ravello, A. Sciarretta, P. Turco, “Smart driving and charging can help reconciliate limited battery capacity and long-distance trips for electric vehicles without compromising on trip time”, Transport Research Arena (TRA), 2022.

[3] G. De Nunzio, I. Ben Gharbia and A. Sciarretta, "A Time- and Energy-Optimal Routing Strategy for Electric Vehicles with Charging Constraints," 2020 IEEE 23rd International Conference on Intelligent Transportation Systems (ITSC), 2020, pp. 1-8.

[4] Sciarretta and A. Vahidi, Energy-Efficient Driving of Road Vehicles. Springer, 2020.

[5] C. Ngo, E. Solano-Araque, M. Aguado-Rojas, A. Sciarretta, B. Chen, M. El Baghdadi, “Real-time eco-driving for connected electric vehicles”, IFAC-PapersOnLine, Volume 54, Issue 10, 2021, Pages 126-131.

[6] X. Zhang, T. Zhang, Y. Zou, G. Du and N. Guo, "Predictive Eco-Driving Application Considering Real-World Traffic Flow," in IEEE Access, Vol. 8, pp. 82187-82200, 2020.

[7] J. Fleming, X. Yan, C. Allison, N. Stanton, R. Lot, “Real-time predictive eco-driving assistance considering road geometry and long-range radar measurements”, IET Intelligent Transport Systems, Vol. 15, Issue 4, p. 573-583, 2021.

[8] Ford Media Center, E-Transit - product overview, https://media.ford.com/content/fordmedia/feu/en/products/cvs/e-transit/e-transit.html

8. Glossary

EV: Electric Vehicle

GIS: Geographic Information System

BEV: Battery Electric Vehicle

BI: Brand-independent

ADAS: Advanced driver-assistance systems

Efficiency Improvement of Automotive Traction Systems by Dynamic Motor Drive

Z. Chen, M. Younkins, P. Carvell, P. Farah, B. Wolk

Tula Technology, 2460 Zanker Rd, San Jose, California, USA

Abstract: Tula Technology has developed Dynamic Motor Drive (DMD) technology to optimize the efficiency of electric powertrains while avoiding the use of rare earth magnets. Similar to the concept of Dynamic Skip Fire (DSF), which is operating in vehicles with internal combustion engines, DMD intermittently operates the motor at high efficiency to seamlessly deliver torque while minimizing losses at low loads. Simulation results show it is possible to reduce the energy consumption of an Externally Excited Synchronous Motor (EESM) by 2 to 3.2% in WLTP and MCT drive cycles.

Keywords: Efficiency, electric vehicle, motor control.

1. Introduction

Electrification is progressing at a staggering pace in the automotive industry. More and more automakers have pledged to phase out development of Internal Combustion Engines (ICEs) and move forward to all-electric solutions as early as the 2030s. This will be a revolutionary change in the history of the automobile.

Nevertheless, Electric Vehicles (EVs) still face various technical challenges. The most notable ones are system efficiency and implementation cost. Increasing the efficiency of EV powertrains plays an important role in reducing grid load, decreasing pollution from electricity generation, and extending the driving distance per charge. However, improvements to efficiency over the past decade have focused on technologies that increase rare earth metal usage.

Although motors with large amounts of rare earth material have extremely high levels of peak system efficiency – above 90% or even 95% – the efficiency at lower loads, frequently encountered during EV operation, is often below 70%, which results in downgraded overall system performance.

Moreover, sources of economically recoverable rare earth metals are concentrated in only a few locations worldwide. Among them, Neodymium and Dysprosium are of critical importance and risk. Although these materials have equipped some of the roughly 10 million EVs in use today, it is unlikely to be an adequate and affordable solution in the future when the entire 1.4-billion-unit automotive fleet consists of EVs. In the next decade, the demand for these metals is estimated to more than double [1, 2]. Although future prices of rare earth magnets are not yet known, the price of equipping an electrical vehicle with these magnets may make these vehicles impractical to own for large portions of the population. We cannot rely exclusively on rare earth metals in the future.

2. Dynamic Motor Drive

The concept of Dynamic Motor Drive (DMD) is shown in Fig.1. With conventional control, the maximum energy efficiency is achieved at 25 to 30% of full load operation. As can be seen, the efficiency of conventional control falls off dramatically at low loads. In contrast, under DMD operation, torque is delivered intermittently at the load that achieves highest efficiency.

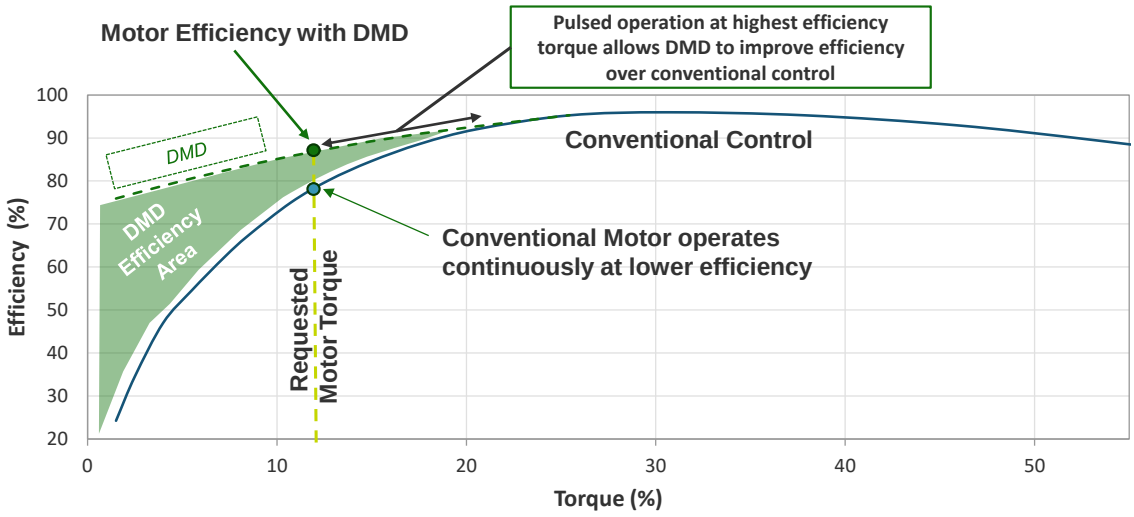


Fig.1 A typical motor system efficiency characteristics at a constant speed.

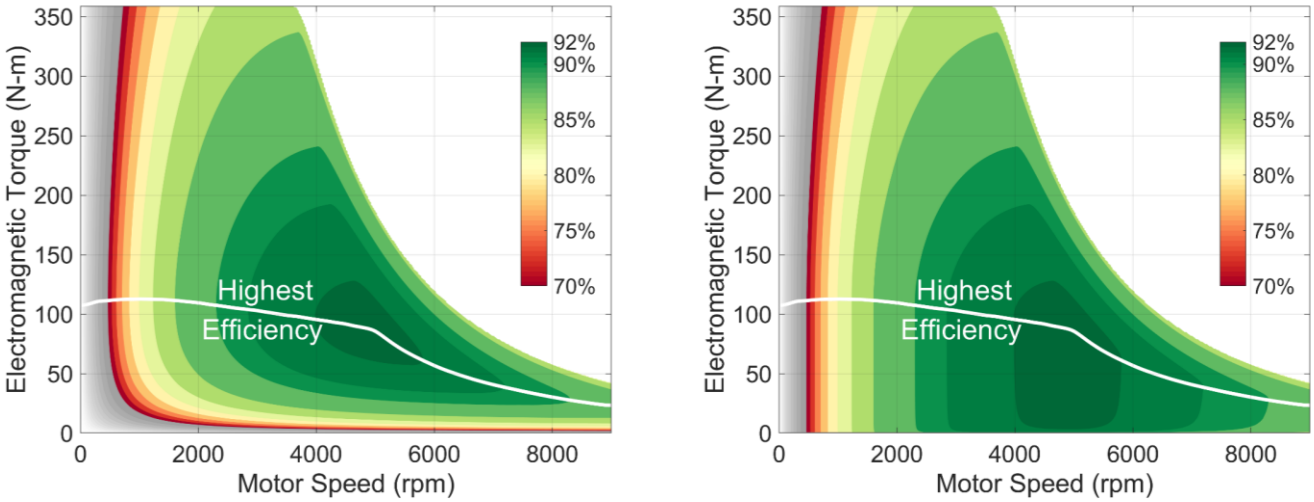


Fig.2 Improved electrical efficiency at low loads from conventional control (left) to DMD (right).

In the example given in the figure, working at a torque request of 12% load is achieved by operating at the more efficient 24% load, but with a 50% duty cycle. This allows the overall efficiency, even at low loads, to approach the levels only previously possible at high loads on the drive cycle.

The resulting motor efficiency is shown in Fig.2 for a 142kW EV powertrain. Efficiency of conventional operation, shown at left, is significantly worse at low loads when contrasted with DMD, shown at the right. For reference, the torque of most-efficient-operation for every motor speed is indicated by the overlaid white line. Torque requests at loads below that line can be improved with DMD. In practice, this means that for most vehicle operation, torque requests below 100 Nm can be improved with DMD. For a large portion of operation during the drive cycle, gains of over 5 or 10% are possible.

3. Loss Analysis

The effectiveness of DMD depends on the relationships between torque, current, and system losses. Detailed discussion can be found from previous publications [3, 4] but are broadly summarized in Fig.3. In the figure, as an illustrative example, conventional operation is contrasted with a motor operating with a simple 50% duty cycle square wave of load.

For most power losses in a motor control system, the relationships with motor current can be categorized into two types: losses that linearly proportional to current, and losses that are quadratically proportional to current. For instance, inverter switching losses are linear, while copper losses and eddy current losses are quadratic. Conduction losses of power switches combine both linear and quadratic terms, while hysteresis losses are nearly linear at low loads and are closer to quadratic at high loads.

The relationship between torque and current differs with motor topologies. For Surface-mounted Permanent Magnet motors (SPMs), torque is proportional to stator current, as expressed in (1).

$$T = pK_e i_q \tag{1}$$

For an SPM at 50% duty cycle operation, the current employed during DMD's intermittent operation is double the peak current that would have been required for conventional motor operation. As a result, the average value of losses that are proportional to current remains the same, but that of losses that are quadratic to current doubles. The net result is, for SPMs, gains are not expected to be found.

In contrast to SPMs, Synchronous Reluctance Motors (SynRMs), utilizing reluctance torque instead of magnetic torque, have a quadratic relationship between torque and stator current.

$$T = p\big(L_d - L_q\big)i_d i_q = p\big(L_d - L_q\big)i_s^2 \sin\delta \tag{2}$$

At the same 50% duty cycle, the peak current increases by only 41.4%, which leads to no change in copper losses. But for losses proportional to current, like switching losses and some part of conduction losses, they are reduced when DMD is utilized.

Another example is Externally Excited Synchronous Motors (EESMs), which have current on both stator and rotor sides. For simplicity, suppose there is no reluctance torque,

$$T = pL_m i_f i_s. \tag{3}$$

The total copper loss of stator and rotor is

$$P_{cu} = R_s i_s^2 + R_r i_f^2. \tag{4}$$

In maximum-torque-per-ampere (MTPA) control, also known as minimal-copper-loss control, the first derivative of total copper loss satisfies condition (5).

$$\frac{dP_{cu}}{di_s} = 0 \tag{5}$$

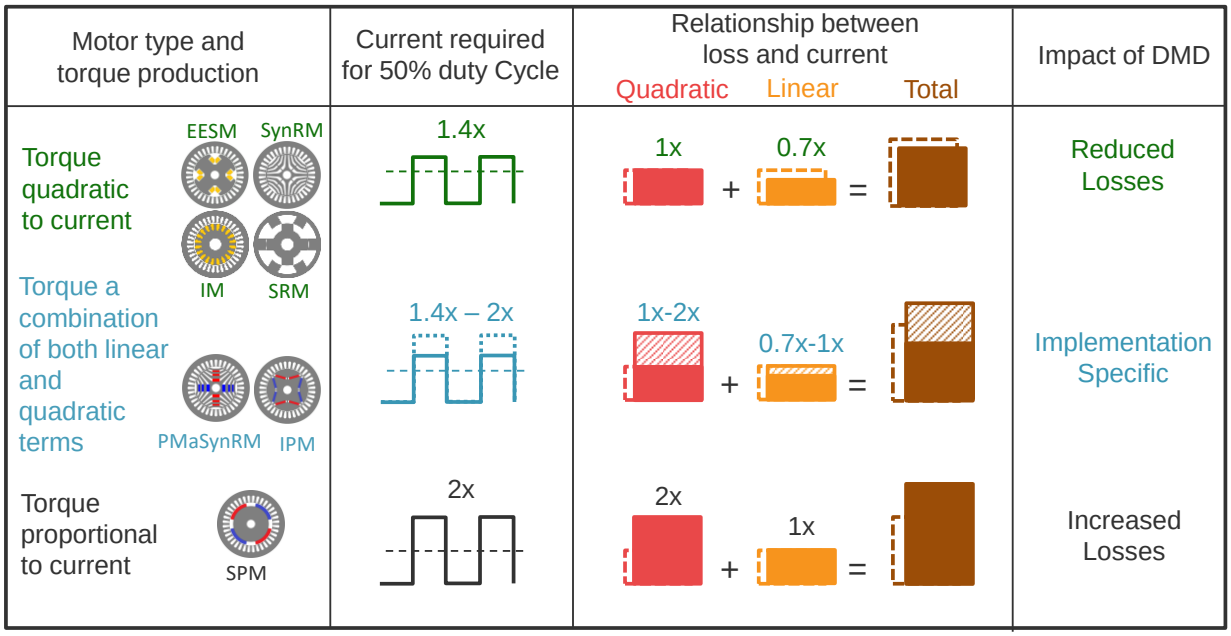


Fig.3 Efficiency improvement possibility of different motor topologies.

By solving (5), it is possible to find out the relationship between torque, stator and rotor currents as follows:

$$T = pL_m\sqrt{R_s/R_r}i_s^2 = pL_m\sqrt{R_r/R_s}i_f^2. \quad (6)$$

This is true only when the motor operates within linear region with no magnetic saturation. It should be noted that even in cases where reluctance torque exists, a similar conclusion can still be achieved although more complicated mathematical deductions are necessary.

Similar to SynRMs, EESMs are characterized by having a quadratic relationship between torque and current in the MTPA region. With this relationship, DMD is also effective to substantially reduce the losses of EESMs.

Other motors, such as Interior Permanent magnet motors (IPMs) and Permanent Magnet Assisted Synchronous Reluctance Motors (PMaSynRMs), combine both magnetic torque and reluctance torque. Torque for these types of motors is a function of both current and the square of current. The ratio between these two factors determines the extent to which DMD can improve efficiency.

From the analysis above, it is known that DMD is most effective for motors without magnets. These types of motors do not contain rare earth metals, and as such eliminate the supply chain volatility inherent in the use of rare earth magnets. On average, since May of 2019, Dysprosium has increased in price by 3.5% every month, or approximately 50% annually [5]. The difficulty in sourcing these magnetic materials is expected to continue indefinitely and will limit the industry's ability to produce high efficiency powertrains across the automotive fleet. Eliminating the use of rare earth metals is an enormous advantage in securing the ability to produce future vehicles. And DMD is an effective way to make up for the efficiency loss due to the removal of magnets.

4. Vibration Suppression Strategy

All vehicle developments have strict constraints on vibration to ensure customer comfort and acceptance. For EVs, this vibration often comes from the torque ripple, a periodic increase and decrease of output torque as the motor shaft rotates. The amplitude, frequency, and phase of the torque ripple are decided by spatial flux distribution and rotation speed. Two exemplar frequencies are shown in Fig.4(c), the first and sixth order harmonics. The torque ripple is not controlled, and thus the vibration induced by it cannot be avoided. This is particularly critical at very low speeds when there are minimal other sources of noise and vibration that could potentially mask operation. At those conditions, the relative kinetic energy of the system means that even modest ripples in torque result in high amplitudes of vibration.

In contrast to the torque ripple that is a common problem in EVs today, DMD algorithms offer control of pulsing strategies, which helps to eliminate perceptible vibration. The modulation frequency of DMD is selectable independently from rotor or vehicle speed. Two factors can be considered. The first is human sensitivity, which is usually between 0.2Hz and 20Hz as shown in Fig.4(a). The second is resonance, which varies from vehicle to vehicle but can be measured by tests. Fig.4(b) shows the Frequency Response Functions (FRFs) of seat track and steering wheel for a

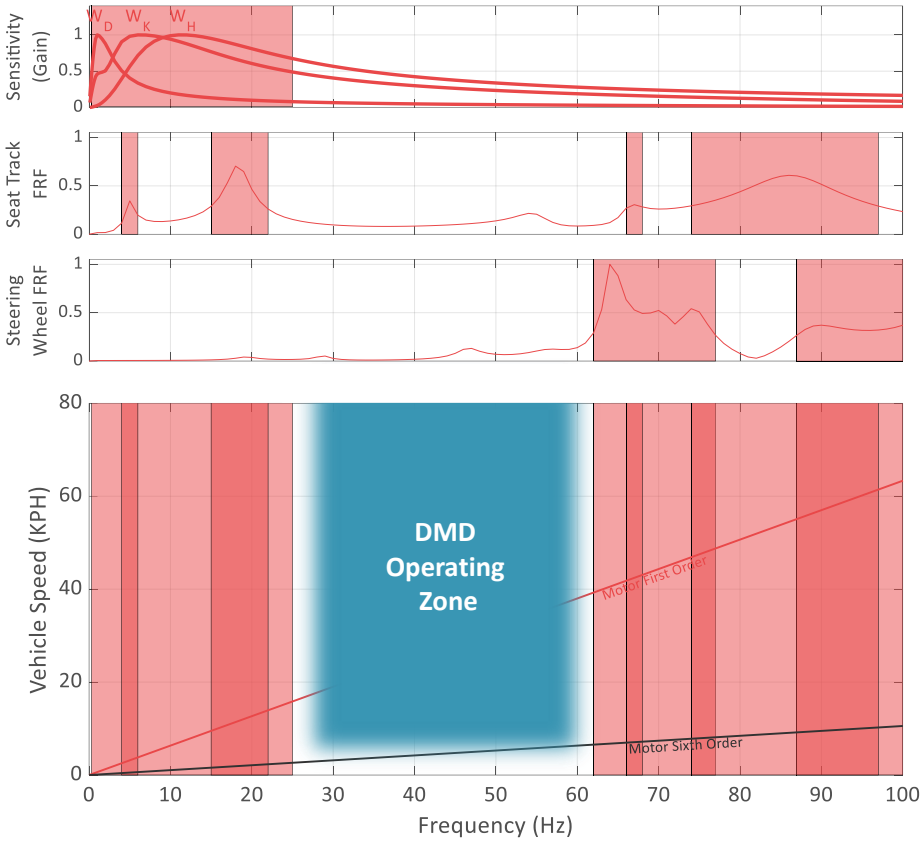


Fig.4 DMD algorithms operates while avoiding resonances and perceptible vibration. (a) top: human sensitivity gain; (b) middle: frequency response functions at seat track and steering wheel for a 2020 Chevrolet Bolt; (c) bottom: DMD operating zone.

2020 Chevrolet Bolt. For both limitations, areas highlighted in red must be avoided. Fortunately, even given these restrictions, there is a generous area in which DMD can operate as shown in blue on Fig.4(c).

Furthermore, it is possible to operate DMD only at the vehicle speeds, torque amplitudes, and operating frequencies at which vibration will not be felt by the passenger. As shown in Fig.4(c), DMD operation is excluded below 10km/h, which avoids the extremely sensitive region of very low speeds.

5. Optimal Motor Control

Selecting DMD modulation frequencies of 20 to 60 Hz requires careful management of transient motor torque. As DMD repeatedly cycles torque on and off to minimize total energy consumption, performance during the transition becomes critical for cumulative efficiency. This, in turn, requires rapid ramping of motor torque between on and off states, as well as a good current tracking to the MTPA curve during the transient. To meet all these requirements, a current control with fast response speed becomes vital.

A current controller's response speed is generally determined by several factors: battery voltage, time constant of the winding circuits, sampling rate, and the controller's cutoff frequency. Nevertheless, even with these physical limitations, it is still possible to obtain the expected DMD control response for most vehicular traction motors, as there are several advantageous factors for control of DMD with electric motors.

First, DMD is primarily used at low loads in the low to medium speed region. Under this condition, there is generally enough DC bus voltage margin for appropriate current control.

Second, for the traction motors that are most suitable for DMD strategy, stator windings usually have time constants which do not hinder fast current response speeds.

Third, the state-of-the-art microcontrollers used for vehicle traction purpose have sampling frequencies several orders of magnitude faster than DMD modulation frequencies. DMD usually operates between 20 and 50Hz, while the microcontrollers on the inverter commonly operate at 10kHz. With such a high rate, even conventional Proportional-Integral (PI) controllers can be implemented with a cutoff frequency of 500Hz. For microcontrollers operating at a slower clock speed, strategies like deadbeat control and direct torque control can be used to achieve the required current response.

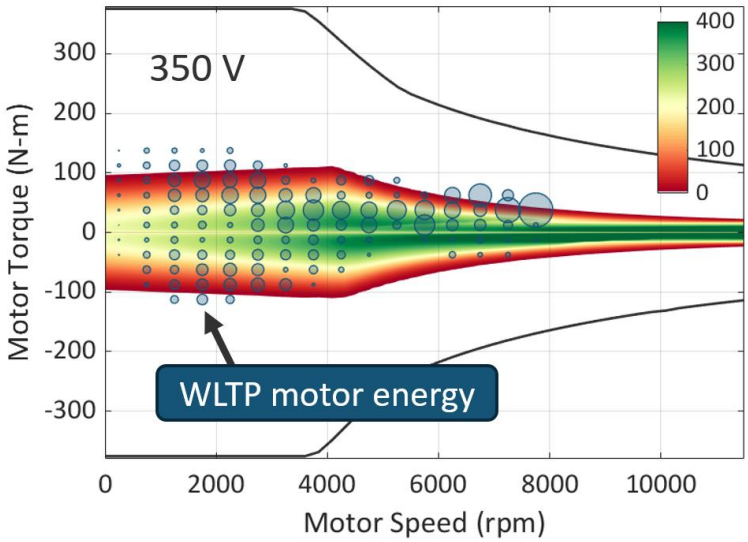
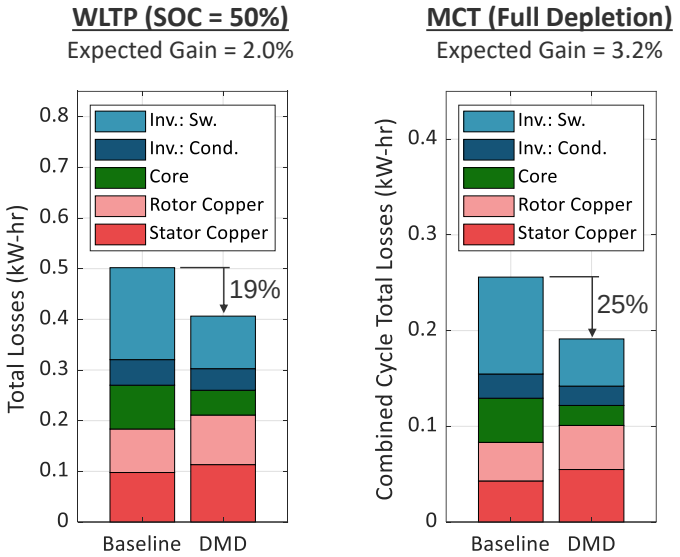


Fig.5 Simulation results of DMD loss reduction in Watts at 350V battery voltage of an 142kW EESM and energy consumption of the motor and inverter system in the WLTP drive cycle.



(b)

Fig.6 Loss breakdown and reduction amount of DMD in the WLTP and MCT drive cycles.

For the above reasons, it is possible to deliver the required transient performance, and achieve the desired DMD modulation frequency.

6. EV Range Improvement

To verify the efficiency improvement made possible with DMD, a simulation study was conducted for an EESM as the traction drive of a 1760 kg subcompact battery EV. Motor parameters are summarized in Table 1. Electrical losses in the motor and inverter were determined using a finite element analysis (FEA) model. Losses at different speed and load conditions with and without DMD operation are compared in Fig.5 with loss reductions by DMD shown as the colored area.

Table 1 Motor Parameters

Parameter	Value
Peak torque	374 Nm
Peak power	142 kW
Peak speed	12,000 rpm

Furthermore, drive cycle simulations of the Worldwide Harmonized Light Vehicle Test Procedure (WLTP) and the US Multi-Cycle Test (MCT) were carried out. Energy consumption on the WLTP is overlaid in Fig.5(a) as circles. The bigger the area of a circle, the

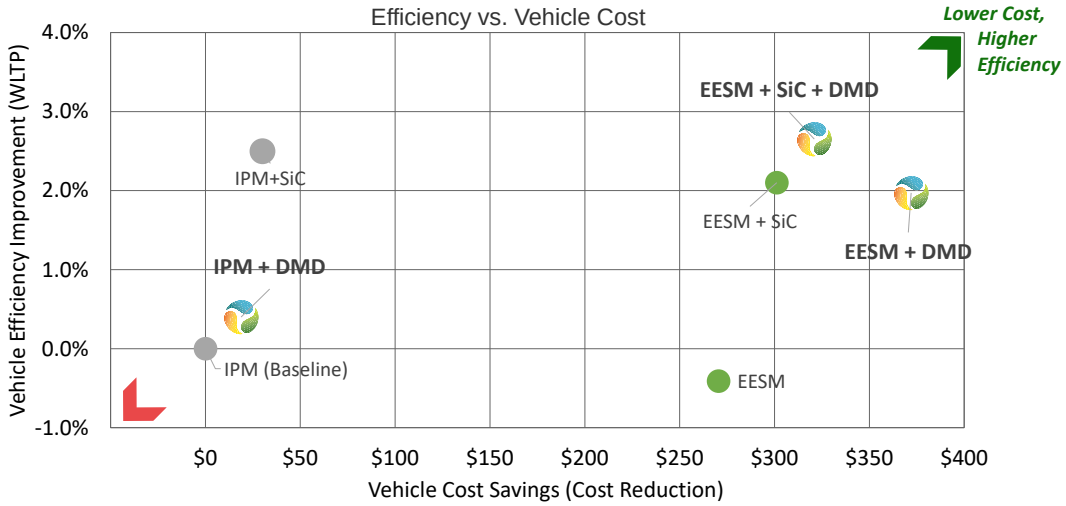


Fig.7 The impact of DMD on an IPM and an EESM for traction drives.

more energy consumed at that speed and load combination. Most operating points are covered in the DMD loss reduction area, implying the effectiveness of the DMD strategy.

The cumulative total loss and breakdown of each type of loss are shown as bar charts in Fig.6. A 19% reduction of losses was observed for the WLTP, and 25% for the MCT. In both cases, large cuts in motor core losses, inverter conduction losses and switching losses offset a slight increase in motor copper losses.

The reduced losses with DMD translate to cycle energy consumption reductions of 2% on the WLTP and 3.2% on the MCT. These are substantial considering they are the result of an easily implementable software strategy.

7. Summary

The impact of DMD on EESM is summarized in Fig.7. Powertrain costs are projected for a battery EV with a range of 400km. Battery size is scaled as appropriate to meet that range. The battery cost is assumed to be $130 per kWh of capacity, and magnet cost is the current 2022 price.

From the figure, it is seen that the EESM and DMD combination is far less expensive and more efficient than the industry standard IPM, with or without an inverter of silicon carbide (SiC) field-effect transistors (FETs). Clearly the benefits brought by DMD have twofold. For end users, it means less energy consumption, and thus cheaper utility bills. For manufacturers, it means less battery capacity for the same distance, and together with the magnet-free design, results in savings of several hundred US dollars on vehicle cost.

All these improvements are achieved with an easily implemented software change in conventional controllers operating with conventional inverters. This makes it possible to improve the efficiency of motors that are free from magnets, and thus significantly reduce the dependence on the rare earth metals that otherwise will limit our ability to electrify the automotive fleet.

8. References

[1] Adamas Intelligence: “Spotlight on Dysprosium”, 2018.

[2] Adamas Intelligence: “Rare Earth Elements: Small Market, Big Necessity”, 2019.

[3] M. Younkins, P. Carvell, J. Fuerst: “Dynamic Motor Drive: Optimizing Electric Motor Controls to Improve Efficiency”, 42nd Vienna Motor Symposium, Vienna, 2021.

[4] Z. Chen, P. Carvell, M. Younkins: “Optimizing Electric Motor Controls with Dynamic Motor Drive”, 30th Aachen Colloquium Sustainable Mobility, Aachen, 2021.

[5] Kitco Metals Inc.: “Strategic Metals”, online: www.kitco.com/strategic-metals/, accessed February 1, 2022.

9. Nomenclature

T: electromagnetic torque

p: number of pole pairs

K_e: back-EMF coefficient

i_d: d-axis current

i_q: q-axis current

i_s: stator current

i_f: excitation current

δ: current angle

L_d: d-axis inductance

L_q: q-axis inductance

L_m: mutual inductance

R_s: stator resistances

R_r: rotor resistance

P_{cu}: copper loss power

Optimal control for serial hybrid coach

A. Delacourt[1], R. Nicolas[1], M. Ponchant[1]

1: Siemens Digital Industries Software, Le campus Carteret – 19 boulevard Jules Carteret 69007 Lyon

Abstract: The objective of this work was to develop closed loop model of a serial hybrid coach. Based on initial inputs from a coach manufacturer, a preliminary system simulation model has been developed. In this configuration, the internal combustion engine (ICE) is not connected to the drivetrain anymore but to an electric generator. This architecture allows the vehicle to decouple ICE performance from the vehicle load.

Nevertheless, with such complex architecture the model cannot be managed easily without a proper energy management strategy. Some specific constraints like zero emission area must be considered to reach a realistic behaviour and dedicated coach mission profile has been implemented using certification tool VECTO (Vehicle Energy Consumption calculation TOol) [1].

By using a dedicated utility within Simcenter Amesim simulation software [2], we were able to generate optimal controller by considering such specificity to fit with coach CO2 reduction objectives.

Furthermore, this controller has been generated automatically thanks to optimization process based on criteria like battery state-of-charge depleting or sustaining strategies.

Finally, integrated hybrid coach simulation model can easily be used to make sensitivity analysis to test several electric motors, internal combustion engines or battery technologies with fast and optimal control.

Keywords: VECTO, hybrid controller, Series hybrid, Coach bus

1. Context

To decrease CO2 from up to 25% and to be allowed to circulate in Low Emission Zones (LEZ); coach needed to go further in powertrain efficiency and electrification. Several propositions have been made in this respect and series hybrid architecture have been chosen. It can achieve long LEZ area without the need of a heavy battery, and the ICE can be optimised to run in a specific area where best efficiency can be obtained. The reference certification tool for heavy trucks, VECTO, will be used to generate cycle dedicated to coach and interurban use, with speed, slope and stops as functions of distance, cycles up to 250km. The study will be performed on Simcenter Amesim software, thanks to its dedicated tool of Hybrid Optimization Tool (HOT) [3]. It is an interactive interface dedicated to get the energetic potential for different vehicle architecture on a given cycle. It can also build the corresponding simulation model.

2. Model generation

Vehicle architecture, series hybrid in this case, offers the choice of various positions for the components, such as a gearbox for the e-motor, the plug-in mode, and the wheel connection for the motor.

E-motor will drive the coach from the rear axle, with hypothesis of a fixed ratio (Rm in Figure1) for the first iteration, then the latter will be replaced by a 2-speed gearbox in a second step.

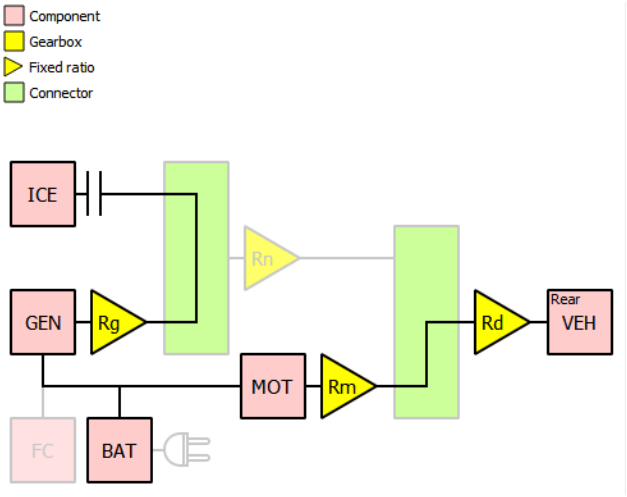


Figure 1: series hybrid architecture for coach bus

Subsystem's parameters have been estimated from real world parts, especially for electric motor/generator, the battery and ICE efficiency (with the help of Engine tables creator tool [4]). The vehicle parameters such as the mass, the roller test bench coefficients or the wheels definition have been taken from an existing vehicle. Mass, with passenger variation, will be a variable to study, especially for vehicle range.

3. Strategy and test case definition

Strategy definition helps to set up the optimal engine torque curve, identifying the best brake specific fuel consumption (BSFC) value for each operating point, transmission, and drivability strategy. Transmission strategy provides the possibility to skip gear or to specify a dedicated transmission mode (Figure2). Regarding drivability setting, it helps setting up the electric penalties for ICE stop and start or

transmission mode change and the macro strategy for battery management such as sustaining or depleting.

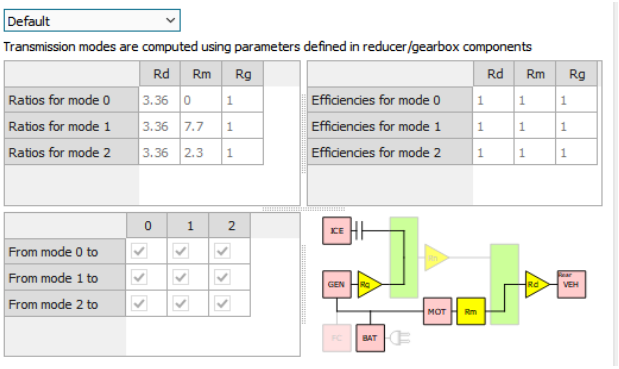


Figure 2 Transmission management

Heavy duty and bus must follow dedicated homologation rules with specific driving cycle adapted to their requirement. Especially by using the European certification tool VECTO for both cycle generation and emissions/CO_2 validations. Thanks to Simcenter Amesim HOT, VECTO cycles can be filled in.

As first example (Figure 3), VECTO coach cycle shows the typical route on a long run coach, doing mostly highway with some steps in city centre, like a high-speed train station. Altitude is also very varying with 600m of difference between the bottom and the top point.

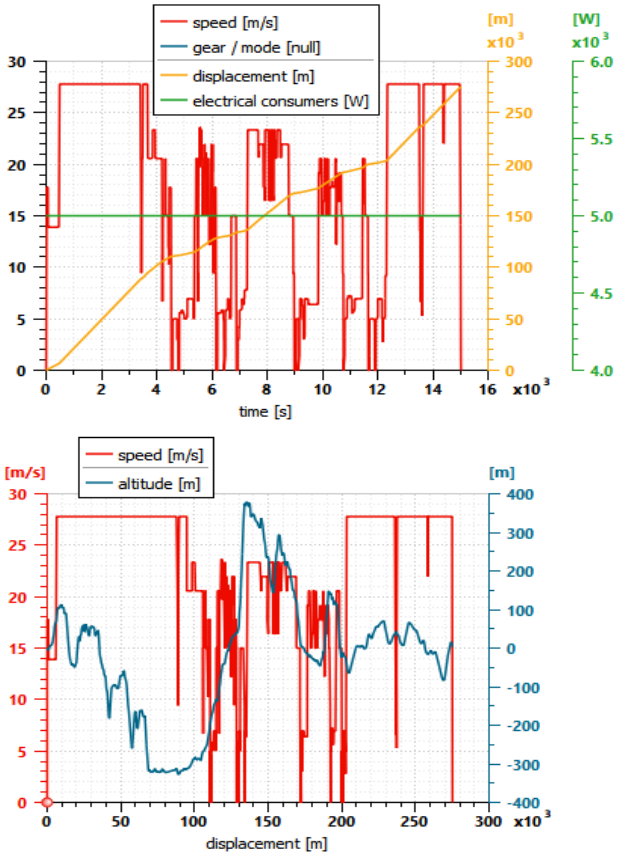


Figure 3 VECTO coach cycle

Regarding VECTO Interurban Cycle (IU) (Figure 4), it represents the exit of a big city, with stops in suburb. Altitude is also a key parameter with 600m of difference between the bottom and the top point. A Low Emission Zone (zone shown in green in Figure 4 where the engine is not allowed to be turned on) is applied based on recent government policies for big cities.

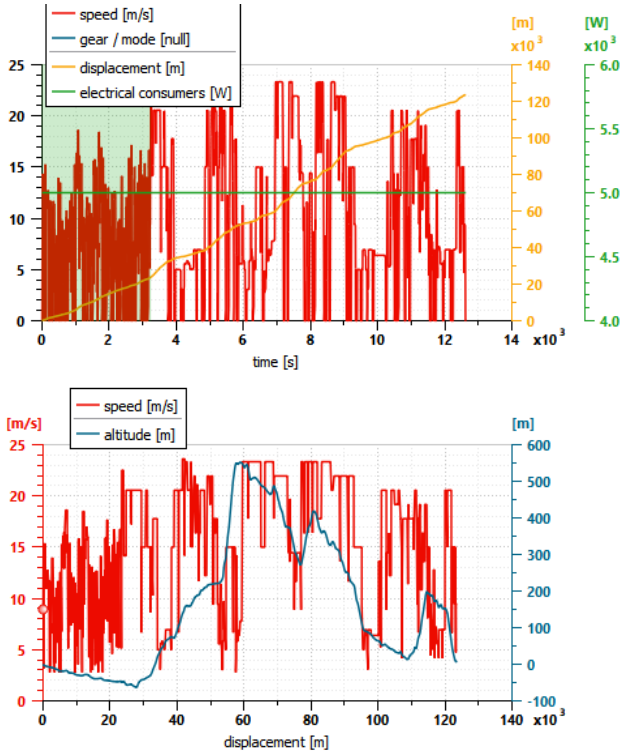


Figure 4 VECTO interurban cycle

4. Different configurations of cycles and gearbox

A comparison has been made between different configurations, with the following model changes:

Number	Cycle	Gearbox
1	Coach	Fixed ratio
2	**Interurban**	Fixed ratio
3	**Interurban + LEZ**	Fixed ratio
4	Interurban	**2-speed gearbox**

Table 1: 4 different configurations

Computation has been performed for each scenario with charge sustaining (start State Of Charge (SOC) = end SOC = 70%) optimisation, all fully managed by the ECMS (Equivalent Consumption Minimization Strategy) [5] which is a component for vehicle control unit dedicated to hybrid powertrain, available with HOT tool.

The focus has been done on the fuel consumption but also the e-motor efficiency, that will depend on driving cycle and gearbox type.

At first, we observe (Figure 5), thanks to HOT post-processing chart, is the different energy demand between the coach cycle and the IU cycle. Both cycles almost have the same duration, but average speed is higher for coach cycle which means more distance and 3 times more energy demand. Therefore, fuel consumption is almost 1L/100km higher for coach. Vehicle range is also lower by 15 km for the coach cycle. Adding LEZ for IU cycle does not make a significant difference for fuel consumption, around 0.1L/100km lower.

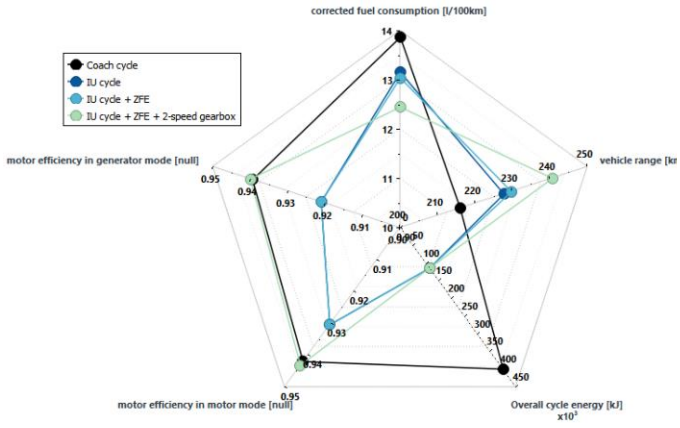


Figure 5 Sipder chart of different architectures

Regarding the implementation of the 2-speed gearbox, an increase of the efficiency of the e-motor, for both generation (+1%) and motor (+2%) modes. The efficiency values of the 2-speed gearbox in IU cycle are similar to coach cycle ones with fixed ratio, because the fixed ratio was optimised for highway where most the coach cycle is running (Figure 6).

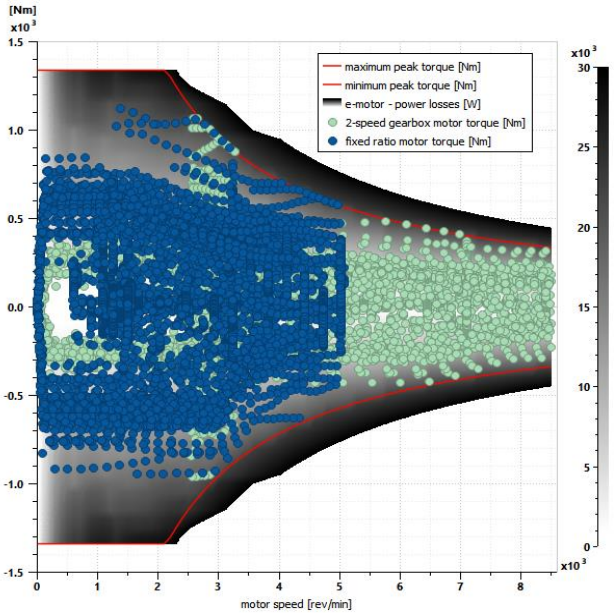


Figure 6 E-motor efficiency map

The two gears have been optimised to reach the e-motor efficiency sweet spot for both highway (longer ratio) and city speed limit (shorter ratio). Therefore, most of the gain is made by having a shorter ratio for city, where the fixed ratio highway was not well matched.

For the whole vehicle, the fuel consumption gain with a two-speed gearbox is around 0.5L/km compared to fixed ratio, and it allows an increase of range of 10km.

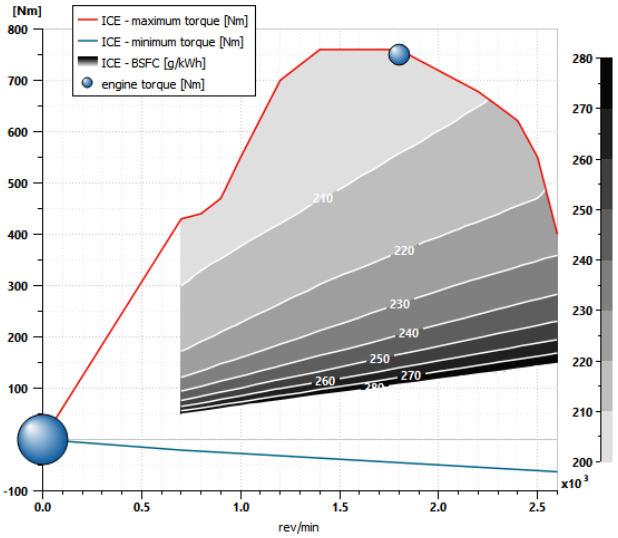


Figure 7 BSFC map

We can also note that (Figure 7), when the ICE is started, it stays on the same operating point, which can be useful to reach higher ICE efficiency by sizing it to run on the specific point.

As a preliminary outcome, a gain of range can also be used to decrease the size of the battery for the same range target, and therefore have a gain of both weight and cost for the entire vehicle. Further gains can be expected by rising the number of gears, at the cost of more complexity.

N°	Cycle	Gearbox	Fuel consumption (L/100km)	Vehicle range (km)
1	Coach	Fixed ratio	13.9	216
2	**Interurban**	Fixed ratio	13.2	228
3	**Interurban + LEZ**	Fixed ratio	13.1	230
4	Interurban	**2-speed gearbox**	12.5	241

Table 2: optimization results

5. Passengers influence on SOC and fuel consumption

Until now, the coach was considered empty of passengers (except the driver). Two more cases will now be studied: no passengers (reference), 25 passengers and 50 passengers. An average weight of 80kg/passenger has been considered.

The computations will be run on the last scenario (IU cycle + LEZ + 2-speed gearbox) since mass will mostly affect the acceleration/deceleration performances.

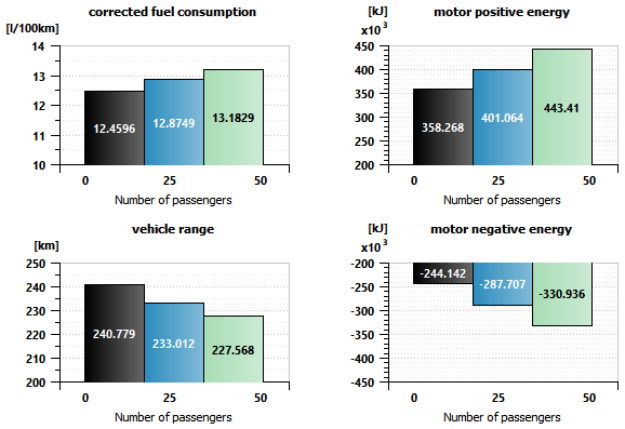


Figure 8 Passengers sweep results

The results show an increase of fuel consumption of around 0.3-0.4L/100km for 25 more passengers (Figure 8). The vehicle range decreases from 240 km with no passengers to 227 km with a full coach (50 passengers).

The most interesting part is the e-motor energy balance. The weight increases the energy needs but also the energy recuperation for almost the same amount.

6. Battery management strategy

Simcenter Amesim HOT allows to choose between 3 different battery management strategies for computation [6]:

- **Sustaining:** to use when initial and final SOC are similar, no specific strategy used.
- **Optimal depleting:** the optimization is done with the constraint to get the final SOC, with the objective of optimal fuel consumption. To use when the final desired SOC is lower than the initial SOC.
- **Regulation depleting:** the optimization is done using preferentially the electric energy at the beginning of the cycle. To use when the final desired SOC is lower than the initial SOC.

In charge sustaining strategy, the final SOC must be equal to initial SOC, 70% in this case. In both charge depleting strategies, the final SOC (40%) is lower than the initial SOC (70%).

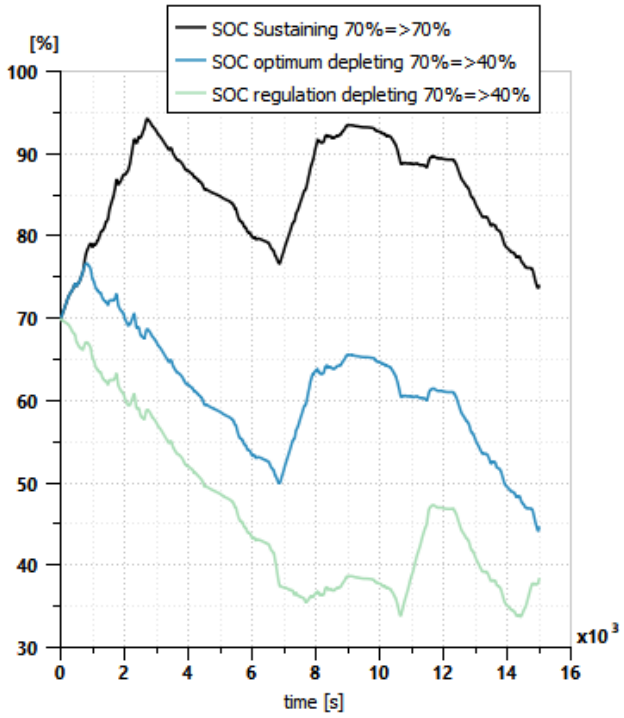


Figure 9 Hybrid strategy SOC comparison

With sustaining strategy, we observe a consistant match between final and initial SOC (Figure 9). Such strategy is mainly used for non-plug-in vehicle. Depleting strategies are advised when the vehicle can be charged because battery energy is preferably used. Fuel consumption is far lower with the depleting strategies (around 6.3L/100km), while sustaining strategy ended at 13.9L/100km.

7. Sketch generation

Once the architecture studies are completed, a Simcenter Amesim model is generated from HOT (Figure 10). All the parameters are directly transferred in the model, as well as maps of the different components. Main subsystems are:

- the driver with the pre-defined driving cycle
- the ECMS (only way to generate it)
- the powertrain

With such a model, sensitivity analysis virtual assessment can be performed to enhance the overall efficiency of the vehicle.

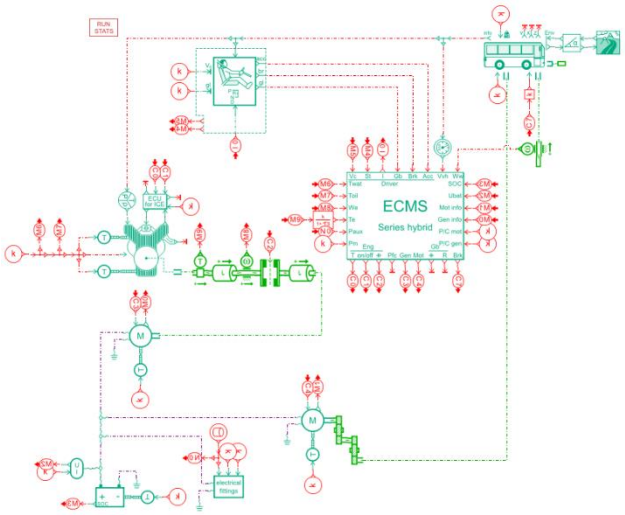


Figure 10 Generated sketch for series hybrid coach bus

8. Conclusion

Due to drastic CO_2 emissions reduction and city policies (diesel ICE ban), being able to provide an electrification solution for any vehicle type is key for the future. Since VECTO certification tool is now used for heavy trucks and buses, simulation software must adapt and find new ways to propose and optimise hybrid powertrains with more advanced controllers and various powertrain architectures. Simcenter Amesim HOT tool demonstrated such a use-case and allows manufacturers, suppliers and third-party users to optimise their powertrains using simulation. It helps to quickly assess and compare powertrain architectures for a given vehicle and save time to further optimise specific components, especially in heavy duty industry.

For this specific coach case, adding a 2-speed gearbox helps increasing the vehicle range and lower the fuel consumption if the coach runs at low speed, high speed cycle tends to not be impacted. Key parameters, like the number of passengers, have been considered and will allow a better and faster battery design.

9. Acknowledgement

This project LONGRUN has received funding from the European Union's Horizon 2020 research and innovation program under grant agreement No 874972



10. References

[1] https://ec.europa.eu/clima/eu-action/transport-emissions/road-transport-reducing-co2-emissions-vehicles/vehicle-energy-consumption-calculation-tool-vecto_fr

[2] https://www.plm.automation.siemens.com/

[3] Dabadie, J., Sciarretta, A., Font, G., and Le Berr, F., Automatic Generation of Online Optimal Energy Management Strategies for Hybrid Powertrain Simulation, SAE Technical Paper 2017-24-0173, 2017, DOI:10.4271/2017-24-0173.

[4] Alix, G., Dabadie, J., and Font, G., "An ICE Map Generation Tool Applied to the Evaluation of the Impact of Downsizing on Hybrid Vehicle Consumption," SAE Technical Paper 2015-24-2385, 2015, doi:10.4271/2015-24-2385.

[5] Manzie C, Grondin O, Sciarretta A, Zito G (2013), Robustness of ECMS-based optimal control in parallel hybrid vehicles, Proc. of the IFAC Symposium on Advances in Automotive Control (IFAC-AAC), Tokyo, Japan, 4-7 Sep. 2013, DOI:10.3182/20130904-4-JP-2042.00120.

[6] Serrao L, Sciarretta A, Grondin O, Chasse A, Creff Y, Di Domenico D, Pognant-Gros P, Querel C, Thibault L (2013), Open issues in supervisory control of hybride electric vehicles: A unified approach using optimal control methods, Oil & Gas Science and Technology, vol. 68, no. 1, p. 23-34, DOI:10.2516/ogst/2012080 (first published in Proc. of the Int. Scientific Conf. on Hybrid and Electric Vehicles (RHEVE), Rueil-Malmaison, France, 6-7 December 2011).

11. Glossary

BSFC:	Brake Specific Fuel Consumption
ECMS:	Equivalent Consumption Minimization Strategy
HOT:	Hybrid Optimization Tool
ICE:	Internal Combustion Engine
IU cycle:	InterUrban cycle
LEZ:	Low Emission Zones
SOC:	State Of Charge
VECTO:	Vehicle Energy Consumption calculation TOol

15 JUNE 2022

COMBUSTION OF HYDROGEN & SYNTHETIC FUELS

Innovating mobility

Competitive technologies, software & web services for a sustainable mobility

ELECTRIFIED MOBILITY

Efficient & cost-effective powertrain electrification solutions for optimum energy efficiency



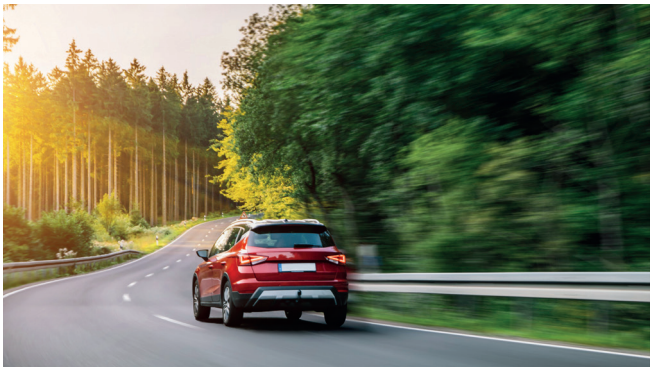


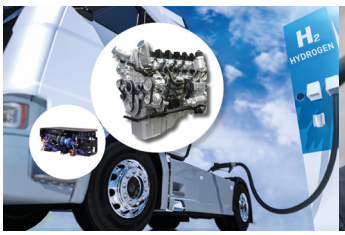
CONNECTED MOBILITY

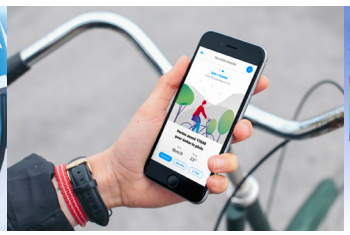
Web services to reduce the environmental footprint associated with mobility and improve air quality

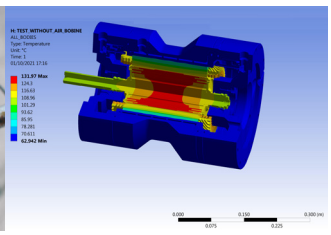
LOW ENVIRONMENTAL IMPACT MOBILITY

Thermal engines & alternative fuels for electrified powertrains









March 2022 - Photos: © IFPEN, X.

Optimizing a Heavy-Duty Hydrogen DI combustion system using experimental and numerical workflow

F. Duffour[1], O. Laget[2], V. Giuffrida[3], T. Valin[4], M. André[5]

1, 2, 3, 4, 5 : IFPEN, 1 et 4 avenue de Bois Préau, 92852 Rueil Malmaison Cedex

Abstract: In the crucial context of global warming, hydrogen is considered as an essential energy carrier to reduce GHG emissions. Its potential applications are numerous and present across all energy sectors. Particularly, our mobility needs are continually increasing: more people, more urban areas and more economic growth in developing countries. All these factors will lead to an upsurge in the energy demand in the very next future. The diversification of the energy sources is urgently required.

Together with electricity and advanced biofuels, Hydrogen mobility has the potential to answer some of the key emissions reduction challenges. Hydrogen may be used to feed a fuel cell, or directly used as a fuel in an internal combustion engine. The latter option offers the advantages of current fossil fuels engines – existing and proven technology, lifetime, controlled cost – with a very low carbon footprint.

The overall objective of the proposed study is to define the specifications of a dedicated Hydrogen direct injection combustion system for a Heavy-Duty application, reach the best fuel efficiency and lowering the raw NOx emissions to minimize the aftertreatment needs.

A complete methodology using experimental data base, 0D and 3D simulation tools has been set up. First, a pre-study with 0D simulations has been realized on two specified operating points (cruise and full load OP) to dimension the air loop system and obtain first results on H2 combustion characteristics (targeted injected mass, maximum in-cylinder pressure, …). Based on this 0D pre-study, 3D simulations have then been realized to optimize the H2/air mixing quality. Thermal management has also been studied tracking high temperature spots (potential pre-ignition and knock areas) in combination with 3D weak coupling between combustion and thermo-mechanical simulations on full load OP.

Finally, the specifications of a dedicated Hydrogen direct injection combustion system for a Heavy-Duty application are defined, including air fluid motion, compression ratio and general settings (piston shape, injector and spark plug positions). The 3D simulation on the final design shows the potential in terms of efficiency and emissions of a dedicated hydrogen direct injection engine compared to a Diesel base piston bowl combustion system.

Keywords: Heavy-duty, Hydrogen, Combustion, 3D CFD Computations.

1. Introduction

The objective of GHG reduction to the carbon neutrality is one of the main challenges for the future of mobility. In order to meet these requirements, hydrogen energy carrier is a key solution for the decarbonation of heavy duty vehicles where an electrical engine (BEV) solution is difficult due to the large distance range needed that would lead to prohibitive mass of battery for energy storage, and refuelling time [1] : medium and heavy trucks, coaches, building and public work. Moreover, the progress in hydrogen production by electrolysis (green H_2) and through Carbon Capture and Storage (blue H_2) combined to the progress in hydrogen storage makes this energy carrier more attractive and political strategy now includes this solution for the future of mobility as the European Union for example [2].

The two main strategies to convert hydrogen energy to mechanical energy are hydrogen fuel cell and hydrogen as a fuel for internal combustion engine. As indicated in the abstract, this latter solution offers the advantages of current fossil fuel engines with a very low carbon foot print [3] and also offers a possible retrofitting of current engine application to hydrogen combustion with few adaptations of the system.

The main advantages of hydrogen combustion rely on his wide flammability range combined with his high flame speed compared to gasoline. Hydrogen offers thus the possibility to burn in high diluted mode with high efficiency [4] and ultra-low NOx emissions.

However, hydrogen shows also some challenging drawbacks for the control of combustion: the low activation energy and the poor volumetric energy density of pure hydrogen force to inject hydrogen as late as possible in the engine in order to avoid pre-ignition/ backfiring [5] and impedes the volumetric efficiency. Therefore, optimization of the mixing process and thermal management to avoid or minimize hot spot inside the combustion chamber is crucial to avoid unwanted hydrogen combustion process, improve combustion stability and reduce mixture heterogeneity and thus NOx.

In the present paper, the specifications of a dedicated hydrogen direct injection system (DI) for heavy duty application will be presented considering a 2.15 litter mono-cylinder engine base.
A complete methodology will be presented beginning from a 0D pre-study to target an injected mass for a cruise and maximum power operating point.
Comparison between Swirl type engine and Tumble type engine in term of mixing will be presented.
Afterwards, correct mixing between air and hydrogen being crucial to avoid potential pre-ignition area due to rich FAER spot [5], optimization by 3D calculations of the direct injection system targeting inside the cylinder head will be presented.
A focus on intake valve law spreading will also be presented to observe the advantages of Miller cycle on hydrogen combustion.
Finally, thermal management using a 3D weak coupling methodology between transient combustion simulation and steady state conduction simulation of the cylinder head will be presented.

2. Engine description and 0D pre-study

2.1 Base engine information and operating points

The multi-cylinder engine target is a 6 cylinders 13 litter engine representative of a heavy-duty application. The base engine chosen for the study is a 2.15 litter displacement mono-cylinder engine. The aerodynamic chosen is Tumble type with a pent-roof cylinder head combined to the Swumble™ concept [6]. This specific choice of aerodynamic is linked to the fact that hydrogen is burning in pre-mixed mode and thus implies a need of high turbulence level to increase the burning velocity, and to improve the turbulent mixing avoiding therefore potential abnormal combustion. Characteristics of this engine are presented in Table 1 and an image of the internal combustion system is presented on figure 1. The base valve laws chosen for this study are respectively 195 spreading and 210 spreading at 1 mm lift for intake and exhaust valve law with a calibration of IVO and EVC of respectively 2 CAD BBDC and 2 CAD ABDC at 1 mm lift. Both valve laws are presented on figure 2 with 720 CAD being the combustion TDC.

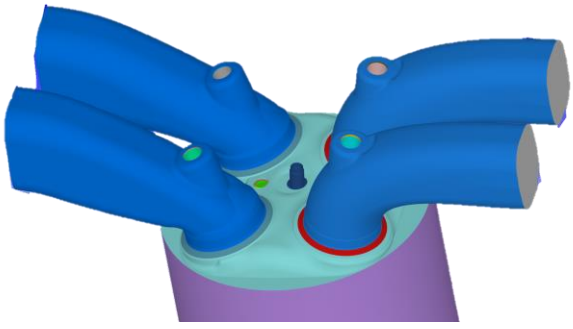


Figure 1: STL of the 2.15 L Swumble™ type engine

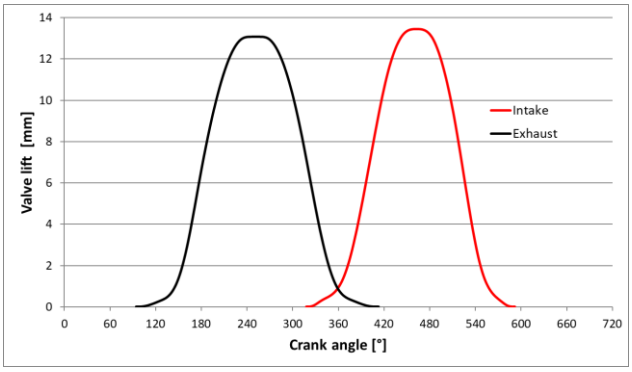


Figure 2: Base intake and exhaust valve laws

Finally, the H_2 is injected directly inside the combustion chamber with injector position in between the intake ports. The injector chosen is a valve gas injector of 40 bar injection pressure, inducing a mass flow rate of around 15 g/s at steady state.

Bore	135 mm
Stroke	150 mm
Displacement	2147 cm^3
Connecting rod length	235 mm
Compression ratio	12

Table 1: Engine main characteristics

Two operating points were studied:

- **Cruise OP:** 1200 RPM x 10 bar IMEP with target FAER 0.4
- **Max power OP:** 1900 RPM x 20 bar IMEP with target FAER 0.5

2.2 0D pre-study

A 0D study was performed to supply the 3D simulations with air loop data (intake and exhaust pressures), representative of a multi-cylinder case, as well as first results on H2 combustion characteristics (targeted injected mass, maximum in-cylinder pressure, …). For that purpose, calculations were performed with AMESim™ for wide variations of different parameters. A schematic of the AMESim™sketch is showed in Figure 3.

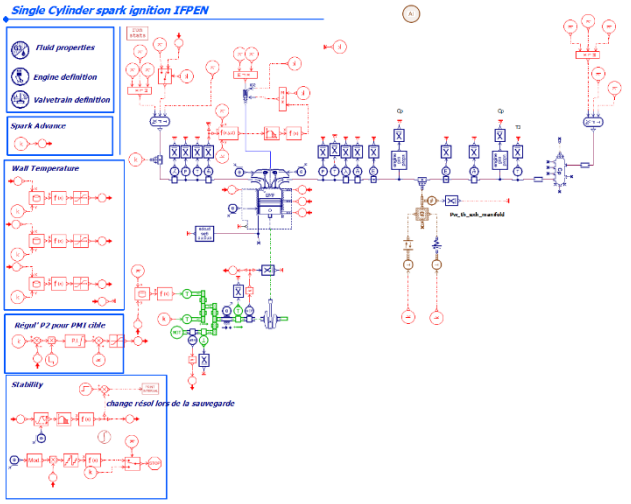


Figure 3: Schematic of the AMESim™ sketch used for 0D simulations

2.2.1 0D input parameters

The following input data were used for the 0D simulations:

- Valves laws: described in Figure 2
- Injection:
  - P_{inj} = 40bar
  - SOI = BDC
  - Injection duration: 20 CAD for cruise operating point, 75 CAD for max power operating point
- Flow coefficients for intake and exhaust valves: based on previous experience and calculations
- Compressor and turbine adapted to the air requirement for the two operating points.

2.2.2 Simulations

Simulations have been performed on the two operating points for wide variations of different parameters and are presented in table 2:

	Cruise OP	Max power OP
T_{in}	317 K	312 K
FAER	0.35 ➔ 0.45	0.5 ➔ 0.6
EGR	0 %	0 %
CA50	5 ➔ 25	5 ➔ 25
CR	10 ➔ 13	10 ➔ 13

Table 2: 0D parameters variations

These 0D simulations supply the 3D simulations with the following data:

- Intake pressure
- Exhaust pressure
- FAER (gas composition)
- Intake temperature
- Exhaust temperature
- Cylinder pressure curve

3. 3D optimization of hydrogen/air mixing

3D simulations were performed with CONVERGE™ for different injector position and targeting inside the cylinder head.

3.1 3D combustion model description

The 3D simulations are realized using the RANS approach. The RNG k-ε model [7] is chosen to solve the turbulence by closing the sub-grid Reynolds stress tensor. Concerning the combustion, the premixed H_2/air flame part and his interaction with turbulence is solved by the Extended Coherent Flame Model (ECFM) [8].

The ECFM turbulent combustion model accounts for the propagation of a stratified premixed flame front in the flamelet regime [9]. A transport equation is solved for the flame surface density and the source term related to the flame surface production by turbulent stretch ($P_1 = \alpha_{ECFM}\Gamma_k$ in ECFM equation) is modelled using an efficiency function. The model constant α_{ECFM} allows then to control the turbulent flame speed.

Concerning the chemistry of H_2, the laminar flame speed and the kinetic of ignition are coupled to ECFM combustion simulation using homogeneous reactor tabulation [10] for various conditions of pressure, temperature, EGR dilution and fuel to air equivalence ratio. The kinetic mechanism of H_2 used for this tabulation is described in [11], and have been already compared to the measurements of Konnov et al. [12] and Kéromnès et al. [13]. This study shows good agreements in term of laminar flame speed and kinetic of ignition for high lambda ratio (>2).

Finally, the spark ignition is accounted through an energy deposition according to the Imposed Stretch Spark Ignition Model (ISSIM) [14] considering the specificities of the ignition system (inductance, resistance, energy deposition, …).

3.2 Physical and numerical setup

The compressible unsteady formulation of Navier-Stokes equations is solved owing to the iterative PISO method. The pressure and the density are coupled according to the Redlich-Kwong-Soave equation of state. Differential critical pressure/temperature and acentric factor between air and hydrogen is used following the methodology of R. Babayev et al [15]. This setup aims at considering temperature increase during hydrogen expansion linked to Joule-Thomson effect. Regarding the spatial schemes, the momentum and species equation are discretized with a second order central scheme while the first order upwind scheme is used for turbulence. The time step

is variable and satisfies a maximal convective CFL number below 5 during exhaust part and 1 for the rest of the cycle. The maximal CFL number based on speed of sound is below 15 during all the cycle. The general mesh strategy follows the same recommendation as the paper of Rouleau et al [5].

Concerning the injection, the numerical injection has been validated and calibrated using experimental Vessel experiment with associated Schlieren and PIV visualizations of the supersonic hydrogen jet. Indeed, knowing that the SOI is close to the BDC (SOI range around 180 to 260 CAD BTDC) with counter pressure varying from 1 to 4 bar (NPR~10), sonic condition are reached inside the injector throat and the expansion from the injector to the combustion chamber is described by the Prandtl-Meyer expansion fan theory of an under-expanded jet of H_2 as described by Hamzeloo et al [16].

Different conditions of counter pressure and temperature representative of the condition inside the combustion chamber during injection have been studied. An image representative of these experiments is shown on figure 6.

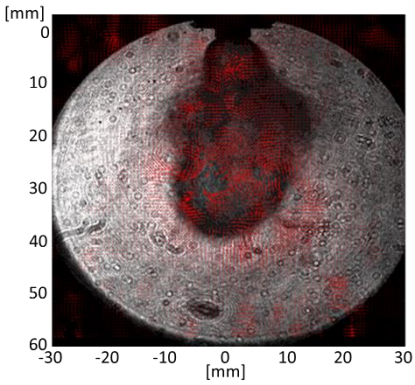


Figure 6: Visualization of the experimental hydrogen jet using PIV combined to Schlieren

Finally, the boundary condition, total temperature and pressure at intake and exhaust are imposed constant and follows the results obtained with the 0D pre-study of paragraph 2.2. Figure 7 presents the injection profile imposed at boundary condition for both operating points.

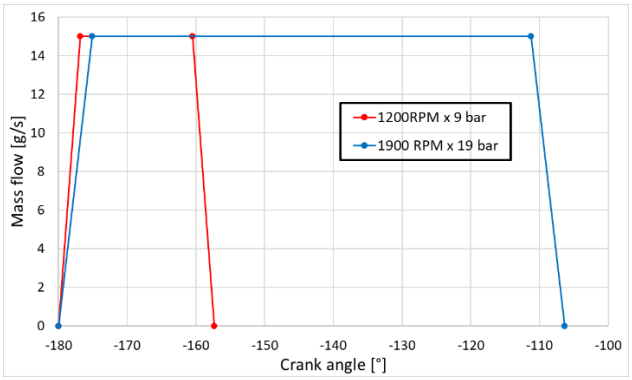


Figure 7: Injected H_2 mass flow rate profiles

3.3 Swirl and Swumble™ hydrogen/air mixing comparison

Aerodynamic and turbulence are first order parameter to improve mixture homogeneity and reduce pollutant emissions for liquid fuel atomization and mixing. To better understand if the impact of turbulence on gas / gas mixing is the same, 3D simulations have been performed considering the Swumble™ engine definition presented in section 2 on typical cruise OP for heavy duty application defined in section 2.1. Comparisons with Swirl type engine definition with the same architecture is realized on the cruise OP. A lateral injector position possible for retrofitting with Swirl type engine is used. An image of this Swirl type engine is presented in figure 8.

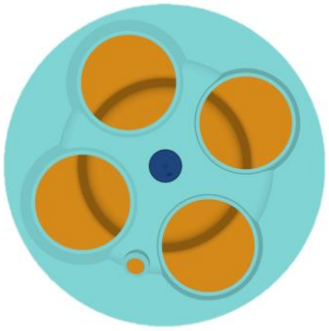


Figure 8: STL of the swirl type engine cylinder head and piston seen from top

Poor mean TKE level can be observed on Swirl type engine with six-time lower TKE level compared to the Swumble™ definition which induces less turbulent mixing between air and hydrogen. Therefore, the mixing, associated to the standard deviation of FAER, is highly impacted and can be observe in agreement with turbulence level in figure 9. Strong heterogeneity of the mixture can also be observed on figure 10 with 3D FAER visualization following y-cut and z-cut plane passing through the spark plug and compared to base Swumble™ configuration.

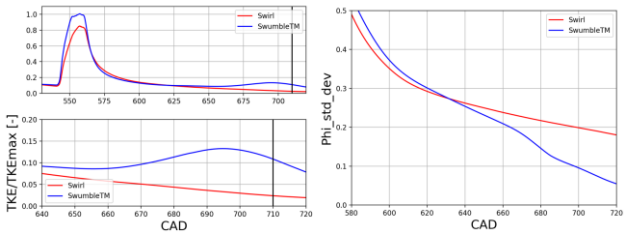


Figure 8: Comparison of TKE and FAER deviation between Swumble™ and Swirl aerodynamics

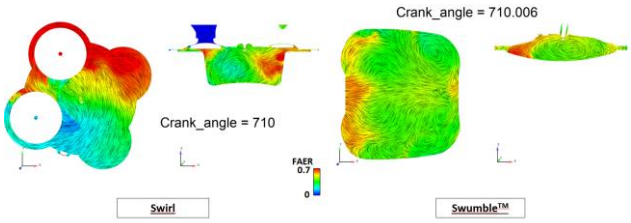


Figure 10: 3D FAER visualization comparison between Swumble™ and Swirl aerodynamic

To conclude, turbulence is a key parameter to improve turbulent mixing between air and hydrogen. Tumble or Swumble™ type motion seem then to be the best solutions to optimize mixing with hydrogen DI engine. However, optimization of the injector targeting by using cap with Swirl type engine and specific injection strategy is also a possible solution to improve mixture quality in a context of retrofit of Diesel engines to hydrogen.

3.4 Optimization of injector targeting

The importance of aerodynamic to improve the mixing process has been presented in the previous part. However, is it possible to further increase this process by optimizing the hydrogen jet targeting by using cap even on a Tumble type aerodynamic with high level of turbulence already observed?

To answer this question, a parametrical study of injector targeting was carried out to optimize the interaction between tumble air motion and supersonic valve jet on the cruise OP. Many targeting has been studied but we are presenting only the results for the best with a comparison to the initial valve type injector without targeting presented in section 2.1.

In terms of global air motion and turbulence, interesting results can be observed when modifying the targeting. A substantial increase can be observed in figure 11 on both Tumble ratio and turbulence level with a gain of 100 % and 66% respectively for the TKE level at second maximum peak of turbulence and for the tumble ratio compared to the base targeting.

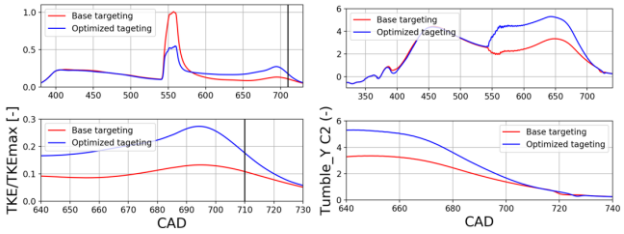


Figure 11: Tumble ratio and TKE comparison for initial targeting and optimized targeting

Consequently, the increase of turbulence implies much more turbulent mixing compared to the base targeting. The global mixing is clearly improved with no more rich spot observed with the optimized targeting as observed on the 3D visualizations of FAER inside the combustion chamber in figure 12.

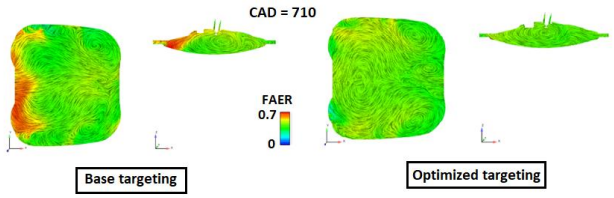


Figure 12: 3D FAER visualization at spark timing between base and optimized targeting (y-cut plane passing through the spark plug and z-cut plane in the middle of the combustion chamber)

To conclude, optimization of the injector targeting thanks to injector cap is important to generate turbulence and improve turbulent mixing. This study shows thus the fact that there is always a required adequation between the injector targeting and the aerodynamic of the engine to optimize mixing.

3.5 Benefit of Miller valve strategy on hydrogen combustion

In order to observe the benefit of Miller valve strategy on hydrogen/air mixing and combustion, three different intake valve spreading have been studied going from standard 180 CAD spreading towards Miller type valve law with spreading of 160 CAD and 140 CAD. The same IVO and EVC have been used for the simulations as indicated in the engine description.

The max power operating point target has been studied for this comparison. Intake and exhaust boundary conditions have been calibrated to target the same trapped mass and 0.5 mean FAER inside the cylinder for all valve laws. Finally, the injection timing has been calibrated for each valve laws to

obtain a SOI at 2mm intake valve lift before IVC and thus avoid hydrogen backflow at intake. The SOI and the level of intake pressure for each valve laws are presented in table 4 and shows reasonable levels of intake pressure considering the compressor studied in 0D pre-study part. The optimized injector targeting has been chosen for this study.

Intake valve laws	SOI (BTDC)	Intake pressure
E180	186 CAD	2.77 bars
E160	208 CAD	3.03 bars
E140	226 CAD	3.42 bars

Table 4: SOI and Intake pressure for each valve laws

Concerning the aerodynamic results, a clear reduction of turbulence when decreasing the intake valve spreading is observed. However, this reduction of turbulence is compensated by the earlier SOI and a correct trade-off in term of mixing seems to be observe with a valve law spreading of 160 as shown on figure 14.

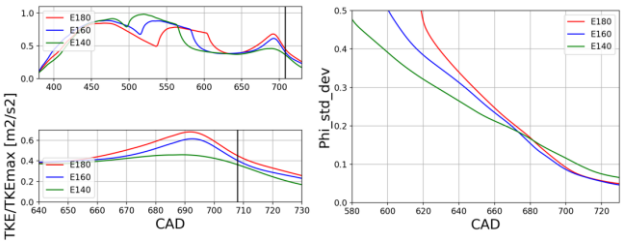


Figure 14: TKE and FAER standard deviation for various intake valve spreading

Finally, Miller thermodynamic cycle induced by reduction of valve law spreading is beneficial for temperature reduction at TDC. A comparison of 3D temperature field between 180 CAD and 140 CAD spreading valve law are presented in figure 15 with a clear reduction of temperature by around 50 K.

A reduction of knock can thus be observed on figure 16 with the ratio of hydrogen mass burnt in auto-ignition mode which allows to monitor the propensity to potential knock of the different configurations. The reduction of temperature induces a reduction of knock level with better CA50 calibration. A global gain of 3 to 4 CAD in CA50 calibration at same 1% auto-ignition limit is observed which represents a 0.5 % indicated efficiency gain.

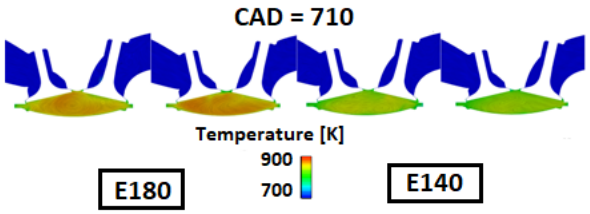


Figure 15: 3D temperature visualization on valve cut planes for 180 and 140 valves spreading

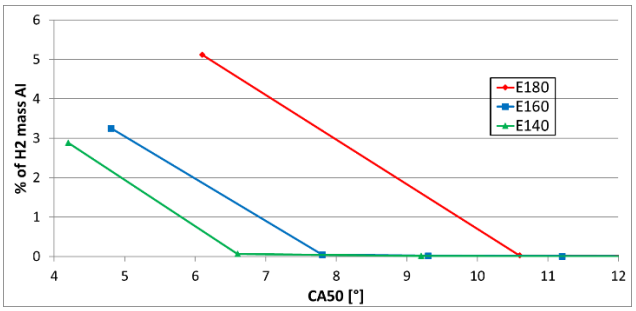


Figure 16: Percentage of H2 mass burnt in auto-ignition function of CA50

To conclude, valve law spreading enable to optimize mixing and reduce temperature inside the cylinder. It reduces mainly knock limitation but can also limit the NOx level.

4. Thermal management study

4.1 Weak coupling methodology

Considering the high sensitivity of hydrogen to auto-ignition phenomena due to his high reactivity when reaching a given level of temperature, thermal management of the combustion chamber is thus mandatory to avoid hot spot and therefore potential knock and/or pre-ignition areas.

The cylinder head cooling system was optimized by a steady state coupling between 3D CFD and 3D Heat transfer FEM modeling using Ansys™ acting as a Conjugate Heat Transfer model of the engine.
Then, a weak coupling strategy between the combustion simulations and the solid heat conduction solver was used. The aim was to feed the thermal conduction calculations with the cycle temporal average of 3D Heat Transfer Coefficient (HTC) map obtained from the combustion simulations. The solid wall temperature field obtained from the steady 3D heat conduction solver is then used as boundary conditions in a new combustion calculation. In the present case, 2 loops were needed to get the convergence between temperature field and mean temporal HTC. A 3D temperature map of the cylinder head obtained by this weak coupling methodology is presented in figure 17.

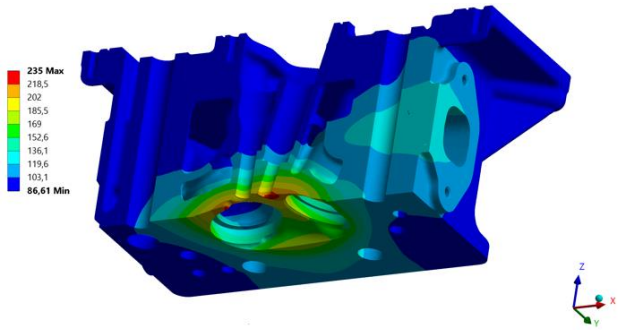


Figure 17: Temperature field inside the cylinder head in °C

Regarding material considerations, due to the thermal conductivity of aluminum, which is four times higher than cast iron, the idea was to evaluate the potential of using aluminum to decrease wall temperatures and subsequently reduce knock or preignition propensity compared to cast iron, was also verified by a FEM thermomechanical analysis to ensure proper operation complying with high in-cylinder pressure.

4.2 3D simulation knock comparison

To better understand the impact of the reduced wall temperature with aluminum on knock intensity, a Spark Advance variation (0 (SA0), 2 (SA2) and 4 CAD bTDC (SA4)) has been realized for both materials. It appears on figure 18 that using aluminum, the knock propensity is reduced by more than 5% at a same CA50 compared to cast-iron.

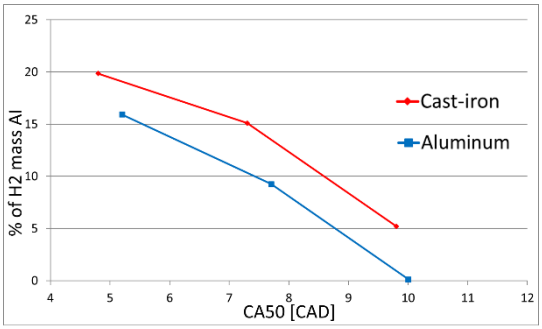


Figure 18: Percentage of H2 mass burnt in auto-ignition function of CA50

To conclude, this part of the study clearly shows the potential of 3D calculation and thermal weak coupling methodology to reduce knock intensity and optimize thermal management of the combustion chamber. The importance of the choice of material is highlighted for the combustion system solid parts. Modification of the design of the cooling gallery using thermal weak coupling is also a possible perspective to further reduce wall temperature and thus knock.

5. Conclusion

A complete study was conducted on a hydrogen DI engine using 0D and 3D simulation tool. Focus has been made on mixing and temperature which are at the origin of potential knock occurrence and high NOx emission levels. Different general conclusions on different topics can be drawn:

- For the engine architecture, solutions with aerodynamic inducing high turbulence level seems to be better for hydrogen / air mixing due to higher turbulent mixing intensity
- Injector positioning and targeting optimization is important to further increase the turbulence by according the global inner-motion to the turbulence
- Miller cycle is beneficial for hydrogen combustion with lower temperature at TDC inducing better phasing of CA50 and reduction of knock
- Weak coupling methodology between 3D CFD and solid heat conduction shows the interest to find the best material properties to avoid abnormal combustion

To conclude, this study clearly shows the potential of coupling experimental and numerical tools to better understand the specificities of hydrogen combustion and then optimize combustion system by assessing the best compromise between different solutions of design, injector integration and even materials.
Finally, mono-cylinder test bench experiments on this specific heavy-duty engine base are planned in the coming months with architecture presented in figure 19.

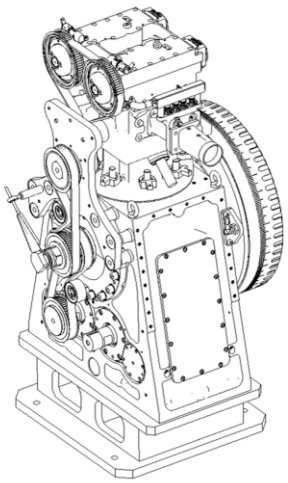


Figure 19: Architecture of the experimental H_2 mono-cylinder engine

6. Acknowledgement

Authors would like to acknowledge their partners, BorgWarner and Tenneco, for the support in this study on injector and spark plug specifications, …

7. References

[1] Forrest, K., Mac Kinnon, M., Tarroja, B., and Samuelsen, S., "Estimating the technical feasibility of fuel cell and battery electric vehicles for the medium and heavy duty sectors in California," *Applied Energy* 276:115439, 2020, doi:10.1016/j.apenergy.2020.115439.

[2] European Commission, "A hydrogen strategy for a climate-neutral Europe," 2020.

[3] Acar, C. and Dincer, I., "The potential role of hydrogen as a sustainable transportation fuel to combat global warming," *International Journal of Hydrogen Energy* 45(5):3396–3406, 2020, doi:10.1016/j.ijhydene.2018.10.149.

[4] Verhelst, S. and Wallner, T., "Hydrogen-fueled internal combustion engines," *Progress in Energy and Combustion Science* 35(6):490–527, 2009, doi:10.1016/j.pecs.2009.08.001.

[5] Rouleau, L., Duffour, F., Walter, B., Kumar, R. et al., "Experimental and Numerical Investigation on Hydrogen Internal Combustion Engine," *SAE Technical Paper Series*, SAE Technical Paper Series, 15th International Conference on Engines & Vehicles, SEP. 12, 2021, SAE International400 Commonwealth Drive, Warrendale, PA, United States, 2021.

[6] X. GAUTROT, M. BARDI, T. LEROY, P. LUCA, L. NOWAK, B. REVEILLE, "SwumbleTM In-Cylinder Fluid Motion for High Efficiency Gasoline SI Engines: development of the second generation," *SIA*, 2020.

[7] HAN, Z. and Reitz, R.D., "Turbulence Modeling of Internal Combustion Engines Using RNG κ-ε Models," *Combustion Science and Technology* 106(4-6):267–295, 1995, doi:10.1080/00102209508907782.

[8] Colin, O., Benkenida, A., and Angelberger, C., "3d Modeling of Mixing, Ignition and Combustion Phenomena in Highly Stratified Gasoline Engines," *Oil & Gas Science and Technology - Rev. IFP* 58(1):47–62, 2003, doi:10.2516/ogst:2003004.

[9] Poinsot, T., "Theoretical and numerical combustion," 2nd ed., Edwards, Philadelphie, ISBN 1-930217-10-2, 2005.

[10] Chevillard, S., Colin, O., Bohbot, J., Wang, M. et al., "Advanced Methodology to Investigate Knock for Downsized Gasoline Direct Injection Engine Using 3D RANS Simulations," *SAE Technical Paper* 2017-01-0579, 2017, doi:10.4271/2017-01-0579.

[11] Xu, B., Chaumeix, N., and West, R., "Compréhension et modélisation de flammes d'essence à fortes charges et fortes dilutions," Thèse de doctorat : Génie des procédés et énergétique : Institut polytechnique de Paris : 2019, 2019.

[12] Konnov, A.A., Mohammad, A., Kishore, V.R., Kim, N.I. et al., "A comprehensive review of measurements and data analysis of laminar burning velocities for various fuel+air mixtures," *Progress in Energy and Combustion Science* 68:197–267, 2018, doi:10.1016/j.pecs.2018.05.003.

[13] Kéromnès, A., Metcalfe, W.K., Heufer, K.A., Donohoe, N. et al., "An experimental and detailed chemical kinetic modeling study of hydrogen and syngas mixture oxidation at elevated pressures," *Combustion and Flame* 160(6):995–1011, 2013, doi:10.1016/j.combustflame.2013.01.001.

[14] Colin, O. and Truffin, K., "A spark ignition model for large eddy simulation based on an FSD transport equation (ISSIM-LES)," *Proceedings of the Combustion Institute* 33(2):3097–3104, 2011, doi:10.1016/j.proci.2010.07.023.

[15] Babayev, R., Andersson, A., Dalmau, A.S., Im, H.G. et al., "Computational characterization of hydrogen direct injection and nonpremixed combustion in a compression-ignition engine," *International Journal of Hydrogen Energy* 46(35):18678–18696, 2021, doi:10.1016/j.ijhydene.2021.02.223.

[16] Hamzehloo, A. and Aleiferis, P.G., "Large eddy simulation of highly turbulent under-expanded hydrogen and methane jets for gaseous-fuelled internal combustion engines," *International Journal of Hydrogen Energy* 39(36):21275–21296, 2014, doi:10.1016/j.ijhydene.2014.10.016.

8. Glossary

CAD: Crank angle degree
BTDC: Before top dead center
SOI: Start of injection
IVC: Intake valve closure
EVC: Exhaust valve closure
OP: Operating point
DI: Direct injection
NPR: Nozzle pressure ratio
TDC: Top dead center
BDC: Bottom dead center
BBDC: Before bottom dead center
ABDC: After bottom dead center
TKE: Turbulent kinetic energy
FAER: Fuel/air equivalence ratio

H2 efficient and near zero emissions operation on a PFI HD single cylinder Diesel ICE

R. Oung[1], F. Foucher[1], J-M. Neveu[2], A. Vucher[2], E. Rieser[2]

1: Université d'Orléans, Laboratoire PRISME, 8 Rue Léonard de Vinci, 45072 Orléans
2: Volvo Group Trucks Technology, 1 Avenue Henri Germain, 69800 Saint-Priest

Abstract: The study uses a heavy-duty single cylinder engine fueled with hydrogen in other to study the excess air ratio, the spark timing and the water injection variations on pollutant emissions and combustion operations. Hydrogen ICE pollutant emissions are limited to small amount of unburnt hydrogen and NOx. While the unburnt hydrogen could be reduced to zero by dedicated exhaust catalyst and lean engine operations. NOx emission could be near zero by adopting lean operation and water injection. The latter two strategies lead to in-cylinder temperature low enough to mitigate NOx formation. Results obtained at low and high load on the single cylinder engine show equivalent power output to it Diesel fueled equivalent. With limited modifications to the Diesel engine, the hydrogen ICE show high efficiency while using port fuel injection and near zero pollutant emissions. The high efficiency measured under lean operation are possible since hydrogen has low activation energy and high laminar flame speed compared to conventional fuel used in ICE. Under low load, the hydrogen ICE operation is set and controlled as conventional spark-ignition engines: spark timing and excess air ratio instead of stoichiometric for gasoline engine for instance. Under high load when high excess air ratio could be difficult to reach, in addition to spark timing, port fueled water injection reduce NOx emissions. Furthermore, the water injection under high load also allow stable engine operations without abnormal combustion events that cannot be avoid without water addition.

Keywords: Zero-emissions, H2 ICE, water injection, indirect H2 injection, lean operation

1. Introduction

Vehicles internal combustion engines (ICE) contribute to global warming through it carbon-kind emissions when they are fueled with fossil fuels. In France, one third of the greenhouse gases originated from transportation [1]. Due to the evolution of pollutant emissions regulations, hybrid or electric vehicles popularize for urban usages since ICE are less efficient under low speeds, stop and start conditions or idle. In order to limit carbon emissions, alternative have to be use in transportation. Additionally, to be the main technology of fuel cell electric vehicles, dihydrogen (H2) can also fuel internal combustion engine. H2 high octane number typically lead to spark ignition engine applications. However, Rosati et al [2] show homogeneous charged compression ignition (HCCI) with air intake temperature (Tin) from 200 °C to 400 °C with a single cylinder optical engine. The engine have a displacement of 0.5 L and run at 1000 rpm. The experiment use H2 direct and port fuel injections (H2-DI and H2-PFI). The need for high Tin can be explain by the low compression ratio (CR) of 7.5. They vary Tin (200 - 400 °C) at a fixed lean air fuel ratio ($\lambda = 1.6$) and the contrary: Tin = 300°C and $\lambda = 1.6 – 2.0$. For a single injection, their results show weaker effects of the temperature sweep on combustion timing than the λ sweep. Yet, H2 combustion timing is not affected as much as conventional fuels: gasoline or Diesel. Adopting high CR can trigger HCCI operations. Lee et al. [3] use a variable CR engine capable of a range from 8 to 45. It displacement is 0.5 L and run at 1600 rpm with H2-PFI. Their results show that cold start operations would need a CR of 32 and 26 otherwise. Those CR are higher than usual conventional engines even for Diesel applications. λ ranges are narrow, typically 0.7 with a CR of 26 and show a indicate thermal efficiency (ITE) above 40 %. Too lean mixture would lead to misfiring operations and too rich mixture trigger knocks or backfires. Ideally, hydrogen combustion product is water but it flames properties can lead to high NOx emissions. H2 combustion due to it low minimum ignition energy (MIE) and wide flammability range compare to gasoline are capable of stable lean operation that is favorable to NOx mitigation. When the in-cylinder mixture exhibit λ higher than 2, NOx emissions are near zero [4–10]. Bleechmore et al. [11] study the λ sweep from 1.1 to 4 at 2000 rpm and to load of 3 and 9 bar of indicated mean effective pressure (IMEP). The engine has a 0.5 L displacement, run at 2000 run with a dual water-H2 direction injection. Their results show a NOx emission peaked at $\lambda = 1.25$ at IMEP = 9 bar and lower values λ above and under. On the IMEP sweep results, NOx emissions are equal or lower to 100 ppm when $2 \leq \lambda \leq 3.3$ depending on the engine load. In that λ range, the ITE vary between 35 % and 50 %. The lean conditions show stable combustions, all measured operating points have an IMEP covariance lower than 4 %. Operating points close to stoichiometric conditions result in backfire and pre-ignition events. Lee et al. [9] investigate a λ sweep from 1 to 2.2 on a 2.4 L four-cylinder engine with H2-PFI with a torque

target of 60 Nm at 2000 rpm. They measure a NOx emissions peak at λ = 1.2. NOx emissions drop significantly at λ = 1.4 and is almost null at λ = 2.2 while showing a 34 % brake thermal efficiency (BTE). Their measurement of the NOx composition show that NO is the dominant form compared to NO2 and N2O for all measured λ. Nguyen et al. [6] investigate a λ sweep from 1 to 2.8 on a 2.4 L four-cylinder engine with H2-PFI and a torque target of 50 Nm at 2000 rpm. Their study compare turbocharged and supercharged solution for boosting the intake. Their results show lower NOx emissions with the supercharger when λ ≤ 2.2 and BTE = 28 % for those lean conditions. Mitigation of NOx emissions can be achieved by other strategies: exhaust gas recirculation (EGR) or water injection [4,5,11–16]. Moreover, those strategies are effective to control backfire and knock. However, management of the correct EGR levels are difficult to execute with high precision especially during transient phases unlike the water injection that can be adjusted precisely and quickly. Verhelst et al. [13] employ EGR in order to limit NOx emissions by lowering the combustion temperature while running the engine under stoichiometric conditions. Their stoichiometric conditions are actually for λ = 0.97 where the excess of H2 is in destination of the three-way catalyst (TWC) to act as a reduction agent. The engine has a displacement of 0.4 L and run from 1500 to 3000 rpm with H2-PFI. Their results show that in order to keep NOx emissions under 100 ppm EGR is only necessary for low load. The maximum load of 12.7 bar of net break mean effective pressure (BMEP) do not need EGR and display a net BTE of 25 %. At lower loads close 4 net BMEP, up to 40 % of EGR is necessary to control NOx emission resulting in a net BTE close to 30 %. The authors also by comparing the stoichiometric + EGR results to and lean burn conditions conclude to better efficiencies achieve overall by lean burn operations. Naganuma et al [16] use a 4.7 L four-cylinder engine with H2-DI for a Japan JE05 emissions test cycle to evaluate the effects of varying injection and spark timing (ST), λ, and EGR rate. Using an EGR rate up to 30 % reduce the mean NOx emission to 1.07 g/kWh instead of 2.02 g/kWh. The reduction by EGR use is not able to lower NOx emissions further because of sudden accelerations from idling included in the test cycle. By using a NOx storage/reduction (NSR) coupled with a Diesel oxidation catalyst (DOC), the mean NOx emission reduces at 0.08 g/kWh. Younkins et al. [5] inject water in the intake runner in a 0.6 L single cylinder engine with H2-DI at 1500 rpm. Without water injection, NOx emissions are near zero when λ ≥ 2.5. At that limit, the engine achieves a net IMEP close to 6 bar and a net ITE just below 42 %. They choose to experiment water injection at λ = 1.67 to obtain from H2 combustion significant NOx emissions. Their results show a decrease of 75 % of NOx emissions when using a single H2 injection and doubling the amount of water introduce (54 mg/cycle instead of 27 mg/cycle) lead to a decrease of the maximum ITE of less than 0.5 %. Dhyani et al. [14] employ both EGR and water injection in a 4.2 L four-cylinder engine run at 1500 rpm with a load of 15 kW and λ = 1.22. Up to 28 % of EGR are use during their experiment and a water to hydrogen ratio (WHR) up to 9.25. Their results show that EGR rate have little impact on the ITE. ITE drop when WHR = 9.25 where the combustion is less stable which could be explain by the increase of the MIE that is more sensitive to WHR than EGR rate. Without applying EGR or water injection, the NOx emission is 10.4 g/kWh. With optimal EGR rate of 25 %, NOx emission is 4.55 g/kWh while it is 0.34 g/kWh for optimal WHR of 7.5.

The previous mentioned studies use light-duty or heavy-duty engines with either stoichiometric conditions combined with EGR in order to lower emissions with a TWC at the exhaust. Otherwise, the lean burn strategy is applied to control NOx emissions by boosting the intake. Water injection is another strategy applied to reduce NOx emissions. Lean burn and water injection are more effective to reduce NOx emission than use of EGR. Water injection in the runner (H2O-PFI) have also the benefit to mitigate pre-ignition, knock and backfire when using H2-PFI. The present experiment study the impact of λ, ST and WHR on engine performances and NOx emissions with a heavy-duty single cylinder of 1.2 L that run at 900 rpm and 1400 under low, medium and high load with H2-PFI and H2O-PFI. Location of both injector help limit the number of modifications needed to the engine head.

2. Experiment set-up and conditions

A Volvo Diesel heavy-duty four-cylinder engine was used as a single cylinder. A summary of the engine geometries is in Table 1.

Geometric compression ratio	12.7
Bore x Stroke [mm]	110 x 135
Displacement [cm3]	1283
Connecting Rod [mm]	212.5 mm
Number of Valves	4
H2 / H2O Injection pressure [bar]	30 / 10

Table 1: Volvo H2 engine specifications

The centrally mounted direct Diesel injector location are modified to fit a cold rated spark plug. Cooling water is heated to 80 °C and was kept under 90 °C during firing operations. Oil temperature and pressure are controlled by the engine circuit. The engine is couple to an electric engine that can ensure motoring operations from 600 rpm to 1900 rpm. An air compressor supplies the engine intake with air that is particle and oil filtered, dehumidified and heated to desired temperature before the heated intake surge tank. Coupled to the exhaust surge tank a valve is

present in order to apply backpressure representative of an exhaust line. K-type thermocouples monitor gas temperatures in the intake surge tank (Tin), in the runner and the exhaust surge tank (Tex). Both intake and exhaust pressure (Pin and Pex) are measured by Kistler 4075A piezoresistive sensors. A Kistler 6125CU20 piezoelectric sensor measures the cylinder pressure and is coupled with an optical encoder ensuring recording of 100 cycles with a 0.1 crank angle degree (CAD) increment. Coriolis mass flow meter measure the air (Emerson CMFS025), water (Bronkhorst M14) and H2 (Emerson CMFS010) flows. A Borg Warner injector supply an H2 spray from a 30 bar circuit. A Plastic Omnium water injection module and control deliver a 10 bar pressure to the water injector.

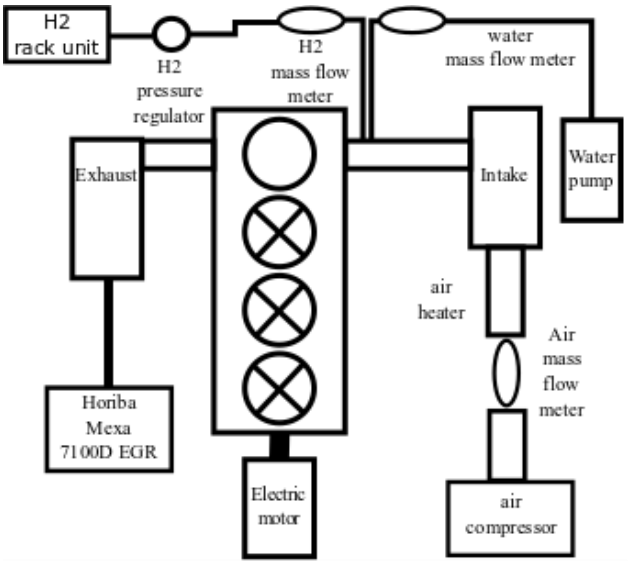


Figure 1: Engine test bench layout

Engine parameter sweeps	IMEP [bar]	Pin Pex [bar]	Tin [°C]	λ [-]	ST [CAD bTDC]	WHR [-]
λ	8	1.6 – 2.4 1.8 – 2.6	30	2.5 - 4	IMEP target	0
ST	8	1.46 1.52	30	2.2	14 - 2	0
WHR	8	1.46 1.52	30	2.2	IMEP target	0 - 5

Table 2: 900 rpm engine settings

Engine parameter sweeps	IMEP [bar]	Pin Pex [bar]	Tin [°C]	λ [-]	ST [CAD bTDC]	WHR [-]
λ	10	1.92 – 3.3 1.92 – 3.3	44	2 – 4.2	MBT	0
WHR	15.5	3.5 3.5	45	3	CA50 = - 15	0 – 4.5
ST	21	3.3 3.25	50	2	10 - 0	3
-	22	3.58 3.5	50	2.2	MBT	3.3

Table 3: 1400 rpm engine settings

All the engine parameters are adjusted by an in-house Labview engine control. The exhaust gas components (O2, CO, CO2, HC and NOx) are measured with a Horiba Mexa 7100D-EGR. Figure 1 show the engine and it environment layout. Table 2 and Table 3 summarized the engine settings of the study. The engine operations are lean in order to avoid the high NOx emissions area located at rich conditions.

3. Results & Discussions

3.1 900 rpm, λ sweep at IMEP = 8 bar

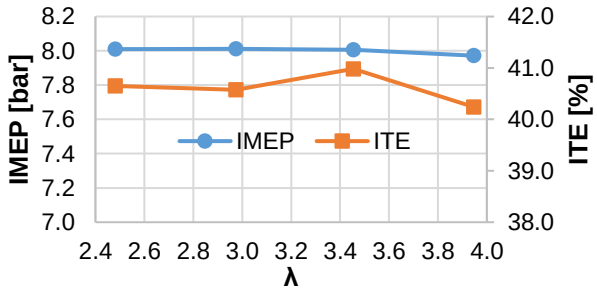


Figure 2 : λ sweep – IMEP & ITE at 900 rpm, WHR = 0, IMEP = 8 bar

Pin increase to vary λ from 2.5 to 4 and the H2 mass flow and the start of injection (SOI) are constants. All conditions have stable operation with an IMEP covariance lower than 1.3 %. Leaner conditions reduce H2 flame speed; it would result in lower IMEP if spark timing (ST) is constant. Slower flame speeds result in an increase of the delay between CA10 and CA50. CA50-CA10 increase from 8.1 to 15.7 CAD at leanest conditions. Therefore, IMEP target of 8 bar is maintain by advancing ST when λ increase. ST vary

from 17 to 38 CAD bTDC for λ = 2.5 and λ = 4 respectively. Consequently, Figure 2 show little influence of λ on ITE; ITE over 40 % is achieved even for λ = 4.

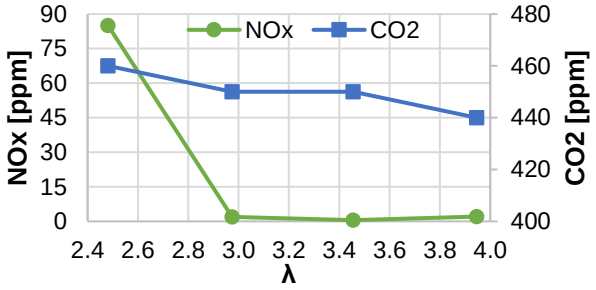


Figure 3 : λ sweep – NOx & CO2 at 900 rpm
WHR = 0, IMEP = 8 bar

show low NOx emissions for λ = 2.5 of 80 ppm. Higher λ results show that NOx emissions is close to null which show that H2 ICE can operate without exhaust after-treatment strategies at medium load without compromising ITE. Tex is at 403 °C for λ = 2.5. That temperature is compatible with selective catalyst reduction (SCR) for active NOx reduction. With higher λ, NOx level might not need active reduction since their values are below 3 ppm. At the beginning of the test day, a motoring reference point show an ambient CO2 level at 430 ppm. CO2 emissions possible formation can originate from the combustion of the residual oil present in the cylinder. Measurements show a decline tendency of CO2 emissions from λ = 2.5 to 5 but the measurement noise of the Horiba AIA-722 CO2 analyzer can be as high as 50 ppm. Those kinds of CO2 emissions are multiple order lower than level measured on Diesel or gasoline engine. A measurement of the CO2 level in the intake surge tank would help to discriminate CO2 of the ambient air and CO2 formed during combustion. Here ST is close to optimal for each λ to account for changes in combustion characteristics. The next discussion focus ST in order to measure influence of ST on engine performances and emissions.

3.2 900 rpm, ST sweep at IMEP = 8 bar & λ

ST move from 14 to 1 CAD bTDC while keeping air and H2 mass flow constant resulting in a constant λ of 2.2. All conditions have stable operation with an IMEP covariance lower than 1.5 %. Figure 4 show that IMEP and ITE are not significantly impact by ST moving from 14 to 10 CAD bTDC. On that range, achieved ITE (> 40 %) is similar to ITE measured during the leaner λ sweep. At ST = 14 CAD bTDC, the combustion is at the knock limit, at which the ST produce combustion with sparse low intensity knock events measured. Consequently, higher ITE might be achieved if knock events could be avoid by water injection, EGR use or λ increase for instance.

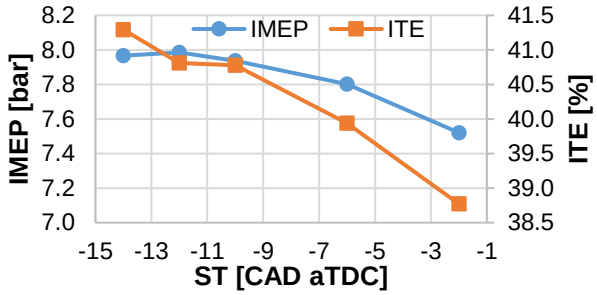


Figure 4 : ST sweep – IMEP & ITE at 900 rpm
λ = 2.2, WHR = 0, IMEP = 8 bar

Moving ST from 14 to 1 CAD bTDC result in increase of CA50 from 4.9 to 9.6 CAD aTDC and also of the delay CA50-CA10 from 5.6 to 5.9 CAD. Those results show that λ near the spark plug might be similar the charge mixture might not be totally homogenized in the whole cylinder volume. Moreover, when ST move closer to TDC at 6 and 2 CA bTDC, CA50 and CA50-CA10 further increase which reduce IMEP and ITE. The maximum NOx emissions of 288 ppm can be lower significantly (89 %) by delaying ST, which lower IMEP and ITE as shown in Figure 5.

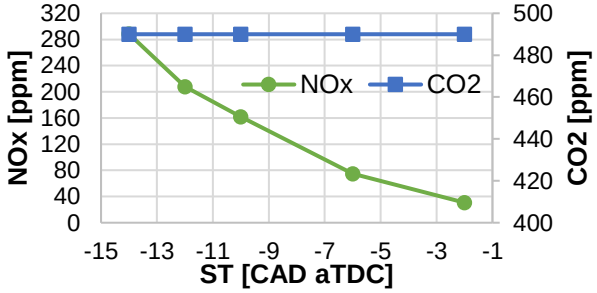


Figure 5 : ST sweep – NOx & CO2 at 900 rpm
λ = 2.2, WHR = 0, IMEP = 8 bar

Without sacrificing engine efficiency, a reduction of 46 % is achieved. At ST = 10 CAD bTDC, NOx is measured at 162 ppm which is almost twice more than the NOx level (85 ppm) measured at λ = 2.5 in the previous λ sweep. λ is a more efficient way to reduce NOx emissions while maintaining high ITE. The higher λ set for the ST sweep increase CO2 emissions to 490 ppm. The CO2 level is constant over the ST range. The increase of NOx and CO2 emissions can be directly link to higher combustion temperature obtain with λ = 2.2 than λ = 2.5 and above. The exhaust gases temperature gap between ST = 14 and 2 CAD bTDC is 30 °C and increase from 416 °C the more ST move closer to TDC. This minimal exhaust gases temperature is a 100 °C higher than the minimum measured at λ = 5. At λ = 2.2, ST and therefore IMEP and ITE are limited by knock events. Water injection is discussed in the introduction as an effective way to avoid knock events. The next focus on WHR to measure it influence on ITE and NOx emissions.

3.3 900 rpm, WHR sweep at IMEP = 8 bar & λ = 2.2

The experimental set-up utilize H2O-PFI, increasing water injected mass can change the volumetric efficiency since the air is regulated by pressure feedback. IMEP target of 8 bar is maintain by correction of ST as WHR increase. All tested WHR produce stable operation with an IMEP covariance lower than 0.9 %. With a thermocouple located just before the intake valve stems, we measure a noticeable drop the intake mixture as soon as water injection is activated. Without water injection, the air close to the intake valve stems are higher (43 °C) than in the intake surge tank which is kept at 30 °C. With water injection, the temperature drop to 34 °C with WHR = 0.5 and stay constant for higher WHR.

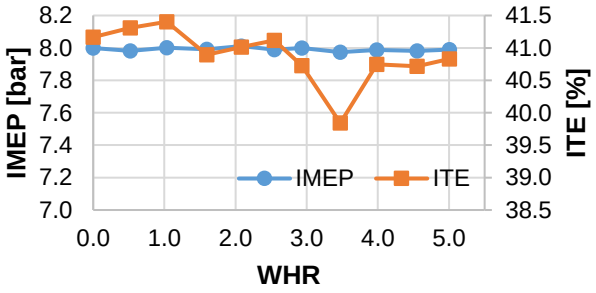


Figure 6 : WHR sweep – IMEP & ITE at 900 rpm
λ = 2.2, IMEP = 8 bar

With Figure 6, we can conclude that water injection does not have detrimental impact on ITE. The lowest ITE at WHR = 3.5 can be explain by a ST not advanced enough to compensate for higher water introduction into the cylinder. ST is constant between WHR = 2.9 and 3.5. When discarding WHR = 3.5, the gap between the maximum and minimum ITE is 0.7 %. Increasing WHR increase CA50-CA10 delay from 5.7 to 8.1 CAD. Water slow the flame as increase of λ does. Previous results show that knock events limit H2 combustion: ST = 14 CAD bTDC at λ = 2.2. With water injection ST can be safely set to 14 CAD bTDC from WHR = 2.0 and to 18 CAD bTDC at WHR = 5.0. When λ increase, previous results show a reduction of NOx emissions.

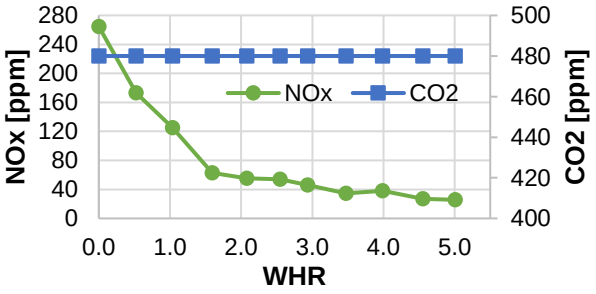


Figure 7 : WHR sweep – NOx & CO2 at 900 rpm
Λ = 2.2, IMEP = 8 bar

Figure 7 show a rapid decrease of NOx level up to WHR = 1.6: 24 % reduction from 264 ppm without water. Then from WHR = 1.6 to 5.0, NOx reduction is 41 %. With WHR = 5.0, the lowest NOx level achieved is 26 ppm. The quick decrease of NOx level with low WHR might imply that most of the water turn into vapor when WHR < 1.6 which reduce the charge temperature and consequently limit NOx formation. With WHR > 1.6, part of the injected water droplet might coalesce during the injection or compression and stay in liquid form while the smallest droplet vaporize. Figure 8 show the exhaust gases temperature does not decrease before to WHR = 1.6. This might validate that most of the injected water is vaporized during combustion when WHR < 1.6. From that threshold, the exhaust temperature reduces linearly with the increase of WHR attaining it minimum of 395 °C at WHR = 5.0. Further increase of WHR might lead to NOx emissions as low as lean conditions results (almost null between λ = 3 and 4). However, a study on water might be more beneficial to ensure that water droplet coalescence is limited.

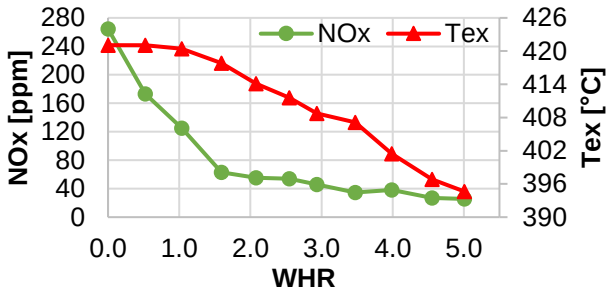


Figure 8 : WHR sweep – NOx & Tex at 900 rpm
λ = 2.2, IMEP = 8 bar

3.4 1400 rpm, λ sweep at IMEP = 10 bar

Pin increase to vary λ from 2.0 to 3.6 and the H2 flow is adjusted to meet the target IMEP of 10 bar. All conditions have stable operation with an IMEP covariance lower than 1.5 %. ST is set for MBT at each λ except for λ = 2 at which knock events limit ST. Consequently, ITE is the lowest of the five measured conditions as shown in Figure 9.

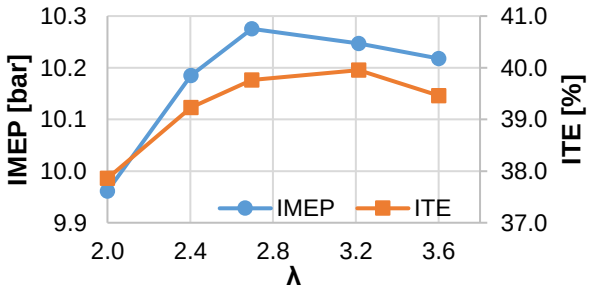


Figure 9 : λ sweep - IMEP and ITE at 1400 rpm
IMEP = 10 bar

For λ > 2, ITE gap between the highest and the lowest value (39.2 %) is 0.8 %. Previous results, at 900 rpm and IMEP = 8 bar, ITE stay almost constant between similar λ range of 1.6. Keeping the target IMEP of 10 bar and setting ST for MBT require moving it further from TDC (see Figure 10) in order to account for slower flame at leaner conditions. Between λ = 2 and 3.6, ST move from 2 to 33 CAD bTDC. The slower flame speed lead to an increase of CA50-CA10 delays which grow linearly from 6.6 to 12.9 CAD.

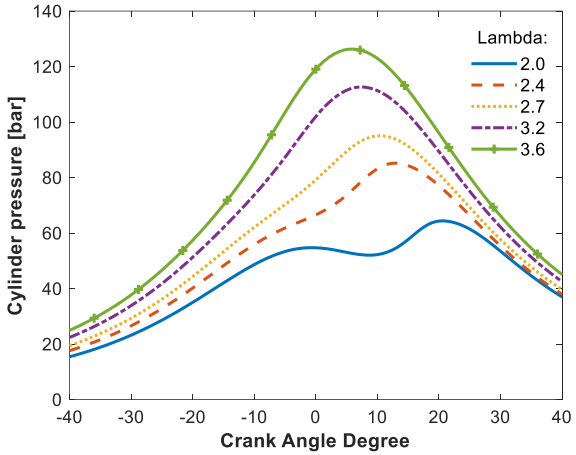


Figure 10 : λ sweep - 1400 rpm & IMEP = 10 bar
Mean cylinder pressure

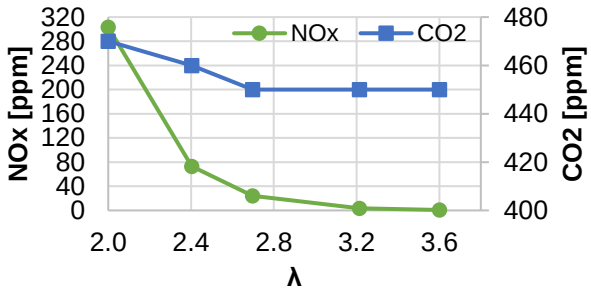


Figure 11 : λ sweep - NOx and CO2 at 1400 rpm
IMEP = 10 bar

Figure 11 indicate that λ = 3.2 and 3.6 conditions achieve near zero NOx emissions. From λ = 2 and 2.4, NOx level reduction is 24 % from 303 ppm. At λ = 2, Tex is 547 °C and drop at 437 °C at λ =2.7. This temperature range enable an active reduction system that could lower NOx level close to zero. As discuss for the λ sweep at 900 rpm, CO2 emissions reduce as λ increase from λ = 2 to 2.7. For leaner conditions, CO2 level measure at 450 ppm which might imply that with the higher combustion temperature at λ = 2 is burning more of the residual lubricating oil than leaner conditions. The next discussion focus on WHR sweep at a higher IMEP and leaner conditions.

3.5 1400 rpm, WHR sweep at IMEP = 15.5 bar & λ = 3.0

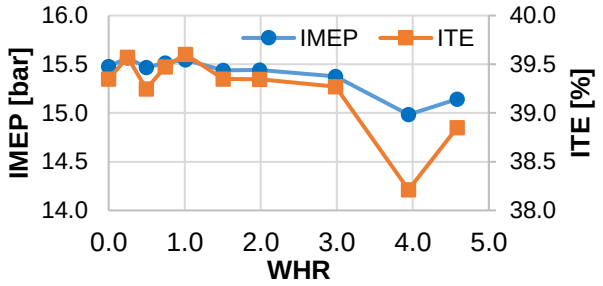


Figure 12 **:** WHR sweep - IMEP and ITE at 1400 rpm
IMEP = 15.5 bar

WHR increase from 0 to 4.6 with settings to have an IMEP of 15.5 bar and similar combustion timing tracked by CA50 set at 15 CAD aTDC. For WHR < 3.9, IMEP covariances are lower than 2.8 % and increase to 4 and 3.6 at WHR = 3.9 and 4.6 respectively. Figure 12 show that IMEP and ITE drop from WHR = 3. With high WHR, setting of CA50 at 15 CAD might not be optimal because of the slower combustion. Figure 13 show the cylinder pressure traces for different WHR which might confirm the previous hypothesis.

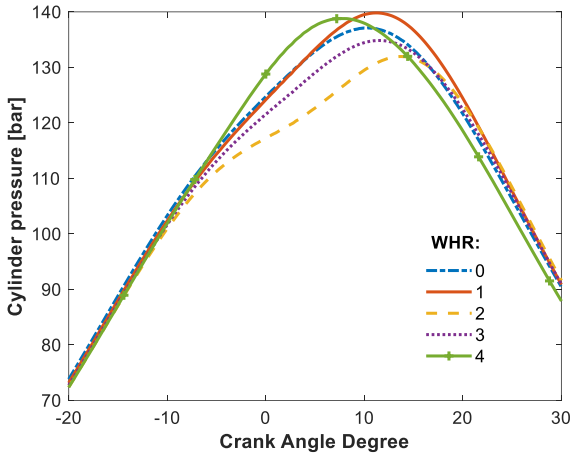


Figure 13 : WHR sweep - 1400 rpm & IMEP = 15.5 bar
Mean cylinder pressure

Previous discussion for 900 rpm show near constant IMEP and ITE up to WHR = 5.0 when ST is set for matching the target IMEP. Figure 15 show that water injection drop Tex linearly as WHR increase while at 900 rpm, the linear temperature drop happen from WHR = 1. This behavior might be explain by lower combustion temperatures for all measured WHR. NOx emissions are almost null even at WHR = 0. On Figure 14 CO2 emissions range level vary between 500 and 520 ppm. Since almost no NOx are formed during combustion, this might signify that applied

engine settings during WHR sweep lead higher amount of residual oil staying in the cylinder. Consequently, despite the low combustion temperature more oil burn resulting in higher CO2 emissions. The next discussion focus ST effects at an IMEP of 21 bar, which correspond to high engine load conditions.

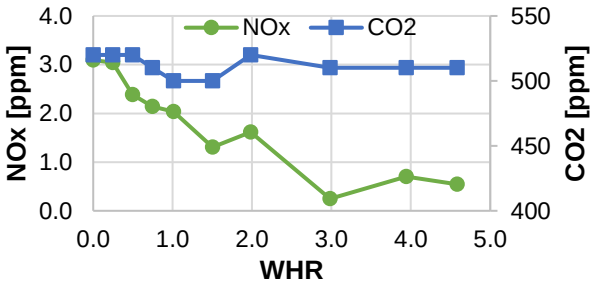


Figure 14 : WHR sweep - NOx and CO2 at 1400 rpm
IMEP = 15.5 bar

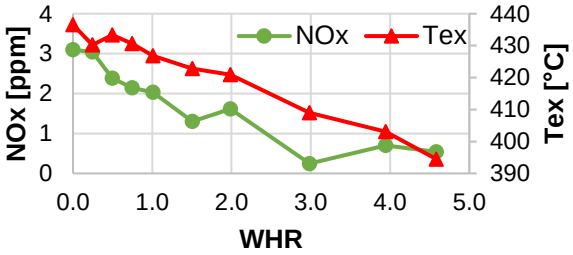


Figure 15 : WHR sweep - NOx and Tex at 1400 rpm
IMEP = 15.5 bar

3.6 1400 rpm, ST sweep at IMEP = 21 bar, λ = 2.0 & WHR = 3

Since the target IMEP is high, WHR = 3 is chosen to avoid abnormal combustion, knock or pre-ignition, during ST sweep. The IMEP target is 21 bar and ST move from 10 (knock limit) to 0 CAD bTDC while maintaining λ at 2. At the knock limit, the combustion is most stable with an IMEP covariance at 1.7 %. For ST = 5 and 0 CAD bTDC, IMEP covariance increase to 3.5 et 3.7 %. Figure 16 show that IMEP and ITE do not draw a linear sensitivity to ST. Moreover, there is no range where IMEP and ITE stay constant while moving ST closer to TDC. During ST sweep at 900 rpm, IMEP and ITE stay constant from ST = 14 to 10 CAD bTDC. Engine setting might need smaller increment to find the ST range where engine performance remain unchanged. However, IMEP and ITE increase when ST = 0. This behavior could be explain by an inhomogeneous charge in the cylinder and/or changes of the local λ near the spark plug. CA50-CA10 delays show little gap between tested ST: 9.1, 10.2 and 9.4 CAD for ST = 10, 5 and 0 CAD bTDC respectively. The CA50 variation is more significant starting from 17 CAD aTDC at ST = 10 CAD aTDC then increasing to 23.8 CAD aTDC before reducing to 19.2 CAD aTDC at ST = 0 CAD aTDC. Despite H2-PFI, the high amount of H2 injected in the cylinder at high load need a study on the mixing process of air and H2.

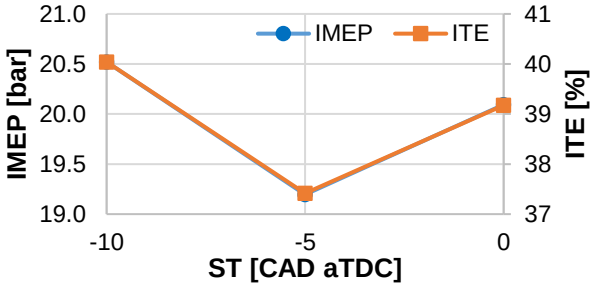


Figure 16 : ST sweep - IMEP and ITE at 1400 rpm
IMEP = 21 bar

NOx emissions of Figure 17 show the same behavior than IMEP and ITE with lower level obtain for ST = 5 CAD bTDC. CO2 emissions vary between 540 and 550 ppm. Previous results show that CO2 emissions might be related to IMEP for same engine speeds and λ since it increases from 470 ppm to 520 ppm. NOx level maximum of 234 ppm is lower than 303 ppm maximum measured for an IMEP of 10 bar and λ = 2. From previous, we could expect that NOx level might be further reduce with WHR > 3 and λ > 2 that is applied for the next discussion.

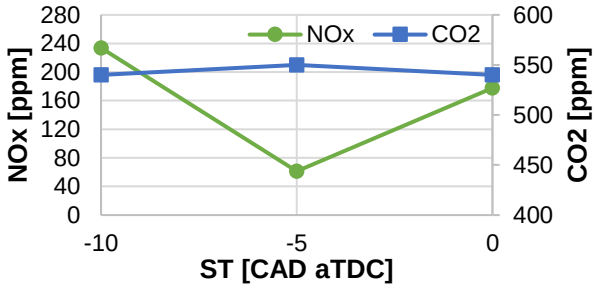


Figure 17 : ST sweep - NOx and CO2 at 1400 rpm
IMEP = 21 bar

IMEP	ITE	NOx	CO2
22.1 bar	42.3 %	101 ppm	510 ppm

Table 4 : 1400 rpm, IMEP = 22 bar, λ = 2.2
WHR = 3.3 & ST = - 15 CAD aTDC

Table 4 show H2 ICE with H2-PFI and H2O-PFI is able to operate at high engine speed and load with an ITE of 42 % while keeping NOx emissions at a low level. As Figure 18 show high intake pressure is required to operate at λ = 2.2. This lead to high cylinder pressure during compression. In order to operate at that IMEP with near zero NOx emissions, higher intake pressure or WHR might be needed. As discussed in the introduction, using EGR might also reduce the NOx and limit knock events but the present experimental set-up does not allow that possibility yet.

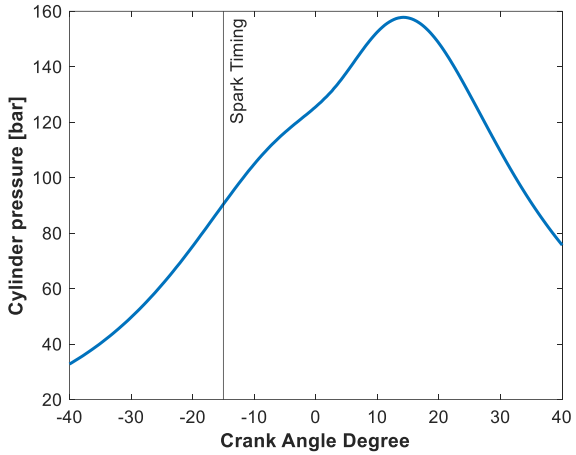


Figure 18 : 1400 rpm, IMEP = 22 bar
λ = 2.2WHR = 3.3 & ST = - 15 CAD aTDC
Mean cylinder pressure

4. Conclusion

Present study use a Diesel single cylinder engine with port fuel injection of H2 and water. The only modification of the engine compare to it Diesel equivalent is replacement if the injector for a cold rated spark plug. The engine is run at 900 rpm and 1400 rpm with engine load ranging from 8 bar to 22 bar of IMEP. The exhaust gases are analyzed in order to track NOx emissions, the main pollutant of H2 combustions. Exhaust gases analysis show that CO2 is present. The small amount measured, maximum at 550 ppm at IMEP = 22 bar, indicate that is CO2 come from the combustion of the residual lubricating oil present in convention engine. Experiment with an optical engine or dry lubrication or other lubricating oils might confirm that hypothesis. Naganuma et al. [17] measure that CO2 emission can be as high as 10 g/kWh.

In this study, lean conditions and water injection are applied to the engine, which mitigate NOx emissions, prevent from backfire and knock occurrences. In order to equal power of it Diesel equivalent high boost level, up to 3.5 bar, is needed for the H2 ICE with low NOx emissions without after-treatment devices at the exhaust. λ and WHR sweeps results show that increasing λ is a more effective way to achieve NOx free operations. The λ threshold depend on the engine load since for near zero NOx operation are achieved at $\lambda \geq 3$ at 900 rpm for an IMEP of 8 bar, $\lambda \geq 3.2$ at 1400 rpm for an IMEP of 10 bar and $\lambda = 3$ at 1400 rpm for an IMEP of 15.5 bar. Water injection is also an effective way to limit NOx formation during combustion. However as discussed at 900 rpm for an IMEP of 8 bar, the actual water injection set-up is not able to bring NOx emissions to zero. A study on the water spray, it induction into the cylinder and it behaviour during compression might help to understand if all the injected water is able to vaporize and therefore reduce the in-cylinder maximum temperature. NOx emissions can also be reduce by ST but at the expense of ITE if drastic change are applied. The reduction obtain by ST is less than increase of λ or WHR.

ST sweeps results show that despite H2-PFI, which would form more homogeneous charge than H2-DI, the mixing between air and H2 might be a subject to address to tend toward high ITE and NOx free operation at lower λ than use in this study. SOI of H2 or water, injectors location in the intake runner, multiple injections, piston shape, injection pressure are some parameters that could be investigate to better understand H2 ICE.

Under lean conditions and a CR of 12.7, H2 ICE achieve at high load (IMEP = 22 bar) ITE of 42 % and 41 % at medium load (IMEP = 8 bar). High ITE can be attain on a λ range of 1.6. Since heavy-duty engine, are majorly use under medium and high load, the present study focuses on IMEP > 8 bar. However, idle is also a crucial engine operation that would need to address in future studies.

5. Acknowledgement

The authors acknowledge the contribution of:

- our colleagues B. Boudeau, Y. Haidous, B. Moreau in the preparation of the single cylinder test bench,
- BorgWarner in the supply of the complete H2 and H2O injector system,
- Plastic Omnium in the supply of water injection system,
- Hynamics in the supply of H2.

7. References

[1] ADEME, “Transitions 2050 choisir maintenant agir pour le climat,” Ademe - Horizons (011627), 2021.

[2] Rosati, M.F. and Aleiferis, P.G., “Hydrogen SI and HCCI combustion in a Direct-Injection optical engine,” SAE Technical Papers, 2009, doi:10.4271/2009-01-1921.

[3] Lee, K.J., Kim, Y.R., Byun, C.H., and Lee, J.T., Feasibility of compression ignition for hydrogen fueled engine with neat hydrogen-air pre-mixture by using high compression, Int. J. Hydrogen Energy 38(1):255–264, 2013, doi:10.1016/j.ijhydene.2012.10.021.

[4] Younkins, M., Wooldridge, M., and Boyer, B., “Direct in-cylinder injection of water into a PI hydrogen engine,” SAE Technical Papers, 2013, doi:10.4271/2013-01-0227.

[5] Younkins, M., Wooldridge, M.S., and Boyer, B.A., “Port Injection of Water into a di Hydrogen Engine,” SAE Technical Papers, 2015, doi:10.4271/2015-01-0861.

[6] Nguyen, D., Choi, Y., Park, C., Kim, Y., and Lee, J., “Effect of supercharger system on power enhancement of hydrogen-fueled spark-ignition engine under low-load condition,” Int. J. Hydrogen Energy 46(9):6928–6936, 2021, doi:10.1016/j.ijhydene.2020.11.144.

[7] Navale, S.J., Kulkarni, R.R., and Thipse, S.S., “An experimental study on performance, emission and combustion parameters of hydrogen fueled spark ignition engine with the timed manifold injection system,” Int. J. Hydrogen Energy 42(12):8299–8309, 2017, doi:10.1016/j.ijhydene.2017.01.059.

[8] Obermair, H., Scarcelli, R., and Wallner, T., “Efficiency improved combustion system for hydrogen direct injection operation,” SAE Technical Papers, 2010, doi:10.4271/2010-01-2170.

[9] Lee, J., Park, C., Bae, J., Kim, Y., Choi, Y., and Lim, B., “Effect of different excess air ratio values and spark advance timing on combustion and emission characteristics of hydrogen-fueled spark ignition engine,” Int. J. Hydrogen Energy 44(45):25021–25030, 2019, doi:10.1016/j.ijhydene.2019.07.181.

[10] Luo, Q. he, Hu, J. Bin, Sun, B. gang, Liu, F. shui, Wang, X., Li, C., and Bao, L. zhi, “Experimental investigation of combustion characteristics and NOx emission of a turbocharged hydrogen internal combustion engine,” Int. J. Hydrogen Energy 44(11):5573–5584, 2019, doi:10.1016/j.ijhydene.2018.08.184.

[11] Bleechmore, C. and Brewster, S., “Dilution strategies for load and NOx management in a hydrogen fuelled direct injection engine,” SAE Tech. Pap. (724):776–790, 2007, doi:10.4271/2007-01-4097.

[12] Antonelli, M. and Martorano, L., “Realization and testing of a low pressure hydrogen direct injection engine using commercial injectors,” SAE Technical Papers, ISBN 2012010652, 2012, doi:10.4271/2012-01-0652.

[13] Verhelst, S., Demuynck, J., Martin, S., Vermeir, M., and Sierens, R., “Investigation of supercharging strategies for PFI hydrogen engines,” SAE Technical Papers, ISBN 2010010582, 2010, doi:10.4271/2010-01-0582.

[14] Dhyani, V. and Subramanian, K.A., “Control of backfire and NOx emission reduction in a hydrogen fueled multi-cylinder spark ignition engine using cooled EGR and water injection strategies,” Int. J. Hydrogen Energy 44(12):6287–6298, 2019, doi:10.1016/j.ijhydene.2019.01.129.

[15] Xu, P., Ji, C., Wang, S., Cong, X., Ma, Z., Tang, C., Meng, H., and Shi, C., “Effects of direct water injection on engine performance in engine fueled with hydrogen at varied excess air ratios and spark timing,” Fuel 269:117209, 2020, doi:10.1016/j.fuel.2020.117209.

[16] Naganuma, K., Takagi, Y., Kawamura, A., and Sato, Y., “Study of NO x Emissions Reduction Strategy for a Naturally Aspirated 4-Cylinder Direct Injection Hydrogen ICE,” (x), 2018.

[17] Kawamura, A., Sato, Y., Naganuma, K., Yamane, K., and Takagi, Y., “Development project of a multi-cylinder DISI hydrogen ICE system for heavy duty vehicles,” SAE Technical Papers, 2010, doi:10.4271/2010-01-2175.

8. Glossary

BTE:	*brake thermal efficiency*
CAD aTDC:	*crank angle degree after top dead center*
CAD bTDC:	*crank angle degree before top dead center*
CA50:	CAD at 50 % mass fuel burned
CA50-CA10:	*delay between 10 % and 50 % of mass fuel burned*
CR:	*compression ratio*
EGR:	*exhaust gas recirculation*
H2:	*dihydrogen*
HCCI:	*homogeneous charge compression ignition*
ICE:	*internal combustion engine*
IMEP:	*indicate mean effective pressure*
ITE:	*indicate thermal efficiency*
NSR:	*NOx storage / reduction*
Pin / Pex:	*intake or exhaust pressure*
SCR:	*selective catalyst reduction*
SOI:	*start of injection*
ST:	*spark timing*
Tin / Tex:	*intake or exhaust temperature*
TWC:	*three-way catalyst*
WHR:	*water to H2 ratio*

Chassis dynamometer and road pollutant emissions assessment on Euro6d Gasoline PHEV vehicles with conventional and synthetic fuels

C. LARRIEU[1], J. WILLIAMS[1], N. RANKOVIC[1], C. CHAILLOU[1]

1: Aramco Fuel Research Center, 232 avenue Napoleon Bonaparte, 92500 Rueil-Malmaison, France

Abstract: In order to limit climate change, the European Commission has recently set two new objectives for GHG emissions for the transport sector, the EU Green Deal and the FitFor55 package. Synthetic fuels (also known as e-fuels), derived from low-carbon hydrogen and captured carbon dioxide, are one of the sustainable solutions available to reduce carbon footprint compared to regular fuel. In parallel, the CLOVE consortium has proposed stringent new emissions targets for the expected upcoming Euro 7 regulation in order to limit the impact of the transport sector on local air quality.

A study was conducted using current-generation Euro 6d-compliant gasoline PHEV to assess the impact of conventional and accurately simulated, surrogate synthetic fuels upon exhaust emissions. All the vehicles were equipped with both TWC and GPF. Chassis dynamometer and on-road tests were performed to ensure a complete picture of emissions under both laboratory- and real-world conditions. On chassis dynamometer, FTIR spectroscopy was used to speciate both hydrocarbon and nitrogen compounds for both engine-out and tailpipe positions. During on-road tests, an innovative PEMS equipped with a FTIR was used to obtain similar measurements. Particle size distributions were measured down to 10 nm in diameter by ELPI in tailpipe positions. For completeness, both charge-depleting and charge-sustaining modes were investigated on RDE cycles.

A detailed analysis of the current and future regulated pollutant emissions was performed for each of the vehicles. Finally, an assessment of the impact upon emission levels of the surrogate fuels compared to a reference conventional fuel is then made, which leads to show that e-fuels are generally equivalent in pollutant emissions while showing potential for improvement in PN levels.

Keywords: synthetic fuel, e-fuel, renewable fuel, RDE testing, pollutant emissions

1. Introduction

To reduce the impact of the transport sector on the environment and especially on the limitation of Green House Gas (GHG) emissions, different technologies and energy vectors are currently developed. Hydrogen is one of these energy vectors which are believed to play a major role for reducing transport GHG in the upcoming decades. Green hydrogen is typically derived from water, using renewable electricity for electrolysis, such as wind or solar. Low-carbon hydrogen (also known as blue hydrogen) is derived from natural gas reforming using Steam Methane Reforming (SMR), Auto Thermal Reforming (ATR) or dry reforming, coupled with a Carbon Capture and Storage (CCS) system. Hydrogen can be used directly in fuel cell or Internal Combustion Engine (ICE). Low carbon hydrogen can also be vectored into synthetic hydrocarbons when reacted with CO_2 captured from different sources, solution widely known as e-fuels. In order to support transport industry and car manufacturers in the transition, various experimental sustainable fuels are being developed with the intent of achieving CO_2 near-neutrality.

Recent studies such as Yugo et at. [1] showed Well-to-Wheel (WtW) CO_2 content for synthetic gasoline of 2.6 gCO_2/MJ, compared to 94 gCO_2/MJ for the RED II Fossil fuel reference, hence a reduction of at least 80% is to be expected depending on the exact scope and hypotheses chosen.

The effects of these fuels on pollutant emissions have to be investigated to ensure that engine and aftertreatment systems are fully compatible with these renewable fuels. Some studies have recently investigated renewable gasoline-type formulations [2-4], generally centering on a reduced number of test platforms.

A study is conducted using four current-generation Euro 6d-compliant gasoline Plug-In Hybrid Vehicles (PHEV) to assess the impact of conventional and surrogate synthetic fuels upon exhaust emissions. These surrogate fuels are accurate simulations of two different industrial processes based on Methanol-to-Gasoline (MtG) and Fischer-Tropsch (FT) technologies respectively.

All vehicles tested are equipped with both Three-Way Catalysts (TWC) and Gasoline Particulate Filters (GPF).

As various studies have recently showed that environmental factors such as traffic congestion and outside temperatures may in some cases induce a high degree of variance in emission levels [5-7], both chassis dynamometer and on-road tests are performed to ensure a complete picture of emissions

Company General Use

under both laboratory and real-world conditions. On chassis dynamometer, Fourier-Transform InfraRed (FTIR) spectroscopy is used to speciate both hydrocarbon and nitrogen compounds (NH_3, N_2O …), with measurements carried out alternatively in engine-out and tailpipe positions. During on-road tests, an innovative Portable Emission Measurement System (PEMS) equipped with a FTIR is used to obtain similar measurements. Particle size distributions are measured down to 10 nm in diameter by Electrical Low-Pressure Impactor (ELPI) in both engine-out and tailpipe positions.

The main objective is not to evaluate the individual vehicle performance, but rather to assess fleet-wide pollutant emissions. The emphasis in the following is on tailpipe pollutant levels, while engine-out levels are also considered and discussed when necessary to give insight into particular findings and points of interest.

This paper will first present the experimental equipment, the fuel characteristics and procedure used to test the selected vehicles. Then, a description of the routes and test plan will be presented. The results section will first deal with the cycle compliance including coolant temperatures and driving dynamics and the specific CO_2 emissions. The second part of the results is dedicated to the analysis of Euro 7 regulated pollutant such as Particle Number (PN), both PN_{10} and PN_{23}, CO, THC, NO_X and NH_3.

2. Experimental Procedure

2.1 Vehicles and vehicle preparation

All four vehicles selected are Gasoline fuel PHEV vehicles homologated under Euro 6d standard. These vehicles are all standard commercial cars, with their Engine Control Units (ECU) as calibrated by the manufacturer.

Vehicles represent varied fuel and air delivery schemes, with both direct and indirect injection technologies being presented, as well as both natural aspiration and turbocharging.

All four have at least one TWC and a GPF. Odometer values at the start of the test campaign are given in Table 1, along with an approximate percentage of distance travelled with ICE on. Vehicle C has a lower actual odometer value but was equipped with a different exhaust line as indicated below.

Vehicle	Approximative odometer at start (km)	Percentage of previous trips with ICE on
A	15000	60-80% (emission tests)
B	13300	>95% (Almost no charge)
C	17300 (exhaust line)	60-80% (emission tests)
D	11500	50% (Hybrid pwt calibration)

Table 1: Vehicle odometers at the beginning of testing

All four vehicles have their exhaust line modified to provide sampling ports in an engine-out position (upstream of the first catalyst) as well as thermocouples along the full length of the exhaust line.

2.2 Measurement apparatus

2.2.1. Chassis dynamometer equipment

The chassis dynamometer is a full HORIBA installation, controlled by STAR VETS operating system, and meets regulatory requirements EURO 6d.
A CVS-7400S HORIBA dilution tunnel is present for diluted measurements. A MEXA-7200H HORIBA device (for diluted emissions) and a MEXA-7500DEGR HORIBA device allow continuous measurement of THC, CH_4, CO, CO_2, NO, NOx and O_2 for engine-out, tailpipe and diluted sampling position. A FTIR is available (AVL Sesam i60 FT Multi Component), and installed alternatively in engine-out or tailpipe position to measure unregulated gas such as N_2O, NH_3, aldehydes, aromatic hydrocarbons and butadiene.
A DEKATI ELPI+ particle sizer is used, which relies on an electrical charger and individual collection stages to sort particles by their aerodynamic diameter. It is installed downstream of the exhaust aftertreatment system and allows the measurement of both PN_{10} and PN_{23}, as well as further distribution analysis (the minimum accepted diameter being 7nm).

A Mass Flow sensor is present to allow for computation of pollutant mass flows and subsequently, cumulative masses.

2.2.2. On-road equipment

Vehicles are set up for on-road testing with an onboard PEMS-LAB® provided by CERTAM (Figure 1). A flexible tube is plugged on the vehicle's exhaust pipe for the purpose of measuring a global flow rate with a Pitot probe (flow rate, temperature, pressure), but also to have a sampling point for exhaust gas.

One of the specificities of this PEMS-LAB® compared to other devices lies in the use of a Fourier Transform Infra-Red spectrometer (FTIR Gasmet AA-4000), allowing simultaneous measurement of each gas in the exhaust. A large library of unregulated gases, which have a great interest for environment and exhaust after treatment systems, can be measured with this device. Obviously, regulated gases are also followed (CO, CO_2, NO, NO_2, THC as well as NMHC/CH_4 split).
Again, a Mass Flow sensor is mounted in the chain to allow for computation of pollutant mass flows and subsequently, cumulative masses.

Company General Use

Additional information is also recorded from the OBD (On-Board Diagnostic) system (engine speed, State Of Charge (SOC), coolant temperature, torque…) if these parameters are available on the vehicle.



Figure 1: Road test equipment as typically installed in the trunk of a test car (source: CERTAM promotional material – not a tested car)

2.3 Data and calculations

Data extracted are mostly modal emission data from test equipment as presented in 2.1 and 2.2, synchronized with OBD and/or CAN data when available. Manufacturers for vehicles A, C and D provided for ECU data acquisition over CAN, while CAN frame decoding was not available for vehicle B.

Lower confidence limits for modal emissions data stand around 1mg/km for most pollutants.

2.4 Overview of fuel characteristics

Fuels tested include a Euro 6 E10 homologation fuel (hereafter "ULG E10" or "Reference fuel"), one E20 fuel, and two mock-up fuels corresponding to simulated large-scale synthetic fuel (e-fuel) production processes, designed with special attention to future evolution of emission norms leading to improved distillation properties and aromatics content.

The 1st surrogate fuel is hereafter known as "E20 2030". It is formulated to correspond to a future conventional E20 fuel, in line with the view of E20 specifications shared by major European industry stakeholders, that could be available in 2030 at the gas station (20% ethanol blend).

The 2nd surrogate fuel, hereafter "E20 MtG", is an E20 ethanol blend based on a mock-up synthetic fuel produced through a MtG process. It is the first e-fuel candidate of this study.

The 3rd surrogate fuel (and 2nd e-fuel candidate) is known as "E20 FT" and is a mock-up of a synthetic fuel produced by upgrading Fischer-Tropsch naphtha into gasoline, again blended with ethanol to an E20 specification. Of note, Vehicle B has not been tested on E20 FT at the time of writing.

An overview of their main characteristics is given in Table 2 below. Note that both E20 MtG and E20 FT e-fuels are above the max E70 and E100 volatility thresholds of EN228, which stand at 48-50% (depending on volatility class) and 71% respectively; this is all keeping in mind that no unified standard exists for E20 fuels at this point in time. Other than these lower temperature volatility thresholds and the ethanol content (thus oxygen content), the "E20 2030", "E20 MtG" and "E20 FT" test fuels are within current EN228 fuel specifications, although e-fuels would not fit volatility class A for Dry Vapor Pressure Equivalent (DVPE) due to a maximum specified DVPE of 60 kPa at 37.8°C.

Property	Unit	ULG E10	E20 2030	E20 MtG	E20 FT
RON	-	96.4	99.0	98.2	98.7
MON	-	86	87.0	86.4	88.5
Density at 15°C	kg/m3	748.9	750.0	732.5	724.9
Vapor pressure (DVPE @ 37.8°C)	kPa	57.3	56.1	66.9	68.0
E70	%v/v	41.6	40.6	62.3	63.2
E100	%v/v	55.3	66.6	79.5	82.1
E150	%v/v	91.5	92.4	88.7	99.0
LHV	MJ/kg	41.47	39.31	39.52	39.59
n-Paraffins	%v/v		5.6	6.0	5.8
Isoparaffins	%v/v		34.4	39.3	53.8
Olefins	%v/v	7	10.7	11.3	0.1
Naphtenes	%v/v		3.4	3.4	1.2
Aromatics	%v/v	28.4	24.7	19.2	18.8
Ethanol	%v/v	9.3	20.6	20.8	20.4
C	%m/m	83.2	79.07	78.27	78.15
H	%m/m	13.3	13.34	13.88	14.07
O	%m/m	3.5	7.58	7.85	7.78
Sulfur	ppm	3.6	<5	<5	<5

Table 2: Fuel characteristics

2.5 Test routes

Vehicles are tested both on road along a defined 86km-long Real Driving Emission (RDE) route around CERTAM's test facilities, and on Chassis Dyno following a speed trace historically extracted from one such RDE trip.

Company General Use

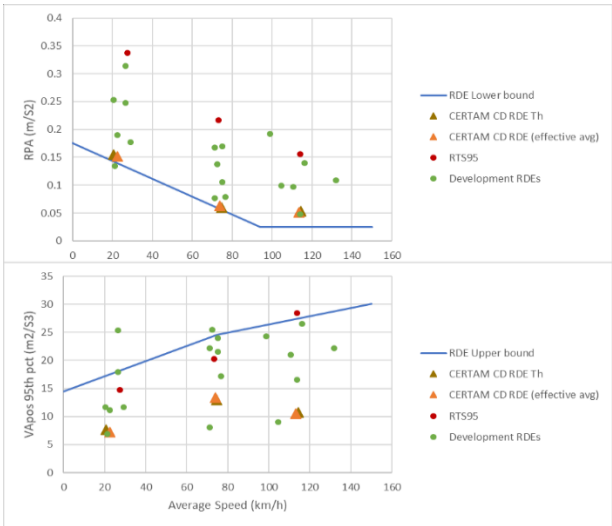


Figure 2: RPA and VApos for CERTAM traces and various Chassis dyno RDE cycles

For this standard RDE cycle, Relative Positive Acceleration (RPA) and 95th percentile of the Speed times Positive Acceleration product (VApos) are computed according to European Commission Regulation [8] and displayed in Figure 2 along with RDE boundaries as well as some other development RDE and RDE-like cycles.

The RDE cycle used at CERTAM is representative of a typical fair road RDE and is shown to not be particularly severe dynamically, for both RPA and 95th percentile of VApos, when compared to other cycles specifically designed to test vehicles to the limits.

2.6 Test plan

Vehicles are tested both on chassis dynamometer and on-road. The procedure is centered on RDE testing, with additional Worldwide harmonized Light vehicles Test Cycle (WLTC) cycles on the reference fuel only, intended to provide reference points to participating manufacturers (these WLTC results won't be discussed in this paper). WLTCs are also run as part of a preconditioning procedure after each fuel change to allow for proper ECU adaptation to new fuel characteristics.

For each vehicle and each test fuel, a standard RDE procedure is conducted based on the homologation WLTC procedure. The vehicle is fully charged, then an RDE cycle is run to deplete the battery to minimum SoC (all vehicles being given for pure electric driving autonomies inferior to 86km). A second RDE cycle is then run and recorded, hereafter known as the "Hot-start" cycle. After soaking at room temperature and at minimum SoC, a third RDE is run and recorded, hereafter known as the "Cold-start" cycle.

All tests are repeated twice, and on chassis dyno the FTIR is mounted alternatively upstream and downstream.

3. Results

3.1 Cycle compliance

As presented by Khalfan et al. [5] among others, an important variation in RDE emission results can occur from test to test based on driving dynamics. Because of this, a brief overview of dynamics and temperature compliance is given here to ensure robustness of emission results, particularly on road.

3.1.1 Coolant temperatures

All coolant temperatures recorded at the beginning of tests are displayed in Figure 3. Hot Start temperatures are shown to be generally lower on road tests due to the added manipulation time before each recorded run, increasing soak time (still below the requested 30 minutes for all tests). Road cold start tests are within a low range of temperature enabling to consider the same start conditions for the four vehicles.

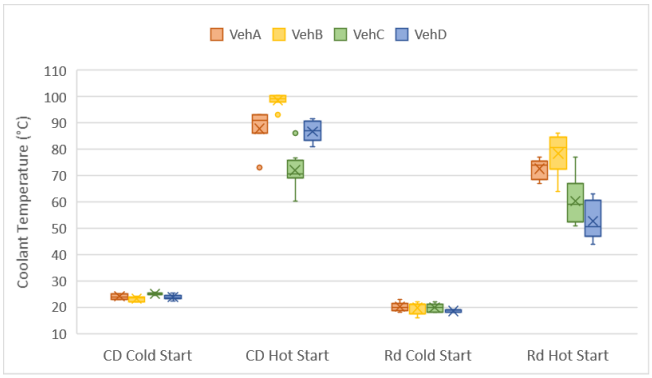


Figure 3: Coolant temperatures at start-up for Hot and Cold starts on Chassis dyno (CD) and Road (Rd) for the four vehicles

3.1.2 Driving dynamics

On chassis dynamometer, standard deviation on RPA values stands at 0.9% of the reference speed trace while VApos standard deviation is at 1.9% of the reference showing a high level of reproducibility (as expected for chassis dyno tests).

On road tests, RPA and VApos are shown in Figure 4. Some deviation is observed as road RDE tests tend to be have slightly higher RPA and Urban average speed but all RDEs are considered valid nonetheless.

Company General Use

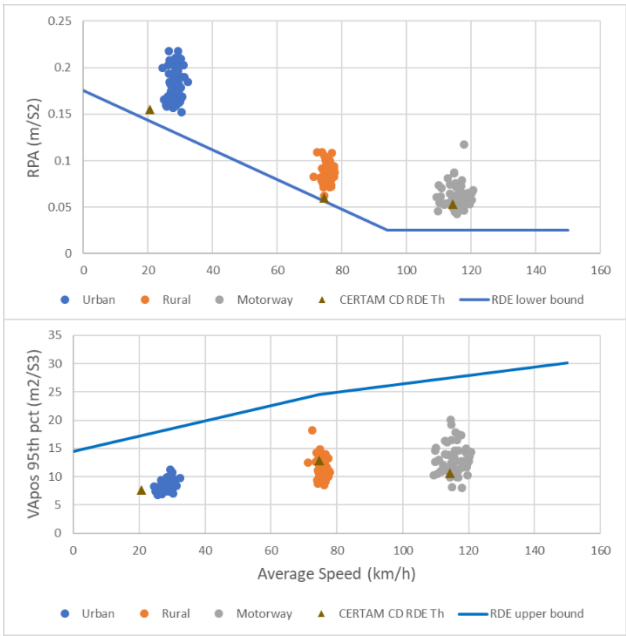


Figure 4: RPA and VApos for road RDE tests as compared with CERTAM's chassis dyno trace

3.1.3 Specific CO_2 emission results

For all vehicles where ECU recordings of torque and engine speed was available (all except vehicle B), a simple engine power computation was applied to compute specific engine-out CO_2 emissions in g/kWh, as seen below in Figure 5. The computation was carried out on a high-load section of the highway phase in order to limit uncertainties due to energy management strategies and ICE activation. Because no engine-out measurement was carried out on road, only chassis dyno results are shown here.

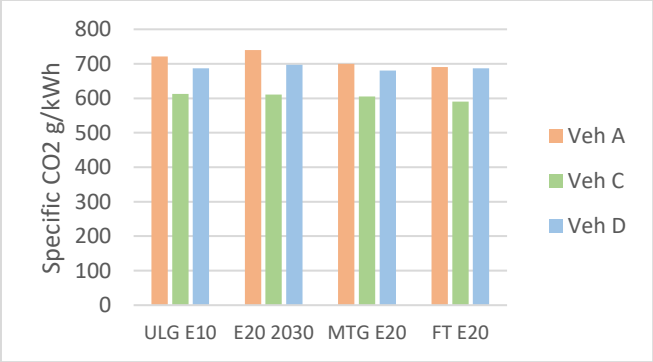


Figure 5: Specific CO_2 (g/kWh) averaged over highway sections

Results relative to the reference ULG E10 fuels are given in Figure 6. The results on vehicle D may be indicative of a difficulty adapting to characteristics of test fuels over the lapse of the preconditioning WLTC cycle. Further tests are being run on ICE-only vehicles of the same engine design to settle on a conclusion.

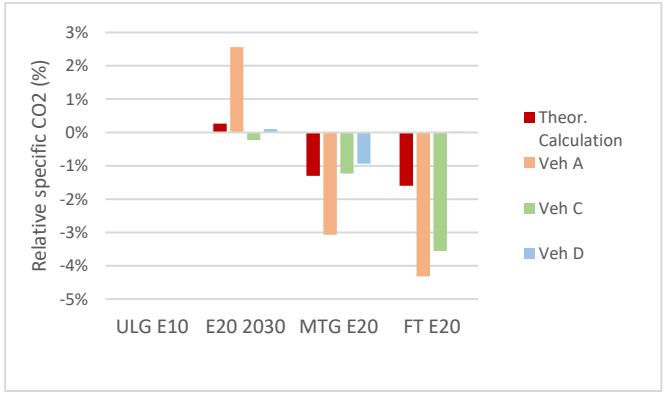


Figure 6: Specific CO2 relative to reference fuel along with theoretical calculation

A theoretical calculation based on physical and chemical properties is given in Figure 6 above as well: it appears all vehicles follow the theoretical trend although it seems amplified in the case of vehicle A and FT E20, which could be due to an offset in the reference level.

3.2 Base results for Euro 7 regulated pollutants

Pollutant levels below are either averaged on all tests, or averaged on only the first 8kms of Cold Start tests ("Cold Phase" emissions). This distance was arbitrarily set in order to minimize effects of inconsistent ICE activation in the first kilometers while allowing for meaningful observations of emissions in cold conditions.

Emission data is shared with manufacturers so that they can further improve emission levels through engine and/or aftertreatment design and control.

3.2.1 PN emissions

As described in 2.2, PN measurements are only carried out in tailpipe position.

Figure 7 shows that PN_{10} and PN_{23} follow the same trends for all vehicles and fuels; as a consequence, and for the sake of simplicity, the following results will be discussed in PN_{10}, keeping in mind that trends in PN_{23} show no appreciable difference.

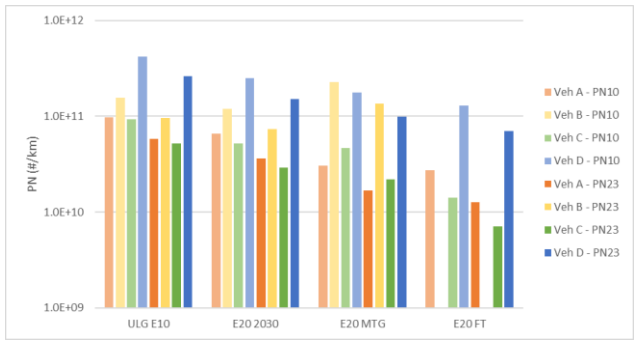


Figure 7: PN_{10} and PN_{23} results on **Chassis Dyno**

Company General Use

Figure 8 shows general averaged results of PN_{10} while a focus on Cold Phase results is shown in Figure 9.

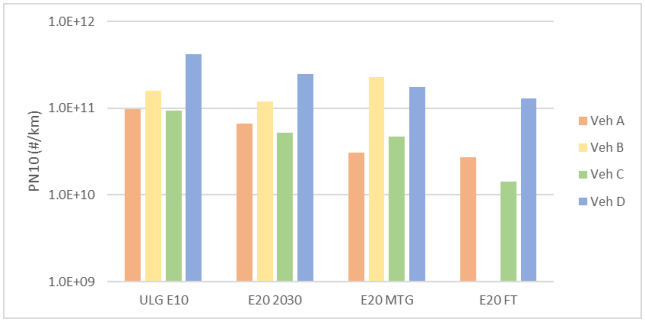


Figure 8: PN_{10} results averaged over **Chassis Dyno** RDE tests



Figure 9: PN_{10} results averaged over **Chassis Dyno** RDE tests – Cold phases

One specific behavior is observed for vehicle B on E20 MTG. It is being investigated with the manufacturer.
Outside of this, results seem to show a promising improvement of PN levels on other vehicles and fuel combinations, with overall improvements ranging between minus 20-40% PN for the E20 2030 fuel up to minus 40-85% PN for the E20 FT fuel.

3.2.2 CO

In engine-out position (Figure 10), CO remains contained within 100% to 110% of ULG E10 results for all experimental fuels and vehicles and appears stable.

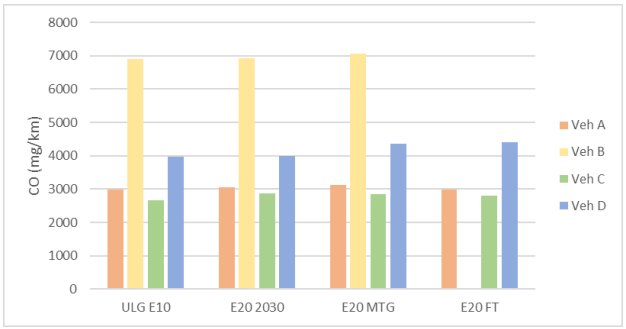


Figure 10: Engine-out CO results averaged over **Chassis Dyno** RDE tests

At the tailpipe, overall CO levels are shown in Figures 11 for chassis dyno and 12 on road. No particular trend emerges although all vehicles are below the ULG E10 on test fuels.

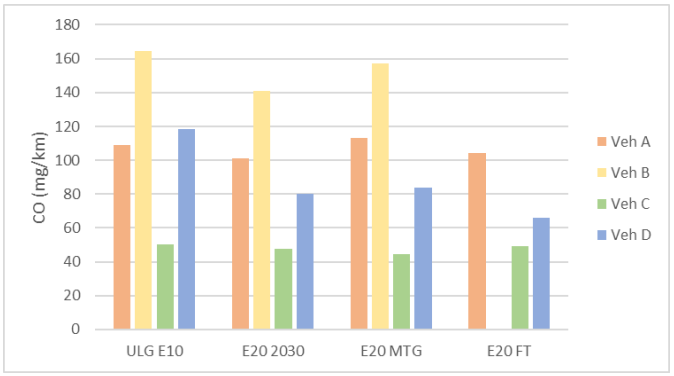


Figure 11: Tailpipe CO results averaged over **Chassis Dyno** RDE tests

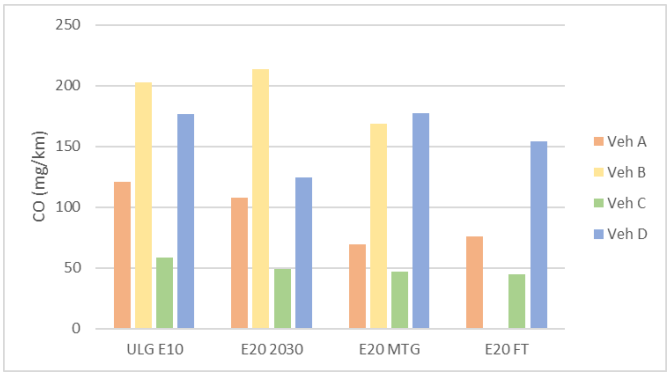


Figure 12: Tailpipe CO results averaged over **Road** RDE tests

It is to be noted that on E20 FT on the cold phase only (see Figures 13 and 14), vehicle C exhibits a degradation that has been attributed by the manufacturer to the specific sensitivity of its richness regulation software to fuels with volatility characteristics outside of the EN228 standard range (cf. Table 2 on fuel characteristics and comment on E70 and E100). This degradation is however compensated overall.

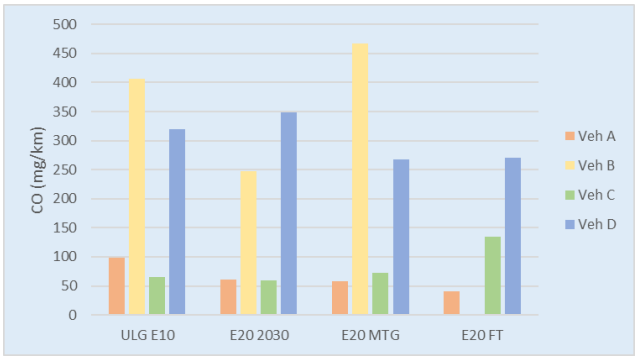


Figure 13: Tailpipe CO results averaged over **Chassis Dyno** RDE tests – Cold Phases

Company General Use

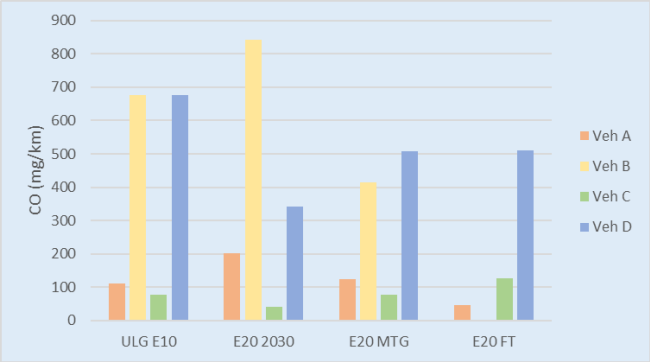


Figure 14: Tailpipe CO results averaged over **Road** RDE tests – Cold Phases

CO results are thus generally considered stable overall while specific attention to richness tuning may further improve results for some manufacturers whose stock calibrations do not properly account for fuels outside of the current volatility standards.

3.2.3 NO_x

NO_x results (Figures 15 and 16 for Chassis Dyno and Road respectively) tend to be low overall, likely owing to the fairly new catalysts (compared to >160000 km homologation design target), and exhibiting no particular trend but a high variance between tests.

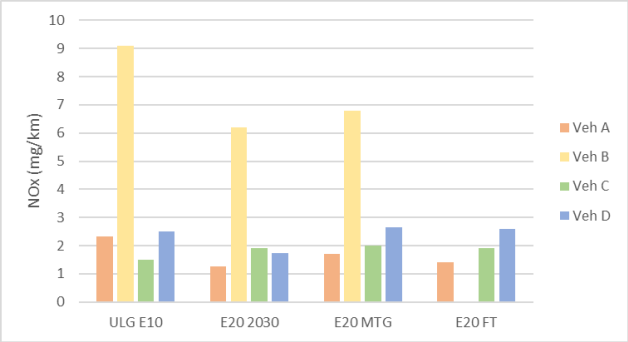


Figure 15: Tailpipe NO_x results averaged over **Chassis Dyno** RDE tests

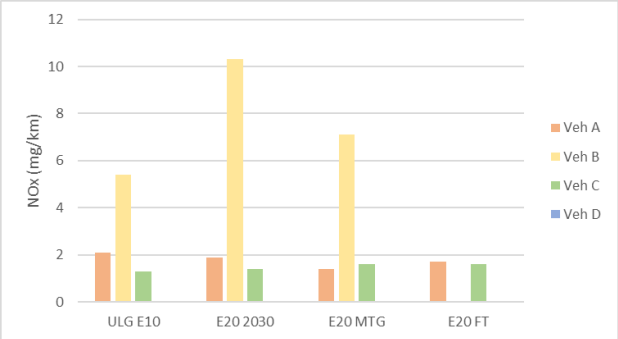


Figure 16: Tailpipe NOx results averaged over **Road** RDE tests

Results for vehicle D are not displayed due measurement inconsistencies.

3.2.4 NH_3 & N_2O

NH_3 and N_2O results are generally very low at the tailpipe on all tests, again likely owing to the fairly new aftertreatment systems in place, with NH_3 results between 1 and 3 mg/km and N_2O around 1 mg/km. Only Vehicle D stands out with NH_3 levels consistently above 10mg/km at the tailpipe, which was confirmed by its manufacturer to be in accordance with internal data as work is in progress to improve performance on this specific topic.

Engine-out levels are even lower and barely detectable: this is generally the expected behavior as most of these pollutants are generated in the TWC.

3.2.5 THC & Aldehydes

THC levels in engine-out position (Figure 17) show potential for slight improvements with e-fuels on vehicles A and B, a neutral trend on vehicle C and a degradation on vehicle D.

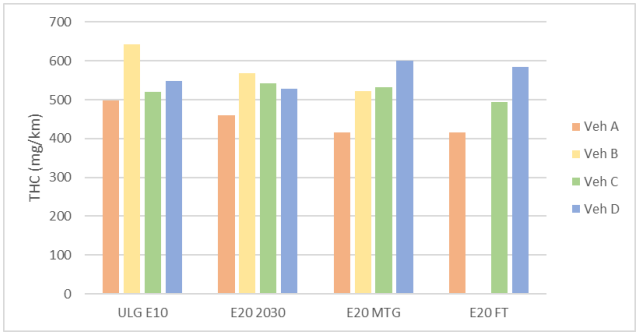


Figure 17: Engine-out THC results averaged over **Chassis Dyno** RDE tests

THC levels at the tailpipe are shown below in Figures 18 on chassis dyno and 19 on road.

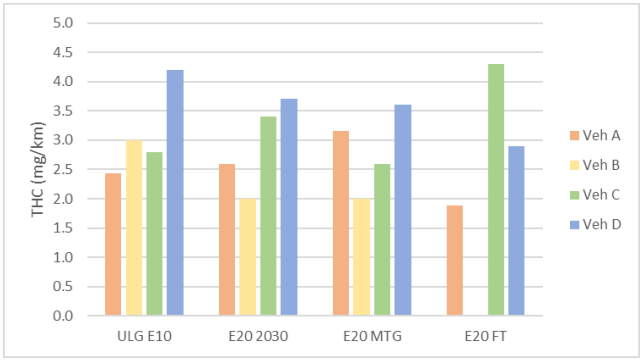


Figure 18: Tailpipe THC results averaged over **Chassis Dyno** RDE tests

Company General Use

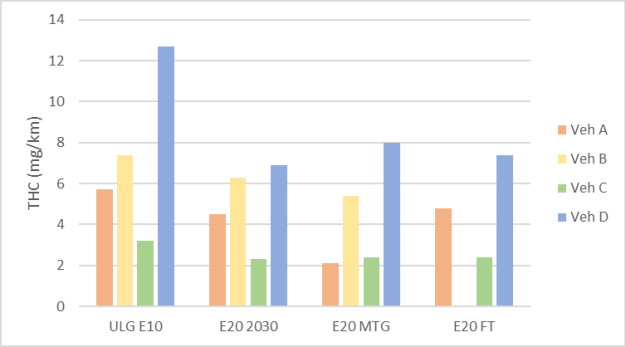


Figure 19: Tailpipe THC results averaged over **Road** RDE tests

Results are generally low and no strong trend emerges. CH_4 is present is stable low quantities across all fuels. Formaldehyde (HCHO) and Acetaldehyde (MeCHO) are at trace levels only at the tailpipe.

Vehicle C's emissions on E20 FT are again traced by its manufacturer to the possible sensitivity of its richness control to fuels with a higher-than-standard volatility.

Regarding aldehydes specifically, tailpipe emissions are not measurable for any vehicle tested (mostly due to efficient, not aged TWC), while engine-out emissions are shown in Figures 20 and 21. Levels are stable for HCHO (note that no results are available on vehicle A on ULG E10 and E20 2030 due to a FTIR issue on tests where it was to be mounted in engine-out position).

For MeCHO, E20 MtG fares generally slightly worse than other fuels. Although it is expected that a higher ethanol content is linked to an increase in MeCHO emissions based on pure ULG, E10 and E85 testing [9-10], results are not highly significant in that case across all E20 fuels.

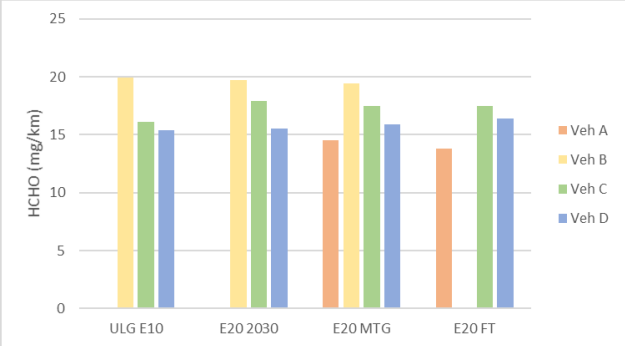


Figure 20: Engine-out HCHO results averaged over **Chassis Dyno** RDE tests with upstream FTIR – Vehicle A partly missing

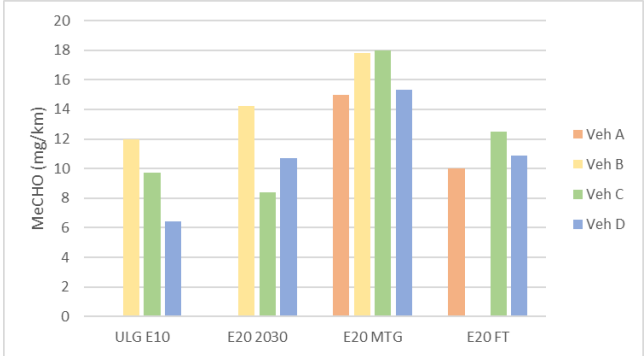


Figure 21: Engine-out MeCHO results averaged over **Chassis Dyno** RDE tests with upstream FTIR – Vehicle A partly missing

4. Conclusion

Given potential reductions in carbon intensity of e-fuels compared to known fossil fuel references [1], the study is motivated by the opportunity to reduce the CO_2 impact of the transportation sector while guaranteeing emission compliance of ICE-equipped vehicles.

The study conducted presents emission results for various surrogate fuel formulations that are in development for future (2030+) use, with the intent of providing insights into the impact of a fleet-wide adoption of e-fuels.

Regarding this objective, there is a benefit to testing a broad selection of PHEV vehicles with differing powertrain designs, as it has been observed in the course of this study that some trends are specific to some manufacturers due to engineering choices at the hardware or software level.

Keeping this in mind, a potential for improvement in PN is observed on surrogate e-fuels, while gaseous pollutants are generally considered stable, with no significant trend emerging across all vehicles in the study.

Going forward, investigations should be targeted towards aged aftertreatment systems, as this study shows levels close to accuracy thresholds for some gaseous pollutants at the tailpipe. With an aged after-treatment system, stability of these emissions could be confirmed on wider scales of concentrations. Furthermore, at the time of writing this article, the Euro 7 regulation has not been officially approved and some elements of it may warrant additional investigation into pollutant stability.

While CO_2 potential reduction has been demonstrated for synthetic fuels, their adoption on a large scale is subject to further European legislation, allowing the recognition of CO_2 gains across the value chain from feedstock production until fuel combustion.

Company General Use

5. Acknowledgement

The authors would like to express their gratitude to the following:

CERTAM for their support and the use of their equipment and facilities.

Participating manufacturers for their technical assistance and their trust regarding this campaign.

Caroline Norsic for her help on background work and redaction.

6. References

[1] Yugo, M.; Gordillo, V.; Shafiei, E.; Megaritis, A.: "*A look into the life cycle assessment of passenger cars running on advanced fuels*", SIA Powertrain & Energy Congress, Rouen, France, 2021.

[2] Puricelli, S.; Casdei, S.; Bellin, T.; Cernuschi, S.; Faedo, D.; Lonati, G.;Rossi, T.; Grosso, M.: " *The effects of innovative blends of petrol with renewable fuels on the exhaust emissions of a GDI Euro 6d-TEMP car*", Fuel, 2021, 294, 120483.

[3] Albrecht, M., Deeg, H., Schwarzenthal, D., and Eilts, P.: "*The Influence of Fuel Composition and Renewable Fuel Components on the Emissions of a GDI Engine*", SAE Technical Paper 2020-37-0025.

[4] Demuynck, J.; Mendoza Villafuerte, P.; Bosteels, D.; Pannwitz, M.; Titze, T.; Sens, M.: "*Zero-impact emissions from a gasoline car with advanced emission controls and e-fuels* ", Vienna Motor Symposium, Austria, 2022.

[5] Khalfan, A.; Andrews, G.; Li, H.: " *Real World Driving: Emissions in Highly Congested Traffic*", Proceedings of the SAE Technical Paper Series. International Powertrains, Fuels & Lubricants Meeting, 16 October 2017, Warrendale, PA, USA, 2017.

[6] Suarez-Bertoa, R.; Valverde, V.; Pavlovic, J.; Clairotte, M.; Selleri, T.; Franco, V.; Kregar, Z.; Astorga, C.: "*On-road emissions of Euro 6d-TEMP passenger cars on Alpine routes during the winter period*", Environ. Sci.: Atmos., 2021, 1, 125-139.

[7] Wang, Y.; Feng, X.; Zhao, H.; Hao, C.; Hao, L.; Tan, J.; Wang, X.; Yin, H.; Wang, J.; Ge, Y.; et al.: "*Experimental study of CO2 and pollutant emission at various altitudes: Inconsistent results and reason analysis*", Fuel, 307, 121801, 2022.

[8] European Commission : "*amending Regulation (EC) No 692/2008 as regards emissions from light passenger and commercial vehicles (Euro 6)*", Official Journal of the European Union, Commission Regulation 2016/646

[9] Li-Wei, J.; Mei-Qing, S.; Jun, W.; Man-Qun, L.: "*Influence of ethanol–gasoline blended fuel on emission characteristics from a four-stroke motorcycle engine*", Journal of Hazardous Materials, vol 123, 1-3, 29-34, August 2005

[10] Graham, L.; Belisle, S.; Baas, C-L.: "*Emissions from light duty gasoline vehicles operating on low blend ethanol gasoline and E85*", Atmospheric Environment, vol 42, 19, 4498-4516, June 2008

7. Glossary

GHG: Greenhouse Gas

WLTC: Worldwide harmonized Light vehicles Test Cycle

RDE: Real Driving Emissions

ICE: Internal Combustion Engine

PHEV: Plug-in Hybrid Electric Vehicle

ATS: After-Treatment System

ECU: Engine Control Unit

OBD: On-Board Diagnostics

CAN: Controller Area Network

TWC: Three-Way Catalyst

GPF: Gasoline Particulate Filter

CD: Chassis Dynamometer

PEMS: Portable Emission Measurement System

PEMS-LAB: PEMS with LABoratory equipment

FTIR: Fourier Transform Infrared (spectroscopy

ELPI: Electrical Low-Pressure Impactor

NOx: Nitrogen Oxides, NO + NO2

MtG: Methanol-to-Gasoline

FT: Fischer-Tropsch

RPA: Relative Positive Acceleration, as described in EC Commission Regulation 2016/646

VApos: 95th percentile of Speed x Positive Acceleration, as described in EC Commission Regulation 2016/646

SoC: State of Charge (implied to be that of the traction battery)

ISC: In-Service Conformity

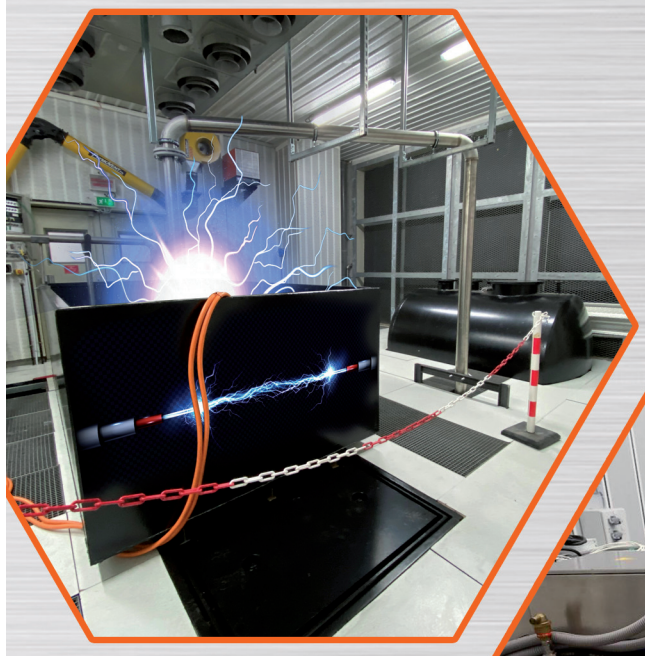
Company General Use

15 JUNE 2022

THERMAL ENGINE FOR HYBRID APPLICATIONS

CRITTM2A

Independent Testing Center









ELECTRICAL ABUSE TEST BENCH

- Short circuit
- Overcharge
- Over discharge
- ECE R100 Homologation
- IEC 62620, IEC 62928
- ISO 16750...

4WD POWERTRAIN BENCH

- Robot driver (pedal, gearbox)
- Battery Simulators up to 500kW
- Performance :
  500kW and 2500Nm/dyno(wheel)

9 PACK TEST CHANNELS
UP TO 1800A, 750kW, 1200V

9 MODULE TEST CHANNELS
UP TO 1200A, 64kW, 100V

96 CELL TEST CHANNELS
UP TO 1000A, 8kW, 8V

INVERTER TEST BENCH

- Battery simulator
  Current : 800A
  Power : 320kW
  Voltage : 1000V
- E-motor emulator
  Current : 400A
  Power : 320kW
  Voltage : 735V

www.crittm2a.com

Future ICE Technologies for High Efficient Hybrid Electric Powertrains

M. Leesch[1], M. Krause[1], J. Böhme[1], T. Arnold[1]

1: IAV GmbH, Auer Straße 54, 09366 STOLLBERG (Germany)

Abstract: Beside improvements on the electric components and operation strategies of hybrid electric powertrains a maximized BTE of the ICE is a key requirement. IAV developed and tested an experimental engine internally called NA16 to investigate and develop new technologies in a full engine environment.

The goal for the thermodynamic development was to achieve a fast and controllable combustion with a high compression ratio and a reduction of the wall heat and gas exchange losses. Thereby the optimal BSFC should be at the range of 20 to 35 kW from the engine power to ensure minimal real world emissions.

The main goal on the mechanic development was to reduce friction losses during cold start operation and especially around the ISFC best point. One of the main measures is using of roller ball bearings for the cam shafts and crank train that reduce the friction and the demand for oil supply dramatically. This allows the use of a small 12V electric oil pump to supply the whole engine on demand. Another advantage of the roller ball bearings is the almost neglectable influence of the oil temperature to the friction. Especially during warm up the friction losses of the roller bearings is much less compared to classic hydrodynamic bearings.

Keywords: High efficient hybrid electric powertrain with Phase Change Cooling, high compression ratio, new piston with a corona shape bowl, roller ball bearings for cam shaft and crank train and iron cast cylinder head and crankcase.

1. Introduction

Beside the local and short range transportation where pure electric powertrains can provide an emission free and energy efficient individual and commercial mobility, practicable pure electric solutions for long range and heavy duty transportation remain unavailable. Especially driving profiles with high power demand combined with long ranges as they are typical for long haul trucks, vacation trips or business trips require the installation of excessive battery capacity or fast charging capabilities as they were not available in the near term future. Also new hybrid electric powertrains can help to ensure low emission transportation for these applications. Especially when they fuelled by biofuels or e-fuels these powertrains can help to achieve a car-bon dioxide neutrality in the whole transportation sector without restrictions in range, driving time or the need to install high capacity charging infrastructure.

To provide a cost optimal and environmental friendly transportation solution with a hybrid powertrain a further improvement of the ICE's efficiency is necessary. The main targets of IAV technologically improvements of the ICE will be a reduced friction, especially cold start friction and a fast and stable combustion with a high com-pression ratio and efficient charge dilution. During the past years IAV as leading tech solution provider has developed several technologies that support these targets. After successfully evaluating the individual technologies and subsequent virtual overall system optimizations at real world driving cycles, IAV has developed a cost effective dedicated hybrid high efficiency demonstrator engine called NA16. In combination with mechanical and thermodynamic testing of the NA16 engine, IAV aims to demonstrate the overall potential of a sustainable biofuel compatible plug in hybrid electric powertrain that combines emission free short range mobility with CO_2 neutral long range capabilities.

2. NA16 Demonstrator Engine

2.1 Development Boundaries

Since the individual transportation in urban and local areas is expected to be pure electric, the focus for an optimized future hybrid powertrain is on longer range profiles such as business trips or extra urban delivery transportation. To easily compare the results of the powertrain optimization with other powertrains the WLTC driving cycle (see Fig. 1) was chosen.

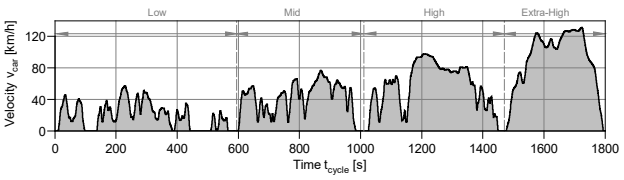


Fig. 1. Operational profile of WLTC driving cycle (cf. [5]).

The efficient high volume use of a new powertrain is largely ensured by its broad application in various vehicle platforms. To allow a broad application the vehicle boundaries for this optimized hybrid electric powertrain were chosen as characterized in table 1. For this purpose, the powertrain is equipped with an electric motor whose power is $P_{e,EM} = 85\ kW$ and a LiFePo-battery with a battery size of $E_{Bat} = 25\ kWh$.

Table 1. target vehicle.

Vehicle class	Compact	Midsize SUV	Full size SUV
Vehicle mass	1555 kg	1935 kg	2105 kg
c_w *x A*	0.29 *x* 2.17	0.30 *x* 2.64	0.34 *x* 2.87
Rolling resistance	0.010	0.0125	0.0137
E-Motor	High Voltage P2 with 85 kW		
HV Battery	LiFePo with 25kWh		
ICE	Baseline 2.0 l T-GDI vs. 1.6 l NA16		

The battery size covers pure electric driving ranges of at least 100 km under real world driving situations. This allows an emission free usability with the most needed range (daily trips to work, etc.) while maintaining the costs little. Based on the customer demands (speed and acceleration) the vehicle has to perform in every driving situation accordingly. Thereby the hybrid electric powertrain offers great opportunities to fulfil the customer demands using ICE and electric motor propulsion and offers more degrees in freedom in operation strategies for the powertrain. Looking at the baseline configuration of the hybrid powertrain (P2 topology) in the driving profile of the WLTC, it becomes apparent that the ICE map areas like high low end torque or high power become obsolete and can be reduced. [1]

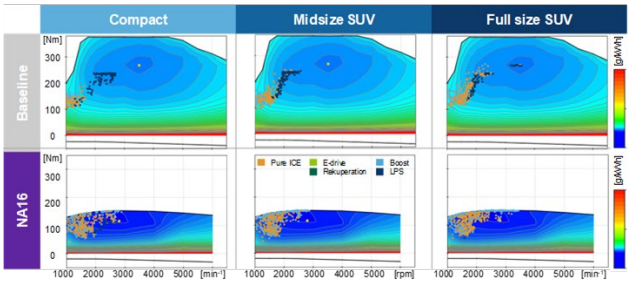


Fig. 2. ICE operating points in P2 topology

In the target powertrain configuration low end torque demands are fulfilled by the electric motor that is generating high torque at low speed. That creates a high acceleration and good towing capability. To bring the BTE best point closer to the typically used operating points a small naturally aspirated engine is beneficial. Even the driving demands of a full size SUV can be fulfilled with the hybrid powertrain and the 1.6 liter (NA16) naturally aspirated engine with better fuel consumption (cf. Fig. 2) . In addition the costs for such an engine are less than turbo charged DI engines.

2.2 NA16 Engine Technology Package

To achieve a maximum BTE of the ICE an optimized thermodynamic process and reduced thermodynamic losses are required.

During the last decades several measures have been taken to optimize the thermodynamic process. The main focus during the last years was to increase the compression ratio while reduce knocking and keep the MFB50 at its optimum. After achieving compression ratios in the area of $\varepsilon = 12 - 14$ with technologies like Miller and Atkinson valve timing leading to BTE's of up to 41 % [2], the focus of development moved to charge dilution combustion processes to further increase the compression ratio and reduce wall heat losses. To maintain an acceptable burning speed at charge dilution (high EGR rates or lean operation), several technologies like pre chamber spark plug or high energy ignition are currently under investigation. [1]

Due to the high ignition energy, the pre-chamber can therefore also ignite mixtures which are diluted with air or residual gas and which usually cannot be ignited with conventional spark ignition. [3] If the design freedom in the engine development is greater, the thermal efficiency can also be positively influenced by the technological change of the cooling system to improve the thermal management of the ICE.

IAV's Phase Change Cooling (PCC) ensure a stable and fast combustion at high charge dilution as well because the cooling of the engine components is carried out according to the principle of cooling on demand and almost independent of the ICE operating point. Therefore the main purpose of the PCC technology is to allow a more accurate and quicker adjustment of the engine and charge temperature.

IAV has developed a phase change cooling system (IAV Advanced Thermal Management) as part of an in-house development project, in which the coolant temperature can be set between $T_{KM} = 95 - 250\ bar$ regardless of the operating point. The closed circuit works for example with a mixture of water and ethanol as liquid coolant. Then it evaporates in the engine and condenses back in the condenser (phase change along the cooling path). A high pressure pump conveying the fluid into the engine at a cooling pressure between $p_{KM} = 1 - 50\ bar$. There is a direct dependence between coolant pressure and coolant temperature, i.e. the higher the pressure, the higher the temperature in the cooling circuit. Depending on the operating point of the engine, it is now possible to set the optimum pressure and thus the most favourable wall temperature for combustion process with high accuracy. Because of the very high heat

transfer coefficient (up to $\alpha_{PCC} = 100{,}000\ W/m^2K$) during the controlled bubble boiling the component temperature follows coolant temperature and can be adjusted very accurately. [4] This can help to adjust the charge constitution depending on the engine operation point optimal to avoid knocking and keep the burning speed high. In addition the more homogeneous combustion chamber temperatures that can be achieved with PCC reduce the knocking tendency. By that the gas temperature in the combustion chamber can be kept in an optimal range that helps to increase the EGR tolerance and burning speed.

The engine parameters for the demonstrator engine were optimized using a combined engine simulation (IAV Engine & 1D engine process simulation incl. IAV port design process). The technology package chosen for the NA16 demonstrator engine is shown in following table (cf. table 2).

Table 2. NA16 engine parameters

Engine type	Inline 4 cylinder
Displacement	1,599 cm³
Power / Torque	84 kW / 160 Nm
Max. Engine Speed	5,500 min^{-1}
Bore *x* stroke	74.5 *x* 91.7
Compression ratio	14.5 : 1
Charge provision	Naturally aspirated
Charge dilution	LP cooled EGR
Cooling system	Phase Change Cooling (PCC)
Combustion chamber	Steel piston with corona style piston bowl Cast iron cylinder head and crankcase
Gas exchange	Pressure loss reduction measures at intake and exhaust system

Compared to conventional engines it was also necessary to reduce the engine friction significant to achieve the BTE target. As a result, the engine hardware had to be completely redesigned.

In the hybrid powertrain are friction losses from the ICE in general and cold start friction in particular an important part in the field of optimization. The main friction losses of modern combustion engines are from pumping power of the oil pump and viscosity related hydrodynamic friction in bearings. To reduce the friction losses modern engines use super light engine oils that have lower viscosity at low temperatures. Even though lower viscosity oils help to reduce hydrodynamic friction and pumping losses they also cause increased mixed friction and oil mass flow demand caused by increasing leakages at higher engine temperatures.

An alternative measure to reduce the oil mass flow demand and decrease the viscosity dependency of the friction is the use of roller bearings. Their demand for fresh oil is so low, that the whole oil supply can be delivered by a 12 V electrical oil pump, what further reduces the mechanical losses of the driving power. With these specifications in mind, IAV has developed a completely new roller bearing crank and valve train. The crankshaft is made of forged pieces that are welded together. This allows a cheap manufacturing and high stability. The conrod is made of a single piece without a cut and the con rod pin is press fitted to the crank shaft. The entire crankshaft design was also subjected to an optimization loop and selected via the IAV Engineering Toolbox using the crankshaft optimization with regard to an optimum of fuel consumption and weight The final design is shown in figure 3.

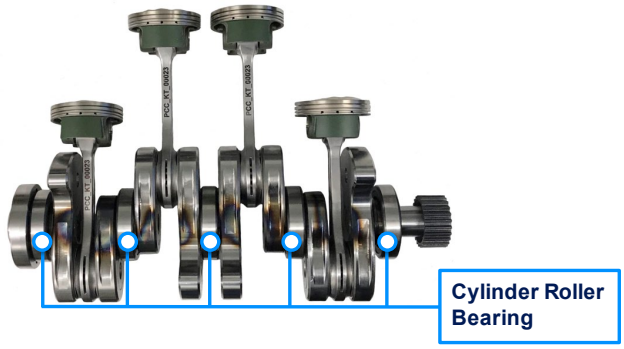


Fig. 3. NA16 roller bearing crank train

Another essential part of the new crank train is also the all new steel piston with a corona shape bowl (cf. Fig. 4). The piston is redesigned to increase the conrod to stroke ratio while keeping the engine block deck height constant. The compression ratio ε increase from baseline ε=10.5 to ε=14.8, to withstand the higher peak firing pressure and temperature, to reduce wall heat losses and to enable a more freely flame propagation throughout the combustion phase. In figure 4 the NA16 steel piston layout and the needle roller bearings on con rod and piston bolt is shown.



Fig. 4. NA16 steel piston and con rod

As the crank train the valve train was also friction optimized and equipped with roller bearings. The

camshafts use 5 needle bearings each and the roller finger followers were equipped with fixed lash adjusters. The fixed lash adjusters reduce oil demand and bearing forces. The oil spray function of the lash adjusters was reduced since it is only required for cooling of the finger followers and needle bearings. The original camshaft bearing oil supply was completely removed. In addition the maximum engine speed was reduced to $n_{mot} = 5{,}500\ min^{-1}$ and by optimizing the engine dynamics it was possible to further reduce the salve spring force and preload. The timing drive is a tooth belt with low friction profile and auxiliaries including the oil pump were removed. The 12 V generator is replaced by a DC/DC converter as typical for hybrid powertrains. In addition the HVAC and oil pump are electrically driven.

The cylinder head and crankcase were equipped with the PCC technology and material was changed to cast iron. Cast iron was chosen to reduce the costs and increase the span of engine temperatures adjustable. Thanks to the increased cooling capacity of PCC local or general overheating is not an issue therefore the higher heat conduction of aluminium is not needed for the target application. With the implementation of PCC the conventional coolant pump becomes obsolete and was removed.

To ensure a stable and controllable high diluted combustion it is important to ensure that the fresh gas entering all cylinders is of the same constitution. This does not only mean the mass flow and temperature to all cylinders must be very equal but also the amount of residual gas, fuel and a good mixture of air, EGR and fuel must be ensured.

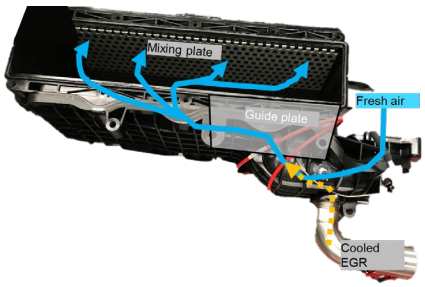


Fig. 5. EGR Fresh Air Mixing

For this purpose IAV developed a dedicated low pressure cooled EGR system for the naturally aspirated engine. That ensures equal distribution to all cylinders, a good air – EGR mixing, high EGR rates at WOT and a condensate trap (cf. Fig. 5).

3. Prototype Testing

3.1 Setup

After manufacturing all the prototype parts in house the engine parts were com-prehensive quality checked and documented. Besides to standardized component verification, particular components (e.g. EGR-Cooler) were also tested on IAV's component test rigs before the demonstration engine was assembled. The engine installed in the test cell can be seen in figure 6.

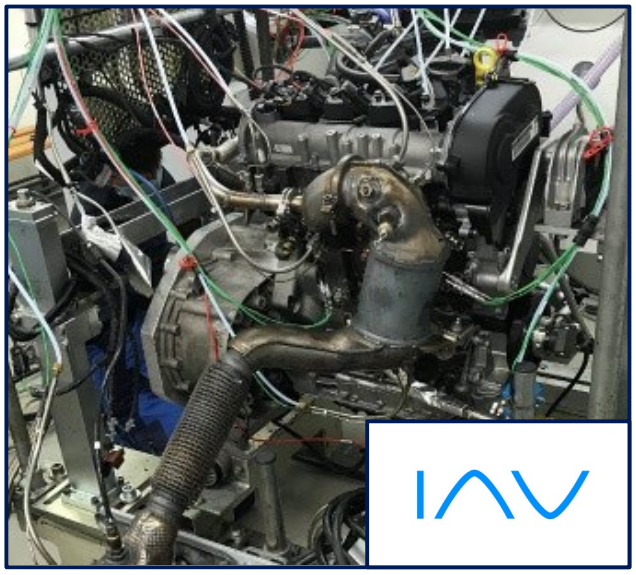


Fig. 6. NA16 engine on dyno

At the same time, the demonstrator was equipped with the characteristic and standardized test bench measurement variables, such as temperature and pressure in the air path, exhaust gas, oil and coolant lines, as well as engine speed and torque, and fuel conditioning. High-pressure indication per combustion chamber was also incorporated into the cylinder head for combustion analysis. The conditioning of the operating media (air, coolant, oil) is carried out via the test bench peripherals.

3.2 Test Results

After commissioning and a conventional run in program the test campaign for the NA16 started. The first step was a strip measurement of the engine to evaluate the engine and component friction measures. The determined engine friction mean pressure (p_{mr}) can be seen in Fig. 7 and in the BTE optimum range, p_{mr} is approximately $p_{mr} = 0.54 - 0.60\ bar$.

Beside the friction optimizations the high dilution burn stability was a major point that was investigated on the dyno. The results of lean burn operation in two relevant operating points can be seen in figure 7. The engine operating points shown are:

- $n_{mot} = 1{,}300\ min^{-1}$; $p_{me} = 8\ bar$ (MP01)
- $n_{mot} = 2{,}500\ min^{-1}$; $p_{me} = 9\ bar$ (MP02)

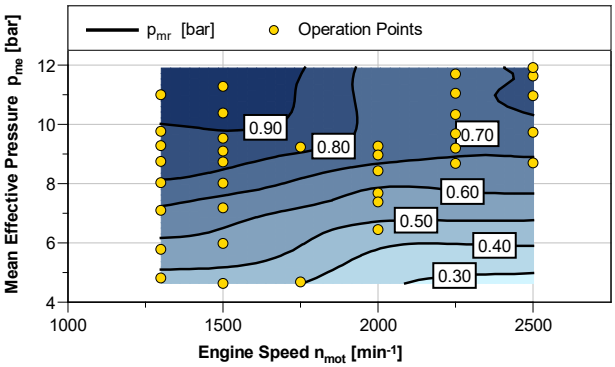


Fig. 7. NA16 friction mean pressure

The test results in figure 8 show the measuring points for indicated specific fuel consumption (ISFC) and coefficient of variation (COV) over the combustion-air ratio λ. At MP01 the combustion-air ratio λ was increased stepwise to $\lambda = 1.65$, while at MP02 was increased to $\lambda = 1.80$ without exceeding a COV limit of 3. The achieved ISFC at MP01 was $b_i = 208\ g/kWh$ (Super E10) and at MP02 which is a key operating point in a hybrid powertrain the NA16 set an ISFC of $b_i = 189\ g/kWh$.

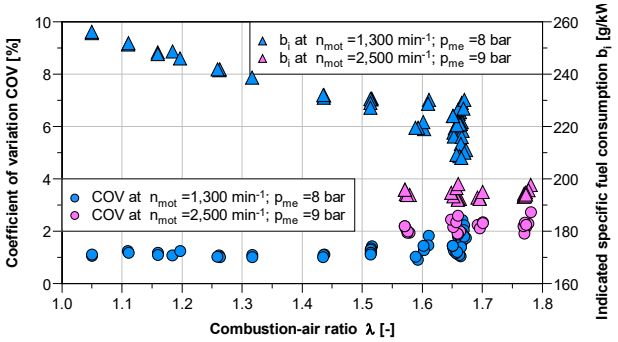


Fig. 7. NA16 NA16 lean burn stability

In addition to an implementable lean operating strategy (additional exhaust gas treatment for NO_x is needed), it is also possible to further reduce CO_2 emissions by using the standard 3-way catalytic converter and biofuels. Especially for vehicle markets or segments that cannot easily be served purely electrically across the board. For this purpose, the NA16 was operated with bioethanol at $\lambda = 1.0$ and with cooled low-pressure EGR.

The measured engine BTE can be seen in figure 8. A peak brake thermal efficiency of $\eta_{BTE} = 44.2\ \%$ was achieved at an engine operating point of $n_{mot} = 2{,}000\ min^{-1};\ p_{me} = 8\ bar$ with an EGR-Rate of 22 %. Furthermore, a wide ICE operating range with $\eta_{BTE} \geq 40.0\ \%$ extends.

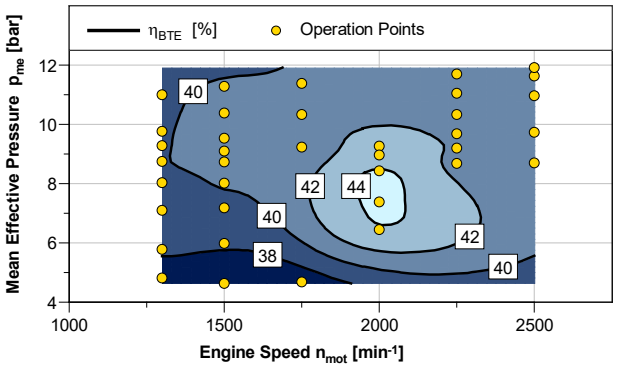


Fig. 8. Measured BTE of the NA16 engine with biofuel operation

4. Conclusion

Driven by the necessity of improving the emissions of internal combustion engines and based on real world driving demands IAV developed an optimized internal combustion engine for hybrid electric powertrains. Thereby IAV using a new approach of engine cooling which offers new degrees of freedom in component cooling depending on the operating point and works consistently according to the principle of demand-based cooling. Additionally extensive measures were implemented in the engine to reduce friction, such as a roller bearings. After transferring the engine design to a demonstrator ready for testing, the successful commissioning of the all new engine, extensive test program were carried out to prove the engine performance and improved efficiency.
The peak brake thermal efficiency of $\eta_{BTE} = 44.2\ \%$ achieved with net zero CO_2 emissions due to the usage of biofuel. Currently further investigations at the test stand are ongoing to extend the $\eta_{BTE} > 43\ \%$ area in the engine map.

5. Acknowledgement

The authors acknowledge the contribution of their colleagues Frank van der Seylberg and Lingjun Xu to this work.

6. References

[1] Matthias Krause, Arnold Thomas: “Future Thermal Management as Enabler for more efficient ICE’s”, JSAE 2021

[2] https://global.toyota/en/mobility/tnga/powertrain2018/engine/

[3] Marc Sens, Emanuel Binder: “Pre-Chamber Ignition as a Key Technology for Future Power-train Fleets”, MTZ 02/2019

[4] Steve Rolfe, Arnold Thomas: “High power density powertrains“, SAE Thermal Conference 2019 Detroit

[5] United Nations: Worldwide harmonized Light vehicles Test Procedure, ECE/TRANS/180/Add.15, 2014

Electrically heated catalyst performance at low ambient temperature

M.Capirchia[1], M.Goncalves[1], V.Lebourgeois[1], E.Jean[1]
1: Forvia Clean Mobility, Bois sur prés, 25550 Bavans

Abstract: Cold start and cold operation have been identified as a key operation area to be improved for coming emissions regulations, especially in Europe and China. A further acceleration of the catalyst heating will be necessary. While in the past huge improvement have been achieved by passive measures, including close coupled mounting of the catalyst, inertia reduction and insulation and refinement in the engine hardware (Secondary Air injection, direct injection...) associated to enhanced catalyst heating strategies, active heating within the exhaust system will be necessary to achieve a breakthrough.

In the Euro7 regulation, the temperature window will be extended and start at negative ambient temperature needs to be considered very carefully.

In this paper we will describe the electrically heated catalyst system and its optimization for the different use cases. A focus is done on the low temperature engine operation, the conditions for a proper efficiency and the performance achieved by the system, using simulation as well as vehicle test results. Different heating strategies are applied to demonstrate the potential of the system depending on available power and activation time.

Keywords: Electrical heated catalyst, Emissions reduction, Very Low emissions, Low temperature, HC, CO, NOx, ICE and Hybrid gasoline engine.

1. Introduction

The Electrically Heated Catalyst (EHC) is considered a key technology to further reduce pollutant emissions after engine start and fulfil future emission standards, especially Euro7. The environmental constraints of the exhaust system (temperatures up to 1000°C, engine vibrations, exhaust gas flow mass and distribution), combined with the endogenic stress linked to the heating operation have driven design and performance of the system. As the constraints and validation work have already been presented in previous papers [2][3], we will focus on the paper on the performances which can be achieved for operation at ambient and at low temperatures. This will complete the picture and show the benefit which can be expected from such a system.

2. Driver: Euro7 emission regulations

The evolution and continuous severization of the worldwide emissions regulations in the last 30 years has been addressed with a continuous improvement and refinement of the technology. Engine components, combustion system and control strategies have been widely redefined. The aftertreatment system has been further optimised, with improved integration, new ultra-thin wall substrates technologies and coatings.
Most of these requirements were then based on a fixed chassis dyno cycle, with clearly defined boundary conditions.
With the introduction of RDE (Real Driving Emissions testing) in Europe (Starting in 2017 with Euro6 phases c and d), the engine operation area is extended, but there is still no strong constraint on HC/CO at low temperature, as the RDE/ PEMS limits only applies to NOx and Particulate Numbers.
At the time we are writing this paper, the Euro7 regulation proposal of the European Commission has still not been released. However, the general objectives set by the European in the Inception Impact Assessment document [1] are the following:
*“The **specific objectives** are to improve air quality, with a particular emphasis on urban areas, by reducing air pollutant emissions from road transport and setting harmonized rules for vehicles. The **operational objectives** are to reduce the complexity and compliance costs of the existing Euro 6/VI vehicle emission standards, to provide appropriate and up-to-date limits for all air pollutant emissions and to ensure that new vehicles keep their air pollutant emissions under control throughout their entire lifetime and in all conditions of use.”*

Following this direction, stronger requirements at low temperature and under typical city driving conditions are expected. Both the emission limits as well as the testing boundary conditions should become more severe for all pollutants (Figure 1).

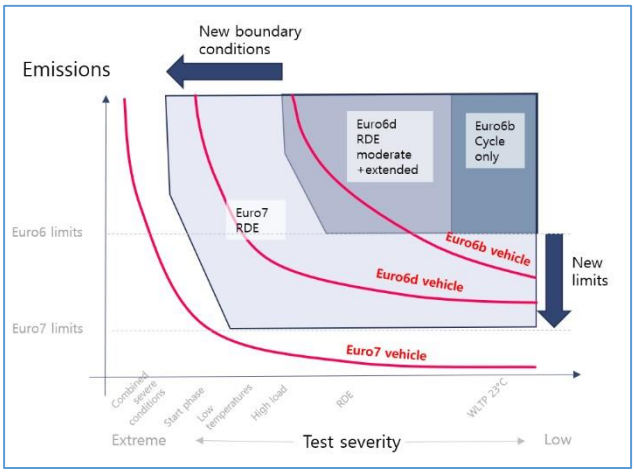


Figure 1: Evolution of the Emission regulation requirements from Euro6 to a futureEuro7

As a result, cold starts and engine warm-up operation, especially at ambient temperatures below 0°C becomes critical for gasoline engines.
Beside all the passive system optimizations mentioned above, we think that a breakthrough is needed to strongly reduce emissions at low temperatures. In addition to the well-known engine control strategies, an active system is required to provide additional heating power at engine start. The Electrically Heated Catalyst (EHC) is a strong candidate. It is providing an external heating source which can be controlled independently from the engine, and therefore helps to get the catalyst ready to pollutant conversion almost immediately.
As the heat source is decoupled from the exhaust flow, the controls can be adjusted to fulfil the needs, depending on the operation modes and boundary conditions. Furthermore, the system can be adapted to different vehicle electrical network and battery specifications.

3. Product description

3.1 EHC single grid

Forvia developed an EHC based on a thin metallic resistive element placed in front of the catalyst, generally named Grid (Figure 2). This component ensures by design a perfect and homogenous heating, with a very dynamic response.
Key aspects along the EHC product development were the compromise to be found between electrical resistance, mechanical robustness, and heating dynamics. This development steps have been already shared on several previous publications **Erreur ! Source du renvoi introuvable.Erreur ! Source du renvoi introuvable.**.



Figure 2: EHC grid product exploded view

The single grid heater has some limitations (Max Power/ Durability) linked to its design. The initial design was targeting 2kW under 12V nominal application, it has been possible to withstand up to 4kW on Faurecia internal tests, under controlled operating conditions.
Deeper work on integration and pre-heating with flow highlighted that:

- The flow distribution and especially the inlet cone design has a big influence on the grid local temperature and therefore on the max power achievable,
- For the most severe emission regulation scenarios, and for near zero emissions applications, there is still a potential need for even higher power around 6 to 8kW

Different improvement paths were elaborated, to increase the exchange surface between heater and exhaust gas.
An easy solution is to multiply the number of heaters, but this might lead to an excessive mass, a loss of performance and to several controllers, having therefore a high impact on system costs.
The best design solution has been found by placing two grids in serial in one electrical loop, allowing to increase the electrical resistance without affecting the mechanical durability of the grids.

3.2 EHC Double grid

From this design demonstrated and validated on single grid, a further improvement of the concept has been developed, using two heaters placed on both faces of a short ceramic catalytic substrate (figure 3).

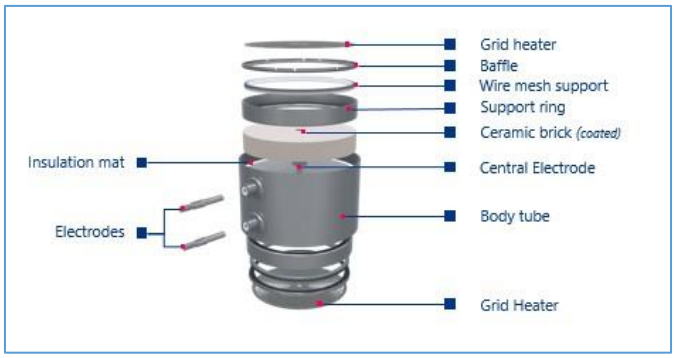


Figure 3: EHC Double Grid Layout

As the two grids cannot be close to each other (to avoid contact), a gap is necessary. To take advantage of this gap a short catalytic converter is installed between the grids.
In addition, this design improves the heat transfer during pre-heating phase (especially without flow), taking full advantage of the increased catalytic surface receiving the radiated heat (figure 4).
Due to the specific geometry, the second grid is radiating to both substrates, the first one on the second substrate and on the cone. Finally, around 75% of the radiated energy (major heat transfer phenomena on the grids) is directly impacting the ceramic, and therefore directly usable for aftertreatment.

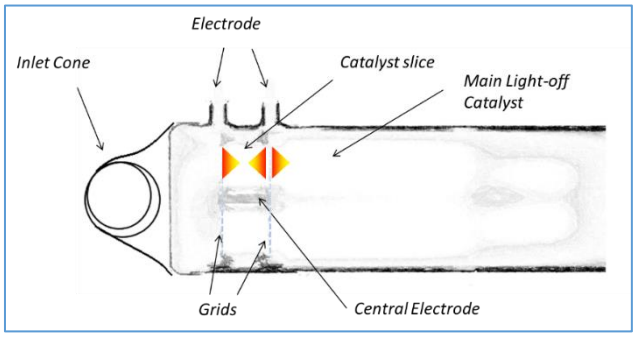


Figure 4: Radiative heat transfer in a double grid layout (radiation is indicated by the triangles)

This enhanced EHC solution is protected by more than 20 patents filings.
The double grid solution offers some freedom in the selection of catalyst (CPSI/wall thickness), and opportunity for a different washcoat and precious metal content in the first catalyst slice than in the main light-off catalyst.
The main manufacturing process of the EHC module relies on Forvia's core expertise, especially canning (using ceramic fiber mats), laser- and arc stud welding. These processes enable the assembly of very thin materials without spatters or surface degradation [5].

4. Emissions and Thermal performance

The first step to assess the performance of the EHC was done based on WLTC at 20°C ambient T. It was the quickest way to highlight the performance without requesting a strong activity on engine calibration (as 20°C is strongly manage and optimized since many decades)

4.1 EHC performance WLTP @ 20°C

The focus is done on the double grid which allows the larger range of possibility on the EHC usage (pre-heating w or w/o flow, higher power.) applied on a 1,6TGDI gasoline engine.

A first picture is given with EHC mission profile based on heating and short pre-heating. This will not impact the final user in his way to use the vehicle (during engine start) specially on pure ICE and MHEV applications.

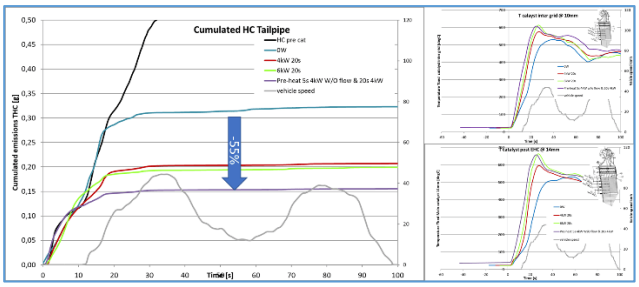


Figure 5: Emissions and Temperature profile with heat and short pre-heat (low energy)

Thanks to low thermal inertia of the EHC double grid, a strong emissions reduction between 30-55% can be achieved (figure 5).
The double grid could be used in a more disruptive way by putting more energy during the pre-heating phase, which is the key driver to reach low emissions targets.
As an example, it is possible to decrease by 75 to 90% the HC (figure 6) with a significant catalyst volume already above 400°C at engine start.

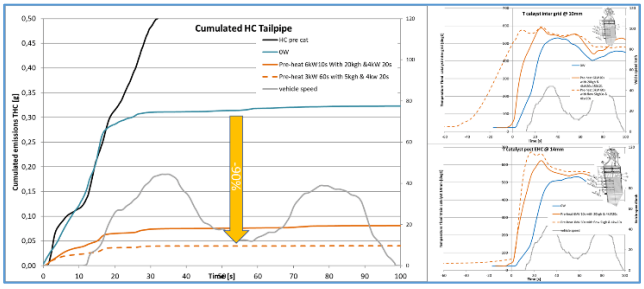


Figure 6: Emissions and Temperature profile with different heat profile to reach Low level (High Energy)

This profile is appropriate for (P)HEV applications with more power available in the batteries and offers opportunity to manage the use of thermal and electrical engine (pre-heating could be done for example during electrical driving).

4.2 -7°C challenge and EHC performance

The emission performance after start at low temperature is expected to be of outmost importance for Euro7 applications and be the key challenge to meet the Euro7. It was therefore decided to conduct a test campaign at -7°C. The objective was to assess the product performances on gasoline engine at very low temperature with different calibrations and heating strategies.

4.2.1 Engine calibration management

Moving from 20°C to -7°C, the first challenge at low temperature is to get the engine revving up properly to the idle speed and to ensure a stable operation without misfiring events. On this purpose most of the engine manufacturers are delaying the ignition timing and using a rich mixture to achieve a quick start and stabilize the engine operation.

The picture below (figure 7) shows the lambda value before and after optimization.

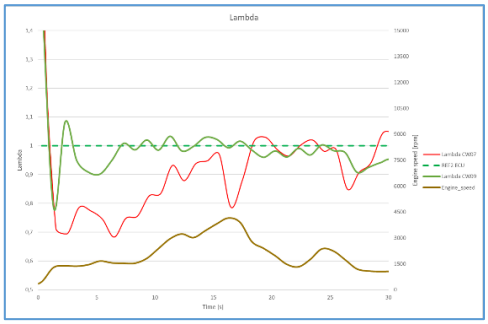


Figure 7: Lambda profile before/after optimization

The baseline calibration (red) curve (lambda between 0,7 to 0,8), is not operating in the optimum stoichiometric window for the TWC. The activation of the EHC single grid has nearly no effect on the emissions (figure 8).

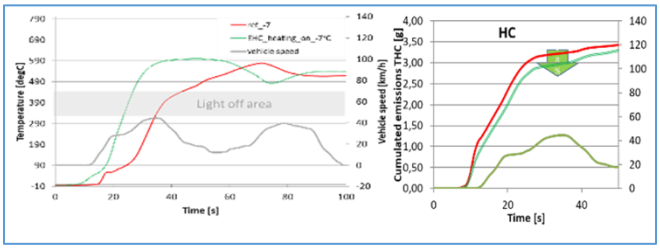


Figure 8: T° and HC emissions w/o calibration update

These results confirm once again that the temperature of the exhaust gases is not the only relevant factor for pollutant emission abatement. An EHC can only work in synergy with an adequately calibrated engine control system.

4.2.2 EHC performance WLTP @ -7°C with improved calibrations

The adjustment of the calibration bas been done with main objective to reduce the time to stoichiometry and to improve the catalyst heating strategy at low temperature. Following adjustments were applied:

- After start enrichment (reduced)
- Upstream dewpoint (reduced)
- AFR setpoint in After start and warmup phase
- Torque reserve in catalyst heating
- Catalyst heating duration

The new baseline calibration (yellow curve) is showing an emission decrease by 45% on HC thanks to improvement of raw emissions (figure 9). The benefits of EHC will be compared to this new baseline.

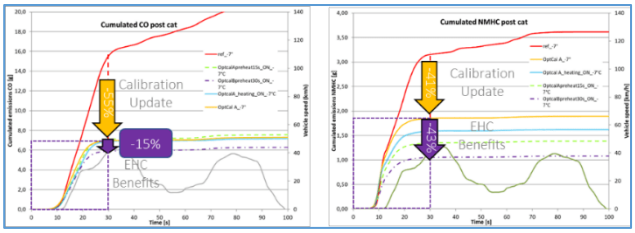


Figure 9: T° and emissions with calibration update

The EHC single grid activation enable a further reduction of around 20% on NMHC, and up to 45% with preheating with a maximum power of 3kw. After 20s, the catalyst is working at high efficiency with no noticeable residual emissions.

For NOx the effect is even stronger with a reduction of 25% without preheating and up to 75% with preheating.

The CO emissions, which have been strongly reduced by the calibration, are only marginally impacted by the activation of the EHC. This can be explained by the extreme sensitivity of CO conversion to lambda and would need a further fine tuning of the calibration.

The tendency seen @ 20°C is confirmed at -7°C. The next challenge is to assess/confirm the potential by combining the low T°C and the RDE conditions.

4.2.2 EHC performance RDE @ -7°C with improved calibrations

A RDE profile has been defined to assess the performance on a more dynamic cycle than the WLTP one. The first idle duration has been reduced (6s, vs 11s for WLTP) which requests a quicker activation of the aftertreatment system (figure 10).

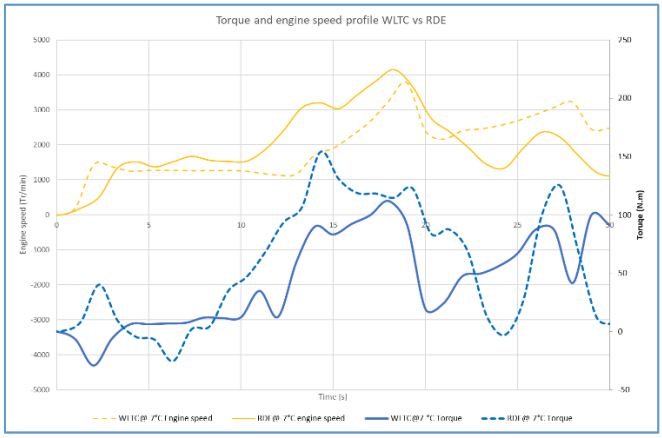


Figure 10: RDE and WLTC profile (engine speed and Torque)

The table 1 is summarizing the key parameters between the different profiles.

	WLTC	RDE
Idle time (s)	11	6
Max Torque (Nm) (% couple max)	110 (45%)	150 (65%)
First acceleration (m.s-2)	1,15	1,83

Table 1: RDE and WLTC comparison

The EHC has to transfer the energy very quickly, a low thermal inertia is mandatory.

As in the previous test, different EHC activation strategies have been evaluated.

The first graph (figure 11) is showing the T°C improvement in the different catalyst thanks to the increase of energy.

The energy injected allows to reach 400°C on the 20mm slice of the double grid even before engine start and significantly reduces the light off time on the main catalyst.

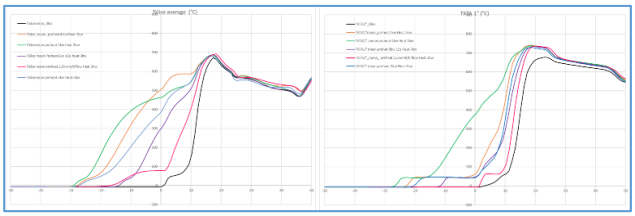


Figure 11: T° behaviour with EHC on RDE profile

However, the emissions benefits are not continuously increasing with the temperature improvement.

As example on the RDE profile (figure 12), the benefits reach quickly around-40% but is not going over 50% with long preheating.

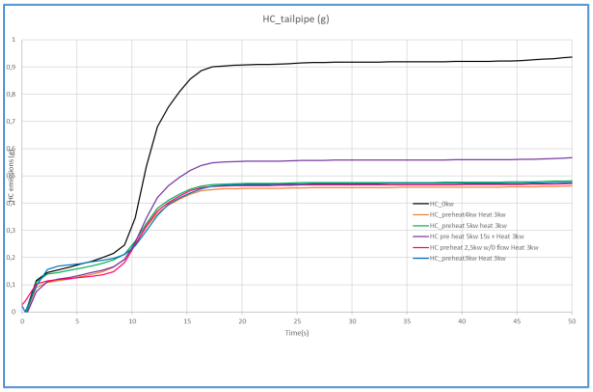


Figure 12: T° behaviour with EHC on RDE profile

The emission improvement potential in this case is limited by the hardware and the calibration status of this Euro6d engine. A stoichiometric lambda value could not be achieved during the first 3-4s. The temperature increase in the catalyst can't be transformed in additional emission reduction as the catalyst is not in his optimal window.

To confirm this statement, additional tests were conducted by keeping air injection (6kg/h) during 5s after engine start.

The lambda measurement before EHC confirmed a leaner mixture (figure 13) and at the same time the tests with same mission profile are now unlocking the limitation on emission reductions.

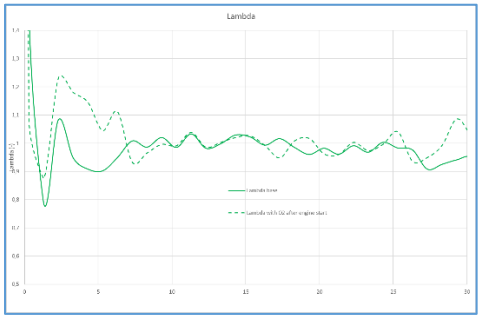


Figure 13: Lambda with additional air injection

A potential of -65% of emissions is now achieved with 5 kw. (figure 14)

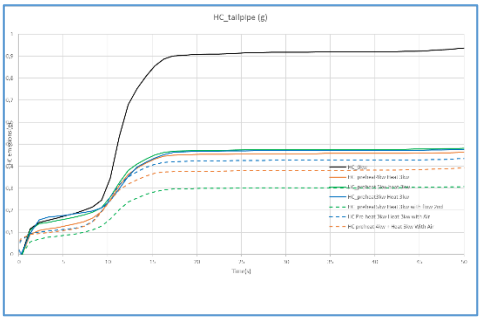


Figure 14: HC emissions with Air injection after engine start

The comparison on the T° profile (figure 15) for a given case (5kw as example) is highlighting the increase of T°C in the slice and confirms with this exotherm the additional conversion rate. This is also showing the 20mm slice is acting as a booster on the double grid.

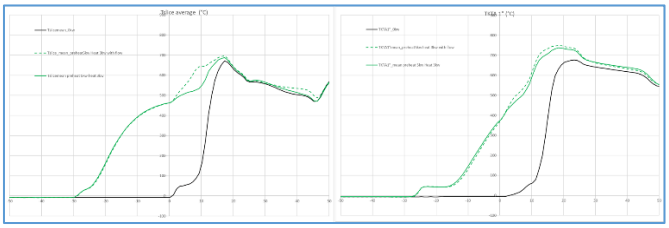


Figure 15: T°C with 5kw and air injection after engine start

Finally, by using the EHC single grid or double grid, with low thermal inertia, strong emissions reduction can be achieved whatever the T°C (-7°C or 20°C) and cycle (WLTP or RDE with more dynamics).

4.3 EHC performance: Energy usage

A product with a design leading to higher thermal inertia will be more impacted on RDE profile with few second of idle before first acceleration. This short idle time on RDE cycle give a faster increase of energy on TWC by exhaust gas so a shorter time before light-off compared to a WLTC (figure 16).

Due to its low thermal inertia the grid family product can address the specific request of RDE profile. Very quick energy transmission of the thermal energy to the TWC is the key point.

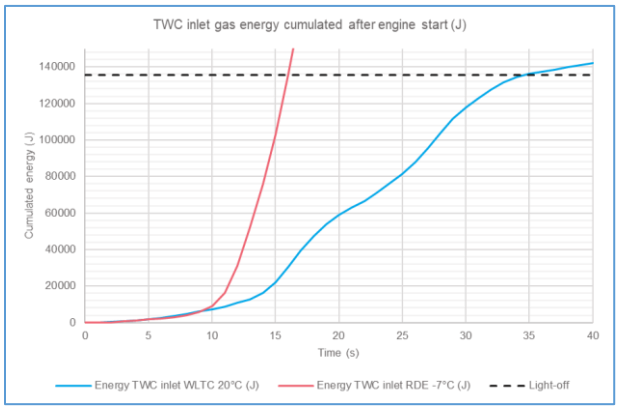


Figure 16: Exhaust gas energy comparison between WLTC and RDE cycle

With test results comparison between WLTC and RDE, confirmation is given that TWC light-off is always reached after the same average level of cumulated thermal energy (gas + EHC thermal energy).

As the exhaust energy in RDE cycle is increasing much faster and the energy rate (J/s) in the exhaust is higher with the RDE cycle, the impact of inertia is even more important than for WLTC. (Figure 17).

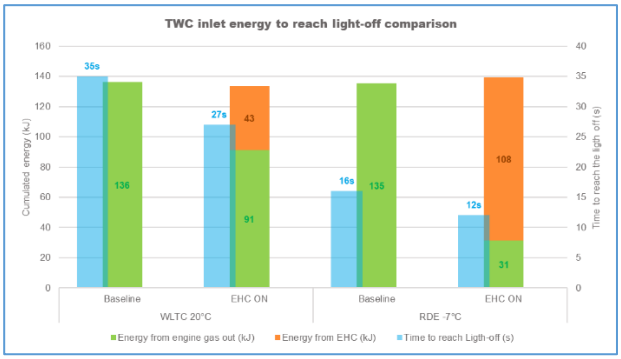


Figure 17: EHC energy contribution comparison between WLTC and RDE cycle

One second reduction of light-off time on RDE cycle gives better improvement of HC emissions than one second on WLTC. At the end, with the low thermal inertia of Grid EHC, similar HC reduction percentage on all cycle with same electrical energy can be obtained.

Figure 18 is showing a summary of tests on different 3 and 4 cylinder engines, temperatures and operating strategies. If the engine calibration is adequate, the HC reduction is proportional to the electrical energy brought onto the system. This gives precious indications for the sizing and for the calibration of an EHC system on future applications.

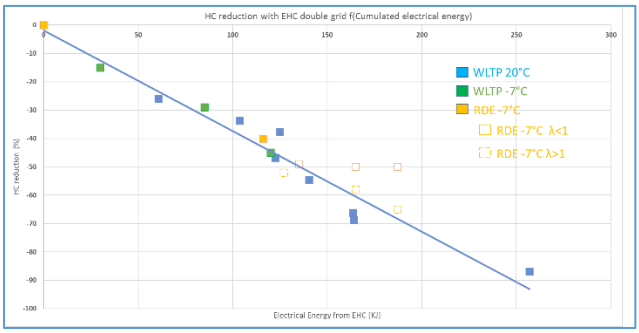


Figure 18: Emission reduction vs energy injected

This clear trend is applicable to the whole EHC grid family product, whatever the T°C and the cycle profile. thanks to its high efficiency (> 90% of heat transfer to the gas after 10s).

5. Conclusion

The significant potential of EHC solution for gasoline applications has been clearly identified and EHC is now a mature and validated technology.

This confirms the EHC as a key player to reach the future stringent Euro7 regulation.

6. Perspectives

This paper highlights that the EHC grid solution thanks to its smart design (low thermal inertia) is able to address several levels of emissions reduction, with different constraints on the controls, depending on the requirements. The application of the EHC function need to be performed in synergy with improved engine calibration and ECU functions, especially during the start phase. Under these requirements EHC is a powerful tool to comply with the most severe regulations to come.

As the product is now available and fully validated, it opens the door for further applications:

- E-fuel / natural gas applications to support the light off, which is very critical due to the fuel characteristics
- Reduction of the PGM content in applications with high PGM content, to be less sensitive to volatile precious metals prices.

These points will be described more in detail in future papers.

7. Acknowledgement

The authors acknowledge the contribution of all the Forvia colleagues involved in the development and the testing of the systems described here above.

8. References

[1] European Commission – Inception Impact Assessment- Development of post-Euro 6/VI emission standards for cars, vans, lorries and buses- Ref. Ares(2020)1800668 - 27/03/2020]

[2] E.Jean & Al.: “Electrically enhanced after treatment system”, HKIPC conference, Hwaseong, Korea, oct. 2018..

[3] A.Sassi & Al.: “Aftertreatment Optimization through Electrical Heating”, SIA Powertrain conference, June. 2019.

[4] Jean, E & al. „Electrically Heated Catalyst: Requirements, Controls and Key Parameters”, 41. Internationaler Wiener Symposium, 2020

[5] M.Capirchia & A.I: “Electrical heated catalyst product and system : the answer for hybrid gasoline clean engine”, SIA Powertrain conference, June. 2021.

[6] E.Jean & A.I: “Electrically Heated Catalyst for Euro7 Hybrid Vehicles, 43. Internationaler Wiener Symposium, 2022

9. Glossary

EHC : Electrically Heated Catalyst

WLTC : Worldwide harmonized Light vehicles Test Cycle

RDE : Real Driving Emissions

TWC : Three Way Catalyst

HC: Hydrocarbon

HCU : Heater Control Unit

Improving the efficiency of P0 and P1 hybrids by valve deactivation strategies

F. Himsel, T. Werblinski, A. Mayer, P. Traversa

Schaeffler Technologies AG & Co. KG

Abstract: Combustion engines will be present for a long period, be it in their classical form or in various architectures of hybrid powertrains. Among those, P0 and P1 hybrids suffer from the fact, that the electric machine is permanently coupled to the combustion engine, so that the crank shaft is always rotating when the electric machine should either generate propulsion or recuperate energy while the vehicle is braking.

By deactivating the exhaust valves of the combustion engine in combination with a cam phasing strategy on the intake valves, air flow through the engine can be disabled, while simultaneously reducing drag torque substantially. This results in increased energy recuperation during overrun mode and enables efficient propulsion through the P0/P1 electric machine. This additional flexibility within the energy management, compared to state-of-the art MHEVs, is another parameter to optimize fuel efficiency. Therefore, advanced strategies for energy usage are discussed.

Besides the CO_2 reduction by efficiency increase, deactivation of the air flow results in protecting the catalyst from oxygen and cold air, which would lead to emission spikes when refiring. Common countermeasures like purging with rich mixture can be avoided, enabling further CO_2 reduction.

The positive effects on fuel consumption and emissions are discussed for vehicles with different powertrain configurations.

Keywords: Valve deactivation, MHEV, overrun, recuperation

1. Introduction

Hybrid powertrains have become more and more popular in the past few years and are widely accepted as a bridge technology from the vehicle which is propelled by the combustion of fossil fuels to the vehicle propelled only by electric energy. Various concepts of hybrids are competing, which differentiate widely in the arrangement of the electric machine(s) with respect to the combustion engine, in battery size and the way the battery can be charged (only during driving or also by external supply of electricity), leading to different requirements to the ever-present combustion engine. The simplest form of hybrids, therefore often referred to also “mild hybrids” are arrangements, where the electric motor is directly coupled to the combustion engine. This can be either in the form of a belt driven starter-generator (P0) or as a crank shaft mounted electric machine (P1 hybrids). For both types, the electric machine can only operate in combination with the combustion engine.

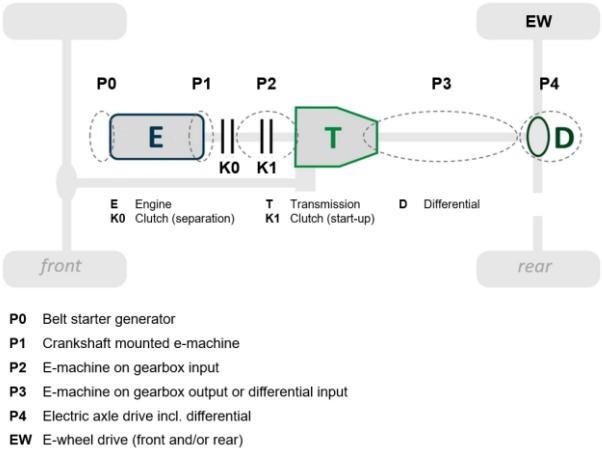


Figure 1: Positions of electric drives for hybridisation

There are also higher forms of hybrids (P2 to P4), as well various forms of parallel and serial hybrids, which enable separation of the electric machine from the crank shaft, and therefore an independent operation from the combustion engine, but are also more complex and therefore more expensive. Therefore, P0 and P1 hybrids are very cost-effective hybrid solutions on the one side but are also proper solutions for vehicles with limited or no access to external charging infrastructure, which differs from market to market or even from customer to customer.

2. Motivation and system description

The combustion engine as the primary source of propulsion, can generally be operated in two modes: It can generate positive torque for the propulsion of the vehicle, or it can be dragged by the kinetic energy of the vehicle in overrun mode. In overrun mode, the electric motor can be used as a generator and recuperate a part of the kinetic energy into electric energy, which can later be used once more for driving. For overrun mode, it would be beneficial to keep the drag torque of the combustion engine as low as possible, because then more kinetic energy could be recuperated.

The drag torque of the combustion engine consists mainly of the frictional torque and torque generated

PUBLIC

by the pumping losses, which still have to be overcome although no combustion takes place. This has two adverse effects: The work for pumping is lost for later usage on the one side, and further on air is pumped through the engine, leading to the catalyst being flooded with oxygen and the overall exhaust system being cooled down. The oxygen reduces the conversion rate of the TWC after refiring, leading to an emission peak, which is usually mitigated by a short phase of rich combustion, known as catalyst purge. This once again leads to an increase in fuel consumption at the end of each overrun phase.

If the unnecessary transfer of air could be avoided, several positive effects could be gained:

- Increased energy recuperation through reduced drag torque
- Avoidance of rich operation after overrun phases
- Avoidance of aftertreatment system cool down

2.1 System Description

Unnecessary pumping of air can be avoided by keeping the engine valves closed at all times. For roller finger follower valve trains, systems in the market, mostly used for cylinder deactivation, are either based on switchable cam followers with hydraulic actuation of the locking mechanism or on switchable cam shafts. In order to combine the benefits of both systems, an electromechanically actuated switchable roller finger follower system was developed [1].

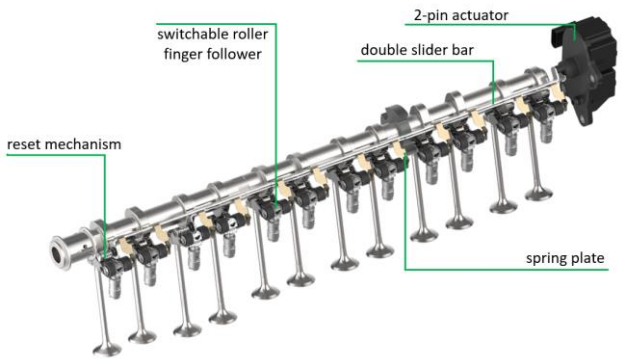


Figure 2: eRocker System for valve deactivation on the example of an inline six-cylinder engine

To avoid the cam motion being transferred to the engine valve, the inner lever of the switchable roller finger follower is uncoupled from the outer lever by retracting a locking pin. The locking pin motion is activated from outside the roller finger follower via an actuation pin. The reverse motion of locking is achieved by a locking spring within the roller finger follower.

The motion from the outside is generated by an electric actuator and transferred by a slider bar. This allows the actuation of multiple valve positions with one actuator. To transfer the motion of the slider bar to the actuation pin in the roller finger, a flexible element in the form of a leaf spring is provided. The flexible element has the purpose to compensate manufacturing tolerances in the system (e.g. positions of leaf spring on slider bar, position of roller finger follower in cylinder head, variations in actuator stroke), differences in position caused by thermal dilatation between cylinder head and slider bar, and also to allow for a slider bar motion although some of the locking pins cannot be moved because they are blocked by a transfer of the cam motion.

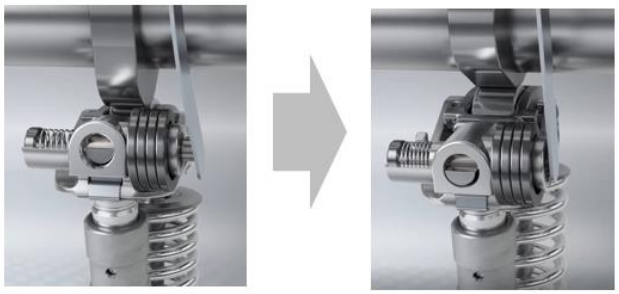


Figure 3: Flexible spring stores slider bar motion until locking pin is free to move

The system was introduced into mass production and its first application is in the new BMW 7 series and X7 in the new inline six-cylinder petrol engine with P1 mild hybridisation, presented in April 2022 [2,3].

During the development of the system, excessive tolerance analysis work has been conducted to bring all parameters and tolerances into the right combination. On the pure geometrical side, it had to be guaranteed, that lowest occurring actuator stroke will still be sufficient to actuate the system reliably under worst geometrical boundary conditions. As the roller finger follower is activated by a leaf spring, which creates zero force in its unactuated state, the actuator stroke exceeds the actuation pin stroke and must still create sufficient stroke with lowest possible spring rate and furthest initial distance from the actuation pin.

At the same time, the system with lowest leaf spring distance to actuator pin, upper spring force tolerances and upper actuator stroke must still fulfil clearance requirements and reliably actuate the system.

Finally, running in and wear at the numerous contacts had to be factored in, and all thermal conditions had to be considered. To mitigate the difference in thermal expansion between (steel) slider bar and (aluminum) cylinder head, the slider bar was realized in stainless steel. An aluminum slider bar would have eliminated the thermal expansion difference from the beginning but was dismissed to allow for a connection between leaf spring and slider bar by resistance welding.

PUBLIC

Resistance welding was selected to enable a precise enough positioning of the leaf spring on the slider bar during production, to keep the overall tolerance chain as low as possible.

As an overall result, the nominal actuator stroke is about 2.5 times higher than the nominal actuation pin motion at the roller finger follower.

After geometrical tolerance analysis, also the system actuation force must be looked at in a statistical manner to consider all variation factors. Excessive force on the actuator had to be avoided for optimum packaging. Also, the electrical supply conditions play an important role. Supply voltage can vary in certain limits and improbable combinations of events are to be considered. Safety relevant systems can cause a sudden supply voltage variation, which should not result in a failed actuation. Also, with minimum voltage and maximum tolerance combination with respect to actuation force, the actuation must take place reliably. Again, at the other side of the spectrum, the maximum voltage and a tolerance combination with minimum force requirement must not result in functional issues. In the developed system, the force required for activation for the maximum worst-case situation is about 50% higher than the force required for the minimum force worst case system. This results in an actuator, which generates about twice the required force in case of the combination of the minimum force worst case system with the maximum supply voltage. In this context, “worst case” is always referring to a “statistical worst case”, not an arithmetical one, that means all tolerance influences are summed up with the probability of their occurrence. Arithmetical worst-case considerations would inevitably lead to an overengineered system.

The subcomponents of the system are delivered to the OEM and only after assembly to the cylinder head, the system is complete. Each subcomponent (SRFF, actuator, slider bar) is tested end-of-line individually at the supplier, so that no further considerations during assembly, like select fitting, classification, or any adjustments, have to take place at the engine assembly plant. Also, cylinder head tolerances are on standard level. After assembly of randomly picked components, each possible system is fully functional within the required limits.

The system is in its first application actuated by a peak and hold actuation strategy, i.e., the initial switching is performed with maximum current (PWM duty cycle 100%) to allow for a fast switching time. As a side effect, the V-shape in the current profile can be used for positive switching confirmation for diagnosis purposes.

After switching is finished, the current is reduced to a substantially lower holding current, to reduce energy consumption and to avoid actuator overheating for longer actuation times.

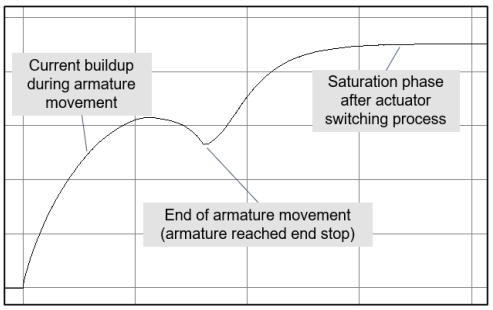


Figure 4: Current profile for system activation (PWM DC 100%)

Deactivation of the system (= reactivation of the engine valves) is achieved by switching off the supply voltage to the actuator. The return motion is performed by the energy stored in the springs of the system, located in the roller finger followers, the leaf springs and the slider bar return spring. To quickly reduce the magnetic force by overcoming the self-induction of the coil, a high negative voltage is necessary. By using a Zener-diode in addition to the negative voltage given by the coil inner resistance, the de-magnetization is accelerated dramatically.

The third dimension for tolerance analysis is the switching time variation. All possible mechanical systems must perform switching in a certain variation range of switching time for all possible boundary conditions (temperature, supply voltage, wear). Knowledge of switching time variation is essential to be able to predict the status of the system for every single valve activation and to avoid trigger angles which would result in incomplete switching at the time of valve opening. For this case, the locking pin could be in an intermediate position, which would enable the valve to start to be opened. However, during the valve motion, the overlap on the locking pin may be insufficient for the increasing force level, the locking pin is displaced and the connection between inner and outer lever is lost. Therefore, this event is often referred to as “misconnection”. Although the occurrence of such an event should generally be tolerable for system robustness against disturbances, it should be avoided systematically for durability and overall engine control, including emission aspects.

The system was modelled with all identified influence parameters in a fast-solving MATLAB model to allow for acceptable calculation times for random-number-based Monte Carlo analyses, requiring thousands of calculations with random tolerance combinations in the probability of their occurrence. The result files were used to train a neural network to enable easier result presentation. The total switching time variation from this analysis and presentation mode can be seen in Figure 5. The variations for system activation and deactivation differ substantially in value and systematic behaviour over temperature. This is due to the nature of both events: Whereas system activation

PUBLIC

is mainly driven by electric energy feeding, system deactivation is driven by the energy stored in the springs of the system. Although at higher temperature oil viscosity and therefore friction effects are lower, the actuator force gets lower due to higher electric resistance.

For deactivation, a temperature effect can be seen below 20°C due to increasing viscosity of the oil in the contacts, but the effect is very low.

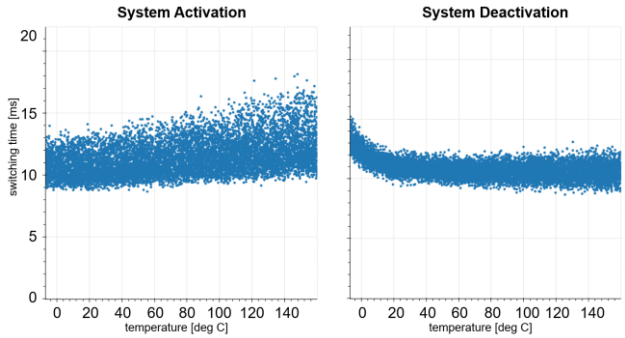


Figure 5: eRocker System switching time variation

Detailed analysis of influence factors showed that voltage variation is the highest single influence factor for system activation. Geometrical and force tolerances have a considerably lower individual contribution, but still add up to the total switching time variation.

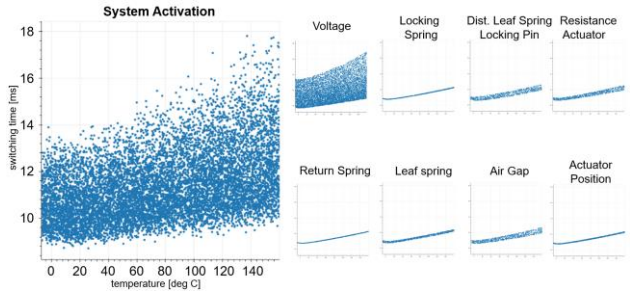


Figure 6: System activation switching time contributors

On the system deactivation side, voltage has very little contribution, as the system deactivates from the PWM holding current level. Voltage difference will cause a different PMW duty cycle due to closed loop control, but the current will drop from the same level.

For the overall switching time variation, factors for system degradation and shot-to-shot variations were factored in. The overall switching time variation was well below the allowed switching time variation, so that further optimization was not required for this application. It should be noted though, that for applications with higher accuracy requirements, a different activation scheme could nearly eliminate voltage influence. With a closed loop PWM control it would be possible to limit the max. current during peak phase. By closed loop PWM, the max. current during peak would be controlled independently of voltage, which would almost eliminate voltage variation. Switching diagnosis would still be possible via PWM frequency analysis, as the PWM duty cycle varies due to the counter induction created by armature motion.

For other dynamic analyses, including dynamic valve lift and force/load analyses under consideration of flexible bodies, also including the switching event itself, a classical dynamic valve train model was built in SIMPACK.

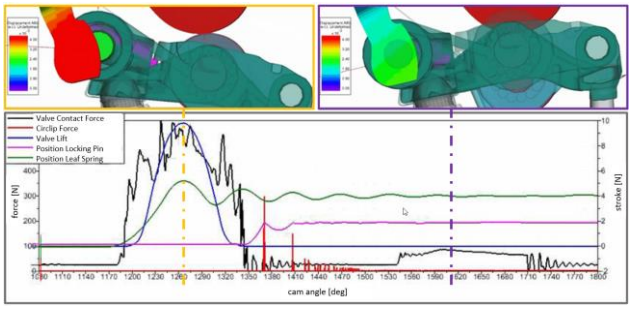


Figure 7: SIMPACK model during valve lift and valve deactivation

This model is also able to simulate misconnections (see above). Misconnections from very high valve lifts can pose a high load on all components through the uncontrolled valve closing by the valve spring. Although probability is mathematically close to zero and most valve trains will not experience any misconnection through their entire lifetime, it was a target during development, that the effect of a misconnection must not pose a threat to system function or engine lifetime.

2.2 Drag Torque Reduction

As mentioned further above, engine drag torque consists of engine friction and pumping work for gas exchange. It was already shown in [4] and [5], that there are different approaches to avoid the losses of the gas exchange.

The maximum reduction can be gained by deactivation of all engine valves. Certainly, this would require a valve deactivation system for intake an exhaust side, leading to substantial on-cost.

A slightly lower but still considerable reduction in pumping work can be achieved by either deactivating only the intake or only the exhaust valves. As a single measure, this would result in an overall increase of pumping work. Only with a combination of an advantageous adjustment of the valve timing of the valves still operating, a substantial reduction of pumping work can be achieved. The deactivation of the exhaust valves in combination with a very late valve timing of the intake valves was shown to be the best compromise [4].

PUBLIC

For the required late intake valve timing, standard hydraulically actuated cam phasers are too limited in their adjustment range. Therefore, an electric cam phaser (ECP) must be used, allowing for quick, precise and very wide adjustment of the intake valve timing. This technology combination was presented as SORS (Smart OverRun System) in [5]. The optimum valve timing was derived by simulation and is engine speed dependent. Overall, intake will have to be retarded by around 70 deg cam angle over the standard position, depending on engine speed. This means that the maximum intake valve lift will be located close to bottom dead center. Hydraulic vane type cam phasers are typically limited to total control angles of around 40 deg cam angle.

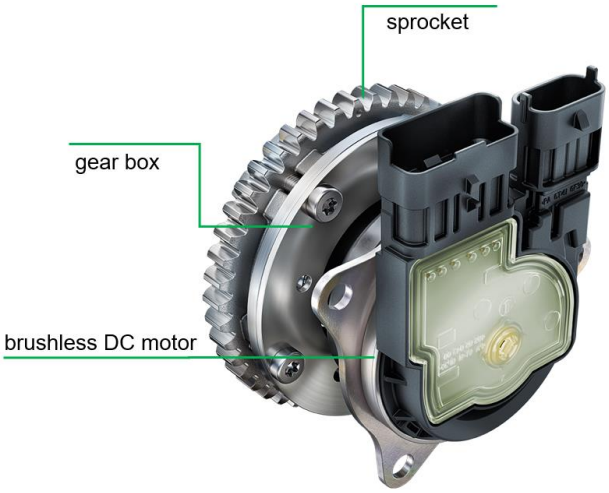


Figure 7: ECP with motor and gearbox (external controller not shown)

Besides this reduction in pumping work, also the engine friction should be reduced by valve deactivation, as the cam shaft motion is no longer transferred into a valve motion to open against the valve spring, but against the inner lost motion spring of the switchable roller finger follower. The force level generated by the lost motion spring is far below the preload of the valve spring, including safety margin, to keep the valve closed against gas forces, otherwise it would result in an unintended valve opening during deactivation stroke. At the same time, the force on the hydraulic lash adjuster (HLA) must be kept above the force generated by oil supply pressure and HLA return spring force.

The frictional torque of an exhaust valve train of a four-cylinder engine equipped with the deactivation system was examined on a classical cylinder head friction measurement test bench. Instead of driving both cam shafts via the timing belt or chain, the exhaust cam shaft is directly driven by an electric motor and the average driving torque is measured over engine speed, which is the standard approach for evaluation of valve train friction. Oil temperatures between 60 and 120°C were measured.

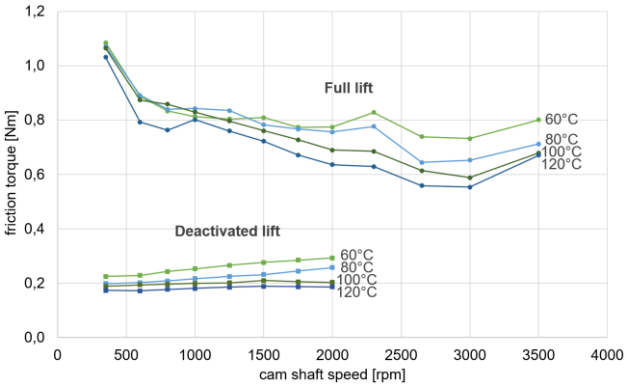


Figure 8: Exhaust valve train friction for full lift and deactivated lift

The friction benefit in the operation range of the deactivation is between 62 and 83% compared to the full lift. The full lift measurement was performed with the SRFF and with the conventional roller finger follower (RFF) of the base application (not shown). Despite the mass increase of the SRFF, the friction of both followers is within the measurement accuracy. This is attributed to the fact, that the standard valve spring developed for the RFF can also be used for the SRFF without valve lift compromises, as the mass increase by the SRFF was kept low enough.

It must be said that the overall crank shaft drag torque reduction by friction reduction for the given valve train, ranging between 0.2 and 0.4 Nm is minor in comparison to the reduction in pumping work, which is between 10 and 14 Nm for the investigated inline-four gasoline engine equipped with SORS. One reason is the very low friction level of the standard valve train of the examined engine. With full deactivation of both intake and exhaust, the benefit by friction reduction could be doubled. Also, secondary effects in the cam shaft drive (chain/belt) by cam driving torque reduction may produce further benefits for overall engine friction reduction but have not been examined.

3. Effect on fuel consumption

In [5], the fuel consumption reduction with SORS was shown for a C-segment vehicle with a 1.0 l inline three-cylinder engine and a 48 V P0 hybridization.

A new approach now analyzed a further engine/vehicle combination, being a 2.0 l inline four-cylinder in an E-segment vehicle. The boundary conditions of the simulated vehicles and powertrains are shown in Table 1.

PUBLIC

	Approach 1	Approach 2
Vehicle	C-segment	E-segment
Vehicle weight	1345 kg	2106 kg
Engine	Inline-3, 1.0 l TGDI, 92 kW	Inline-4, 2.0 l TGDI, 135 kW
Transmission	7-speed DCT	8-speed automatic
Hybridization	48 V P0 15 kW	48 V P0 15 kW
Battery	48 V 0.5 kWh	48 V 1.8 kWh

Table 1: Base data of simulation approaches

The simulation approach with a combined simulation of the engine being modelled in GT Power and the overall vehicle including hybrid mode control being modelled in MATLAB Simulink was comparable. The baseline modelling was calibrated with engine and vehicle measurements.

	Approach 1	Approach 2
SORS[1)] + boosting	- 2.5%	-1.9%
SORS[1)] + eCoasting	-4.0%	-4.4%
SORS[1)] + eCoasting + ECP benefits	-5.2%	- 5.6%

[1)]Includes benefits of recuperation and avoidance of purging

Table 2: CO_2 benefits for WLTC

As a first simulation step, SORS was applied in combination with the P0 boosting strategy of the base vehicle. The fuel consumption benefit for approach 2 came out at 1.9%, which is slightly lower than the 2.4% in approach 1. This is attributed to the overall higher power of the base engine, which has less operation range above the sweet spot of best specific fuel consumption. Therefore, boosting results in more operation points in areas of lower specific fuel consumption. Also, the calibration of the catalyst purge, which was included in the model as the respective OEM has applied it in the vehicle, are causing the difference.

As next step, the P0 strategy was changed to eCoasting instead of boosting. In the standard configurations as they are on the market nowadays, the P0 is used to lower high load torque points to have the combustion engine operated in more efficient operating areas. eCoasting uses the electric machine as only means of propulsion of the vehicle in low load operation points, which would otherwise have to be covered by the combustion engine with high specific fuel consumption. With eCoasting the combustion engine is only dragged along but not firing in these operation points. The benefit increased to 4.4% over baseline for approach 2, whereas it was 4.0% for approach 1 [5]. The difference in combustion engine load points is considerable and can be seen in Figure 9.

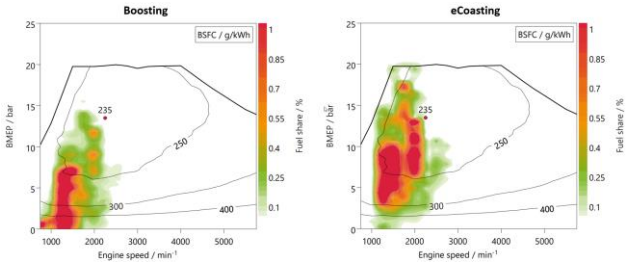


Figure 9: Heat map of operating points between boosting and coasting in WLTC

Finally, the projected benefit of 1.2% for the application of an ECP was added to both simulation results. This benefit was transferred from an independent examination and is mainly based on the more precise cam timing control, which enables the reduction of safety margins against higher EGR levels with an ECP versus and hydraulic cam phaser for a turbo charged engine.

4. Effect on vehicle emissions

The negotiation of the EURO 7 vehicle emission levels is still ongoing in the respective committees. Especially the consideration of short driving cycles is still open and may pose a severe challenge to the combustion engine, as most of the emissions are generated at the beginning of the cycle. At engine start, the catalytic converter has not yet achieved light-off temperature.

The main emission challenges for EURO 7 will be cold start and real driving emissions with high occurrences of overrun periods containing fuel cut-offs and catalyst purging events.

The emission levels for CO and NO_X were simulated for an aggressive EU6d RDE cycle, which was proposed by the Consortium for Ultra Low Vehicle Emissions (CLOVE).

Emission simulation for the vehicle of above-described approach 2 showed, that NO_X mainly depends on the initial increase when the catalytic converter is not yet at light-off temperature. It is very interesting to see, that with exhaust deactivation, the increase at the beginning of the cycle is even bigger. Catalyst purge is avoided with the exhaust valve deactivation strategy, which is beneficial for fuel consumption and maybe beneficial for emissions as well. With the current calibration, the emissions are on a similar level, but additional potential for the SORS calibration may exist.

PUBLIC

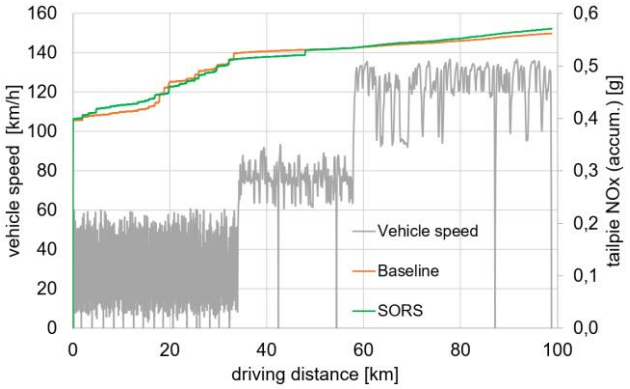


Figure 10: NO_X (accumulated) for the aggressive RDE cycle

The CO emissions show a different behaviour over the cycle than the NO_X emissions. Also here, the initial phase after engine start produced a big part of the overall accumulated emissions, but not as dominant as for NO_X. Also, the CO emissions over cycle develop slower with exhaust deactivation, which is a direct effect of the avoidance of catalyst purge after overrun phases in the investigated application.

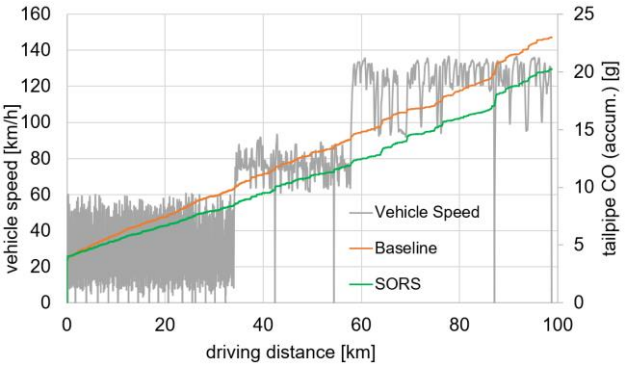


Figure 11: CO (accumulated) for the aggressive RDE cycle

It must be said that the observed behaviour and also the relation between CO and NO_X to each other is considered to be very vehicle and application specific. Different hardware configurations of the exhaust aftertreatment system as well as different purging strategies result in different emission levels. It was shown in [6], that the shape and duration of the rich purge peak will influence the NO_X to CO relationship. The present base vehicle was obviously optimized during calibration for NO_X emissions on the cost of CO. Therefore no benefit could be achieved on the NO_X side, but only on CO.

For other applications and overall system configuration, avoidance of rich purge through valve deactivation can provide a fine tuning tool for the OEM to balance out NO_X and CO and to further optimize the overall emission behavior of the vehicle.

A simple strategy will not be optimal for all driving conditions. For heat up of the exhaust, purging after overrun will result in quicker heat up of the catalytic converter, although this will be on the cost of CO_2. Once the TWC (three-way catalytic converter) is on temperature, the avoidance of catalyst purge results in overall lower NO_X and CO emissions

5. Transition between operation points

The purpose of a valve deactivation strategy is the avoidance of air throughput in overrun phases. However, air throughput is essential to keep the inlet manifold vacuum for load control of the ICE via the throttle valve. Consequently, the amount of air drawn into the cylinders at the first cycles may be too high for the desired refiring operation point.

There are theoretically several possibilities to solve this issue:

1. Evacuate the intake manifold before refiring
2. Spark retard for short term torque control
3. Apply gradual reactivation of cylinders
4. Balance ICE torque peak by electric machine
5. Use intake lift (phasing and/or lift height/duration) to control amount of air

All possibilities could solve the issue, but have either a CO_2 penalty, or require further systems which are not present in each engine. The system in [2] and [3] could for example use intake valve lift control, as a fully variable intake valve lift system (BMW Valvetronic) is present in these engines.

With the proposed exhaust valve deactivation strategy in the Smart OverRun System (SORS), an Electric Cam Phaser is present on the intake cam shaft. Although it is usually not used for load control, it could for this application take over this function through continuous control of intake valve closing time.

The strategy is shown in Figure 12: The transition to deactivated state should be controlled in a similar manner as current fuel cut off overrun. Exhaust valves are deactivated and the intake ECP is adjusted to the corresponding late position (1). Recuperation is maximized, depending on driving mode and brake pedal.

After the requirement for changing back to fired mode is identified (2), the intake valve lift is advanced from its drag torque optimal position. An air mass model in the ECU calculates the cam timing for the refiring load and speed. Then the exhaust valves are reactivated together with injection and ignition (3). After tip-in, the intake manifold pressure would drop down very quickly in a few cycles. The ECP position would be adjusted according to the manifold pressure level. Fine tuning of the load could still be done with spark retard (which will not be CO_2 optimal), but the amount would be drastically reduced. Also, the electric machine could support the smooth transition (see possibility (4.) above).

PUBLIC

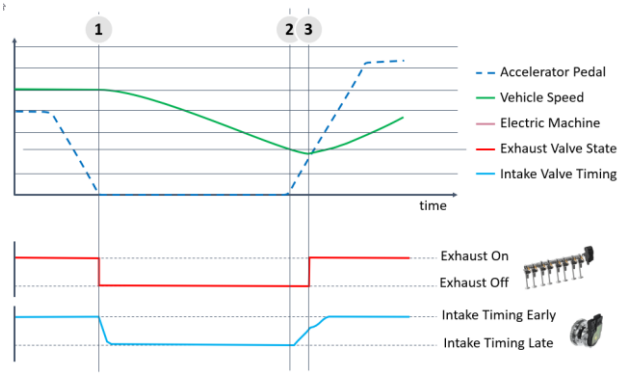


Figure 12: Transition to overrun and back to fired operation (schematic)

The transition from fired to overrun condition is generally seen less critical, altough a similar approach as described above, but the other way around could be considered for increased comfort.

6. Conclusion

Valve deactivation and electric cam phasing, combined in the SORS system, can be a considerable contributor for reduction of CO_2 emissions for P0 and P1 hybrid vehicles. Total CO_2 reductions of above 5% in the WLTC driving cycle are realistic for different engine/vehicle configurations and are the main motivation for system implementation.

Through the SORS, eCoasting becomes more efficient than boosting and contributes with around 2% to the overall reduction.

RDE emissions CO and NO_X can also be influenced in a certain range and balanced out versus each other, dependent on the application of the respective OEM, but the overall reduction is small with respect to the emissions caused at engine startup and will therefore typically not be the main driver for system implementation.

The eRocker System as well as the electric cam phasing systems have entered mass production successfully and are available for further applications.

7. Outlook

Schaeffler is continuing the effort to examine further use cases of the SORS system, for example usage of valve deactivation at engine start, for comfort as well as for emission purposes.

8. Acknowledgement

The authors would like to thank all team members at Schaeffler Technologies AG & Co. KG and at FEV for their contribution to this study. Special thanks and acknowledgment for their outstanding work go to the development team of the first eRocker System mass production application.

9. References

[1] Himsel, F.: "Schaeffler eRocker System", Schaeffler Kolloquium (Baden-Baden, Germany), 2018

[2] The new BMW X7; https://www.press.bmwgroup.com/global/article/detail/T0378353EN/the-new-bmw-x7; 13.04.2022

[3] The new BMW 7 series; https://www.press.bmwgroup.com/global/article/detail/T0380173EN/the-new-bmw-7-series; 20.04.2022

[4] Himsel, F., Werblinski, T., Christgen, W.: "Schaltbare Ventiltriebsysteme – von der Hydraulik zur Elektromechanik", Ventiltrieb und Zylinderkopf (Würzburg, Germany), 2019

[5] Werblinski, T., Christgen, W., Traversa, P., Schroder, C.: "Valve Train System for P0 and P1 Hybrid Powertrains", 30th Aachen Colloquium Sustainable Mobility 2021 (Aachen, Germany), 2021

[6] Görgen, M., Nijs, M., Thewes, M., Balazs, A., Yadla, S., Scharf, J., Uhlmann, T., Claßen, J., Dorscheidt, F., Krysmon, S., Sterlepper, S., Düzgün, M.: „Holistic Hybrid RDE Calibration Methodology for EU7", 8th International Engine Congress 2021 (Online)

10. Glossary

CLOVE: Consortium for Ultra Low Vehicle Emissions
DC: Duty Cycle
DCT: Dual Clutch Transmission
ECP: Electric Cam Phaser
HLA: Hydraulic Lash Adjuster
MHEV: Mild Hybrid Electric Vehicle
OEM: Original Equipment Manufacturer
PWM: Pulse Width Modulation
RFF: Roller Finger Follower
SORS: Smart OverRun System
SRFF: Switchable Roller Finger Follower
TWC: Three-way catalytic converter
WLTC: Worldwide Harmonized Light Vehicles Test Procedure

PUBLIC

15 JUNE 2022

BATTERY ARCHITECTURE

Supercap-Battery Hybrid for Board- and Powernet Applications

H. Hauf*, S. Court*, B. Dunne*, G. Maisonneuve*, M. Tommasi*

* NAWATechnologies, 190 av. de la Plaine, 13106 Rousset, France

Abstract: The ever-accelerating transition towards electrification brings massive changes to vehicles' architectures with great focus on the density of electric energy storage [EES].

In addition to energy density, the limitations of power density of EES must be taken into account as well.

This paper illustrates how a supercapacitor with electrodes based on vertically aligned carbon nanotubes [VACNT] [5] can stabilize a vehicle's boardnet voltage, reduce the battery's C-rate and insure stable functioning at extremely low temperatures.

The transients of supercapacitor-battery hybrids will also be shown comparing the results between standard EDLC [4] supercapacitors and VACNT-based EDLC [1-3].

Keywords: boardnet, supercapacitor, hybridisation, ESR, EDLC, nanotechnology, VACNT

1. Electric energy storage, looked at differently

First a different, simple method of how to identify the most suited EES technology for a given application is proposed. It resides on the very basics of energy storage, where energy is always stored inside a volume and power (often expressed in C-rate) transits through a surface of that very energy-volume. This holds true for both worlds, ICE and EV.

Some representative examples of EES, commercially available technologies are shown in fig. 1. Many others exist but are omitted for clarity.

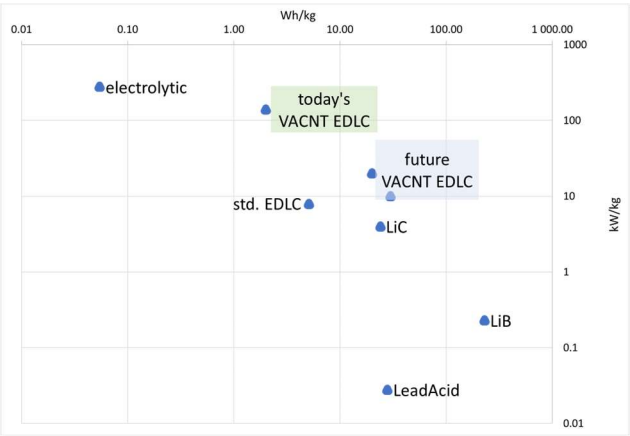


Figure 1: mass-density Ragone for selected EES

The overall scale ranges over several orders of magnitude for both, power, and energy densities. The different technologies typically line up on one (log-log) line (with only lead acid technology shifted due to the higher specific density of lead).

The VACNT-EDLCs densities represent the characteristics of today's VACNT-EDLC (green) and the characteristics of future VACNT-based EDLC (blue), the latter still being in development.

Whereas these Ragone plots are common, they do not allow to select the best of breed for anyone given application. To select the most suited EES technology the plot can be rescaled on its power-axis

$$\left.\frac{P}{m}\right|_{EES}\left[\frac{kW}{kg}\right] \mapsto \frac{\left.\frac{E}{m}\right|_{EES}\left[\frac{Wh}{kg}\right]}{\left.\frac{P}{m}\right|_{EES}\left[\frac{kW}{kg}\right]} \cong t \qquad [1]$$

so that the EES-technologies can be compared to the application's requirements (fig. 2).

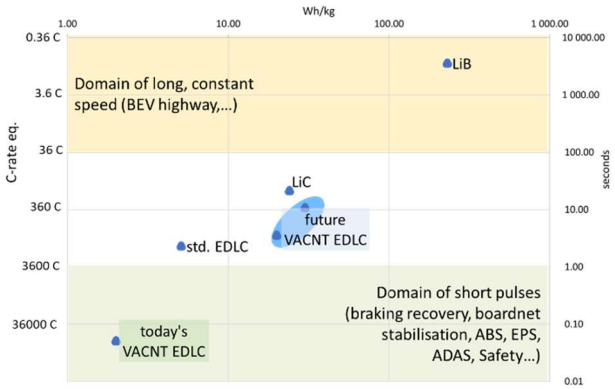


Figure 2: rescaled Ragone for selected EES

The EES-technologies shown in fig. 2 are the same as in the Ragone of fig.1, only that power densities are given as a duration on the right axis. As battery applications are often expressed in terms of C-rates, the left axis has been added for sake of completeness.

It is evident that there is no one-fits-all storage technology across the different requirements. Certainly, a higher battery density (or an oversized battery) can address higher absolute powers despite their relatively low C-rates.

Still, the combination of batteries with other EES technologies such as supercapacitors is in many cases the best suited solution.

2. Electrode morphologies at the nanoscale

Before describing the hybrid examples, the usage of VACNT-based EDLC [1-3] requires some explanation.

Fig. 3 compares the impedance measurements of a VACNT-EDLC (A) with the ones from commercially available std. EDLC (B). VACNT-EDLC have a twenty-fold lower equivalent serial resistance [ESR], which is clearly brought to evidence throughout the whole spectrum of measurement.

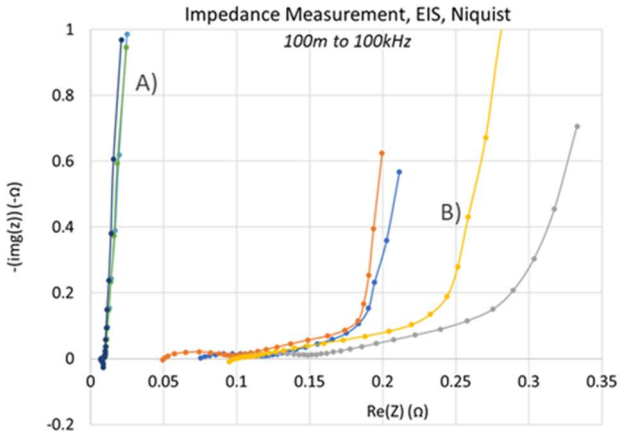


Figure 3: Impedance comparison of VACNT-EDLC with std. EDLC

The electrodes of std. EDLCs consist of a porous material, mostly of activated carbon, whereas VACNT-EDLC electrodes are made of highly anisotropic carbon nanotubes (fig. 4). Their density is around $10^{11}\frac{1}{cm^2}$ of 80µm length.

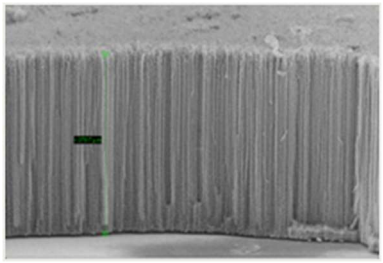
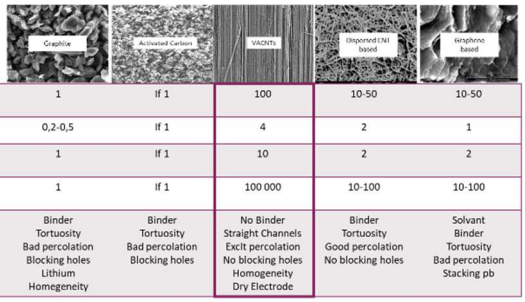


Figure 4: SEM of VACNT crosscut

As the channels in between VACNT provide for the shortest path of charged species to get in (whilst charging) and out (whilst discharging), the ESR of VACNT-based is twenty-fold lower than std. EDLC.

The nanotechnology of VACNT brings many more advantages to the electrode material properties which are summarized in fig. 5.



Electrical conductivity	1	If 1	100	10-50	10-50
Ionic conductivity	0,2-0,5	If 1	4	2	1
Thermal conductivity	1	If 1	10	2	2
Mechanical cohesion	1	If 1	100 000	10-100	10-100
Main features	Binder Tortuosity Bad percolation Blocking holes Lithium Homegeneity	Binder Tortuosity Bad percolation Blocking holes	No Binder Straight Channels Exclt percolation No blocking holes Homogeneity Dry Electrode	Binder Tortuosity Good percolation No blocking holes	Solvant Binder Tortuosity Bad percolation Stacking pb

Figure 5: Comparison of material properties of different electrode morphologies

Although the materials are all made from carbon, it is the nanoscale morphology making for the massive differences.

3. Boardnet stabilisation through hybridisation

Fig. 6 shows the electric power measurement of the boardnet for a 1000s drive.

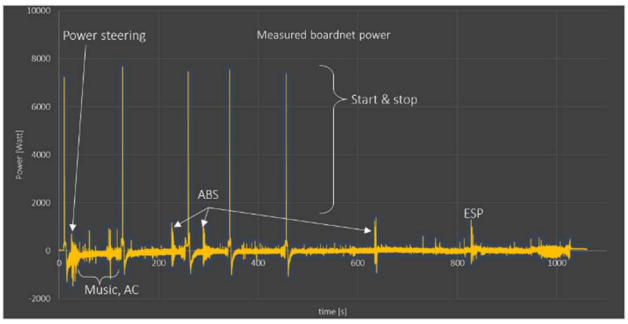


Figure 6: Measured 12V-boardnet power of a Golf7 1.6 tdi

Based on the measured power requirement a Spice model was build (fig. 7) to explore the resulting electric transients when supercapacitors are supporting the battery.

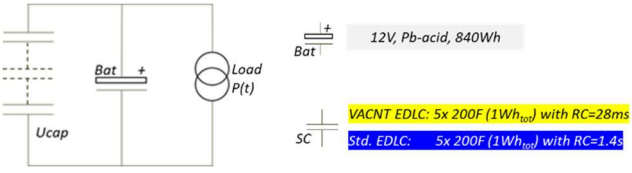


Figure 7: simplified view of schematics and components' KPI

The transient of the boardnet voltage is shown in fig. 8 and 9 for three distinct cases:

- Battery alone, i.e., without supercapacitor
- Battery supported by a std. EDLC
- Battery supported by VACNT-EDLC

Although not scope of this paper, it shall be mentioned that the boardnet hybridisation can be done with and

without the use of a DCDC amplifier. The differences reside in supercapacitor sizing, electric architecture, and cost.

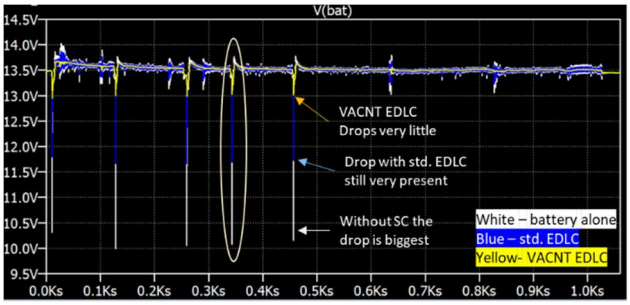
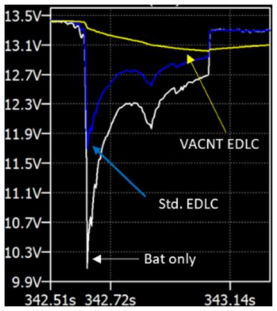


Figure 8: transient of boardnet voltage

The voltage drop for high load discharge is highest for a battery alone solution (Δ3.5V), lower for a hybridisation with std. EDLC (Δ2V) and lowest for VACNT-EDLC (Δ0.5V).

The battery's inner resistance and the load's impedance constitute a voltage divider where the voltage drops for the relatively high battery resistance during high current draws.



The use of supercapacitors lowers the voltage drop due to their low ESR.

As VACNT-EDLC exhibit a 20-fold lower ESR than std. EDLC their voltage drop is thus lowest.

Figure 9: zoom on a single, S&S voltage transient

By plotting the transients $V_{boardnet}(t), I_{load}(t)$ in parametric format, the stabilisation can be shown more clearly (fig. 10).

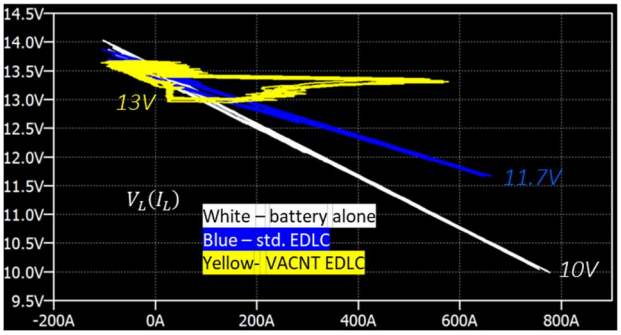


Figure 10: boardnet voltage as a function of boardnet load current

The C-rate of the battery is 9.5C during the discharge phases (fig. 11) for a battery alone solution, 5.5C when hybridized with a std. EDLC and 2C when a VACNT-EDLC is used instead.

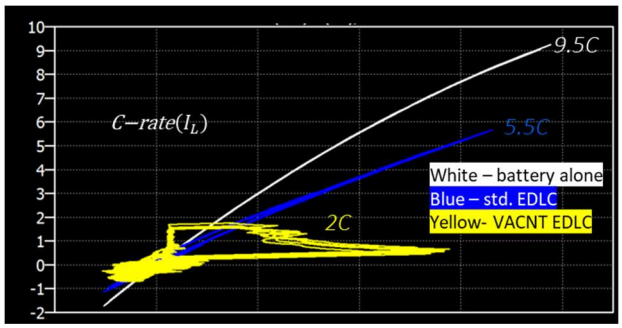


Figure 11: battery's C-rate as a function of boardnet load current

It shall be mentioned that supercapacitors operate well, with little change in performance at extreme low temperature (-30°C) so that the boardnet stabilization can be insured over a broad range of temperatures.

4. MHEV powernet hybridisation

The hybridisation of the EES for the MHEV powernet of a passenger car by a premium German brand, C-segment has been studied. The P0 configuration for the battery-alone reference is shown in fig. 12.

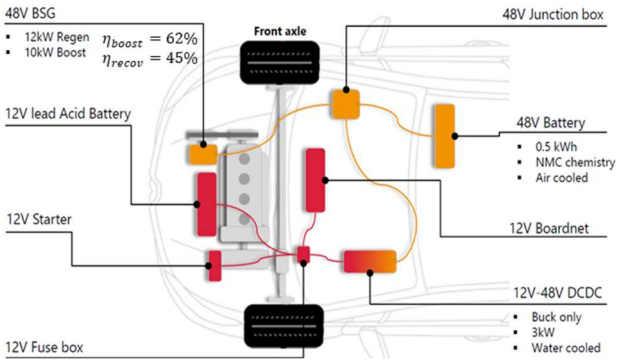


Figure 12: MHEV, P0 configuration

The vehicle's mechanical crankshaft power and the electric motor power has been measured over a (driven) WLTP cycle (fig. 13).

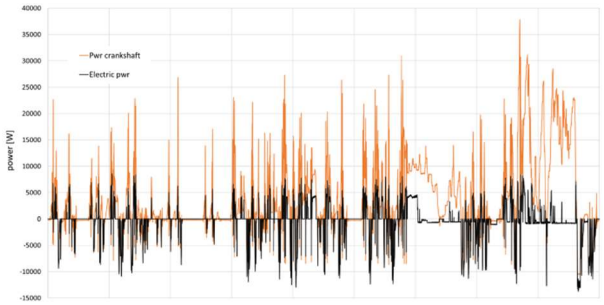


Figure 13: measured mechanical and electric power, WLTP-cycle

To study the benefit of hybridisation, i.e., adding a supercapacitor to support the battery a Spice model was developed (fig. 14).

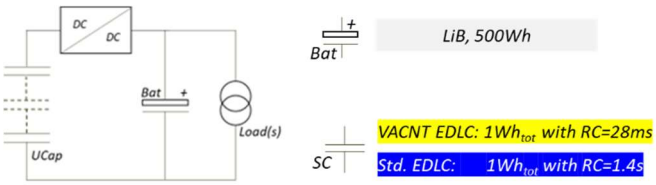


Figure 14: simplified view of schematics and components' KPI

The hybridisation greatly reduces the battery's C-rate (fig. 15).

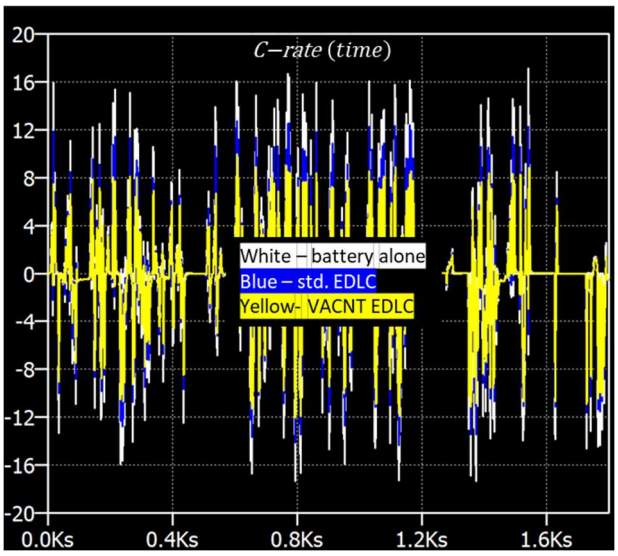


Figure 15: C-rate of battery throughout a WLTP-cycle for different hybridisations

For sake of clarity the transient plot is plotted parametrically (fig. 16).

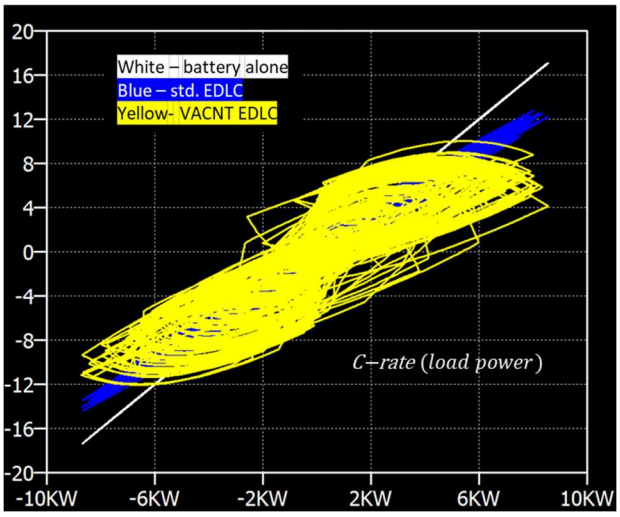


Figure 16: C-rate as a function of load power

The overall C-rates are reduced massively when using VACNT-EDLC (fig. 17).

C-Rates (min/max)	Battery alone	With VACNT-EDLC	
Discharge	+17 C	+10 C	-41%
Recuperation	-18 C	-12 C	-33%

Figure 17: C-rate reduction of hybrid using VACNT-EDLC with a battery of 500Wh

It is alternatively also possible to reduce the battery's size by keeping the C-rate (fig. 18).

Battery size (-33%)	Battery alone	With VACNT-EDLC
Discharge	500 Wh	335Wh

Figure 18: size reduction of the battery, keeping the C-rates at +17C/-18C

Alike in the boardnet case before, it shall be noted that the supercapacitors' performance does almost not alter at extreme low temperatures (-30°C).

5. Conclusion

The hybridisation of supercapacitors with a battery will lower massively any voltage drop for boardnet applications and shows benefits for C-rate reduction of the battery for both, boardnet and MHEV-powernet applications.
The lower the supercapacitor's ESR, the better the results.
It is the electrodes' nanoscale morphology which yields the extremely low ESR of VACNT-EDLC.
A Ragone rescaling method has been proposed for quickly identifying the best suited EES technology for anyone application.

6. Acknowledgement

The entire technical staff at Nawatechnologies is gratefully acknowledged for their contribution to the achievements presented herein.

7. References

[1] Dorfler et al., High power supercap electrodes based on vertical aligned carbon nanotubes on aluminum,

Journal of Power Sources, Volume 227, 2013, Pages 218-228,.

[2] Dogru et al., Flexible supercapacitor electrodes with vertically aligned carbon nanotubes grown on aluminum foils, Progress in Natural Science: Materials International, Volume 26, Issue 3, 2016, Pages 232-236

[3] Nassoy et al., Single-Step Synthesis of Vertically Aligned Carbon Nanotube Forest on Aluminium Foils, Nanomaterials 2019, 9, 1590.

[4] Conway, Brian Evans (1999), Electrochemical Supercapacitors: Scientific Fundamentals and Technological Applications, Berlin, Germany: Springer, pp. 1–8, ISBN 978-0306457364VACNT

[5] Chen, Hao et al., 22 November 2010, "Controlled growth and modification of vertically-aligned carbon nanotubes for multifunctional applications". Materials Science and Engineering: R: Reports. 70 (3–6): 63–91. doi:10.1016/j.mser.2010.06.003.

Modular and Distributed Battery Design with Integrated Multi-Level Power Electronics Converter

J. Al-Tayie[1], X. Zeng[2], J. Dalby[3], R. Tappin[4]

1,3,4: Ricardo plc, Shoreham Technical Centre, Shoreham by Sea, West Sussex, BN43 5FG, United Kingdom
2: University of Bath, IAAPS, Claverton Down, BA2 7AY, United Kingdom

Abstract: This paper presents the outcomes from a concept feasibility study that designed a battery pack for Electric Commercial Vehicles (ECVs) to combine the functionalities of the traction inverter and onboard charger (OBC) into the existing battery management system using a distributed power electronics converter topology integrated into the battery pack, thus enabling modular solutions to be created for a range of applications.

Using multi-level converter topology in automotive applications to provide both traction power and battery charging is an innovative application of converter technology that could reduce vehicle cost and mass. The Modular Multilevel Converter (MMC) manages the charging of the battery and drives the traction motor(s).

A concept of a battery pack with an integrated MMC was designed and analysed thermally and mechanically to assess its integrity. Electromagnetic emissions analysis was also performed to evaluate the impact of the converter on the rest of the vehicle operation from increased emissions.

Immersion cooling technology was implemented to cool the battery pack and the MMC in an efficient and integrated manner to drive higher specific power ratings.

Keywords: Pouch, Battery, MMC, modular, distributed converter, immersion

1. Introduction

As part of our mission to support the decarbonisation of the global transport and energy sectors, Ricardo has partnered with the University of Bath (UoB) to develop a novel solution for heavy-duty electric vehicles focusing on improving efficiency and performance and reducing the cost of future electric trucks.

The Multi-Bat project, funded by the Faraday Battery Challenge and supported by Innovate UK, saw Ricardo and the UoB investigate the feasibility and benefits of integrating a power electronics converter into a battery pack.

The vision of the project was for a multi-functional, modular battery pack to enable reduced cost of electric vehicles in sectors with lower production volumes. The battery, with its integrated MMC, will combine the functionalities of the traction inverter and onboard charger into the existing battery management system (BMS) using a distributed converter topology integrated into the battery pack, thus enabling modular solutions to be created for a range of applications.

Using multi-level converter topology in automotive applications to provide both traction power and battery charging energy is an innovative application of converter technology that could reduce cost and mass of the electric vehicle by reducing components count and sharing functionalities as will be explained in section 2 of this paper.

Additionally, as electric commercial vehicles already operate at 600-800 V, this layout is a cost-effective method of power conversion that can be readily adapted for future Electrified Road Systems (ERS), which could operate at 1500 V.

There were six main focus areas to the concept study; a) development of the battery sub-module (SM) and battery pack with immersion cooling methodology, b) development of a concept power electronics converter to perform the required functions, c) development of a thermal concept to mitigate any adverse effects that the power converter integration could have on the battery system, d) assessment of the mechanical feasibility for the installation of the distributed converter into a commercial vehicle battery pack, e) the impact of the distributed converter layout on electromagnetic performance and signature of the integrated battery pack system f) and finally cost analysis.

The next sections of the paper have been structured to address the six areas of the Multi-Bat concept study.

2. Multi-Level Converter Topology and Control

The requirements of the MMC in this application are to provide the functions of battery management, voltage balancing, state of charge and state of health monitoring and the ability to detect and isolate problematic SMs and cells.

The MMC is also to provide bidirectional charging/discharging from a three-phase power supply directly to the battery pack and to support DC fast charging at over 1 MW. The MMC will provide drive/regen braking functionality, supplying the traction motor with AC power and receiving recovered energy from the prime mover.

The concept architecture selection for the MMC was based on comparison to other competitive multi-level topologies such as neutral clamp and flying capacitor converters. MMC topology was chosen to achieve high modularity and to have integrated control of battery and electric machine, [1], [2].

The electrical circuit of the chosen MMC topology is drawn in Figure 1. It is composed of three phases or legs. Each phase has two arms, an upper arm and a lower arm. Each arm is a string of sub-modules, shown as SM1, SM2, SMx…, connected to an arm inductor, which helps to control and reduce the arm current.

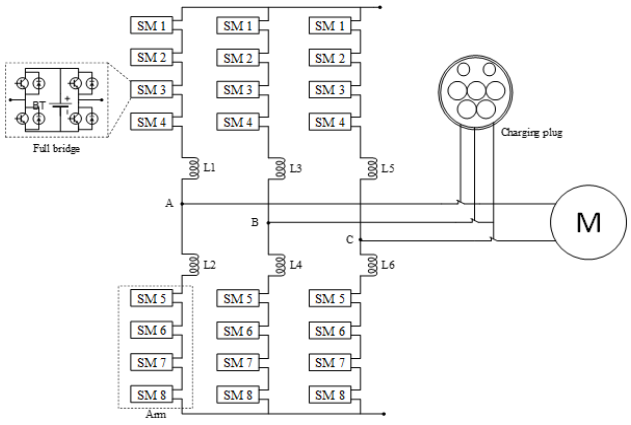


Figure 1: MMC Concept System Diagram

A range of different MMC levels were considered, and components selected for each topology that could meet the requirements of breakdown voltage and continuous current handling. Multiple options for each level were studied and for each component, the cost and power losses were noted at the particular operating point. These results are summarised in the bars on Figure 2.

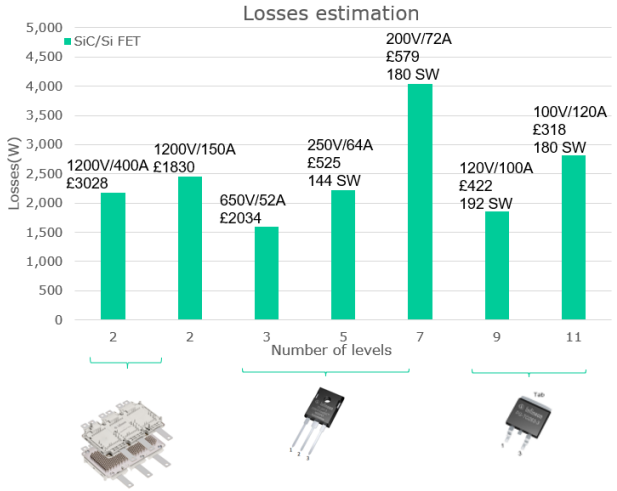


Figure 2: Cost and losses comparison for a fixed output power and duty cycle

Converter SM design and voltage level optimisation has led to the selection of a 9-level (9L), full bridge (FB) converter, [3], [4], [5].

The topology can produce full line-line voltage with good total harmonic distortion (THD), lower operating losses and lower cost.

It was identified by our analysis that while the number of power semiconductors unsurprisingly increased with the number of levels offered by the MMC, the overall cost did not follow the same trend. Since a lower rated component can be used for the SM of the MMC to achieve the desired output voltage, the cost of the power stage is reduced, as can be seen for the 9L option of Figure 2.

A calculation of THD for the different inverter levels, can be seen in Figure 3, where there is a reduction in THD as the number of voltage levels in the MMC is increased. It is worth noting according to our analysis that the 9L converter can achieve a minimum THD of under 10.0% in theory. (Not including switching frequency harmonics and intermodulation).

This lower THD will reduce the electromagnetic signature and losses in the electric machines and will reduce filter requirements, should they be needed.

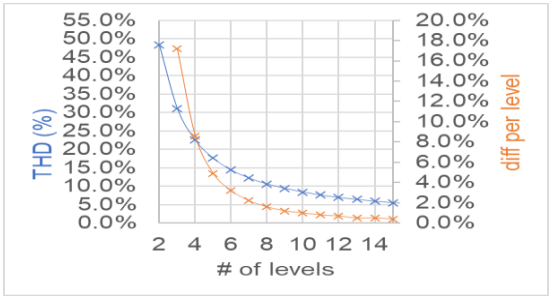


Figure 3: Trend in THD reduction for ideal staircase waveforms

The output of the 9L MMC produces a staircase-like waveform, as illustrated in Figure 4. This causes the reduction in THD and dv/dt stress on the electric motor windings in comparison to a two-level inverter (TLI). The 9L can produces much smoother voltage and current waveforms.

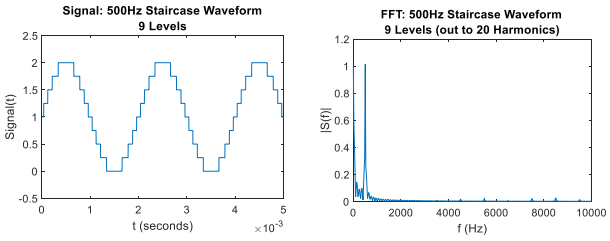


Figure 4: Staircase waveform with THD spectrum for 9L waveform

2.1 MMC Energy Balance and Electric Drive

The stage-of-charge (SoC) imbalance between battery cells is a key issue since it shortens battery lifetime and decreases vehicle performance.

The battery based MMC topology operating in each arm can be considered as a voltage source comprising a DC component and an AC component. The DC component is used to maintain DC bus voltage while the AC component (quasi-sinusoidal wave) balances the energy between the upper and lower arms, as indicated on figure 5.

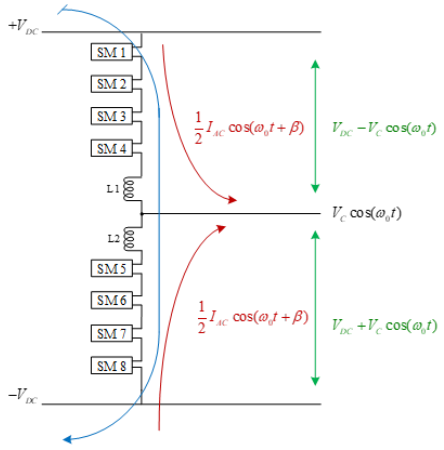


Figure 5: Simplified conversion for One phase to show energy flow

A battery management control algorithm was developed including individual SM control, arm balance control and cluster control.

The imbalance of SMs can be mitigated by controlling the duty of each SM and circulating current.

The individual balancing control aims to balance the battery's SoC of every SM in each of the six arms. The power balance creates DC current flowing between the bottom and top DC rails as illustrated in Figure 5. Three phase AC currents are equally shared between upper and lower arms with a neutral point in the DC rails.

A MATLAB/Simulink model was built to conduct the system design and simulation. The MMC features field-oriented control (FOC) for the motor and individual SoC balancing for the battery SMs.

The impact of individual balancing of the battery SMs from a MATLAB simulation can be seen in Figure 6. The SoC of each battery SM is balanced until the last SOC being balanced for all SMs in that arm. As the system was set in motor mode that the energy of batteries is consumed by its loads, the battery modules are in discharge mode.
Figure 6 shows that the individual balance algorithm helps the SMs in the same arm to balance because initial SoC for every arm is different, the SMs are still imbalanced in different arms but the arm balance algorithm can solve the problem. In this case, arm4 is firstly drained but then other arms tries to compensate the arm under the impact of individual balance algorithm until all arms are drained.

Figure 7 shows one arm current measured while driving the electric motor. There are both AC and DC current components flowing through each arm. The median value indicates the amplitude of the DC current component. Due to the AC and DC components, the decoupling effect to drive and balance energy was maintained

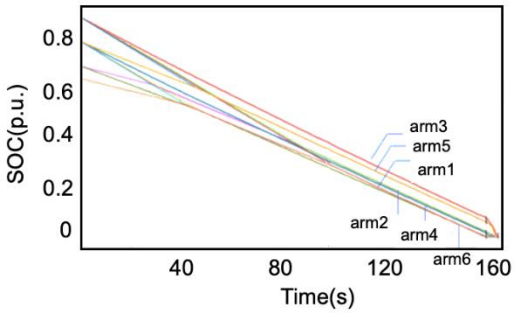


Figure 6: SoC values for each MMC arm

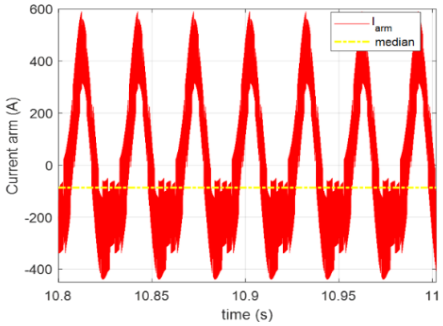


Figure 7: MMC arm current while driving electric motor

It is important to state that the proposed battery management does not have an impact on the three-phase output voltage and current of the traction motor which means it has a minimal impact on the electric driving performance and efficiency.

3. Battery Concept Design

This section of the paper is covering the mechanical concept design of the Multi-Bat project.

The objective of battery concept design work area is to design a modular battery that packages into a 6x4 tractor chassis and satisfies the vehicle energy storage and voltage targets.

Immersion cooling was selected based on Ricardo experience to have high heat transfer, to limit thermal runaway and to have a robust design. The immersion cooled design was developed to meet thermal and

structural requirements supported by 3D CFD and FE analysis. Pouch cells were chosen to have high energy density and high space utilisation [6].

The feasibility study developed the battery pack concept with the 9L MMC arrangement (developed by UoB), allowing for a gate driver and power converter unit to be integrated at a module level, with the battery pack to be controlled by the BMS and no external converter.

The battery SM assembly contains 12 rows of 4 cells, supported by a base tray cassette, common 4 cell cassettes and coolant channels, as illustrated in Figure 8. The overall battery SM configuration is 24S3P.

The power electronics (PE) converter SM assembly is then located into the battery SM assembly at this point, utilising an aluminium fastening plate and bolts for fixing to the module.

8 rows of 3 cells are then assembled, supported by 3 cell cassettes and cooling channel components.

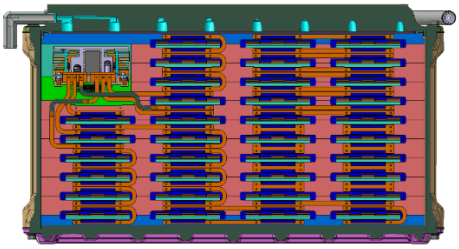


Figure 8: Internal assembly of the battery SM with PE converter SM

A top cassette is located on top of the cell cassette stack, with the assembly being secured at this point on the upper side of the threaded rods.

Cassettes are pre-assembled with compression limiters at fixing points to control the interference with cells.

PE SM output busbars are then assembled along with the internal side of the terminal assembly.

A compression pad is placed on top of the cassette stack and contacts the top cover. A complete SM is shown in Figure 9.

The battery SM design was modified and optimised with inputs from the thermal and mechanical analyses to have a viable concept.

Busbars connection between cells and PE SM was optimised based on current requirement during charging as the worst-case scenario with 2.5C charging rate and to take advantage of the immersion dielectric cooling to minimise the amount of copper used for the busbars.

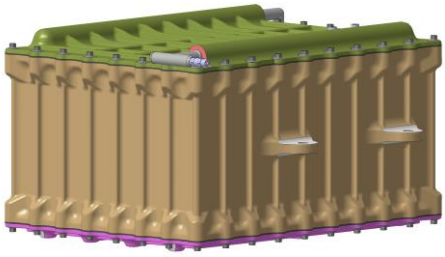


Figure 9: Battery SM assembly showing external structure

The coolant fluid enters the SM by the inlet manifold on the top cover and flows over the cells through three channels. The coolant also passes through the PE SM before exiting the module at the outlet manifold.

Even distribution of dielectric fluid into the SM is ensured by the inlet manifold design.

Figure 10 shows a plenum with reducing diameter which coincides with reducing port sizes. The resulting steps and cross-section reduction allows the earlier ports to gather an even amount of coolant to the downstream ports.

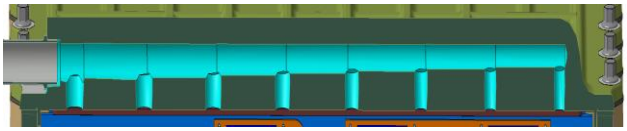


Figure 10: Section view showing coolant inlet manifold of the coolant channels

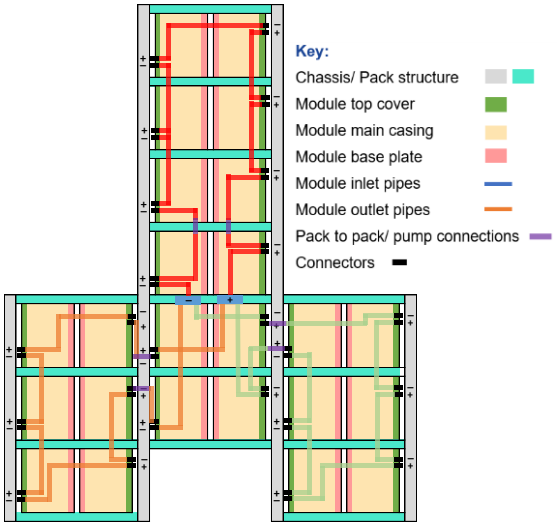


Figure 11: Battery Pack – Module to Module Busbars

The PE SM has DC bus film capacitors included in the assembly to provide a low impedance path for the high frequency ripples, to protect the battery from excusive heat due to the high frequency ripples and to improve dynamic performance.

The PE SM assembly is a self-contained module that is designed to be dropped into a battery SM.

Flow restriction geometry has been developed to ensure an even distribution of coolant across the entire module by not allowing a low resistance path for coolant flow via the PE SM assembly.

To achieve the desired battery pack properties, the SMs are organised in an 8 series 3 parallel configuration, the three parallel series denoted in different colours on Figure 11.

Pack level busbars are mounted rigidly to the module terminals and are shrouded in a polymer high electrical resistance coating.

High voltage electrical connections are required between sub-packs for this configuration and are indicated in Figure 11.

Cooling pipe connections are required for coolant supply and exhaust from the SMs. The battery pack concept design has provided a feasible piping solution that has been packaged within the battery pack, shown in Figure 11.

4. Thermal Analysis and Assessment

This section of the paper covers the thermal analysis and assessment that was performed on the battery SM.

Thermal analysis has been performed to select a thermal concept and to perform 1D and 3D analyses to evaluate the performance and immersion fluid distribution.

The battery SM uses pouch cells with a single side of the cells being directly cooled. The PE SM is part of battery SM and cooled by the same immersion dielectric fluid.

1D thermal models of battery and PE SM components have been built to assess temperatures (and gradients) of critical components

Charging conditions with the highest power dissipation for battery cells and converter components have been investigated. Sensitivity studies were carried out to find the optimal battery coolant channel size, converter heatsink size and coolant flow rate requirement.

Several intake manifold variants were investigated with the design progressing based on both CFD results and CAD, aiming to uniformly distribute the coolant to the cell channels.

The coolant flow in the SM was optimized through multiple design iterations considering various parameters (inlet manifold, baffle, and PE SM flow).

Venting gas analysis was performed for two cases; single pressure release valve (PRV) and two PRVs. Peak pressures of 10.3 bar and 6.3 bar respectively were predicted, these values were provided for mechanical analyses of the design robustness.

The heat transfer coefficient (HTC) values predicted are acceptable for the current design, as verified by the 1D thermal analysis of the battery and converter SMs.

Figure 12 shows the optimized results of the pressure of the battery SM and the circulation of the cooling fluid.

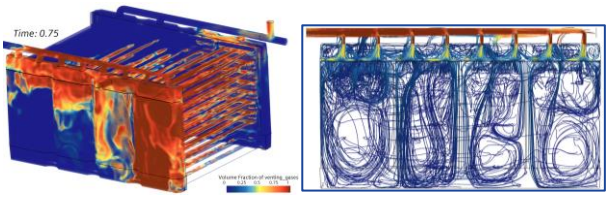


Figure 12: Battery SM showing peak pressure and uniform dielectric circulation

To verify the thermal performance further, long haul and regional vehicle delivery cycles have been assessed to see the impact on battery cell temperature and gradients.

The maximum cell temperature is around 43°C (coolant temperature is 27.3°C) with 2.5C charging rate which is lower than the targeted limit of 50°C. Results are shown in the traces of Figure 13.

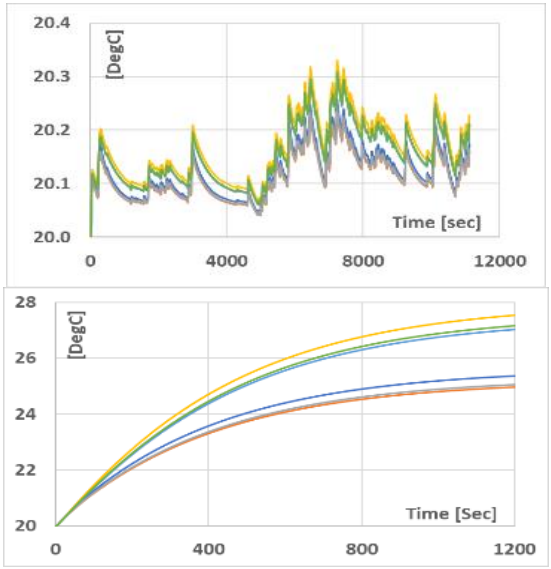


Figure 13: Coolant temperature rise with long haul cycle and with 2.5C charging rate

5. Mechanical Analysis and Assessment

This section of the paper covers the mechanical analysis and assessment of the battery SM and its integrated PE SM.

Finite Element Analysis (FEA) has been conducted to support the design and development of the battery and the PE converter SM concept.

The FEA studies have been performed in line with Ricardo CAE design verification plan (DVP). The load cases are a combination of selected industry standards, Ricardo experience and load cases specific to this project.

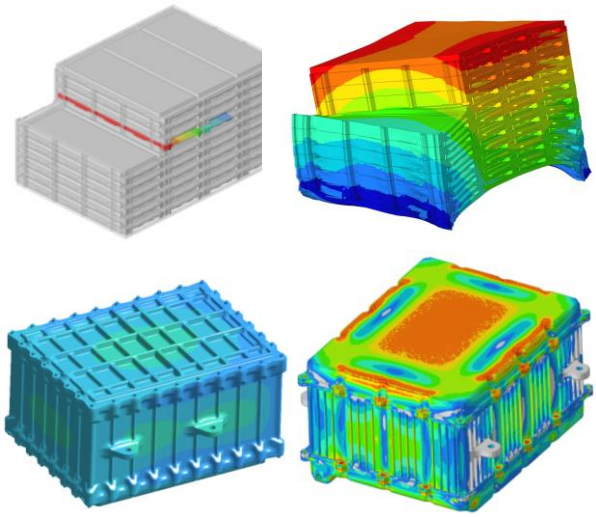


Figure 14: SM FEA analysis modal & vibration, deformation, and maximum stress in MPa

Bolted joint performance on the selected cast material was performed at 10 bar internal pressure to assess the bolt and casting integrity against high internal pressure during cooling failure events.

Shock analysis has shown a maximum stress of 100 MPa, below the 159 MPa limit.

Figure 14 shows some results of the mechanical analyses for modal, vibration, deformation, and maximum stress observed during the analyses studies.

Modal analysis on the PE SM has shown 1st modal frequency achieves the 30Hz target as per Ricardo DVP process.

The stress levels predicted in the PE SM PCB were well below the ultimate tensile strength (UTS) limit, results shown in Figure 15.

The maximum bolt load is equivalent to a stress of 690 MPa which is below the UTS of 800 MPa therefore the result is acceptable according to the CAE DVP.

Battery SM enclosure iterations to improve internal pressure results and enclosure mass were performed. Wall thickness and rib pattern and design were optimised during this study. Wall thickness was reduced from 10 mm to 6 mm to reduce cost and mass.

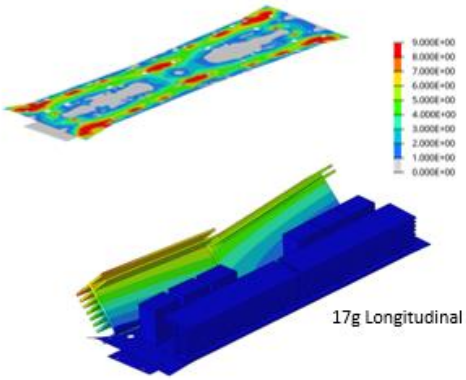


Figure 15: Modal analysis of the PE SM assembly

If the cell stack components are not in contact and are allowed to vibrate freely the predicted modal frequencies are very low, especially those of the spacers which can be less than 1 Hz.

The module casing stress under shock and abuse load cases is relatively low except for areas around the lugs, but the maximum stress levels are still below the yield and UTS targets.

The 10-bar pressure load case caused some the deformation of the casing covers and that led to the selection of casting material to withstand the requirement.

In conclusion, mechanical analysis has identified the areas for the mechanical design to address to make a working concept design.

6. EMC Virtual Validation

Section 6 of the paper is to address the EMC analysis performed during the Multi-Bat project.

The connections from the central BMS to the distributed gate drivers of the SMs converter create a risk for electromagnetic emissions. While not as critical in truck applications compared to passenger cars, it has been evaluated at this early stage to quantify the level of risk in the battery concept.

EMC/EMI simulation is an emerging discipline, therefore the approach was first focused on building and validating a model of the Innovate UK REVB BMS (Project Number 101573) to existing test data from that project, giving confidence in the accuracy of the tools.

The validated model was then modified to reflect the MMC layout and used to predict the impact on the electromagnetic emissions, highlighting any potential risks for its future application.

The approach is to numerically analyse EMC/EMI of printed circuit boards within the chosen Dassault Systems CST EM Studio simulation suite.

The PE SM configuration considered within the frame of the project is the H-bridge power converter illustrated in Figure 16.

Battery cells are connected directly to the DC side of the H-bridge, with capacitors added to provide a low impedance path.

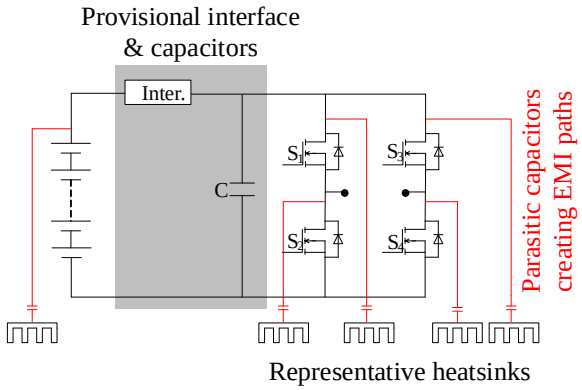


Figure 16: Converter H-bridge SM for EMC analysis

The PE SM described in the CST microwave environment has the semiconductors devices and the capacitors replaced by discrete ports. The frequency domain solver is used in the 3D field simulation for creating a matrix of the 3D model.

The 3D field simulation generates a circuit in CST schematic studio. All ports are now electrically accessible and for each component a SPICE model was assigned.

Due to the increased mutual inductances between the parallel-connected devices of the PE SM, current unbalances are observed, creating EMI propagating paths with different impedances.

Oscillations during switching events in the voltage and current waveforms of the power devices are known to create additional EMI noises.

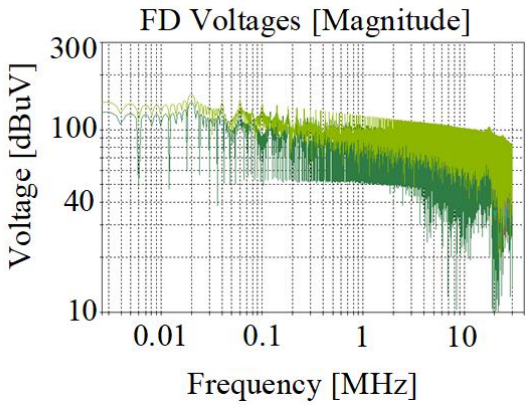


Figure 17: Voltage frequency response

The oscillation frequency is estimated to be equal to 16 MHz. The voltage frequency response of the parallel-connected devices has shown maximum average voltage in dBµV that is more than the maximum threshold voltage recommended by CISPR standard (average limit is 50 dBµV). Results are given in Figure 17 for illustration purposes.

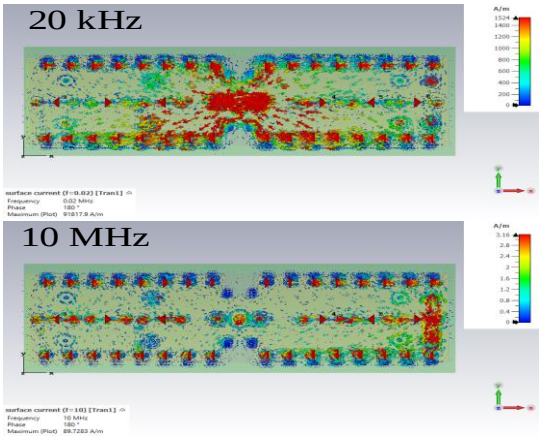


Figure 18: 3D surface current captured at 20 kHz and 10 MHz on the PCB by H-field monitor

Figure 18 depicts the surface current obtained by using the combined transient capability of CST studio.

At the switching frequency of 20 kHz, the current flows through the power devices via the normal operating paths (depending on whether the devices are conducting or by-passed).

However, at the frequency of 10 MHz, a conducted EMI propagating path appears at the vicinity of the battery's terminals. This helps to visualise propagating paths and recommend the use of adequate EMI reduction methods.

The conclusion of this initial EMC analysis is that further work is required to optimise the design of the power electronics SM and techniques to reduce the EMI signature is to be investigated. Ricardo and UoB are confident to have suitable EMC solution that meets the requirements.

7. Cost Analysis

Ricardo and UoB cost analysis conducted during the course of the project has shown that due to the selection of the 9L MMC topology with low voltage discrete power devices and the eliminating of the OBC as separate unit, there is potential for cost saving of £1975 and mass reduction of 36 kg as illustrated in Figure 19.

The data presented in Figure 19 is for the MMC and for the separate OBC and inverter topologies.

Further optimisation works will be performed during the next stage of the project to articulate the design and to optimise the battery pack energy and power densities which may have impact on cost saving and mass reduction.

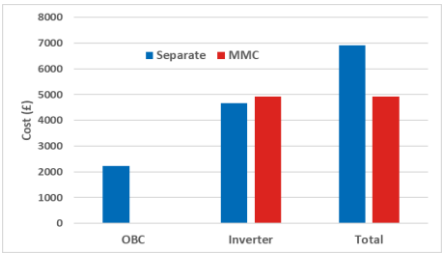


Figure 19a: Potential cost saving of the MMC concept

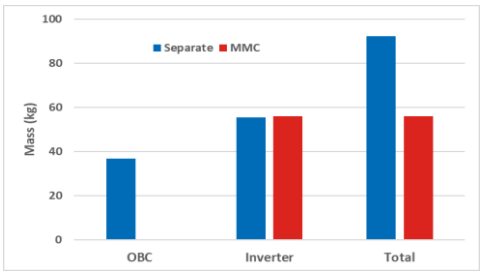


Figure 19b: Potential mass reduction of the MMC concept

8. Discussion and Conclusion

The scope of this paper was to generate a concept of an immersion cooled battery pack with integrated power electronics MMC to facilitate traction and onboard charging functionality into an existing BMS.

The designed concept features immersion cooled pouch cell technology and with 9L multi-level converter to form the MMC topology and control strategy.

EMC virtual validation process has shown some areas of concerns regarding EMI and those concerns will be addressed during the next design phase of the project and we are confident those concerns can be solved by optimising and refining the concept design.

MMC based drive and energy management system can replace and integrate three electronics system into one structure, including inverter, OBC and SM battery balance methodology.

The project managed to generate a working concept MMC system that would lead to cost and mass saving as the OBC is integrated within the MMC and the distributed converter can be directly integrated in the battery pack and share same dielectric immersion cooling medium.

The next phase of the project is to refine the design and to optimise the mass and volume of the battery SMs and pack to achieve the desired power and energy densities that satisfy the requirement of the heavy-duty trucks. Another phase of the project is to build a demonstrator unit.

9. Acknowledgement

The authors would like to thank Innovate UK and the Faraday battery challenge boards for providing funds to conduct this study.

The authors would like also to thank Ricardo Plc. for providing co-funding.

The authors would like to thank and acknowledge the contributions of colleagues at Ricardo and UoB.

10. References

1) P. L. M. A. J. R. Samir Kouro, “Multicarrier PWM With DC-Link Ripple Feedforward Compensation for Multilevel Inverters,” IEEE TRANSACTIONS ON POWER ELECTRONICS, vol. 23, no. 1, pp. 52-59, 2008.
2) S. N. S. S. P. D. Ankit Yadav, “Modular multi-level converter topologies: Present status and key challenges,” in 2017 4th IEEE Uttar Pradesh Section International Conference on Electrical, Computer and Electronics (UPCON), Mathura, India, 2017
3) T. D. A Rakesh Kumar, “Multilevel Inverters: A Review of Recent Topologies and New Modulation Techniques,” in International Conference on Recent Trends in Electrical, Control and Communication (RTECC), Malaysia, 2018
4) M. N.O. Sadiku. Computational Electromagnetics with MATLAB. Talor & Francis Group
5) J. Yang, X. Xiao, S. Gao, X. Jiang, X. Zhan, J. Wang and Z. Wu, “Average Model of MMC with Full-bridge Sub-modules for Blocking Situation,” in 8th Renewable Power Generation Conference, Shanghai, 2019V
6) Verma, D. Hawke, C. Rouaud “Highly integrated oil cooling solutions for power electronics and electric motor” in SIA PWTE 2021

11. Glossary

ECV: Electrified Commercial Vehicle
MMC: Modular Multi-Level Converter
ERS: Electrified Road Systems
TLI: Two-level Inverter
EMC/EMI: Electromagnetic Compatibility/ Interference
DVP: Design Validation Plan
NPC: Neutral point clamped converter
FC: Flying capacitor converter
CHB: Cascaded H-Bridge Converter
SiC: Silicone Carbide
CFD: Computational Fluid Dynamics
HTC: Heat transfer coefficient
PRV: Pressure Release Valve
UTS: Ultimate Tensile Strength
FEA: Finite Element Analysis

Design of a battery pack module for mHEV application with Multi-Physical Simulation

Julien TRUONG CANH[1], Franck DHAUSSY[1], Yannick RAYNAUD[1]

1: PLASTIC OMNIUM CLEAN ENERGY SYSTEM (FRANCE), 214 Av. de la Mare Gessart, 60280 Venette

Abstract:

This study will present the simulation work and result that were performed in the context of the development of a 48V battery pack with innovative cell electrochemistry based on Sodium-ion instead of usual Lithium-ion technology. With a complete simulation platform composed of all elements of a battery pack, we are able to design sub-component of the pack as well as predict its future performance.

First chapter gives a brief approach to the Sodium-ion cell chemistry. NVPF cells cathodes present interesting characteristics especially for power applications needed for Mild-HEV, Full-HEV and also FECV.

The focus here is given to the battery pack and its internal components. While simulations at vehicle level are interesting, we here focus on the behavior of subcomponents inside the pack, and simulation of every cell independently in the pack.

We run WLTC type cycle in our simulation platform to assess the behavior of our pack, prior to evaluation in real driving (RDE) cycles.

Keywords: Electrical Vehicle, Mild-Hybrid, battery pack, Amesim simulation, driving cycles, pack configurations,48V, Ncells, Thermal management

1. Introduction

With new regulation, regarding greenhouse gases emissions, the electrification in transport industry has become a major topic of development and innovation, and a focus for the engineering teams. Electric and hybrid vehicle development is a response of the automotive industry to these policies, but new challenges have emerged. One of the main difficulties of electrification of vehicles is the battery pack sizing without compromising volume, weight and safety. The battery pack design is extremely important, as electrical power takes a larger part in the total power output of the vehicle. Car manufacturers are asking increasing power and more current to be drawn from the battery pack.

Therefore, the design of the pack needs to be carefully addressed, and design choice need to be accompanied with clear data. Because cell testing require quite long time to get accurate results and are therefore expensive, it is necessary to rely of computer assisted design and simulation methods. Modelling can then play a crucial role in order to define the right sizing of a battery pack, compare chemistry and cell performances, prevent design error, and finally validate the choices made on driving profiles.

In this context, PLASTIC OMNIUM has developed a battery pack model for mild-HEV application for 48V P0 to P4 architectures. 48V hybrid system can be seen as a smooth transition from gasoline/diesel ICE vehicle to full electrical vehicle. The 48V battery pack can be easily integrated in already existing platform, and a powerful electrical machine can be used to support thermal engine for torque shaving, heating of the engine coolant or the catalyst, stop & start, regenerative breaking, comfort functions like electric air conditioning or active suspensions…

The other asset of a 48V network in the vehicle is that high consumption component can be switch to 48V a power supply, meaning a reduction of thermal losses due to lower current for the same power, as well as a possibility to reduce cable section in the vehicle.

2. Cell chemistry presentation

The development of large-scale electrical energy storage systems is the greatest challenge for both mobility and stationary applications. Lithium-ion battery is the predominant technology in the market today. Despite the great success of this technology and the variety technology in the Li-ion batteries family, several major performance and production weaknesses remain. Sodium is an obvious substitute for Lithium thanks to its similar chemical properties. In the early days of lithium-ion battery research, also sodium-ion batteries had been studied. The research, however, was largely discontinued, most likely because progress was slow compared to the lithium-ion chemistry success. Today, research on Na-ion batteries is mainly motivated by the large abundance of sodium.

TIAMAT's Sodium-ion technology is patented with the right for commercial exploitation. This technology is based on the use of a active positive electrode material phosphate based. Its formula is **$Na_3V_2(PO_4)_2F_3$.** Active negative electrode material is carbon based and shows a partially amorph disorganized structure, commonly named Hard Carbon. The electrolyte is made of carbonate solvents and sodium salt. This combination forms an efficient system for fast ion transfer without damaging the electrode's structure. As internal resistance is lower, the heat generation is lower too, securing the electrode integrity. These combined differentiators put TIAMAT Na-ion battery cells technology as an excellent candidate by design, for 48V battery pack.

For the pack construction, we are integrating prismatic cell format. The cell specifications ck battery are detailed in the following table:

Table 1. Sodium-ion NVPF26148PP7.1 specifications [1]

Capacity	Typical	15Ah 55.5Wh
Nominal voltage	Nominal Charge Discharge	3.7V 4.25V 2V
Charge current	Standard Maximum Peak (10s)	7.5A 150A 500A
Charge time	Standard Fast charge	120min 12min
Discharge current	Standard Maximum Peak (10s)	7.5A 225A 700A
Internal Resistance	AC (1 kHz)	0.5mΩ
Ambient temperature	Charge Discharge	0 to 55°C -30 to 55°C
Energy Density	Volumetric Gravimetric	170Wh/L 90Wh/kg

The cell offers high power performance as presented in the following figure, and noticeable symmetric behavior of power in a discharge and in charge

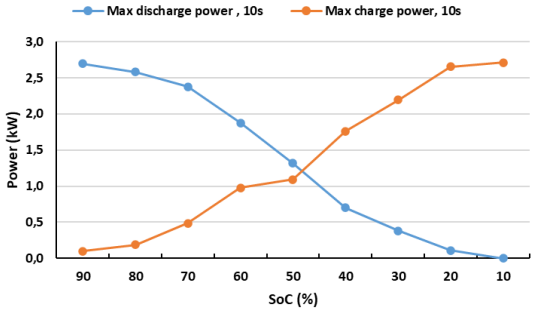


Fig. 1. Charge and discharge max power at 25°C, 10s [1]

In addition to the high-power performances, the safety is an important advantageous of NVPF-HC cells. In a rapport published by Ineris [2], Bordes et al. tested the thermal runaway propagation using six 18650 charged cells positioned vertically and in close contact to each other but not electrically connected, The abused cell was positioned at one extremity of the line-up. The cells 'temperature evolutions are presented in the following figure:

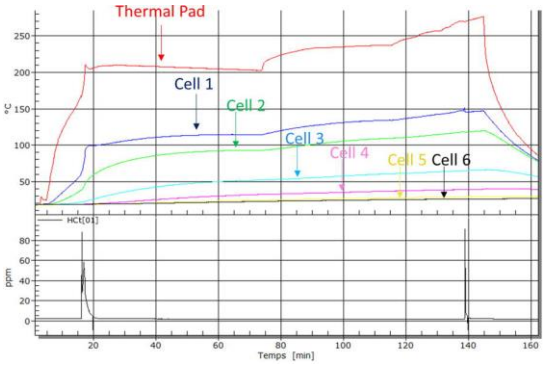


Fig. 2. Temperature recorded on each cell and the heating pad

The maximal temperature recorded on Na-ion cell is 210-260°C whereas most of Li-ion cells reached temperatures higher than 800°C, indicating a more energetic release during thermal runaway. This ensures that the thermal runaway stays limited to one in a sodium-ion NVPF-HC pack compared to lithium-ion behavior, where it is quickly propagated from one cell to another.

3. System Simulation platform

3.1 Global Architecture Simulation platform

Amesim™ is a powerful tool to model multi-physics and systems.

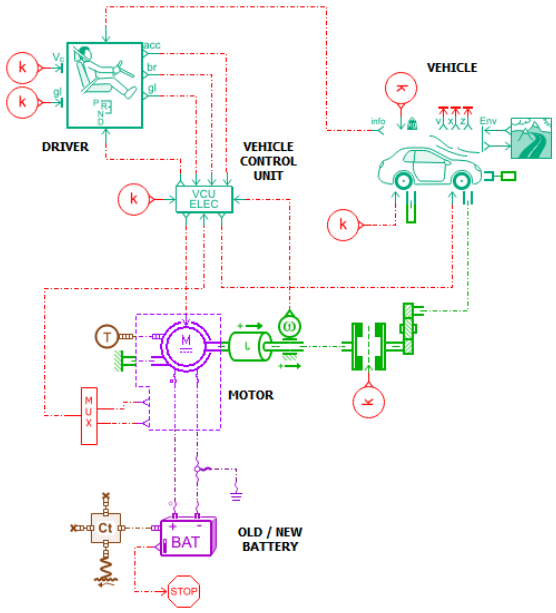


Figure 3: Sketch of an electric vehicle simulator under Simcenter Amesim™

From vehicle dynamics to electro machine behaviour and performance and of course Batteries the global simulation platform can modelized the complete vehicle. In the study presented in this paper we consider only the battery pack. The power and energy drawn from it are used as inputs of the model. This energy request is based on both real driving data recorded and other simulations.

Pack specifications

- Over 30Kw power output with high SOC
- 0,9kWh energy
- Liquid cooled
- Integrated BMS+DC-DC converter

Simulated part

- All cells simulated independently
- All electronics components (busbar, fuse …)
- The innovative liquid cooling system developed by PLASTIC OMNIUM Clean Energy Systems for the cells and the integrated DC-DC converter
- The input is simulated as a power source that can draw and give power to the pack. The power profile is an input of the model and is given from a data file.

3.2 Amesim Battery pack Model

The figure below presents the schematics of the 48V battery pack, developed by PLASTIC OMNIUM Clean Energy Systems under Simcenter Amesim™ software

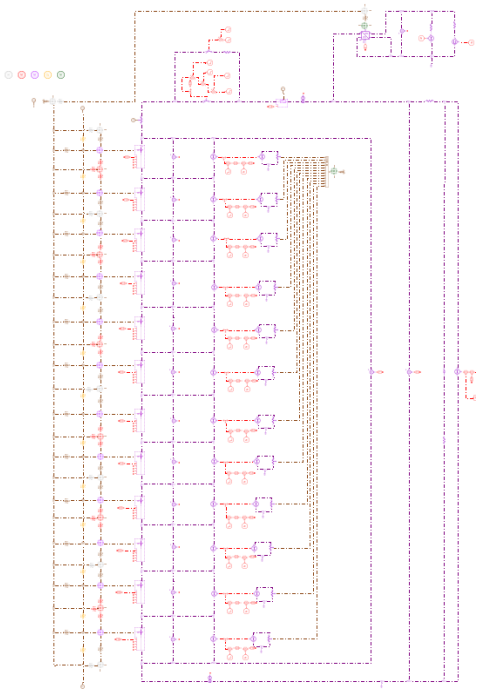


Figure 4: Sketch of the Battery pack 48V

The main components of the simulator are the following :

- The cells: for our pack application, with TIAMAT Sodium-ion technology a configuration of 12 cells in series and 1 branch in parallel (12s1p) is used to reach a nominal voltage of 48V. The goal of the simulation is not to check different configuration of cells, so number of cells is not a parameter. The cell model is based on a network a resistance and capacities in parallel to model voltage diffusion [7]

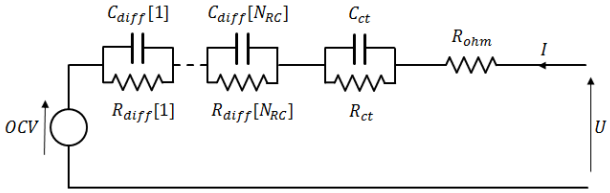


Figure 5: Cell electrical model

- The busbar network: Cell tabs and busbar are modelled as resistances that can vary with temperature. To simplify the sketch, some busbars in series are grouped together to form a single resistance which is the sum of both busbars. This method does not allow for an accurate estimation of the busbar temperature

but is electrically accurate which is sufficient to assess pack electrical performance.

- Fuse: to protect the cell from overcurrent, our pack design includes a fuse that will open the circuit in case it reaches a certain current for a certain duration. To ensure that the fuse is correctly design the simulation must check that the fuse does not blow during normal operation of the battery pack.
- Main contactor: To isolate the battery pack from the rest of the vehicle. It is a controlled switch which is placed in the battery pack. This switch is controlled normally closed and contribute to the network resistance.
- Pre-charge contactor: On the vehicle, the loads the battery pack supply are often capacitive. This means high current pics can happen when connecting the pack to the vehicle load. To prevent this phenomenon and associated safety risks, a parallel electrical branch to the main contactor is done with a switch and a high resistance which limits the current at the start of operation.
- The cooling system: To ensure that the cell does not overheat during operation, and to guarantee life duration cooling system is necessary. An air-cooled system design was initially considered but simulation showed that this solution was not sufficient to cool the cell at high power output targeted. Simulation used in pre-development phase enables to sort out design solutions and avoid unnecessary prototype costs. The active cooling that was selected in the system is using a cooling plate located under the cell. The plate is cooled with a flow of liquid. Fins are placed in-between cells and connected to the cooling plate to increase cooling surface with the cell on the side. The cell heating part is handled in the cell model [3]
- BMS: The electronics as a whole is not modelled as it plays a little role in the electrical performance, but one key function of a battery management system is the cell balancing, which is modelled in this sketch. The model is capable to evaluate the performance of the balancing function and ensure that the BMS balancing resistance are correctly designed.
- Current voltage and temperature sensor are also present and modelled in the sketch, currently the output is not used as the real value of variables is available but future application of the model with BMS software function will use these measurement output to monitor Battery pack and compute SOC

3.3 Detail design of main functions

The model is parametrised using numerical optimisation methods based on tests data and datasheet of component [4], [5].

With this, we are able to test scenarios and check how the model physics react to the input stimulus.

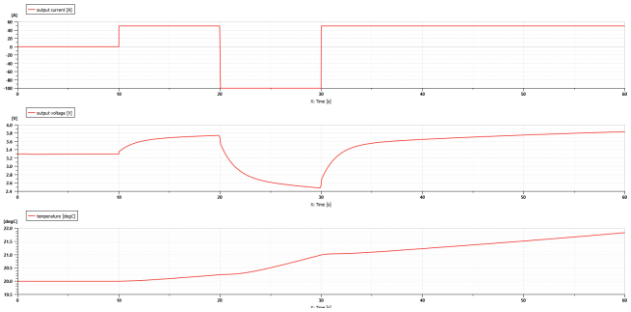


Figure 6: Simulation of behaviour of 1 cell given a pulse current input

The figure above shows the dynamic behaviour of one cell when pulse currents are applied to the battery pack. As expected, the voltage is changing when current is applied. But in real applications we must ensure that, this voltage will remain within the useable range of voltage for the cell that the cell supplier recommend for safety and warranty. The current also have an effect on the cell internal temperature, as the model estimate the temperature increase when a current load is applied. Similarly, to voltage limits, the battery pack design must ensure that the temperature cannot exceed a certain limit. This is the role of the liquid cooling and the simulation on real driving condition will show that our design prevent correctly over temperature in the simulated drive.

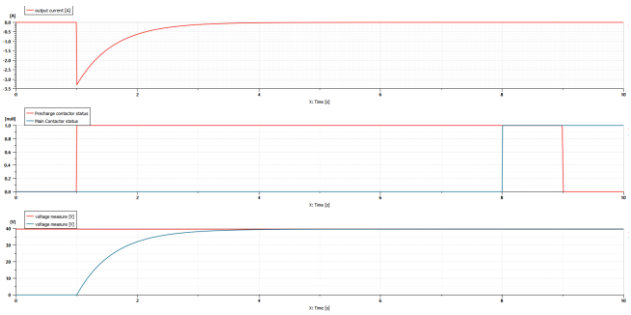


Figure 7: Simulation of pack precharge sequence

The pre-charge function can also be simulated to help the design of the component. Indeed, the resistance choice is critical. With too low resistance the inrush current will be high damaging the battery pack, with a value too low, the time to be ready for operation will be long and unacceptable for customer. Usual pre-charge must ensure, that current is lower than 50A, which is the case in our design.

4. Battery Pack simulation results

4.1 Electrical Results

To evaluate the performances of the battery pack on real driving condition, this study focuses on the WLTC profile [7].

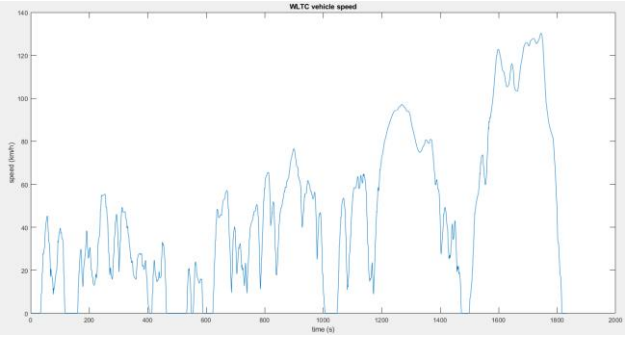


Figure 8: Driving profile of WLTC

WLTC, from WLTP, can be considered an average cycle. Several other homologation type cycles exist (NEDC: New European Driving Cycle …). From the driving cycle database, we can extract the current profile necessary for the vehicle to perform the cycle and input it to our battery pack model.

The nominal voltage range is from 36V to 52V; all electrical components are validated to operate within window. Therefore, we must ensure that the battery voltage stays within that range in our simulation.

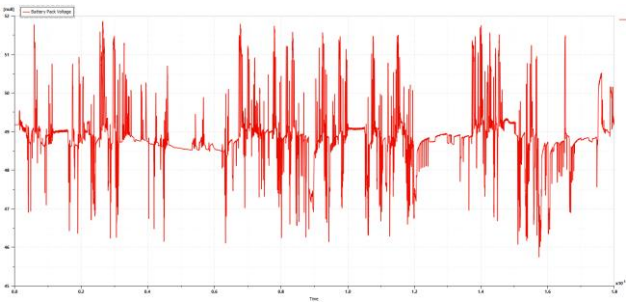


Figure 9: Battery Pack voltage simulation

The intrinsic resistance of the cell, as well as the one from the battery pack component give some voltage variation around the nominal value at 48V.

The battery voltage stays within the acceptable range but is close to the maximum value. The pack busbar resistance increases the pack internal resistance. To improve pack performance, this resistance must be decreased with an improved design (larger busbar, less connection …)

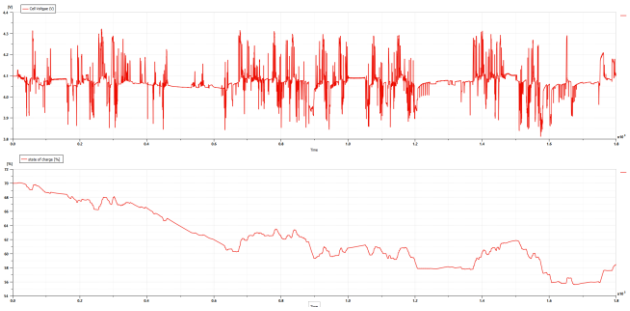


Figure 10: Cell Voltage simulation

At cell level, we can also check the SOC variation during our cycle. The profile is slightly discharging as we lose around 10% of SOC on the drive. The cell voltage stays within the acceptable voltage range. We still have some margin in discharge as the cell have a lower resistance for discharge.

4. Thermal results

The thermal behavior of the cell can also be assessed during the driving cycle. Here we will focus on the temperature of one cell. Because of their relative position in the pack, each cell has its own temperature behavior, and simulation with 3D model have to come in complement of the 0D simulation to find hot point in the battery pack.

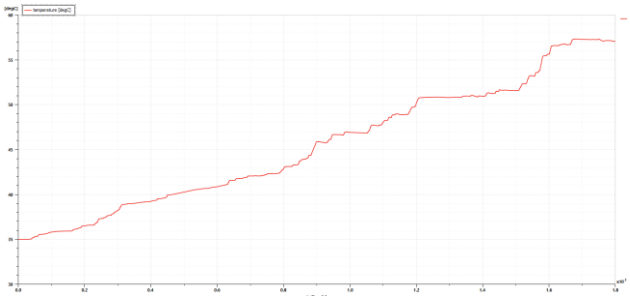


Figure 11a: Cell temperature without thermal management simulation

In the figure 11a, the thermal management function is deactivated to check the actual need for a cooling system. The temperature rapidly increases above 55°C which is the maximum allowed with TIAMAT Sodium-ion cells in operation

On the figure 11b, the thermal management is activated with a cooling fluid. The temperature still increases but stabilize around 42°C. The cooling system keeps the cell at an optimal operating temperature while allowing a lower resistance value.

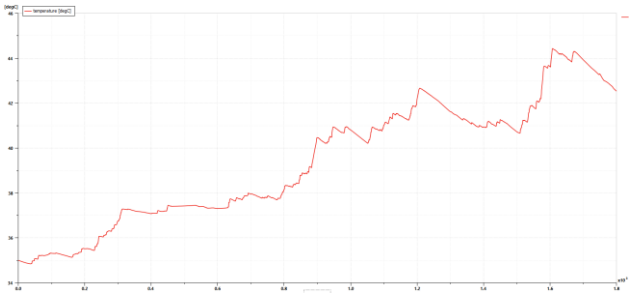


Figure 11b: Cell temperature simulation with thermal management activated

4.3 Parametrical study

The model has several parameters used as input. These are system parameters, which are more dependent on the battery pack integration within the vehicle. One of the key parameters for the system is the cooling fluid. The value for fluid temperature and flowrate is normally an input for the battery pack design. With parametrical study, we can find what the maximum temperature value to ensure a proper cooling. This value can be shared for a good vehicle integration. The battery pack can then operate only if the vehicle cooling system is supplying the correct fluid temperature.

Table 2. Temperature study

Cell initial temperature	Fluid cooling temperature	Cell Maximum Temperature
35°C	20°C	38°C
35°C	30°C	44°C
35°C	45°C	55°C
35°C	50°C	60°C

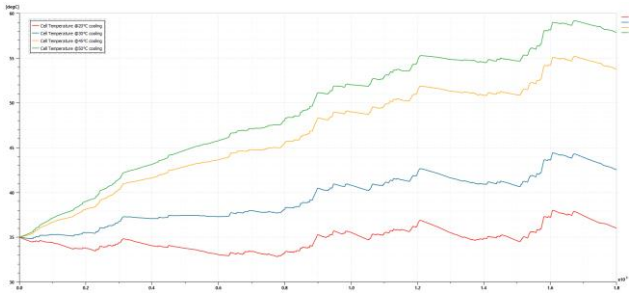


Figure 12: Cell temperature simulation for different cooling parameters

In real driving condition, the battery pack should request a derating power from the vehicle if the liquid coolant temperature is above a certain threshold. We can here estimate that the cooling system should be closed to 30°C in order to have a good margin from the maximum cell temperature at 55°C. In addition, maximum liquid temperature should not exceed 45°C. Of course, these simulations only give an average cell temperature. To identify hot spot within the cell, we need to use more accurate 3D thermal model.

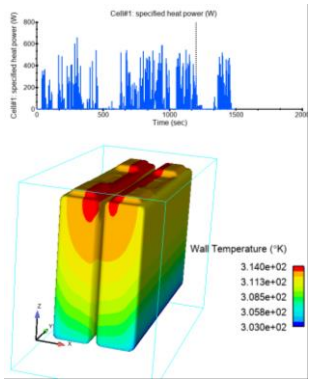


Figure 13: 3D thermal simulation

3D modeling drawback is that it takes time and requires a defined design to get result. With our fast-computing 0D model, we can provide the cell thermal losses dynamically and use it as an input for the later and more precise 3D thermal model. In fig. 13, the cell heating losses are extracted from the simulation from the 0D model, to run on a simplified 3D two cells model. The bottom of the cell is close to the cooling temperature and thus the top of the cell is the hot spot, but still within cell thermal limits.

Table 3. SOC study

Cell initial SOC	Fluid cooling temperature	Cell Maximum Temperature
70%	30°C	44°C
50%	30°C	52°C
40%	30°C	56°C
30%	30°C	58°C

Another key factor in cell management is the cell state of charge. This is because cell resistance is a function of SOC and temperature. The Battery pack must remain within a given SOC range to ensure correct operation. While at low SOC, other problem can arise (e.g. increased aging of cell) it is also a factor in the thermal design as the cell heating is directly linked to the cell resistance. For low SOC at the beginning of the cycle because the resistance is higher, the maximum temperature is also higher. In practice, the battery management system must apply a derating at lower SOC.

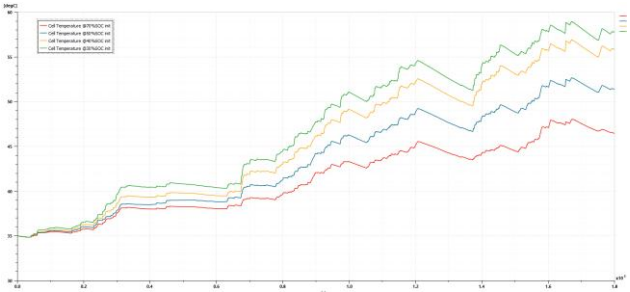
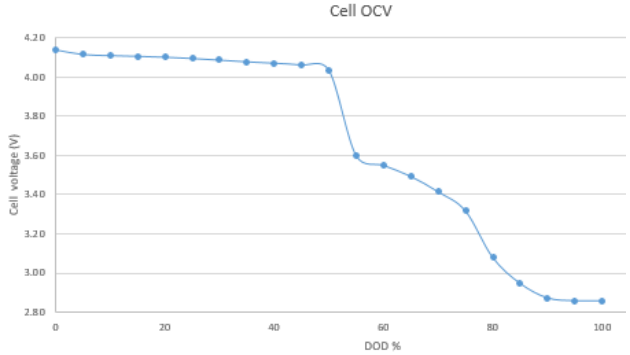


Figure 13: Cell temperature simulation for different initial SOC parameters

Furthermore, Sodium-ions cell, have a high non-linearity for their OCV curve. Lower SOC value would lead to higher current to compensate for lower voltage leading to even more heat losses. It is best to limit cell SOC above 50% as shown in the Table 3.



5. Conclusions

This paper presented the development of the simulation platform and means that have been set to develop a battery pack 48V. In the early phases of the project development, the use of simulations are powerful tools that allow testing designs and concepts in advance and optimizing them to ensure optimal performance of the final system. The current set-up shows promising result for the battery pack without test yet being done and give confidence in the design and in the components sizing choices. It also can be used to show the limits of the design and the improvement points to increase the overall pack performances in power.

The model can also be used for validating or calibrating BMS function such as advanced SOC, SOP, and SOH algorithm.

The model can be continuously improved over the course of the development of the product, always improving its accuracy based on tests data.

6. Acknowledgement

The authors thank all the PLASTIC OMNIUM Clean Energy Services and TIAMAT and IFPEN colleagues who contributed to this work as well as the French agency for ecological transition (ADEME) for the financial support it granted to the project.

7. References

[1] TIAMAT, *Cell datasheet,* 2022.

[2] B. ARNAUD et L. Jerome, «Comparison of propagation rate between Na-ion and Li-ion cells,» Ineris, October 2021.

[3] Damay, N., Friedrich, G., Forgez, C., & science, H. o. (2016). Modélisation thermique en vue du dimensionnement d'un pack batterie, avec prise en compte du couplage électro-thermique pour la caractérisation des pertes électriques. Grenoble.

[4] Jackey, R. A., Plett, G. L., & Klein, M. J. (2009). Parameterization of a Battery Simulation Model Using Numerical Optimization Methods.

[5] Plett, D. G. (2013, 2015). Battery Management and Control>>Simulating Battery Packs. Colorado.

[6] DieselNet. WLTC Test Cycles details. https://dieselnet.com/standards/cycles/wltp.php.

[7] Plett, D. G., & Colorado, U. o. (2021, 10). Equivalent Circuit Cell Model Simulation. Colorado.

[8] Ahmadou Samba. Modélisation Electro-thermique 2D d'une batterie lithium-ion de type "pouch". Journées JCGE '2014-SEEDS, June 2014, Saint-Louis, France.hal-01083934

[9] Diagnostic de l'état de vieillissement des systèmes de stockage de l'énergie électrique Application : Véhicule, Asmae EL MEJDOUBI 2015

8. Glossary

SOC: State of Charge
SOH: State of Health
SOP: State of Power
CAD: Computer assisted design
EM: Electrical machine
BMS: Battery management system
WLTC: Worldwide Harmonized Light Vehicles Test cycle
WLTP: Worldwide Harmonized Light Vehicles Test Procedure

15 JUNE 2022

ELECTRIFIED PROPULSION SYSTEMS TESTS AND SIMULATIONS

Real-Time Multi-Physics Simulation of BEV VTM for X-in-the-Loop Control Development

Eduardo Graziano[1], Giulio Boccardo[1], Luca Panizzolo[1], Asveen Seebooa[2], Santhosh Jayaraju[2], Ioannis Argyridis[2],

1: POWERTECH Engineering S.r.l., Torino, Italy
2: Jaguar Land Rover, Coventry, UK

Abstract: Battery Electric Vehicles (BEVs) have demanding constraints for the thermal management of their sub-systems, requiring proper thermal conditioning based on the vehicle state and environmental conditions. In order to address all the different requirements with the minimum energy consumption, a BEV cooling system is typically characterized by an articulated layout enabling different cooling or heating modes that must be properly controlled. In this perspective, X-in-the-Loop (XiL) simulation is an effective and innovative means to develop and validate the thermal management control system coupling a real or virtual ECU with a fully-physical system-level plant model. In this paper, a methodological approach for the set-up of real-time capable 1D models for a complex BEV architecture is presented, providing a valuable tool for the control system development process with visible benefits in terms of time-to-market and development costs, thanks to the reduced need for time-consuming and expensive experimental campaigns.
Keywords: BEV, Thermal Management, 1D simulation, HiL, Real-time

1. Introduction

The advent of electric powertrains introduced new challenges for the automotive industry, often contrasting with time-to-market and cost reduction constraints OEMs and their suppliers are asked to comply with. Electric components like batteries and e-drive units have more stringent thermal requirements compared to internal combustion engines, as they require lower operating temperatures – sometimes even lower than ambient – and a narrower temperature operating range too. These can be achieved adopting dedicated cooling solutions that typically lead to more complex systems, more components and actuators, a higher number of degrees of freedom for the control system [1]. In addition, the battery pack is the only energy source available onboard, thus the control strategy must be optimized not only to satisfy performance, thermal and safety requirements, but it must also guarantee a suitable vehicle range and durability [2]. In this scenario, CAE tools have further increased their popularity thanks to clear benefits in terms of reduction of development time, prototyping and experimental testing needs. Virtual models can be built during the early product development phases and used as a digital twin even when the real system is not available yet. XiL simulations based on real-time models are a key enabler for the virtual design and validation of complex vehicle thermal and energy management control systems [3].
Within this context, a workflow was needed to convert complex and computationally demanding 1D Vehicle Thermal Management (VTM) models of its electric platforms to still fully-physical but faster variants (up to real-time), usable for both offline and online system-level energy management and optimization studies. In this demonstrative project a BEV VTM 1D detailed model already available was selected as case study. As a first step, a reduction methodology was defined and applied to obtain a Fast-Running Model (FRM) variant of the baseline detailed model, intended for offline analyses. Secondly, the FRM built was used as a starting point to set up a real-time (RT) model for online applications, eventually deployed and validated on a Hardware-in-the-Loop (HiL) simulator.

2. Baseline 1D Model Description

A virtual model of a full-electric SUV used to carry out integrated performance, energy management and range optimization studies was selected as test case for this demo project. The model was built in GT-SUITE – the multi-physics software used in the automotive industry for mono-dimensional vehicle and powertrain simulation – and it included the following sub-domains (Figure 1):

- Vehicle longitudinal dynamics and driveline
- E-drive performance and thermal model
- Battery pack electrical and thermal model
- Coolant circuit
- Refrigerant loop
- Vehicle cabin
- Underhood compartment
- Energy and thermal management control system

The VTM model required the user to input a vehicle speed profile target and some boundary conditions for the analysis, e.g., ambient temperature, battery state of charge, etc. The control logic implemented in the model automatically determined the instantaneous traction/braking power request as well as the status of

all the cooling system actuators, trying to attain the performance and thermal targets without exceeding safety limits.

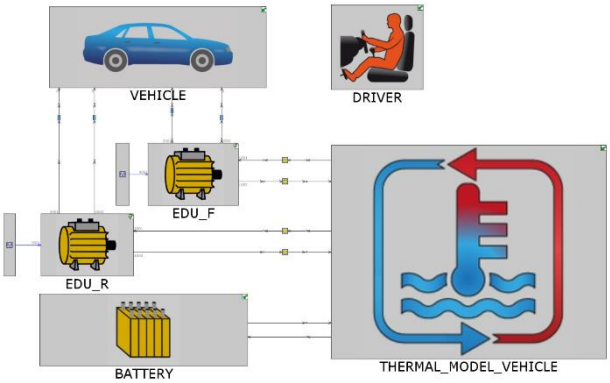


Figure 1: System-level GT-SUITE VTM model

The heat generated by the powertrain components was dissipated by the cooling system, which predicted the instantaneous fluids and hotspot temperatures, with these latter ones used to more accurately look-up components losses. The energy consumed to move the vehicle and the one regenerated during slowdowns, as well as the power absorbed by the actuators, contributed to the estimation of the instantaneous battery state of charge and residual vehicle range.
This comprehensive model was characterized by a Factor of Real-Time (FRT) in the range of 5÷30 (Figure 2), i.e., the computational time required was on average 5÷30 times higher than the actual duration of the maneuver simulated. The variability of FRT was related to the aggressiveness of the maneuver and different heat transfer conditions, that have an impact on the model stability and convergence time.

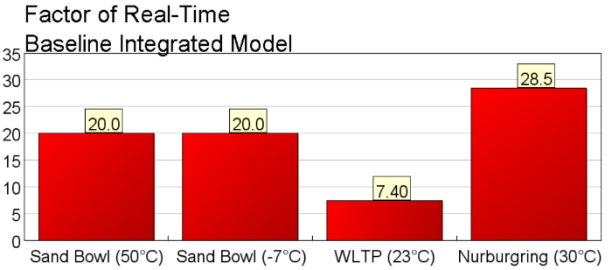


Figure 2: Average FRT of baseline model on some maneuvers at different ambient temperatures

Although compatible with the complexity of the VTM model, this computational effort limited the number of analyses that could be carried out in a certain time frame, especially when long transient maneuvers were involved. This aspect motivated the need of a more computationally efficient model, capable to further expand the VTM model simulation capabilities up to real-time applications.

For the purpose of the study, the baseline VTM model was run over several relevant transient maneuvers to generate reference results to be used as a target during the following model reduction and speed-up process.

3. Fast-Running 1D Modelling

3.1 Overview

FRM is a term used to indicate 1D fully-physical models showing a quite fast computational time in the range of 1÷5 and a level of accuracy comparable with the one offered by the more detailed variants. This is achievable thanks to a coarser discretization of the model accompanied by a dedicated calibration of the tuning factors, typically required to compensate for some physical phenomena that might not be captured anymore with a simplified geometry.
The reduction of the baseline model to a FRM was carried out in three steps:

1) Identification of the most computationally demanding flow circuits in the baseline model
2) Geometrical reduction and calibration of flow circuits identified at point 1) in standalone models
3) Integration of the reduced and validated flow circuits into the complete VTM model

In GT-SUITE, each closed- or open-loop flow path is handled and solved as an individual flow circuit. In order to minimize the effort and the impact on results, the FRM reduction process was applied to a limited number of flow circuits, in particular the ones representing the actual bottlenecks for the simulation runtime. A CPU breakdown analysis was carried out on the baseline model to identify the flow circuits with the highest impact on the computational time. Figure 3 reports the fraction of the total CPU time required by each flow circuit included in the model, evaluated over a complete simulation run. It was straightforward to recognize the refrigerant loop, the coolant circuit and the underhood sub-model as the most demanding parts of the model and the best candidates to be reduced to FRM.
The FRM reduction process was carried out separately on each sub-system, isolated from the complete VTM model and set up to run standalone over steady-state points. This was done for a couple of reasons:

- Speed up the FRM calibration process limiting the modelled domain and the required simulation time
- Clearly assess the impact of geometrical reduction on the sub-model results, replacing interacting systems with imposed boundary conditions

Approximate CPU Breakdown by Cluster

Cluster #	Circuit #	Type	Name	CPU %
2	2	Flow	refrigerant	41.86
1	1	Flow	Battery_Circuit	39.97
"	12	Flow	Flow 12 (Column 1)	"
3	3	Flow	Airpath_Cool3D_Centre	14.89
1	1	ODE/Mech	ODE 1 (Column 1)	1.64
"	2	ODE/Mech	ODE 2 (Column 1)	"
"	3	ODE/Mech	ODE 3 (Column 1)	"
"	4	ODE/Mech	ODE 4 (Column 1)	"
"	5	ODE/Mech	Controls (Column 1)	"
7	7	Flow	Flow 7 (Column 5)	0.54
"	8	Flow	Flow 8 (Column 5)	"
			Thermal	0.25
10	11	Flow	Flow 11 (Column 5)	0.2
8	9	Flow	Cabin Air	0.16
4	4	Flow	Airpath_Cool3D_2	0.14
6	6	Flow	coolant heater	0.13
9	10	Flow	Flow 10 (Column 5)	0.11
5	5	Flow	Airpath_Cool3D_Vanes	0.11

Figure 3: CPU breakdown analysis reporting the circuits with the highest impact on computational time (highlighted with arrows on the side)

3.2 Coolant Circuit Reduction

The coolant system was made of two hydraulic loops put in communication with a coolant-to-coolant Heat eXchanger (HX) and sharing the same expansion tank: one loop was dedicated to the thermal management of powertrain components (e-drive, battery, OBC), the other to the cabin heating. The former loop, referred as “main loop” in the following, included a n-way valve enabling different flow paths and operating modes, such as:

- E-drive passive cooling with radiator and battery active cooling with chiller
- Combined e-drive and battery passive cooling with radiator
- Cabin heating exploiting e-drive and battery heat
- Cabin heating with an e-heater or heat pump
- Battery heating with an e-heater or heat pump

Both the main and the cabin loops were geometrically reduced to FRM according to the following guidelines:

- Pipes placed between two components or flow junctions were replaced with a single straight pipe with constant diameter, maintaining the total length and volume of the baseline geometry (Figure 4).
- Each equivalent straight pipe was discretized over its length with a single sub-volume (i.e., the Navier-Stokes equations were solved in the centroid of the pipe only).
- A coarser single sub-volume discretization was used on HXs as well except the chiller, where a less severe reduction was adopted to avoid refrigerant-side instabilities.

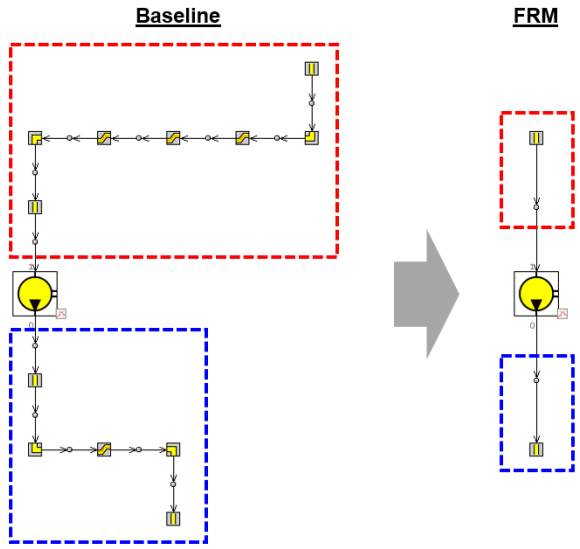


Figure 4: Example of geometrical reduction of pipes upstream and downstream of the coolant pump

Although not required for the FRM purposes, in order to reduce the global effort, the geometrical reduction was carried out targeting a maximum number of 100 sub-volumes for each individual flow circuit, which was a requirement for the RT model to be developed as a second step.

The number of sub-volumes for the main and cabin coolant loops characterizing the baseline model and FRM is reported in Table 1. In the FRM, the two loops were set as separate flow circuits in order not to exceed the 100 sub-volumes threshold.

Table 1: Number of sub-volumes for the coolant system, before and after the geometrical reduction

N° of Sub-Volumes	Baseline	FRM
Main Loop	1650	97
Cabin Loop		40

As in a FRM some information in terms of pipes bends and tapers were missing because of the simplified geometry, the out-of-the-box pressure drops predicted by the model were underestimated compared to the baseline scenario with detailed geometry. For this reason, some concentrated flow restrictions were placed at relevant locations along the hydraulic circuit to restore the total permeability of the system. The equivalent diameter of these flow restrictions was calibrated on a subset of steady-state points with pumps running at maximum speed, targeting the reference flow rates through the different branches of the circuit. After that, the calibrated FRM was run and validated against baseline model results over a complete pumps speed sweep and with different n-way valve positions/hydraulic modes.

Figure 5 reports some correlation plots in which the steady-state outputs of the FRM running over a pumps speed sweep at constant coolant temperature

("FRM", solid line) are compared against the baseline model reference results ("Base", dashed line). Two series of results are represented, corresponding to different hydraulic layout modes: Mode 1 with e-drive and battery loops running separately ("M1", in red), Mode 2 with e-drive and battery loops running as a single circuit ("M2", in blue). The X and Y axes report the pumps speed and volumetric flow rate, normalized with respect to the values from the Base (M1) maximum speed operating point. The FRM showed a satisfactory correlation against reference results throughout the circuit over the pumps speed sweep, especially in Mode 1 (i.e., separate loops) that was the most relevant from the thermal standpoint. A gap was noticed between FRM and baseline model on battery pump flow rate in Mode 2 (i.e., combined loops), likely related to the impact of model simplification on the complex n-way valve internal flow distribution. However, since Mode 2 was expected to be used less extensively than Mode 1 during normal vehicle operations, given the purpose of the project it was decided to accept this correlation status without proceeding with further tuning of FRM results.

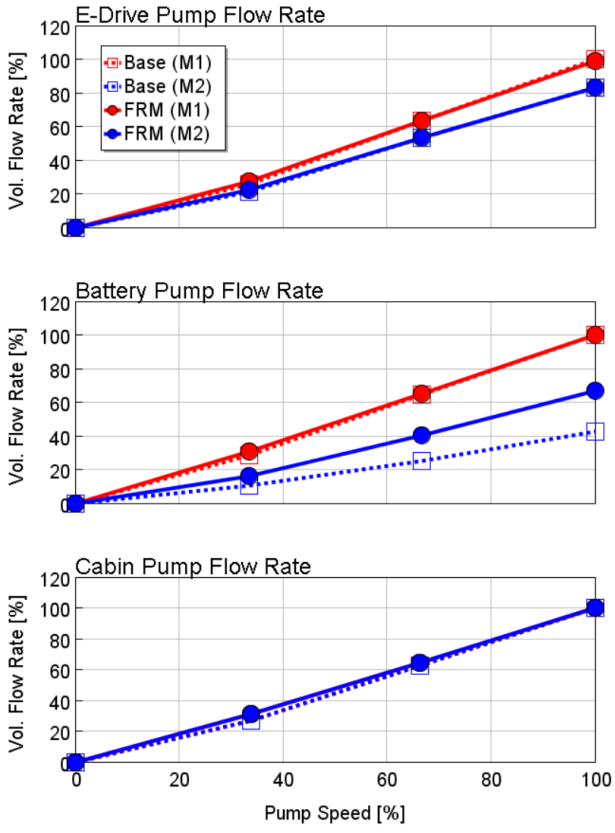


Figure 5: Correlation plots between FRM and baseline model for the standalone coolant circuit

The FRM behavior was validated from the computational efficiency standpoint as well. Figure 6 reports the FRT averaged over the steady-state points of the pumps speed sweep, for both the baseline (left) and FRM (right) variants. A huge decrease of the required computational effort was observed on the FRM, characterized by a simulation speed on average 20 times faster than the original baseline model.

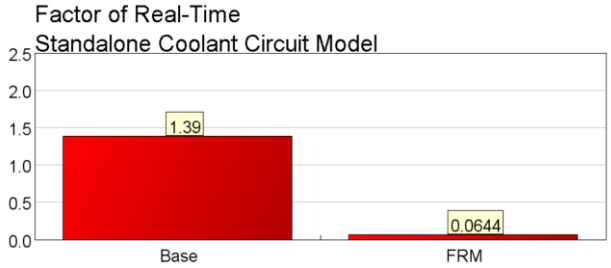


Figure 6: FRT characterizing the standalone coolant circuit baseline model and its FRM variant

3.3 HVAC Circuit Reduction

The HVAC loop of the vehicle under study was quite complex and articulated, featuring valves used to define flow direction and operate the system either in cooling or heating mode via heat pump. In addition, 3 Electronic eXpansion Valves (EXV) were used to regulate the thermal load on the battery chiller and two cabin evaporators (front/rear).

Two-phase HVAC models are typically trickier to reduce to FRM since they are more sensitive to the discretization level adopted compared to coolant loops. For this reason, the procedure followed to build the HVAC FRM featured slight differences from the one described for the coolant circuit:

- Each group of pipes separating two or more components was arranged in a standalone flow bench model, imposing suitable refrigerant pressure/temperature/flow rate conditions at the boundaries. This was carried out both on the baseline detailed geometry and its reduced counterpart.
- Due to the two-phase nature of heat transfer, HXs results were strongly affected by the discretization level adopted. In order to mitigate the impact on heat transfer results, a sweep of number of sub-volumes was carried out on each HX to identify the minimum value required to achieve a good correlation with reference results.
- The refrigerant pipes were reduced following the same guidelines adopted for the coolant part and targeting the maximum 100 sub-volumes criterion for compatibility with RT model requirements. To comply with this constraint, in some cases it was necessary to adopt an even stronger reduction on pipes to compensate for the higher number of sub-volumes required for HXs.

Each group of pipes was individually reduced until the maximum number of sub-volumes limit was satisfied (Table 2) and calibrated by means of concentrated

flow restrictions to correlate FRM results with the ones obtained with the baseline geometry.

Table 2: Number of sub-volumes for the HVAC loop, before and after the geometrical reduction

N° of Sub-Volumes	Baseline	FRM
HVAC Loop	676	100

The individual portions of the system were then reassembled into a FRM variant of the complete HVAC circuit, which was run in several cooling and heating operating conditions as listed in Table 3.

Table 3: HVAC system operating modes

Operating Mode	Description
1	Shut-off
2	Front evap.
3	Front + rear evap.
4	Front + rear evap. + chiller
5	Front evap. + chiller
6	Chiller
7	Heat pump

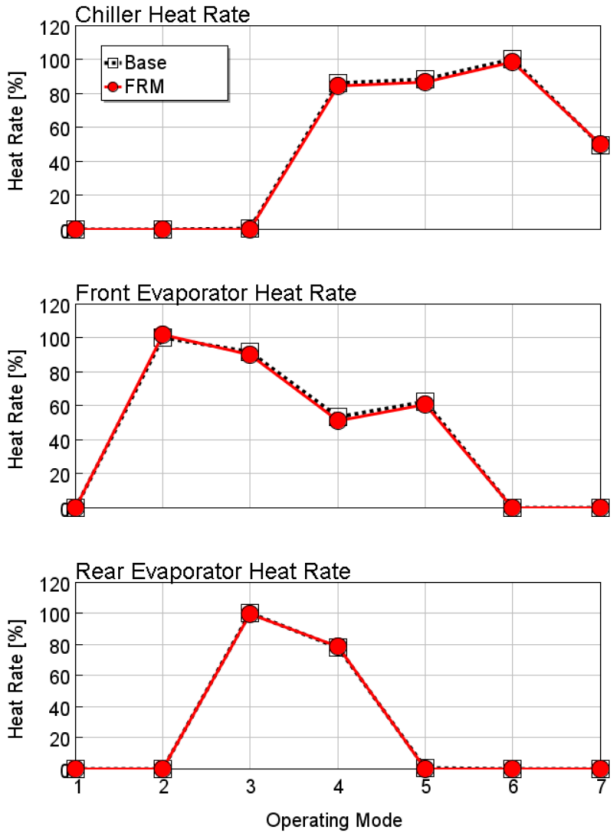


Figure 7: Correlation plots between FRM and baseline model for the standalone HVAC circuit

Some steady-state correlation plots between the standalone HVAC FRM ("FRM", solid red) and the baseline model ("Base", dashed black) are reported in Figure 7. The X axis represents the HVAC system operating mode, the Y axis reports the chiller/evaporators heat transfer rate normalized with respect to the maximum value evaluated from the "Base" results for each component. The correlation level achieved was satisfactory in all the operating conditions explored.

The computational speed of the standalone HVAC model improved on average by a factor of ~15 when passing from the baseline model to FRM, as depicted in Figure 8.

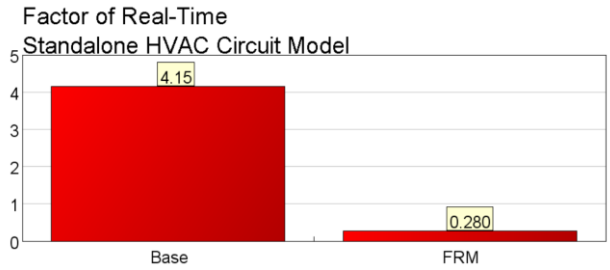


Figure 8: FRT characterizing the standalone HVAC circuit baseline model and its FRM variant

3.4 Underhood Model Reduction

The underhood sub-model included a quasi-3D representation of the Condenser Radiator Fan Module (CRFM), built in COOL3D. A COOL3D model is discretized with a 3D matrix of control volumes, applied to both CRFM components and air domain. The quasi-3D approach adopted allowed a more accurate prediction of air flow distribution compared to a conventional 1D approach.

The COOL3D-based representation of the CRFM was maintained in the FRM variant as well, just adopting a coarser discretization level and some geometry simplification techniques aimed to the reduction of the total number of sub-volumes (constrained to 100 as in previous cases). Figure 9 reports on the left side the baseline CRFM geometry, compared against the FRM variant on the right.

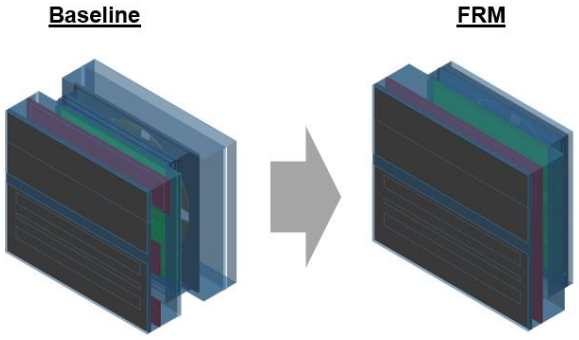


Figure 9:COOL3D model of the CRFM, before (left) and after (right) the geometrical reduction

A significant reduction of the number of sub-volumes was obtained with the FRM, as reported in Table 4.

Table 4: Number of sub-volumes for the underhood model, before and after the geometrical reduction

N° of Sub-Volumes	Baseline	FRM
Underhood	2554	88

As already observed on the hydraulic circuits, the geometrical simplification of the CRFM led to an underestimation of predicted pressure losses along the air path. Three resistance planes were placed in the COOL3D FRM and tuned to restore both the baseline CRFM overall permeability and the air flow distribution between the radiators and the surrounding void space. The COOL3D FRM behavior was validated on a standalone model where a vehicle speed sweep (i.e., external air velocity sweep) from 0 to 200 km/h was reproduced, assuming the fan running at maximum speed with the active grille shutter fully opened. Figure 10 depicts the condenser and LT radiator air flow rate correlation between the baseline model ("Base", in black) and the FRM ("FRM", in red). The X axis represents the external air velocity at CRFM inlet, the Y axis reports the air mass flow rate normalized with respect to the baseline condenser flow rate evaluated at maximum speed. The satisfactory accuracy of FRM results was assessed.

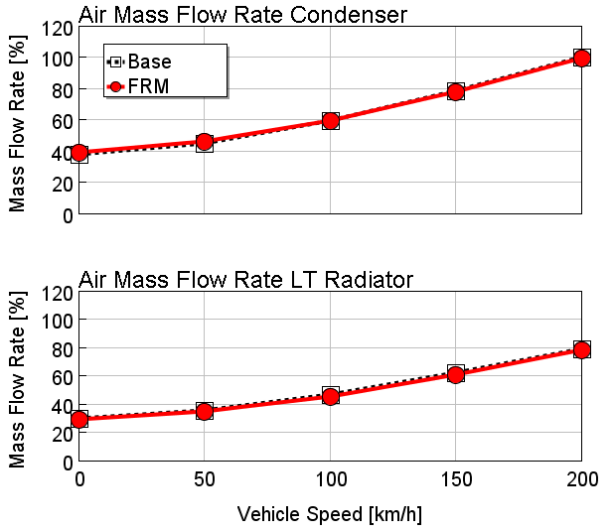


Figure 10: Correlation plots between FRM and baseline model for the standalone underhood

A visible increase of the computational efficiency was noticed with the underhood FRM as well, which showed an average ~10 times increase in simulation speed, as depicted in Figure 11.

3.5 Integrated VTM FRM Validation

The standalone coolant, HVAC and underhood FRMs were integrated into the complete VTM model, replacing their baseline counterparts.

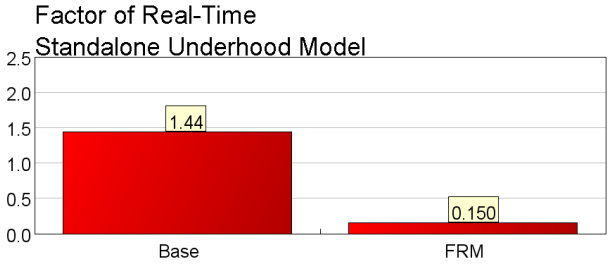


Figure 11: FRT characterizing the standalone underhood baseline model and its FRM variant

The vehicle and driveline part, the control system as well as the flow circuits showing a negligible impact on computational time were not modified. All the input/output signals exchanged between the different sub-models were maintained.

In order to further speed up the integrated FRM, an optimization of solver settings was carried out. The simulation timestep used in the baseline model (0.05 s) was swept towards higher values to identify the threshold beyond which the FRM results started to deviate from the baseline model reference values. A timestep of 0.15 s was eventually selected and implemented in the VTM FRM, keeping some margin from the critical threshold identified from the sweep.

The relative impact of each reduced sub-model on the computational time is depicted in Figure 12, which reports from left to right the incremental variation of FRT when implementing each standalone FRM in the baseline integrated model.

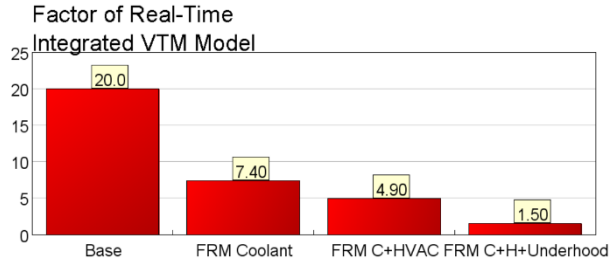


Figure 12: FRT decrease with FRM sub-models

The integrated VTM FRM was run over several transient maneuvers to validate its behavior against the baseline model reference results. The outputs observed on two relevant scenarios are reported in Figure 13: the "Sand Bowl", a steady-speed driving mode in a hot environment at 50°C and the "Nürburgring", the well-known German track at 30°C ambient temperature. The upper plot represents the front e-motor coil temperature predicted by the e-drive heat distribution model; the plot in the middle reports the predicted coolant temperature at the battery pack inlet; the bottom plot reports the heat rejection from the condenser to the external environment, sensitive to both battery and cabin cooling requirements. In each plot, the solid lines represent the VTM FRM results ("Sand Bowl" in red, "Nürburgring" in green),

while the black dashed lines refer to the baseline VTM model reference outputs.

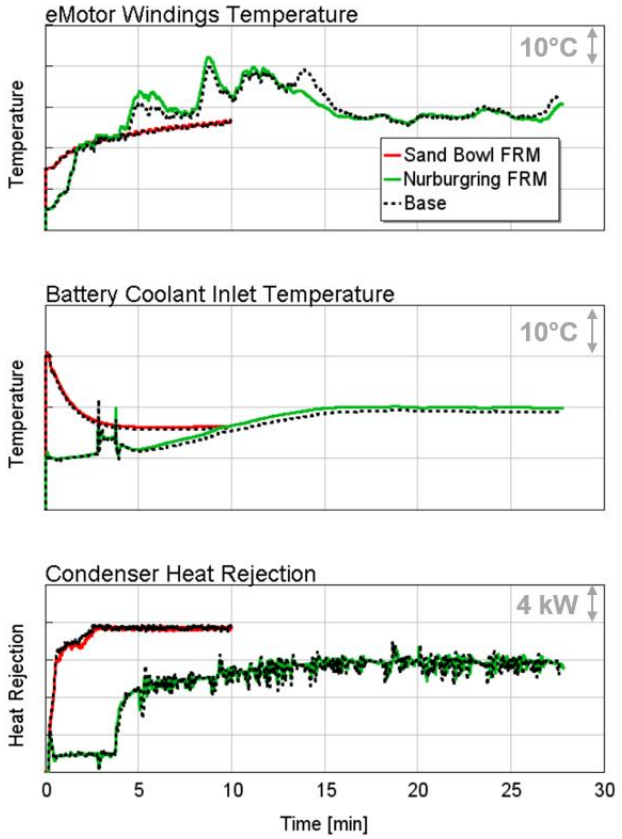


Figure 13: Correlation plots between FRM and baseline variants for the integrated VTM model

The satisfactory correlation level demonstrated by the standalone FRMs in steady-state conditions was confirmed by the integrated VTM FRM as well. Negligible differences were observed between FRM and baseline VTM model over the “Sand Bowl” maneuver. Small but still acceptable correlation gaps were observed on few quantities in the “Nürburgring” test case, due to the highly dynamic operating conditions which made the FRM outputs more sensitive to the coarser discretization level and larger timestep. The VTM FRM proved its higher computational efficiency in all the driving scenarios tested, showing a computational time on average more than 90% faster than the original baseline model.

The proposed methodology for VTM models reduction proved to be effective in significantly reducing the computational time still maintaining a satisfactory accuracy of results, expanding the simulation opportunities for such kind of complex integrated applications.

4. Real-Time Model Set-up and HiL Deployment

Although the FRM built was intended for offline simulations, the smart practices taken during its set-up (e.g., the 100 sub-volumes limit) made it a robust basis for the RT model set-up, with a limited number of adaptations. Since the maximum number of sub-volumes requirement was already satisfied, most of the effort was concentrated in the set-up of the model to run with the so-called GT-SUITE-RT solver, which is a specific version of the standard solver dedicated to RT applications. As the GT-SUITE-RT solver is optimized to maximize the computational speed, it lacks some non-essential features that made it not compatible with some of the objects used in the VTM model, which required to be replaced with equivalent alternatives.

The perimeter of the RT model was limited to the cooling system, as the vehicle and control parts were expected to be handled by other tools in the HiL simulation environment (e.g., the ECU). The latter sub-systems were then removed from the VTM RT model and replaced by an input/output interface enabling signals transmission during co-simulation between the GT-SUITE physical cooling system and the Simulink® platform model.

For the scope of RT model online validation it was not required to integrate the GT-SUITE model within the complete HiL simulation environment, thus a simplified co-simulation approach without a physical ECU was adopted to test the model behavior. The input requested by the cooling system model (i.e., the ones expected to be provided by the control part) were extracted as time profiles from the reference results, imposed as signal sources in a Simulink® model and fed to the GT-SUITE model encapsulated into a S-Function. The outputs provided by the GT-SUITE model, although not required as feedback for the controls in this simplified set-up, were passed back to Simulink® for validation purposes.

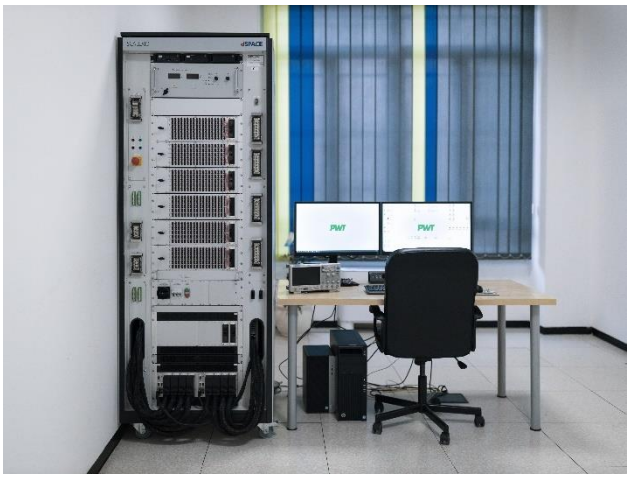


Figure 14: PWT in-house HiL dSPACE simulator

The co-simulation model was eventually deployed on the dSPACE Scalexio HiL hardware available in PWT’s laboratory (Figure 14) and run online on a single CPU core over the same transient maneuvers used for offline validation.

Figure 15 depicts the results from the online RT simulation compared against the ones from the offline VTM FRM and baseline model over the Nürburgring (30°C) maneuver, which showed to be the most critical among the ones tested. It can be noticed that the modifications applied to the RT model in terms of signals processing and solver type did not affect the correlation level, which confirmed to be satisfactory. The RT model showed an even better correlation with Base model results compared to FRM: this behavior was due to the fact that in the online simulation the controllers actuations were imposed as time profiles (i.e., control outputs were not sensitive to VTM model thermal results as in the FRM case).

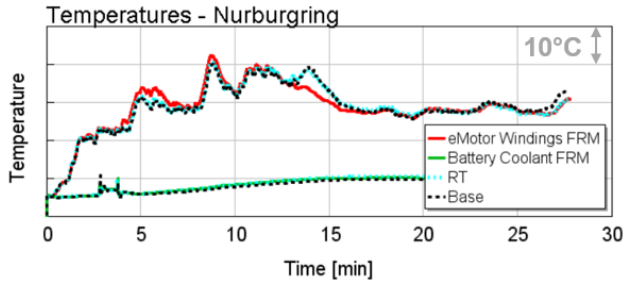


Figure 15: Temperatures correlation plot between RT online model and offline variants

The average FRT showed by the RT model was lower than 1 and thus aligned with the requirements, although some spikes above the threshold were noticed in highly dynamic maneuvers like the Nürburgring (Figure 16). These spikes did not represent an issue for the current test case, but in presence of less performant CPUs and/or more complex models they might generate simulation overruns. In that case, further tuning of the RT model might be needed to limit the occurrence of overruns within an acceptable threshold.

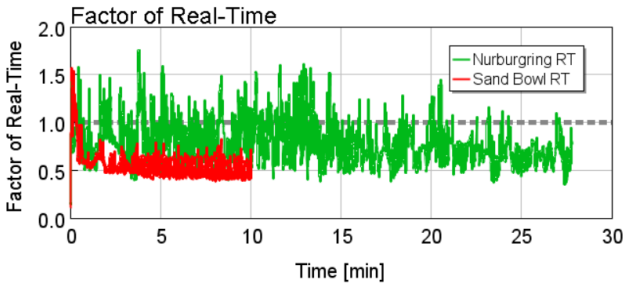


Figure 16: Instantaneous FRT showed by the RT model running online on dSPACE HiL hardware

5. Conclusion

In this demonstrative study a complex BEV VTM model was converted to a FRM, which showed an average 90% improvement in computational time with a limited impact on results accuracy. It proved to be an effective and fast solution to carry out intensive system-level analyses and optimizations. Furthermore, the potential of such kind of physical models to be used as a virtual plant for the development and validation of control systems was assessed. A RT model of the cooling system was obtained from the FRM with limited modifications, set up to run in co-simulation with Simulink® and tested online on a dSPACE Scalexio HiL simulator at PWT's laboratory, proving a suitable computational speed and an accuracy level comparable with what observed from the offline counterparts. The RT model was further validated in-house by Jaguar Land Rover in conjunction with a complete control system and the methodology proposed was adopted as a standard for the new vehicle development programmes.

6. Acknowledgement

The authors acknowledge the contribution of Mr. Pantelis Dimitrakopoulos from Gamma Technologies, LLC for his valuable support during this work.

7. References

[1] Piao, C., Chen, T., Zhou, A., Wang, P., Chen, J.: "*Research on Electric Vehicle Cooling System Based on Active and Passive Liquid Cooling*", Journal of Physics: Conference Series, 2020.

[2] Shelly, T., Weibel, J., Ziviani, D., Groll, E.: "*Comparative analysis of battery electric vehicle thermal management systems under long-range drive cycles*", Applied Thermal Engineering, Volume 198, 2021.

[3] Boccardo, G., Graziano, E., De Rosa, L., Mrkvica, T., Pautasso, S.: "*Virtual Approach for Control System Design: Integrated Simulation of Battery Cooling and Cabin Comfort Circuits to Develop a BEV Thermal Management Control Logic*", SIA POWERTRAIN, Versailles (France), 2019.

8. Glossary

BEV: Battery Electric Vehicle
XiL: X-in-the-Loop
ECU: Electronic Control Unit
OEM: Original Equipment Manufacturer
CAE: Computer Aided Engineering
VTM: Vehicle Thermal Management
FRM: Fast-Running Model
RT: Real-Time
HiL: Hardware-in-the-Loop
SUV: Sport Utility Vehicle
FRT: Factor of Real-Time
CPU: Central Processing Unit
HX: Heat eXchanger
OBC: On-Board Charger
HVAC: Heating Ventilation Air Conditioning
EXV: Electronic eXpansion Valve
CRFM: Condenser Radiator Fan Module
LT: Low-Temperature

Virtual Calibration of a detailed HEV thermal management system

H. Sara[1], P. Dimitrakopoulos[2], N. Framke[1], H. Pandit[2], A. Koniec[3]

1: Gamma Technologies GmbH, Danneckerstraße 37, 70182 Stuttgart, Germany
2: Gamma Technologies LLC, 601 Oakmont Ln, Westmont, IL 60559, United States
3: Gamma Technologies SAS, 27 Rue d'Aubuisson, 31000 Toulouse, France

Abstract: With the latest trends of electrification, the requirements to design controls systems without prototype hardware are increasing and the focus is shifting to virtual testing of vehicle systems including SiL and HiL simulations. The ability to forgo prototype testing demands numerical and simulation methods that are quick to model, fast to run, accurate and scalable. A real time thermal EV plant model centered around geometry based 1D flow simulation offers a feasible way to meet these requirements. Offering precise information on the energy losses required for thermal management of different subsystems, it can be efficiently extended with mechanical and electrical systems to represent a transient, holistic xEV powertrain system. To further increase the reliability of the numerical representation, the 1D model can be enhanced by coupling it to higher fidelity and models, e.g., for flow, electrochemistry, or heat transfer mainly at the expense of HiL compatibility. Using a high-fidelity plant model of a Through the Road hybrid vehicle including 3D thermal FE models for engine, this study investigates methodologies of efficient model complexity reduction, that preserve the governing physics, align with the development process and are modular. The study includes HiL compatibility and integration of the model subsystems via FMI standard.

Keywords: Holistic thermal management system, Real time Simulation, hardware in the loop, HiL simulation.

1. Introduction

Reducing the emission of conventional vehicles by means of electrification of the powertrain brings new opportunities and challenges for automotive engineers, especially in the field of thermal management and thermal security of components. Thermal management systems for xEVs usually have a high degree of topological complexity, integration of new function, more interaction between different circuits, new thermal management strategies and high level of complexity of the control algorithms [1] [2].
On top of that the key factor for the market acceptance of an xEV is its range. Thermal management can play a crucial role in optimizing the vehicle range [3]. Cooling systems in conventional powertrain were based on passive means where the ambient air was used to extract the excess heat of the engine. Due to limited energy capacity of BEVs, the interaction between the different thermal management systems increased and heat pump system were used to ensure the correct operating temperature for not only the battery, but also the e-motor and the power electronics from the perspective of range and life cycle, as well as occupant comfort. The electrical energy needed for thermal conditioning of battery or cabin and for propulsion can be of the same order of magnitude [4]. Therefore, the industry focus is on a holistic approach to thermal management [5].
The aim is to validate new technologies early and without the presence of hardware, decreasing testing costs and development cycle time and increasing the security of the decision making throughout the powertrain development. Because of these requirements, the focus is shifting to a complete virtualization of the complete vehicle design and validation through virtual testing of (XiL) of vehicle systems: including Software and Hardware in the Loop simulations [6] [7].
In this study, using a high-fidelity plant model of a Through the Road hybrid vehicle including 3D thermal FE models, methodologies for efficient model complexity reduction are investigated. The methodologies preserve the model physics, accuracy, and predictability, align with the development process and are modular. The study includes HiL compatibility and integration of the model systems.

2. System Modelling

The case study used in the article is representative of a Through the Road hybrid vehicle as presented in Figure 1. An internal combustion engine with an 8-kW belted starter generator and a 6-speed manual transmission power the front axle while a larger 27 kW electric machine propels the rear axle. The TTR model has a holistic thermal management system modelled including:

- 3DFE thermal representation of the engine.
- Detailed electro and thermal battery pack module.
- Quasi 3D underhood model.
- Parametric thermal representation of the electric motor.

- Two-Phase system for battery cooling and passenger comfort.
- Detailed piping network for low and high temperature cooling circuits.

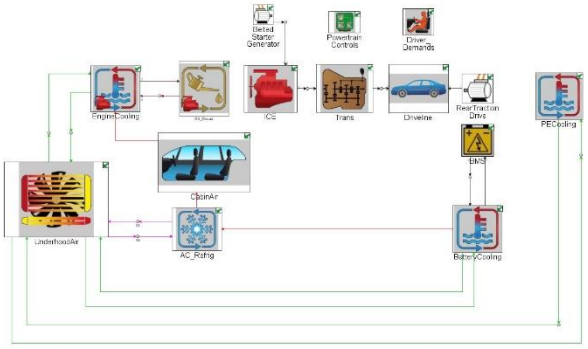


Figure 1: Structure of the integrated system level.

In addition to the detailed thermal management system, the TTR model contains a detailed control system. Based on the vehicle speed target, battery state of charge, ambient and system temperatures, and other inputs, the controls algorithms determine dynamic operating modes. The control logic ensures safe operation of the battery and rear electric machine within temperature limits. Based on the ambient conditions, the battery, the electric machine and the cabin temperature, the controls determine which mode to use to condition the battery using a refrigerant circuit or ambient air as heat sink.

The driving cycle used to compare runtime models is a WLTC.

3. Reduced Order Model

3.1 Runtime improvement potential

Such type of integrated model is usually a result of combining sub-models and components from different stakeholders, who may have different requirements on model accuracy and runtime. When the different sub-systems are not developed for fast runtime, the integrated model will often run slower than real time.

For the TTR model of figure 1, figure 2 shows an example of such situation. The model's highest computational domain is "Thermal", representing the finite element representation of the engine in the model. Following are the various cooling circuit such as refrigerant, battery coolant, underhood and engine coolant. These circuits where modelled as a detailed 1D flow network representing the CAD geometry very closely.

Cluster #	Circuit #	Type	Name	CPU %	CPU time
					min
-	-	-	Thermal	84.43	183.69
3	5	Flow	Refrigerant	4.90	10.65
4	6	Flow	BatteryCoolant1	3.68	8.01
"	7	Flow	Flow 7 (Column 5)	"	
9	3	ODE/Mech	Battery-module%93	1.22	2.65
6	10	Flow	Underhood	1.09	2.38
2	2	ODE/Mech	ODE 2 (Column 1)	1.05	2.29
7	11	Flow	Air	0.91	1.97
1	1	ODE/Mech	ODE 1 (Column 1)	0.75	1.62
2	3	Flow	Coolant_engine	0.45	0.99

Figure 2: CPU breakdown by cluster of the TTR model

The detailed TTR model has a real time factor of 7.3: meaning that its solution time is7.3 times slower than real time, requiring more than 3.5 hours to run a WLTC driving cycle. In order to make such model accessible for HiL activities, the highest potential of runtime gain lies in the reduction of the FE based thermal representation of the engine and the number of flow volumes in the different coolant systems.

3.2 3D-FE to 1D Lumped Mass

GT-SUITE is known for its successful 1D-3D synergic simulation approach as shown in Vijay Studies for Battery [8]and E-motor design analysis [9]. The fluid is solved one-dimensionally through a 1D Navier-Stokes equations. While the heat conduction within the solids is solved on a 3D finite element mesh. This approach presents several advantages for detailed component modelling, for example faster design iterations to achieve optimized component design, control strategies and faster transient analyses for design validation. However, this solution when integrated in a complete model, can lead to high computational time.

For lower simulation time, it is desired to further simplify the model by replacing the detailed finite element structures with lumped masses. The lumped mass model characterized with correct mass, heat transfer and material thermal properties account for accurate component thermal inertia as desired for the system analyses. The thermal finite element template in GT-SUITE offers the possibility to maintain two different levels of detail (Figure 3):

- 3D finite element
- 1D lumped mass

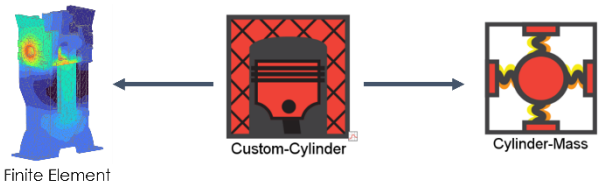


Figure 3: Different options for a detailed component

The left part of Figure 3 presents an overview of the 3D FE cylinder structure. It is representative of the actual engine geometry, and it gives an accurate solution of the spatial heat fluxes using detailed structure geometry along with accurate boundary selection for coolant, oil, gas, and ambient interfaces.

It is always desired to calibrate the 1D models so that they can reproduce the same results as their 3D counter parts. For this, when switching from 3D-FE to 1D lumped mass, effective length, and cross-section for the 1D conduction paths are calculated automatically from the existing 3D FE mesh. Those can be scaled at user discretion to fine tune the derived reduced order 1D model with the results shown in Figure 4.

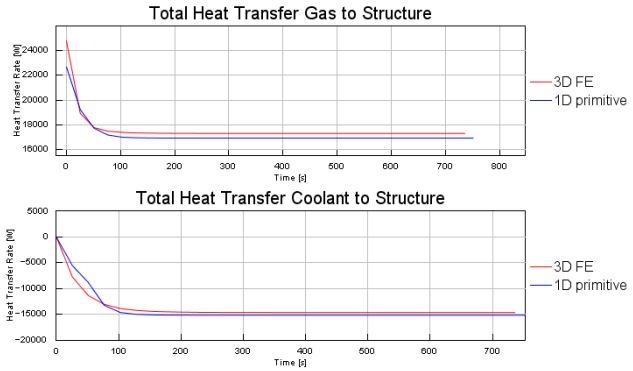


Figure 4: Results of a calibrated 1D lumped mass vs 3D FE thermal cylinder

3.3 Reduction of flow system complexity

With the electrification of the powertrain, the complexity of the hydraulic circuits was increased. Alongside multiway valves, the cooling systems include corrugated pipes, longer pipes with multiple bends and different cross-sections. Hence, a detailed representation of the hydraulic circuits is necessary to accurately account for its pressure drop. On one hand, to improve model's accuracy, discretization of the hydraulic circuits is necessary. On the other hand, modelling thermal management circuits in GT-SUITE uses an implicit iterative solution, with a fixed timestep. Therefore, the simulation time is just a function of the number of sub-volumes in the system. Coarse discretization will normally result in faster simulation time, but sometimes this is at the expense of accuracy. Finer discretization may result in better accuracy and resolution, but with longer computational times.

To reduce the number of flow volumes in the model, the GT-SUITE "Combine Flow Volume Wizard" is used. The wizard merges a flow branch into only two flow volumes and auto-calibrates the simplified flow branch. The volume of the total branch is equally divided between the two flow volumes which are separated by a pressure loss connection that will account for the pressure drop of the detailed flow branch.

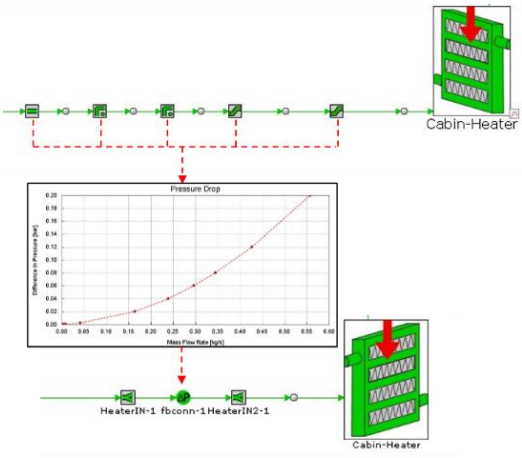


Figure 5: Combine flow volumes

The pressure drop is calibrated using a virtual flow bench where the operating conditions are inspired from the operating conditions of the detailed flow branch. After defining the maximum operating pressure drop expected in the system, the flow bench will simulate different flow rates in the system to derive a pressure loss correlation representative of the system. Figure 6 shows the accuracy of the derived cooling circuits of the presented model where the flow volumes were dropped by around 70% from 263 to 84.

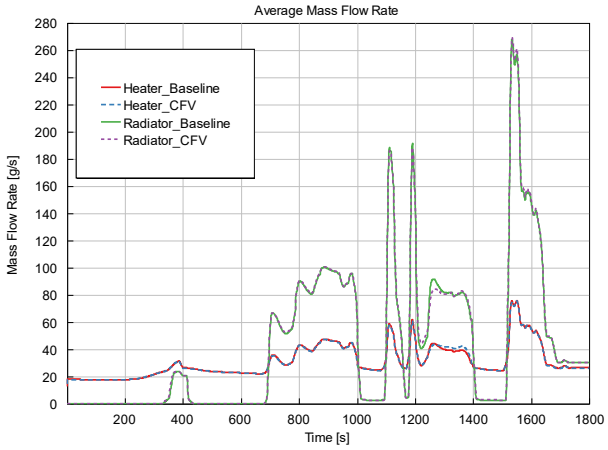


Figure 6: Flow rate accuracy after combining flow volumes

4. Results

4.1 Runtime improvement

The detailed physical model ran with a real time factor of 7.3. By using the different GT-SUITE tools, namely switching from a 3D-FE thermal to a 1D lumped mass representation of the engine and reducing the flow systems geometric complexity, a fast-running model was derived from the previous detailed TTR case

study model. The derived model has a real time factor of 0.7. It runs 30% faster than real time, completing a WLTC cycle in 21 min, while still including the governing physics.

The fast-running model shows a high result accuracy when compared to the detailed model, as demonstrated using the coolant, the battery and the cabin temperature shown in Figures 7, 8 and 9 respectively.

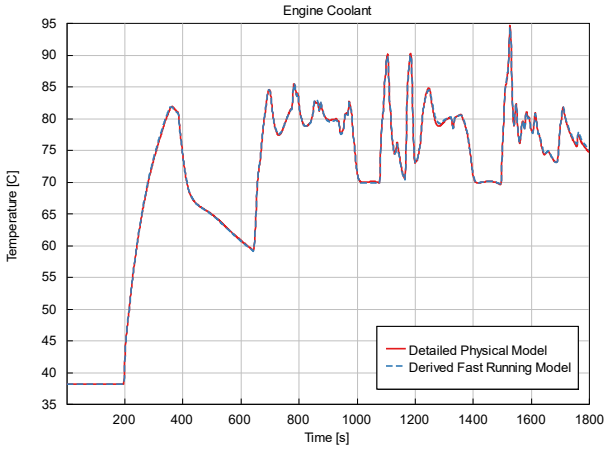


Figure 7: Engine coolant temperature of the detailed physical model vs the derived fast running model

4.2 Predictability of the fast-running model

The process used to derive the fast-running model maintained the governing physics of the system. Compared to other methods relying on static maps or mathematical system characterization, the fast-running model maintains most of the predictability of the detailed physics-based model. For many late design changes during the project, such as scaling a heat exchanger or updating pump, fan or valve information, the derived fast-running model will be able to predict the new system characteristics as a result of the design change

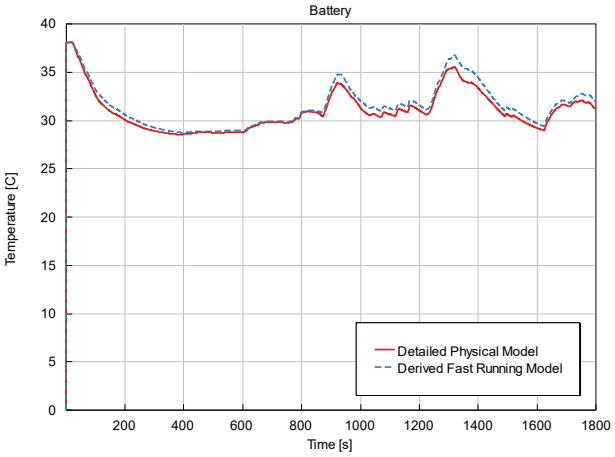


Figure 8: Battery temperature of the detailed physical model vs the derived fast running model

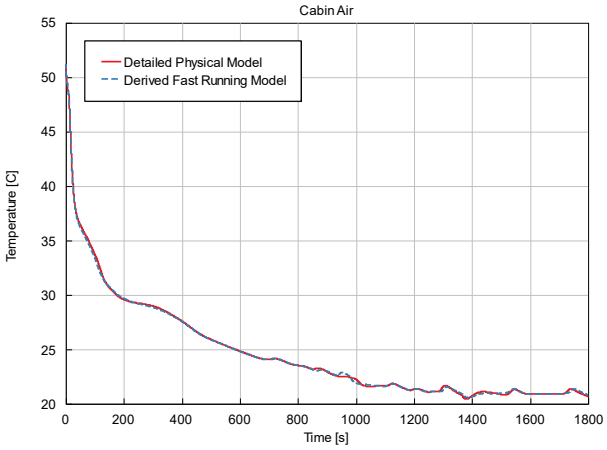


Figure 9: Cabin air temperature of the detailed physical model vs the derived fast running model

To assess the predictability of the fast-running model, the high temperature radiator is scaled down in the detailed and in the fast-running TTR model. This scaled down heat exchanger will affect not only the heat transfer rate to the coolant, but also the air distribution in the underhood model, the power consumption of the pump and many other important system parameters.

The heat transfer of the HT scaled radiator, as well as the engine coolant and the battery SOC presented in Figures 10, 11 and 12 respectively prove that the fast-running model has the same predictivity as the detailed model thanks to the physics-oriented model optimization. The changes resulting from the scale down heat exchanger are comparable for flow distribution, heat transfer rate, coolant temperature, and SOC of the battery in both models.

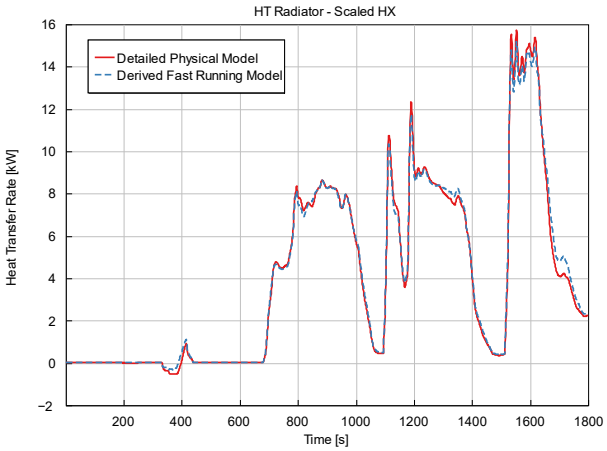


Figure 10: Heat transfer rate of the scaled down radiator for both detailed and derived models

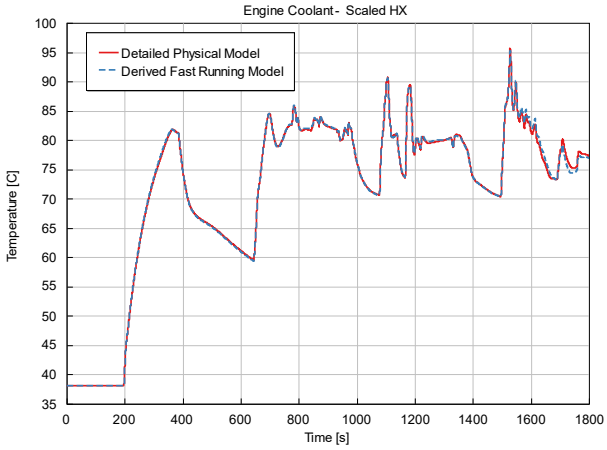


Figure 11: Engine coolant temperature for detailed and derived models with a scaled down radiator

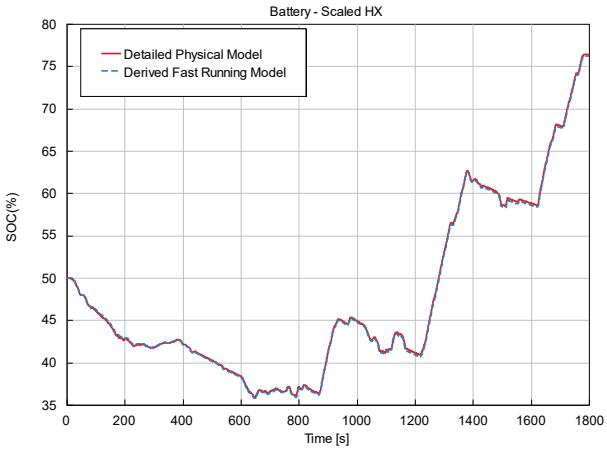


Figure 12: Battery state of charge for detailed and derived models with a scaled down radiator

5. HiL Application

5.1 Co-Simulation on Parallel Cores via FMI

To further reduce the simulation time of the studied case, the model can be divided into parallel sub-models by means of FMI and run on parallel cores.

The model splitting aims for a balanced CPU load of all sub systems. Based on the CPU breakdown by cluster of the derived fast running model, the circuits with the highest computational cost are the 2-phase circuit or the refrigerant loop, followed by the battery coolant circuit. Therefore, the fast-running model is further divided in three subsystems: the refrigerant loop, the battery loop, and the rest of the vehicle.

Figure 13 shows the results of the temperature of the engine, battery, and the cabin of the HiL capable TTR model over a WLTC cycle. At the end, the TTR detailed model runtime was reduced by around 96% leading to a HiL capable model run with a real time factor of 0.3. For a WLTC cycle of 30 min, the high-fidelity model needs more than 3.5 hours of simulation time. The fast-running, holistic thermal management model is capable to achieve the WLTC cycle in 9 to 10 minutes.

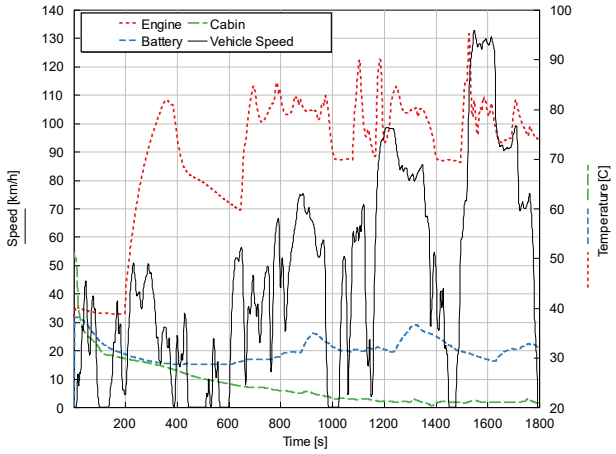


Figure 13: Results of the fast-running model

5.2 Run on HiL system

The last stages of the V cycle demand for fast running model, faster than Real-Time, that will provide accurate data to the sensors of the various software and hardware components. Special Real-Time computers, that are called Hardware in the Loop (Hil) systems, are employed to run the plant models and deliver results to the various components through standard industry ports, protocols and cables. The hardware in the loop system used in this study is equipped with a 4 core Intel CPU and it allows for running up to 4 different plant models, one per core. As shown in the previous paragraph, the fast-running Vehicle Thermal Management model is split into 3 different models due to computation reasons on desktop. The same three models are used on 3 different cores of the HiL system and the WLTC cycle is exercised again. There are two requirements for the HiL test:

1. Real time execution time at all time steps
2. Maintain the same simulation results when simulation on the Real-Time OS as the desktop results

Deploying a GT-SUITE plant model is a three steps process that involves special solver code, Simulink Code Generation (formerly known as the Simulink Real-Time Workshop) and the respective HiL vendor preparatory software. Some HiL vendors are compatible with FMI but this study relies on Simulink as the wrapper. First, the three fast-running models are switched from GT-SUITE to the GT-SUITE-RT to be compatible with the special HiL solver libraries that consume less memory and are compatible with the OS and CPU architecture of the HiL system.

GT-SUITE-RT solver results are verified once again on the desktop before running on the HiL system. They are identical with the GT-SUITE solver (Figure 14).

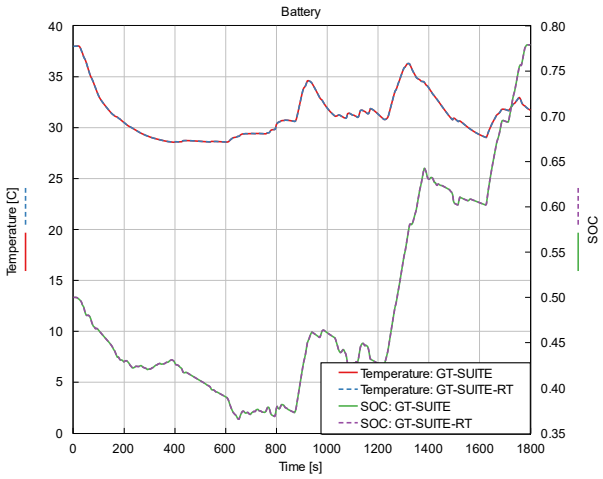


Figure 14: Results of GT-SUITE vs GT-SUITE-RT solver

The second step in the process is to wrap the GT-SUITE-RT models around the Simulink Coder framework. Each Simulink model is used to exchange input and output data between the different software components and a GT-SUITE-RT plant model. GT offers a Simulink library to facilitate the connection between plat models and Simulink ECU logic. The same GT Simulink library is compatible with both desktop simulation and the HiL system used in this study. Each GT-SUITE-RT plant model is wrapped around a Simulink model as a reference model. HiL systems OS detect the Simulink models connections and can automatically transmit data between the different plat models, even though they are simulating on different cores without affecting the execution time or the plant model results. Each model is configured to use the special HiL libraries that are compatible with the HiL system OS and CPU configuration and the HiL code is compiled. The GT-SUITE-RT model files remain separate from the resulting HiL application, and they must be copied via the file transfer protocol on the HiL system. This approach allows for quick iterations between the plant model developers and the Hardware in the loop engineers.

All three models are loaded at the same time on the HiL system and simulate on different cores. Each one of them is executing below the real time loop duration (200ms) at all timesteps and the data exchange between them is handled without any problems (Figure 15). The WLTC cycle is followed in the exact same manner as on the desktop and the plant model results are the same as presented in Figure 16 for the cabin air temperature.

Splitting of the models is verified as a generic approach to run complex multi-domain full vehicle thermal management plant models below Real-Time on Hardware in the loop environment and therefore take advantage of the accurate simulation results of a plant model software as GT-SUITE.

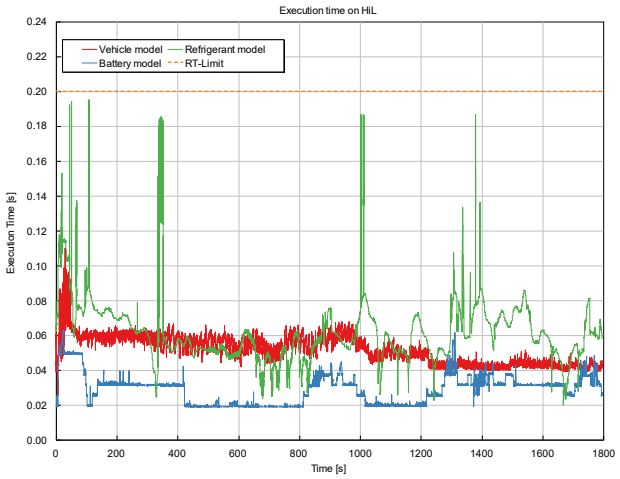


Figure 15: Execution time of the three models on the HiL machine

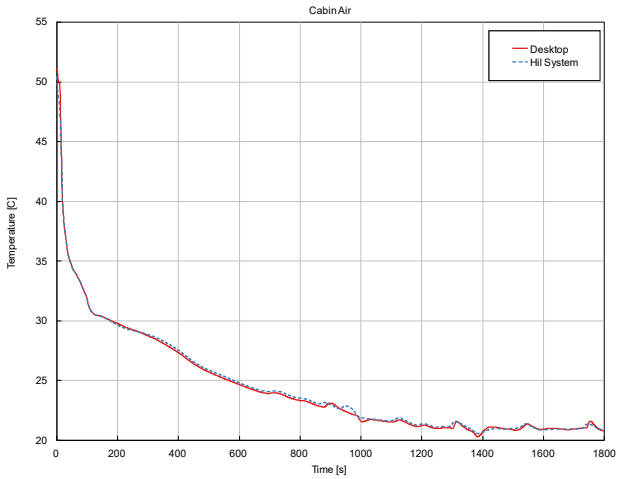


Figure 16: Cabin Temperature on Desktop vs HiL System

6. Conclusion

The case study involves a holistic thermal management system of a TTR hybrid vehicle which ran on a WLTC cycle.

The aim of the paper was to highlight a novel methodology for physics based derived fast running model that maintains the accuracy and the predictability of a detailed 1D HEV thermal management model and is fully deployable on a HiL

machine. The work was carried on GT-SUITE and can be divided in three main parts:

- Assessing of runtime improvement using a report of CPU usage of each circuit in the model.
- Switching from a 3D-FE to a 1D lumped thermal mass representation of a component. The 1D lumped thermal mass characteristic details are calculated from the 3D-FE mesh.
- Reduction of the flow system complexity while keeping its physical characteristics: volume and pressure drop.

It is important to note that because of the governing physics of the systems were maintained during the process, the derived fast running model not only showed high accuracy but also kept the same predictability of the detailed physics model. This enables the possibility to account for late design changes with the derived fast running model.

To further reduce the simulation time and deploy the model on HiL machine, the derived fast running model was divided into 3 sub-models with a balanced CPU load and ran on the HiL system on different cores successfully.

7. References

[1] Bennion, K., and Thornton, M.: "*Integrated vehicle thermal management for advanced vehicle propulsion technologies"*, SAE 2010 World Congress (Detroit, USA), 2010.

[2] Shah, S., Vijay, D., and Lehocky, M.: *"Thermal management of electrified vehicle by means of system simulation",* SAE Technical Paper 2020-28-0033, 2020

[3] Zhao, C., Li Y., Yang, Y., et al: "*Research on electric vehicle range under cold condition"*, Advances in Mechanical Engineering, Vol. 14(3) 1-11, 2022

[4] Umezu, K., and Noyama, H.: "*Air-conditioning system for electric vehicles (i-MiEV)*", SAE 2010 Automotive Refrigerant & System Efficiency Symposium (Scottsdale, USA), 2010.

[5] Yuan R., Fletcher, T., Ahmedov, A., et al,: *"Modelling and co-simulation of hybrid vehicles: a thermal management perspective",* Applied Thermal Engineering, Volume 180, 2020

[6] Guardabascio, V., Pesce, M., Magistrali, S., Marcigliano, F. et al.: "*AModel-based control development using real-time 1D thermal management in co-simulation for high performance BEV digital twin"*, SAE Technical Paper 2022-01-0200, 2022.

[7] Liu, Y., Hong, S., and Ge, T., *"Real-Time Hardware-in-the-Loop Simulation for Drivability Development,"* SAE Technical Paper 2017-01-0005, 2017.

[8] Vijay, D., Framke, N., Stopp, P.: *"Fast running detailed battery thermal management models based on 1D-3D synergetic approach",* 20. Internationales Stuttgarter Symposium. Proceedings. Springer Vieweg, (Wiesbaden, Germany), 2020

[9] Vijay, D., Framke, N.: *"Synergic 1D-3D reduced order modeling techniques for electric motor design analysis",* 22. Internationales Stuttgarter Symposium. Proceedings. Springer Vieweg, (Wiesbaden, Germany), 2022

8. Glossary

BEV: Battery Electric Vehicle

CAD: Computer Aided Design

CPU: Central Processing Unit

E-Motor: Electric Motor

ECU: Electronic Control Unit

EV: Electric Vehicle

FE: Finite Element

FMI: Functional Mock-up Interface

HiL: Hardware in the Loop

HT: High Temperature

OS: Operating System

SiL: Software in the Loop

SOC: State of Charge

TTR: Through the Road

WLTC: Worldwide Harmonized Light Vehicles Test Cycles

xEV: all Electromotive Vehicles such as hybrid, plug-in hybrid, fuel cell …

Influence of Measurement Uncertainty on the Range and Efficiency Evaluation of Electric Cars

A. Stock[1], P. Potereau[2], T. Kevenaar[3]

1: Hottinger Brüel & Kjær GmbH, Im Tiefen See 45, 64293 Darmstadt, Germany
2: Hottinger Bruel & Kjær France SAS, 46 rue du Champoreux, 91540 Mennecy, France
3: Hottinger Bruel & Kjaer Benelux B.V., Schutweg 15a, 5145NP Waalwijk, The Netherlands

Abstract: The maximization of efficiency is one of the central design criteria during the development, and the operation of electric drive systems. In order to calculate the efficiency of an electric vehicle or to predict its remaining range, relevant physical quantities of the powertrain, such as voltages, currents, speed and torque, must be measured. Due to the manufacturing tolerances of sensors and measuring devices as well as the influence of environmental conditions on the measurement process, every real measurement is inevitably subject to measurement errors and a resulting uncertainty in the measurement results. This measurement uncertainty of the measurands is propagated to the quantities calculated from them, such as the power or energy and the efficiency as well as the range. A reduction of the measurement uncertainty in measured quantities allows a higher range specification, which illustrates the high relevance of calculating and minimizing measurement uncertainty for optimizing the performance of an electric vehicle.

Keywords: measurement uncertainty, electromotive, efficiency, inverter, electric drive

1. Introduction

Loss minimization or efficiency maximization is one of the central criteria in both, the development, and the operation of electric drive systems. Therefore, the reliable and precise measurement of the relevant system quantities (e.g., electrical, and mechanical quantities) is an essential and challenging task in the field of metrology. Due to environmental conditions influencing the measurement process as well as manufacturing tolerances of any sensor or measurement equipment, every real measurement is associated with a certain measurement uncertainty (MU). Knowledge of this MU is important for assessing the quality of the measurement results. In this context, the propagation of the MU on parameters calculated from the measured quantities is also of great relevance. This can be clearly highlighted by the following application example. The MU of the measured voltages, currents, torque, and speed of an electric vehicle are subject to MU. This MU is propagated to the resulting power quantities, which in turn result in a MU of the efficiency and the range estimation of the measured electric vehicle. A more precise estimate of the measurement uncertainty allows a higher range specification. However, this is just one of many examples that illustrate the great relevance of determining and minimizing the MU. For this, both the use of high-precision measurement equipment and a suitable MU analysis method applicable for inverter-fed drives, are indispensable. The content of this paper will address these topics in detail. A suitable, powerful measurement setup as well as MU analysis for non-sinusoidal signals will be presented.

2. Measurement on the Electric Power Train

2.1 General system topology

Figure 1 shows the basic topology of an electric powertrain as it may be installed in an electric vehicle. The electric machine is fed by a power inverter transferring energy from the battery to the machine. During recuperation of the vehicle, mechanical energy may be transferred in electrical energy and fed back to the battery.

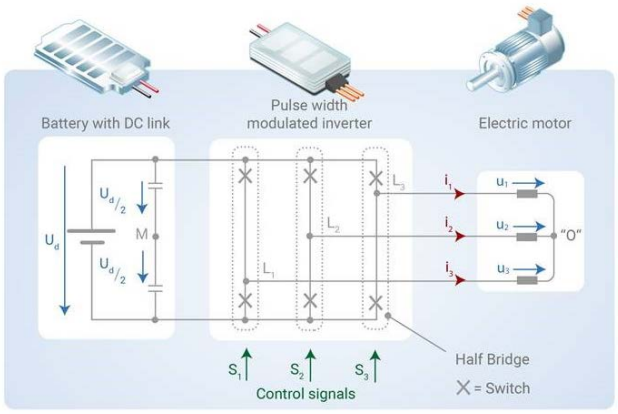


Figure 1: Basic topology of an electric power train

During both motor and generator operation, the aim should be to achieve optimized energy transfer for the entire operating range. In addition to the efficiency of the individual components of the powertrain, the overall efficiency is very important. For this reason, it is essential to measure all relevant physical quantities of the powertrain in a time synchronous manner. This includes the output voltages and currents of the

battery and the power inverter as well as the mechanical torque and speed of the electrical machine.

2.2 Electrical power

As it is well-known from scientific literature [1-3], the instantaneous power $p_{\mathrm{el}}(t)$ of an electrical n-phase system is defined by (1), including the n phase voltages $u_{\nu r}(t)$ and phase currents $i_{\upsilon}(t)$, with $\nu \epsilon \{1,2,\dots,n\}$.

$$p_{\mathrm{el}}(t) = \sum_{\upsilon=1}^{n} u_{\upsilon r}(t) \cdot i_{\upsilon}(t) \tag{1}$$

In general, the voltages should be measured against a common reference potential *r*. If the voltages are not measured against a uniform reference potential *r*, which is for example the case in phase-to-phase measurements with different reference phases, further conversions will have to be done, see [2,3]. Assuming periodic voltages $u_{\nu r}(t+T) = u_{\nu r}(t)$ and currents $i_{\upsilon}(t+T) = i_{\upsilon}(t)$, the active power is defined as the average of the instantaneous power in (1) over the fundamental period T:

$$P_{\mathrm{el}} = \frac{1}{T} \cdot \int_{t-T}^{t} p_{\mathrm{el}}(\tau)\,\mathrm{d}\tau \tag{2}$$

2.3 Mechanical power

From the fundamentals of drive technology, e.g. [4], it is well-known, that the instantaneous mechanical power $p_{\mathrm{mech}}(t)$ of a rotating machine results from the product of the torque $m_{\mathrm{mech}}(t)$ and the angular velocity $\omega_{\mathrm{mech}}(t)$ of the drive shaft, where the latter can be represented by the time-derivative of the mechanical rotor position angle φ_{mech}.

$$\begin{aligned} p_{\mathrm{mech}}(t) &= m_{\mathrm{mech}}(t) \cdot \omega_{\mathrm{mech}}(t) \\ &= m_{\mathrm{mech}}(t) \cdot \frac{d\varphi_{\mathrm{mech}}(t)}{dt} \end{aligned} \tag{3}$$

During steady state, with constant mechanical speed $n_{\mathrm{mech}} = \frac{\omega_{\mathrm{mech}}}{2\pi}$ and constant torque $M_{\mathrm{mech}} = m_{\mathrm{mech}}$, the steady state mechanical power results in:

$$\begin{aligned} P_{\mathrm{mech}} &= \frac{1}{T} \cdot \int_{t-T}^{t} p_{\mathrm{mech}}(\tau)\,\mathrm{d}\tau \\ &= 2\pi \cdot M_{\mathrm{mech}} \cdot n_{\mathrm{mech}} \end{aligned} \tag{4}$$

2.4 Efficiency

As mentioned in the introduction, efficiency maximization is one of the fundamental design criteria. Since the efficiency is defined as the ratio of output power P_{out} to input power P_{in} of the system under consideration [4],

$$\eta = \frac{P_{\mathrm{out}}}{P_{\mathrm{in}}} \tag{5}$$

it is essential to determine the power quantities with the lowest possible MU. For this reason, the following section will describe a procedure to estimate the MU of electric and mechanical active power, as well as efficiency.

2. Measurement Uncertainty and Error Propagation

2.1 Categorization of error influences

In every real measurement, the measured value differs from the actual true value of the measured physical quantity. The reasons for this can be manufacturing tolerances of the measuring devices and sensors, uncontrollable environmental influences, incorrect handling by the user, etc. Although there are numerous reasons for the deviation of the measured value from the true value, the error influences can be divided into two different categories.

On the one hand, these are systematic error influences. These influences are characterized by the fact that they always lead to the same deviation between the measured value and the true value under the condition of an exactly identically repeated measuring process with equal environmental conditions. They are therefore reproducible and can be detected and compensated for, at least in the theoretical ideal case. Examples of systematic errors are, a measuring scale that is always read incorrectly in the same way by the operator, a component of the measurement equipment that deviates from its nominal value due to manufacturing tolerances, or a neglected consideration of the influence of temperature on a measurement process.

In addition, there are random error influences. These are characterized by the fact that they vary randomly in sign and amplitude even with repeated measurements using the same measurement method and (approximately) equal and constant ambient conditions. They are therefore usually difficult to reproduce or compensate for. Examples include quantum mechanical processes such as thermal

noise, but also highly complex deterministic processes, which react very sensitively and apparently randomly to external influences and fluctuations such as environmental conditions. Although in the latter case the causes are deterministic in origin, the measured variables change in a seemingly unpredictable and random manner ("apparent" randomness) and the corresponding measurement error appears random, when in fact it is the lack of system knowledge (incomplete or inaccurate mathematical/physical model) that leads to the apparently random error [5].

Those observations illustrate that error influences cannot always unambiguously be labelled as a random or systematic error. By improving the system knowledge about the measurement process and the environmental conditions, apparently random errors can be transformed into systematic errors and in this way also reduced or compensated [5].

The error influences described so far are clarified based on the example diagram in Figure 2.

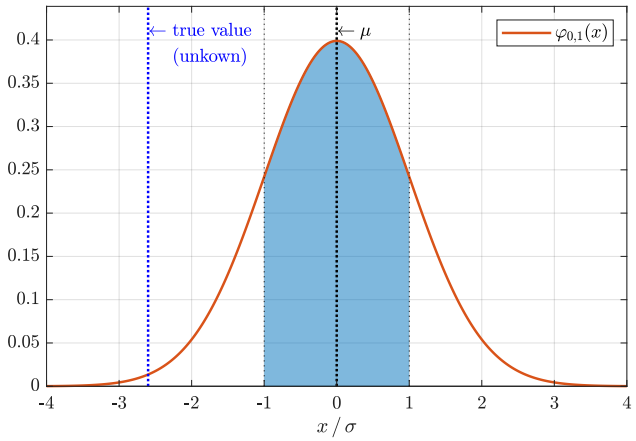


Figure 2: Basic topology of an electric power train

Generally, the true value is unknown. If a measurement were exclusively subject to systematic errors, repeated measurements under constant environmental and measurement conditions would always show the same constant deviation between the measured value and the unknown true value. For example, the measured value could be equal to μ and thus deviate from the unknown true value, see Figure 2.

In addition, however, random errors with a certain typical measurement uncertainty $u(x) = \sigma$ and an associated probability density function

$$\varphi_{\mu,\sigma} = \frac{1}{\sigma\sqrt{2\pi}} \cdot \mathrm{e}^{-\frac{(x-\mu)^2}{2\sigma^2}} \tag{6}$$

can occur, for example with expected value $\mu = 0$ and a standard deviation of $\sigma = 1$ may occur. This results in the standard normal distribution $\varphi_{0,1}(x)$, see [5]. In this case, the repeated measurement results scatter around the value μ. In this context the typical MU of this measurand $u(x) = \sigma$, caused by random errors, indicates that an individual measured value will be in the interval $[-\sigma, \sigma]$ around the expected value μ with a probability $P([-\sigma, \sigma]) = \int_{-\sigma}^{\sigma} \varphi_{0,1}(x)\,\mathrm{d}x \approx 68{,}27\,\%$. This reasoning considers random errors only.

This means that the exact true value can never be determined from real measurement results. On the one hand, an infinite number of measured values and the exact knowledge of their probability distribution would be necessary to determine the expected value μ based on a sample. On the other hand, in practice it is not possible to fully compensate for all systematic errors. The reasons for this are, for example, unknown environmental influences or environmental influences that cannot be described due to their physical complexity or the fact that measurement equipment cannot be produced without manufacturing tolerances and these tolerances cannot be fully compensated by adjustment or mathematical consideration.

Before performing a measurement, the MU can be used to determine the interval around the measured value, that is already compensated for (known) systematic errors, in which the (unknown) true value will lie with a certain probability.

2.2 Error propagation

The maximum systematic error Δy of the quantity y, which is calculated from n different variables or measurands $x_1, x_2, \cdots, x_n$ with the respective systematic measurement errors $\Delta x_1, \Delta x_2, \cdots, \Delta x_n$, is approximated by the total differential [5]:

$$\Delta y = \sum_{\upsilon=1}^{n} \left| \frac{\partial y}{\partial x_\upsilon} \cdot \Delta x_\upsilon \right| \tag{7}$$

Based on the MUs related to random error influences $u(x_1), u(x_2), \cdots, u(x_n)$, the resulting MU $\mathrm{u}(y)$ may be approximated by the Gaussian MU propagation. In case of uncorrelated variables $x_1, x_2, \cdots, x_n$, it is defined by (8), see [5,6]:

$$\mathrm{u}(y) = \sqrt{\sum_{\upsilon=1}^{n} \left(\frac{\partial y}{\partial x_\upsilon} \cdot \mathrm{u}(x_\upsilon) \right)^2} \tag{8}$$

If the variables $x_1, x_2, \cdots, x_n$ are correlated, the covariances $\mathrm{Cov}(x_v, x_\mu)$ have to be considered by the correlation terms $2\sum_{v=1}^{n-1}\sum_{\mu=v+1}^{n}\frac{\partial y}{\partial x_v}\cdot\frac{\partial y}{\partial x_\mu}\cdot\mathrm{Cov}(x_v, x_\mu)$ in addition to $\sum_{v=1}^{n}\left(\frac{\partial y}{\partial x_v}\cdot \mathrm{u}(x_v)\right)^2$ [5,6].

The GUM [6] in general recommends compensating for systematic errors. However, if this is not possible for reasons given above, the influence of random and systematic measurement deviations can be expressed in an increased measurement uncertainty $\mathrm{U}(y)$ taking additionally into account the systematic error influence [7]:

$$\mathrm{U}(y) = \sqrt{(\mathrm{u}(y))^2 + (\Delta y)^2} \tag{9}$$

3. Error Propagation for Power and Efficiency Measurements

3.1 Electric instantaneous power

The electrical instantaneous power is calculated using the measured voltages and currents. For a simple two-pole system ($n = 2$), this results in an instantaneous power, see [2],

$$p_{\mathrm{el}}(t) = u(t)\cdot i(t) \tag{10}$$

where $u(t) = u_{12}(t)$ is voltage measured between the two poles and $i(t) = i_1(t)$ is the current in the first conductor.

Like all measurands, the voltages and currents are subject to a certain MU, which can be determined using data sheets, calibration protocols and knowledge of the measurement process and ambient/environmental conditions. Regarding the following equations, for reasons of clarity, the time dependence of the physical quantities is not explicitly indicated. Furthermore, it is assumed that voltage and current are uncorrelated.

The systematic error (worst case) of instantaneous power Δp_{el} of a simple two-pole system, see (10), is calculated applying the total differential from (7), based on the systematic error of the measured voltage Δu and the systematic error of the measured current Δi:

$$\begin{aligned}\Delta p_{\mathrm{el}} &= \left|\frac{\partial p_{\mathrm{el}}}{\partial u}\cdot\Delta u\right| + \left|\frac{\partial p_{\mathrm{el}}}{\partial i}\cdot\Delta i\right| \\ &= |i\cdot\Delta u| + |u\cdot\Delta i|\end{aligned} \tag{11}$$

The relative systematic error of the instantaneous power $\Delta p_{\mathrm{el}}/|p_{\mathrm{el}}|$ is therefore defined as:

$$\begin{aligned}\left|\frac{\Delta p_{\mathrm{el}}}{p_{\mathrm{el}}}\right| &= \frac{|i\cdot\Delta u| + |u\cdot\Delta i|}{|u\cdot i|} \\ &= \left|\frac{\Delta u}{u}\right| + \left|\frac{\Delta i}{i}\right|\end{aligned} \tag{12}$$

The relative systematic error of the instantaneous power $\mathrm{u}(p)$ of a simple two-pole system, see (10), is calculated applying the Gaussian error propagation from (8), based on the MU of the measured voltage $\mathrm{u}(u)$ and the MU of the measured current $\mathrm{u}(i)$:

$$\begin{aligned}\mathrm{u}(p_{\mathrm{el}}) &= \sqrt{\left(\frac{\partial p_{\mathrm{el}}}{\partial u}\cdot\mathrm{u}(u)\right)^2 + \left(\frac{\partial p_{\mathrm{el}}}{\partial i}\cdot\mathrm{u}(i)\right)^2} \\ &= \sqrt{\left(u\cdot\mathrm{u}(i)\right)^2 + \left(i\cdot\mathrm{u}(u)\right)^2}\end{aligned} \tag{13}$$

The relative MU of the instantaneous power $\mathrm{w}(p)$ is therefore defined as ratio of the absolute MU and the instantaneous power:

$$\begin{aligned}\mathrm{w}(p) &= \frac{\mathrm{u}(p_{\mathrm{el}})}{p_{\mathrm{el}}} \\ &= \frac{\sqrt{\left(u\cdot\mathrm{u}(i)\right)^2 + \left(i\cdot\mathrm{u}(u)\right)^2}}{u\cdot i} \\ &= \sqrt{\left(\frac{\mathrm{u}(u)}{u}\right)^2 + \left(\frac{\mathrm{u}(i)}{i}\right)^2} \\ &= \sqrt{\left(\mathrm{w}(u)\right)^2 + \left(\mathrm{w}(i)\right)^2}\end{aligned} \tag{14}$$

3.2 Electric active power

Assuming ideal DC conditions by means of constant voltage $u(t) = U$ and constant current $i(t) = I$ the active power in (2) is equal to the instantaneous

power in (1): $P_{\mathrm{el}} = p_{\mathrm{el}}(t) = u(t) \cdot i(t) = U \cdot I$. Therefore, the error propagation from voltage and current to active power in the DC case is given by evaluating (13) or (14).

For arbitrary voltage and current waveforms, the active power defined in (2) would have to be inserted directly into the error propagation laws (7) or (8). However, since active power is calculated digitally on modern power analyzers, it is given by the associated discrete-time expression of (2). Without loss of generality, the integral is discretized on the interval $[0, T]$. Neglecting amplitude quantization and assuming that the fundamental period is a multiple integer of the sampling period, the discrete definition of the active power of a two-pole system can be represented by (15), including the sample period T_s, the number of samples in the fundamental period $N = T/T_s$ and the sampled values of voltage $u_k = u(kT_s)$ and current $i_k = i(kT_s)$:

$$P_{\mathrm{el}} = \frac{1}{T} \cdot \int_0^T p_{\mathrm{el}}(\tau)\,\mathrm{d}\tau \approx \frac{1}{NT_s} \cdot \sum_{k=1}^{N} u_k \cdot i_k \cdot T_s = \frac{1}{N} \cdot \sum_{k=1}^{N} u_k \cdot i_k \tag{15}$$

To calculate the maximum systematic error of active power as a function of the systematic errors of voltage and current, (15) is inserted into (7), see [3,8]:

$$\Delta P_{\mathrm{el}} = \frac{1}{N} \cdot \sum_{k=1}^{N} |u_k \cdot \Delta i_k| + \frac{1}{N} \cdot \sum_{k=1}^{N} |i_k \cdot \Delta u_k| \tag{16}$$

To determine the MU of active power related to random error influences, (15) is inserted into (8), see [3,8]

$$\mathrm{u}(P_{\mathrm{el}}) = = \sqrt{\frac{1}{N^2} \cdot \left(\sum_{k=1}^{N} (u_k \cdot u(i_k))^2 + \sum_{k=1}^{N} (i_k \cdot u(u_k))^2 \right)} \tag{17}$$

Considering the ideal DC case for this discrete-time calculation with constant ambient conditions and influencing parameters, i.e. $u_k = u,\ i_k = i,\ u(u_k) = u(u)$ and $u(i_k) = u(i)$ for all k: It becomes clear that systematic errors

$$\Delta P_{\mathrm{el}} = |u \cdot \Delta i| + |i \cdot \Delta u| \tag{18}$$

are independent from the length N of the averaging interval, that is, the systematic error cannot be reduced by taking more samples and measuring over a longer time. The MU related to random errors is reduced by a factor of $\frac{1}{\sqrt{N}}$:

$$\mathrm{u}(P_{\mathrm{el}}) = \sqrt{\frac{1}{N} \cdot [(u \cdot u(i))^2 + (i \cdot u(u))^2]} \tag{19}$$

Due to the possibility of mutual compensation of random errors, the MU of active power decreases as the number of voltage and current samples used for averaging increases.

From the preceding derivations, it follows that (16) and (17) are suitable for estimating the error influences propagated from the measured voltage and current to the electric active power of a two-pole system. Of course, these equations can also be extended accordingly for multiphase systems. For real measurements, the influence of the limited measurement bandwidth and sampling rate of the measuring devices and sensors must be considered in addition to these equations.

3.3 Mechanical power

The error propagation of torque and speed to the mechanical power (see (3)) can be calculated analogously to the electrical active power. This results in a systematic error of mechanical power of

$$\Delta P_{\mathrm{mech}} = = \frac{2\pi}{N} \cdot \sum_{k=1}^{N} |M_k \cdot \Delta n_k| + \frac{2\pi}{N} \cdot \sum_{k=1}^{N} |n_k \cdot \Delta M_k| \tag{20}$$

and a MU estimated by

$$\mathrm{u}(P_{\mathrm{mech}}) = = \sqrt{\frac{4\pi^2}{N^2} \cdot \left(\sum_{k=1}^{N} (M_k \cdot u(n_k))^2 + \sum_{k=1}^{N} (n_k \cdot u(M_k))^2 \right)} \tag{21}$$

3.4 Efficiency

Analogous to the instantaneous power, the error propagation can be performed from the averaged power quantities to the efficiency. As an example, if we consider the efficiency of an electric machine in motor operation, the input power corresponds to the active electric power $P_{\mathrm{in}} = P_{\mathrm{el}}$ and the output power corresponds to the associated averaged mechanical power $P_{\mathrm{out}} = P_{\mathrm{mech}}$. Based on (5), (7) and (8) the error propagation leads to the relative results:

$$\left|\frac{\Delta\eta}{\eta}\right| = \left|\frac{\Delta P_{\mathrm{el}}}{P_{\mathrm{el}}}\right| + \left|\frac{\Delta P_{\mathrm{mech}}}{P_{\mathrm{mech}}}\right| \tag{22}$$

$$\mathrm{w}(\eta) = \sqrt{\left(\mathrm{w}(P_{\mathrm{el}})\right)^2 + \left(\mathrm{w}(P_{\mathrm{mech}})\right)^2} \tag{23}$$

3.5 General recommendations

So far, the error/MU propagation from measured quantities to quantities calculated from these has been considered. The MU or the systematic deviations of the actual measured quantities are contained in the data sheets or calibration sheets of the respective measuring equipment and sensors. A major challenge is to utilize the respective information in a suitable manner. On the one hand, the entire measurement chain must be taken into account, for example, in the case of a current measurement, the current transformer, if necessary, a burden resistor and finally the measurement channel of the power meter. Each individual component of the measurement chain depends on different influencing factors, for example aging effects, temperature influences or influence by the earth's magnetic field, etc. The respective influencing factors can be specified on the measuring range, the currently measured value or as absolute value. Regarding (15), the calculation of an active power value is influenced by N samples of voltage and current respectively. Due to the averaging, random deviations can mutually average out, whereas systematic deviations remain unaffected by the averaging. It is therefore also essential to categorize the data sheet information into systematic and random errors. While noise varies in both magnitude and sign and can therefore compensate from one sample to the next, a systematic error, such as a faulty resistor in the input amplifier of a measurement device, will affect every sample on that channel in the same way. Of course, this must be taken into account in the error propagation in a suitable way. Systematic deviations should be added by absolute values, random deviations should be considered by Pythagorean addition.

4. Conclusion

This paper presents the challenges of measuring power/energy and efficiency in automotive powertrains. It explains why measurements are essential to optimize individual components and the entire powertrain. Since every real measurement is subject to a certain MU, this paper examines its influence in power and efficiency measurements. With regard to eDrive applications, reducing the measurement uncertainty of power/energy enables a more optimistic range specification. In order to estimate the MU as low as possible, it is important to consider different error influences in an appropriate way to be able to use compensation effects. The paper explains the necessary methods for the propagation of measurement deviations and MU of the measurands into calculated quantities. Furthermore, basic information on the evaluation of specifications, data and calibration sheets of the measurement equipment is given.

5. References

[1] IEEE Std 1459-2010: "*IEEE Standard Definitions for the Measurement of Electric Power Quantities Under Sinusoidal, Nonsinusoidal, Balanced, or Unbalanced Conditions*", 2010.

[2] Staudt Volker: "*Fryze - Buchholz - Depenbrock: A time-domain power theory*", International School on Nonsinusoidal Currents and Compensation, Łagów, Poland, 2008.

[3] Stock Alexander: "*Messtechnische Analyse der Energieverluste von stromrichtergespeisten Antriebssystemen im nichtstationären Betrieb*", Dissertation, Shaker Verlag, 2021.

[4] Teigelkötter Johannes: "*Energieeffiziente elektrische Antriebe*", Springer Vieweg, 2013

[5] Kiencke Uwe, Eger Ralf: "*Messtechnik, Systemtheorie für Elektrotechniker*", Springer, 2008

[6] BIPM: "*Evaluation of measurement data — Guide to the expression of uncertainty in measurement (GUM)*", 2008.

[7] Krystek Michael: "*Berechnung der Messunsicherheit, Grundlagen und Anleitung für die praktische Anwendung*", Beuth, 2020

[8] Schneider Simon Michael: "*Test Bench Design for Power Measurement of Inverter-Operated Machines in the Medium Voltage Range*", Dissertation, Universitätsverlag der TU Berlin, 2018.

6. Glossary

MU: Measurement Uncertainty

16 JUNE 2022

ELECTRIC VEHICLE ARCHITECTURE

Electrification, efficiency and fun to drive – Hyundai Motor Group's E-GMP

Dr. Michael Winkler[1], Dr. Jinhwan Jung[2]

1: Hyundai Motor Europe Technical Center GmbH, Hyundai Platz, 65191 Ruesselsheim, Germany
2: Hyundai Motor Group, R&D Division, Namyang-eup, Hwaseong-si, Gyeonggi-do, 18280 Korea

Abstract: Manufacturers are making notable efforts to respond to the rapidly changing customer needs of each market, not only for conventional ICE models but also for battery electric vehicles. The dedicated all new EV platform "E-GMP" was launched in late 2020 as a response to different lifestyles and use-cases of Hyundai, Kia and Genesis customers. In 2021, Hyundai Motor Group successfully launched the Hyundai ioniq 5 as well as the Kia EV6 on this all new EV platform in Europe; the Genesis GV60 is being introduced to the European market in 2022. Further models such as the Kia EV6 GT will be introduced to the European market this year, and additional models such as the ioniq 6 are already announced.

Whereas the conventional all-wheel drive Kia EV6 already offers 239kW (325PS) and a 0..100kph acceleration in 5.2s, the EV6 GT delivers outstanding acceleration performance with 0..100kph in only 3.5s. In order to achieve this outstanding driving performance, the system power is increased to 430kW (585PS).

Energy efficiency and driving performance are traditional KPI's for automotive customers. Due to packaging limitations and the cost impact of increasing the battery size, vehicle efficiency and charging speed will be major factors to enable long distance driving.

In this paper, the key features of the E-GMP platform such as platform modularity, 800V battery and charging system, Silicon Carbide (SiC) inverter and Permanent Magnet Synchronous E-Motor (PMSM) design will be described and their benefit for the customer will be highlighted.

Keywords: Electrification, 800V, platform, modularity, charging, E-motor

1. Introduction

Whereas in the years 2018 and 2019 the market share of EVs in Europe remained below 2%, recently sales took off and reached a market share of 11% in 2021. We can see that disruptive changes, mainly driven by climate change, accelerate the transition towards e-mobility.

In accordance with the "law of diffusion of innovation", we are currently witnessing the transition from "early adopters" to the "early majority" of EV customers. Despite all the inaccuracies in forecasting, EV's will change from a niche product to mainstream by 2030, Fig. 1.

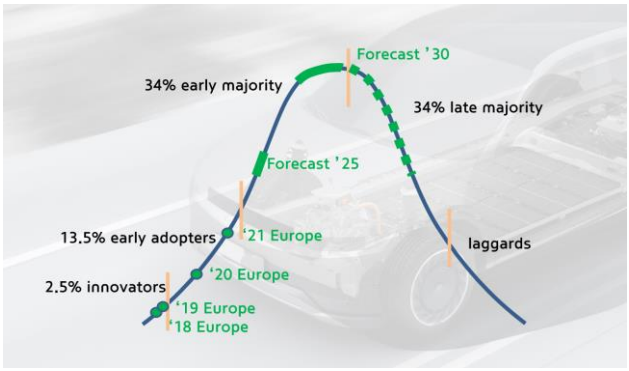


Figure 1: Law of diffusion of innovation /1/ and EV sales and market trends in Europe

As one of the innovators, HMG introduced the first EV to the European market in 2014, Fig. 2. The KIA Soul EV was a derivate of the gasoline and diesel variant. Being a pioneer in this new era, in the same year, Hyundai launched the first mass production fuel cell car, the IX35 fuel cell.



Figure 2: HMG Electrification in Europe

In the meantime, we see a change in EV car usage. While the Soul EV had a driving range of 210km, the range of the Niro, launched in 2019, was dramatically increased up to 485km, allowing EV's to qualify as the main car in a household. Since these EV's shared the

vehicle platform with ICE or hybrid (HEV) and plug-in hybrid (PHEV) variants, this placed several restrictions on the EV's due to the usage of common parts and package limitations.

To overcome these limitations, HMG recently introduced the E-GMP vehicles such as the Hyundai ioniq 5, Kia EV6 and Genesis GV60.

Today we experience an EV boom, and our 800V technology sets the standard in the automotive industry.

2. Electric – Modular Global Platform – E-GMP

Based on our learnings from previous EVs, our development is now fully focused on the benefits we bring to our customers. As a result of this approach, the following features has been successfully applied:

- currently up to 528km range in WLTP (Kia EV6)
- ultra fast charging (18 min from 10 to 80% SOC or up to 100 km range in 5 minutes.)
- acceleration of just 3.5s for 0..100km/h (Kia EV6 GT)
- Vehicle to Load (V2L) with 230V / 3.6kW socket

Breaking the platform down to its core, it can be characterized by 3 main sub-systems, Fig. 3:

1. Bi-directional charging system
2. Integrated drive system
3. Modular 800V battery

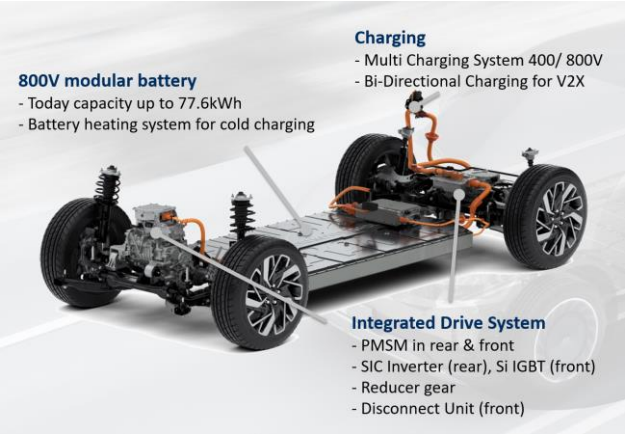


Figure 3: Overview E-GMP sub-systems

This new architecture allows modularity for rapid and flexible adaption to markets, the usage of efficient and powerful power electronic (PE) systems and finally keeps costs competitive.

2.1 Charging System

The highly sophisticated charging system allows for a performance focused on customer convenience. As the 800V battery allows high power charging in under 5 minutes for 100km driving range or in other words up to 80% SOC in just 18 minutes.

E-GMP vehicles can be charged hassle free with 400 & 800V chargers with Hyundai's patented Multi Charging System using the rear E-Motor as inductor and inverter for boost control, Fig. 4 This technology permits the minimization of added components for weight, package and cost benefit.

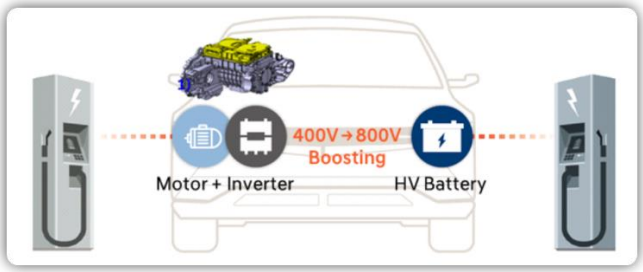


Figure 4: Hyundai's Multi Charging System /2/

Charging performance can be best explained by the charging power over SOC. When considering customer experience, the peak charging power is not the only relevant factor; it is also important to look at the average power over a relevant SOC range. In Fig. 5, a competitor 800V system offers a higher peak power, but nevertheless the average charging power between 10 and 80% SOC is highest for the EV6 as a representative of E-GMP.

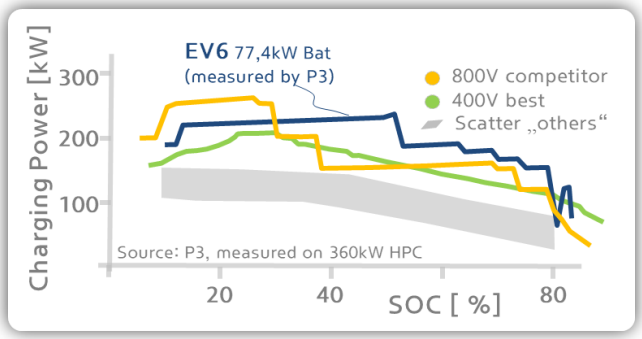


Figure 5: Charging Performance /3/

Vehicle to Load (V2L) functionality offers bi-directional (AC) charging up to 3.6kW. The integrated Charge Control Unit, as a further development of the On Board Charger, is an E-GMP standard. Furthermore, the bi-directional charging is an enabler for upcoming charging models such as Vehicle to Grid (V2G).

A proof of concept for V2G is currently being conducted in Utrecht / Netherlands with 25 ioniq 5 cars being charged during the daytime and being discharged at peak times or during the evening/night.

2.2 Integrated Drive System

The integrated drive system consists of two PMSM for front and rear drivetrain, an SI-C inverter for the rear and SI inverter for the front motor, a transmission / reducer gear and a disconnect unit for the front drivetrain.

2.2.1 E-Motors

Permanent Magnet Synchronous Motors (PMSM) are used to achieve highest efficiency in combination with the disconnect unit of the front drivetrain. The modular concept is based on a 200mm core diameter, which covers a wide operational range of torque and power, Table 1.

Table 1: Modularity for E-Motors front / rear

	Front for AWD 	Rear 
Power	70 / 160 kW	160 ~270 kW
Torque	255 ~ 350 Nm	350 ~ 390 Nm
Stator Core	Φ 200 mm	Φ 200 mm

In order to achieve the best performance with the smallest packaging demands, the drive system offers reduced volume (-35%) and weight (-6%) by a high system integration level and the usage of a high speed motor design. ioniq 5 and EV6 – our latest dedicated EVs – can rev up to 15.000 rpm. This is approximately a 33% increase compared to the current design of e.g. Hyundai Kona. Genesis' GV60 offers more powerful performance with a boost mode that instantly increases power output and allows higher vehicle speed. These models use a high-speed electric motor (up to 19.000 rpm) with a significantly higher top speed than their competitors, whereas most EVs in the market nowadays can feature up to 15.000 to 17.000rpm. The highlight of Hyundai Motor Group's high-speed electric motor technology is embedded in the EV6 GT, which boosts up to the highest RPM among state of the art EVs. The electric motors in the front and rear axles of the EV6 GT, scheduled to be released in the second half of 2022, rev up to 21.000 rpm., Table 2

Table 2: E-Motor Evolution

	ioniq / Kona	E-GMP
Motor Speed	11.200 rpm	15. ~ 21.000 rpm
Winding	Round Coil	Hairpin
Cooling	Water cooling PE System	Oil spray E-Motor only

The cross-section of the coil inside the novel motor has a rectangular structure, which is similar to the shape of a hairpin. As a consequence, the coil can be wound more tightly compared to the current round wire, which reduces winding resistance, increases efficiency, Fig. 6.

This concept of fitting more copper in a given amount of space is quantified by a metric called "copper fill factor". In this particular hairpin design, an improvement of 10% can be achieved compared to the traditional "pull-in winding" stator setup. Actually by increasing the copper fill factor, the e-motor performance is increased. Hence the hairpin winding and oil cooling as described below lead to an efficiency enhancement of ~2%.

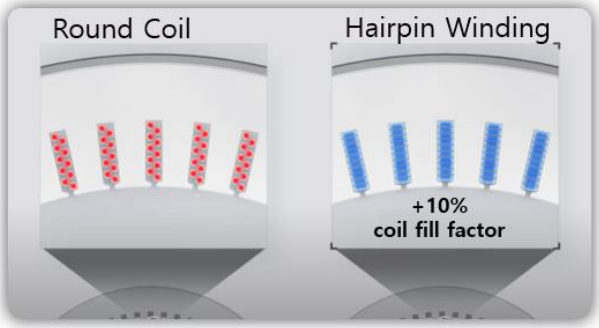


Figure 6: Hairpin Winding

For the inevitable heat generation of the motor due to high speed, the cooling performance of the motor was strengthened by implementing a design that minimizes power loss. The typically used electric motor's water-cooling jacket have a heat transfer to the coolant only on the stator's outer diameter without being able to directly reach the coil itself or deeper inside the motor assembly. As a result, those sub-components remain hottest, since the coolant flows only through the housing.



Figure 7: Oil cooling

Both E-Motors (in the front and in the rear) have the same oil spray cooling concept applied, Fig. 7. The cooling performance is greatly improved because the oil is directly sprayed on all heated up sub-components, stator and rotor. Simultaneously, the oil is lubricating all mechanical components such as bearings and also reducer gears.

2.2.2 The disconnect system

The structure of the E-GMP uses a disconnector technology for the front axle that is not easily found in existing BEVs. This technology makes it possible to physically connect and disconnect the drive motor and drive axle freely, which are located on the front wheel side, Fig. 8.

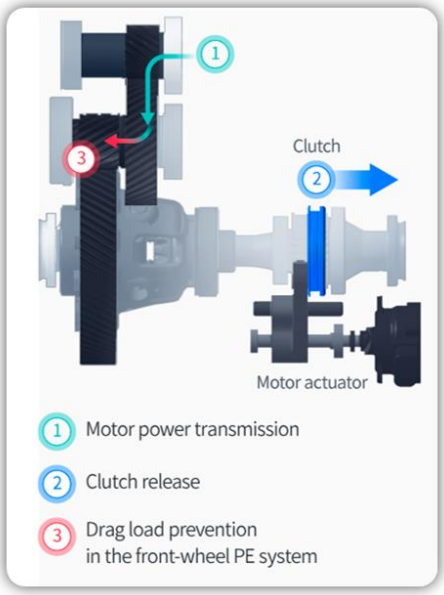


Figure 8: Disconnect System Front Axle /4/

The drive connection to the front wheels can be engaged or disengaged within 0.4 seconds by attaching and detaching the dog clutch on the drive axle operated by a motor-type actuator.

Disconnecting the front drive this way increases the energy efficiency by preventing the drag load of the front wheel PE system and shifting rear motor operating point to areas of higher efficiency. At the same time, it enables dynamic driving by offering all-wheel drive capabilities, which for EVs is also an important factor for customer experience. Overall the driving range can be improved by about 6 to 8%.

2.2.3 The inverters

The material composition change of the power semiconductor is a great example of the advantage provided by the E-GMP's EV-dedicated concept. The major task of the inverter is to convert direct current (DC) to alternating current (AC). In order to do so, most common applied power semiconductor materials are Silicon Carbide (SiC) or Silicon (Si). For highly cost driven systems, Silicon is applied due to its lower overall cost. SiC has significant performance advantages, such its ability to work in high-voltage, high-current, and high-temperature settings with comparable low losses, Fig. 9. Losses in the inverter can mainly be separated in switching and conduction losses.

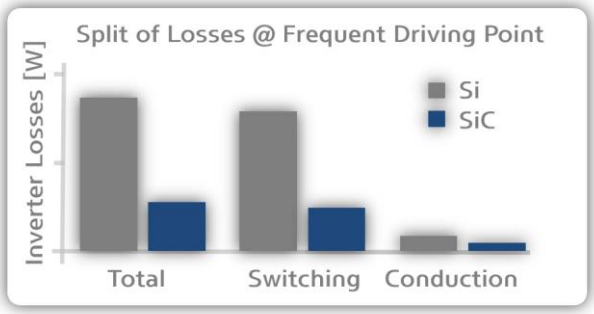


Figure 9: Inverter Losses

Since the E-GMP is designed to operate in the sophisticated high voltage range of 800V, SiC was selected to increase the inverter efficiency. Consequently, the rear motor, which is the main powering motor of the E-GMP, is built as a SiC power module. This step leads to a range benefit of ~5%, or which corresponds to a battery capacity of approximately 1.5 battery modules.

These savings make the vehicle lighter or allows and increase of the all-electric driving range. Yet the switching losses enable additional higher efficiency even in fast driving, as their impact increases with higher frequencies, Fig. 10.

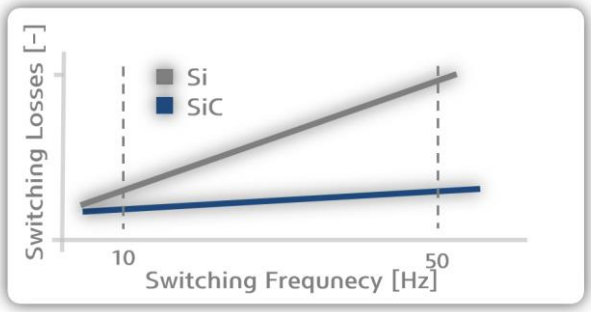


Figure 10: Switching Losses over Frequency

Usually switching losses increase with rising switching frequency, limiting switching frequency of conventional SI inverters to ~10Hz. By changing to SI-C inverters switching frequency can be increased with reduced losses. This supports the application of high speed motors and high power application: a well-suited match for the 21.000 rpm fast rear-axle drive unit with up to 270 kW.

2.3 The modular 800V battery system

The battery pack of the E-GMP consists of standard modules with 12 cells each. Cell capacity is 2.42 kWh, Fig. 11.



Figure 11: Standardized battery module

The pouch-type battery cell used for E-GMP is highly competitive with respect to energy efficiency and manufacturing costs. With a volumetric density of 618 Wh/l on the cell, level the standardized E-GMP battery system improves energy density by 10% compared to existing electric vehicles, allowing for more efficient and lightweight battery system configuration.

The modular approach allows flexible battery pack capacities currently available with 24 modules (50kWh), 30 modules (72,6kWh) or 32 modules (77,4kWh). The modularity additionally allows us to adapt battery capacity based on market and model demands and available space.

3. Summary and Outlook

Based on a long history of working on EV vehicles, Hyundai Motor Group developed the modular electric platform E-GMP with the focus on meeting the customer needs for an EV being able to serve as the main car in the household. Long distance driving is enabled due to the 800V battery system and fast charging capability. The platform is currently used along the three brands Hyundai, Kia and Genesis and the model variety will continue to expand over the next years. These new benchmark setting for EV's performance are also noticed and welcomed by customers as well as critics. The Hyundai ioniq 5 as well as the KIA EV6 are winners of several prizes, such as "The Car of the Year" Award 2022, Fig. 12.



Figure 12: KIA EV6 car of the year 2022

As described above, Hyundai Motor Group's dedicated EVs are not just eco-friendly but also fun to drive. With a 0-100km/h acceleration of 7.4sec in the basic 2WD version up to an amazing 3.5sec in the KIA EV6 GT, the EV platform offers a large scale of options from a range optimized 2 wheel drive up to a high performance variant with a maximum speed of 260kph.

4. References

[1] Simon Sineck: "https://www.ted.com/talks/simon_sinek_how_great_leaders_inspire_action?language=de".

[2] J. Jung, PE Modular Strategy Based on e-GMP / IMA, The 10th China International Automobile Powertrain Summit, China 2022

[3] Company P3, charging index.

[4] https://tech.hyundaimotorgroup.com/article/interview-with-researchersthe-story-of-ev-technology-on-e-gmp

48 Volts Innovative EV kit for Cross Car

Autors : Anthony Puget, Guillem Enjalbert
Keywords : Electrification / Low Voltage / Valeo / Motorsport

Abstract : Valeo has designed a full electrified propulsion kit for Cross Car composed with 2 eDrive, DC/DC, Control Unit , Display, Batteries and all necessary ancillaries.

This kit is meeting 5 key objectives :

1. Performant : Able to offer comparable performances vs ICE powered Cross Car.
2. Smart in Torque Repartition : one machine per rear wheel offering different possibilities of torque management (Torque vectoring)
3. Affordable : To make a 48V propulsion kit adapted for Cross Car championship and actors.
4. Respect the environment : 48V voltage enables recharge @home and affordable infrastructure on track, avoiding ICE generators for electricity charging.
5. Safe : Use of non lethal voltage (< 60V) easing the use and intervention on kit by end customers

1. Context

This project is driven by 2 main axis : the evolution of motorsport towards electrification and the significant growth of low voltage electrification for small electric vehicles

1.1 Motorsport electrification

The FIA and its previous President Jean Todt have reorganized all sectors of Motorsport (single-seater, endurance, rally) in order to make them more readable, attractive and more global to bring out the future talents of the federations that make up the FIA.

One of the biggest challenges for the FIA is to support Motorsport towards new technologies (hybrid, electric and hydrogen) to be in phase with the transformation of the automotive industry. This approach has already been started for several years with the electric Formula, hybrid engines in Formula 1 and in endurance.

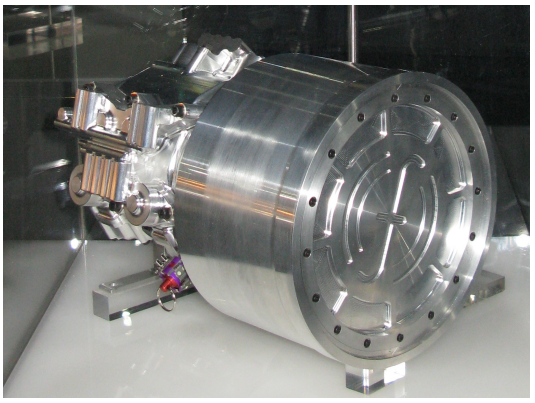


Figure 1 : Kinetic energy recovery system for Formula 1

The Rally sector (rally, rallycross and autocross) is beginning this transition with the introduction of hybrid cars in the world rally championship and electric cars in the world rallycross championship from 2021



Figure 2 : RX2e electric race car

The problem with all these new technologies lies in the fact that they are only applicable to global programs, supported by manufacturers because the technology to be efficient is extremely expensive. Finally, to have an acceptable performance in the eyes of the pilots, the teams and the public, the voltage currents used (300v to more than 600v) make it a technology that can only be used by professional and trained actors.

Finally, how to imagine and justify the World Championship of electric rallycross with thermal support series that will trouble the message of the FIA and the manufacturers committed to this approach.

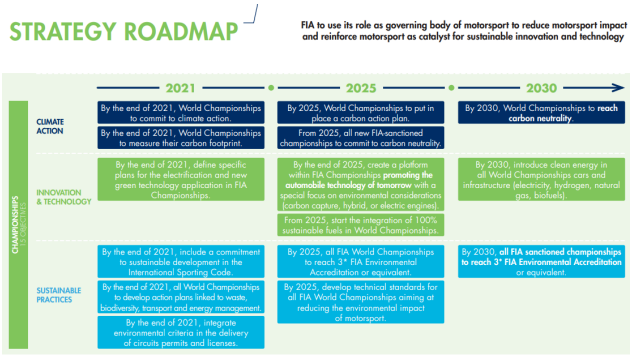


Figure 3 : FIA Championship roadmap

The covid 19 crisis is accelerating the need to switch from thermal vehicles to clean energy vehicles (hybrid, electric, hydrogen). However, this expensive sector and its restricted use in motorsport is not accessible to promotional formulas.

1.2 Valeo is a key player in New Mobility electrification

The automotive world is now moving towards electrifications for 3 major reasons

- Increasingly drastic CO2 regulations and emission standards:
- Decrease in diesel sales following the impact of the VW Diesel Gate
- Gradual ban on thermal vehicles in urban areas

Based on these reasons, Valeo anticipates a significant growth in vehicle electrification and more particularly on New Mobility Market

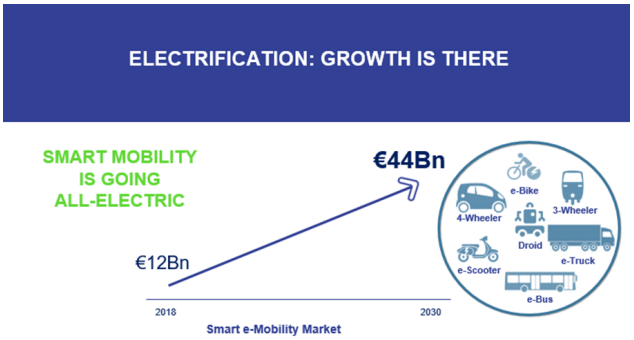


Figure 4 : Evolution of New Mobility Market

On top of that, Valeo is the pioneer and world leader in automotive 48V systems. Valeo has recorded 40% of worldwide order intake to date for these electrical systems. The first mass-produced new vehicles equipped with this hybridization technology, some of which will be sold worldwide, are gradually arriving on the market.

It is estimated that nearly 4 out of 10 new vehicles produced worldwide in 2030 will be equipped with mild hybrid electrical systems (light hybridization, up to 48V). The value potential in a vehicle equipped with a 48V device will double for Valeo. It can even

triple in certain applications. At the end of 2019, order intake for Valeo's 48V and mild hybrid solutions amounted to 7.5 billion

The strong 48 Volts experience combined with the New Mobility playground is the perfect combination for Valeo to enter this market. As a result, In addition to traditional cars, new small 100% electric urban vehicles, mass-produced and powered solely by Valeo 48V machines has entered in circulation in 2020. By the sole use of this device, Valeo is opening up to new markets by becoming an engine manufacturer and powertrain solutions supplier.



Figure 5 : Example of vehicle powered by Valeo 48V powertrain



Figure 6 : e-Access, the 48V eDrive powering Citroen Ami

so many players are innovating, different cargo architectures, different engines or even the positioning of the load.

2. Cross Car 48V electrification, an ambition that makes sense

2.1 Key Actors

The project consists of the study, production and development of an electric cross car demonstrator. It is a complete vehicle project carried out in collaboration between the companies MYGALE (chassis part), VALEO (complete electrification kit) and NOVUM TECH (battery part).

VALEO is a key player and brings the added value on electrification in order to meet the following objectives

2.2 Objectives

• Transversalization objectives: Valeo also aims to reuse the solutions developed on this vehicle to electric and hybrid vehicles. The electric motors, transmission, controller and software will be directly applicable on the following vehicle types:

o 48V hybrid vehicle: Demonstrate fuel savings and CO2 emissions in real driving conditions, with up to 25% fuel savings for city driving and more than 30% for the urban phase of the WLTP cycle (compared to the same non-hybrid vehicle). These vehicles can also handle maneuvers (parking, low speed, etc.) in ZEV (zero emission) mode.

o 48V plug-in hybrid vehicle: with a larger 48V battery to extend the range of the ZEV for urban driving. It will be possible to reach more than 30 kilometers in zero-emission mode in the city, demonstrating the advantage of electric all-wheel drive on safety and driving pleasure thanks to its powerful torque assistance.

o 48V smart electric city car: demonstrate the feasibility of a "double 100" electric

vehicle (range of 100 km and top speed of 100 km/h) thanks to the 48V propulsion system. This concept could reach an affordable price, offering electric mobility for all without worrying about autonomy for urban travel. Indeed, the average daily journey by car is only 20 km per day in France!

o 48V All-Electric Light Truck: 4WD meets last mile delivery and loading with 48V electric propulsion. The 48V eDrives can be placed in the front and/or rear to ensure better maneuverability with the capability of electric 4WD with a payload of 350 kg. It is a simple, easy to maintain and robust system.

• Technical objectives: The electric cross car developed aims to have performance almost identical to that of a thermal vehicle by paying particular attention to the weight of the vehicle in its design. The use of an electric motor will bring increased driving pleasure through greater torque on low-grip tracks. Target is to be at least at the level of Junior Rallycross series. The use for the first time of a non-lethal voltage (less than 60v) also makes this project particularly attractive and innovative because it will allow the marketing phase to distribute it to traditional motorsport players (individuals, teams, organizers, curators)

• Economic objectives: For a championship of 20 vehicles, we are aiming for a kit leading to a complete vehicle not exceeding 120% a thermal cross car (€30,000 excl. VAT for a thermal) with the same performance, increased driving sensations

• Safety objectives : Use a non-lethal voltage allowing this kit and vehicle to be put in the hands of all the traditional players in motorsport. No special HV certification is needed for maintenance.

• Environmental objectives: The use of a non-lethal current voltage, the capacity of the battery and its cost will allow for the first time “home” charges with a change in the circuit so as not to have to recharge in significant local load means that are not very ecological (diesel generators). Valeo also aims to mainstream the solutions developed for this product on 48 Volt 100% electric vehicles.

3. Valeo is putting together a brand new 48 V kit for Cross Car

3.1 A complete kit

As explained, the Valeo objective is to develop and supply a kit ready to be fitted and used in the Cross Car
Valeo is directly in charge to design and procure the the following parts

- 2 eDrive (motor + reducer) with a power of 25 kW each
- DC/DC 48V / 12V
- Powertrain Control Unit
- Harness
- Powertrain cooling system (including battery)
- Interfaces: Drive/Rear Selector, Dashboard
- Accelerometer

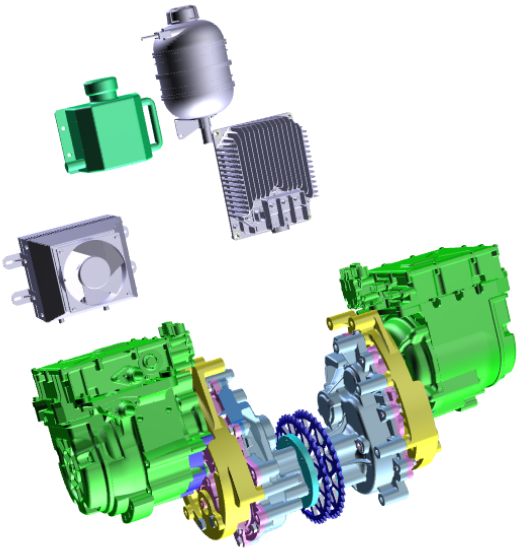


Figure 7 : Kit exploded view

On top of that, Valeo has specified the battery and worked in close collaboration with Novum Tech to develop this item



Figure 8: Example of battery pack 48V

3.2 Specifications

• Motors:
Power = 2x 25kW
Max Torque = 2x 85Nm
Speed range = -14000 to 18000 rpm
48V Brushless technology
Backpack 25kW inverter
Water cooling (motor & inverter)

• Reduction:
2 stages reduction global ratio = 10.1
(1 Gear driven reducer ratio 9.21 + 1 Chain ratio 1.1)
Automotive validated reducer

• Battery:
Voltage = 36 to 49.2V
Discharge max power = 54 kW
Nominal Energy = 10.5 kWh
Weight = 82kg (+PDU)
Discharge use T° = -10 to 55°C
Size = 590 x 248 x 355 mm (+PDU)
Water cooled

• DC/DC Converter:
Buck converter 48V to 14V
Output power = 1500W continuous (1800W peak)
Efficiency = 92 to 94%
Air cooled

• Motors cooling:
Fan power = 375W
Minimum flow rate = 6L/min
Outlet coolant temperature = 65°C
Max dissipated power = 14.8 kW (at 25°C)

• VCU (Vehicle Control Unit):
32bit microcontroller
VALEO developed embedded SW
CAN communication
Analog & digital I/O
H-bridge switch
IP67
Operating voltage = 9 to 18V
Ambient T° = -40 to 85°C

• HMI:
Race designed dashboard
Fully configurable
CAN communication & Analog/digital I/O

4. Design & Technical Choices

4.1 Mechanical integration

• As the battery is the heaviest component of the kit (~85 kg), it has been integrated right at the back of the driver, on the floor, to keep the main weight centered so as not to modify too much the handling of the vehicle.

• To share the platform with the ICE powered version, the FIA homologated chassis could not be modified. Taking into account this constraint, the whole powertrain has been moved close to the battery and a second stage of reduction (in addition to the gear-driven reducer) done by chains has been added to reach the rear axle.

The motors have been fixed to the chassis by the bottom, and maintained in position on the top by a support linking the two

motors together and attached to the chassis.

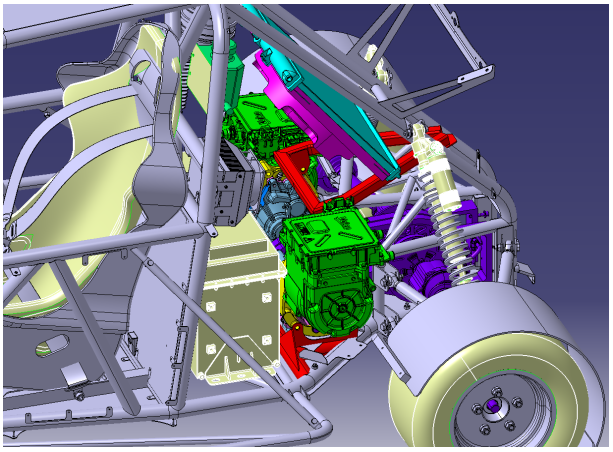


Figure 9: Overview of integration

• Contrary to the ICE version Cross Car which has a rigid rear axle with a unique brake disk in the center, A specific rear axle has been designed to adapt one motor on each wheel: 1 chain per wheel, 1 brake system per wheel.

• The cooling fan & radiator are suspended to the chassis above the powertrain.

• The Fusebox and the VCU have been fixed inside the drive compartment and the other accessories (DC/DC, Cooling parts) have been positioned on the wall behind the driver.

4.2 Powertrain

As explained previously, the kit should re-use existing 48V VALEO products to ensure an affordable and safe solution. This led to a bi-motor powertrain (2x 25kW), as VALEO off-the-shelf motors originally designed for hybrid architectures don't provide more than 25kW per motor at 48V. Each motor is connected to one wheel with its own reducer and a chain.

The performances of this powertrain have been evaluated by simulation and compared to an ICE powered Cross-car.



Figure 10: Example of simulation report

The difference between the Mygale ICE Cross-car and the Electric solution on the Issoudun Cross-car track was estimated at 3s in the worst case (low battery voltage).

4.3 Cooling sizing

To design the cooling system, several assumptions have been made : worst case thermal losses, external air temperature = 25°C for Europe, 45°C for GCC (potential market), flow rate = 6l/min minimum.

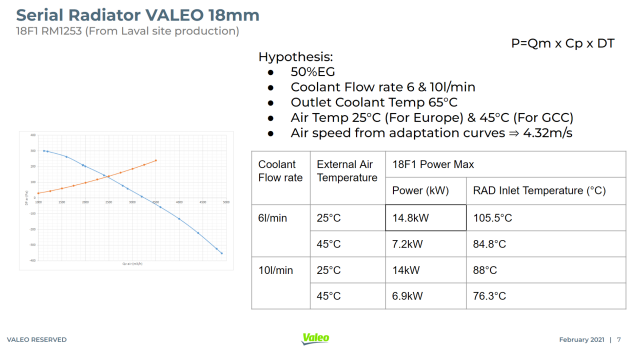


Figure 11: Cooling simulation results

Cooling simulations show that the solution installed on the Cross-car can dissipate 7.2kW in a warm environment, and 14,8kW at 25°C.

These results validate the components selected for our electrical application for the European market AND GCC market or other warm countries.

4.4 DC/DC Converter

12V Electrical maximum consumption = 840W

VALEO DC/DC Off the shelf can provide up to 1800W.

In the same logic as for the other components, using here an off-the-shelf solution has been prefered, even if for this component in particular, the impact on the cost is minimal.

4.5 Torque vectoring

The dual eDrive solution chosen to power the electrical Cross-car allows to apply a different torque on each wheel to correct the vehicle trajectory to improve the handling : the Torque vectoring.

A specific software brick has been developed to calculate the ideal torque to apply to each wheel to maximize the speed in a curve in function of several data : steering wheel angle, vehicle accelerations, wheels slipping, …

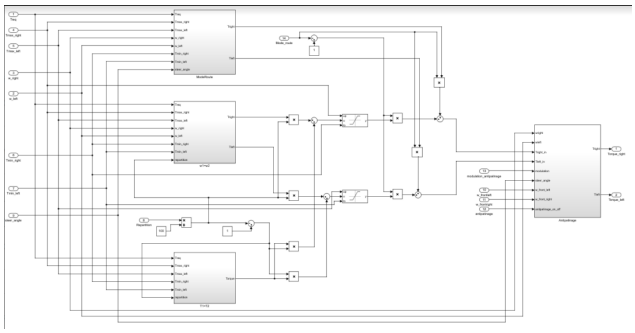


Figure 12: Extract of Torque Vectoring SW

5. Commissioning and Testing

5.1 Issoudun Cross-Car track

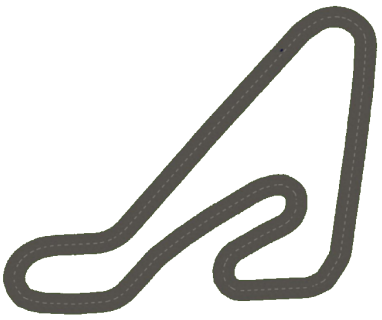


Figure 13: Overview of Issoudun track

The Cross Car first tests on a real track took place on the Issoudun Cross Car track in November 2021.

Few important points have been learnt from this session :

• Torque Vectoring: with a dual eDrives powertrain, when one wheel is not transmitting the power to the track (slipping, not in contact), the power is not transferred to the other wheel as no link exists between both wheels. The global power is therefore halved.
As Cross Car tracks are made to turn skidding, the Torque Vectoring appears to be more of a disadvantage in this discipline.
⇒ A rigid link has been installed between both wheels to ensure full power even when slipping.

• On very muddy tracks, the Cross Car is always functioning on its peak power points. The battery's protections were set to hold these points for only a few seconds. So they had to be pushed close to the battery's limits.

• The general behavior of the system was ok (Vehicle Control Unit software, Energy management, HMI, Cooling).

5.2 RallyCross at Nurburgring track

The FIA set up an exhibition for electric Cross Car solution during the last race of the RallyCross World championship in Germany, on the Nurburgring track.



Figure 14: Nurburgring RallyCross track

Other competitors on the electric Cross Car market, Peters Auto, were also participating in this exhibition, but with a High voltage solution (400V).

• On a faster track (due to RallyCross specificities), we managed to stay close to the high Voltage Cross Car and to our objective, the ICE Junior Cross Car: 2s a lap.

• But more than the current gap with our objective, these tests highlight that we were facing some power limitations due to the battery maximum voltage.

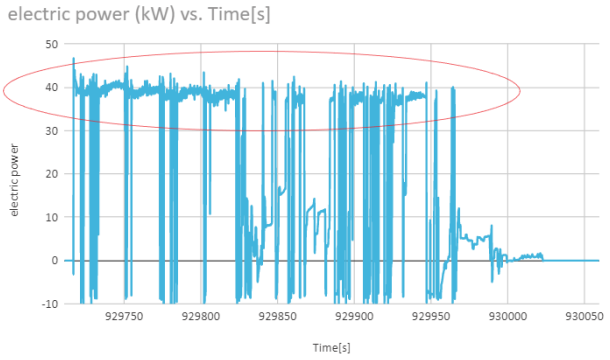


Figure 15: Power measurement in race

Indeed, to maximize the motors output power, the system should run close to the maximum admissible voltage, i.e. 58V.
We could gain more than 10kW in the best case. To do so, a new battery needs to be developed.

• To stay in the potential improvements category, the global weight of the system could be lowered: lighter cooling solution specific for Europe, more appropriate DC/DC, transmission and brake system designed for one rigid axle instead of 1 system for each wheel, chain only transmission, …

• Despite these limitations and points to improve, the overall behavior of the system was good and the electrification kit robustness is a big achievement, especially to prove the FIA the pertinence of the 48V solution.



Figure 16: Ready to Go !

6. Outcomes and Next Steps



Figure 17: Happy Team !

Key outcome is obviously the high satisfaction and proudness for having succeeded to put a 48V Cross Car on wheel to successfully demonstrate the potential of this solution. In a frame of 10 months time.

Positive outcome

- Successful demo during a FIA world rallycross round
- Performance close to the objective : around 2 seconds / per lap vs iCE Junior rallycross and Peters High Voltage solution
- Full potential still to release
- High interest from FIA and promoters
- Developed in less than 10 months !

We noticed during testing some limitations to correct & understand

- Battery voltage to increase to maximize machine power output
- Weight to gain (transmission, cooling?)
- Autonomy to confirm

These improvements are planned for 2022 with the objective to bring an updated kit for FIA Motorsport Games

System Design of Optimized 800V eDrive Systems

J. Bonifacio[1], V. Warth[1], F. Prausse[1], M. Sperber[1], T. Schupp[1], W. Haege[1]

1: ZF Friedrichshafen AG, Graf-von-Soden Platz, 1 88046 Friedrichshafen, Germany

Abstract: Increasing the DC-link voltage up to 800V brings significant advantages in automotive applications. Faster charging times, lower weight and better efficiencies are some aspects associated with these systems. In this work, a holistic system optimization for an 800V automotive powertrain with Si-IGBTs and SiC-MOSFETs is discussed. The consideration of the specific challenges for optimizing an inverter for fast switching as well as its consequences at system level are discussed. The choice of the optimal PWM frequency as well as the impact of fast switching on bearing currents are also demonstrated. The efficiency gap between the Si and SiC solutions is derived experimentally and is shown to be very significant in cycle relevant areas. It is demonstrated that only a thorough consideration of the system trade-offs and physical properties can lead to an optimal solution regarding efficiency, costs and reliability at system level.

Keywords: Automotive System, e-drives, 800V, Silicon-Carbide, System optimization

1. Introduction

Environmental concerns and stringent legislation regarding emissions are having a decisive impact on the adoption of electric vehicles for personal and commercial applications. Despite recent developments in this area, long charging times and limited range are still perceived as drawbacks of this technology by the end-customers. 800V architectures arise in this context as an answer to these issues. Raising the battery voltage up to these levels enables higher charging powers when compared with current 400V solutions with the same current. With a higher charging power, it is possible to significantly reduce the charging time or to increase battery capacity, i.e., also increasing vehicle range [1]. Another advantage associated with 800V architectures are the weight savings across the vehicle especially due to the reduction of the cross section of high voltage cables [2]. Due to the aforementioned reasons, 800V e-drives have gained much attention in the automotive industry, not only for heavy duty, but also in passenger car applications.

Increasing the battery voltage has, however, several impacts on the e-drive system. At this voltage level, Silicon Carbide (SiC) MOSFETs can offer significant efficiency advantages over the Si-based IGBTs. To maximize this efficiency potential, it is necessary to optimize the whole system design for reaching high voltage steepness, which minimizes the switching losses but also increases EMI issues, voltage overshoots on the semiconductor devices and voltage stress on the insulation system of the electric machine. For reaching the desired voltage steepness without endangering the semi-conductors, it is necessary to minimize the DC-link stray inductances. This last aspect brings main design constraints for the power electronics design and must be considered carefully. On the electric machine side, the question regarding the optimal Pulse-Width-Modulation (PWM) frequency, which minimizes the system losses, for the SiC technology and its effects at system level also arises. It becomes clear that a whole system optimization is the necessary solution for designing an 800V system with maximum performance and efficiency at optimal cost.

In this work, the holistic system development and optimization for an automotive 150kW 800V SiC based electric drive is discussed. High voltage steepness up to 40V/ns is reached and the related switching loss reduction of more than 30% is demonstrated. Loss reduction at system level compared to the 400V Si-IGBT system of the same power class reach around 1-2% in cycle relevant operating regions. The impact of the fast switching SiC power electronics over other system components like bearings is also demonstrated and possible countermeasures are discussed.

2. 800V specific requirements and system-level optimization issues in automotive applications

The design of 800V e-drive systems must take relevant electrical and mechanical requirements into account. At this voltage level, higher creepage and clearance distances compared to 400V systems may introduce issues regarding the geometrical placement of the components and the need to develop alternative solutions. These values depend on the application conditions, e.g., altitude, and the voltage levels reached by the system. The definition of the limits for the battery voltage is also paramount for a system optimization. For the system developed in this work, a rated battery voltage of 650V was set for the power of 150kW, which was set to be completely available up to the voltage of 820V. Outside these limits, a power limitation was set and the withstand voltage was defined to be 1150V. All the components and the geometry of the whole system were designed for coping with these requirements. Figure 1 shows

the 800V inverter developed in this study, which was compatible with both Si-IGBTs and SiC-MOSFETs.
For reaching a cost and efficiency optimal solution at system level, considering the limitations of the inverter, machine and mechanics, it is necessary to analyse in detail the trade-offs inherent to the system. For example, increasing the switching speed might be an interesting solution for improving the efficiency, but may increase the probability of bearing damage due to parasitic currents and insulation failure. Higher switching speeds also influence the choice of the loss minimal PWM frequency for driving the system, which has also implications regarding costs and computational burden for online control. In general, it can be stated that optimized components do not necessarily yield an optimized system.

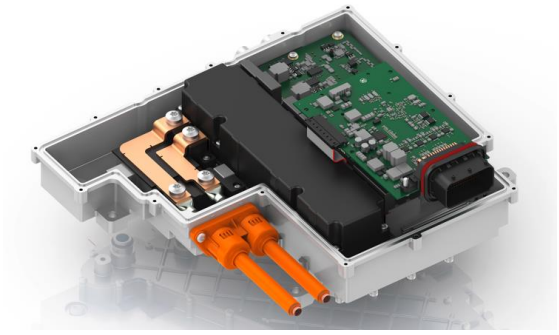


Figure 1: ZF 150kW 800V Si/SiC inverter

3. Power electronics design for fast and efficient switching

The design of an 800V SiC power electronics for fast switching is not a straightforward task. Besides the consideration of all normative requirements regarding for example clearance and creepage distances and geometric limitations imposed by the available space, it is also necessary to consider and optimize technical aspects that are influenced by the fast switching. The thermal and supply conditions affect and are also subject to the influence of the switching speed.

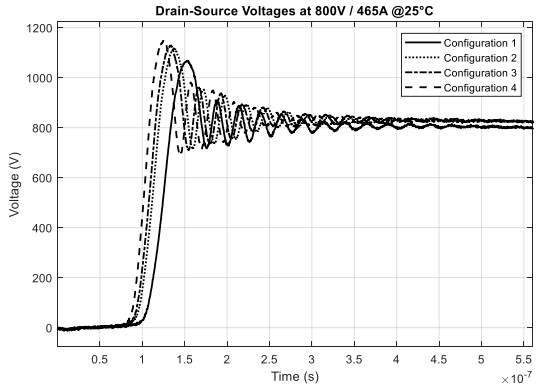


Figure 2: Drain-source turn-off voltages for four different driver configurations at 800V 465A

It is generally desirable to increase voltage steepness because it yields to a reduction of the switching losses. This reasoning is even more advantageous with SiC because it can reach faster switching due to the high drift velocity of this material [3]. The switching speed can be controlled by optimizing the driver configuration for reaching the desired result. Figure 2 shows drain-source voltages for four different driver configurations at 800V 465A. It is possible to see that the reached voltage steepness changes with the driver configurations. Configuration 1 is set to the slowest voltage steepness and Configuration 4 to the fastest one.
Figure 3 shows the switching energies in per-unit (p.u.) at turn-on and turn-off for the four tested driver configurations. The energy loss reduction between Configurations 1 and 4 reach around 33% and 15% for the turn-on and turn-off losses respectively. This result highlights the importance and potential of the optimization of the driver configuration for fast and efficient switching.

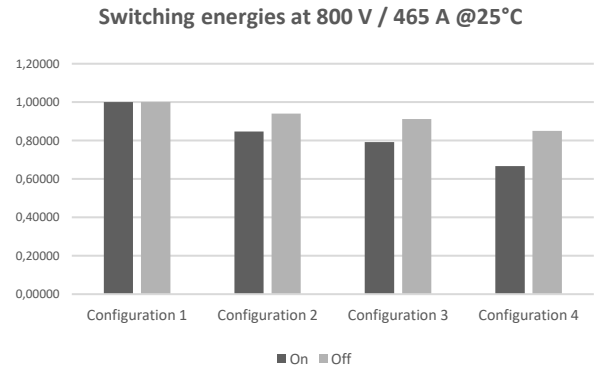


Figure 3: Turn-on and turn-off switching energies (in p.u.) for four different gate-driver configurations

In Figure 2 it is also possible to see that the drain-source voltage overshoot changes with as a function of the switching speed. In fact, higher switching speeds yield higher voltage overshoots over the switches at turn-off, as it is stated in Eq.(1), where $L\sigma_{DC\_link}$ is the stray inductance of the DC-link. Since the maximum voltage rating for the devices typically used in 800V 2-level inverters is 1200V, this limitation must be strictly observed in order to guarantee an operation inside the Safe-Operation-Area. It becomes clear that a minimization of the DC-link's stray inductance is a mandatory step to reach high switching speeds.

$$v = L\sigma_{DC\_link}\frac{di}{dt} \qquad (1)$$

The total DC-link stray inductance is defined by the sum of the stray inductances of the power-module ($L\sigma_{PM}$), of the mechanical interconnection between

DC-link capacitor and power-modules ($L\sigma_{mech}$) and of the DC-link capacitor itself ($L\sigma_{Cap}$), as shown in Eq.(2).

$$L\sigma_{DC\_link} = L\sigma_{PM} + L\sigma_{mech} + L\sigma_{Cap} \quad (2)$$

For the design of the present system, a very low stray inductance of 9.15nH has been reached, as demonstrated by the results in Table 1. It is also important to highlight that the simulation and measurement of the stray inductance match very well. The validation of the simulation tools for this aspect of the power electronics was an enabler for performing the optimizations which lead to the final low value of stray inductance This was accomplished by a thorough optimization of the DC-link capacitor design and its connection with the power module. The rationale of these optimization was to reduce to a minimum the size of the busbars between power-module and DC-link capacitor as well as finding a geometric placement of the HV-DC busbars which ensures low stray inductances while providing good cooling properties.

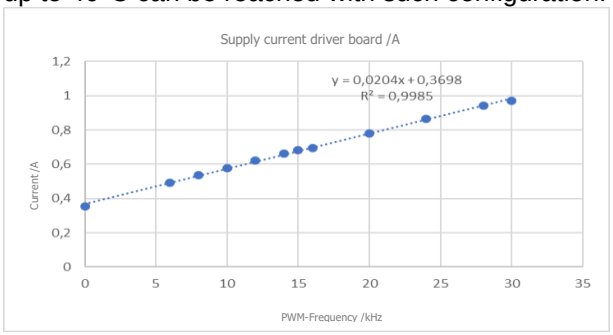
Table 1: Simulation and measurement of the DC-link's stray inductance

	Stray inductance
Simulation [nH]	8.9
Measurement [nH]	9.15
Deviation	2.81%

With these optimizations at driver level and regarding the DC-link's stray inductance, it was possible to reach a voltage steepness of 40V/ns with the optimized setup. Further optimizations are possible and still ongoing since the parameters of the power-module are also currently being optimized to reach even lower values of DC-link stray inductances and higher switching speeds.

Another important requirement for an 800V SiC power electronics, is that it should allow higher PWM frequencies for minimizing system losses and DC-link ripple. The effect of the PWM frequency at system level will be discussed in the following section. For the inverter design, increasing the switching frequency has dramatic consequences for its thermal design and impacts the choice of components that can be used in a particular application. Figure 4 (top) show the supply current needed by the driver board as a function of the switching frequency. The supply current increases, as expected, in order to cope with increased switching energy needed for higher PWM-frequencies. The current increase defined by the targeted frequency will define the design of the power supply circuits as well as the components that will be selected for driving the power-modules. In this specific case, the maximum frequency was chosen to be 30kHz.

In Figure 4 (bottom) it is also possible to see the implementation of the connection between driver board and the power-modules. The losses on the driver board increase with increasing current for driving the switches at higher frequencies. Due to this reason, a Thermal Interface Material (TIM) and a power-module bracket are used for cooling the driverboard. This effect is reached by thermally connecting the driver circuit with the cooling channels below the power-modules. Simulations and measurements show that a temperature reduction of up to 40°C can be reached with such configuration.



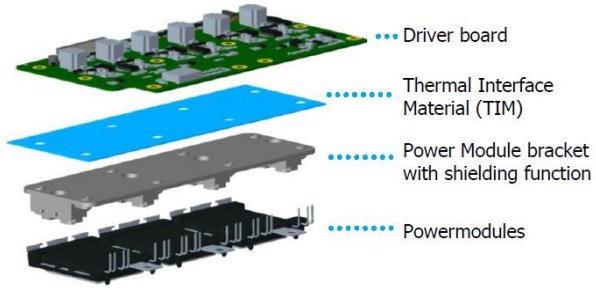


Figure 4. Necessary supply current for the driver board (top) and cooling concept of power-modules and driver board using a Thermal Interface Material (bottom)

Another function achieved by the power-module bracket is shielding the driver board from the electromagnetic noise produced by the power-modules. This function becomes more important for fast-switching converters, since the risk of electromagnetic interference increases significantly.

4. The optimal choice of PWM frequency

As demonstrated in the previous sections, tuning the switching speed of 800V SiC power electronic devices enables a significant loss reduction under operation. Another important parameter, which also has an important impact on the losses at system level is the choice of the PWM-frequency. It is known from literature [4], [5] that the high-frequency electric machine losses reduce asymptotically with increased switching frequency. At the power electronics, the switching losses increase linearly with the PWM frequency [6]. Therefore, there is a unique switching frequency which minimizes the overall losses at

system level. In modern automotive e-drives a full variable switching frequency strategy is typically implemented in order to guarantee an energy optimal state at every operating point.

Figure 5 shows the loss difference between the frequencies of 10kHz and 4kHz for the electric machine and the 800V SiC inverter at two different operating points: 5000rpm with 100Nm and 4250rpm and -275Nm. The variation of the electric machine losses is mainly negative - except for some outliers which were caused by measurement and interpolation errors at border regions, whereas the variation of inverter losses is mainly positive. This confirms the expectation that the e-machine losses decrease while the inverter losses increase with higher PWM frequencies. It is also possible to conclude that the potential for loss reduction at system level through a manipulation of the PWM-frequency depends strongly on the operation point.

Figure 6 shows the loss difference for machine and inverter for 16kHz and 10kHz. The machine losses, although still negative, are lower compared to the variation between 4kHz and 10kHz, which indicates that the potential for high frequency loss reduction of the machine reduces with increasing PWM frequency. For the inverter, the losses are positive as in the previous case.

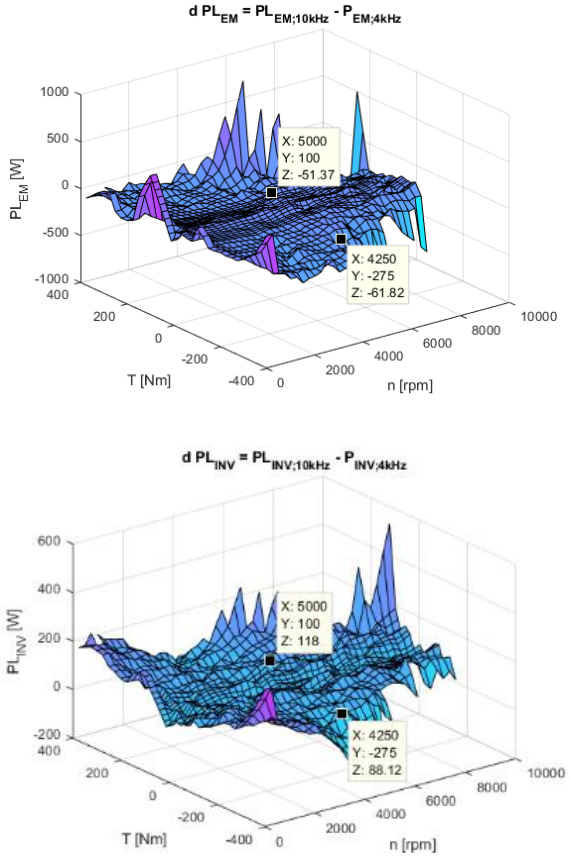


Figure 5. Loss difference between PWM frequencies of 10kHz and 4kHz for e-machine (top) and inverter (bottom)

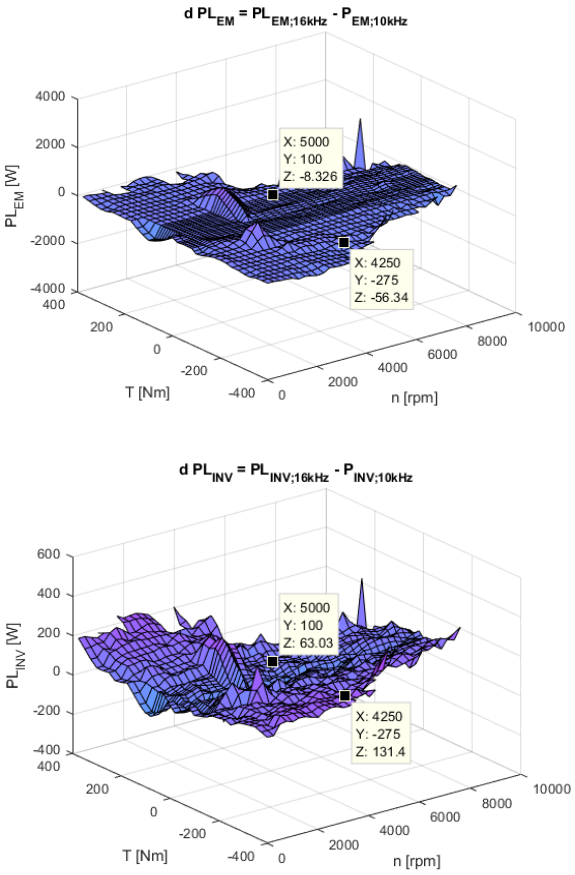


Figure. 6. Loss difference between PWM frequencies of 16kHz and 10kHz for e-machine (top) and inverter (bottom)

Measurements up to 28kHz have been carried out with the SiC system for establishing the optimal switching frequency for each operating point. Figure 7 (top) shows the results of the optimization using only the overall loss at system level as criteria. The optimal PWM frequency lies around 10kHz in the low torque region and around 14kHz at the high torque region. Frequencies higher than 14kHz lead to increased losses at system level because the higher switching losses at the inverter are not fully compensated by a loss reduction at the e-machine side. For the optimization two boundary conditions were also considered: the minimal switching frequency for ensuring the controllability of the electrical machine, which is particularly relevant at higher speeds and the DC-ripple boundary, which might prevent the use of very low switching frequencies in order to keep the DC-ripple in an acceptable range. In Figure 7 (bottom) it is possible to see that for the SiC system the controllability and the DC-ripple conditions were always satisfied with the efficiency optimized frequency. This is the case because the optimal frequencies are relatively high, due to the reduced weight of the switching losses compared to the high frequency losses of the machine.

Performing the same optimization with a Si power electronics yields the results shown in Figure 8. The optimal frequencies are rather low compared to the optimal ones from the SiC system, ranging from 2 to 6kHz. If the boundary conditions regarding the controllability and the DC-ripple are considered, it is possible to see in Figure 8 (bottom) that the controllability condition determines the PWM frequency at higher speeds and the DC-ripple condition determines the frequency for some points at the mid-speed range. This can be explained by the fact that the efficiency optimal frequencies for Si are rather low because the switching losses of the inverter are more significant compared to the e-machine high frequency losses. It is important to mention that other aspects such as NVH (noise, vibration and harshness) will also have an impact on the choice of the optimal PWM frequency.

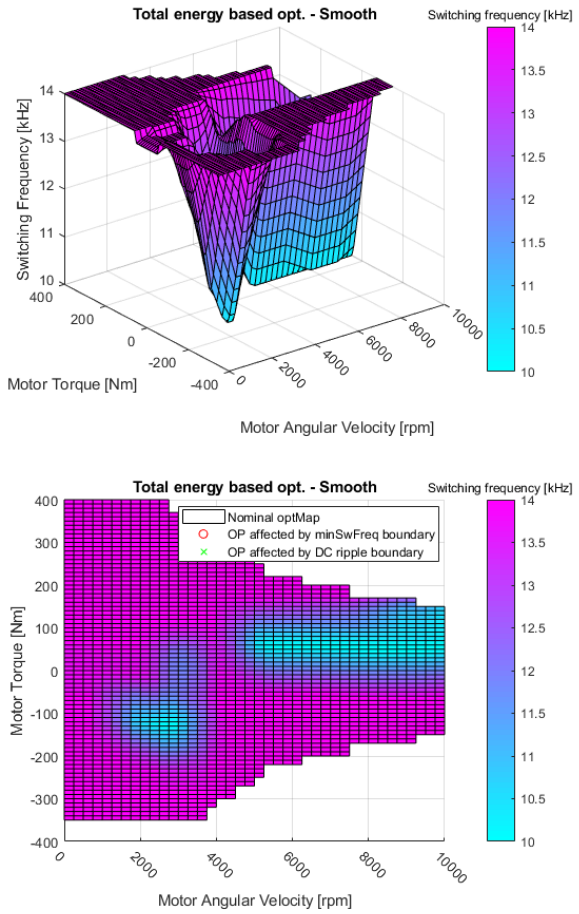


Figure.7. Operation point dependency of the optimal switching frequency (top) and consideration of boundary conditions (bottom) for the 800V SiC system

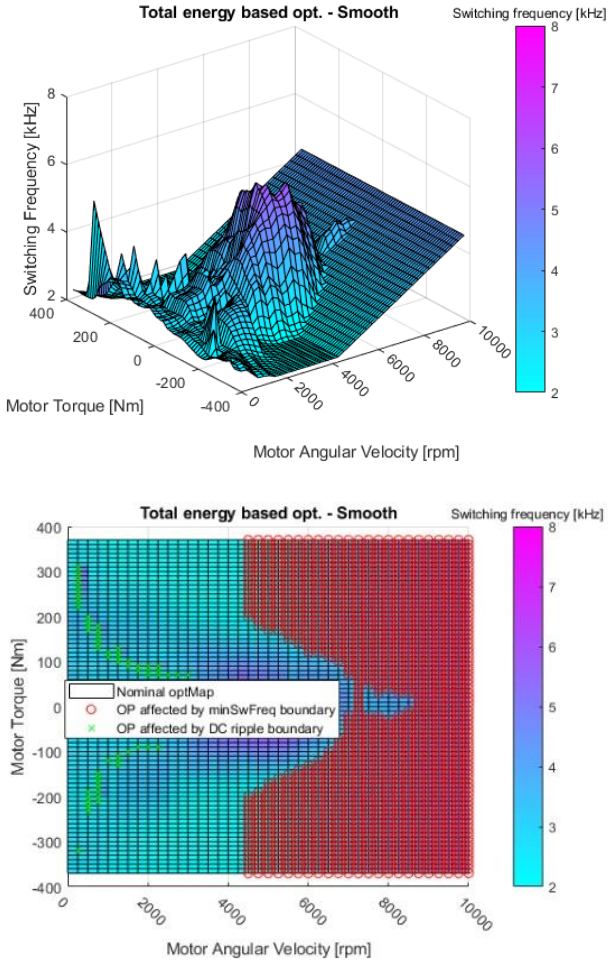


Figure 8. Operation point dependency of the optimal switching frequency (top) and consideration of boundary conditions (bottom) for the 800V Si system

It is possible to conclude from these energy optimizations that the use of SiC enables and requires the application of PWM-frequencies that are higher than the ones typically used for Si-IGBTs. For assessing the loss reduction potential of 800V SiC compared to the 400V Si solution, measurements at rated voltage were carried out for both systems. In Figure 9 the loss difference between both systems is shown. The 400V-Si system was operated with 325V voltage and 8kHz switching frequency whereas the 800V-SiC system was operated at 650V and 10kHz. The electric machine was the same in both cases, with the only difference being the windings connection for allowing the operation at higher voltages. The measured loss difference reaches up to 2-3%, indicating the 800V SiC system is more efficient than the 400V-Si. In cycle relevant areas, the loss advantage that can be achieved lies around 1-2%. This result confirms the expectation that the use of SiC has a significant potential for increasing the efficiency and consequently the range of electric vehicles [7].

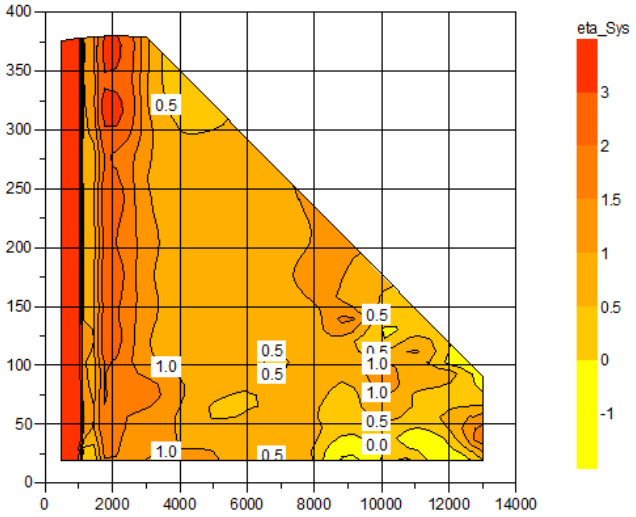


Figure 9 : Loss comparison at system level between Si-IGBTs at 325V 8kHz and SiC-MOSFETs at 650V 10kHz with an automotive PMSM

5. Influence of power electronics parameters on the electric machine and mechanics

An often-neglected aspect of a whole e-drive optimization is the influence of power electronics parameters on other components, especially on the mechanics' side. One of the most significant aspect of these interactions is the effect called bearing currents. These currents typically arise in power-electronics driven e-drive systems because of the switching events. There are in general three types of power-electronics induced bearing currents [8]:

- EDM (electric discharge machining) currents: These currents arise as a pulse when the voltages over the bearings exceed the threshold voltage of its lubrication film. The voltage over the bearing mirrors the common-mode voltage and is proportional to a ratio between electric machine and bearing capacitances (the so-called bearing voltage ratio, which is geometry dependent).
- Circulating bearing currents: The pulsating voltages in the machine terminals cause a ground current at the stator. This current excites a circular magnetic flux, which induces a voltage along the shaft of the e-machine. If this voltage is high enough to break the insulation film, a current flowing from one bearing to the opposite one will appear.
- Rotor ground currents: These currents appear when the machine is grounded by the load and can reach considerable magnitudes.

Bearing currents are a very critical phenomena because they generate premature failure of the bearings, reducing the useful life of the whole e-drive system. In this project, a measuring setup was designed for characterizing the bearing currents. Figure 10 shows the e-drive shaft, which contains three bearings (L1, L2 and L3, from left to right). For measuring the bearing currents, a set of five Rogowski-coils has been used. These coils are enumerated from L1_1 to L3 and placed as shown in Figure 10. A voltage measurement through shaft grounding elements has been placed in L1 and L2 in order to measure all relevant characteristics of the arising bearing currents.

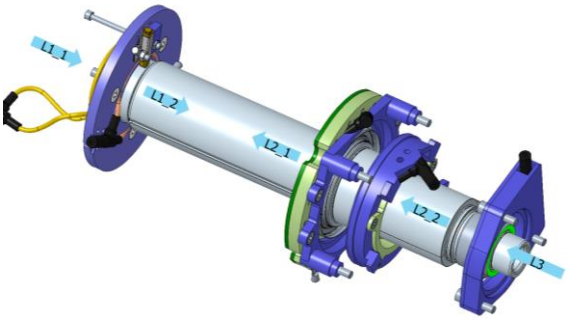


Figure. 10. Setup for bearing currents' characterization

Figure 11 shows the bearing currents' measurement at 3000rpm, 0Nm and 650V with Si-IGBT switching devices. The currents measured by the Rogowski-coils are equal in all measuring points, which indicates that circular currents are present in this e-drive. At each switching event, a current flows into the shaft from the left side of bearing L1 and finally goes back to the housing through bearing L3. The current could also in some cases flow through the gears between L2 and L3 into other bearings in this path. No EDM currents have been detected in this system. It is important to highlight that these measurements have been carried out without any counter-measure for better assessing and characterizing the bearing currents.

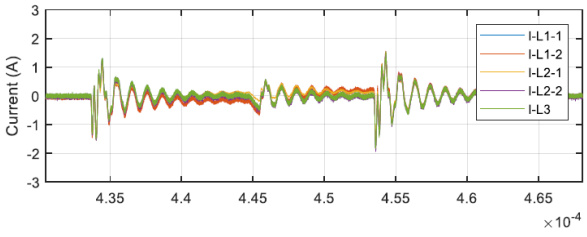


Figure. 11. Circulating currents at 3000rpm, 0Nm and 650V with Si-IGBTs

In Figure 12 a comparison between bearing currents under Si and SiC at 5000rpm, 0Nm and 800V can be analysed. The switching speeds are around 40V/ns for the SiC-MOSFETs and 2V/ns for the Si-IGBT variant. The current under SiC is almost the double of that under Si, which confirms the expectation that circular currents are negatively affected by increasing the switching steepness.

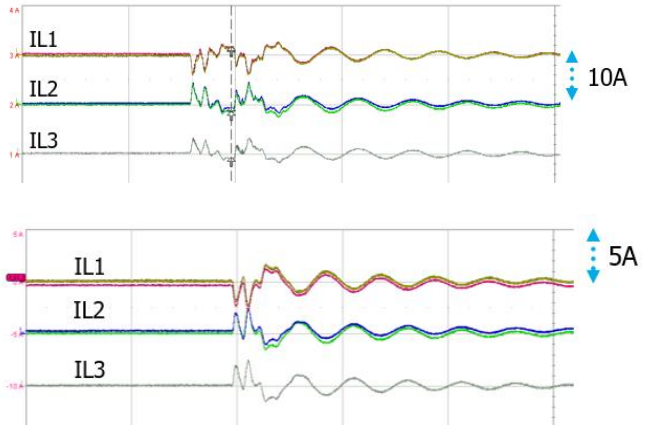


Figure. 12. Measured circulating currents with SiC (top) and Si (bottom) at 800V, 0Nm and 5000rpm

There are several counter-measures for coping with circulating currents that can be applied to an automotive e-drive system. The selection process for the most suitable strategy in a particular case must take several aspects into account, e.g. available installation space, durability requirements, application environment and costs. Figure 13 shows the effectiveness of an AC filter for reducing the circulating currents at 800V, 0Nm and 5000rpm.

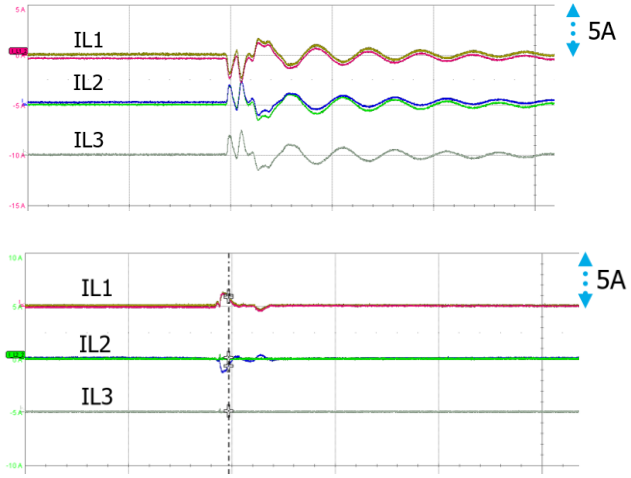


Figure. 13. Measured circulating currents with Si-IGBTs at 800V, 0Nm and 5000rpm without (top) and with (bottom) an AC-filter

6. Conclusions

In this work, a holistic optimization procedure for designing an 800V system with Si-IGBTs and SiC-MOSFETs was discussed. Besides the design constraints for reaching fast switching with SiC, like the optimization of the DC-link stray inductances and the component choices for the driver board, the implications of fast switching regarding the overall system efficiency, the optimal PWM frequency and EMC effects have been discussed. The efficiency advantages of SiC related to Si became very clear from the measurement of the overall system losses, as well as the possibility offered by SiC of using higher PWM-frequencies for minimizing the system losses. The overall efficiency advantage of 800V-SiC compared to 400V-Si lies around 1-2% in cycle relevant operating regions. Moreover, the effects of the fast switching on the properties of bearing currents, as well as the effectiveness of an AC-filter for coping with this issue, have been demonstrated experimentally. These issues indicate that only a holistic and interdisciplinary design approach can yield a functional, cost competitive and efficient automotive e-drive system.

7. References

[1] Aghabali, I.; Baumann, J.; Kollmeyer, P.; Wang, Y.; Bilgin, B.; Emadi, A.; 800-V Electric Vehicle Powertrains: Review and Analysis of Benefits, Challenges and Future Trends; IEEE Transactions on Transportation Electrification, Vol 7, No 3, 2021

[2] Jung, C.; Power Up with 800-V Systems: The Benefits of Upgrading Voltage Power for Battery-Electric Passenger Vehicles, IEEE Electrification Magazine, Vol 1, Issue 5, 2017

[3] Shang F.; Arribas, A.P., Krishnamurthy, M.; A Comprehensive Evaluation of SiC Devices in Traction Applications, IEEE Transportation Electrification Conference and Expo (ITEC), 2014

[4] Rasilo, P.; Martinez, W.; Fujisaki, K.; Kyyrä, J.; Ruderman, A.; Simulink Model for PWM-Supplied Laminated Magnetic Cores Including Hysteresis, Eddy-Current, and Excess Losses, IEEE Transactions on Power Electronics, Vol. 34, Issue 2, Feb/19

[5] Zhang, D.; Liu, T.; Zhao, H., Wu, T.; An Analytical Iron Loss Calculation Model of Inverter-Fed Induction Motors Considering Supply and Slot Harmonics; IEEE Transactions on Industrial Electronics, vol. 66, No 12, 2019

[6] Stempfle, M.; Fischer, M.; Roth-Stielow, J. Loss modelling to optimize the overall drive train efficiency; 17th European Conference on Power Electronics and Application- EPE'15 ECCE-Europe

[7] Hain, S.; Meiler, M.; Denk, M.; Evaluation of 800V Traction Inverter with SiC-MOSFET versus Si-IGBT Power Semiconductor Technology, Proceedings of PCIM Europe, Nuremberg, Germany, 2019

[8] Plazenet, T.; Boileau, T.; Caironi, C.; Nahid-Mobarakeh, B.; A Comprehensive Study on Shaft Voltages and Bearing Currents in Rotating Machines; IEEE Transactions on Industry Applications, Vol 54, No 4, 2018

16 JUNE 2022

ENERGY FOR SUSTAINABLE MOBILITY

e-Fuels and 2nd Gen. Biofuels as possible complementary strategy to e-mobility targeting Europe's 2050 climate goals.

J.Ullrich[1], S.Hoffmann[1], R.Steininger[1], A.Kapp[1], I.S.Ryu[1], Dr.Y.Chi[2]

1: Hyundai Motor Europe Technical Center GmbH, Hyundai Platz, 65428 Rüsselsheim / Germany
2: Hyundai Motor Group, Hyundai Yeonguso-Ro, Gyeonggi-Do / Korea

Abstract: Despite that future mobility might be mainly electric, there will be no instantaneous swap from chemical energy carriers (=fuels) to electrical energy storage systems (=batteries). Because of this, HMG also evaluates low carbon, climate friendly fuels made from green electricity (water, wind or solar power = e-Fuels) or from bio mass (plant oils, cellulose or algae =Bio Fuels) for their market perspectives but also their impacts on powertrain systems. If e-Fuels or Bio Fuels dominate, depends on cost, raw material availability and infrastructural as well as climatic boundaries and legal circumstances. This paper deals with pro's & con's of sustainable fuels and related market perspectives. To anticipate a bit of the papers conclusion: It is very likely that fuels will affect the automotive sector in Europe beyond 2035 and even more in global scale to a not foreseeable time.

Keywords: e-Powertrain, e-Fuels, synthetic fuels, Bio-Fuels, sustainability, CO_2, climate goals, Europe

1. Introduction

About 125 years after the 4-stroke internal combustion engine was patented, this technology combined with chemical energy carriers is still by far the dominant "motor" for mobility. Fundamental advantages of fuels today are the existing distribution infrastructure and the long term bunkering as well as the outstanding energy density especially of liquid fuels, ensuring that energy storage in a vehicle is simple, safe and cost attractive.
The authors do not doubt that e-mobility will grow fast and to a high level but there is also not doubt that the duration of the transition period isn`t easy to predict.

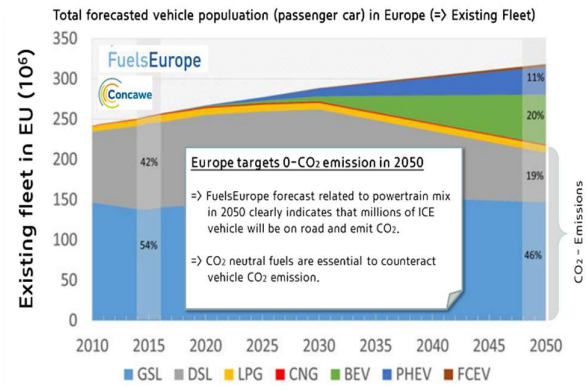


Fig. 1 Possible powertrain mix in Europe [1]

Complementary to this, also the phasing out and final end of internal combustion engines and its fuels is difficult to estimate, particularly for fuels an add-on period of 10 to 20 years have to be considered reflecting on how long vehicles will stay in use within various markets. As a consequence, this paper basically deals with two aspects of fuels:

1) How modern fuels can create benefits on engine performance, efficiency and how fuel composition should be tailored to maximize the advantages for a maximum of powertrain concepts.
2) How future fuels can represent a part of the solution in decarbonizing the existing vehicle population in the market.

In the frame work of this paper and especially in the final conclusion, the authors try to sketch some answers to the above questions, also taking into account market aspects related to country specific requirements, energy costs and political statements.

2. Internal Combustion Engines & Fuels Quality

2.1 After decades and thousands of presentations on combustion engine technology, the reader might forgive the authors, if a detailed explanation of this technology is not repeated here. Moreover, some special engine aspects are chosen with respect to the latest ICE development trends that are linked to fuel quality - the below list does not claim completeness:

- Compression ratio of diesel and gasoline engine are approaching each other to values between 14 to 16:1 basically to compromise thermal efficiency and engine out emissions.
- Injection pressures increase for both engine concepts e.g. 250 ⇒ 750 bar for gasoline and 2.000 ⇒ 2.500 bar for diesel.
- High EGR to achieve a low-temperature combustion and so to limit NO_X and to stabilize combustion are standard – at least for passenger and light duty vehicles.
- Lean-burn concepts using $\lambda \gg 1$ are also on the future road map of modern electrified ICE to further increase the efficiency and resulting in potentially very low exhaust gas temperatures.

PT System Development / Johannes Ullrich / 10.122.130.27 / 2022-06-10 15:45 / This document is not allowed to copy or distribute illegally as a information property of HMETC. If you violate this rule, you can be punished by policy of HMETC and related local law.

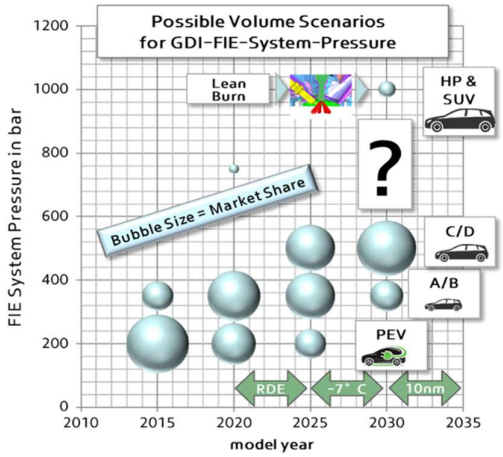


Fig. 2 Prognosis on future fuel injection pressures [2]

- Multiple injection events per cycle are used to reduce PN emission especially in cold conditions.
- Last but not least, frequently happening start-run-stop-events of modern electrified powertrains are also a challenge in many ways in particular for FIE component temperature transients and thus deposit formation.

2.2 Fuels Quality (=Fuel Performance Parameters)
In previous paragraph some features of modern engine concepts were listed. In this paragraph it shall be discussed in how far these features can be linked to the fuel characteristics in a reasonable way.

• To ensure satisfying engine operation with nowadays compression, fuels for diesel should have very good self-ignition properties (CN ≫ 52), the higher the better is an un-contradicted rule. So, it is for gasoline where RON should have 98 points, at least. Applications with a sophisticated knock-control can take additional efficiency benefits from even higher values that would come in reach with Methanol for example.

• Increase of the fuel pressure asks further special properties to the fuel. In case of diesel where servo-driven injectors create high fuel return flow temperatures, fuel degrading (aging) is one challenge aside from sufficient lubrication to prevent from wear. Field experience tells us that not only proper additive packages are needed but also the final boiling point of diesel fuel is a crucial parameter against fuel aging and fuel born deposits. In case of gasoline the main challenges from injection system point of view are sufficient lubrication and proper media separation with regard to the high pressures and fuel leakages in critical zones – the high pressure pump is the by far most critical component here.

• High EGR – or in other words – low oxygen partial pressures do make ignition and combustion substantially more critical. As a consequence, diesel fuels should have high CN and good evaporation characteristics to avoid combustion instabilities, misfire and vehicle jerking. Similar also gasoline fuels should ignite – not in an autonomous way – but reliably even with moderate spark energies.

• In case of future gasoline lean burn concepts, the specific engine demand for fuel properties is still under investigation. Despite ongoing research, it can be said that with regard to an overall lower combustion and exhaust gas temperature level, the evaporation of the fuel becomes quite important to avoid oil dilution and to ensure high conversion efficiencies of the after-treatment system.

• The today`s gasoline engine calibration strategy of multiple injection (1 to 4 injections per cycle) is an appropriate measure to reduce PN emission as well as oil dilution effects by shorting the spray length and so to avoid high amounts of liquid (non-evaporated) either distributed as liquid droplets in the combustion chamber or even located on the combustion chamber walls. Alternatively, the boiling characteristic of the fuel could be utilized as a fuel tuning parameter in the future because with a faster evaporation of the fuel, the PN emission can be reduced even without complex injection control strategies requiring additionally a highly careful function validation over the entire life of a vehicle e.g. 250.000 km for coming legislations.

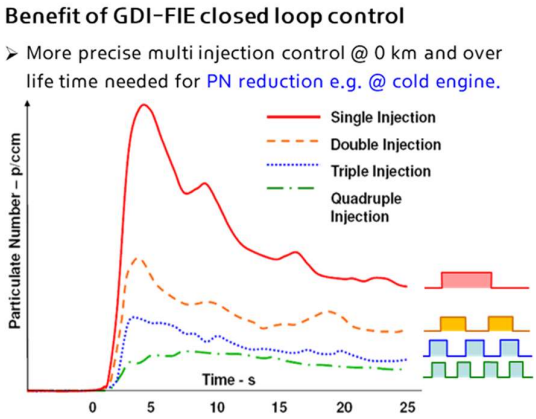


Fig. 3 The impact of multi injection on PN emission [2]

• Frequent start-run-stop or even long periods of pure electric driving could lead to fuel degrading effects not only via overheating of the fuel after short full load operation with sudden stop afterwards but also to a “natural” fuel degradation by presence of air (=oxygen) in the fuel tank in worst case also associated with water during long time periods between the tank re-fill events by the customer.

PT System Development / Johannes Ullrich / 10.122.130.27 / 2022-06-10 15:45 / This document is not allowed to copy or distribute illegally as a information property of HMETC. If you violate this rule, you can be punished by policy of HMETC and related local law.

3. Production and CO_2 Impact of Fuels

Fuels can be made and provided to the market in a variety of ways starting with conventional (fossil) fuel with the highest CO_2 impact, over 1st and 2nd generation bio fuels and ending with hydrogen and hydrogen products that are in best case entirely CO_2 neutral along the entire production chain and so leading to a "Near Zero" CO_2 impact to environment.

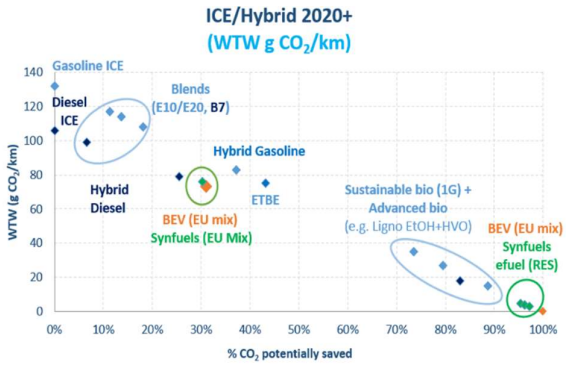


Fig. 4 Different energy carriers and its CO_2 saving [3]

The diagram in Fig. 4 shows clearly that different technologies could lead to very low CO_2 emission in a holistic view and so any decision to prefer one technology versus another. The main message that can be taken is that "100% CO_2 saving" is possible with BEV (but only with 100% green electricity) or alternatively with synthetic fuels (also only when feedstock and electricity is 100% green) – in other words both concepts are equivalent and the question arises whether an entire renewing of the energy distribution infrastructure of a society is really worth it just to "go electric".

3.1 Political and economic background

One political request that came up in the recent weeks is to no more accept bio fuels as energy carriers if they are considered as a competition to food production facing food shortages and high food prices also in Europe. If this request becomes effective by law, the fuel composition in the future could not only affect diesel fuels for their biodiesel or maybe also HVO content, but also gasoline fuels that are using 5 – 10% Ethanol today and planned to contain 20% Ethanol in the near future while staying within a minor modified EN228 spec. In how far the above intention to skip bio fuels might affect even the use of Methanol as a base-product for producing MtG (Methanol to Gasoline) is unclear.

3.2 Technical pathway

The pathway to produce fuels from fossil source is quite clear and needs no detailed explanation except for the fact that for sure green hydrogen will be used more and more during all refinery processes and so fuel makers can fulfil their commitments to cut down CO_2 emission of their business operations.
Referring to the previous expectation that also bio components will have lower importance in the future, bio fuel production processes shall not be discussed in this paper – as this was done in many other papers of the last decades.

As a fact only two production pathways seem to be an accepted part of future sustainable e-fuel production:

1) Fuel production via Fischer Tropsch
2) Fuel production via Methanol Synthesis

From a process and chemistry point of view, the Fischer Tropsch process is the more fundamental concept as it is using the generic elements (hydrogen and carbon) plus energy to form higher molecules of any structure and size. The FT-Process is quite energy intensive but in turn allows substantially more degrees of freedom during the tailoring of the fuel to the needs of automotive but also aviation demands.
Of course the yield of the FT-Process is not one but a variety of products and hence has to be understood and evaluated in a bigger context. Aside from the direct FT-Product "Naphta" that is a very basic and immature kind of gasoline fuel with an RON < 70 only, also very good qualities of Diesel and Kerosene and last but not least waxes and other chemical products that are important for the chemical industry are made.

On the other hand, the methanol pathway leads to a much more straight forward approach for liquid energy carriers at very attractive product costs. Undesired components like sulfur and benzene are quite low and also knocking resistance of MtG is – with RON values between 90 to 94 - even without any post-treatment substantially higher than for a FT-Base Gasoline. On top, however depending on the particular process parameters, aromatics content is also very low which is beneficial for PN emission. A challenge is still to compromise boiling behavior, aromatics and RON to avoid costly add-on process steps or even performance additives.

Beside of the favorable functional properties of MtG, the main advantage could be seen that the base-product Methanol is already today available in big scale and traded, bunkered and distributed around the globe. For that reason, MtG is truly close to market, immediately after sufficient number of refineries were modified to produce this new fuel.
As explained in the previous two paragraphs, two processes for synthetic fuels are available and well understood. Even though there might remain some requirements for even better fuel performance parameters, today`s fuel additive industry has proper solutions to recover production related fuel quality

PT System Development / Johannes Ullrich / 10.122.130.27 / 2022-06-10 15:45 / This document is not allowed to copy or distribute illegally as a information property of HMETC. If you violate this rule, you can be punished by policy of HMETC and related local law.

mismatches and demerits by suitable performance additives regardless if the goal is to enhance knocking resistance (ETBE or MTBE) or increase ageing robustness (detergents) to name only two aspects.

4. Sustainable Fuels of the Future

Below picture is frequently used internally (HMC) to give a rough overview on modern fuels – without claiming for completeness of course:

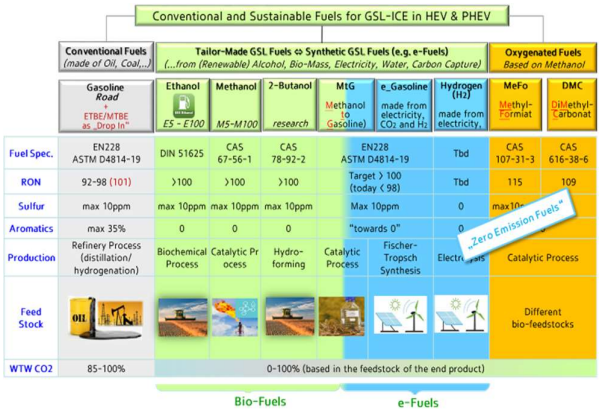


Fig. 5 Overview of selected gasoline fuel types [4]

4.1 Bio-Fuels of 1st Generation

Fatty Acid Methyl Esters (=FAME), well established alcohols like Ethanol and Methanol and blends of those shall be understood as 1st Gen. Bio-Fuels here. Whereas E5 and E10 – despite former media discussion – are technically not that challenging, FAME that can be produced from very different feed stocks can have some risky properties.

Based on that, Hyundai did some intensive research on fuel quality and fuel stability as well as on the fuel effects on vehicle performance, emission, after-treatment behavior, FIE control logic and fuel born deposits with special focus of 1st Gen. Diesel Bio-Fuels. The results were very promising and did not give evidence that 7% might be a strict limit for blending FAME into fossil Diesel fuel.

As long as the fuel qualities are within the given specs of EN590 and EN14214 not only emission like soot are positively affected but also other aspects such as oil dilution and the ash loading is uncritical for example in particular if the vehicle calibration and related software algorithm's are suitable for that.

Last but not least, and after end of all evaluation tests (vehicle mileages up to 240.000 km and test durations longer than 3 years), all FIE components showed perfect function and less fuel born deposits than parts operated with standard market fuels. Since the results were confirmed by the related FIE supplier, also Hyundai did not fear a legislation towards FAME blend rates of 10%, 20% and 30% or even pure FAME operation if legislation would demand for it one day.

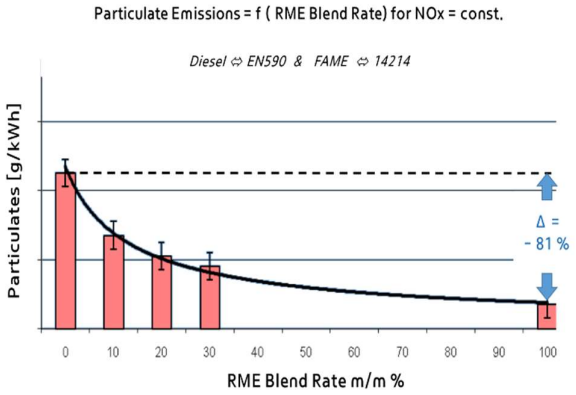
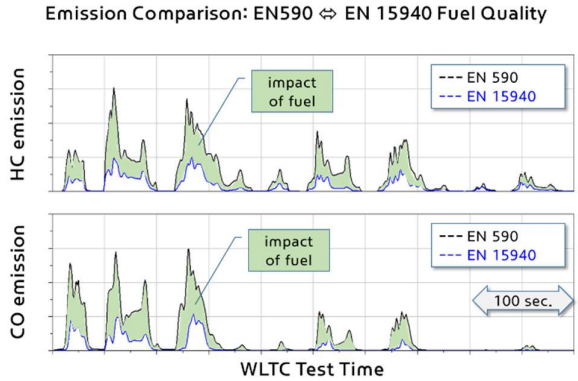


Fig. 6 Effect of FAME on particulate emission [5]

4.2 Bio-Fuels of 2nd Generation

HVO fulfilling EN 15940 specification is a typical 2nd Gen Bio-Diesel-Fuel with outstanding and highly desirable properties for the Diesel combustion process such as a pure paraffinic molecule structure with CN ≫ 70 and fast boiling that ensures a good fuel evaporation, fast and soft ignition and a stable combustion that in turn leads to advantages especially in cold and warm-up HC and CO emission but also for soot formation and for combustion noise.



Fig, 7 Effect of HVO on HC & CO emissions in WLTC

As a very interesting add-on advantage, the authors observed also lower tailpipe CO_2 emissions between 4 to 6 % without any vehicle modifications. A dedicated calibration for EN 15940 fuels would lead to 8 –10% CO_2 reduction a further Hyundai study showed.

In so far, HVO – or more generally speaking – Paraffinic Diesel, that possess a clear specification and has meanwhile been released for many passenger cars, light duty and heavy duty applications would be a very fast and easy way to instantaneously decarbonize the existing Diesel fleet and at the same time improve not only air quality but

PT System Development / Johannes Ullrich / 10.122.130.27 / 2022-06-10 15:45 / This document is not allowed to copy or distribute illegally as a information property of HMETC. If you violate this rule, you can be punished by policy of HMETC and related local law.

also noise emission. A simple facilitator to gain these benefits would be to create the framework for Paraffinic Diesel according to EN15940 as a certification fuel.
Also, the advantages of HVO on particulate emission are not only an effect in some operation points on engine dyno but can be turned into a valuable benefit for the entire vehicle to elongate the particulate filter regeneration intervals, for example.

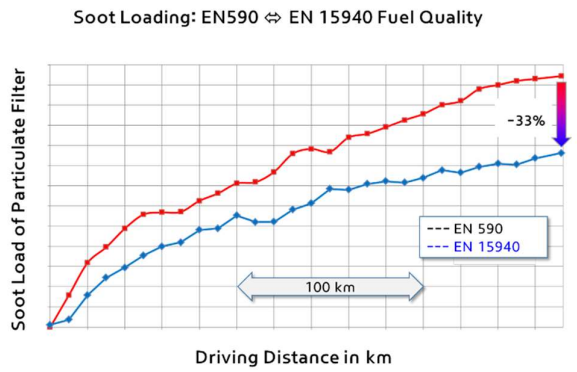


Fig. 8 Effect of HVO on particulate filter loading

An aspect that is not that frequently reported is the so called « nozzle hole coking » caused by fuel born deposits which is influencing the maximum injection rate, the area of max. engine torque as well as power and thus top speed and acceleration of the vehicle.

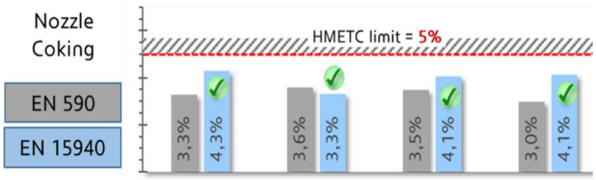


Fig. 9 Nozzle spray hole cokung: Diesel vs. HVO

Hyundai did a dedicated investigation (see picture 9) and found that there is only a minor demerit of 0,6% of Paraffinic Diesel against B7-Diesel. As this value is only slightly above the test repeatability of ± 0.5% and due to the fact that the formation of fuel born deposits could be well controlled and further reduced by suitable detergents, no field issues like power loss for the customer have to be feared.

For the gasoline case with Methanol and Ethanol made from bio mass (the straight forward way to make it) as well as MtG respectively EtG can be judged as a 2nd Gen. Bio Fuel. Hyundai`s experiences with MtG are very different and – as expected – depends less on the idea of MtG itself than more on the production details that is the efforts made to supply either a quite costly “High End” or a very cheap “Low End” product. Following this argument MtG produced via Bio-Matter pathway or green electricity pathway could almost have the same properties and so the related test results that will be shown in the following chapter are valid for both concepts.

4.3 Synthetic Fuels (synthesized from H_2 and CO_2)

- Synthetic Diesel Fuels: Also among the synthetic fuels, different processes are possible. Aside from the option to build higher HC-molecules from C and H atoms using in best case green electricity to produce so called e-Fuels (e-CNG, e-Gasoline, e-Diesel) other processes do exist as well to produce GtL from fossil or also green natural gas. Here GtL is a dedicated brand name for a special kind of Paraffinic Diesel that like HVO meets EN 15940 standard. Depending on the feedstock, GtL can be pure fossil or partially green in the WtW thinking. In fact, the effects of GtL on vehicle equals those of HVO.

- Synthetic Gasoline Fuels: MtG (or EtG) made from H and C plus green electricity shall be by definition seen as a fully synthetic gasoline fuel. Hyundai is evaluating those kinds of fuels since the very beginning in close cooperation with fuel and additive producers. The R&D focus is not only to demonstrate how outstanding fuel properties (e.g. ultra high RON) could be utilized for all new engine generations (e.g. ultra-lean burn w. $\varepsilon \gg 12$) but also to judge what could be a realistic that is “close to market” quality of such a fuel, able to be sold to a reasonable price and so has good perspectives for a fast and wide market acceptance.
Some results on how, for example PN and CO_2 emissions, could be affected by the quality of synthetic fuels that utilized the tolerance borders of EN 228 specification are shown below. So it is not about saying synthetic gasoline is good or bad or e-Fuels from FT-Process are better or worse than those from Bio-Methanol pathway but moreover to show that it simply depends on the particular fuel parameter adjustment.

The very interesting question whether e-Fuels or 2nd Gen. Bio-Fuels (both might be called MtG) will dominate the market is just depending on production cost of the fuel and the taxation. Hence countries with highly attractive electricity cost may be able to supply e-Fuel-MtG at a similar price. Just like other countries with higher Bio-Mass availability could offer MtG from Bio-Methanol.
In view of this, it is clear that not the feedstock but the fuel parameters that can be realized is relevant and has to be balanced between several target conflicts as usual. A reduction of the aromatics content for example is desirable from PN emission but critical from gasket swelling aspect.

A fast boiling (e.g. low final boiling point) is desirable for low PN, low HC and low CO emission.

PT System Development / Johannes Ullrich / 10.122.130.27 / 2022-06-10 15:45 / This document is not allowed to copy or distribute illegally as a information property of HMETC. If you violate this rule, you can be punished by policy of HMETC and related local law.

Furthermore – like seen also in case of HVO – the molecular structure of synthetic gasoline e.g. the C/H-ratio of the fuel – offers direct benefits for tail pipe (=TtW) CO2 emissions.

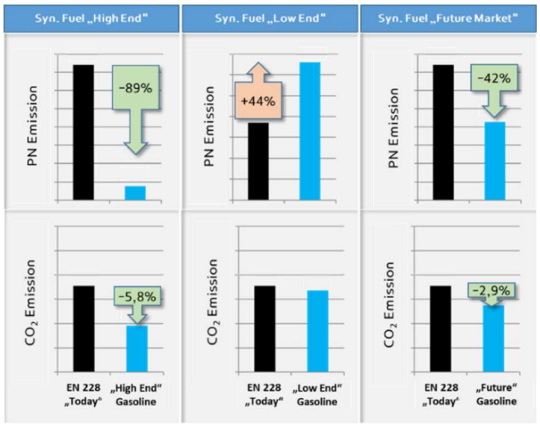


Fig. 10 Impact of synthetic fuel quality on emissions

A high "H" to "C" ratio gives lower tail pipe CO_2 emissions but goes – if not counteracted by additives for example – in the wrong direction with respect to knocking resistance of the fuel. Also the volumetric energy density is negatively affected and could lead to a noticeable fuel consumption increase for the vehicle user.

One little insecure item is the usage of fuel additives that is not that detailed in the fuel specifications and could cause unintended incidents for deposits formation, wear in side of the injection system, fuel degradation, corrosion or other today unknown phenomena.
However, in the eyes of the authors synthetic fuels offer more opportunities than risks basically for two reasons:

- Synthetic fuels allow the elimination of undesired properties resulting from the fossil origin of the fuel that usually have to be eliminated by costly post treating counter measures in the refinery. Synthetic fuels could be tailored to the functional demand from the very beginning to improve also the performance and the emission of any existing or planned powertrain concept improving air quality in urban sectors and elsewhere. Hyundai found that synthetic fuels can have several generic advantages for PN, CO, HC and even tailpipe CO_2 that can be used to improve almost any powertrain concept even without any modifications (see Fig 10).
- Synthetic fuels represent – in the WtW thinking – a fast and effective way for de-carbonization of any existing vehicle that is already in the market and that will come to market as HEV or P-HEV until a ban of ICE might be agreed and be effective by legislation. On top, this can be achieved without any substantial rebuild of the fuel distribution infrastructure like it will be mandatory for EV or FCEV where huge amounts of electricity or hydrogen will be needed. Such an advantage should not be underestimated with respect to customer acceptance that in the end is the basis for market success in a free society.

4.4 Oxygenated Fuels
Although FAME as well as Methanol and Ethanol contain oxygen and therefore show interesting emission advantages mainly for PM and PN, chemicals like OME (for Diesel) and MeFo and DMC (for Gasoline) belong to the category of modern oxygenated fuels. Those not only possess oxygen but in addition avoid C=C-double bonds as the key design feature of this fuel molecule that is decisive for the "near zero particulate emission" behavior. This is why OME is discussed here shortly.

Within a public founded project Hyundai took the chance to evaluate OME in more detail and confirmed for own powertrain concepts the known advantages of OME and its blends such as a nearly soot free combustion and so to break up the classic PM/NO_X trade-off. Blends with up to 7% OME could be used directly and without any modifications to gain emission and CO_2 benefits. Blends between 7% and 15% would require some calibration adaptations but can be managed with the same powertrain hardware. Higher OME blend rates as well as even higher usage of pure OME, will finally require a new layout of injection systems and combustion chambers due to the 35% lower energy content of OME and the substantially more intense combustion.

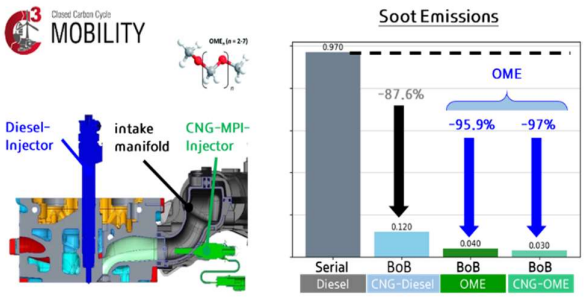


Fig. 11 Impact of fuel oxygenation on soot emission Hyundai Dual-Fuel Study within C3-Mobility

PT System Development / Johannes Ullrich / 10.122.130.27 / 2022-06-10 15:45 / This document is not allowed to copy or distribute illegally as a information property of HMETC. If you violate this rule, you can be punished by policy of HMETC and related local law.

Already by a swap from B7 diesel to OME the emission benefits are that strong that a combination of a complex dual fuel strategy to further lower soot emissions gives no significant additional benefits like it is the case when CNG injection is combined with the injection of Diesel fuel realizing a kind of "jet-ignition-concept". An open task of Diesel-Dual-Fuel combustion concepts is still the inhomogeniety caused by the Diesel jets and leading an intolerable increase of CO and HC engine out emissions.

Despite the production of OME is quite simple when made from green Methanol and despite of the listed advantages of OME, the authors do not believe in a market success of OME in Europe because the current discussion about banning of ICE from 2035 is of course not a good basis to promote new fuel types that can show their advantages only in combinations with substantially modified engine hardware. For the same reasons the market perspectives for fuels like MeFo, DMC, DME to name only a few are similar.

4.5 Hydrogen based fuels and Hydrogen based on the feedstock "electricity" seem politically to be the fuels with best acceptance among other fuel types. Here, the main critics are still the generated tail pipe emission and the cost that may not be competitive. Fortunately, they are not judged to be in competition with food production. They are also not considered to represent a danger for our biosphere (flora & fauna) as even waste bio matter is not a feedstock and last but not least they allow for some freedom to decide how to use green electricity like as follows:

4.5.1 Direct use of green electricity
Best overall efficiency (70% to 90%) but entirely new energy infrastructure needed and so requiring high investments and making market acceptance a challenge – especially on global scale.

4.5.2 Producing hydrogen from green electricity
Second best overall efficiency (40% – 65%) and good energy storage density but also high investments in hydrogen infrastructure needed. Weather using fuel cell or internal combustion engine (=ICE) as energy converters is surely a question if cost reduction of fuel cell is coming true or if the real market with all their severe operation conditions might request a more robust system like an ICE.

4.5.3 Producing e-Fuels from green energy has the lowest overall efficiency (15% to 35%) but almost no add-on cost for fuel distribution, and depending on fuel type, also no new powertrain technology needed. In addition, especially liquid hydro-carbon-products have good customer acceptance on global scale that offers a greater market in terms of "second life utilization".

P.S.: The term "overall efficiency" shall be understood as the ratio between the gross input (e.g. solar) energy and the energy that is available at the car wheels.

So, in the end it might be to some extend a philosophical question which way to go. If the highest overall energy efficiency is the decisive criteria, then e-mobility is for sure the best solution.

If – for a transition phase for example – very high energy density is needed and the electric grid is not yet powerful enough, green hydrogen can be the first choice of a complementary energy carrier for some decades.

If last but not least the hypothesis is true that 1000 times more solar energy is reaching the earth than really needed by mankind, then the overall energy efficiency would no more be of relevance and the concept of making e-Fuels from H2 and CO_2 using green electricity might not only option for a fast de-carbonization of the existing fleet and for countries with insufficiency performance of the electric grid, but could be more over be seen as a mid-term and even long-term solution for mobility that could be pioneered from Europe by exporting the related technologies for produceing e-Fuels globally. Mandatory or at least helpful for such a scenario would be of course more capacity for electrolyser and extensive use of solar, wind and water power to supply the electricity at low cost. However, e-Fuels themselves might most likely not be produced in Europe due to the (currently) high cost of green electricity, but moreover in countries with cheap solar, wind or water power. A game changer could be if nuclear power would be judged to be green one day – of course.

5. Market Perspectives of Fuels

5.1 Fuels in Europe

It is obvious from the current political discussions that the long term perspective for new powertrains e.g. new ICE and new specially fuel tailored types are not very promising in Europe.

However, there is an existing fleet in Europe to be decarbonized until 2050 and if this shall not be done only via CCS or certificated trading with CO2, most likely also sustainable fuels will still play a role in Europe.

In addition, there is also a market that is called "rest of the world" were unlike in Europe mobility is less seen as a burden for the climate but a basis for economic growth.

PT System Development / Johannes Ullrich / 10.122.130.27 / 2022-06-10 15:45 / This document is not allowed to copy or distribute illegally as a information property of HMETC. If you violate this rule, you can be punished by policy of HMETC and related local law.

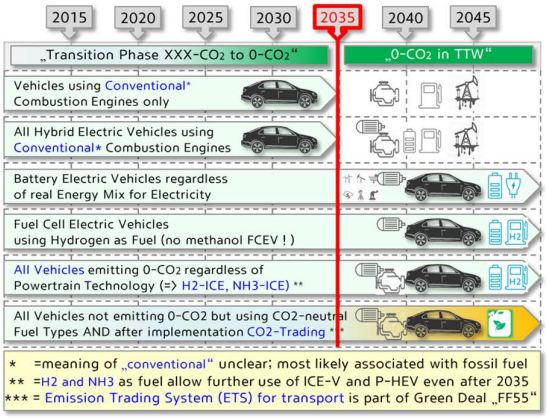


Fig. 12 Possible passenger car scenario in Europe

Since the introduction of B5, B7, E5, E10 the fuels in Europe are not purely fossil. In the last decade future components were blended into the EN590 respectively EN 228 fuels while making sure that the specifications are still kept. Through this strategy, fuel makers launched – invisible for the customer at the filling station – paraffinic diesel and also gasoline pendants to replace fossil fuel with renewables and so to lower the effective net CO_2 emissions – even without CO_2 accountability for the CO_2 fleet targets.

Outside of Germany also pure paraffinic fuels according EN 15940 are offered because of a request by a big number of customers. Inside of Germany some innovative fuel providers and TIER I suppliers succeeded to launch EN590 or EN228 compliant fuels under product names such as “Blue Diesel” or “Blue Gasoline”, for example, that offer a reduction of the CO_2 impact by at least 20% and are said to be suitable for the entire existing vehicle fleet.

5.2 Fuels in China

China, a country that relies on own energy resources like nuclear power, water, solar but also substantially coal to stay energy independent, announced to modernize their definition of “new energy vehicles” by 2025. From that year onward, EV emission will not be “0” by definition as in Europe, but calculated based on the true energy mix. In return, other technologies like H2-FCEV or cars powered by highly efficient ICE running on Methanol or hydrogen will be considered as CO_2 neutral because Methanol and hydrogen is judged as climate neutral fuel in China.

5.3 Fuels in USA

Internal exchanges between the various Hyundai overseas centers confirm the trend for e-mobility in USA that will predominantly be a phenomenon of big east and west coast area and California, of course. Based on that background, it appears a bit strange on a first glance that California announces also to fully replace fossil Diesel by HVO until year 2025.

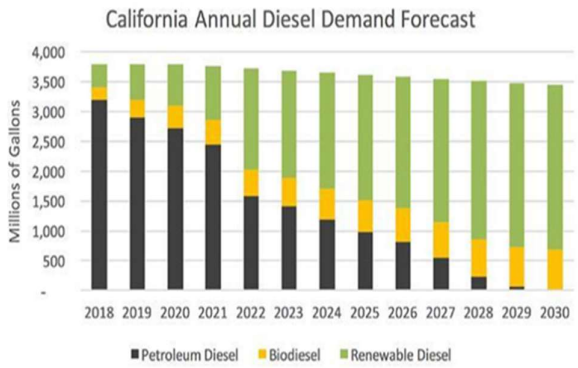


Fig. 13 Diesel fuel market in California by 2030 [6]

By now no information about banning of combustion engines in USA are available and so also no severe concerns against use of chemical energy carriers in in this country do exist. However, it looks that H2-ICE will not be judged as zero CO_2 technology unlike it could be expected for Europe – at least by now.

5.4 Fuels in South America

It is well known that South America is trys to be energy independent by use of locally produced bio alcohol (=Bio-Ethanol). In addition, “…Brazil does not want to wait 20 years until electrification arrives...” [8]

Also media news revealing an investment of about 1 billion € to develop pure ICE but also hybrid powertrains running on Bio-Ethanol of local production indicates that “It could still make sense to use synthetic fuel cars in Latin America in 2035.” [7,9]

Such news may be interpreted in a way, that many OEM statements related to product strategy may be only valid for Europe and might have only little meaning as trend forecast for the much bigger, entire world market. This is in line with local politicians who made clear that not all countries give their highest priority to e-mobility but rather to the prosperity of the economy and the living standard of the inhabitants.

5.5 Fuels in other countries

Fuel market in Japan

- Since decades country of Japan and the biggest car maker in the world are famous for offering outstanding innovative products but at the same time providing robust and affordable mobility for the entire world.
- No wonder that with such a big picture and a wide product scope a self-limitation to only one technology and the related economical risks is unintended. In fact, the biggest car maker in the world not only generated great headlines in the newspapers when revealing its intention to launch a passenger car powered by an ICE and fueled

PT System Development / Johannes Ullrich / 10.122.130.27 / 2022-06-10 15:45 / This document is not allowed to copy or distribute illegally as a information property of HMETC. If you violate this rule, you can be punished by policy of HMETC and related local law.

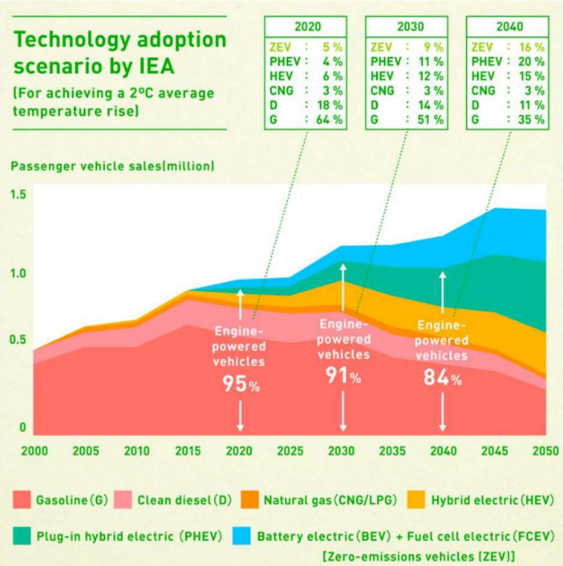


Fig. 14 Outlook future mobility in Japan until 2050 [12]

by hydrogen in parallel to the well-known in-house fuel cell cars, but lately also made a clear commitment to the usefulness of modern climate neutral fuels – no matter if bio-mass or green electricity based. [12]

Fuel market in India

- Cost of ownership is the key motivator for customers in India when fixing their vehicle purchasing decision. Whereas, in the last decades the trend for higher FAME blend rates up to B20 were counteracted by more severe emission legislation (Barat 6) and the associated price increase of diesel cars causing a move to gasoline engines running on LPG. The latest trend to go for CNG (Fossil –CNG and Bio-CNG) seems to become effective with high probability.

  After politicians from India informed that India will take over a big part of the free capacities of the global CNG market, it could be read in related news that the sales figures of CNG fueled passenger cars have increased in 2022 by 55% followed by an announcement that the local production of Bio-CNG could supply a further substantial increase of the CNG market. India refuses to define a timely based milestone for an ICE ban as EV is seen prohibitively expensive.

Fuel market in ASIAN countries

- More or less the same motivation is the driver in countries such as Malaysia and Indonesia to strongly increase the blend rates of FAME up to 40% using locally produced palm oil as feedstock.

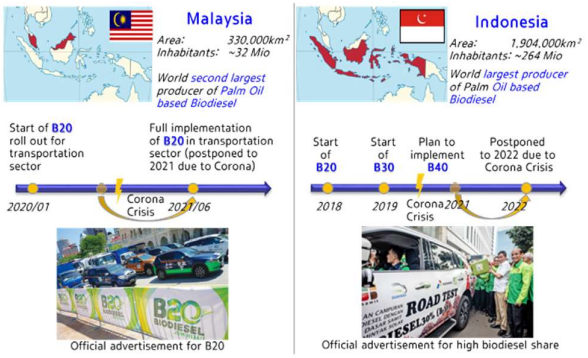


Fig. 15 FAME Road Map in ASIAN countries

6. Conclusion

E-Mobility is said to be an important, maybe the most important pillar of future individual mobility and goods transport. The difficulty for precise planning will be to estimate which markets will grow to what extent in which time, to what saturation level and what kind of obstacles might have to be overcome in our rapid changing global economy with respect to political movements, economic conditions influencing not only the production cost of an EV but also related energy infrastructure.

However, depending on the final decision made by European commission in the weeks to come it is also possible that the only ICE that might remain for new registration at least in Europe after 2035 might the H2-ICE – and eventually ICE running on NH3 for special applications.

But looking to the big picture at this time, from a global point of view, it seems very reasonable not to give up technologically interesting topics too early, such as sustainable, affordable energy carriers e.g. modern synthetic fuels, and for sure this might be seen also as one motivation of “Hyundai Motor Group to Collaborate with Aramco and KAUST on New E-fuel Development to Support Clean Mobility” during the coming years to identify the pro’s and con’s of e-Fuels. [10, 11]

Following the argumentation of FuelsEurope it is very likely that synthetic fuels produced in Europe will be mainly based on bio-mass, whereas synthetic fuels from electricity will come from MENA states plus countries like Chile and Australia of course.

Hence, a reasonable roll-out scenario of how climate neutral fuels can be launched in the market could look as follows:

1) Maximizing the renewable (non-fossil and climate neutral) drop-in-rate in today`s market fuels, to speed up de-carbonization of the existing vehicle fleet, while staying within given specifications (e.g.

PT System Development / Johannes Ullrich / 10.122.130.27 / 2022-06-10 15:45 / This document is not allowed to copy or distribute illegally as a information property of HMETC. If you violate this rule, you can be punished by policy of HMETC and related local law.

BlueGasoline ↔ EN228 for Gasoline & R33 ↔ EN590 for Diesel) even in Europe.

2) Large scale launch of fuel derivate such as paraffinic diesel (EN15940) and E20 (EN228*) that require only a “no-harm-test” program for validation and release even in Europe.

3) Capacity build up for eFuels in countries offering green electricity at low cost (e.g. Chile, Saudi Arabia) and capacity build-up for Bio Fuels of 2nd Generation such as HVO, MtG form Europe that is within given fuel specification allowing 80% to 95% CO2 reduction even in Europe.

4) Development of new and tailor made synthetic climate neutral fuels (=new fuel qualities) in parallel with engine development (=new engine variants e.g. lean burn) to gain even more emission and efficiency benefits for those countries that do not plan a banning of ICE – or go for hydrogen or ammonia as fuels – maybe even in Europe.

7. Acknowledgement

The authors would like to thank Hyundai management for the innovative work environment that finally enables a technology open R&D process and so to investigate a wide spectrum of technologies for many years. Many thanks also go to the C3-Mobility Consortium especially TÜV-Rheinland and the German Ministry of Economy (BMWi) for their cooperation and support.

8. References

[1] Marta Yugo: "The Low Carbon Pathways Project", Chapter 2, Page 9, Figure 5, Concawe, 2018.

[2] Johannes Ullrich et Al.: "Internal Paper - Trend Report on FIE Technology”, HMETC Powertrain FIE & Fuels Team, 2019.

[3] Marta Yugo:"The Low Carbon Pathways Project", Chapter 2, Page 30, Figure 18, Concawe, 2018.

[4] Andreas Kapp, Roland Steininger.: "Internal Paper - Trend Report on Fuels Market Perspectives”, HMETC Powertrain FIE & Fuels Team, 2021.

[5] Andreas Kapp, Diploma Thesis „Grundsatz-untersuchungen zur Vorbereitung eines Pkw-Flottentests mit Biokraftstoffbeimischungen“ , University of Applied Sciences Gießen, 2008

[6] Media News, California Advanced Biofuel Alliance, www.biodieselmagazine.com/articles/2516583/biodiesel-renewable-diesel-set-to-replace-petro-diesel-in-california, 2019

[7] Herbert Dies, Volkswagen AG, Media News, globalhappenings.com/markets/59290.html, 2021

[8] Pablo Di Si, Volkwagen Latin America. Media News, industryeurope.com/sectors/transportation/vw-hopes-to-turn-a-profit-in-latin-america-with-1bn-investment/, 2021

[9] Herbert Dies, Volkswagen AG, Media News, www.euronews.com/next/2021/11/11/germany-autos-volkswagen, 2021

[10] Media News, Aramaco - DHAHRAN www.aramco.com/en/news-media/news/2022/aramco-and-hyundai-motor-group, 2022

[11] Media News, Hyundai News Room, www.hyundai.news/eu/articles/press-releases/hyundai-to-collaborate-with-aramco-and-kaust-on-new-e-fuel-development.html, 2022

[12] Media New, Toyota News Room, https://toyotatimes.jp/en/report/hpe_challenge_2022/005.html

9. Nomenclature & Abbreviations

CCS	Carbon Capture System
CN	Cetane Number
CO	Carbon-Monoxide (-Emission)
DMC	Dimethylcarbonat
e-CNG	CNG made using electricity
e-Diesel	Diesel made using electricity
e-Gasoline	Gasoline made using electricity
ETBE	Ethyl-tertiär-butylether
EtG	Ethanol to Gasoline
EV	(pure) Electric Vehicle
FAME	Fatty Acid Methyl Esters
FC	Fuel Cell
FIE	Fuel Injection Equipment
GtL	Gas to Liquid (=Paraffinic Diesel)
HC	Hydro-Carbon (-Emission)
HVO	Hydro Treated Vegetable Oil
ICE	Internal Combustion Engine
MeFo	Methylformiat
MON	Motor Octane Number
MTBE	Methyl-tert-butylether
MtG	Methanol to Gasoline
OME	Oxymethylenether
PM	Particulate Matter
PN	Particulate Number
RON	Research Octane Number
Soot	Solid Matter Emissions
TtW	Tank to Wheel
WtW	Well to Wheel
EN 228	Specification of Gasoline Fuel
EN 590	Specification of Diesel Fuel
EN 14214	Specification of FAME Fuel
EN 15940	Specification of Paraffinic Diesel Fuel

PT System Development / Johannes Ullrich / 10.122.130.27 / 2022-06-10 15:45 / This document is not allowed to copy or distribute illegally as a information property of HMETC. If you violate this rule, you can be punished by policy of HMETC and related local law.

How will the VALEO Smart Ebike system simplify the last mile delivery ?

Autors : Edgar Dépagneux, Simon Beslin, Benjamin Morliere
Keywords : e-Bike / Cargo bike / Last Mile Delivery / Valeo's e-bike System

Abstract : Cities becoming more and more polluted and congested, and the multiplication of legislation, malus, and taxes to reduce or even ban the use of combustion vehicles. However, these changes are opening up new opportunities, such as the evolution of last-mile delivery, towards softer forms of mobility, like electric vehicles. Among them, the cargo bike seems to have a legitimate place in the sector. In countries that are very advanced in new mobilities, such as Germany, there is a significant number of cargo bikes. 230k units were sold there in 2021 against 15k in France, indicating an undeniable trend (according to the annual analysis from "observatoire du cycle 2021").

1. The Market

1.1 The e-Cargo Market

According to the latest market analysis (from Persistence Market Research) on electric cargo bikes, the worldwide market is growing significantly in 2021, with global revenue up 9.1% year-over-year. Revenue worldwide is expected to triple by 2031.

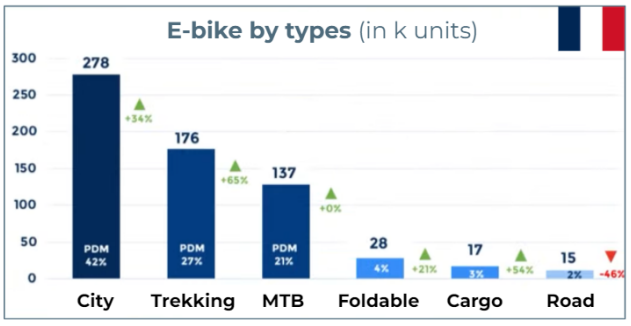


Figure 1 : eBike by types

Despite the fact that the cargo type electric assist bike is a small segment of e-bike, they still doubled in volume in 2021, even with often high prices, so this is excellent progress. In countries such as Germany, Holland or Belgium, which are far ahead of France in this type of mobility and last mile delivery, the figures are growing and with much higher volumes. This will result in an increased demand in the coming years among individuals and professionals.

It is also a very competitive market, with new entrants all the time as the market is not mature. This e-Cargo market is growing, so many players are innovating, different cargo architectures, different engines or even the positioning of the load.



Figure 2 : Different uses of cargo

According to a study in London, eCargo bikes could replace...



Figure 3 : eCargo could replace…

1.2 The Last Mile Delivery Market

With the explosion of e-commerce, the pandemic has put the spotlight on the already sensitive subject of so-called last mile logistics : how to ensure deliveries to

city centers, to individuals and to businesses? The issue is ecological : in urban areas, road transport of goods contributes to 15% to 20% of greenhouse gas emissions, according to the French Agency for Ecological Transition. It is also a major emitter of local pollutants (40% of NOx (nitrogen oxides) emissions and 50% of particulates).

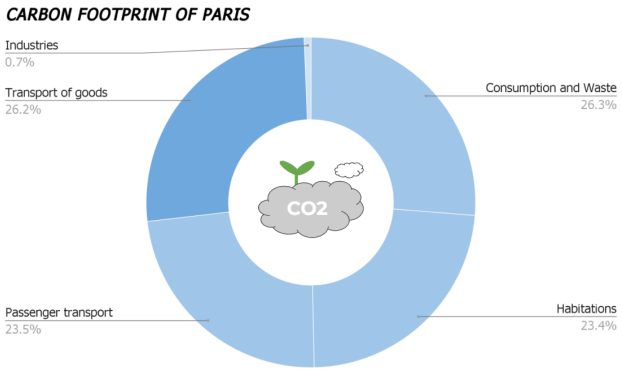


Figure 4 : Paris carbon footprint

But the issue is also economic : the "last mile" market is worth 1.5 billion euros, and has grown by 63% in the last five years. For operators, this logistics represents about 30% of the total cost of delivering a good or service.

The Last Mile Delivery has changed their relationship with end customers, who now require a higher level of service because they rely on parcel delivery for more and increasingly immediate needs. Being able to meet those demands has become a competitive edge for players looking to increase their share of the market. Moreover, delivery giants such as Amazon or DHL are already in the midst of a transition to cargo bikes for delivery in major metropolitan areas.

2. Regulation of ICE in cities

More and more processes are being put in place to drive out combustion vehicles, such as the Low Emission Zones (LEZ) which are intended to protect people in the most polluted dense areas (such as Paris).

The principle is to encourage the circulation of the cleanest vehicles while preventing the most polluting and "unclassified" ones from driving, so in the LEZ, polluting vehicles are prohibited during certain time slots. This is just one of the many regulations put in place to encourage people and professionals to use vehicles such as electrically assisted bicycles for example. In addition, to achieve its goal of climate neutrality in 2050, the European Commission is proposing a reduction in new car emissions of 55% in 2030 and 100% in 2035. This would mean the end of combustion car sales by that date.

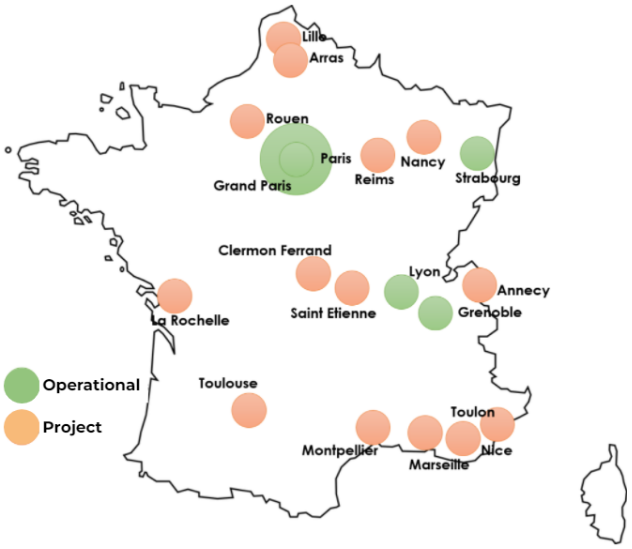


Figure 5 : LEZ examples in France

3. A game changer eBike system

Valeo, the world leader in automotive electrification, has adapted its 48V motors to bikes by coupling it with an integrated automatic gearbox, resulting in a high-performance electric assistance system for bikes, combining performance, efficiency, intelligence, comfort, robustness and ease of use.

Designed and assembled in France (Mid Drive Unit and Battery), the system comprises a 48V eMotor & an adaptive automatic gearbox (7 gears with an instantaneous shifting). As in a car with an

automatic gearbox, you are free to choose between an automatic mode or a manual mode for shifting. Thanks to sensors, the system predicts the environment and cyclist behavior and gives the optimum shifting to provide the perfect power.



Figure 6 : Valeo's MDU

With the eBike smart system : your only job is to pedal, you don't have to worry about shifting gears at all, which is perfect for a delivery use, because the delivery person is not necessarily familiar with cycling. Ease of use is a key expectation for LMD companies regarding their delivery drivers. The complete gearbox system developed allows automatic gear selection without having to choose its ratio, and increases the comfort of the user especially in long use such as delivery use.

With 130 Nm of torque (eight times the cyclist effort), electric assistance allows carrying a 300kg load to climb a 14% gradient like a parking ramp for example.

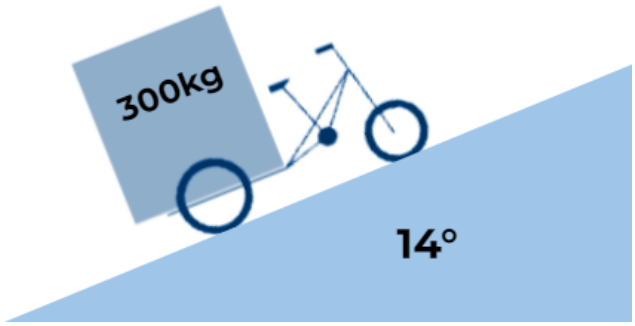


Figure 7 : Parking ramp

Taking advantage of sensors and the ability to read cyclist behaviors and their environment, electronics & algorithms are able to adjust electrical assistance, cranking frequency and pace to the optimum level.

Valeo has designed the project in its entirety, by accompanying this powerful and innovative system with a whole connected environment. The service that accompanies this product is materialized by a mobile application that will act as a diagnostic tool for the aftermarket part.

This system is suitable for cargo use and adapted to last mile delivery. It includes an integrated anti-theft function that blocks the use of the ebike, a reverse feature & regenerative function to save brake usage & charge batteries back for cargo applications.



Figure 8

3.1 The MDU

The MDU (Mid Drive Unit) assists the cyclist through an electric motor. When the cyclist pushes the pedal, a torque and rate measurement is done on the primary shaft to indicate the BCU (Bike Control Unit) which torque at wheel the cyclist is expecting. Depending on the selected mode, the BCU calculates which level of torque the motor will provide to assist the cyclist.

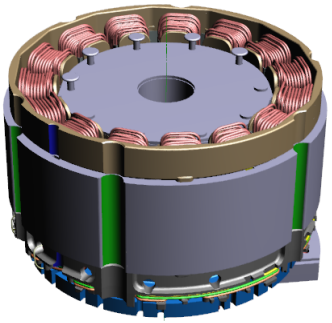


Figure 9 : Electric motor

On his side, the cyclist can select the gear he is more comfortable in, independently from the torque the assistance will give: as MDU is an all in system, the motor torque can go directly to the output of the MDU. It is designed to provide constant assistance whatever gear is selected, hence it gives a high level of assistance even when the cyclist has selected the seventh gear to start with.

3.2 The gearbox

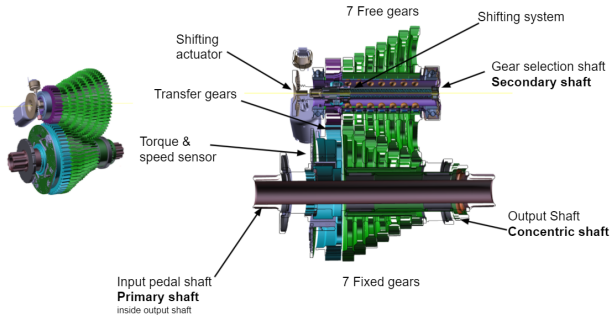


Figure 10 : Double shaft gearbox

Each gear can be selected individually : a small DC motor activates a worm screw that drives a shuttle under each gear. The shuttle pushes outwards a pawl that engages a notch in the free gears. The gear is then selected.

The shuttle travels alongside the worm screw and its guide to select the gear demanded by the Bicycle Control Unit (BCU).

The position sensor is feeding back the BCU with the location information to ensure the shuttle is sitting under the correct gear.

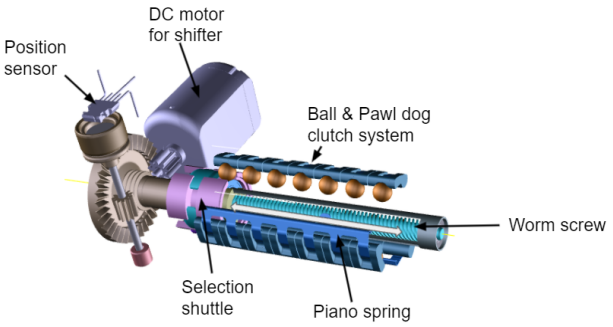


Figure 11 : Gear selection shaft

3.3 The BCU

The BCU (Bike Control Unit) is the controller that runs all the control loops inside the MDU. It receives information of cyclist torque & cyclist pedaling cadence, and adapts the motor torque assistance to the demands.

By interpreting the information received by CAN from the bike HMI, the BCU adapts the actual driving mode. By interacting with automatic or manual gearbox mode, the BCU will adapt the commands to control the gearbox shifting actuator.



Figure 12 : HMI (display + remote control)

The HMI has a simple ergonomics, it is composed of a screen part and a remote control part. You can switch to sequential mode and shift gears manually with the plus and minus buttons. There is also a thumb trigger for the walk assist or reverse.

The BCU adapts the level of assistance taking into account the battery state.

Finally, the BCU, based on sensor data, is able to adapt the assistance applying some limitations and derating.

4. Why e-Cargo Bike for last mile delivery ?

The e-Cargo bike can completely revolutionize the world of delivery in cities. This responds to real societal issues : pollution (particles, CO2 and noise) and congestion. More and more European cities are closing their urban centers to cars.

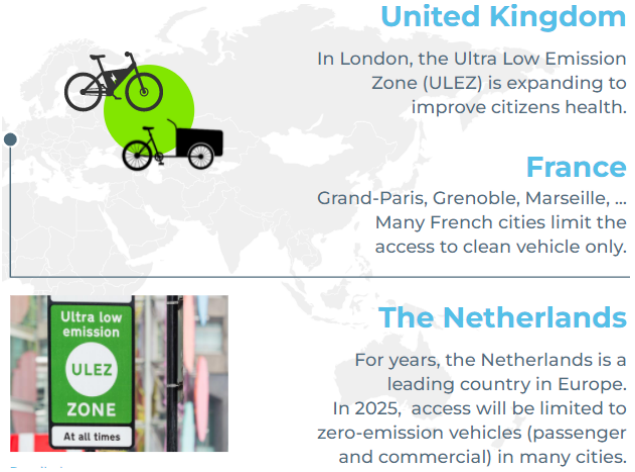


Figure 13 : example of regulations

Indeed, the relatively small size of cargo-type electric bikes, compared to a van or a delivery truck, would allow cities to be relieved of congestion. The unloading of the cargo can be done without hindering the circulation of other road users, and consequently find a more fluid traffic in the big cities.

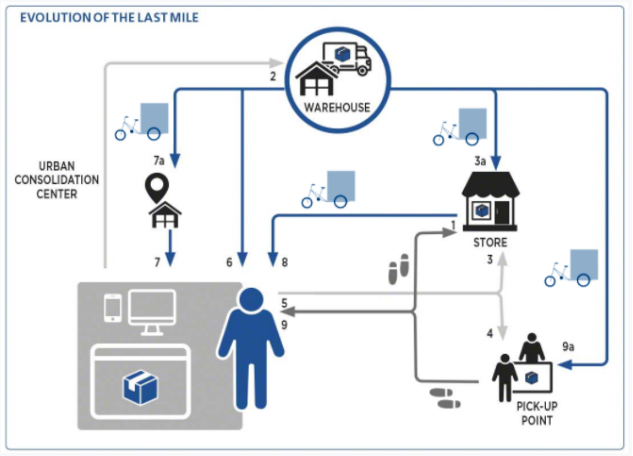


Figure 14 : Last Mile Delivery (https://www.mecalux.com/blog/last-mile-delivery)

In general, a delivery person with an electric cargo bike can make his rounds faster than with a van. It is more agile and narrower, and can be driven more easily through the city. On average, a delivery person on a cargo bike will travel at an average speed of 8 to 12 km/h during his tour. If we assume that a cargo bike for delivery travels an average of 30 to 40 km per day to make its rounds, it would avoid the emission of about 2 tons of CO2 per year compared to the use of a commercial vehicle (van type).

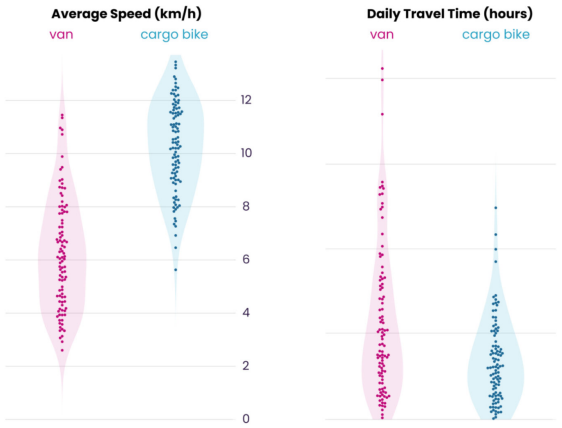


Figure 15 : Comparison between e-Cargo and classic delivery van

5. Valeo's solution perfectly adapted to last mile delivery

5.1 Safety & Comfort

Thanks to VALEO expertise coming from the automotive industry and supply chain, we have been rethinking the Cargo bike electrification system bringing new functionalities and performances which are necessary for the safety and comfort of the deliverers.

The MDU from Valeo raises the bar in terms of safety:

- First, the MDU provides full commitment to local legislation requirements (thanks to its modular platform software).
- The MDU software is also secured with a dedicated Checksum.
- From an on-road safety standpoint, the MDU carries CAN protocol which is compatible with safety devices such as lighting, turn indicators, etc.
- The system is more reliable, so there is less risk of being immobilized in traffic.

The Valeo ebike system is equipped with a reverse mode, allowing more maneuverability to the driver especially when he is fully loaded. And also allows the delivery person not to put his foot on the ground to make a reverse if he has a 3-wheel cargo. It's also equipped with a regenerative braking system, to recover energy to the battery and reduce brake pad wear thanks to the engine natural brake. Valeo also developed anti-theft and park lock (like the "P" function of a car automatic gearbox) systems with fully integrated features, and allow you to secure your eBike cargo in a blink of an eye when you are about to unload. Electrical assistance automatically shuts-down and the integrated gearbox automatically switches to neutral position without any possibility to crank, moreover, it starts the synchronization with the add-on GPS tracker module (optional).

Indeed Valeo is developing a Mid Drive Unit with high torque (perfect for a fully loaded cargo bike) and Integrated gearbox, that way we can remove the classical and annoying derailleur. It also simplified the maintenance. The automatic gear shifting is perfectly adapted to the user behavior and the environment thanks to 4 key sensors (cadence, torque, wheel speed and tilting). The sensors and the algorithm coupled with an automatic gearbox provide the smoothest ride you can imagine.



Figure 16 : MDU specifications

5.2 Reliability

Valeo comes with significant advantages in terms of reliability, with the torque developed by the motor not going through gearbox for enhanced reliability preventing bearings, gears axis and pinions, pawls, and decreasing noise and vibrations.
In the current market configuration with MDU coupled with a classic derailleur, torque goes into the derailleur, coming with a high solicitation. But with the MDU supplied by Valeo, torque goes directly to the rear wheel pignon. By eliminating the derailleur and the external gear cassette, the system becomes more reliable, greatly reducing the need for maintenance. The first MDU revision (oil replacement) will be necessary after 1000 hours of use, the equivalent of 4 and a half months in last mile delivery use. In fact, in cargo bike delivery companies, 30% of the fleet is not

running because of mechanical problems, hence the interest in simplifying the transmission (like with the Valeo solution).



Figure 17 : Derailleur

This is a matter of business continuity with the integrated gearbox avoiding derailing, preventing delivery delays. Finally, the MDU is designed to work with belts and chains of any size which have a direct impact on reliability (classic derailleurs require thin chains whereas MDU can carry chains or belts 2 to 3 times larger).

5.3 Efficiency

The on-road efficiency is mainly driven by the following specs:

- Automatic gear shifting in any circumstances (stop or when pedaling) and linked to environment (slopes, descent, etc.)
- Reverse engage for more maneuverability especially when fully loaded
- Transparent onboard intelligence to adapt the bike control to its environment and its user : Optimum electrical assistance level and cranking cadence to simplify the driving experience and ergonomy at maximum (only pedaling and driving). This simplicity of use for the deliverers is an asset in terms of security too.

The 3 main components, known as electric motor, reducer and layshaft gearbox are designed to offer best in class efficiency (above 90%) saving battery consumption while decreasing the losses of electrical assistance and muscular torque developed by the user.

5.4 Equipments et maintenance

The system also includes a display that shows all the necessary information for the driver. GPS applications (used permanently by delivery drivers) are often power-hungry and can accelerate the loss of autonomy of the phone, that's why he has the possibility to plug his phone to the USB-C socket of the display in order to recharge it. The display is well equipped with Bluetooth and coupled with a mobile application.

The connectivity aspect is addressed for 2 main uses : daily use & maintenance.

Daily use is necessary for our end customers so they have a more complete experience with their bike. They can configure their bike by tuning assistance levels, upgrade their bike, manage the security and lock their bikes. They also have access to detailed information about their rides. End-users will have access to a mobile application.

Maintenance on the other hand, aims to improve lifetime and repairability. Bike manufacturers, shops & repairmans will have access to a diagnostic tool allowing them to fix eBikes. This tool will be a gateway to get a more complete view of a bike, errors codes, usage values, and overall a complete logbook of a bike. Allows for quick identification of the breakdown, thus reducing downtime.

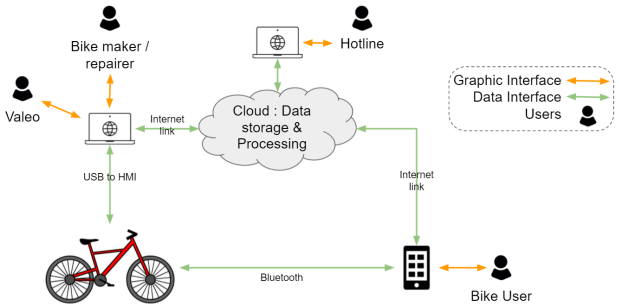


Figure 18 : Connectivity



Figure 19 : MDU Features

The system offers the possibility to embark a battery of 1240Wh. Which allows the driver to deliver all day within the city, and a range around 70km (in the worst conditions) with the 150-250kg load. The average delivery route in last mile delivery is between 10 & 15km, so with the Valeo system, the driver will be able to multiply delivery and be more efficient. Without forgetting than the regenerating braking system will extend the range of the eCargo.



Figure 20 : 1240 Wh Valeo Battery

The Valeo eBike solution also allows the use of smaller vehicles for delivery, such as cargo bikes. They move more easily through the city and take up less space when the driver unloads, compared to a conventional truck or van. As a result, Valeo is helping to make cities less polluted, less congested and safer. And in any case, with the multiplication of regulations, malus, taxes, and even the banning of the combustion engine, the cargo bike will eventually be an unavoidable solution for last mile delivery.

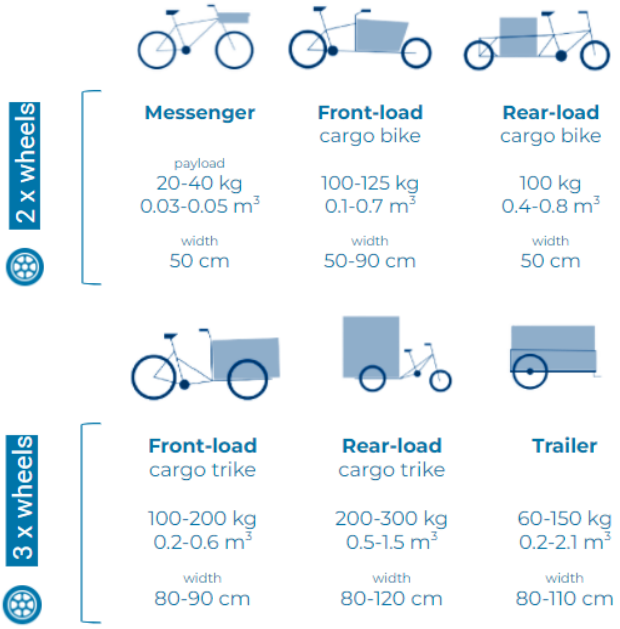


Figure 21 : Types of Cargo bikes

Combination of advanced emission control technologies and sustainable renewable fuels on a long-haul demonstrator truck

P. Mendoza Villafuerte[1], J. Demuynck[1], D. Bosteels[1], T. Wilkes[2], C. Chaillou[3], M. Hultman [4]

1: Association for Emissions Control by Catalyst (AECC aisbl), bd. Auguste Reyers 80, 1030 Brussels, Belgium
2: FEV Europe GmbH, Neuenhofstraße 181, D-52078 Aachen, Germany
3: Aramco, 232 Avenue Napoléon Bonaparte, 92500 Rueil-Malmaison, France
4: Neste Corporation, Vasagatan 7, 111 20 Stockholm, Sweden

Abstract: Reducing CO_2 emissions from road transport is key to mitigate climate change. Heavy-duty vehicles are a hard-to-abate sector. Wider usage of sustainable renewable fuels significantly reduces Well-to-Wheel CO_2 emissions of new and existing vehicles in addition to electrification. It is also important to further reduce pollutant emissions to improve air quality, which is achieved with the application of advanced emissions control technologies.

This paper investigates compatibility of advanced emission control technologies for ultra-low pollutant emissions with two examples of sustainable renewable fuels: Hydrotreated Vegetable Oil (HVO) and e-diesel. Emissions are measured in real-world driving with a demonstrator truck and compared to reference emissions results with a market diesel.

The emissions control system of the truck integrates a close-coupled Electrically Heated Catalyst (EHC) and Diesel Oxidation Catalyst (DOC), a catalysed Diesel Particulate Filter (cDPF) and a dual Selective Catalytic Reduction (SCR) system with twin AdBlue® dosing. Both SCR catalysts contain an ammonia slip catalyst.

A reference In-Service Conformity test is run as well as an urban delivery test. Analysis of the initial cold-start phase and warm operation show ultra-low emissions are confirmed when using sustainable renewable fuels. Currently non-regulated pollutants (NH_3, N_2O and PN10) are measured in addition to standard species with a prototype Portable Emission Measurement System (PEMS).

An analysis is carried out to understand the potential Well-to-Wheel CO_2 emission reduction for the different fuels. The results of the calculation show that considerable CO_2 reductions are possible for both fuels tested. This reduction can be achieved for new and existing vehicles due to the drop-in capability of these sustainable renewable fuels.

Keywords: sustainable renewable fuel, Well-to-Wheel, ultra-low pollutant emissions

1. Introduction

The European Union has started the process to become the first climate-neutral continent by 2050. On 11 December 2019, the European Commission presented the European Green Deal [1] which sets out a detailed vision to safeguard biodiversity, establish a circular economy and eliminate pollution. Further to this, in the Commission work programme for 2021, the revisions and initiatives linked to the European Green Deal climate actions and in particular the climate target plan's 55 % net CO_2 reduction target are presented under the 'Fit for 55' package [2]. The work programme included an important revision of the regulation setting CO_2 emission performance standards for new passenger cars and for new light commercial vehicles [3]. In the Commission's work programme for 2022, the review of the CO_2 emission standards for heavy-duty vehicles has been included [4]. It is worth clarifying that both regulations for light- and heavy-duty vehicles are based on tailpipe emissions, what is known as Tank-to-Wheel (TtW).

The legislative landscape, with the review of such legislations and the challenges ahead to make Europe the first climate neutral continent by 2050, sets the scene for increased awareness and discussion on alternative pathways that will allow for substantial overall reduction of CO_2 emissions from road transport.

From the pollutant emissions' perspective, significant efforts have been made in the past decades to reduce these emissions from internal combustion engines. Since the implementation of on-road testing for light- and heavy-duty vehicles in the legislation, pollutant emissions have been drastically reduced from these applications. In December 2020, the European Commission adopted the Sustainable and Smart Mobility Strategy (SSMS) [5]. The adopted strategy calls for more to be done: the upcoming proposal for stringent air pollutant emissions standards for combustion engine vehicles, Euro 7, will ensure that only future-proof ultra-low emissions vehicles come to the market.

The expected introduction of Euro 7 standards for light- and heavy-duty vehicles is intended to further reduce emissions significantly from heavy-duty vehicles with internal combustion engines in order to improve air quality on the roads and especially in cities.

This manuscript reports the pollutant and CO_2 emissions from a heavy-duty demonstrator vehicle with state-of-the-art emission control technologies tested with sustainable renewable fuels over a broad range of operations. The testing with sustainable renewable fuels was conducted within two phases of the AECC project. The emission control system used in phase 2 was updated with an active thermal management described in section 3. Well-to-Wheel (WtW) CO_2 emissions are reported.

The sustainable renewable fuels chosen for these tests were HVO and e-diesel. HVO was selected as an already available fuel at European service stations which is able to substantially reduce CO_2 in a WtW assessment. E-diesel was also tested. This fuel is expected to be available in the mid-term and will allow substantial CO_2 reductions provided that the hydrogen is produced from low carbon renewable energy and the CO_2 is captured from the atmosphere or from an unavoidable source.

2. Base vehicle and powertrain characteristics

The heavy-duty vehicle used in the project is an N3 Daimler Actros 1845 LS 4x2 tractor equipped with a 12.8 l engine with high pressure Exhaust Gas Recirculation (EGR) and homologated to Euro VI-C. The rated power of the engine is 330 kW at 1600 rpm and the type approval reference work in the World Harmonised Transient Cycle (WHTC) is 29.4 kWh.

3. Emission Control Technology system

Previous publications have described in detail the system implemented in phase 1 of the AECC heavy-duty demo vehicle project [6 - 8].

In the first phase of the project, the innovative emission control system was composed of a close-coupled (cc) DOC, SCR and Ammonia Slip Catalyst (ASC). The ccSCR/ASC is placed as the first component in the boxed system followed by a DOC, catalysed Diesel Particulate Filter and SCR/ASC, with twin AdBlue® injection and a hydrocarbon (HC) doser to support DPF regeneration. A novel twin AdBlue® dosing system was implemented to the demonstrator truck and controlled using FEV's in house developed twin dosing control software. The software controls both injection systems individually and coordinates the AdBlue® dosing. The system determines if the front or rear system should be used to optimise conversion efficiency.

In phase 2 of the project work, the emission control system was modified to further reduce cold-start emissions. The ccDOC which is located directly after the engine turbo and consists of two substrates was changed. An electrically heated catalyst (EHC) was implemented as the first substrate within the DOC canning, as can be seen in Figure 1.

In the phase 2 setup, the vehicle was fitted with an external 48 V system allowing for efficient use of the EHC and applying the power required when needed. The AC/DC converter installed in the vehicle supplied 10.8 kW maximum power, defining the EHC capacity.

The EHC was calibrated to hold a ccSCR temperature (front face) of 220 °C. At idle, EHC performance in the heavy-duty demonstrator truck is capable of achieving average gas temperatures downstream of the EHC between 350-400 °C and temperatures upstream of the ccSCR > 200 °C.

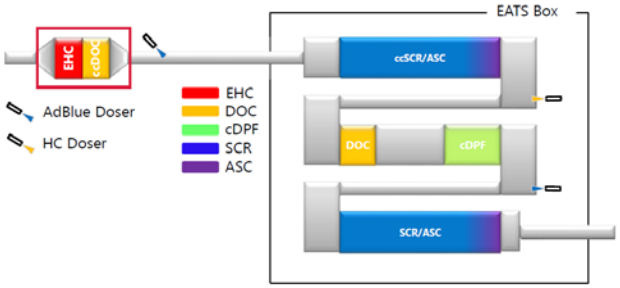


Figure 1. Phase 2 emission control system

The EHC supports the clean operation of the vehicle by reducing high NOx emissions from the cold-start and preserves the system temperature when the operating conditions include long idle phases. A dedicated paper on the phase 2 of the work is in the process of being published and for this reason the discussion in this manuscript will focus on the results achieved with the sustainable renewable fuels.

4. PEMS equipment integration

The emission results reported in this paper refer to tests conducted on the road with the vehicle instrumented with a Portable Emissions Measurement System (PEMS). To fully quantify both cold-start NOx emissions and secondary emissions compliance, a prototype PEMS was fitted to the demonstrator vehicle as shown in Figure 2. The tailpipe was modified to contain the Exhaust Flow Meter (EFM) for the PEMS kit and the equipment itself were set up on the trailer.

The PEMS kit contained NO (Chemiluminescence Detector) and NO_2 (Photoacoustic spectroscopy) analyzers to determine tailpipe NOx speciation, as well as CO and CO_2 measurement devices (Non-Dispersive Infrared Sensor). In addition to the

gaseous measurements, PN10 is measured using a condensing particle counter (CPC).



Figure 2. PEMS installed in the vehicle

In addition to the standard PEMS equipment, the truck was fitted with portable NH_3 and N_2O measurement technology. N_2O was measured using a Non-Dispersive Infrared Sensor and the NH_3 was measured using a Quantum Cascade Laser setup.

5. Fuels

All measurements in project phases 1 and 2 have been done on EN 590 'B7' diesel fuel. Extra measurements were conducted on sustainable renewable fuels to validate the ultra-low pollutant emissions while significantly reducing Well-to-Wheel CO_2 emissions.

For the test with sustainable renewable fuels, in phase 1 of the project, the choice was to use 100% Hydrotreated Vegetable Oil. HVO is increasingly produced from waste and residue fat fractions coming from the food industry, as well as from non-food grade vegetable oil fractions. HVO could achieve up to 90% WtW CO_2 reduction straight from the pump depending on feedstock, this fuel meets the requirements of EN 15940 for paraffinic diesel fuels [9], for this reason, the calibration of the engine of the vehicle can be used without any adjustments.

Table 1. Fuel properties

Fuel property	Units	B7	HVO	e-diesel
Density	kg/l	0,835	0,78	0,7987
Cetane number		52	>70	74,8
Carbon content	%m/m	85,94	84,8	85,06
Hydrogen content	%m/m	13,35	15,2	14,94
Net heating value (m)	MJ/kg	42,74	43,6	43,91

During phase 2, an e-diesel was used to conduct on-road tests. The specifications of the fuel stayed within the limits of EN 15940 and therefore, no changes to the engine calibration were necessary.

Life Cycle Assessment (LCA) is an internationally standardised methodology (ISO 14040 ff), it helps quantifying the environmental footprint related to goods and services. For the moment, the LCA is not being used within the European regulatory framework to calculate CO_2 emissions from road-transport. Nevertheless, some companies and researchers are looking at such an approach to compare different technologies [10-12]. A first step towards LCA can be given by the well-to-wheel analysis.

In this paper, a WtW CO_2 analysis was conducted according to the JEC (JRC-Eucar-Concawe) methodology version 5 [13] and will be reported in the following section. The JEC methodology was chosen as its objective is to establish, in a transparent and objective manner, a consensual Well-to-Wheel energy use and GHG emissions assessment of a wide range of automotive fuels and powertrains relevant to Europe in 2025 and beyond. Furthermore, current JEC version 5 is the first one including assessment data for heavy-duty vehicles.

$CO_{2,WtW}$ in g/km is calculated with equation (1) as described below.

$$CO_{2,WtT,fuel\ production}\left[\frac{g}{km}\right] - CO_{2,biocredits}\left[\frac{g}{km}\right] + CO_{2,TtW}\left[\frac{g}{km}\right] \quad (1)$$

The $CO_{2,WtT,fuel\ production}$ is calculated with equation (2).

$$\frac{Q_{fuel}\left[\frac{MJ}{100km}\right]}{100} * \left(\sum_{all\ compounds,i} CO_{2,intensity,WtT,i}\left[\frac{gCO_2}{MJ}\right] * NRJ_i\right) \quad (2)$$

Where Q_{fuel} is the measured fuel energy in MJ used by the vehicle for 100 km driven on the chassis dyno, $CO_{2,intensity,WtT,i}$ are the Well-to-Tank CO_2 emission factors for the compound i blended in the fuel, NRJ_i is the share of energy of the compound i blended in the fuel. The biocredits are calculated in a similar manner based on the value for each component blended in the fuel which is not from fossil origin.

An overview of all the data used is given in Table 2. Well-to-Tank (WtT) input data is coming from the JEC WtW report. Tank-to-Wheel input data is from on-road testing.

Well-to-Tank data from the JEC report is expressed in CO_{2eq} emissions as also the impact of other

greenhouse gases is considered. This is not the case for the measured Tank-to-Wheel values.

Table 2. WtT data used on the WtW calculations

Fuel property	B7	HVO		e-diesel
		EU mix	Waste cooking oil	
$CO_{2\ intensity}$ (gCO_2/MJfuel)	73,73	71,31	71,31	71,03
WtT $CO_{2\ emission\ factor}$ (gCO_2/MJfuel)	18,20	30,00	11,10	0,81
$CO_{2\ biocredits}$ (gCO_2/MJfuel)	-5,03	-71,31	-71,31	-71,03

Note: JEC pathways chosen - B7: COD1+WOFA3a; HVO EU Mix.[14]; HVO Waste cooking oil: WOHY1a; e-diesel: RESD2.

6. On-road testing

On-road tests were defined to verify the broad range of driving conditions covered in the base project [6, 7] with conventional diesel.

Two routes were used, a typical In-Service Conformity (ISC) and an urban delivery route. The tests covered a significant range of the operating map of the engine. Speed profile of the routes can be seen in Figure 3.

Both route speed profiles are meant to replicate typical missions of the vehicle.

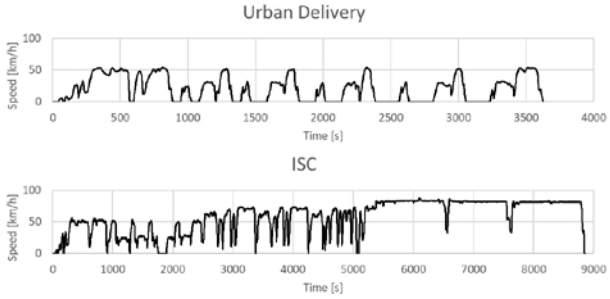


Figure 3. Speed profiles of the different routes completed

These routes ensure a broad coverage of the engine operating map as can be seen in Figure 4. The ISC test ensures a complete operation of the engine torque, including full load operation. The urban delivery route covers lower load operation compared to the ISC as it contains continuous 1, 2- and 3-minute stops where the engine is kept idling.

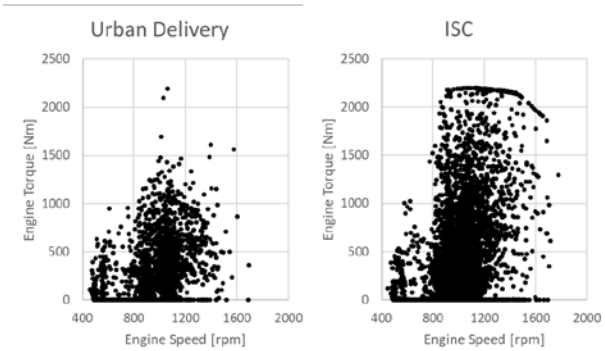


Figure 4. Operating engine map covered by the different routes completed

Similar to the base project, during the sustainable renewable fuel campaigns all tests were conducted with the vehicle preconditioned. Such preconditioning included running the vehicle at constant speed with high engine load to prepare the vehicle for the next day of testing. The protocol was implemented to investigate a severe condition for the emission control system. The preconditioning depletes the ammonia storage of both SCRs as well as passively regenerating the diesel particulate filter.

7. Results

A general remark on the results shown in this section is that the pollutant emissions figures include a summary of the emissions results of several tests. Error bars indicate the level of variability observed in the measurements. In particular, during the cold-start and the urban operation, there is a certain variability due to the impact of driving conditions and initial status of the emission control system.

The testing campaigns in phases 1 and 2 included different numbers of tests, ambient temperatures, payloads, and traffic conditions. Details on the conditions covered are reported below.

NOx emissions

A summary of the NOx emissions of the on-road test results obtained with the system with conventional diesel during phases 1 and 2 can be seen in Figure 5. The figure includes the results achieved by testing the vehicles with sustainable renewable fuels as well.

Phase 1 results show emissions from urban delivery and in-service conformity testing, focussing on the urban share of operation as emissions were near-zero in the other parts of the test. The on-road tests were conducted within a broad range of ambient temperatures from 4 to 25°C. With 10, 50 and 100% payload, as well as with an empty and a normally ammonia-loaded SCR.

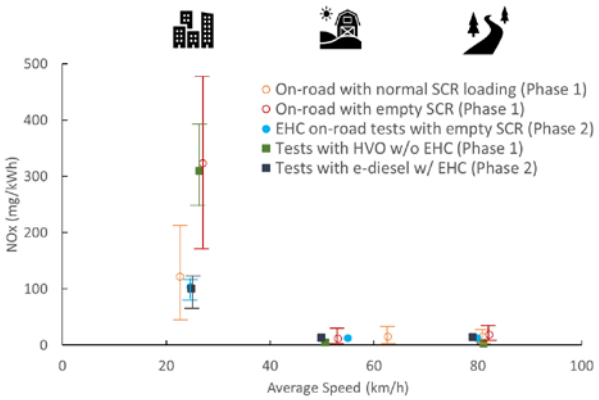


Figure 5. Summary NOx emissions of phase 1, phase 2 and testing with sustainable renewable fuels.

The on-road NOx emissions results with normal SCR ammonia loading are between 42 and 208 mg/kWh. For these tests, no preconditioning was conducted and the loading in the SCR at the beginning of the trip is how it remained at the end of the testing the previous day. On the other hand, results of on-road testing with empty SCR show a higher range of NOx emissions, from 168 to 475 mg/kWh. As can be seen, rural and motorway operation show very low tailpipe NOx values, all below 30 mg/kWh, as the emission control system is warm.

Figure 5 shows the range of emissions achieved in phase 2 of the project as well. As noted, at this stage the system includes the EHC. Tests were conducted with empty SCRs and with ambient temperatures between 5-8 °C. The NOx emissions under urban operation vary from 88 to 112 mg/kWh.

The tests conducted with HVO and e-diesel were similarly conducted with empty SCRs at the beginning of the trip. The HVO testing was conducted in phase 1 of the project. The results show the urban NOx emissions from 248 to 399 mg/kWh. The testing conducted with e-diesel in phase 2 of the project achieved urban NOx emissions from 65 to 137 mg/kWh. In both cases, this is within the variability observed in the results with market diesel. The rural and motorway emissions from the testing with sustainable renewable fuels are below 16mg/kWh.

Particulate number (PN10) emissions

A similar analysis was made for the particulate emissions. Phase 1 results show urban emissions with normal SCR loading from $6{,}07 \times 10^{10}$ to $1{,}38 \times 10^{11}$ #/kWh. Results from phase 1 with an empty SCR and a regenerated DPF show PN10 emissions varying from $1{,}74 \times 10^{11}$ to $4{,}16 \times 10^{11}$ #/kWh. The results of phase 2, with a system upgraded with the EHC, an empty SCR and regenerated DPF vary from $2{,}38 \times 10^{10}$ to 1.34×10^{11} #/kWh.

HVO on-road tests from phase 1 show results varying from $2{,}86 \times 10^{11}$ to $5{,}37 \times 10^{11}$ #/kWh. In addition, the testing with e-diesel conducted on phase 2 of the project achieved $9{,}88 \times 10^{10}$ to $1{,}03 \times 10^{11}$ #/kWh. In both cases, this is within the range observed on market diesel.

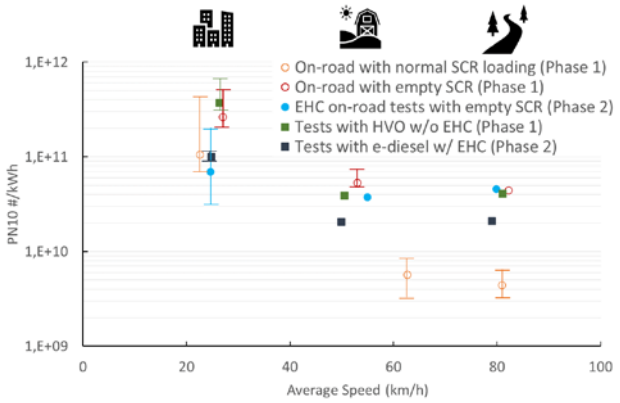


Figure 6. Summary of PN10 emissions of phase 1, phase 2 and testing with sustainable renewable fuels.

Ammonia (NH_3) and nitrous oxide (N_2O) emissions

As described in section 4, the vehicle was equipped with a PEMS system able to measure NH_3 and N_2O. In general, all tests conducted in phases 1 and 2 showed extremely low ammonia emissions. This is mainly due to the system being equipped with ammonia slip catalysts after each SCR. Phase 1 results have been published and can be found in previous publications [6 - 8].

Regarding N_2O emissions, these emissions occur due to unselective catalytic reactions within the DOC or even the ammonia slip catalyst via unselective oxidation of unreacted NH_3. As previously reported [6 – 8], the N_2O is produced throughout the length of the trips. Figure 7 shows the summary of N_2O emissions for phases 1 and 2 of the project. The resulting urban emissions from on-road testing with normal SCR loading on phase 1 of the project vary from 58 to 78 mg/kWh. In rural operation the N_2O emissions varied from 42 to 68 mg/kWh and in motorway operation from 27 to 40 mg/kWh. The N_2O urban emissions achieved with an empty SCR in phase 1 varied from 18 to 59 mg/kWh, rural emissions from 19 to 37 mg/kWh and in motorway driving from 16 to 58 mg/kWh.

In phase 2, the urban N_2O emissions achieved with an empty SCR ranged from 65 to 87 mg/kWh, with the ISC test achieving rural N_2O emissions of 25 mg/kWh and 47 mg/kWh in motorway operation.

N_2O urban emissions from the testing with HVO in phase 1 vary from 54 to 106 mg/kWh. There was one in-service conformity test with N_2O urban emissions of 196 mg/kWh. This test is considered an outlier and

further analysis need to be conducted to understand what could have caused these higher N_2O emissions. The N_2O urban emissions from the e-diesel testing in the project's phase 2 vary from 89 to 106 mg/kWh.

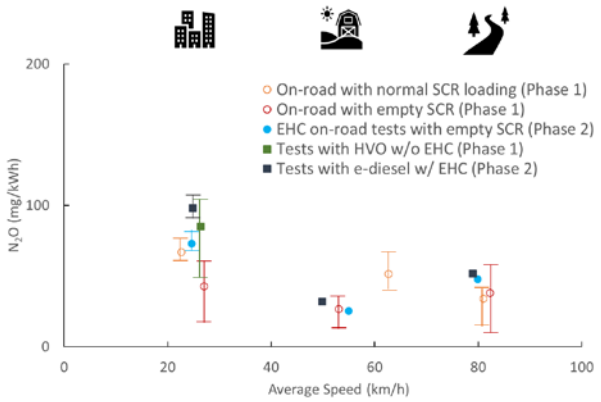


Figure 7. *Summary of N_2O emissions of phase 1, phase 2 and testing with sustainable renewable fuels.*

Well-to-Wheel CO_2 emissions reductions

From the beginning of the project, the intention was to implement an emissions control system which would impact as low as possible the WtW CO_2 performance of the vehicle. Phase 1 of the project kept this impact to less than 3% on average. For phase 2, the calculation of the fuel consumption/CO_2 included in Figures 8 and 9 does not include the power required to use the EHC. This is the case for both diesel and e-diesel calculations, so it is not impacting the fuel comparison. However, the external power required for the EHC to be used within an in-service conformity test has been calculated to be about 1%.

It is important to note that the CO_2 emissions vary within the on-road tests due to the many factors found on the road, including traffic conditions, ambient temperature, road closures or driver dynamics. The average of the CO_2 emissions of the tests has been identified as the best approach to compare the results.

Figure 8 shows the average Tank-to-Wheel CO_2 emissions of urban and in-service conformity tests at ambient temperatures between 4 to 23 °C. All tests have been conducted with 10% payload, as the data available for this condition was larger.

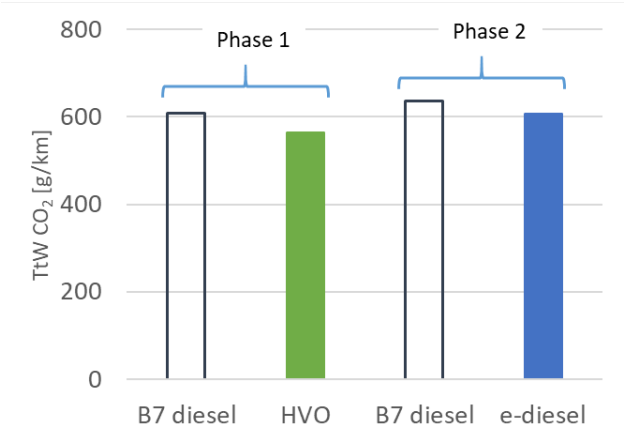


Figure 8. Average TtW CO_2 emissions of urban and in-service conformity tests with conventional and sustainable renewable fuels

Figure 9 shows the results of the Well-to-Wheel CO_2 emissions from the analysis conducted using the JEC version 5 methodology and pathway assumptions [11]. The WtW methodology estimates the energy use and GHG emissions in the production of a fuel and its use in a vehicle. Results show substantial WtW CO_2 reductions can be obtained by using this approach.

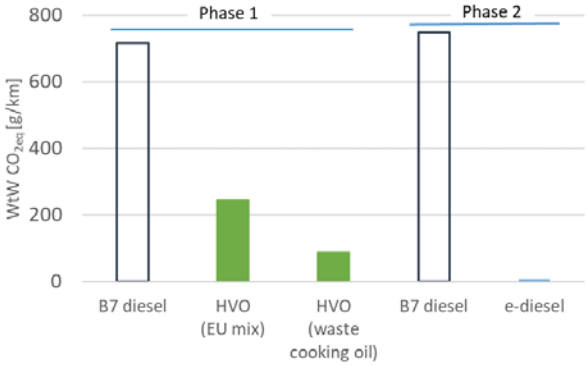


Figure 9. WtW CO_2 emissions reductions

Results show that HVO can reduce the WtW CO_2 emissions up to 89% with respect to B7 diesel if the feedstock used is waste cooking oil. Using the HVO mix found within the EU reduces the emissions up to 70%.

E-diesel used within the current study achieves 99% WtW CO_2 emissions reduction.

8. Conclusions

This work summarised the ultra-low pollutant and Well-to-Wheel (WtW) CO_2 emissions of an demonstrator N3 (long-haul) vehicle with an advanced emission control system and in 2 project phases.

The vehicle was equipped with a state-of-the-art emission control system including close-coupled

components. The vehicle was tested with conventional and sustainable renewable fuels and all data presented relates to on-road testing.

The results show ultra-low pollutant emissions on the vehicle in both phases of the project.

While significant cold-start NOx emissions reductions are achieved in phase 2 of the project, the phase 1 system (without the EHC) already achieves very low NOx emissions when the SCR systems are used with normal ammonia load at the beginning of the test.

PN emissions for all cases are very low. However, test results indicate that cold-start remains the main event for the particulates. These pollutant emissions reductions are confirmed when the vehicle is tested with sustainable renewable fuels.

Furthermore, regarding WtW CO_2 emissions, results show significant reductions can be achieved by the use of sustainable renewable fuels. It is important to note that HVO is already available in several European countries and such WtW CO_2 emission reductions can be achieved by the current in-use vehicle fleet. The e-diesel shows potential for further reductions almost reaching CO_2 neutrality on a WtW basis.

Based on the ultra-low pollutant emissions achieved through the combination of close-coupled catalysts as well as the use of sustainable renewable fuels contributing towards very low WtW CO_2 emissions, internal combustion engined heavy-duty vehicles will continue to support a sustainable European economy for the next decades.

9. Acknowledgement

The authors would kindly like to thank the members of AECC for supplying the catalyst and filter parts and for their highly valuable contributions to this study; as well as the International Platinum Group Metals Association (IPA) and Corning Inc. for the financial support. We also like to thank NESTE and Aramco for supplying the sustainable renewable fuels for this study. Thanks to Daimler Trucks for providing the basic production truck and FEV for their continuous support during the development of this project.

10. References

[1] European Commission, ‘The European Green Deal’, COM(2019) 640 final, 2019

[2] European Commission, ‘'Fit for 55': delivering the EU's 2030 Climate Target on the way to climate neutrality’, COM(2021) 550 final, 2021

[3] European Commission, ‘Commission Work Programme 2021’, COM(2020) 690 final, 2020

[4] European Commission, ‘Commission work programme 2022’, COM(2021) 645 final, 2021

[5] European Commission, ‘Sustainable and Smart Mobility Strategy – putting European transport on track for the future’, COM(2020) 789 final, 2020

[6] Mendoza Villafuerte, P. et al.; ‘Ultra-Low NOx Emissions with Close-Coupled Emission Control System on a Heavy-duty Truck Application’, 30th Aachen Colloquium Sustainable Mobility 2021, 2021

[7] Mendoza Villafuerte, P. et al.; ‘Ultra-Low NOx Emissions with a Close-Coupled Emission Control System on a Heavy-Duty Truck Application’, SAE Paper 2021-01-1228, 2021

[8] Selleri, T.; et al. Measuring Emissions from a Demonstrator Heavy-Duty Diesel Vehicle under Real-World Conditions—Moving Forward to Euro VII. Catalysts 2022, 12, 184

[9] NESTE Renewable Diesel Handbook, https://www.neste.com/sites/default/files/attachments/neste_renewable_diesel_handbook.pdf

[10] C. Ternel, A. Bouter, J. Melgar, “Life cycle assessment of mid-range passenger cars powered by liquid and gaseous biofuels: Comparison with greenhouse gas emissions of electric vehicles and forecast to 2030”, Transp. Res. Part D Transp. Environ. 2021, 97, 102897, https://doi.org/10.1016/j.trd.2021.102897.

[11] M. Yugo, V. Gordillo, E. Shafiei, A. Megariti, “A look into the life cycle assessment of passenger cars running on advanced fuels”, In Proceedings of the SIA Powertrains & Power Electronics Conference, Paris, France, 9–10 June 2021

[12] https://www.scania.com/content/dam/group/press-and-media/press-releases/documents/Scania-Life-cycle-assessment-of-distribution-vehicles.pdf

[13] M. Prussi, M. Yugo, L. De Prada, M. Padella, R. Edwards, “JEC Well-To-Wheels Report v5”, EUR 30284 EN, Publications Office of the European Union: Luxembourg, 2020, JRC121213, ISBN 978-92-76-20109-0, https://doi.org/10.2760/100379

[14] Demuynck, J. et al.; ‘Advanced Emission Controls and Sustainable Renewable Fuels for Low Pollutant and CO2 Emissions on a Diesel Passenger Car’. Sustainability 2021, 13, 12711, 2021.

Ammonia powertrain for a carbon free mobility

C. Dumand[1], C. Mounaïm-Rousselle[2], P. Gaillard[3], E. Gérard[4], J. Dedeurwaerder[5], J. Op de Beeck[5]

1: Stellantis, Technical Center of Vélizy, Route de Gisy, 78140 Vélizy-Villacoublay, France
2: PRISME, Université d'Orléans, 8 Rue Léonard de Vinci, 45072 Orléans, France
3: Aramco Fuel Research Center, 232 avenue Napoléon Bonaparte, 92500 Rueil-Malmaison, France
4: Plastic Omnium Clean Energy Systems Research, ZAC de Bois de Plaisance, 214, avenue de la Mare Gessart, 60280 Venette, France
5: Plastic Omnium Clean Energy Systems Research, Rue de la fusée 98, 1130 Brussels, Belgium

Abstract: Limiting global warming to 1,5°C is the common goal of the worldwide economies. On this basis Europe has launched its Green Deal, and the European Commission has proposed its Fitfor55 Program reducing the tank to wheel CO_2 emissions from transport by 55% in 2030, and by 100% in 2035.

Meeting such Tank to Wheel (TtW) emissions requires carbon free energy carriers for all type of mobile applications.

In line with the focus of this year SIA Powertrain and Energy conference on passenger cars and all types of commercial vehicles, this paper will describe the use of ammonia as a carbon free fuel.

All aspects from production of ammonia, through its transport and its distribution to the service station are considered. Then the storage of ammonia onboard the vehicle and its use in the vehicles' powertrain are laid out and described.

The ammonia eco-system is compared with other carbon free powertrain solutions in terms of overall energy efficiency, CO_2 emissions and Total Cost of Ownership (TCO). An example of Light Commercial Vehicle (LCV) application is detailed in this article.

Keywords: Ammonia, thermal engine, zero emission, zero CO_2

1. Introduction

1.1 Tank to wheel CO2 emission regulations evolution

Fuel economy standards are evolving and becoming more and more stringent in most of the regions of the world. The European Commission has launched its Fitfor55 program, sharpening its CO_2 requirements to a reduction of 55% compared with the 2021 value). In 2035 a CO_2 emission reduction of 100% is proposed, which will then ban all powertrains with CO_2 emissions (Figure 1).

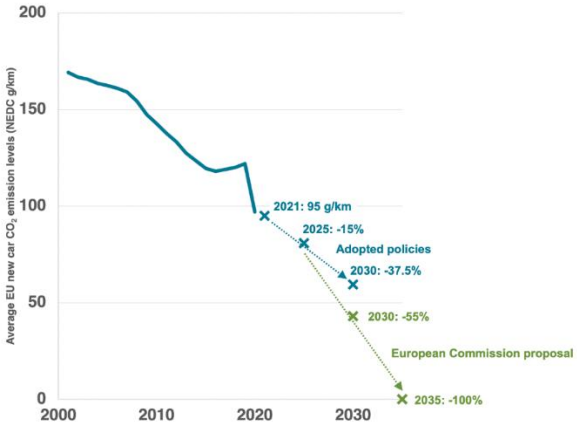


Figure 1: CO_2 emissions standard evolution for passenger cars according EC Fitfor55 proposal [1]

On top of that, since 2020 on-board fuel efficiency measurement equipment has been installed in all vehicles sold. By this means fuel efficiency in all driving conditions can be determined and analysed. Analysis of the first set of measured fuel efficiency data is currently being analysed in Europe and the results may lead to a further evolution of the regulations.
This represents a strong challenge for all OEMs to optimize the powertrains for whatever driving conditions occur in real life.

1.2 Zero CO_2 vehicle enablers and challenges

A steep uptake of zero emission vehicles is mandatory. Latest by 2035, 100% of the vehicles in Europe are required to be Tank-to-Wheel zero CO_2 emission.
For all zero emission technologies, the challenge remains to cover sufficient range, and to have a guaranteed available energy distribution network.
The cost and complexity have to be kept as low as possible, to maintain vehicle affordability for most car drivers.

2. Ammonia thermal engine

Although the idea of using ammonia as a fuel dates back almost 100 years as recently summarized in the review by Mounaïm-Rousselle et al. [2,3], few studies have been carried out on engines in operation with the objective of using ammonia only. within the framework of the H2020 project, ARENHA (https://arenha.eu/), several studies have been carried out on single-cylinder engines based on standard engines in order to evaluate the feasibility of an 'all' ammonia conversion [4,5]. The intrinsic properties of ammonia combustion such as its ignition resistivity and low flame speed made it necessary to choose only a spark ignition engine.

3 engines were selected to perform experiments and to evaluate what load with acceptable stability (%) could be reached as a function of different engine speeds to guarantee the good operating conditions and sufficient energy output. The engines characteristics, summarized in Table 1 are, overall, two spark ignition engines based on a classic design (EP6), i.e. with a tumble motion, one limited to the usual compression ratio (10.5) and the other allowing a variation of the compression ratio from 11.75 to 14 but with a long stroke (LS) and a diesel type engine (DV6) whose ignition is helped by the addition of a spark plug on the cylinder head with a compression ratio varying from 14 to 17.

Table 1. Main characteristics of 3 engines	Spark ignition Engine (EP6)	Long Stroke Spark ignition Engine (LS)	Spark assisted Diesel engine (DV6)
Displaced volume (l)	0.4	0.54	0.39
Stroke (mm)	85.8	115	88.3
Bore (mm)	77	77	75
Connected rod length (mm)	138.5	177	136.8
Compression ratio	10.5	11.75 to 14	14 to 17

An example of results as a function of the engine characteristics is presented in Figure 2 to highlight the difference between two engine architectures at 1000 rpm. With standard EP6, it is possible to run with ammonia only for medium load but impossible to select operating conditions (equivalence ratio and intake conditions) to run at low load as it can happen when restarting or slowing down a vehicle. For that, small content of hydrogen has to be added in the fuel to help ammonia combustion.

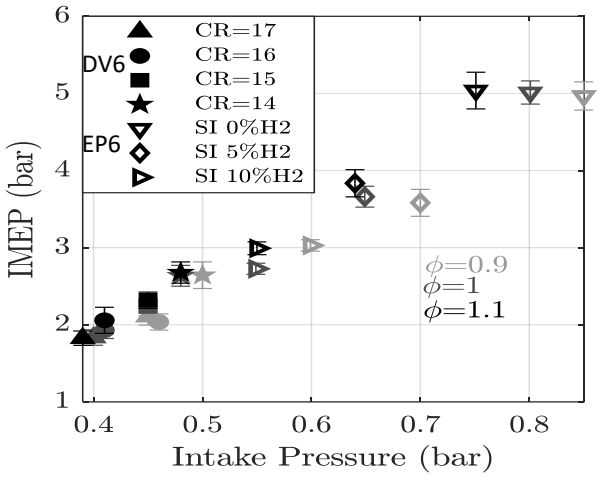


Figure 2: example of low load limits for EP6 and DV6 as a function of CR and equivalence ratio at 1000 rpm.

In the case of diesel architecture, it is evident that a good improvement of NH_3 combustion with CR increase is obtained despite of 'diesel' type flow (swirl motion), which allows to extend the low load limits (less than 2 bars of IMEP). This limit is affected slightly by the air/fuel ratio but consider a lambda of 1.1 limits a little the high ammonia consumption rate related to its low energy content compared to gasoline. The main improvement of the overall engine performances was obtained also at different engine speeds from 650 to 2000 rpm [5]. The use of a non-standard engine (LS) allows to decrease the needs of hydrogen doping but a ratio of 14 enables to reach only 3.5 b of low load (against 2.6b for DV6 with the same compression ratio). It has to be noted from these studies that the indicated efficiency is in the same order than those obtained by gasoline fuelled engines.

After the flexibility of the operation of an ammonia engine, the other most important point remains the pollutant emissions, i.e. nitrogen-based ones and ammonia slip. Some examples of typical emission tendencies are shown in Figure 3. In Figure 3a the effect of engine architectures is compared for same compression ratio (CR14) : as expected due to the nitrogen-fuel route, NOx reaches a maximum for lean mixture (between 0.8-0.9), with slightly lower emissions with diesel architecture. But from all these studies, it was concluded that the use of classical diesel bowl induces a strong drawback: a very important NH_3 slip due to NH_3 trapping, with as a function of the air/fuel mixture and the compression ratio, a parallel H_2 emission due to in-cylinder ammonia decomposition. In Figure 3b, NO, NO_2 and N_2O are plotted as a function of the equivalence ratio for the S engine at 2 different CR : NOx emissions are composed roughly by NO, affected by the CR value. N_2O remains below 100 ppm, value reached for lean mixture. This value could not be neglected as it

corresponds to an equivalent 3% of CO_2 as warming impact.

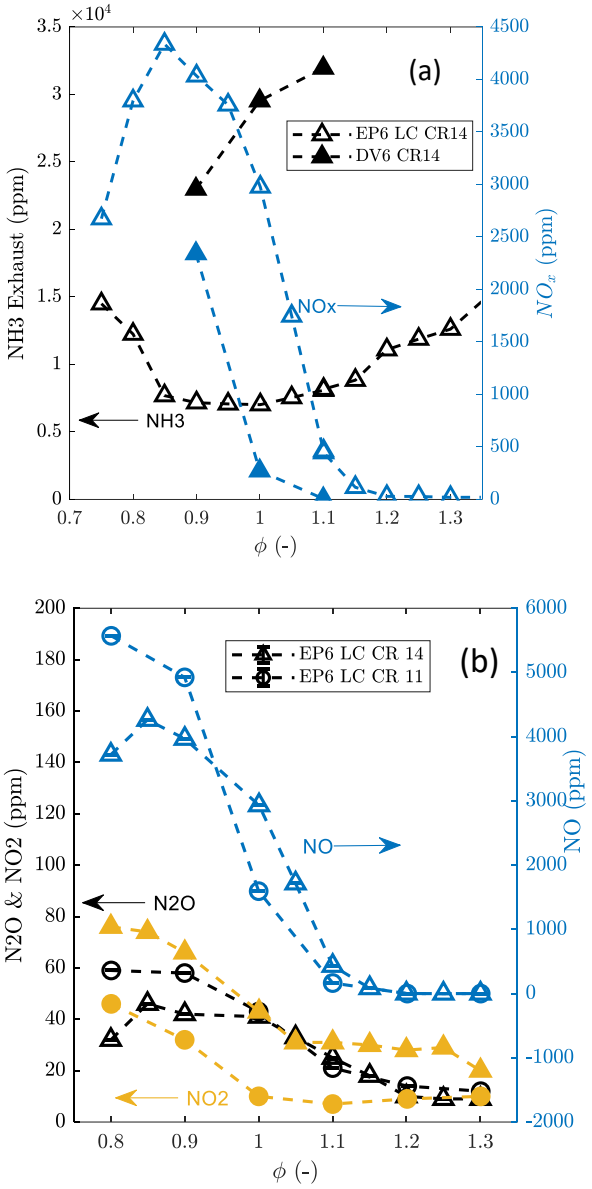


Figure 3. Example of exhaust emissions as a function of equivalence ratio for different engine architecture and compression ratio. (a) unburnt NH_3 and NOx, (b) nitrogen species.

In conclusion, it is possible to run with ammonia as fuel in standard engines: in SI architectures, it is necessary either to add hydrogen (by onboard cracker) to the engine during the various starting phases [6] or to increase the compression ratio considerably, in Diesel architectures, spark igniter has to be added and optimisation of combustion chamber is required to avoid too strong ammonia slip before the post-treatment system. The indicated efficiency is the best around an equivalence ratio of 0.9 which reduces the fuel consumption but induces higher NOx emissions (even N_2O). Therefore, the best compromise for operating conditions has to be defined and selected as a function of exhaust post-treatment technology.

3. Ammonia Storage System and autonomy

3.1 Energy density

The energy density of carbon free fuels is quite different from the energy density of conventional fuels. Additionally, the powertrain efficiency of a battery electric vehicle is more than 2 times higher than the efficiency of a powertrain based on a combustion engine on WLTC. This has a significant effect on the quantity of energy to store onboard the vehicle.

Therefore, it is crucial to include the powertrain efficiency factor in the energy storage system design and base the vehicle concept on a desired autonomy.

Underneath a comparison chart of various energy storage volumes required for a vehicle autonomy of 100 km.

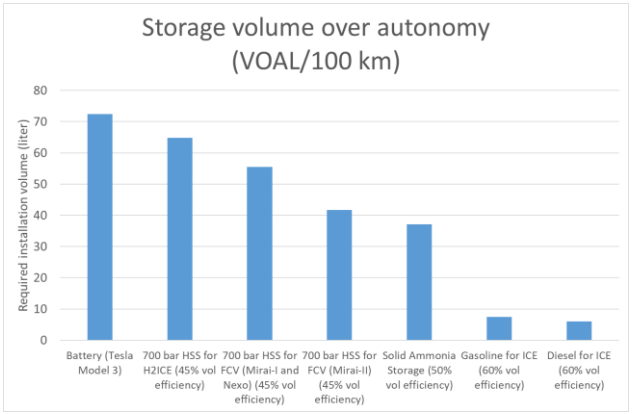


Figure 4: Required car body volume over vehicle autonomy on WLTC [7]

The chart in Figure 4 takes into account that the volume available in a car body is never exactly the optimal shape for the energy storage system. On batteries a distance is to be kept to adapted and fit standard cell modules. 700 bar hydrogen vessels have a cylindrical shape and can therefore not go in all corners on a vehicle. Conventional gasoline and diesel tanks have a rounded shape as well.

The battery takes up the largest space for a given autonomy. Using hydrogen as a fuel and this in combination with the most efficient fuel cell technology can almost halve the required energy storage space compared to a battery.

Storing Ammonia on a solid structure in combination with a conventional combustion engine further reduced the required volume for 100 km autonomy.

3.2 Autonomy on highway

Vehicle integration of batteries and 700 bar H_2 compressed tanks in terms of mass and volume is one the main challenge to ensure reasonable vehicle ranges to these technologies.

In Figure 5, an assessment of the volumetric energies between solid NH_3 and 700 bar H_2 storages in the vehicle tanks is performed, but also the residual available energies at the wheels considering the losses for highway conditions. For comparison, NMC batteries are also included.

We can notice that the solid NH_3 storage is quite competitive compared to the other solutions:

- at the tank location, volumetric energy equals for NH_3 1.5kWh/L, 0.72 kWh/L for 700bar H_2 and 0.3kWh/L for NMC battery.
- at the wheels, NH_3 keeps a margin over the other solutions with 0.54 kWh/L vs 0.25 kWh/L for the other solutions.

It makes the NH_3 solid storage a competitive candidate in terms of vehicle volume integration versus the achievable range, that could reach more the double range with the same storage volume.

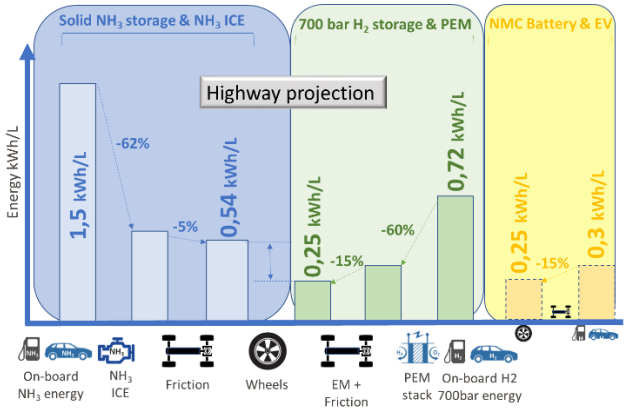


Figure 5: Volumetric energies in kWh/L for solid NH_3 and 700 bar H_2 storages

4. Ammonia retail cost

With an annual production of 180 million tons and 120 ports already equipped with ammonia trading facilities [8], ammonia is a widely used and traded commodity, which, in its liquid form, at 20 bar and ambient temperature or atmospheric pressure and - 33°C, has a 50% higher volumetric energy density than liquid hydrogen, making ammonia a convenient hydrogen carrier but also an alternative decarbonated fuel to hydrogen. Ammonia is produced from the combination of hydrogen and nitrogen, through the century-old Haber Bosch process, and its production cost depends significantly on the hydrogen cost production, making low-cost green hydrogen producing regions potential cost competitive green ammonia exporters. In MENA (Middle-East-North Africa) countries, green ammonia production cost is anticipated to be 400USD/ton by 2030 [9], and its shipping transportation cost to EU can be assumed to be 50USD/ton [10].

Figure 6 shows the retail cost breakdown of green ammonia imported from MENA region to France, assuming distribution cost equivalent to gasoline and Diesel fuels of 0.2EUR/L [11], an energy-based energy tax (TICPE) equivalent to the tax on ED95 [12], the greenest available road fuel [13], and 20% VAT. With a cost of 175EUR/kWh, equivalent to 0.9EUR/kgNH_3, ammonia retail cost is potentially comparable to hydrogen at 6EUR/kgH_2, home charging [14] and Diesel fuel without considering the powertrain efficiency.

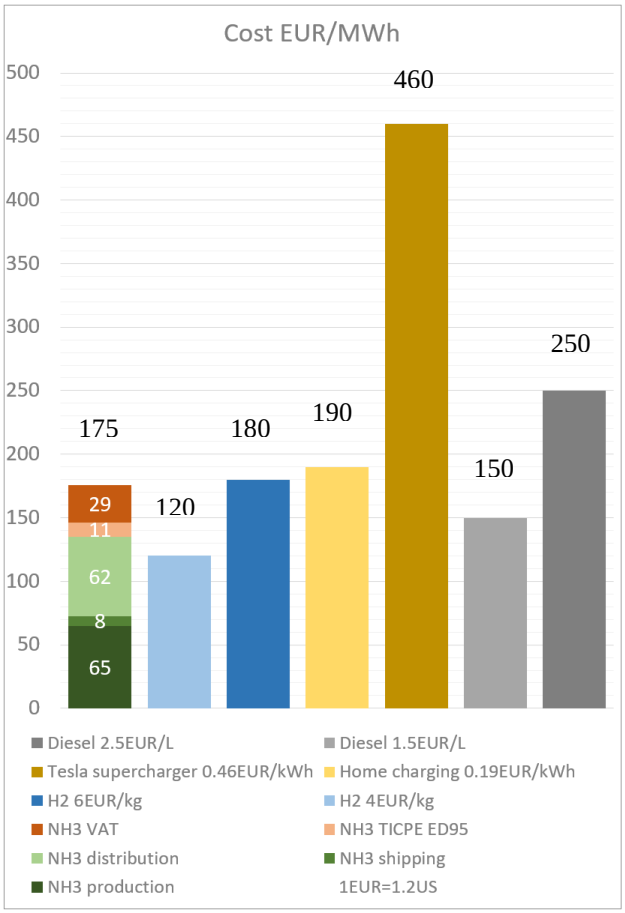


Figure 6: 2030 energy retail cost

5. TCO evaluation

We present in this section a first assessment of the Total Cost of Ownership of the NH_3 ICE technology versus the current Diesel ICE but also versus a Battery Electric Vehicle (BEV) and a Plug-In Fuel Cell

Electric Vehicle (FCEV) for a Light Commercial Vehicle (LCV) type.
Indeed, for commercial vehicle application, the TCO is one of the main purchasing drivers for the customer. Nonetheless, TCO estimation is a complex exercise because of all the prices that will have a major impact on the results and are not well known for 2030 as the future energy prices (H_2, fast charging, etc.), the future battery ones, the maintenance costs (battery of fuel cell replacement mandatory), the vehicle residual values, … The calculations are done with the current estimations and will be continuously refined with the carrier and technology maturity improvement.
We opt for a 500 km WLTC range hypothesis for the NH_3 ICE, BEV and FCEV. Diesel will not really be impacted by the range because of the low-cost storage system compared to the other technologies.
We also proceed to some energy cost swaps.
In Figure 7 & Figure 8 we compare the TCO for WLTC and highway usages, for 120 000 km on 4 years leasing base.
We can notice that the NH_3 ICE stays competitive compare to the Diesel reference @2.5€/L for all the usages.
Because of their high efficiencies on WLTC, BEV and FCEV have the lowest energy costs except for BEV if we assume a fast charge @0.46€/kWhe.
On highway, because of the BEV/FCEV decreased efficiencies compared to WLTC, the NH_3 ICE appears to be a quite competitive solution compared to the other candidates.

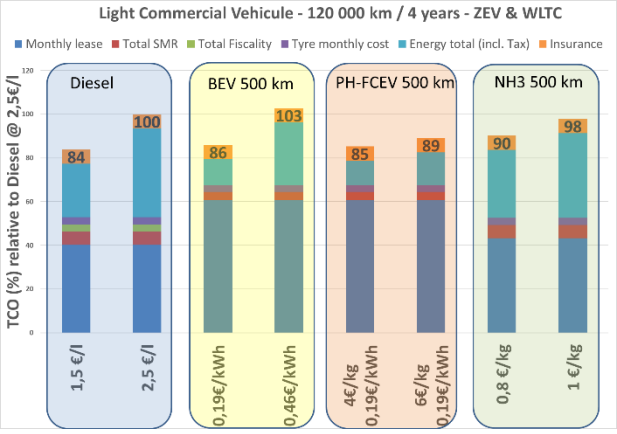


Figure 7: TCO evaluation for ZEV & WLTC usage

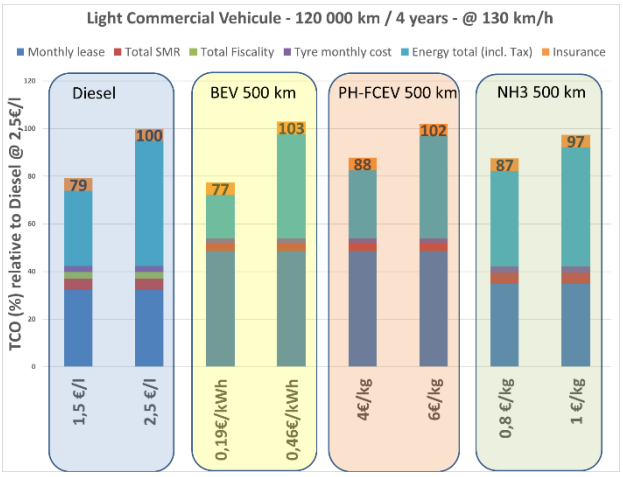


Figure 8: TCO evaluation for highway @130 km/h

6. Conclusion

European Commission and European countries adopted politics mitigating greenhouse gases promoting electrified and hydrogen powertrains. Nevertheless, in future, other decarbonized energies and powertrains could be used beside BEV and FCEV. We demonstrated in this article that ammonia as a fuel presents some benefits in energy density and TCO compared to conventional decarbonized powertrains.
Moreover, ammonia could be used directly in well-known ICE and hybridized powertrains. Those technologies are robust and cheap compared to BEV and FCEV.
Authors also expect some benefits in Life Cycle Assessment of this ammonia and ICE powertrain compared to other decarbonized powertrains, lowering the needed amount of rare metals. This point will be assessed in the coming months.
Further research and innovation work remain to make this ammonia fuel a concrete alternative:

- the combustion processes in engine must be further studied to be sure to cover all driving conditions,
- the aftertreatment system (NO_x, N_2O & NH_3) must be designed and validated,
- the on-board ammonia storage system using salt and adsorption, must be safe in any using case.

Major thresholds for this technology development will be to see ammonia becoming a worldwide green energy carrier and decarbonized fuel for shipping industry. In those conditions, local retailing will become realistic also for road transport.

7. Acknowledgement

This study based on engine experiments has received funding from the European Union's Horizon 2020 research and innovation programme under grant agreement No. 862482 (ARENHA project).

8. References

[1] European Commission, Communication from the Commission to the European Parliament, the Council, the European Economic and Social Committee and the Committee of the Regions, 'Fit for 55': delivering the EU's 2030 Climate Target on the way to climate neutrality, July 14th 2021

[2] C. Mounaïm-Rousselle, P Brequigny, Ammonia as fuel for low-carbon spark-ignition engines of tomorrow's passenger cars, Frontiers in Mechanical Engineering 6, 70, 08 September 2020 | https://doi.org/10.3389/fmech.2020.00070,

[3] C. Mounaïm-Rousselle, P. Bréquigny, A. Valera-Medina, E. Boulet, D. Emberson, T. Løvås, Ammonia as Fuel for Transportation to Mitigate Zero Carbon Impact, in Engines and Fuels for Future Transport (2022), Springer pp. 257-279, hal-03501644,

[4] C. Mounaïm-Rousselle, P. Brequigny, C. Dumand, S. Houillé, "Operating Limits for Ammonia Fuel Spark-Ignition Engine", Energies (2021), Special Issue Ammonia as an Energy Carrier, 14(14), pp. 4141, https://www.mdpi.com/1996-1073/14/14/4141

[5] C. Mounaïm-Rousselle, A Mercier, P Brequigny, C Dumand, J Bouriot, Performance of ammonia fuel in a spark assisted compression Ignition engine, International Journal of Engine Research (2021), hal-03519268

[6] A. Mercier, C. Mounaïm-Rousselle, P. Brequigny, J. Bouriot, C. Dumand, Improvement of SI engine combustion with ammonia as fuel: Effect of ammonia dissociation prior to combustion, Fuel Communications, Volume 11, 2022, 100058, https://doi.org/10.1016/j.jfueco.2022.100058SIA

[7] Position Paper on Hydrogen Combustion Engine, SIA, Paris, 2022

[8] Ammonfuel – an industrial view of ammonia as a marine fuel. TOPSOE report, August 2020 https://www.topsoe.com/hubfs/DOWNLOADS/DOWNLOADS%20-%20White%20papers/Ammonfuel%20Report%20Version%2009.9%20August%203_update.pdf

[9] IEA Global Hydrogen Review 2021, https://iea.blob.core.windows.net/assets/3a2ed84c-9ea0-458c-9421-d166a9510bc0/GlobalHydrogenReview2021.pdf

[10] Argus Ammonia, Argus Media Group, September 2018,https://www.argusmedia.com/-/media/Files/sample-reports/argus-ammonia.ashx?la=es&hash=BC748B7D73D15785ECF389E958403C2D4C4EBEEC

[11] Décomposition des prix des carburants, Ufip Énergies et Mobilités, May 29th 2022, https://www.energiesetmobilites.fr/actualites/decomposition-des-prix-des-carburants

[12] Filière française des biocarburants, Rapport d'information n° 136 (2019-2020), Sénat, Novembre 20th 2019, https://www.senat.fr/rap/r19-136/r19-136_mono.html#toc64

[13] JEC Well-To-Wheels report v5. EUR 30284 EN, Publications Office of the European Union, Luxembourg, 2020, ISBN 978-92-76-20109-0, doi:10.2760/100379, JRC121213

[14] Electricity prices for household consumers first half 2021, Eurostat, 2021, https://ec.europa.eu/eurostat/statistics-explained/images/4/42/Electricity_prices_for_household_consumers%2C_first_half_2021_v5.png

9. Glossary

BEV:	Battery Electric Vehicle
CR:	Compression Ratio
FCEV:	Fuel-Cell Electric Vehicle
ICE:	Internal Combustion Engine
IMEP:	Indicated Mean Effective Pressure
LCV:	Light Commercial Vehicle
MENA:	Middle East and North Africa
NH3:	Ammonia
RPM:	Rotation per Minute
SI:	Spark Ignition
TCO:	Total Cost of Ownership
TtW:	Tank to Wheel
VAT:	Value-Added Tax
WLTC:	Worldwide Harmonised Light vehicles Test Cycle
WLTP:	Worldwide Harmonised Light vehicles Test Procedure
ZEV:	Zero Emission Vehicle

16 JUNE 2022

FUEL CELL AND HYDROGEN STORAGE

Optimization of PEMFC cold-start strategy using multi-physical real-time capable system simulation

C. Pötsch[1], D. Ritzberger[1], J. C. Wurzenberger[1]

1: AVL List GmbH, Hans-List-Platz 1, A-8020 Graz

Abstract: Cold-start from sub-freezing temperatures is an immanent technical challenge for PEM fuel cell systems. The process water from the electrochemical reaction forms liquid water which further freezes in the membrane and the adjacent reaction layers. Simultaneously, the system is heated by system losses. If the catalyst layer is covered by ice before the system temperature is above the freezing point, the electrochemical reaction stops. A self-sustained system cannot recover from this state and ice formation can cause serious structural damage.

The paper presents a multi-physical, real-time capable system level simulation model for PEMFC systems. The stack model features 1D gas channel flow and a 1D transient thermal model. Cell performance is described by a reduced dimensionality electrochemical model. For cold-start simulation, the transient water content model is extended to account for frozen water in the membrane and liquid and frozen water in the catalyst layer and GDL. The impact of frozen water is consequently considered in the performance model.

In a computational study, different control strategies for cold-start from sub-freezing conditions are investigated. In four case studies, the impact of varying start current, external heat, dry purge at shut-down and active voltage control is shown. The analysis documents the impact on cold start characteristics, heat-up time and the system energy balance.

Keywords: Fuel cell, cold start, simulation

1. Introduction

In PEM (Polymer Electrolyte Membrane) fuel cells, hydrogen and oxygen are supplied at two separate electrodes (anode & cathode). The active reaction and diffusion layers which separate the reactants feature a sandwich design, as shown in Figure 1. In the core, there is the solid membrane electrolyte which acts as separator for gas species and electron transfer while allowing the conduction of protons (i.e. H^+). The membrane also dissolves process water, which is crucial for the ionic conductivity of the membrane. This storage capacity opens the possibility for active water management.

On either side of the membrane, there are thin catalyst layers (CL) consisting of porous support structures holding dispersed platinum particles to enable the two essential half-reactions. At the anode, that is the oxidation of hydrogen, $H^2 \rightarrow 2{\cdot}H^+ + 2{\cdot}e^-$ and at the cathode the reduction of protons in the presence of oxygen, $2{\cdot}H^+ + 0.5{\cdot}O_2 + 2{\cdot}e^- \rightarrow H_2O$. Hence, the process water is generated in the cathode CL and needs to be removed from there. Therefore, it needs to pass the gas diffusion layers (GDL) located on the outside of the sandwich between the catalyst layers and the adjoined gas channels.

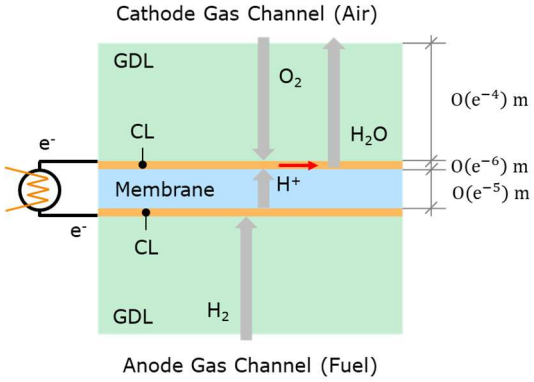


Figure 1: Schematic of the membrane electrode assembly (MEA)

1.1 Phases of cold start

When starting a PEM fuel cell at sub-freezing conditions, the water produced by the reaction can liquidize and further freeze inside the catalyst and gas diffusion layers. Simultaneously, the system is heated by process losses. It is crucial for a successful start that the heat-up is fast enough. Otherwise, the catalyst layer (which is the thinnest layer in the Membrane Electrolyte Assembly, MEA) is covered by ice before the system temperature reaches the melting point. In that case, the electrochemical reaction stops. A self-sustained system cannot recover from this state – it would require external heating or warm ambient conditions to recover. Needless to say, ice formation can cause serious structural damage in the fragile layers.

1.2 Cold start from sub-freezing conditions

The following section describes principle behaviours when starting a fuel cell at sub-freezing temperatures. For this purpose, two freeze start events at different start temperatures and galvanostatic stack operation are compared. Figure 2 shows a start from -15°C.

Current is applied at ~98 s, which causes a subsequent decay of cell voltage (a). The water formed in the electrochemical reaction accumulates in the membrane (c). When saturation is reached at ~102 s, liquid water forms and accumulates in the (cathode) catalyst layer, where it almost entirely freezes (d). The heat generated by process losses warms up the system, which is operated otherwise in adiabatic conditions (b). When the temperature approaches the melting point, there is a transition from ice to liquid water, which causes a residence phase of the temperature around 0°C. Due to the heterogeneous temperature distribution in the stack (1D model), the freezing and melting phases overlap. At ~128 s, the stack has entirely passed the freezing point. During the entire cold-start process, the CL reaches a maximum frozen water saturation of ~0.6, which is sufficiently low to sustain stack operation.

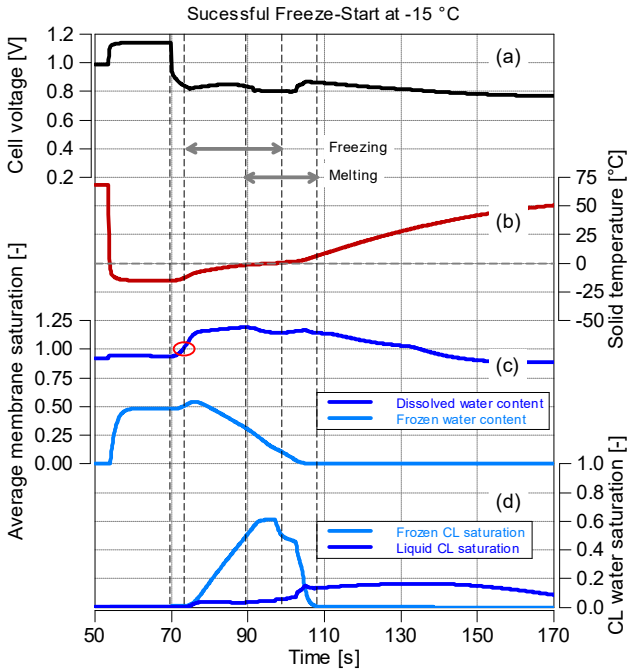


Figure 2: Successful cold start from -15°C

When starting the system at -25°C (Figure 3), the membrane water content and saturation in the CL (c)/(d) are initially similar to the previous case. However, ice formation continues as system temperature remains below the freezing point (b) for a longer period. From ~118 s onwards, when the CL water saturation exceeds ~0.7, a significant drop in the cell voltage is observed (a)/(d), which is caused by the increased transport and activation losses in the CL. Fate takes its course until the cell voltage drops to zero. At that point, the stack cannot generate any further electric power or heat.

The behaviour demonstrated above correlates qualitatively with the one observed in measurements, as e.g. reported in [1].

The case shown in Figure 3, with start temperature of -25°C and a current density of 0.417 A/cm² will serve as a reference case for further investigations of different measures to facilitate cold start.

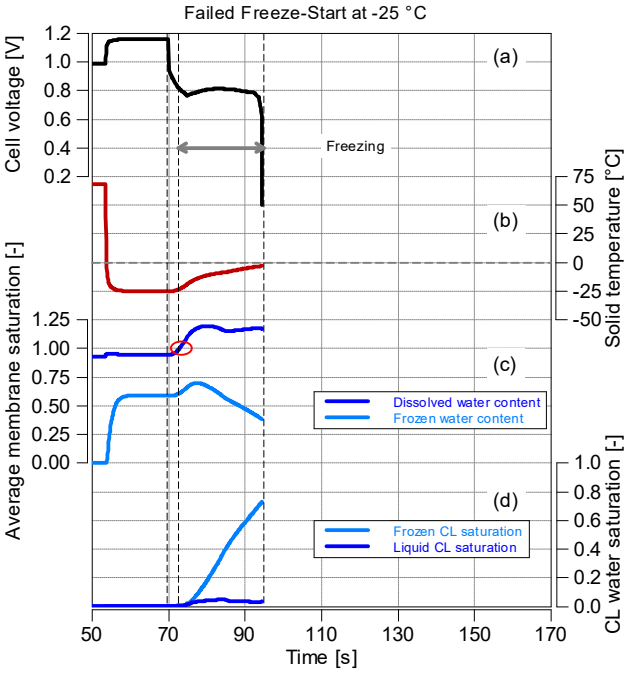


Figure 3: Failed cold start from -25°C

2. Simulation model

The models and workflows presented in this paper are implemented in the system simulation environment AVL CRUISE™ M [2].

2.1 System simulation platform

Fuel cell powered propulsion systems are a textbook example of a multi-physical system, comprising the following domains: Rotational mechanic components describe the driving resistances of the vehicle and the power flow from the motors to the wheels or propellors. An electrical network describes the power distribution between fuel cell, battery and e-motor and its resistances and losses. A liquid flow network covers needs on thermoregulation, cooling or heating different components. Fuel and air supply at the electrodes are described by a compressible gas flow network. The energy conversion in the fuel cell stack is modelled by an electrochemical fuel cell model, which is outlined below in further detail. Generic signal processing components are used to consider control functionalities.

2.2 Fuel cell stack model

The fuel cell stack component models the electrochemical processes, gas flow and thermal behavior in 0D, 1D or 3D resolution. To comply to hard real time constrains, prerequisite on the (virtual) testbeds, and to provide fastest simulation times in office, the gas flow in the electrodes is described in a

quasi-dimensional manner. The electrochemical conversion and transport processes in the MEA, together with the current vs. voltage characteristics are described by a thermodynamically consistent reduced dimensionality model. Herein, the model also considers transient water content, as well as cross diffusion of nitrogen, hydrogen and oxygen through the membrane and the related parasitic reactions. For details on the stack and electrochemical model please refer to [3] and [4].

The simulation of cold and freeze start events builds on a transient thermal model to describe the heat-up of the solid structure, a performance model to describe the energy split, and a detailed transient water content model. The related model extensions are outlined in detail in the following section.

2.3 Water content & cold start

The water content model comprises the relevant water balance, transport and phase change phenomena as schematically shown in Figure 4. In each of the three MEA layers, the model considers a liquid (dissolved) and a frozen water state. Further, it describes the mass transfers due to diffusive transport and capillary action between adjacent layers, as well as phase change processes (i.e. freezing and melting). The water content states (dissolved, liquid, frozen) impair the physical properties of the active reaction and diffusion layers i.e. conductivity, diffusion resistance and reactive surface area which consequently determines the overall fuel cell performance. In detail we have:

- The membrane humidification model calculates the water balance in the ionomer taking into account diffusion between the gas channels and the membrane, as well as electro-osmotic drag. At normal (warm) conditions, the membrane water is dissolved in the ionomer. At sub-freezing conditions, a part of the membrane water freezes (1) in Figure 4. The dissolved water content determines the membrane ionic conductivity and therefore ohmic loss. Frozen membrane water does not contribute to the ionic conductivity and thus it enhances ohmic loss. The frozen membrane water model is based on [1].
- When the membrane reaches saturation, due to cold and/or very humid conditions, liquid water forms and enters the (cathode) catalyst layer (2). At sub-freezing conditions, the water freezes (3). Liquid and frozen water in the CL hinder the diffusive transport in the porous layer and block the active surface area for the electrochemical reaction. This results in higher activation and transport losses in the CL.
- The model considers the transfer of liquid water in the porous structures of the catalyst and gas diffusion layers due to capillary action (4) and freezing of water in the GDL (5). Liquid and frozen water in the GDL block the diffusive gas species transport. At high GDL water saturation, water is dragged to the gas channels (6).

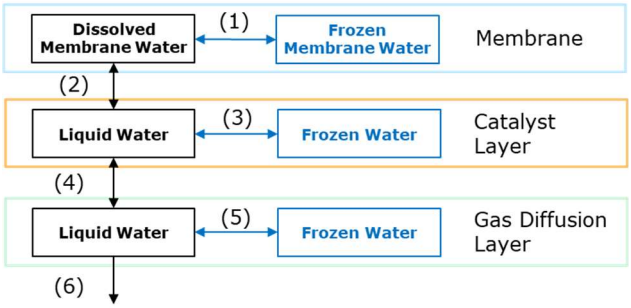


Figure 4: Water content states and transport mechanisms considered in the model

3. Case studies

In the following section, the cold start process of a PEM fuel cell system is investigated. For this purpose, four operating parameters are studied with respect to their impact on the cold start behaviour:

- Variation of current density
- External heating
- Dry purge during shut down
- Active voltage control

The cold start behaviour is assessed via cell voltage during the start sequence as first indicator for a successful or failed start. The second relevant aspect is the warm up duration, i.e. the time the system takes to reach operating temperature. Another relevant aspect for the system is the energy balance during start up, which defines the electric energy that needs to be consumed or stored in the battery.

3.1 Variation of current density

The value of the current is one of the main operating parameters during a PEMFC cold start. Therefore, it is also one of the most studied parameters in literature on the topic, e.g. [1], [5], [6]. As outlined in previous sections, a successful freeze start event is determined by the rate of water formation and rate of system warm up. In this regards, current and the rate of water formation are directly proportional as given by the stoichiometry of the electrochemical reaction. When assuming constant efficiency, the process heat generation would as well directly scale with the current. Under these assumptions, in a first approximation the value of the current would not affect the probability of success or failure, it would only determine the duration of the warm up process.

In reality, additional second order effects need to be taken into consideration. On the energy side, the system efficiency decreases with higher current. This

causes an enhanced internal heat generation which would be beneficial for cold start. On the water side, the effect of current is diverse. Faster water formation provides less time for storage and uniform distribution of the water in the MEA. Furthermore, the effect of the electro-osmotic drag (i.e. the transport of water from the anode to the cathode due to proton flow) increases with current, thus more water is transported to the cathode CL. These water transport effects would impede cold start at high current. Hence, the second order effects with respect to warm up and water management are counteracting.

The following case study investigates freeze start events at different ambient temperatures and current density values at otherwise constant conditions. The stack is operated adiabatic (only internal heat generation) and galvanostatic (defined current). Figure 5 compares two cases at the same start temperature (-25°C). The solid lines show results at high current density of ~0.417 A/cm², which corresponds to the reference case shown in Figure 3. The dashed lines show results for a reduced current density of ~0.29 A/cm². The lower efficiency at high current determines a lower cell voltage during start-up (a). The heat generation is expectedly enhanced at higher current which reflects in a faster temperature rise (b). The faster water generation at high current causes a faster membrane and CL saturation (c/d). While the frozen membrane water content declines faster due to higher temperature (c), the CL frozen water saturation (d) increases over proportional for the high current case, which causes a failed cold start at ~95 s.

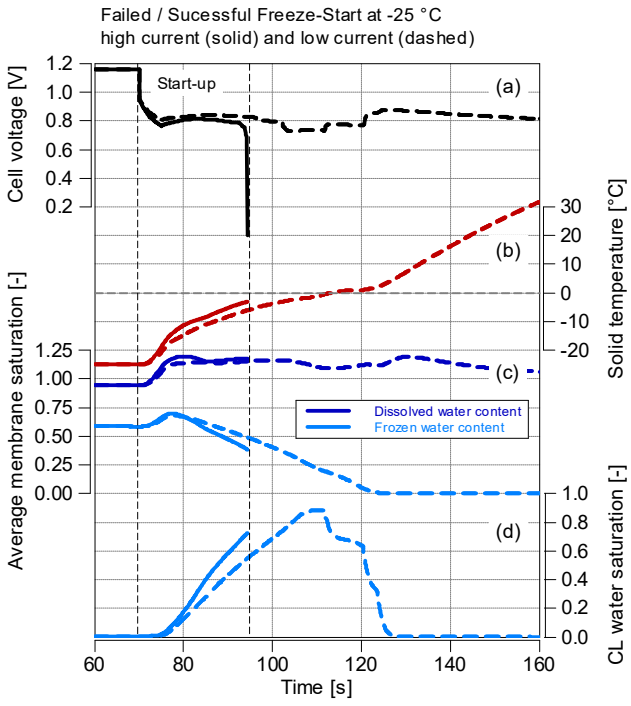


Figure 5: Freeze start at -25°C at different start current

The above results indicate that the second order effect of the water content overcompensates the impact of the enhanced heat generation due to reduced efficiency. The is qualitatively in line with the behaviour observed in measurements which is reported e.g. in [6].

The current value determines the heating velocity. To quantify the effect, Figure 6 shows a variation of start current at two different start temperature values. The figure at the top shows the minimum cell voltage that is observed during the start process. At high temperature (-15°C), no significant voltage drop is observed. The figure at the bottom shows the warm up time, i.e. the time the system takes to reach 20°C. At -15°C the system successfully starts at any given current, which allows to choose the value to reach the desired warm up rate. For the low temperature series (-25°C), a significant voltage drop is observed at current densities greater than 0.35 A/cm². This, the minimum warm up duration is limited at ~65 s by water generation and freezing.

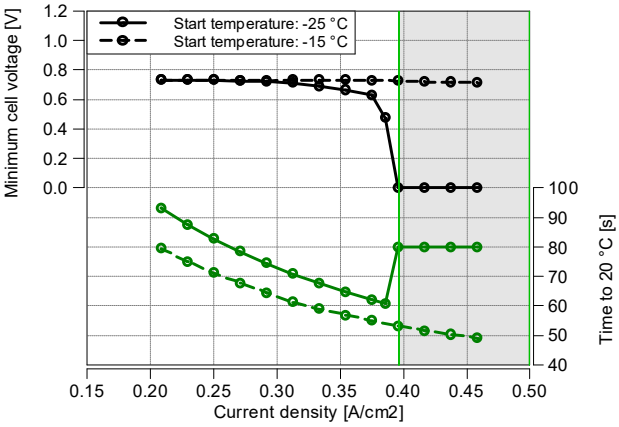


Figure 6: Variation of start current at different start temperature

3.2 External heating

An evident measure to facilitate the cold start capabilities of a fuel cell stack start is to apply electric heat from an external source. In the actual system, this can be achieved by installing an electric heater in the thermoregulation circuit upfront the stack which is electrically sourced e.g. from the battery of the fuel cell hybrid vehicle. For the present case study, an electric heater with a maximum power density of 750 W/m² is modelled, which corresponds to 1/10 of the nominal electric power density. Further, it is assumed that heat generation is equally distributed across the stack.

The effect of applying 750 W/m² external heat is compared to the reference case at -25°C in Figure 7. As expected, the temperature rise after the start is enhanced due to heating (b). This reflects in the lower frozen membrane (c) and CL (d) frozen water content. At the given operating conditions, the stack generates

~3750 to 4500 W/m² internal heat. The additional 750 W/m² of external heat are sufficient to sustain a successful start at -25°C.

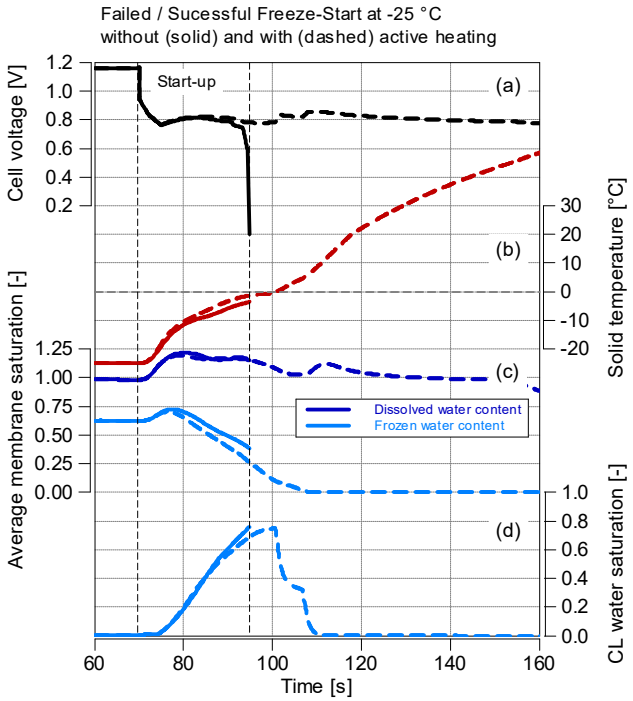


Figure 7: Freeze start at -25°C with and without external heating

The case study is extended to a wider range of operating conditions with respect to start temperature and external heat generation. Results for characteristic cold start values are shown in Figure 8 as a function of the two variation parameters. The figure at the top shows the minimum cell voltage during the start sequence. A value of 0.5 V is defined as a limit for a successful start. Applying an external heat source of 375 W/m² shifts the start temperature by ~5°C as indicated by the blue arrow in the top image. At the same time it reduces the warm up time from ~58 s to ~52 s as indicated by the blue arrow in the middle figure.

The figure at the bottom shows the accumulated energy utilized for external heating during the warm up. The values refer to a passenger car sized system with a nominal power of 100 kW. The white line indicates the 0.5 V voltage limit. The accumulated heat value reaches up to ~0.12 kWh. During the same time, the stack produces ~0.45 kWh electric work. In this regard, the active heater is not only suitable to facilitate cold start, it also provides an additional degree of freedom for energy management.

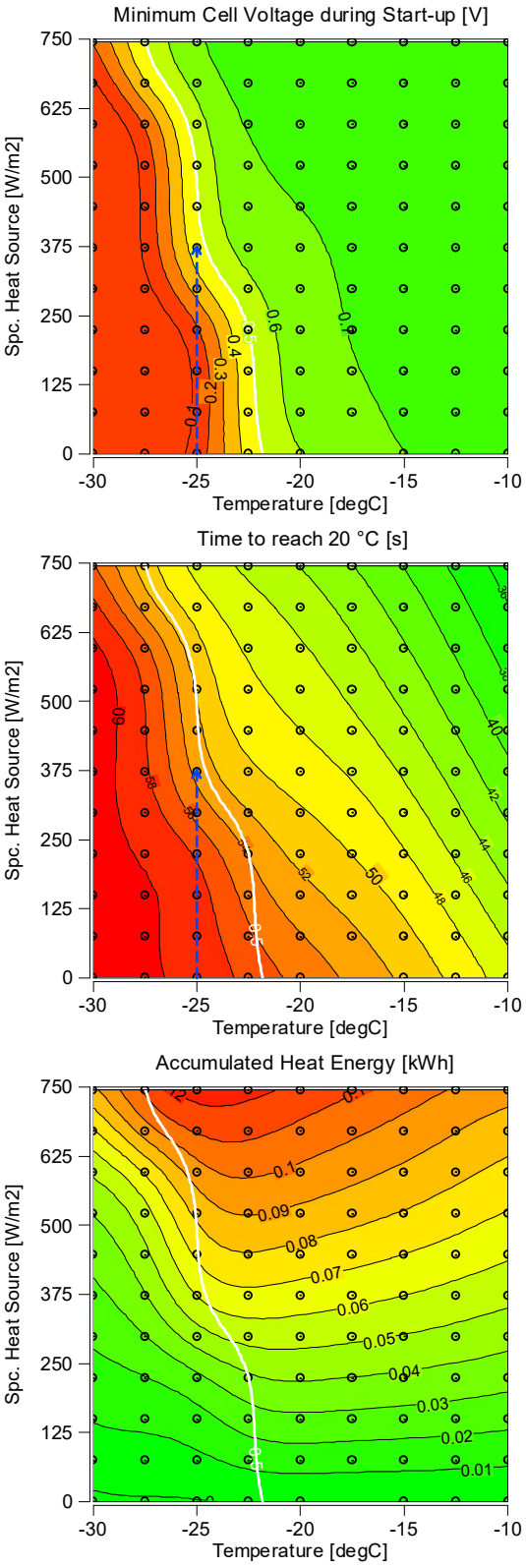


Figure 8: Variation of start temperature and external heat power

3.3 Dry purge during shut down

Every successful start-up has its roots in a prescient, well controlled, shut down. It would leave the stack in a condition which steers the race between freezing and heat-up in favour of the latter. Here, the membrane humidification state offers one degree of freedom for optimization. A low initial water content would offer a higher storage capacity for the process water in the membrane to be filled before liquid (frozen) water formation starts. At the same time, the membrane needs to retain a certain minimum water content to enable ionic conduction. The following section simulates various cases of the sequence: shut-down at warm conditions – active dry purge – rest and cool down – start up.

Figure 9 compares two variants: the baseline case without (solid lines) and the reference case with (dashed lines) active dry purge of the membrane during shut-down. The simulation starts at warm conditions (b) in a constant current / voltage point (a). At ~25 s, the system is shut down to zero current. In case of active dry purge, the cathode is flushed with warm and dry air for a defined time period. This drains a part of the dissolved membrane water. As a consequence, the water content drops from full saturation to 75 % saturation (c). From 50 – 60 s, the system cool down to the ambient temperature of -25°C. For demonstration purposes, this phase is artificially accelerated in the simulation. At ~66 s, the system is started again and a constant current is applied. Process water forms and partially accumulates in the membrane. If the membrane is already saturated (no drying), water would immediately liquidize & freeze in the CL, as shown in the solid lines (d). Consequently, the start-up process terminates at ~92 s due to CL freezing (a). If the membrane provides water storage capacity (thanks to previous dry purge), it can dissolve a larger part of the process water, which establishes a time margin of ~5 s for heat-up before liquid water formation starts (d). This provides a sufficiently large margin to start the system at -25°C.

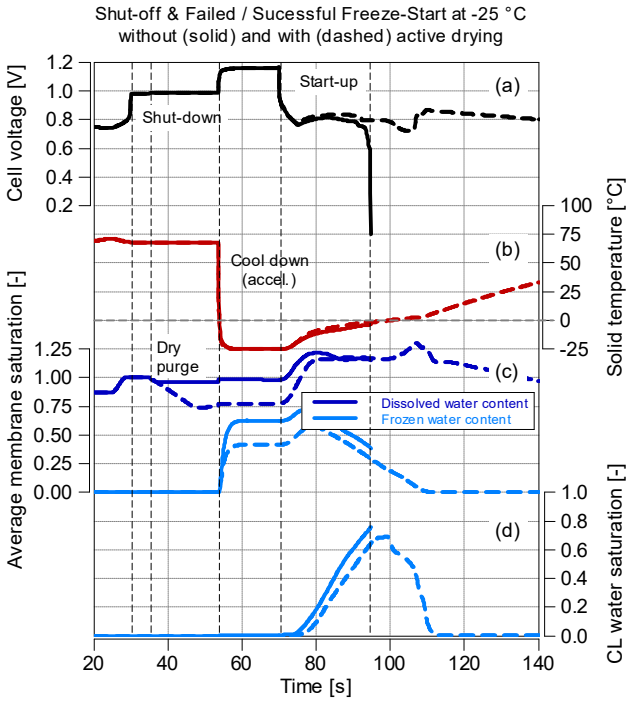


Figure 9: Freeze start at -25°C with and without active dry purge

The case study is extended to a wider range of start temperature and dry purge intensity. Figure 10 (top) shows the minimum cell voltage during start up, which represents a measure for CL freezing leading to cold start failure. Without dry purge (maximum membrane water saturation), start temperature is limited at ~-20°C. By active dry purge, the temperature range can be extended down to -30°C.

The warm up duration (time to reach 20°C) is shown in the bottom image of Figure 10. As expected, the warm up time increases with lower start temperature. As another notable aspect, the results also show that warm up duration is reduced by active dry purge. This is explained by the reduced heat capacity of the stored water and the lower latent heat to defrost the system.

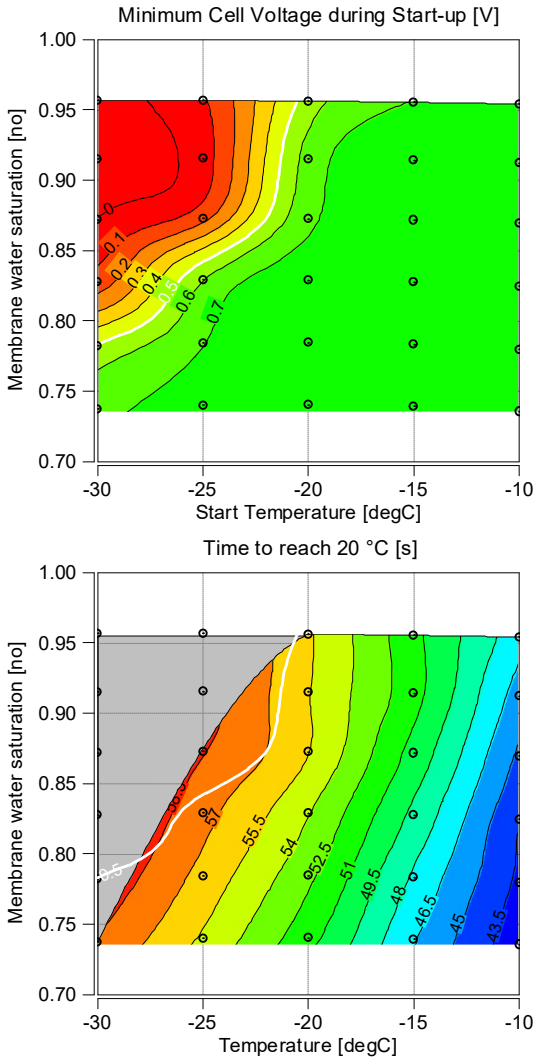


Figure 10: Variation of start temperature and dry purge intensity

3.4 Active voltage control

Previous cold start results in this work are obtained for galvanostatic operation. The current is held constant and the voltage and power output result from the operating point on the polarization curve. With respect to the electric operation this provides a single set point value – the current density. The maximum value may be limited by water generation and freezing (see case study 'Variation of current') and/or by the actual electric power demand and the charge characteristics of the battery. However, a large current may be desired with respect to internal heat generation for a faster warm up time.

One way which is studied here to reconcile the two opposing requirements is to steer both the current density and voltage simultaneously. The simultaneous control of current and voltage is achieved by reducing the cathode stoichiometry. The reduced oxygen supply deliberately enhances concentration, activation and transport losses to deteriorate the efficiency and thus to enhance the internal heat generation.

The background of the control concept is schematically represented in Figure 11, showing the steady-state polarization behaviour. The baseline curve is shown in the solid line with markers. The coloured frames indicate the target current density and cell voltage operating range during start up. The dots represent the target operating points for the case study. The dashed lines show the polarization curves for reduces cathode stoichiometry. As indicated by the steady-state results, the stoichiometry needs to be reduced to very small values just above 1.0 to reach the desired operating range. In the system, this requires an exact steering of the compressor, which can be a demanding control task.

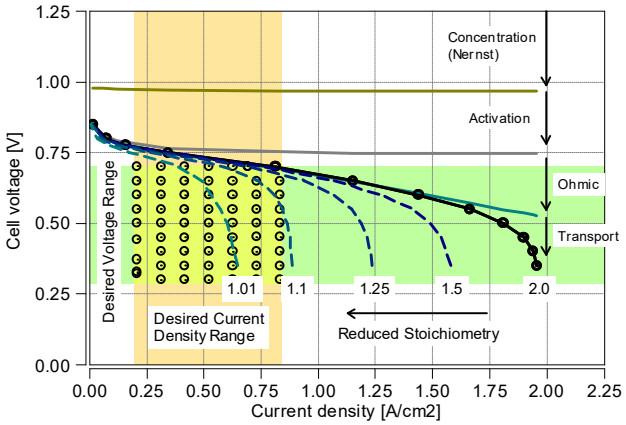


Figure 11: Fuel cell electric operating range, cell voltage vs. current density

The following case study investigates the feasibility of an accelerated warm up by active voltage control. Herein, current and voltage are used as variation parameters, while the same start temperature of -5°C is used for all cases. A PID controller steers the compressor to reach a desired stoichiometry for the given current / voltage point.

As the simulation starts with fresh air in the cathode, the stoichiometry would initially drop below 1.0 until the surplus oxygen in the cathode gas volume is consumed, Figure 12 (d). As also shown, the controller reaches the desired operating point after after ~1.5 s (a), (b). Thereafter, the stoichiometry remains close to 1.0 during warm up. For the high voltage case (dashed lines), the stoichiometry increases when the system reaches operating temperature due to the drop of thermodynamic efficiency at higher temperature. As can be observed in the temperature results, the low voltage case features a significantly faster warm up due to higher internal heat generation. Thus, the system reaches the operating temperature of 75 C after ~47 s, while the high voltage case requires ~82 s (c). When system temperature is reached, the thermoregulation system controls the stack temperature by external

cooling. The membrane humidity is controlled to the desired saturation value of ~0.9 by steering the cathode inlet humidity (e).

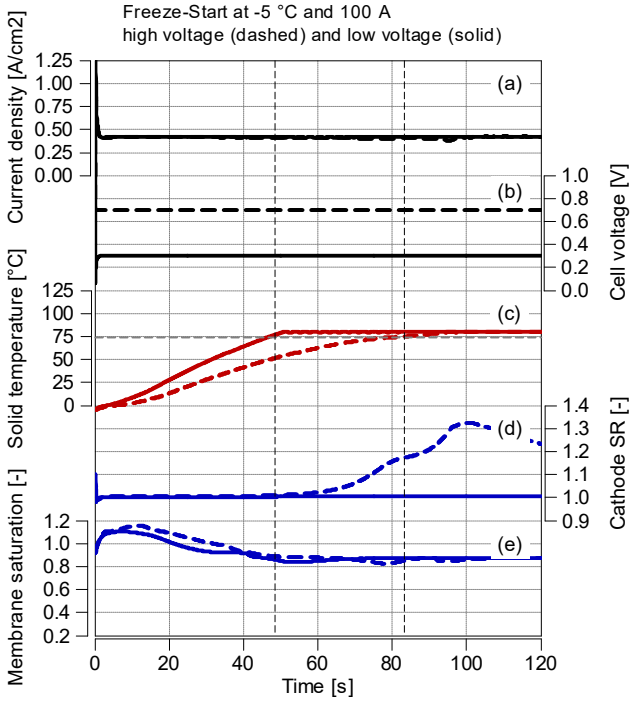


Figure 12: Cold start at -5°C at constant current density and different cell voltage levels

The study is extended to a wider current density / cell voltage range and the results are presented in Figure 13. The image at the top shows the warm up time until the stack reaches its operating temperature of 75°C as a function of the cell voltage for three different values of the current density. It shows that the warm up velocity can effectively be steered by voltage control at constant current density (and thus fuel energy supply). For the current density reference value of 0.417 A/cm², the duration is reduced from 82 to 47 s, by reducing the voltage from 0.7 to 0.3 V. As a reference, an external heat source of 750 W/m² at 0.7 V/0.417 A/cm² yields a warm up time of 68 s. The figure in the middle shows a plot for the warm up time against current density and cell voltage. The white lines show the cell electric power output density which naturally features a hyperbolic characteristic.

Another relevant aspect for the cold start characterization would be the amount of electric energy produced by the stack before it reaches an operating temperature suitable for transient operation. This energy needs to be utilized by the system power consumers or stored in the battery. The battery storage capacity may be limited by the battery temperature or state of charge. The electric energy production results for the current case study are shown in the figure at the bottom. The value ranges from 0.225 kWh to 1.05 kWh and it correlates mainly with the cell voltage.

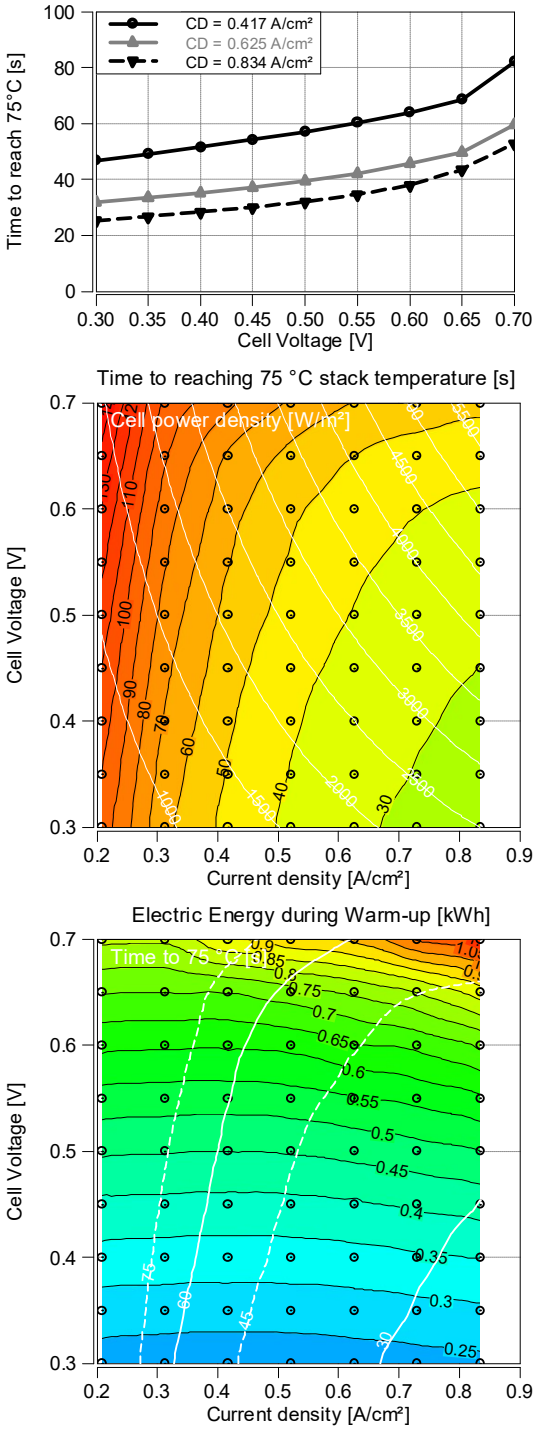


Figure 13: Warm up time and power balance for a variation of start current and voltage

4. Summary and Conclusion

The paper presents a multi-physical, real-time capable system level simulation model for PEMFC systems. The transient water content model is extended to consider dissolved, liquid and frozen water in the membrane, CL and GDL with the target to simulate freeze start events. The electrochemical

performance model is adopted to take into account the water content in the MEA.

The paper investigates four measures to facilitate a successful start from sub-freezing temperatures. Therefore, the following case studies are conducted:

- A variation of start current shows that water formation and freezing is enhanced at high current due to enhanced electro-osmotic drag. This prevents high current freeze start that would enable fast warm up at low temperatures.
- Applying external electric heat to the stack is an effective measure to facilitate cold start and to reduce the warm up time. The related hardware requirement of an electric heater in the cooling circuit elevates system complexity and costs.
- Active dry purge of the MEA during system shut-down raises the storage capacity for process water in the membrane at start-up before liquid and frozen water formation starts. This can be crucial to sustain a successful start.
- Simultaneous current and voltage control during start-up is an effective measure to reduce system efficiency and enhance the internal heat generation to facilitate a self-sustained cold start. The required exact closed loop control of the air supply adds complexity to the system.

Each of the investigated measures features specific advantages and disadvantages with respect to the hardware requirements and their related system complexity and costs. Furthermore, the optimal cold start control strategy also depends on the specific boundary conditions, such as start temperature, system electric power demand, battery state and storage capacity. System simulation with appropriate physical depth and high computational performance is an effective tool to support PEM FC cold start strategy development.

5. References

[1] Kui Jiao, Xianguo Li, "*Three-dimensional multiphase modeling of cold start processes in polymer electrolyte membrane fuel cells*", Electrochimica Acta, Volume 54, Issue 27, 2009, Pages 6876-6891, ISSN 0013-4686, doi: 10.1016/j.electacta.2009.06.072

[2] Knaus, O., Wurzenberger, J.C., "*System Simulation in Automotive Industry*". In: Hick, H., Küpper, K., Sorger, H. (eds) "*Systems Engineering for Automotive Powertrain Development*." Powertrain. Springer, (2020) Cham. doi: 10.1007/978-3-319-68847-3_34-1

[3] Pötsch, C., Henigman, U. & Wurzenberger, J.C., "*Modellbasierte Entwicklung von Brennstoffzellensystemen*", ATZ Extra 26, 16–19, 2021, doi: 10.1007/s35778-021-0464-5

[4] Kravos, A., Ritzberger, D., Tavčar, G., Hametner, C., Jakubek, S., Katrašnik, T., "*Thermodynamically consistent reduced dimensionality electrochemical model for proton exchange membrane fuel cell performance modelling and control*", Journal of Power Sources, Volume 454, 2020, 227930, ISSN 0378-7753, doi: 10.1016/j.jpowsour.2020.227930.

[5] Yun Wang, Partha P. Mukherjee, Jeff Mishler, Rangachary Mukundan, Rodney L. Borup, "*Cold start of polymer electrolyte fuel cells: Three-stage startup characterization*", Electrochimica Acta, Volume 55, Issue 8, 2010, Pages 2636-2644, ISSN 0013-4686, doi: 10.1016/j.electacta.2009.12.029.

[6] Kocher, K., Kolar, S., Ladreiter, W., Hacker, V.: "*Cold start behavior and freeze characteristics of a polymer electrolyte membrane fuel cell*", Fuel Cells – From Fundamentals to Systems, Volume 21, Issue 4, Wiley, ISSN 1615-6854, 2021, doi: 10.1002/fuce.202000106.

Development of fuel cell retrofit kit for commercial vehicles and TCO analysis

A. Ennever[1], P. Fussey D[1]. Sweet[1], E. White[1], M. Tomlin[1], S. Tate[1], M. Parrett[1], J. Richart[1]

1. Ricardo plc Shoreham-by-Sea, West Sussex, BN43 5FG, United Kingdom

Abstract: Hydrogen fuel-cell powered buses offer a solution to decarbonisation, however dealing with the existing fleet of vehicles is a significant challenge for the industry. Ricardo will present the development and design of an affordable (one third of the cost of a new fuel-cell bus), modular, scalable, quickly deliverable fuel-cell retrofit kit to transition the existing Diesel-powered fleet (38,000 buses in the UK in 2020) to zero-emissions vehicles.

It will help to extend the life of otherwise serviceable stranded assets, reducing unnecessary waste. Ricardo will present the analysis that has led to the sizing and specification of the fuel cell and the battery pack, together with the development of the powertrain (including hydrogen storage tank) and its integration on the bus.

Total Cost of Ownership is an important factor for the bus operators to select their vehicle and powertrain. Ricardo will present the TCO comparison between a Diesel-engine, a Battery Electric and a Fuel Cell powered double decker bus in 2022 and 2030. The TCO analysis will include the maintenance requirements with battery and fuel-cell ageing models.

The article/presentation will also highlight the details of the thermal management system that has been developed to maintain the same thermal comfort inside the bus but also improve the hydrogen consumption thanks of the use of a holistic thermal management (HTM) approach. The HTM enables the heat recovery from electrical components thanks to the use of a heat pump and heat recovery from the fuel cell to avoid using electrical heaters for warming up the cabin and the battery in cold and mild ambient temperatures.

Keywords: Retrofit, TCO, LCA, modular FC design, FC thermal management, FC system sizing

1. Introduction

Earlier this year, Ricardo and Stagecoach secured funding from the Tees Valley Hydrogen Transport Hub to demonstrate a double decker bus, retrofitted with a hydrogen fuel cell system. A retrofitted Alexander Dennis Enviro400 is now available for demonstrations in the UK.
The Enviro400 acts as a proof-of-concept vehicle; it is driven on the road but is not to be used in passenger-carrying service. The bus model selected was chosen due to its small package space. A modular solution is being developed that will be transferable, with minimal adaption, to other bus models already being considered.

The fuel cell and hydrogen tank packaging will depend upon bus architecture and it is possible that “some sacrifices” may be necessary. Ricardo says that the required 300-mile range of the retrofitted Enviro400 means loss of one row of seats in the saloon to permit installation of a sufficient number of hydrogen cylinders.
Ricardo is using its in-house modelling toolset to optimise the combination of fuel cell, battery and associated thermal management solution considering factors including total cost of ownership, performance requirements, battery and fuel cell degradation and remaining bus life.
Power is transmitted to the wheels via an electric axle that is well proven in bus electrification projects. There is no separate motor or driveshafts. This enables Ricardo to package the rest of the powertrain, including the fuel cell, battery and electrified ancillaries, in the engine bay.
At the start of the project, it was expected that a retrofit solution should cost around 50% the cost of a new fuel cell bus however the more detailed analysis revealed that TCO is likely to be on parity as the addition of FC system depreciates over a smaller number of years. It is important to note that total investment needed to support such uptake of zero emission busses is much less for retrofit then for new buses.
Another important aspect is the total impact of CO2 generated. Various scenarios are described in this article showing significant benefit when adopting retrofit model.
A production retrofit solution could be ready in 2023 subject to operators’ commitment to commercially viable uptake.
In parallel with the purchase of new fuel cell buses, retrofits provide the opportunity to more affordably increase the scale of hydrogen bus fleets, supporting the case for investment in hydrogen infrastructure. The opportunity to retrofit existing diesel buses to hydrogen power could support the conversion of entire fleets to zero-emission operation by the early

2030s (or sooner) without compromising the lifetimes of any fossil fuel-powered vehicles.
In the longer term, it is possible that operators could carry out production conversions in-house, or that the hydrogen fuel cell package is provided to OEMs to fit into new vehicles. This article will elaborate on the modification required.

2. Simulation tools for system design

2.1 Introduction to AIM

To assist with the fuel cell vehicle system sizing, Ricardo have adapted the Architecture Independent Modelling (AIM) toolchain, originally built for hybrid vehicle architecture comparison. The AIM toolchain exploits ultra-fast vehicle models, containing the physics relevant for comparison between varying system specifications, within an optimisation algorithm – with the objective of optimising the hybrid control strategy to minimise the fuel consumption over a target drive cycle. This approach, combined with Ricardo parallel computing capability, allows for potentially hundreds of thousands of various hardware specifications and control strategies to be simulated and compared in a matter of hours. For the development of the fuel cell bus retrofit hardware specification, the AIM toolchain was enhanced to include fuel cell capability.

2.2 Input Data Acquisition

Rather than relying on a generic drive cycle for system sizing activities (e.g. SORT), a real life cycle was preferred due to the potential significant impact of hill climb events on the vehicle performance and system degradation. A realistic cycle was obtained representing a real bus route in the Brighton and Hove region, incorporating several steep hill climbs (up to 15% grade). The duty cycle used is shown in FIGURE 1

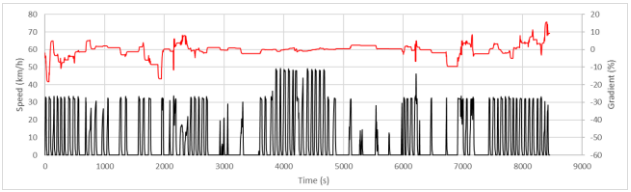


Figure1: Duty cycle (speed and gradient) as used in AIM analysis

Initial data for the bus and powertrain specification were obtained based on Ricardo experience of electric drive units suitable for a double decker bus application. Initial fuel cell characteristic data was based on Ricardo forecast of likely future fuel cell efficiency (as a function of relative load), while the fuel cell transient power response was modelled as a 2s transition between 10% and 90% load (applied as a rate limit). These assumptions were deemed adequate for the initial stage of the project and would be revisited later in the process, once supplier engagement had begun.

2.3 Modelling Methodology

AIM was used in conjunction with the Design of Experiment (DoE) methodology to ensure that results were generated across a large range of hardware specifications. In this instance, a DoE was created combining fuel cell peak power, battery capacity, and battery peak power as variables. A list of 150 cases was generated, where each case represented a unique combination of these variables. Each case in the DoE was then passed through the AIM optimisation algorithm several thousand times, where the control strategy would be optimised to ensure best possible efficiency.
To do this, a basic control strategy was created, with several optimisable parameters based on a simple lookup curve of fuel cell power against vehicle electrical power demand. This is shown in FIGURE 2. At very low power demand, the fuel cell would move to an optimisable idle condition (minimum 7% fuel cell load - P_{idle}). At a specific power demand (D_1 - optimisable), the fuel cell would transition to a second optimisable load level (P_{opt}). The vehicle was then allowed to remain at this operating point until demand reached a secondary, higher power demand (D_2 - also optimisable), before entering a “load following” phase, up to maximum fuel cell demand at a final optimisable vehicle power demand (D_3).

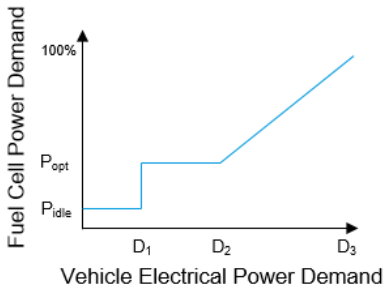


Figure 2: Example of control strategy as used in AIM analysis

The hybrid strategy could be overridden if the system detected that the resulting battery power would exceed the battery power limitation, in which case, the fuel cell demand would be increased in order to protect the battery. Due to the backwards facing nature of the models, it was not always possible to respect the battery power limitation (if the fuel cell power was limited by the transient rate limiter), in

which case a fuel penalty was enforced to assist the optimisation algorithm in avoiding these solutions.

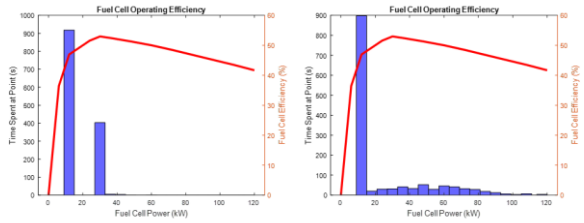


Figure 3: Potential control outcomes of AIM control analysis. High power battery utilising peak shaving with fuel cell at best efficiency (L) and low power battery with highly transient fuel cell (R)

A requirement of the optimisation process was to ensure net neutral SOC over the full duty cycle. As this cycle was representative of a full round trip (starting and ending in the same place), and the vehicle was not considered to include plug-in capability, this was considered a valid assumption.

2.4 Results Analysis

After completion of the set of cycle simulations, battery and fuel cell ageing models are applied. Fuel cell ageing is modelled as a reduction in efficiency per cycle (higher average load leads to higher degradation) based on correlation data available to Ricardo at the time of the study. No data relating to power degradation of the fuel cell was available at the time of the study. Battery ageing is applied using the HiFi Elements toolchain, where battery state of health (SOH) is predicted using correlated datasets, impacted by mean C-rate, Depth of Discharge and charge throughput (temperature sensitivity was not considered in this analysis as adequate cooling was assumed).
The results of the simulation were then applied as inputs to a preliminary Total Cost of Ownership (TCO) model. Components were considered end of life (EOL) when fuel cell efficiency had reduced by 20%, and battery SOH had reduced to 80%. Upon reaching the EOL, components were assumed to be replaced (at a cost representative of the predicted pricing at the time of replacement). Fuel consumption was assumed to increase linearly with efficiency reduction, up to the point of hardware replacement, at which point fuel consumption reverted back to the “new” value. The TCO was calculated over a 10-year lifespan, considering 11.5hrs operation per day (average) and 300 days per year. FIGURE 5 shows an example response of TCO vs Fuel cell stack power, with minimum TCO visible at approximately 65kW.

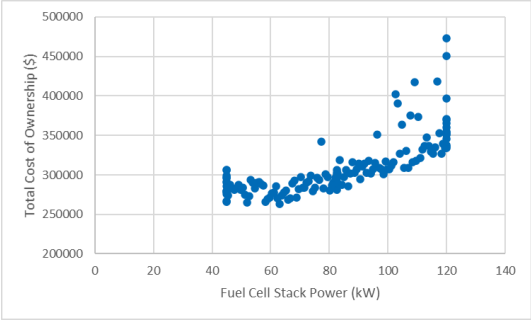


Figure 4: Example AIM output – sensitivity of TCO to Fuel Cell Stack Power

Assessing the produced data factoring in the TCO, component life expectancy, performance attributes, expected vehicle range (with defined tank size) alongside other subjective factors resulted in the definition of the final hardware specification.

3. System mechanical integration

During the simulation phase the engineers collaborated with mechanical integration team to validate that the proposed system sizing can be accommodated in the available space. Subsequent work packages included: packaging concept, bus modifications, H2 fuel tank system, system specification with focus on thermal integration (an entire main chapter is dedicated to this topic due to its importance in the overall integration project), control system and functional safety.

3.1 Packaging concept

Ricardo assessed buses currently in service and of an age to qualify for commercially viable retrofitting. From this work, the E400 was chosen as the basis for the first demonstrator because it has the smallest engine bay. A repower solution developed to fit the E400 is likely to fit all other buses that have larger engine bays, and with interface brackets the solution could be carried across to other buses with minimal modifications.

An important aspect of the repower design is minimising the cost of the kit and the bus modifications needed to the bus to accept the repower kit. So, the solution was designed such that the plated weight and CofG were not affected by the conversion. The implication of this was that five rear-most passenger seats had to be removed from lower deck to offset the additional mass and volume of the new hydrogen power train, but no requirement to change the vehicle braking or suspension systems were needed as a result. Upper deck seating remained unaffected as all hydrogen tanks fit underneath the rear seats in upper saloon.

The HYRBUS Demonstrator bus had to be designed and built and commissioned in 7 months. To achieve this, the selection of 'off the shelf' components was necessary, and the engineering focus was on integration; mechanical, electrical and control. In some instances, suitable components were not available in the time required, and a compromise had to be sought. For example, the batteries selected were energy batteries and twice the physical size specified by analysis, just to achieve the continuous electrical power needed. Such a compromise was useful for development to be able to explore the boundaries of operation, but a production solution can be further optimised to realise a smaller module size.

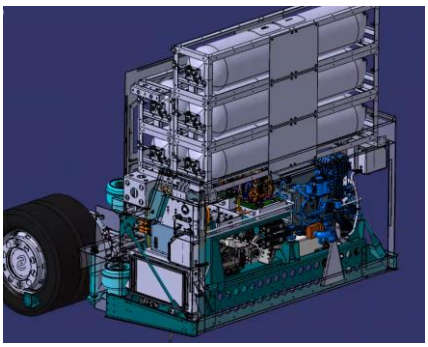


Figure 5: FC retrofit packaging

3.2 Bus modifications

To fit the repower kit into the bus, some bus modification had to be done. Clearly the engine, transmission intake and exhaust are removed, but there was further surgery needed as the Hydrogen repower kit is larger than the diesel solution. The rear five-way seat on lower deck was cut out. Some of the ceiling of lower deck above these seats was also removed to make room for the hydrogen tanks. Numerous brackets and trim also had to be sacrificed to provide a clear volume for the Propulsion Module. To reinstate a lower saloon, a new bulkhead panel was fitted to separate the passengers from the repower area. Panels within this bulkhead are removable to enable access to fuses.

The conversion itself consists of three modules, the first is the Hydrogen storage. This consists of five type 3 storage tanks each with a capacity of 5kg of compressed gas at 350 bar (a total capacity of 25kg of Hydrogen). Each tank has a mass of approximately 100 kg and the aluminium frame and hydrogen distribution pluming increase the mass of this module closer to 600kg. The frame assembly was analysed for compliance to regulation EC 79 and is readily configurable to other shapes (to suit the roof of a single deck for example), as each frame is identical. The assembly includes all valves, pipework and fill plate as a single assembly, enabling testing off the vehicle. The assembly can be fitted into the bus as one-piece.



Figure 6: Hydrogen storage

The second module is the electric axle which was necessary as there was insufficient package space for a solution that retains the original mechanical axle and power it by an electric motor. The axle chosen was a direct-drive, which offers good efficiency and very low maintenance. It is a direct replacement for the ZF 132 mechanical axle which resulted in a straightforward installation. The axle provides regenerative braking (Category A) so the driver can use 'one pedal' driving technique for most of their driving. Something that that drivers of the bus very quickly became accustomed to. The footbrake feel is slightly different, as the first portion of travel was dedicated to the retarder, but as that system has been deleted with the transmission this first portion of the brake pedal does nothing. However, further depression of the pedal will active the service brakes as normal. The Park brake system remains unchanged.



Figure 7: Electric Axle

The third module is the Propulsion Module, which was developed to contain the remainder of the powertrain in one assembly, that can be viably tested off-line (out

of the bus) and provided with the other two modules as certified tested assemblies.

The Propulsion Module includes;

- Lithium-Ion batteries from Akasol, 2 batteries in parallel providing 60kWh and 300kW peak, 100kW continuous
- The fuel cell, providing up to 80kW of electrical power. The fuel cell operates continuously maintain a target battery state of charge. This enables the fuel cell to operate in an area where it is most efficient.
- On long downhill descents significant brake energy can be harvested if the battery has capacity to accept it. If the battery approaches a full state of charge energy is diverted to a brake resistor to dissipate energy to atmosphere and maintain a consistent driver experience. A further advantage of the brake resister is that it has been integrated such that it can absorb voltage spikes should they arise (from an e-stop activation for example)
- Compressed air and hydraulic fluid are provided by electric pumps and compressors in the Propulsion Module. These provide the same performance as the original engine driven components.
- The complete thermal management system for the fuel cell, pump, compressors and power electronics, covered in Section 4.
- Low voltage power distribution and fusing. DCDC converted for the 24 and 12V consumers
- High Voltage Power Distribution unit, containing the fusing solution, and all HV cables between energy sources (fuel cell, battery) and consumers (axle, electric ancillaries for example)

The design offers the operators good access to service items and the interface with the existing bus systems (pneumatic, hydraulic, electrical, and coolant) remain in the same place to ease integration with the vehicle. The module includes all the high and low voltage wiring, fuse boxes and control systems. The construction of the framework was developed to be easily manufactured from sheet steel, and easily adapted to enable alternative components (different electrified ancillaries, or batteries for example) to be accommodated simply.

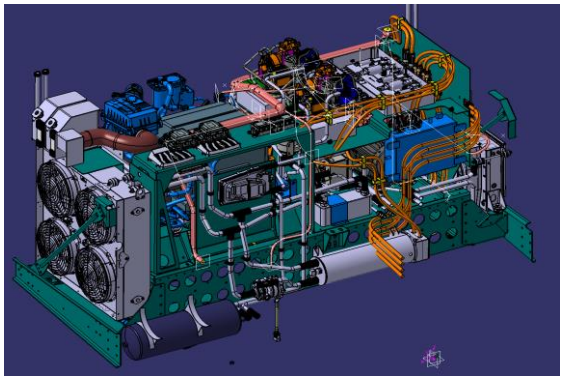


Figure 8: Fuel Cell Propulsion Module

3.4 Control system

To develop the repower solution as quickly as possible, the HYRBUS project developed the control system from Ricardo's hybrid control library in parallel with the vehicle build using models of the vehicle systems to test the strategies. This is known as a Model in the Loop (MIL) approach.

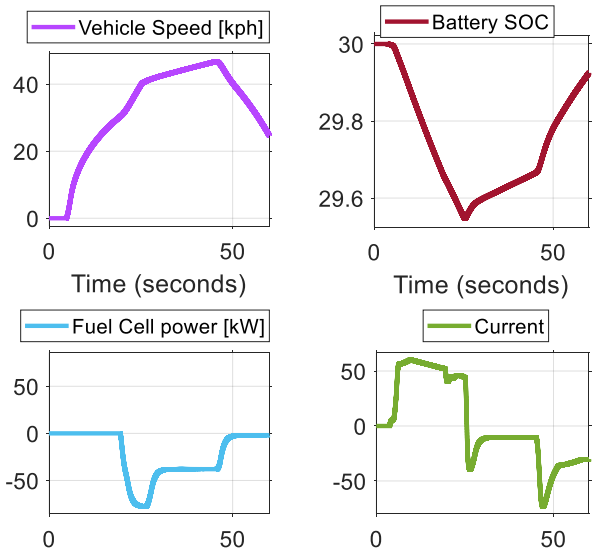


Figure 9: Example of MIL output for Fuel Cell power request at low SOC

As physical parts became available, Hardware in the Loop (HIL) was used to test the control system response, function and physical fit, saving valuable time on the vehicle later.

The control system was developed to provide a range of functions. It orchestrates the operation of the new (the repower kit) and old bus systems. Control functions include thermal management (pumps, fans logic), fuel cell demand, battery state of charge target and outputting signals to the bus so that it runs without an engine and gearbox it would otherwise expect.

A driver display completes the package. The display offers a visual health status, battery state of charge and fuel level. This was developed to minimise integration effort into the existing bus dash system and offers a solution that can be transferred to other vehicles that benefit the repower kit.

3.5 Safety Analysis

The converted bus was developed to be road legal and its development was supported by a comprehensive safety analysis which looked at the safety credentials of all the new components, their interaction and whole vehicle operation.

The known hazards which could result from malfunction of the new or modified systems were collated from experience with systems of the same type deployed in similar applications. For each hazard, a set of external measures which could be employed to prevent or mitigate the effects of hazard were specified, including

- Driver actions in response to malfunctions and faults
- Operating procedures and processes (for all users including drivers, passengers, maintenance/service operatives)
- Other technologies (i.e., mechanical measures to override or disable malfunctioning electronic controls).
- Restrictions of use (i.e., in certain environmental conditions)
- Vehicle Packaging (i.e., the placement and positioning of physical functional elements to minimise the impact of any malfunctions to reduce or prevent harm).
- Design guidelines.

The defined external measures were captured into a set of requirements with unique identifiers to be referenced in subsequent validation and verification activity.

An analysis of the designs for the new and modified systems was then performed to identify malfunctions which could result in the previously identified hazards. For each identified malfunction, safety measure(s) were specified to mitigate its effects (i.e., prevent its development into a hazard) by functional means (where possible) including

- detection and driver warnings
- performance/functional degradation
- functional redundancy

Subsequently, tests were undertaken on closed circuit tracks to ensure the performance of the braking and steering systems of the vehicle installed with the new and modified systems was as intended by the OEM for the base vehicle, in dry and wet conditions.

Mitigation included using the existing bus venting in upper saloon to provide good venting on three sides at the highest level to ensure no escaped Hydrogen could collect. Constant Hydrogen monitoring (4 places) was installed and displayed in the driver's area with the associated audio and visual alarms.
The batteries are compliant to ECER100 but as they are mounted in a potential impact zone, analysis was used to design a replacement rear ‘bumper’ structure that forms part of the conversion kit.
In common with other high voltage powered vehicles, the system includes a High Voltage Interrupt Loop (HVIL), Emergency Stops and integrated automatic fire suppression system.
An Acoustic Vehicle Alarm System (AVAS) has also been fitted to warn other road users and pedestrians of the otherwise silent running bus.

4. Thermal integration challenge

Integrating fuel cell system into the vehicle architecture brings new challenges. To successfully retrofit a diesel engine vehicle, the new propulsion system must be designed to fit the existing system in terms of package space, mass distribution, and electrical and fluid interfaces. The added complexity of a hybrid powertrain architecture, comprising a traction battery and fuel cell system (FCS), pushed the replacement system towards a highly integrated design. To achieve such integration, a holistic approach to thermal management was envisaged and developed.

Relative to a diesel engine, PEM fuel cells operate at lower temperature which poses challenges for both heat rejection and heat recovery. The fuel cell cooling pack size increasing to compensate for lower temperature difference to ambient air, although this can be moderated by optimal balancing of power demands between the fuel cell and battery. Heat recovery through existing fan-cooled heat exchangers within the bus is challenging for a lower temperature source, particularly when the hottest fluid, the deionised coolant from the fuel cell stacks, is incompatible with traditional hose materials.

Additional thermal functions complicate the situation further. A pure electric powertrain relies on regenerative braking to dissipate much of the braking power, but a hybrid system must demonstrate brake power dissipation even when the battery is at full state of charge. The battery requires cooling below ambient temperature to support fast charging rates and to improve battery life in hot climates. Finally, a host of

new power electronics devices are required to replace the shaft-driven mechanical devices of diesel engine buses; many of these devices require liquid cooling due to their compact design and sensitive components.

4.3 Heat Recovery

The saloons of a double-decker city bus are designed for convenience and capacity. High inertia, low insulation and high ventilation rates lead to relatively large peak heating demands. At the same time, demand is difficult to forecast and stabilise due to large stochastic variations in solar loading, passive gains (from occupants) and vehicle speed. To complete the challenge, the heat must be delivered through existing fan-cooled heat exchangers which are sized for high temperature coolant and low speed airflow.

A system of heat recovery is evidently required to minimise reliance on resistive heating, but each solution presents a trade-off between efficiency and complexity.
Concept 1: Direct heat recovery from FCS to Saloon heaters using deionised coolant loop
Concept 2: Indirect heat recovery from FCS to Saloon heaters using plate heat exchanger and a dedicated pumped coolant loop
Concept 3: Indirect heat recovery from FCS and Power Electronics and E-Motors (PEEM) circuit to Saloon heaters using two plate heat exchangers and a dedicated pumped coolant loop
Concept 4: Heat recovery from FCS and Power Electronics and E-Motors (PEEM) circuit to Saloon heaters using one plate heat exchangers, a dedicated pumped coolant loop and a heat pump to upgrade and stabilise the temperature delivered to the saloon heating.

Concept 4 was initially selected but was found to be highly challenging to package. A compromise was found with Concept 3 which offers energy saving at mild heating conditions, although the bus will remain reliant on a HV resistive heater for severe heating demands.

4.4 Brake Cooling

Unlike a diesel engine, a pure electric powertrain relies on electrical capacitance to absorb brake power during a descent. Once the battery has reached 100% SoC all additional brake power must be dissipated through resistive loads. Ancillary low voltage power consumers can absorb up to 10kW but, for a double-decker bus, a further 90kW must be rejected to ambient through alternative routes.

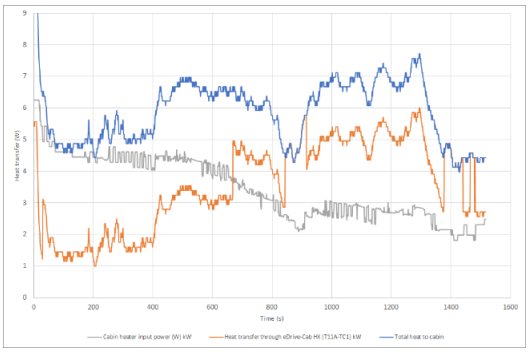


Figure 10: Results from early trials showing transition of cabin heating from electric cabin heater to heat recovery from the eDrive coolant circuit as the system warmed up.

Concept 1: Direct cooling through a dedicated radiator
Concept 2: Indirect cooling to the FCS through a plate heat exchanger
Concept 3: Direct cooling to an on-board tank of coolant with a supplementary radiator
Concept 4: Direct cooling through a dedicated radiator PLUS indirect cooling to the PEEM cooling circuit through a plate heat exchanger.

Concept 4 was chosen to minimise overall package volume, to avoid the risk of disturbing the fuel cell temperature control, and to create a solution which is agnostic of the centre of gravity of the donor bus.

Thermal System Summary

Understanding the different temperature requirements of each function and the interactions between their timing enables a holistic thermal management approach to minimise the overall package into the available space.

5. TCO and beyond

The TCO is shown in figure 13 and compares different powertrains for a double deck bus on a high utilisation suburban route operating around 20 hours per day. The powertrains are hydrogen fuel cell retrofit bus against a new diesel, a new battery electric and a new fuel cell bus. Employment costs are high as there are multi-shifts of driver for a single bus.

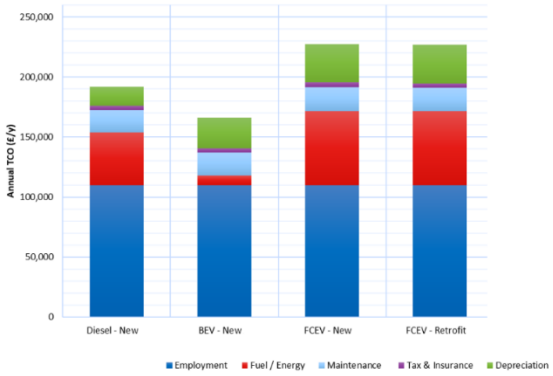


FIGURE 11: Total cost of ownership for a double deck bus in 2022 with BSOG subsidies

The fuel costs are significant again due to the long operating day. The English Bus Service Operators' Grant (BSOG) is applied with a 35p/L subsidy for diesel and a 22p/km zero emission vehicle subsidy. The result of these subsidies is that the difference between hydrogen and diesel fuel costs are narrowed, but neither can compete with the low energy costs of the battery electric bus.

The maintenance costs are broadly similar, dominated by lubricant changes for the diesel bus, mid-life battery replacement for the battery electric bus and periodic fuel cell stack refurbishments together with a mid-life battery replacement for the fuel cell bus. The replacement and refurbishment periods are based on supplier data applied to a typical suburban bus duty cycle.

The deprecation allowance covers the annualised cost of the initial capital outlay. For the new buses this assumes an industry typical 15-year straight-line depreciation, while the retrofit kits and their installation are depreciated over 10 years. The retrofit includes the full retrofit kit, its installation, mid-life refurbishment of the bus and the cost of purchasing a 10-year-old bus at typical market value.

The TCO difference between new and retrofit fuel cell bus is very similar, despite the difference in capital cost of several hundred thousand pounds. This is due to the difference in depreciation period previously noted.

However, there are important other criteria to consider. Overall benefits from a lifecycle greenhouse gas perspective and the upfront lower capital costs of retrofit.

The impact of bus fuel cell refit using Life Cycle Analysis (LCA) was assessed. Previous Ricardo studies for DG-Climate Action [ref] have shown significantly lower lifecycle emissions have been calculated for fuel cell buses. Assuming a 2020 energy mix and hydrogen production methods, global warming potential (C02e) for a fuel cell bus is calculated in the study to be 52.5% of the total equivalent C02 generated by the diesel equivalent. This is a worst-case assumption, as it is expected increase in renewable energy used in hydrogen production over the future lifetime of fuel cell vehicle would decrease emissions further. The benefits of re-fit fuel cell, in comparison to replacement fuel cell bus, can be calculated from the data in the study to be 85,000 kg CO2eq based on the energy savings from re-using the non-powertrain components, for example the chassis and body shell.

The total cost for decarbonising the UK bus fleet through natural fleet renewal (i.e., replacing naturally scrapped buses with zero carbon buses) will help achieve 2035 decarbonisation ambition which much of the bus sector is aiming for. A simple model, applying the distribution of bus scrappage age to the existing UK bus fleet, shows that the annual number of buses requiring natural replacement will increase from circa 1,500 in 2022 to between 2,500 and 3,500 between 2025 and 2030. The cost for this number of vehicles will proportionally increase for diesel. However, when factoring in the upfront capital cost for a zero-emission mix of new battery electric and new fuel cell buses, the capital cost is expected to increase from circa £300m in 2022 to between £950m and £1,300m annually between 2025 and 2030. This is a very significant cost for the bus industry and will require significant government support. However, the use of retrofit kit installations could reduce the annual capital cost to decarbonise (through natural fleet renewal) down to below £700m. This would be a significant saving for government in capital support costs and / or for bus operators. Additionally, the use of retrofits has the potential to allow a much more rapid decarbonisation of the bus sector with the government and industry budgets available.

6. Acknowledgement

The authors acknowledge the contribution of their colleagues to this work.

7. References

[1] Nik Hill et al, Determining the environmental impacts of conventional and alternatively fuelled vehicles through LCA, Final Report for the European Commission, DG Climate Action

CO_2 free Hydrogen Mobility for Passenger Cars without compromises

B. Criel[1], F. Jannot[1], E. Wahlmüller[2], U. Hanessen[3], J. Op de Beeck[4]

1: Plastic Omnium New Energies, Rue de la fusée 98, 1130 Brussels, Belgium
2: Plastic Omnium New Energies, Maria-Theresia-Straße 46/2, 4600 Wels, Austria
3: Plastic Omnium New Energies, Passage du Cardinal 1, 1700 Fribourg, Switzerland
4: Plastic Omnium Clean Energy Systems Research, Rue de la fusée 98, 1130 Brussels, Belgium

Abstract: On one hand, the Fitfor55 proposal of the European Commission, published in July 14th 2021, requests a reduction of CO_2 emissions from passenger cars of 55% by 2030. In 2035, 100% of the passenger cars and light duty vehicles are to become free of any CO_2 emissions. This proposal is purely focussed on Tank-to-Wheel emissions and demands a carbon free fuel or energy storage onboard the vehicle.

On the other hand, car buyers are looking for vehicles that can suit all their needs. These are not limited to everyday commuting, or nearby shopping, or any average driving cycles. Their needs include occasional weekend trips to the seaside, yearly holiday travels over 1000 km or more per day, and occasional driving under high load, high speed or with a trailer.

All this is combined with the need for passenger space and comfort, as well as a convenient and large luggage space.

Current CO_2-free passenger car offerings cannot meet these combined requirements like the current internal combustion engine vehicles do. Compromises in travel time or flexibility are currently needed.

This paper presents the various use cases and performances we expect from our current ICE driven vehicles. It then applies these to a CO_2-free passenger car, using hydrogen and electricity, in search of a solution meeting at least the same level of performance and comfort as our current vehicles, without compromises.

The study describes a vehicle architecture and the related powertrain components combining the various means of energy storage and transformation.

It then goes in the details of the hydrogen storage system, as well as the fuel cell system and its balance of plant. This is illustrated with test results and applied on the various relevant use cases expected from our current ICE powered vehicles.

Keywords: Hydrogen, Fuel Cell, zero emission, CO_2-free

1. Introduction

1.1 Tank to wheel CO_2 emission regulations evolution

Fuel economy standards are evolving and becoming more and more stringent in most of the regions of the world. The European Commission has launched its Fitfor55 program, sharpening its CO_2 requirements to a reduction of 55% compared with the 2021 NEDC value of 95 gCO_2/km. In 2035 a CO_2 emission reduction of 100% is proposed, which will then ban all powertrains with CO_2 emissions.

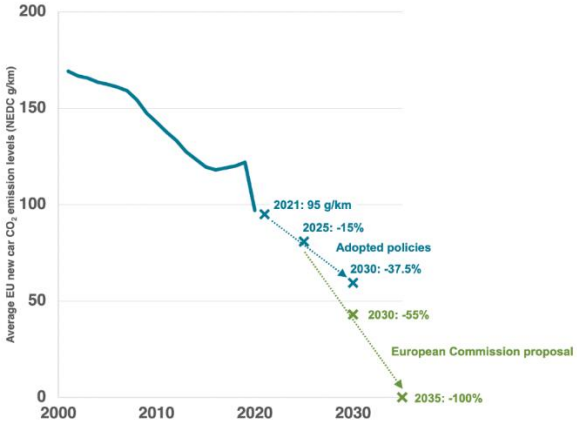


Figure 1: CO_2 emissions standard evolution for passenger cars according EC Fitfor55 proposal [1]

Additionally the applicable test cycle and driving conditions for fuel efficiency determination have evolved. The NEDC has been replaced by the more representative WLTP test cycle.
On top of that, since 2020 on-board fuel efficiency measurement equipment has been installed in all vehicles sold. By this means fuel efficiency in all driving conditions can be determined and analysed. Analysis of the first set of measured fuel efficiency data is currently being analysed in Europe and the

results may lead to a further evolution of the regulations.
This represents a strong challenge for all OEMs to optimize the powertrains for whatever driving conditions occur in real life.

1.2 CO_2 reduction enablers

Various technologies enable the reduction of CO_2 emissions from passenger cars. Engine efficiency improvement can be reached by increasing engine compression ratio, rightsizing and eventually by applying lean burn engine operation. A strong improvement of internal combustion efficiency is realised by using the internal combustion engine only in its most efficient operation condition. Strong hybridization of the powertrain is helping to achieve this goal. Nevertheless, none of the above technologies realise a zero CO_2 emission powertrain.

Therefore, a steep uptake of zero emission vehicles is mandatory. Latest by 2035, 100% of the vehicles in Europe are required to be Tank-to-Wheel zero CO_2 emission.

For all zero emission technologies, the challenge remains to cover sufficient range, and to have a guaranteed available energy distribution network.

4. Hydrogen storage integration

4.1 Hydrogen Storage integration challenges and constraints

The required available chassis volume (VOAL) for energy storage for a range of 100 km in WLTP conditions is compared for a given vehicle. It takes into account the shape of the storage and its capability to fill the available volume on the vehicle. For the sake of simplification, all energy storage means are considered to be placed in a crash protected zone on the vehicle, and none are allowed in the crash deformation zone.

For the BEV, the Tesla Model 3 MY2021 is taken as a base. The long-range version has a WLTP autonomy of 580 km, and the battery with junction box takes 420 litres of space on the vehicle. The battery is assumed capable to fit well in any available space in the vehicle.

For the hydrogen 700 bar high pressure storage, 2 cases are illustrated. The case with a fuel cell driven powertrain based on the 1 kgH_2/100km WLTP fuel economy from the Toyota Mirai-I and Hyundai Nexo. With the newest generation Toyota Mirai-II, the WLTP consumption is around 0.75 kgH_2/100km, which further reduces the required Hydrogen Storage System (HSS) installation volume.

A second hydrogen case is an H_2ICE driven vehicle with a fuel efficiency close to nowadays diesel and gasoline vehicles.

The hydrogen storage itself has a volumetric efficiency (hydrogen storage volume versus volume available in chassis) of about 45-50% due to the round shape of the 700 bar hydrogen vessels.

For the gasoline vehicle, a WLTP fuel economy of 4.5 l/100 km is considered which corresponds to 105 gCO2/km. The volumetric efficiency is at 60% since a fuel tank's shape creates some unusable space in sharp corners and close to the fuel delivery module.

For the diesel vehicle, a WLTP fuel economy of 3.6 l/100km is considered, which corresponds to 95 gCO2/km. The volumetric efficiency of a diesel tank is considered 60%, same as the gasoline tank.

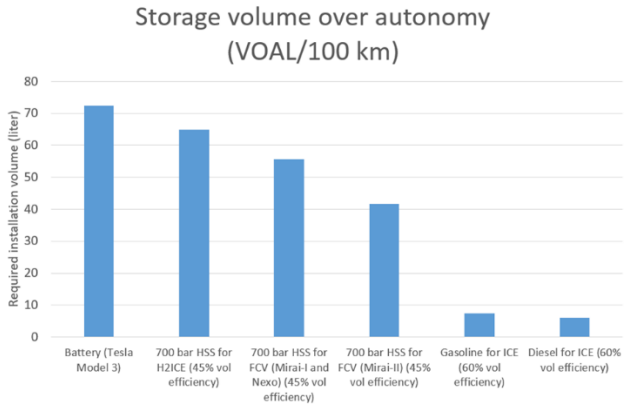


Figure 2 : Required available energy storage volume on a chassis for a WLTP autonomy of 100 km.

The particular challenge of integration in a passenger car is the compact environment and the need to keep luggage and passenger compartment space available.

For safety reasons the HSS needs to be placed in the crash protected zone of the vehicle.

The current hydrogen driven vehicles on the market use 700 bar hydrogen vessels under the rear seat and at the front of the booth. This system is sometimes completed with a vessel in the central tunnel of the vehicle. This requires the availability of the tunnel space for hydrogen storage, and there is less applicable to rear wheel drive vehicles.

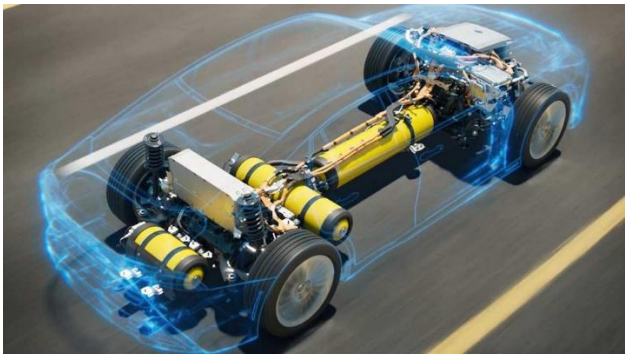


Figure 3 : HSS location in Toyota Mirai-II [2]

High pressure hydrogen storage typically finds peak gravimetric and volumetric efficiency by creating an increasingly spherical pressure vessel. This creates 2 main problems in terms of vehicle design.

1. The placement of a sufficiently spherical vessel generally means that the vehicle trunk space must be sacrificed. This is especially challenging because, unlike a battery electric vehicle, the front end of the car generally houses the fuel cell and balance of plant, which significantly limits the storage space in the vehicle. As a result, vehicles to date have tended to put a smaller tank under the rear seat of the car and another in the trunk itself. This as well has a disadvantage because the seat height of the rear seat becomes excessively high especially for a typical passenger car.

2. The placement of such a tank system tends to require a specific vehicle platform, which imposes additional capital expenses for OEMs.

If a high-pressure hydrogen storage system were able to utilize the same space allocated for a propulsion battery, it could enable a vehicle variant with increased range due to the increase in volumetric and gravimetric efficiency of 700 bar hydrogen storage with respect to lithium-ion batteries.

Architectures storing hydrogen in the floor of the vehicle are currently being developed. Such concept is fitting in the battery location of a skateboard BEV vehicle.

It is illustrated in the picture below.

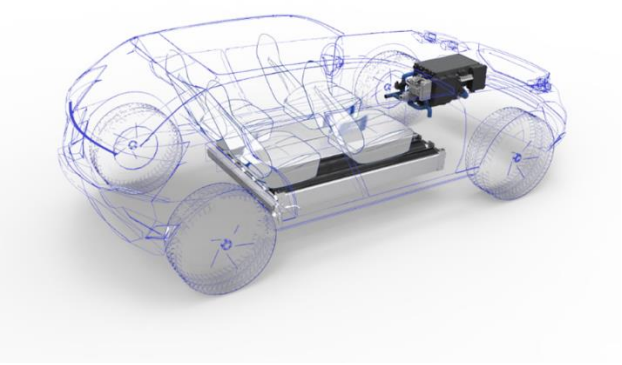


Figure 4 : Integration of HSS in the floor of a skateboard vehicle platform.

For this study, a battery pack volume with the outer dimensions of 1300 x 1800 x 140 mm³ is applied. The challenge is to integrate a partial or entire hydrogen storage system in such a thin volume.

A possible integration of hydrogen vessels in such a volume is represented in figure 5.

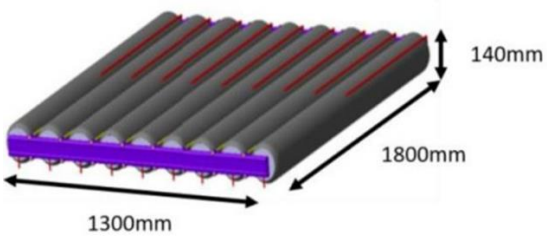


Figure 5 : 700 bar vessels in a volume of 1300 x 1800x 140 mm³

To make efficient use of this space, a volumetric efficiency of more than 40% is targeted. This volumetric efficiency is calculated as the volume of hydrogen in relation to the available volume in the vehicle. It results in a storage capacity for 5.7 kg of H_2. 95% of this storage capacity is usable under worst case temperature conditions of -40°C and a remaining system pressure of at least 20 bar. Therefore, the usable H_2 capacity amounts to 5.4kg.

Such a hydrogen storage architecture is studied and demonstrated in the context of the European SH_2APED project.

Weight is a crucial factor for energy efficiency. Therefore, a gravimetric efficiency of more than 5.7% on tank basis is targeted. The gravimetric efficiency is calculated as the weight of hydrogen stored versus the overall storage system weight. Achieving this, requires optimizations in gas management and hydrogen cylinder design. Optimizations in gas management can become achievable provided certification of a multi-vessel system is allowed according to future versions of regulations such as UNECE R134. Currently regulations require that each vessel is required to have an individual on-tank valve, and TPRD, resulting in unnecessary system mass and complexity. Additionally, optimizations in the boss-liner interface of a hydrogen storage tank can improve the overall weight of the system, by optimizing carbon fibre loading.

A nominal pressure of 700 bar is set, since it is the latest standard for hydrogen vehicle nominal pressure, and since it allows a relatively compact storage system.

5. Energy storage modularity

Both batteries and hydrogen storage vessels can be combined in 1 vehicle. This way all combinations ranging from a full hydrogen fuel cell vehicle to a full battery electric vehicle can be explored. Some options for combinations are illustrated in the next table.

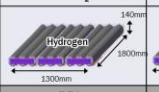
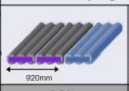
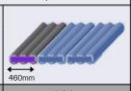
	Option 1	Option 2	Option 3	Option 4
	Full H_2	Hydrogen + Battery		Full Battery
Energy Storage (H_2 + Battery)				
H2	5.7 kg	3.8 kg	1.9 kg	–
Range by H_2	758 km	511 km	256 km	–
Battery Energy	–	17 kWh	36 kWh	59 kWh
Range by Battery	–	130 km	275 km	450 km
Total Range	**758 km**	**641 km**	**531 km**	**450 km**

Table 1 : Hydrogen storage and battery combinations

Selected configuration

As documented in the SIA paper from 2021 [3], the combination of a large hydrogen storage combined with a small battery is one of the most versatile powertrain combinations. Therefore the rest of the study will be based on the configuration where the energy storage is mainly taken by a hydrogen storage system (for long travels) completed by a battery sufficient for most daily commuting distances, and both located in the bottom of the vehicle

- Battery : 17 kWh
- Hydrogen storage : 3.9 kg H_2

Underneath an illustration of an existing hydrogen storage system developed to fit in the floor of a skateboard platform.



Figure 6 : 6 vessels in a module (830 x 1300 x 140 mm³)

The dimensions of this module is 830 x 1300 x 140 mm, and it has a rated capacity of 3.2 kg of H_2.

It can be completed by a module of 2 additional vessels adding up to an overall dimension of 1100 x 1300 x 140 mm. The hydrogen storage capacity rises therefore up to 4.3 kg of H_2.

This leaves a volume of more than 127 litres for the battery, which suffices for more than 17 kWh of energy, which is close to today's standard PHEV battery capacity.

6. Fuel cell system options

Various fuel cell systems are currently under development at Plastic Omnium. The rated power goes from 40 kW up to 150 kW.

Version 1: FCM 40 fuel cell system

The efficiency of the FCM 40 kW fuel cell system is illustrated in the graph below.

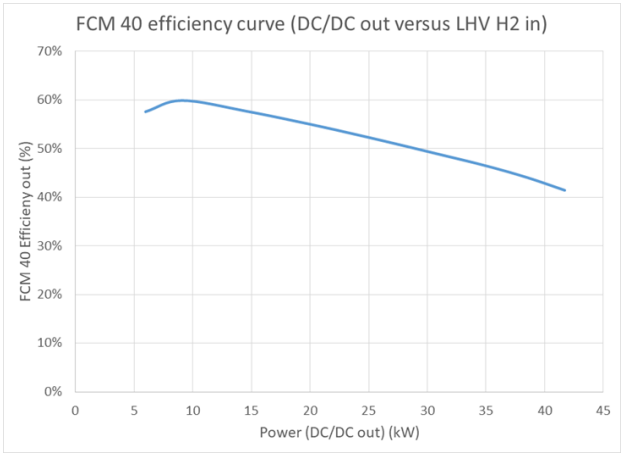


Figure 7 : Efficiency to net power at DC/DC outlet for FCM 40 fuel cell system

Its optimum efficiency lies at around 8 kW, which covers most of the city drive and low speed cruise control drive conditions.

Version 2: FCM 50 fuel cell system

The FCM 50 fuel cell system has a rated power of 50 kW.

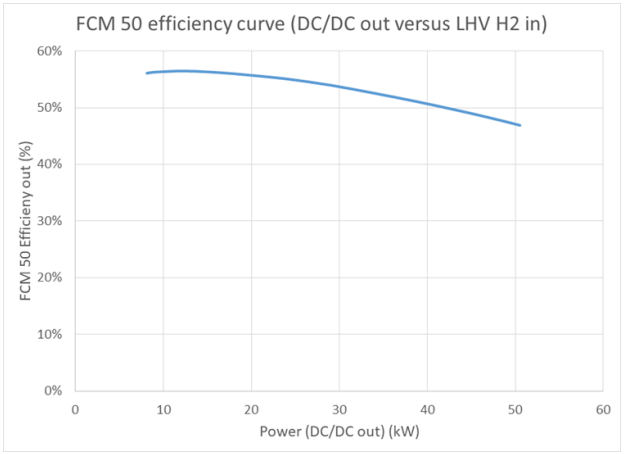


Figure 8 : Efficiency to net power at DC/DC outlet for FCM 50 fuel cell system

This fuel cell maintains well its power above 48% at full power and reaches its optimal efficiency of more than 56% between 8 and 18 kW.

The complete FCM 50 system is illustrated in the picture below.



Figure 9 : FCM 50 system

Version 3 : FCM 100 fuel cell system

The FCM 100 fuel cell system has a rated power up to 100 kW.

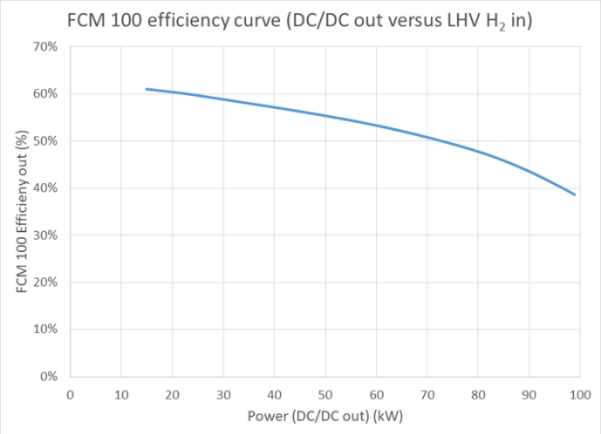


Figure 10 : Efficiency to net power at DC/DC outlet for FCM 100 fuel cell system

It reaches its maximum efficiency of more than 60% at a load below 20 kW.

Version 4 : FCM 150 fuel cell system

The FCM 150 fuel cell system has a rated power of 150 kW and beyond.

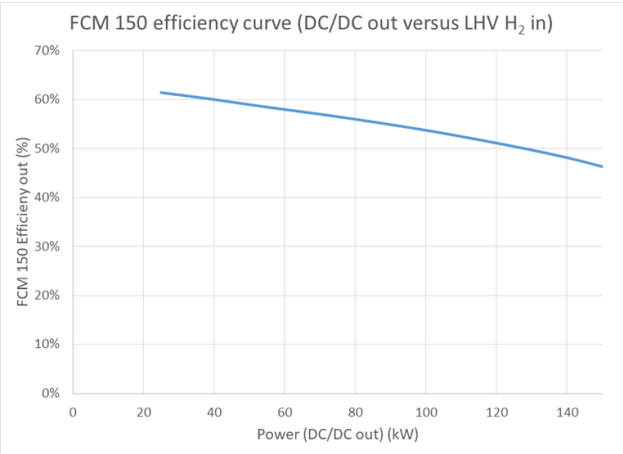


Figure 11 : Efficiency to net power at DC/DC outlet for FCM 150 fuel cell system

It reaches its maximum efficiency of more than 60% at a load below 40 kW.

7. System performance requirements and comparison in various use cases

7.1 Overall power and energy consumption data depending on vehicle speed

The average air and mechanical resistance of European cars has been recorded and documented, and is represented in figure 12.

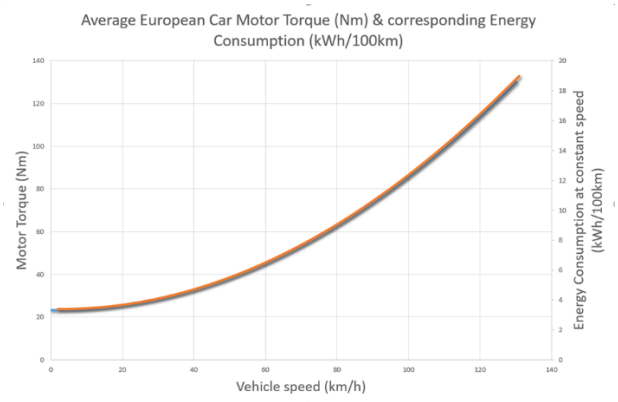


Figure 12 : Average European Car Motor Torque & corresponding Energy Consumption.

7.2 Reference vehicle description

In this study, the aim is to observe the effect on powertrain efficiency of various driving conditions and to verify the selection of powertrain combination.

Reference measurements are crucial, especially in the extreme driving conditions, to assure consistency of simulation data with reality.

As a reference, a BMW 530e vehicle is used. This is a very versatile vehicle able to cover all types of driving conditions ranging from low speed traffic jam driving up to German Highway high speed driving. This vehicle is equipped and various drive cycles are recorded.



Figure 13 : BMW 530e xDrive PHEV reference vehicle selected for driving conditions testing.

To avoid considering electricity supplied by the grid, and in order to simulate only energy generated onboard the vehicle, the drive cycle was started with the battery at low level (empty). This means that the vehicle is mainly driven in 3 modes :

- Regenerative braking
- Load point moving
- Electric boost

These same driving modes are available and applicable for a PHEV Fuel cell Powertrain. Nevertheless the calibration and for load point moving and electrical boost will be adapted to the fuel cell specific efficiency curve.

Electrical drive is only used, when the energy harvested from regenerative braking or load point moving suffises for a short electric operation, for instance in a traffic jam.

The reference vehicle is a PHEV, which uses a direct injection turbocharged gasoline engine combined with an electric powertrain.

Vehicle type : BMW 530e xDrive, US Lev-II

Vehicle mass : DIN 1868 kg (DIN)

Combined Powertrain power output 185 kW (combined electrical motor and combustion engine)

Maximum torque 420 Nm (combined electric motor + internal combustion engine).

Top speed : 211 km/h (US version)

7.3 WLTP as a representation of daily commuting

For an average European passenger car driven in a WLTP cycle, the power evolution curve can be determined. It has to take into account vehicle mass, acceleration and deceleration profiles, and drag and resistance forces. The below graph represents this power profile.

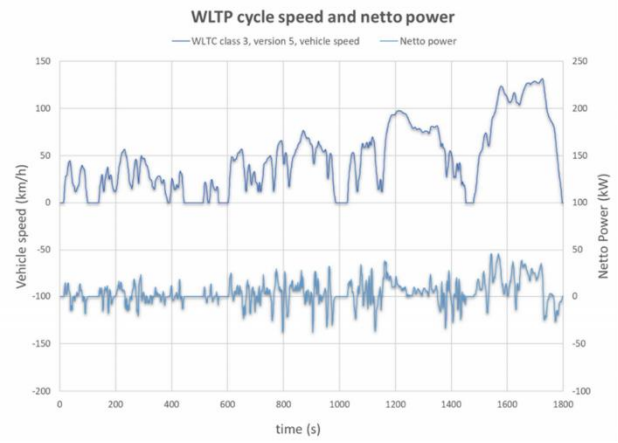


Figure 14 : WLTP speed and power profile for an average European passenger car (1395 kg + 500 kg load)

During WLTP driving, the average speed (excluding stops) is 53 km/h.

The propulsion power remains moderate (up to 45 kW). Brake power occurs up to 35 kW. This cycle is well known, and the basis for fuel efficiency evaluation of a vehicle during its initial certification.

7.4 WLTP extra high as a representation of highway driving

The WLTP extra-high speed profile, with an average speed of 94 km/h, is representative of average highway driving with regular stops and speed limitations at 120 or 130 km/h.

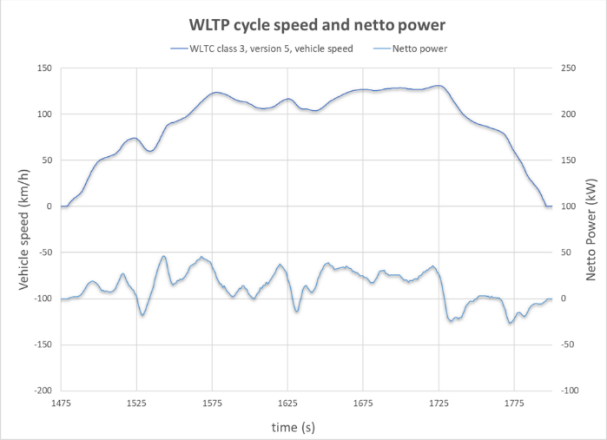


Figure 15 : Highway drive speed profile

The propulsion power remains moderate (up to 45 kW). Brake power occurs up to 35 kW.

7.4 Dynamic highway driving (no speed limitation)

The WLTP extra high speed section goes up to speeds of 130 km/h.

On highways in Germany, traffic at substantially higher speeds is frequently observed. The below graph has been recorded during highway driving in a non speed regulated zone

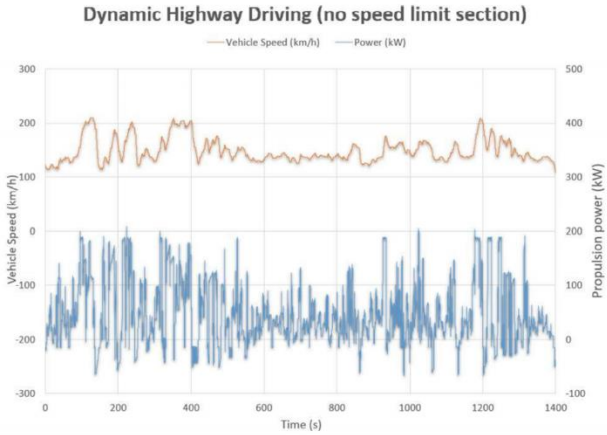


Figure 16 : Dynamic highway driving speed and power profile for a passenger car

In this dynamic highway drive cycle the vehicle speed goes up to 210 km/h. The vehicle propulsion power goes up to peaks of 185 kW. These power peaks of 185 kW occur during full acceleration. As soon as the vehicle has reached speeds above 200 km/h, no further forced acceleration was attempted, and the power required to keep the vehicle at this speed lies around 95 kW.

During the acceleration phases both fuel cell and battery can work together, for as long as the energy stored in the battery suffises. This enables to cover all peak demandes during acceleration or during a short slope

However, for long uninterrupted driving at constant speed (even at this speed above 200 km/h) the power has to be supplied by the fuel cell alone.

A high level of hybridisation can create an eBoost function and help to lower the need for peak power from the combustion engine. The electrical energy for this peak power needs to come from energy harvesting, electrical energy transformation and storage, combined with a high electrical powertrain efficiency. When the energy from braking does not suffise, it has to be generated by the fuel cell, taking into account its efficiency in the power generation operation mode. Therefore, for such conditions, the electrical architecture, battery, motor/generator and the overall efficiency of this pure electrical powertrain remains important, but it is not sufficient.

Fuel cell power is key to create at least the constant power to drive the vehicle at its max speed (in our case study i.e. 95 kW). Of course a car is not always driven at its max speed/load, and the fuel cell efficiency in any driving mode below the 95 kW is to be optimal.

Selection of FCPHEV powertrain

The target of this study is to define a powertrain that allows driving the zero emission vehicle without any compromises. This means that the vehicle must be able to cover all of the above driving cycles.

Since we know dynamic driving on a German Highway can require up to 95 kW constant power, with the battery covering all peaks, both the FCM 100 and FCM 150 are practical options.

Considering that most driving cycles do not require more than 50 kW of power, the FCM 100 is selected for the powertrain efficiency study. This allows to benefit from the maximum power of the fuel cell for extreme conditions of high-speed driving and towing. Most driving conditions needing less than 50 kW average power will allow the fuel cell to run in its most efficient conditions at more than 55% efficiency.

From the previously mentioned SIA Powertrain paper [3], which favours option 3 for hydrogen versus battery capacity for long distance travel, we know that priorising hydrogen fuel cell driving over EV (Electric Vehicle) driving helps to keep the travel time low.

Indeed recharging a battery takes more time than refilling the hydrogen storage system. The latter is comparable to refilling a vehicle with diesel or gasoline, which takes less than 10 minutes.

Therefore, the selection of powertrain parameters for this study are:

- Fuel Cell maximum Power : 100 kW
- Electrical motor Power : 185 kW
- Electrical motor Torque : 500 Nm
- Peak Battery electrical power : 85 kW
- Continuous battery electrical operation power : 55 kW up to 30 minutes
- Battery capacity : 17 kWh
- Hydrogen storage capacity : 4.3 kgH_2

To optimise the usage of the fuel cell, a maximum usage of the battery capacity is applied, which smoothens the continue power supply requested by the fuel cell. The result of such an optimisation on the dynamic highway driving, can be found in the figure below.

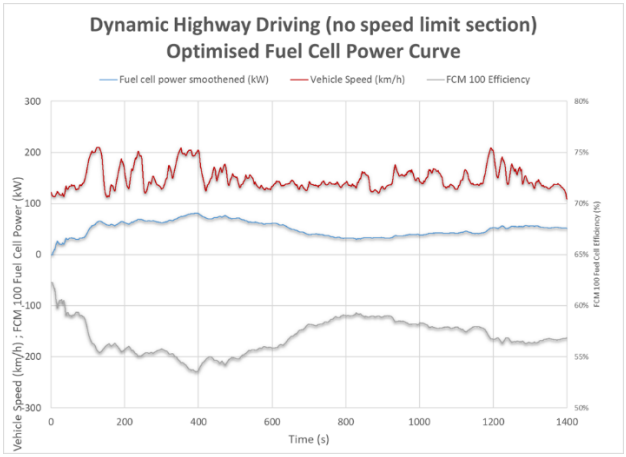


Figure 17 : Optimised fuel cell power curve for dynamic unlimited highway driving

For such driving, the maximum power from the fuel cell can limited to a peak value of 81 kW, and an overall average power of 50 kW. This can be easily handled by the FCM 100 fuel cell system.

The fuel cell efficiency for such an extreme driving cycle is between 50 and 60% for the vast majority of the driving cycle. When taking into account the losses over the AC/DC conversion (brake energy recuperation), battery charge/discharge, the DC/AC conversion and finally the efficiency of the electric drivetrain, the corresponding average hydrogen consumption is 2.48 kgH_2/100 km.

The same optimisation is applied on a prolonged highway section (extra high) based on the WLTP

extra high speed profile. The result is shown in the curve below.

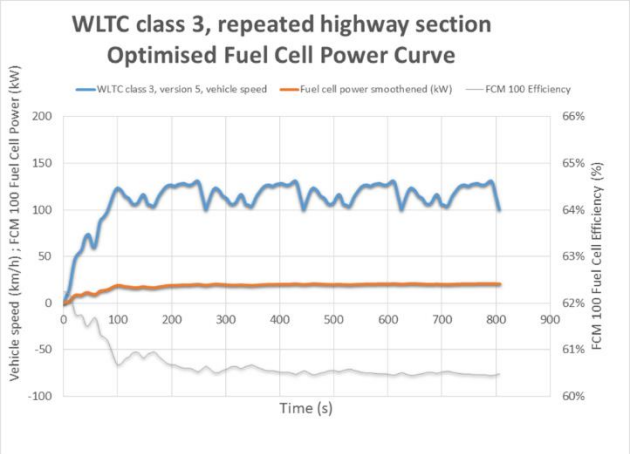


Figure 18 : Optimised fuel cell power curve for prolonged highway driving based on WLTP extra high

For such driving, the maximum power from the fuel cell can be limited to a peak value of 21 kW, and an overall average power of 18.5 kW. This can be easily handled by the FCM 100 fuel cell system.

The fuel cell efficiency for such a moderate highway driving cycle is always above 60%. When taking into account the losses over the AC/DC conversion (brake energy recuperation), battery charge/discharge, the DC/AC conversion and finally the efficiency of the electric drivetrain, the corresponding average hydrogen consumption for such a highway drive is 1.12 kgH_2/100 km.

8. Use case selection

Use case 1 : high speed highway travel

Most of the use case are a combination of city driving, rural driving and highway driving. These use cases are represented in the WLTP cycle, and most powertrains are fit to cover such a driving cycle.

On top of the daily commuting in Europe, most of the vehicles are used at least once per year for a travel during the holiday period. The distance travelled is often 1000 km or more.

This is one of the most challenging uses cases and is therefore selected for this use case study.

In this case, as an example, a travel from Brussels to Vienna is considered.

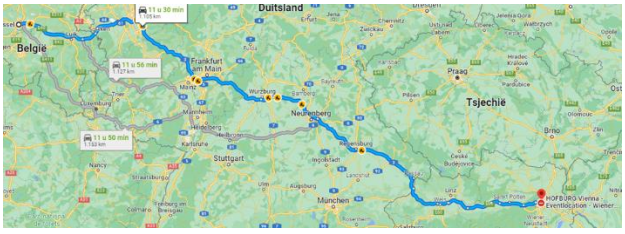


Figure 19 : Travel from Brussels to Vienna (source google maps)

The total distance is 1 100 km and the expected travel time about 11 hours and 30 minutes.

It is crucial to identify the possible locations for hydrogen refuelling.

These can be found for instance on the website H2.live [4].

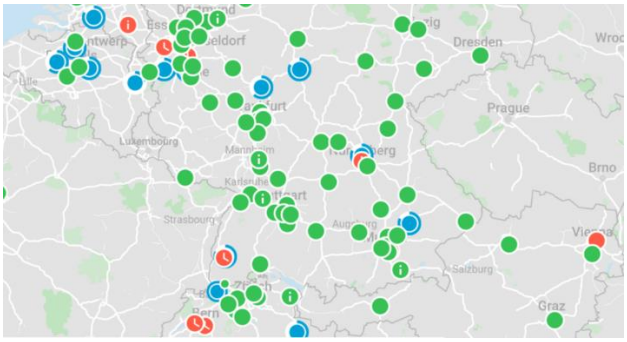


Figure 20 : Hydrogen refuelling stations (source H2.live)

As there is a 700 bar hydrogen refuelling station in the Brussels area (Zaventem), the hydrogen storage is considered full at the beginning of the travel.

From the previous SIA Skateboard study, we know that maximum usage of the fuel cell and hydrogen storage over long distances is beneficial thanks to the short refuelling interval.

Nevertheless it is important to have available fast recharge station to recharge the battery when depleted. An example of a tool to find recharge stations is PlugShare.com [5].

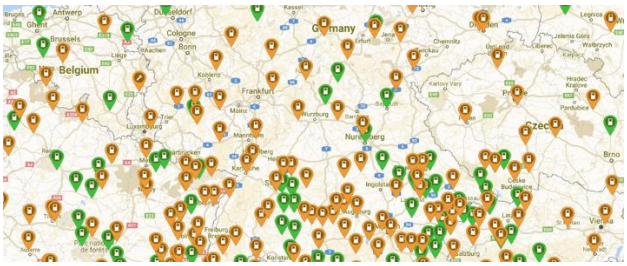


Figure 21 : Electrical Fast Charging Stations (source : PlugShare.com)

Well spread over the trajectory from Brussels to Vienna, we find public stations and fast charge stations.

8.1 Travel from Belgium to the German border

Leaving the city of Brussels requires to start with a city drive, then followed by larger roads and then finally highway drive. This is well represented by an entire WLTP cycle.

Over the Belgian highway, a speed limit of 120 km/h applies. There is also a lot of traffic most of the time during the day. Therefore, a repeated WLTP extra high cycle is applied until Germany.

The total distance travelled in Belgium is 140 km.

The Hydrogen power and consumption over the initial WLTP cycle (23 km) is far below 1 kgH_2/100km. This corresponds to a consumption of 0.23 kgH_2.

This is followed by 117 km of extended WLTP extra high cycles with an average consumption of 1.12 kgH_2/100km This corresponds to a consumption of 1.31 kgH_2.

The overall consumption of hydrogen over travel in Belgium adds up to 1.54 kgH_2. The remaining mass of H_2 in the tank is therefore 2.76 kgH_2.

8.2 Travel in Germany

In Germany there is a mix between sections with speed limit and section without speed limit. To represent this, half the distance is covered by a WLTP extra high-speed profile and the other half is the dynamic German Highway cycle as previously described.

The total distance travelled in Germany is 705 km.

Half of this distance occurs on non-limited high-speed section, and the other half on speed limited section similar to the ones found in Belgium.

The hydrogen consumption in the high-speed section is 2.48 kgH_2/100km and the hydrogen consumption on the speed limited sections is 1.12 kgH_2/100km. Therefore the average hydrogen consumption in Germany is 1.80 kgH_2/100km.

An intermediate Hydrogen refuelling stop can be found in Köln/Bonn, close to the airport. This is at a distance of 85 km from the border. A perfect mix of German highway styles leads to a consumption of 1.53 kgH_2 (versus 2.76 kg H_2 still available).

Then it is 183 km towards Offenbach (Frankfurt) for a next stop at a Hydrogen refuelling station. The overall consumption over this distance in Germany is 3.29 kgH_2 (versus 4.3 kgH_2 available).

Then follows a section of 239 km towards Nürnberg for a next refuelling stop. The overall consumption on this section is 4.30 kgH_2 (versus 4.3 kgH_2 available). In case of hydrogen shortage, the battery will briefly take over the energy supply.

Then a last section of 212 km towards Passau for a last refuelling stop in Germany. The overall consumption on this section is 3.82 kgH_2 (versus 4.3 kgH_2 available).

After Passau, the speed is reduced towards entering Austria.

8.3 Travel in Austria

In Austria, highway speed is limited. Therefore, the WLTP ultra high is used for driving on Austrian highways until nearing Vienna. For the last section entering Vienna, the combination of the entire WLTP cycle is applied, as it covers an evolution between city and highway driving.

From the hydrogen refuelling station in Passau to the hydrogen refuelling station in Vienna, a total distance of 315 km applies. On this section 3.52 kg H_2 is consumed (versus 4.3 kgH_2 available). The refuelling here is optional, since there is still some hydrogen range left, and the battery is still full and available for more than 100 km of city drive.

9. Results

The overall consumption of H_2 on this travel is 17.73 kg of H_2.

The total travel requires 4 stops, with an optional 5th stop to refuel at the destination in Vienna. At the end, the full battery is available for city commuting.

In total 4 times 5 minutes of stops have been passed, and the car has been driven dynamically, including high speed driving sections in Germany, without additional restrictions compared to a conventional diesel/gasoline vehicle.

Underneath the time chart for the entire travel.

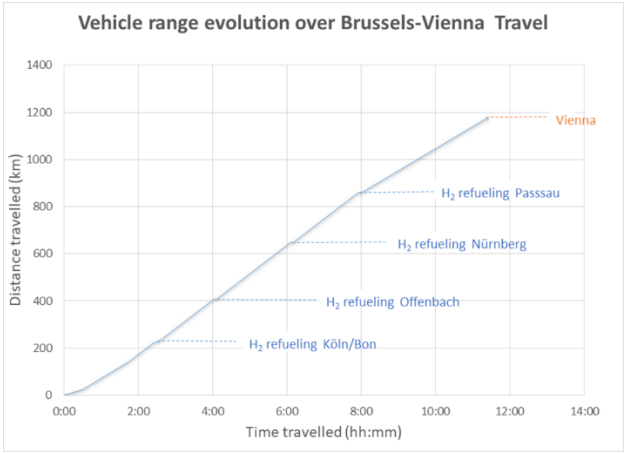


Figure 22 : Travel time chart including hydrogen refuelling stops

We can therefore conclude that zero CO2 emissions driving without speed limitations or any other compromises, is possible.

The combination of a fuel cell system such as the FCM 100, together with a battery of up to 17 kWh and a hydrogen storage in the floor of a vehicle makes this possible.

10. Acknowledgement

The authors of this paper would like to thank their colleagues of Plastic Omnium New Energies Wels, Austria, Genk, Belgium and Fribourg, Switzerland.

11. References

[1] European Commission, Communication from the Commission to the European Parliament, the Council, the European Economic and Social Committee and the Committee of the Regions, 'Fit for 55': delivering the EU's 2030 Climate Target on the way to climate neutrality, July 14th 2021

[2] Website https://toyota.jp/mirai/, 2021

[3] SIA Powertrain & Power Electronics Conference 2021, The era of Skateboard EV platforms : how to integrate hydrogen storage in the platforms of the future, J. Op de Beeck, D, Hill, B. Criel, E. Deparis, A. Seifert, Paris, 2021

[4] Website https://h2.live/en/, 2022

[5] Website https://www.plugshare.com, 2022

12. Glossary

EV:	Electric Vehicle
ZEV:	Zero Emission Vehicle
NEDC:	New European Driving Cycle
WLTP:	Worldwide Harmonised Test Procedure
PHEV:	Plug-in Hybrid Electric Vehicle
BEV:	Battery Electric Vehicle
FCEV:	Fuel Cell Electric Vehicle
CFRP:	Carbon Fibre Reinforced Polymer
TPRD:	Thermal Pressure Relief Device
OEM:	Original Equipment Manufacturer
UNECE:	United Nations Economic Commission for Europe
FCPHEV:	Fuel Cell Plug-in Hybrid Electric Vehicle

16 JUNE 2022

BATTERY THERMAL MANAGEMENT AND SAFETY

SAFE BATTERY SYSTEMS: INNOVATIVE MATERIALS AS A KEY FACTOR FOR BATTERY SYSTEMS

Dr. Uwe Franken[1]

1: Henkel AG&Co. KGaA, Henkelstraße 67, 40191 Düsseldorf, Germany

Key words: Thermal propagation prevention, fire retardant, safe battery systems,

Abstract: The topic of Thermal Propagation Prevention (TPP) is increasingly coming into focus in the e-mobility industry. With an increasing number of reported cases of fire on electric vehicle roads, legislation in China has caught up and is placing new safety requirements on electric vehicle manufacturers, and NA and EU are expected to follow soon. [1]

1. Introduction

The presentation and paper will provide an overview of various products and solutions for specific application areas such as lid coating (epoxy and water-based), potting and foam technologies. Together with classical thermal management, bonding and sealing technologies and products, this will ensure that the safe integrity of the batteries meets and follows the regulatory requirements for prevention in electricity storage systems of a battery.
.

2. Background

Number of electric vehicles have increased in recent years and a battery is the main power source in the electric vehicles. Since the battery is the main power source for the electric vehicles, battery capacity, energy density, and fire safety are major concerns for all electric vehicle manufacturers. However, the battery safety is one of the most important challenges. In accidents involving collisions, an electric vehicle can catch a fire, and therefore, the battery should be capable to withstand an external heat and fire, thus extending the time for passengers to evacuate the electric vehicle.

3. Strategic approaches

1. One way to enable the battery of the electric vehicle to withstand elevated external heat and fire is a fireproof coating. The fireproof coating is suitable for both traditional battery casings made of iron, steel and aluminium alloy as well as light-weight plastic casings made of PPS, SMC, flame-retardant PP, nylon and glass fibre. The fireproof coating is a light-weight and effective way to protect the battery from fire compared to alternative fire protection conception.

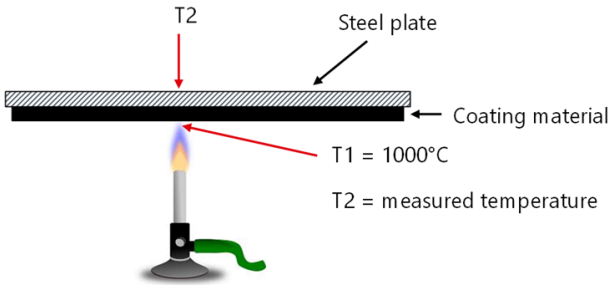
2.
Generally, the fire protection coating is a material that, in the event of fire, the material comes into a contact with heat and fire, it expands from a coating thickness of few millimetres to a thick foam layer of several centimetres (up to expansion rate of 40 times the thickness of the coating layer). This type of coating is also called to an intumescent coating. The expanded coating layer effectively insulates the battery compartment from the elevated temperature and fire, and therefore, prevents burns caused by a drastic rise in temperature inside the battery, stabilizes the structure of the battery box, and ultimately provides more time to the passengers to evacuate the vehicle.

One way to provide a fire protection coating is to use of mica sheets as a fire protection coating. However, the use of mica sheets is a manual and labour-intensive process. Therefore, this coating type is not suitable for large production volumes, which require high speed and accuracy.

Another way to provide the fire protection coating is to apply a fire retardant composition on a surface of a battery box. There are various 1k and 2k fire retardant compositions available for different surfaces, however, most of such compositions do not meet required heat and fire-retardant properties or meet the high process speed and accuracy requirements for battery box coating applications.

4. Testing set up

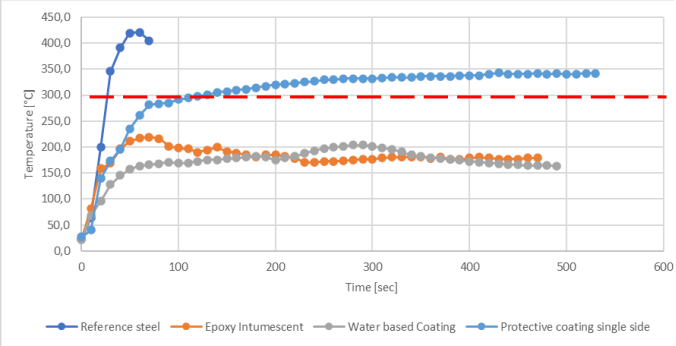
Figure 1 illustrates a test method used to determine ability of coatings to resist heat and fire over a defined period of time.



.

5. Findings

The below diagram shows the temperature development over time of a steel sheet protected with coating systems in case of a fire event. [3]



6. Conclusion

Henkel's technologies for prevention of thermal propagation of battery cells are suitable for a high degree of automation for mass production. Today there are no standard solutions available for a cost efficient mass production.

Compared to standard and expensive mica fibre foils the above-described technologies are lower in both. Potting materials or liquid applied foams can be applied on top of the cells on busbars

Additionally, sprayable coatings of the battery lid allow a protection against extreme temperatures a during a thermal runaway causing a fire.

7. Acknowledgement

I acknowledge the contribution of my colleagues Umesh Harkal, Abhijit Hirekerur and Sandeep Kothawade to this work.

8. References

[1] GB/T 38031-2020; Electric vehicles traction battery safety requirements

[2] Ruiz Ruiz, V. and Pfrang, A., JRC exploratory research: Safer Li-ion batteries by preventing thermal propagation, EUR 29384 EN, Publications Office of the European Union, Luxembourg, 2018, ISBN 978-92-79-96565-4, doi:10.2760/786907, JRC113320

[3] Patent application: IN 202241021136 "Fire retardant coating for battery boxes"

Smart Thermal Management

B. van Moergastel[1], S. Visser[1], R. Puts[1], P. Mosca[1], C. Massano[2], F. Planté[3], J. Basset[3]

1: DENSO AUTOMOTIVE, Friedrich-list-allee 42, Wegberg - Germany
2: DENSO Thermal System Frazione Masio 24, Poirino - Italy
3: RENAULT GROUP, 1 avenue du Golf – 78084 Guyancourt - France

Abstract: Smart Thermal Management is a novel vehicle system and control concept developed in close collaboration between DENSO and Alliance in which RENAULT is belonging. The aim is to optimize the energy distribution and utilization between the different subsystems inside the vehicle to maximize the customer satisfaction. The proposed concept has been developed by carefully listening to the end-customer voice and understand what the real needs of the end-customers are when it comes to real-world usage of a BEV. Cross-divisional members from diverse backgrounds (Thermal, Powertrain, Electrification, Mobility and Electronics) aim to maximize the total vehicle performance effectively using the expertise of all members. The holistic approach adopted by the team leverages on elements of 'Optimization-Based (OB) controls' and 'Artificial Intelligence' (AI) to guarantee best vehicle operation. Both in-car and out-car information are used in a Model Predictive Control (MPC) framework to determine an optimal control over a complete driving trip, taking into consideration past and future states of the vehicle system. Prerequisite of the control structure is modularity and scalability of the proposed solutions. For this reason, each technological upgrade part of the solution, can be seen as plug and play module to be integrated in the pre-existent architecture.

Background

The most common reason for not buying a battery electric vehicle is the lack of trust of the customer performance (range and charging duration) against ambient temperature, route trajectory and driving behavior. It is of the highest interest for the OEMs to solve this issue in the development of their products to keep competitiveness and increase their profitability.

One challenge for battery electric vehicles is to accurately predict the range expectation. An inaccurate display of the expected range can lead to increased range anxiety, stress, and quality of driving an electric vehicle. Particularly for very long trips it is more difficult to schedule due to required charging events. To be consistent along the trip, it is important to predict what would occur during the trip in terms of the vehicle's drivetrain and thermal management as a result of the selected route, traffic and weather conditions (disturbances).

The second challenge is to maximize customer satisfaction by maximizing range and reducing the charging durations, and to keep such planned route in relation to the actual driving events. This issue addresses for all trips, even though different seasonal circumstances. The higher-level goal of this study is to provide a set of leverages to the Alliance, with the help of "avant-gardish" approaches and methodologies, that have been determined by a fine process of design, grounded on to "from customer to design" approach. Both Alliance and DENSO share the same mindset in trying to solve this issue and to increase customer performance.

Below two root causes of inaccurate range predictions are described.

1: Battery electro-chemical processes. Figure 1 shows an example of temperature sensitivity on the battery performance. Batteries are used over a wide range of temperatures, which result in different power utilization during discharging and charging events.

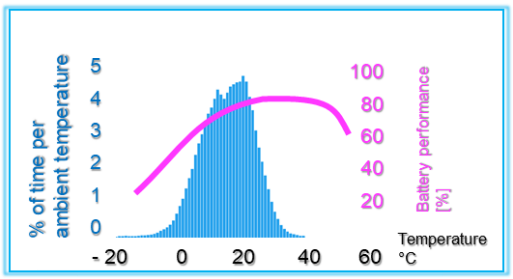


Figure 1: Battery pack temperature sensitivity

2: Thermal system's efficiency. The efficiency of the thermal system realizing the requested propulsion power required cabin conditioning while considering component efficient operating temperatures.

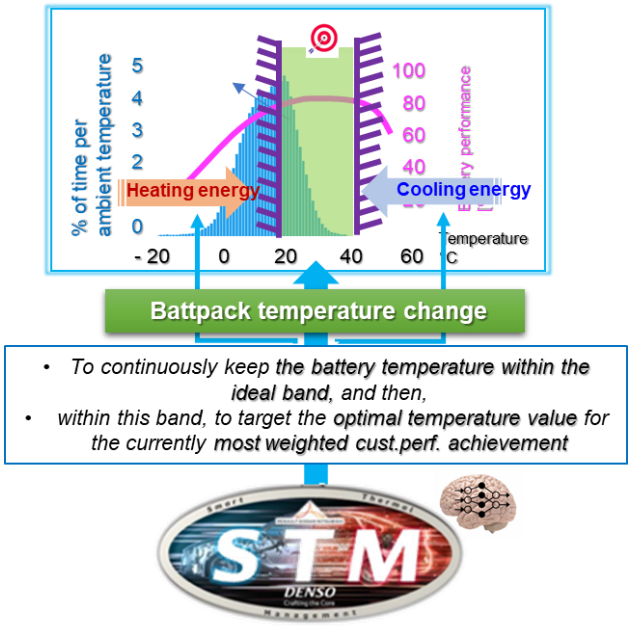


Figure 2: How Smart Thermal Management shrinks range of battery temperature

This Smart Thermal Management study does not include changes in the battery pack architecture, neither the chemistry, but as can be seen in Figure 2, it explores advanced controls to reach and keep optimal battery cell temperatures in a certain safe operating range for maximum customer performance.

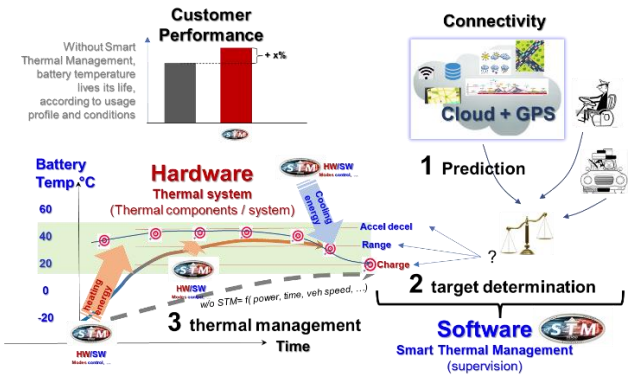


Figure 3: Three-step approach of Smart Thermal Management

As can be seen in figure 3, there is a three-step approach to be taken by a combination of high tech components and advanced controls to improve the customer performance level

1 Gather and collect in real time, the necessary information coming from outside by connectivity to GPS and Cloud, and from observation of the driver behavior, and of the vehicle state as far as possible (mass, CdA, ...).

2 Mix all these inputs into a "cauldron", to let a supervision device process this content, and thus balance in real time what is the most recommended customer value to be served, on the considered time. The considered time can serve an immediate driver need or request, or even anticipate for example, the next charging event. Afterwards, the battery temperature targeted value is given that supports the desired customer performance.

3 Assuming such a given targeted value, the Hardware of the vehicle thermal management system needs to be managed accordingly: after having right sized the single components, and having selected high efficient technology for the component systems, it is to get as quick as possible, and continuously with always the lowest quantity of energy, the targeted temperature value of the battery. This could be then summed up in the improvement of the COP of this system, and in optimizing either the sourcing of heat (for heating), or dissipation of heat (for cooling), from the least expensive one (like heat recovery concepts), up to the most expensive one, in terms of consumption of available energy in the battery.

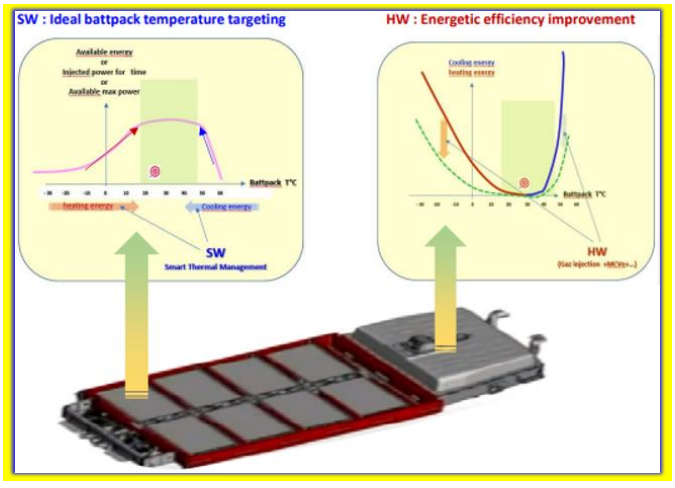


Figure 4: Individual contribution of Hardware and Software to Smart Thermal Management

1. Introduction

Three pillars have been identified as Key Performance Indicators (KPIs) towards customer performance:

Convenience: Total cost of ownership and practical utilization of the vehicle is essential to overcome the hurdle of BEV ownership. E.g., range anxiety that is commonly known mainly when driving in extreme cold or hot weather conditions.

Comfort: user feeling while driving the vehicle is a key factor for the customer satisfaction as the passengers need to feel at ease by not being too hot or too cold.

Fun to Drive: BEV is known for having a good amount of low-end torque and instant response compared to conventional powertrains. This aspect while driving the vehicle should not only be available in sport mode, but it must be maintained under all driving conditions.

The interrelation and trade-off between these three pillars define the multi-domain nature of the complex problem, requiring a holistic vehicle system solution. Starting from scratch and without preconceptions, both novel hardware and software solutions have been developed by a cross-divisional team of experts from both DENSO and Alliance. In this way the vehicle values are considered as a whole and managed by considering thermal, powertrain and electrification aspects as one system.

2. Smart Thermal Management (STM)

One of the core elements in the approach is the usage of high-tech components and state-of-the-art functionalities. The increasing complexity of the vehicle's thermal system is tackled using distributed approach inside a modular control architecture. Digital engineering is considered as development method, which means that there is a strong focus on the development and usage of simulation models.

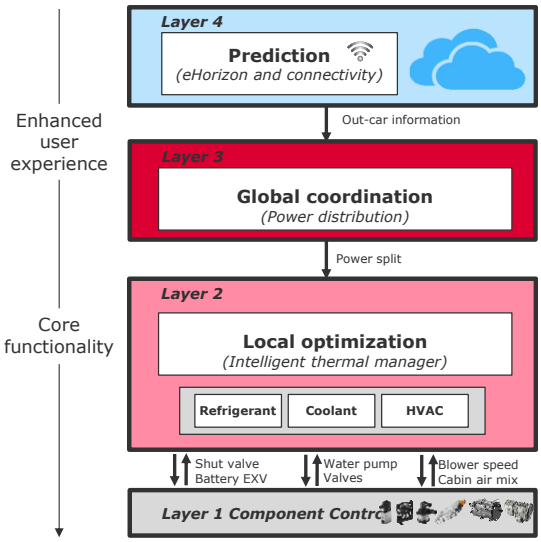


Figure 5: Thermal System modular control architecture

The control of the thermal system is a layered structure in order to improve the modularity of the system is visualized in Figure 5. The Layer 1 low level control acts directly on the actuators, containing mainly the base functionalities of the components to achieve the target setpoints (PID control, control maps). The layer 2 controls consist out of subsystem domain specific controls. With the focus on the thermal system, it includes the refrigerant, coolant, and HVAC controls. Layer 1 and 2 combined are treated as core functionalities, which are essential to operate the vehicle's main features.

Layer 3 is introduced to further enhance the user experience using global coordination functionalities. Predictive inputs are used to allow accurate energy coordination. The Layer 3 control therefore sets the heating and cooling demands of the heat pump, electric powertrain and cabin conditioning system.

Processing of prediction information is performed in the top Layer 4. With the data that is available within the vehicle, from the cloud and navigation systems, it is possible for modern systems to predict the required route trajectories for the energy usage of the vehicle.

3. STM - Prediction

All external inputs that could affect the in-vehicle's energy flow are considered within the prediction layer to allow optimal energy distribution. Four main sensitivities were identified to realize an accurate prediction for the vehicle's propulsion, cabin and battery conditioning for a given route. The main sensitivities are:

1) Actual traffic information
2) Weather information
3) Driving behavior
4) Charging station

To allow long route predictions, route segmentation is applied to meet the computational performance of the hardware selected. An optimal trade-off between the prediction accuracy and computational performance is set.

By using the connectivity to cloud services, it is possible to get that information in a real-time fashion that allows the feeding of the required information. This is fed as data that is processed smartly into segments inside the vehicle.

3.1 Traffic information

One essential item is the route prediction that contains the actual and predictive road & traffic conditions that determine the requested powertrain energy consumption.

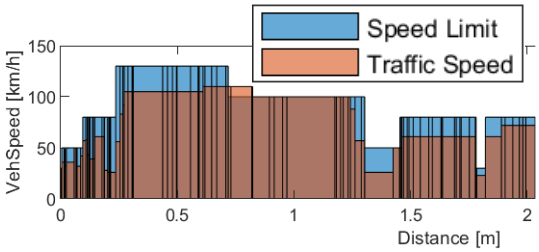


Figure 6: Cloud-based traffic speed information

Figure 6 shows an example of the available vehicle speed information of a route. This information is used into the prediction layer to compute the energy required to realize this trajectory.

3.2 Weather information

Another item that affects the energy consumption of both the cabin conditioning system as well as the battery conditioning system are (changing) ambient conditions like temperature (e.g. sunshine) and humidity (e.g. rain). In cold conditions there is a need for (additional) heating and in hot conditions there is a need for (additional) cooling. The use of predictive weather information into the prediction layer allows the passengers to feel comfortable while driving under changing circumstances. Additionally, the battery can be conditioned optimally to keep the performance of the vehicle and prevent excessive battery degradation.

3.3 Driving behavior

Another influence on the vehicle's energy consumption is the driving style of the user. An aggressive driving style typically leads to an increased powertrain energy consumption and is a property of the driver that can be reflected in the prediction of the route.

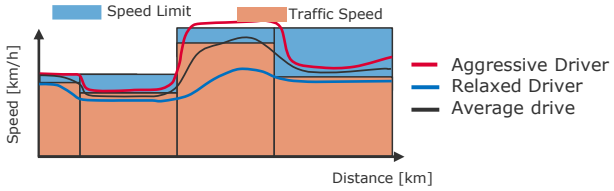


Figure 7: Driving behavior based correction factor

The prediction layer allows to correct the anticipated vehicle speed trajectory. Figure 7 shows an example of the predicted vehicle speed trajectory as a function of a certain driving behavior.

3.4 Charging stations

Charging station connectivity is essential to provide the information of the charging power to prepare the battery effectively towards the charger specifications. This can enable a reduction of over-conditioning the battery and realize quick charging time by ensuring the battery characteristics. Overheating can be avoided increasing the battery lifetime. can handle the charging power without incurring overheating and consequent degradation or thermal runaway.

These four inputs are considered within STM prediction layer. An accurate prediction is essential to reach the destination effectively and quickly as possible. Due to inaccurate or false information or unexpected events, the predicted energy trajectories can still differ compared to the real world. Global coordination functionalities anticipate prediction inaccuracies while further enhancing the driver satisfaction.

4. STM – Global Coordination

Layer 2 Global Coordination is an essential element between long range predictive inputs and the vehicle's core functionalities. The scope of this control layer is to distribute the energy between the vehicle's main subsystems. The electric powertrain, heat pump system and cabin conditioning are monitored simultaneously to guarantee the maximum satisfaction of the driver in terms of Comfort, Fun to Drive and Convenience, while reaching the destination with sufficient battery State of Charge.

The need for a coordination function at this stage is justified by the resolution of a multi-objective problem consisting in the optimal split of the finite amount of energy available in the battery, being the only energy source in a BEV.

The focus of the Alliance and DENSO is to generally maximize and prioritize user's satisfaction over the complete route. Satisfaction assumes different meanings based on the user's attitude and the operation context. In the case of a family trip in the countryside, cabin comfort assumes priority role over the propulsion aspect. A completely different scenario is given by the driver desire to feel the power of the BEV by rapid accelerations and high solicitation and energy consumption from the powertrain, typical of sporty driving style on a hilly landscape.

A Human Machine Interface (HMI) is available in the vehicle's cockpit allowing to transfer the driver's request to the control logic. Pure priority or combination of Comfort, Fun to Drive and Convenience express the driver preferences and are translated in the optimal control problem.

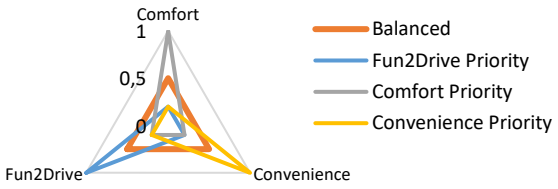


Figure 8: Driver Prioritization

Figure 8 reports an example of possible combinations of KPIs selection. The relative importance of the KPIs is expressed by a number between 0 and 1 (0% - 100%) for ease of representation. The translation of the driver's demand in mathematical terms is required for the formulation of the target cost function for the optimal control problem formulation. The cost function includes a term for each of the target KPIs which are weighted in importance based on the HMI values. Specifically, the cost function terms represent the degree of user satisfaction expressed as the available energy in respect to the energy demand at each of the subsystems for each of the road segments identified.

The most popular algorithms for the optimal energy split have been identified as a combination of classical Model Predictive Control (MPC), Dynamic Programming (DP) and Pontryagin's Minimum Principle (PMP). The foundation of Dynamic Programming makes the algorithm a good candidate for the resolution of a multi-states multi-input final state constrained problem.

The algorithm for the computation of the optimal control inputs can be broken down in four steps:

1: Computation of the sub-systems energy requirements. Predictive inputs in combination with inverse sub-models are used to calculate the energy demands of each road segments constituting the whole trip. Figure 9 shows an example of daily commute. The predictive vehicle speed is used to compute the propulsion energy demand with a calibrated physical vehicle model corrected based on the user's driving style.

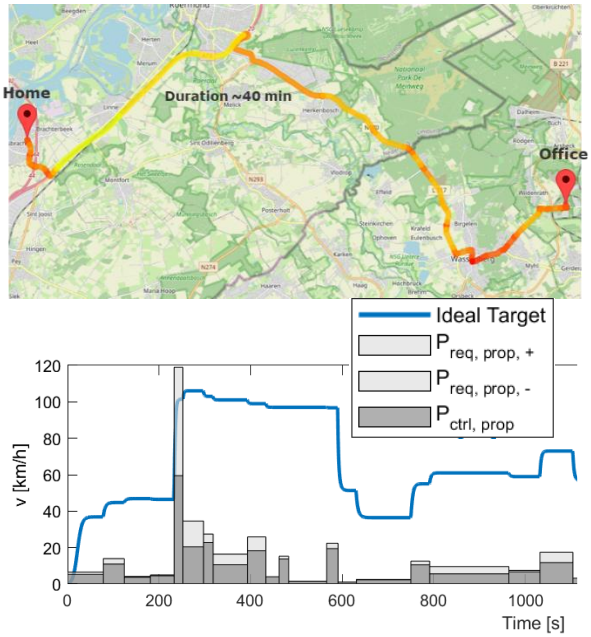


Figure 9: Energy demand computation based on target predictive vehicle speed trajectory

Together with the Propulsion energy requirement also the required thermal energy at the HVAC and Battery are computed in order to achieve respectively a cabin cooling/heating requirement and battery cooling requirement.

2: Problem formulation. The optimal problem could be formulated to guarantee the maximum user satisfaction (in terms of Fun2Drive, Comfort and Convenience) over the trip ensuring the arrival to the destination with predefined minimum residual energy in the battery. The available energy is a function of the control inputs accordingly to a must/want logic. The must/want logic ensures always a certain minimum level of available energy (and therefore driver's satisfaction).

3: Computation of the available energy for each subsystem in a Dynamic Programming Framework. The optimization problem represented by the cost function is solved backwards in the DP framework starting from the end time backwards to the initial instant in order to guarantee the final state to be

between the selected boundaries. The optimal control policy is computed by following the lowest cumulative cost over the complete trip (Cost-to-Go-Map). The state and the inputs are opportunely discretized and to reduce the computation burden, the time domain is discretized based on the segment duration (long and short segments result in same computational efforts).

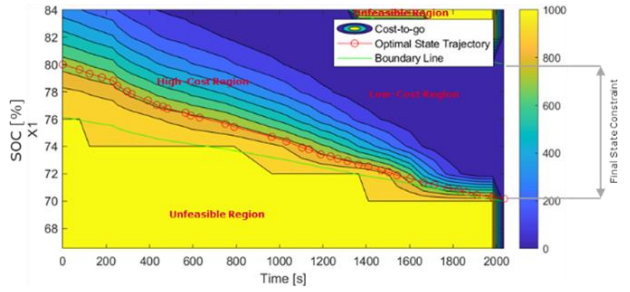


Figure 10: Cost-to-Go map

Figure 10 shows an example of Cost-to-Go map and the computed optimal SOC trajectory. The battery SOC is located at the limit of the unfeasible region where the user satisfaction can be maximized by keeping the final SOC in the target Final State Constraint interval.

4: Optimal Control Inputs actuation. The available energy for each subsystem is used in each subsystem as a constraint for the local optimization. In figure 11 there is an illustration of the energy available (dark grey) and the requested (light grey). Not all the requested energy is provided to the Coolant Subsystem in order to reach the destination with the actual SOC in the target final region. With this constraint and the optimization an optimal satisfaction is achieved at the price of not completely meeting the target temperature trajectory.

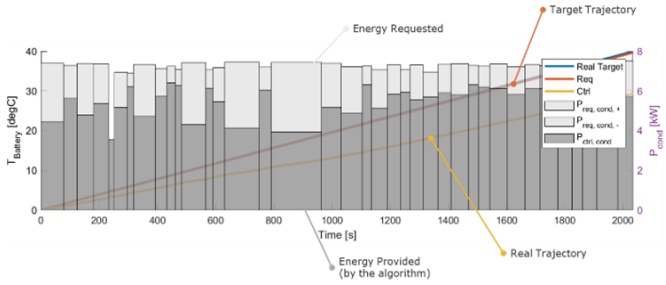


Figure 11: Optimization result

5. STM – Local Optimization

Layer 2 Local Optimization control aims to reduce the amount of calibration effort that normally would increase together with system complexity. Optimal Model Predictive Control (MPC) is enabled by the training of surrogate models by Deep Learning techniques. By using advanced Machine Learning (ML) methodologies it is possible to optimize the control of both refrigerant and cooling subsystem by characterizing these subsystems, e.g. in the form of Neural Networks, in a real-time fashion.

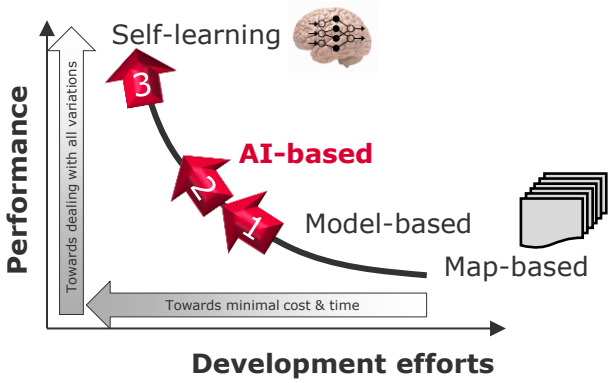


Figure 12: Performance vs. development efforts

A cost function expressing the optimization problem leverages a surrogate system representation to determine the optimum for best subsystem efficiency while fulfilling the required performance. This type of optimization-based control removes the need of operating modes and the rule-based calibrations required for each mode, enabling a significant reduction in calibration effort. This is supported by the fact that the amount of physical testing can be reduced when using an accurate digital plant in Model in the Loop (MiL) environment. Component testing, system testing and demo-car testing become less critical during the development phase reducing the development efforts further. Due to the modular control architecture, calibrations could be easily updated using actual vehicle data to make sure optimum control is guaranteed.

The selection of the most suitable Supervised Learning (SL) based model depends on the system complexity and the computational performance available of the hardware selected. A heat-pump model requires a high complexity and good accuracy. The selected model is the neural network.

Extensive research for the selection of a suitable optimization algorithm has been carried out and population-based optimization algorithm has been selected instead of more classical approaches such as first-derivative, second-derivative or Blackbox methods based on the following criteria:

- Simplicity and easiness of calibration (low amount of calibration parameters)
- Bounded optimization domain (particularly suitable for control)
- Avoidance of local minima convergence
- Multidimensional optimization
- Potential for parallel computation

Figure 13 demonstrates the initial and optimal outputs for cabin cooling for a given time instance

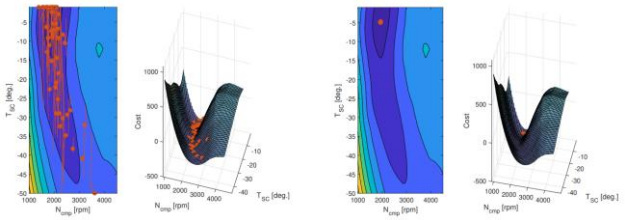


Figure 13: Swarm optimization, initial iteration (left) and optimal output (right)

Main objective of the heat pump system is to control towards the desired heating or cooling performance. Secondly, controls should maximize the system efficiency. In the case of a heat pump system, the system efficiency is defined by the Coefficient of Performance (COP), which is the ratio of the delivered cooling/heating performance and the electrical energy used. Thirdly, the control targets must be selected such that stable operation of the system is guaranteed.

Figure 14 shows that by implementing the local optimization methods in an Intelligent Thermal Management (ITM) a 24% reduction of compressor energy can be achieved, resulting in driving range increase as customer value.

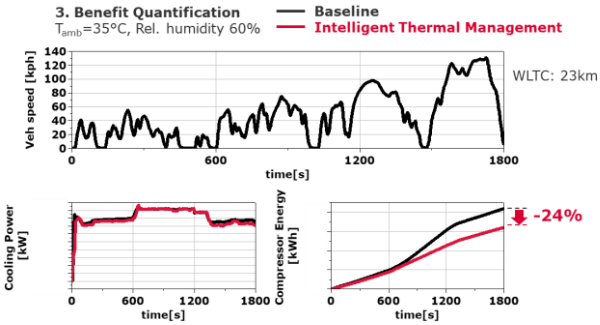


Figure 14: WLTC evaluation, base vs. ITM

It can be concluded that by implementing machine learning model in combination with the optimization function to create the control references, the total performance of the thermal system can be significantly increased. Additionally, the selection of the right control method allows the best performance of the computational power available.

State-of-the-art heat pump and coolant systems are getting more complex over time as battery thermal management becomes more important. A multi-dimensional control problem needs to be solved. An increase of recovered waste heat and reduction of electrical energy has been identified using local optimization controls. This then includes the coolant system with advanced hardware solutions linked to smart controls.

6. Summary

Smart Thermal Management consists out of 3 essential parts with their own purpose

- Connectivity is key to accurately estimate vehicle's energy flows
- Global coordination realizes optimal energy distribution for optimal customer satisfaction
- Local optimization method enable control towards optimal efficiency while reducing development efforts

In a next step, the performance of STM's virtual developed advanced functionalities shall be demonstrated in a real vehicle on the road.

Glossary

AI: Artificial Intelligence

Alliance: RENAULT, NISSAN, MMC (Mitsubishi Motors Corporation)

CdA : Drag coefficient times frontal area

COP: Coefficient of performance

DP: Dynamic Programming

HMI: Human Machine Interface

ITM: Intelligent Thermal Management

KPI: Key Peformance Index

MiL: Model in the Loop

ML: Machine Learning

MPC: Model predictive controls

OEM : Original Equipment Manufacturer

PMP: Pontryagin's Minimum Principle

SOC: State of charge

SL: Supervised learning

STM: Smart Thermal Management

Artificial Intelligence methodology for electric vehicle battery modelling

Daniele Gatto[1], Leonardo Canzio[1], Raffale Farina[1], Jeonghan Park[1]

1: Hyundai Motor Europe Technical Center, Hyundai-Platz, 65428 Rüsselsheim am Main, Germany

Abstract: Li-ion cells performance is heavily impacted by temperature. Smart battery thermal management can improve overall performance for Battery Electric Vehicle (BEV) via predictive heating or cooling. Current solutions are based on experimental data collection and heating/cooling system calibration to reach a specific temperature target. For improving the current status, higher system prediction capability is achieved via Artificial Intelligence (AI), with an emphasis on reducing road test so to limit assets usage and cover an entire car range without long and expensive tests for each vehicle. New methodology aims at temperature evaluation and energy-efficient management rather than target temperature achievements. Flexible structure allows for implementing thermal management evaluation in real time. Given a specific route prediction, this model targets a temperature prediction within 1°C accuracy. The current development showed promising results but, to reach the target value, an increase in gathered data is required.

Keywords: Battery model, Artificial Intelligence, Battery Electric Vehicle, Battery thermal management

1. Introduction

Battery Electric Vehicles (BEV) have become increasingly popular in recent years and market predictions are pointing at a continuation of this trend for the near future [1]. This growth in usage has shown a limitation of the current battery technology. Lithium-ion batteries (LIB) are affected by very poor performance in low temperature conditions [2] due to their chemical limitations. To achieve the same level of usability expected by driver in these situations, most commonly apparent during winter times, who are accustomed to Internal Combustion Engine, it is imperative to find solutions to achieve battery temperatures that allow for optimal performance by BEVs. Moreover, high temperature conditions may be detrimental for battery health during its lifespan, thus strategies for battery cooling are in place when deemed necessary.

These operations are possible by actuating thermal management solutions which are intrinsically very energy demanding due to the high thermal inertia of this kind of energy storage.

An optimisation process is thus required. This is achievable through the development of a battery thermal model that will allow for better temperature evolution prediction, which will be used to minimize the energy expense for thermal management and allowing for improved consumption and reduced charging times.

The goal of this paper is to present a battery thermal model that can predict the temperature evolution in a 30-minute window into the future given the predicted user case, may it be for the vehicle to be driven to a selected destination, charge, used for Vehicle-To-Load (V2L) or left stationary. The predicted temperature has to replicate the behaviour of the temperature measured by the Battery Management System (BMS), which is installed on the vehicle, since the project had to rely on existing hardware to minimize the working hours required for its development.

Since the battery is a highly complex system with a temperature gradient dictated by its chemical, geometrical and thermal configuration, the model must predict both the maximum and minimum measured temperature within the battery pack in order to actuate both predictive heating and cooling solutions.

Additional conditions are connected to the modelling phase: the battery and vehicle systems are considered as “grey boxes”, with the only available data coming from press material. This consideration is dictated by, respectively, the inherit danger of sharing highly sensitive information such as battery chemistry and operational functioning, and the cost of complex analysis such as multibody thermal and computer fluid dynamics analyses.

The desired temperature prediction has to achieve maximum punctual error less than or equal to 1°C for both values separately. This accuracy is required by the current battery thermal solutions strategies.

In order to further minimize the required operative work for its development and usage, the model has to be trained with the data gatherable during one week work on a single vehicle. Additional requested were posed for increased flexibility on multiple vehicles from the same family, which share similar architectures and, thus, the comparable battery hardware.

The final result will be used in optimisation solutions which will focus on minimizing the required energy to

reach a specific target temperature, either for the maximum or minimum value, or to minimize the charging time, given the hard limitation on power input strictly related to the battery temperature. For this reason, the model has to allow for thermal management influence implementation: to reduce the complexity, a heat exchange parametrization has been chosen, so further evolution can implement this feature with reduce effort.

2. Model structure

2.1 Model functional structure

The battery thermal model works in conjunction with an operative prediction model: this component absolves the requirement of providing information on the desired time horizon regarding the supposed user case and the environment in which the vehicle will be used. To do so, the model relies on Sat-Nav information, such as current position, road profile, traffic and weather forecast, and user inputs, such as set destination, driving style and usage style parameters, and scheduled usages.

This model requires an accurate power request prediction, given the information on possible usage scenario in the predictable future (driving, charging, inactivity). Since driving condition is the main focus for this battery thermal model, the power request is calculated according to road profile to reach the specified destination by the driver, his/her driving style, predicted traffic and other information.

The model has to output the following signals as time series for the desired time horizon: power input/output to/from the battery, predicted speed, predicted ambient temperature along the selected route.

This model is built separately, and in-depth accuracy is under investigation.

The battery thermal model has been built from data available via CAN-BUS signals on the tested vehicles to allow for a seamless conversion from offline to online usage and mass production deployment.

The battery thermal model is based upon the concept of produced heat by the battery due to ohmic resistance, and heat exchange with the surrounding ambient and elements.

The battery model can be divided into two sections: electric and thermal subsections.

Due to the restrictions imposed to the project, it was required to find a solution that would have facilitated the conversion from one vehicle to another from the same family of cars. The electric model aims at calculating the generated heat from a single cell, which can then be multiplied for the number of available cells. This means that vehicle sharing the same cell chemistry can be described by the same model, scaled to fit the available battery configuration.

The dispersed heat is then used in the battery thermal subsection to compute the temperature evolution, combining the influence of ambient factors and chemical behaviour.

2.2 Electric model

The main objectives for the electric model were:

- Predicting battery voltage drop under load.
- Allowing for current determination, given a specific power request (adjusted for accounting of inefficiency between powertrain components from the tires to the battery inlet.
- Evaluating the amount of heat produced by the battery

This section is, also, responsible for predicting the State of Charge (SoC) evolution, given the battery capacity (expressed in kWh) and the requested power, adjusted for the operative conditions, which may cause a variation in both values.

To simulate such system with the specified requirements, the approach has been to divide the battery into single cells which have been represented individually, for them forming the entire battery in its complexity. For this representation, multiple solutions for both physical and empirical models were analysed: the former were discarded due to the large amount of sensitive data required for its current operation.

Battery equivalent circuits have multiple degrees of complexity, meant to represent the different characteristic behaviours presented by LIB.

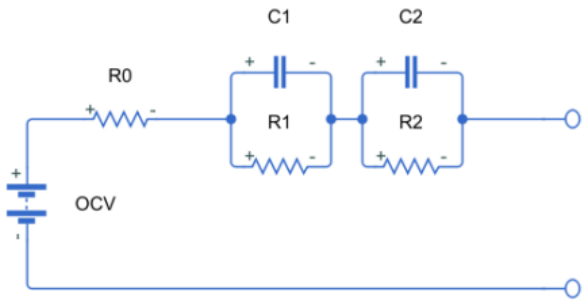


Figure 1: Thevenin battery equivalent circuit

The final choice in equivalent electric model settled on Second Order Thevenin Model (Figure 1), due to the fact that was extensively proven in multiple occasions to offer more accurate results [3] than other models, its computational cost is on the lower spectrum compared to other solutions and has already been proven for battery thermal prediction [4] [5]. This model il composed by 6 elements: an ideal voltage generator, 3 resistances and 2 capacitances. Those unknown physical proprieties will be determined by optimisation methods. As such, the main equation to calculate the single cell voltage V is:

$$V = V_0 - V_d - V_r \quad [1]$$

Given:

$$V_d = K \cdot Q \cdot \frac{it}{Q-it} + Ae^{-it} + K_f \cdot Q \cdot \frac{i_{f1}}{Q-it} \quad [2]$$

$$V_r = R_0 \cdot i + R_1 \cdot i_{f1} + R_2 \cdot i_{f2} \quad [3]$$

Where:

- $V_0 =$ open circuit voltage [V]
- $V_d =$ discharge-related voltage drop [V]
- $V_r =$ resistance-related voltage drop [V]
- $i =$ current requested to the battery [A]
- $i_{f1} =$ electrochemical polarisation current [A]
- $i_{f2} =$ concentration polarisation current [A]
- $it = \int i\, dt =$ discharged energy [Ah]
- $Q =$ cell capacity [Ah]
- $R_{0,1,2} =$ equivalent resistances [Ω]
- $K, A, B, K_f =$ parameters for typical battery discharge curve representation [ ] [6]

Electrochemical and concentration polarisation currents can be calculated using the equivalent capacitance according to the proprieties of second order systems.

These parameters that govern the electrical behaviour of each cell are affected by external influences. Temperature is one of the most prevalent: within the standard range of usable temperature, its effect can be seen on the internal resistance, which tends to increase at the decrement of the temperature [6], on capacity, which tends to decrease with the temperature [7], and on Open Circuit Voltage (OCV), with a general decrement in low temperature conditions [8]. To evaluate the three most prevalent variables (SoC, C-Rate and temperature) influence on the parameters, studies suggest that polynomial equations are sufficient to model fully represent the variation during exercise [9]. These variations have been accounted by optimizing the coefficients k_{ij} in polynomial functions that are hereby presented. Given a base value for each parameter y_o and *n* influence values x_i , normalised in value, the third-degree polynomial that gives the correct parameter result *y* is:

$$y = y_0 \left(1 + \sum_{j=1}^{3} \sum_{i=1}^{3} k_{ij} \cdot x_i^j\right) \quad [4]$$

The main approximations for this model are as follow:

- Supposed battery State of Health (SoH) is 100%
- No regulation intervention by BMS is required: all the battery cells are perfectly balanced
- No permanent chemical mutation in operation
- No performance degradation or self-discharging phenomenon
- Battery chemistry and electric behaviour is constant between each cell
- No other impedance is present inside the battery rather the battery cell
- Ideal measurement system
- Temperature between themselves and the module enclosure
- Perfectly symmetrical condition between the two parallel that compose the battery

When the model is completely optimised, a lookup matrix is generated to allow for faster computation in current – voltage split, given a predicted power request in a specific set of boundary conditions (SoC and temperature).

2.3 Thermal model

Battery packs are highly inertial systems from a thermodynamic perspective, whose temperature cannot be defined as a single value but rather as a continuous gradient within the structure due to the reduced thermal conductivity. Usually, a battery is mainly composed by very closely packed cells to increase the energy density, which limits the ability to exchange thermal energy with the outside ambient. Other elements present within the battery pack are connecting tabs, connecting wires, sensors and embedded systems for safety purposes. The battery system is usually contained in a robust and isolated structure, with added exterior elements such as insulation, reinforcements and thermal management systems. This structure is usually bolted directly to the vehicle chassis with added passive safety elements. The thermodynamic state of each cell, as for any other body in existence, is linked to its enthalpy. The variation of this physical propriety, inside a battery cell, can be divided into two different contributing factors: irreversible and reversible heat. Irreversible heat is always positive (thus, heat is generated), but reversible heat can be both positive and negative, depending on the current thermophysical status of the analysed cell. So, it can be stated that a battery cell in thermal equilibrium with the environment surrounding it, can not only generate heat but also absorb it. The reversible contribution in overall heat variation, however, is not predominant in thermal evolution, but shall not be ignored. It has been proven that heat generation as a contribution of only static resistance is not reliable for temperature prediction [10], in some situation amounting for 10-20% of thermal energy variation inside the cell [11]. The turning point in which irreversible heat generation becomes prevailing is when C-Rate is greater than 0.5 C. Moreover, for general cell studies purposes, reversible heat can be included in irreversible heating effects [12], just by modifying its contribution accordingly. In terms of physical proprieties, cells heat capacity is directly linked to their SoC [13]. The variation in value has been quantified at around 15% from full charged to fully discharged [14] [15] and the common behaviour may be approximated through a

linear regression. Moreover, temperature itself varies heat capacity proprieties on all materials, in particular for LIB. The variation in specific heat capacity is very dependent on battery chemical composition, shape and temperature difference, with some tests reporting small variation [16] while others report as much as 38% variation within a 60 degrees window (from −5 °C to 55°C) with strong evidence of an effective linear regression model being accurate to predict the expected evolution [17]. In terms of heat exchange with the surrounding ambient, the two main mechanisms are convection and conduction. Speed has been investigated as an additional factor in convective heat transfer as shown by some studies [18], the heat transfer coefficient of underbody is non-negligible and can be approximated via linear interpolation as a function of speed.

The main approximations for this model are as follow:

- Heat inside the battery is generated only by cells.
- Any other heat source is negligible or compensated by other inputs
- Heat generation within the cell is homogeneous: no hotspots formation
- Heat generation is not affected by SoH
- Chemical or physical proprieties do not change irreversibly over time, no hysteresis effects
- Irreversible heat is negligible or compensated by other inputs
- Temperature dependent variation of parameters are compensated by the model itself
- Ambient temperature is uniform around the vehicle
- Heat exchange with outside environment is only function of ambient temperature
- Any other element exchanging heat with the battery is considered at ambient temperature
- Elements in the HVAC system do not exchange heat with the battery
- Predicted temperature is supposed to behave exactly as a predictive thermometer sensor: the model will not predict exactly the temperature of the cells, just the predicted thermometer reading

The electrical model is heavily influence by the temperature of each cell, but those values are the requested output. To overcome this issue, these solutions were developed:

- The battery has been divided into modules, each one composed by a fraction of the total cells in this system. Each module has been represented by a single cell with a specific temperature in a lumped mass representation model
- A static temperature distribution has been supposed; to estimate such distribution, thermal resistance was supposed equal on all directions, ignoring physical proprieties
- The entire thermal model is run iteratively until it converges. For the first iteration, battery temperatures are supposed constant with the same value as in the prediction instant, then they are updated until convergence is reached

3. Model construction

3.1 Data acquisition

All the available data has been acquired on a Hyundai Ioniq 5 Long Range AWD. The data acquisition took place on May 2021 in the state of Hessen (Germany). All the data was acquired with the stochastic ambient condition in the defined test week. Data acquisition has been performed via an OBD-to-USB connector and a decrypting program to analyse the CAN-BUS signals. The speed has been estimated from data used for ABS system.

The goal of this testing phase was to recreate the largest variety possible in data point for the training phase. For this reason, the test procedure has been divided into 3 sections: driving, charging and soaking.

1. Driving: the vehicle has been driven on urban, extra urban and highway roads with a driving style based on homologation test such as the Worldwide Harmonised Light-Duty Vehicles Test Procedure (WLTP). Moreover, the driver has been instructed to perform the manoeuvres with different vehicle maps (sport, normal and eco), different regenerative strategies and with different power requests (from more aggressive to tamer). To compensate for the lack of data at very low temperature condition, the vehicle has been soaked overnight for half of the testing days at sub-zero temperature to recreate the driving with low battery temperature during the first driving phase

2. Charging: the vehicle has been charged from different SoC (varying from 5% to 40%) with different power inputs (AC 230V, DC 400V, DC 800V)

3. Soaking: the vehicle has been left turned off in a given ambient, most of the tests required the usage of a climate chamber, which recreated a specific ambient temperature; these tests were meant to acquire data on the heat exchange

Total measured data amounts at:

1. 20 hours of driving
2. 5 hours of charging
3. 26 hours of soaking

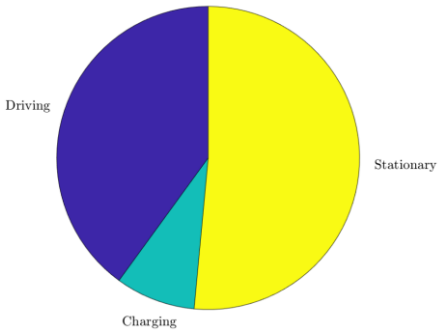


Figure 2: Data division between 3 sections

To compensate for the lack of data at different temperatures, synthetic time series have been included to cover the entire spectrum from -20°C to +50°C with data sets meant to simulate thermal equilibrium conditions. Due to the high thermal inertia of the battery system, the synthetic data represents a quasi-equilibrium state, often seen after a period of 2-6h of stationarity in any given ambient, as presented in Figure 3.

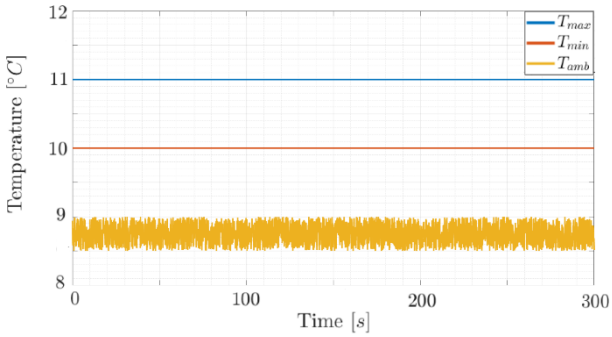


Figure 3: Example of synthetic dataset added for training purposes

White noise has been added to the ambient temperature to simulate a realistic measurement. For the electric signals, time series from other stationary acquisitions similar in temperature have been copied and used for these synthetic series. This data amounted to 5 more hours of stationary conditions.

3.2 Electric model development

For the electric model, all the necessary parameters have been optimised thanks to the usage of Genetic Algorithm (GA).

The parameter optimisation has been divided into two phases:

1. OCV optimisation, in which all the parameters related to the voltage and its dependency on SoC and temperature were extrapolated from the soaking datasets
2. Resistance optimisation, in which all of the data acquisition has been used to optimise the values for the resistance response during charge and discharge events.

The target function has been defined as the average of difference between measured and simulated voltage. When the results have been deemed satisfactory, these two steps have been halted and the electric model has been declared as defined, with the optimal results as the de-facto parameters for the next simulations.

3.3 Thermal model development

The thermal model has been developed with an Artificial Neural Network (ANN) architecture meant to represent the physical behaviour of the analysed system.

Every Neural Network is formed by layers, structures in which nodes are grouped, and neurons, in which every input signal is multiplied by a specific weight and combined to a specific bias. The training process for a Neural Network is meant to optimise the values for factors and addends to minimize the error function output.

The designed Neural Network is divided into five main sections, as presented in Figure 4:

1. Input section
2. Input processing
3. Battery-inspired section
4. Output processing
5. Output section

The input section is composed by 5 signals:

1. *H:* Battery Generated Heat [J]
2. *C:* Current [A]
3. *AT:* Ambient Temperature [°C]
4. *Sp:* Vehicle Speed $\left[\frac{km}{h}\right]$
5. *SoC:* State of Charge [%]

Current signal has been added to account for reversible heat.

While the output section is composed by 5 signals:

1. *Tmax:* Maximum battery temperature [°C]
2. *Tmin:* Minimum battery temperature [°C]

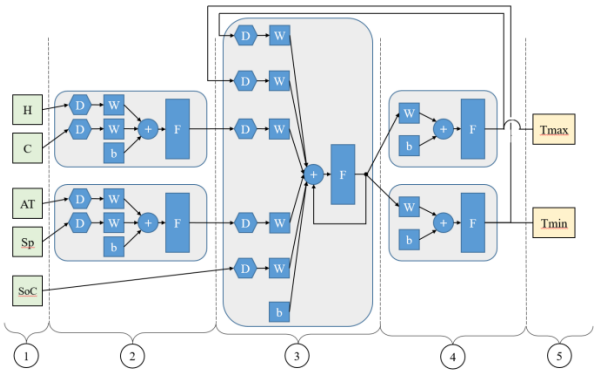


Figure 4: Artificial Neural Network

Each section contains either one or two layers, which are meant to represent the specific physical behaviour of the system: in the second section, the heat generation process is separated from the heat exchange with the ambient.

After iterative optimisation, the best result has been achieved with the following configuration:

- Second section: 80 neurons per each layer and hyperbolic tangent activation function
- Third section: 250 neurons and hyperbolic tangent activation function
- Forth section: 1 neuron per each layer and linear activation function

The architecture hereby presented can be classified as a Deep Neural Network, due to the presence of multiple layers, a Nonlinear Autoregressive Network with Exogenous Inputs since the outputs from previous time steps are combined to inputs to produce a new time step prediction, a Recurrent Neural Network, since the battery layer output is closed in a loop with its inputs, and a Time Convolution Network, since the inputs are convoluted with dynamic kernels to optimise the outputs. To evaluate the performance of this ANN, the chosen parameter has been the Root Mean Squared Error. The dataset has been divided into:

- 70% training
- 30% validation
- 0% test

The datasets have been divided into blocks to replicate a more accurate testing scenario.

The training process has been divided into 2 phases:

- Open Loop Training, in which the temperature data points from previous time samples have been given as input, to minimize the error propagation during the first epochs and to allow for more accurate temperature prediction for the next time sample. This training does not produce a valid ANN since the requirements ask for a multiple time steps prediction into the future, but it allows for faster convergence during the Closed Loop Training
- Closed Loop Training, in which the Neural Network is trained to operate as demanded to, with multiple time steps prediction into the future relying only on the temperature prediction it's able to perform

A down sampling in data frequency has been actuated to reduce the amount of data for training purposes and, thus, reducing the required training time to generate the working network. In has been decided that a down sample from 10 Hz of the original signal to 0.1 Hz was acceptable, since temperature variation frequency can be estimated with the same or lower order of magnitude. To avoid lost of information, all the signals have been averaged over the new time period, except for the generated heat, which has been integrated over time to produce a new signal whose information respected the original one.

4. Results

4.1 Electric model validation

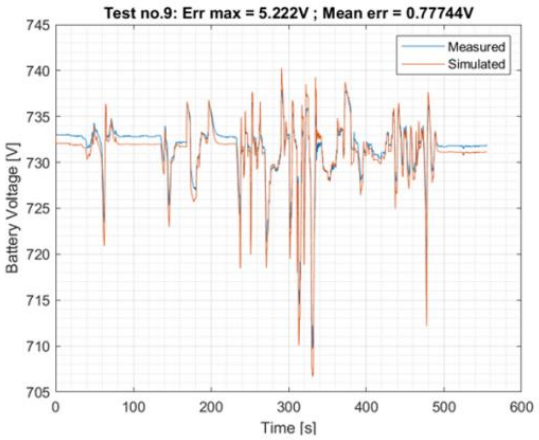


Figure 5: Voltage correlation between GA optimization and target value - best result

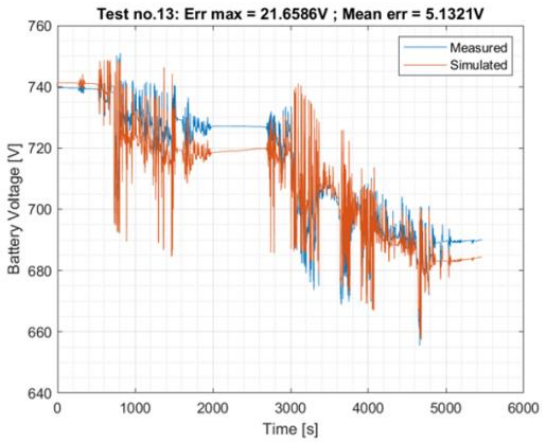


Figure 6: Voltage correlation between GA optimization and target value - worst result

The main goal for the genetic algorithm was to optimise the variables to obtain a proper fitting in voltage curves during operative conditions. The algorithm produced the following results:

The average result registered a RMSE = 3.872V. The maximum error is 21.65V and it's related to a very rapid change in current flow.

This result was deemed accurate enough for the heat estimation. The main problem with this technique, due to OCV estimation in stationary and post-cool-down conditions, the value measured when current I = 0A has a constant gap from predicted to target. To improve the performance, new time-dependant OCV compensation strategies have to be studied.

4.2 Thermal model validation

With the resistance value extrapolated in the previous analysis, the generated heat is calculated to produce a temperature prediction from the thermal model.

For testing the resulting Neural Network, new data from a vehicle with the same characteristics as the one used for the first data acquisition has been generated and measured. This process was meant to demonstrate the validity of said ANN on multiple vehicles in different ambient conditions. New test data amount to 30 minutes, divided into two sessions, performing a driving cycle on public road in urban and highway conditions. On this phase, it has been decided to pursue an offline validation to reduce production time. The results have also been post-processed using a moving average function with a data span of five points. This process is meant to reduce the oscillation in resulting signal, since the temperature evolution is much slower than predicted.

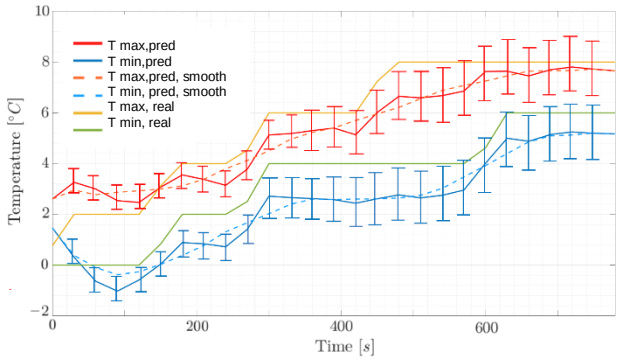


Figure 7: Test results for battery temperature prediction, comparison – session 1

		Prediction	
		As is	Smoothed
Tmax	RMSE [°C]	0.7881	0.7608
	Max Error [°C]	1.8436	1.8436
Tmin	RMSE [°C]	1.0627	1.0331
	Max Error [°C]	1.5622	1.9749

Table 1: Test results for battery temperature prediction, output and smoothed value – session 1

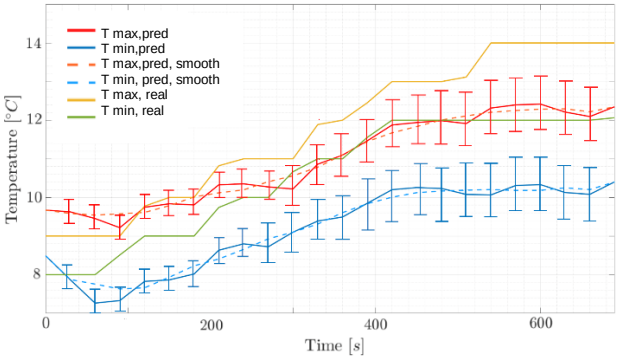


Figure 8: Test results for battery temperature prediction, comparison – session 2

		Prediction	
		As is	Smoothed
Tmax	RMSE [°C]	0.9664	0.9390
	Max Error [°C]	1.7945	1.9055
Tmin	RMSE [°C]	1.4079	1.3830
	Max Error [°C]	1.9341	1.9940

Table 2: Test results for battery temperature prediction, output and smoothed value – session 2

As supposed, the smoothed predictions result in lower RMSE values, but higher maximum absolute errors, causing a slightly worse performance given the specified evaluation metric.

5. Conclusion

Results show only a partial compatibility with measured values and the maximum error for both minimum and maximum temperature, while on the same order of magnitude, are above requested target (1.8 °C and 1.9 °C against 1 °C). RMSE is lower but still above target value (0.9 °C for maximum temperature and 1.2 °C for minimum temperature, calculated as combination of both sessions).
The results from this procedure are considered promising but not on target for the requirements. This solution may be pursued for future application but has to be improved upon.
After further analysis, here are further ways in which the model can be improved:

- More test with different driving conditions and driving scenarios
- More tests at different soaking temperature and different battery starting temperature
- Tests distributed on different months of the year or recreated on clematises chassis dynos: the departure from an ambient with high temperature difference compared to the test scenario may have caused a non-realistic data input

- Specific tests on speed influence on thermal exchange
- Accurate data from battery bench testing may be used for improved electric model accuracy.

In total, it has been estimated that the amount of test has to be at least doubled in order to achieve the desired accuracy and it has to be distributed in different month of the year or must be conducted in thermally controlled environments.

6. Acknowledgement

The authors acknowledge the contribution of ePT Performance development department colleagues from Hyundai Motor Europe Technical Center.

7. References

[1] I, T. D, and L. N, “Li-ion batteries for mobility and stationary storage applications,” Scientifc analysis or review KJ-NA-29440-EN-N, 2018.

[2] Shuai Ma, Modi Jiang, Peng Tao, Chengyi Song, Jianbo Wu, Jun Wang, Tao Deng, Wen Shang, “Temperature effect and thermal impact in lithium-ion batteries: A review”, Progress in Natural Science: Materials International, vol. 28, Issue 6,2018

[3] G. Wu, C. Zhu, and C. Chan, “Comparison of the frst order and the second order equivalent circuit model applied in state of charge estimation for battery used in electric vehicles”, Journal of Asian Electric Vehicles, vol. 8, July 2010

[4] C. Zou, A. Klintberg, Z. Wei, B. Fridholm, T. Wik, and B. Egardt, “Power capability prediction for lithium-ion batteries using economic nonlinear model predictive control,” Journal of Power Sources, vol. 396, 2018

[5] M. F. Niri, T. Q. Dinh, T. F. Yu, J. Marco, and T. M. N. Bui, “State of power prediction for lithium-ion batteries in electric vehicles via wavelet-markov load analysis,” IEEE Transactions on Intelligent Transportation Systems, vol. 22, no. 9, 2021.

[6] L. Gurjer, P. Chaudhary, and H. K. Verma, “Detailed modelling procedure for lithium-ion battery using Thevenin equivalent,” 2019 IEEE International Conference on Electrical, Computer and Communication Technologies (ICECCT), 2019

[7] C. Zhang, K. Li, S. Mcloone, and Z. Yang, “Battery modelling methods for electric vehicles - a review,” 2014 European Control Conference (ECC), 2014

[8] R. Zhang, B. Xia, B. Li, L. Cao, Y. Lai, W. Zheng, H. Wang, W. Wang, and M. Wang, “A study on the open circuit voltage and state of charge characterization of high-capacity lithium-ion battery under different temperature,” Energies, vol. 11, 2018.

[9] V. Sangwan, A. Sharma, R. Kumar, and A. K. Rathore, “Equivalent circuit model parameters estimation of li-ion battery: C-rate, soc and temperature effects,” 2016 IEEE International Conference on Power Electronics, Drivesand Energy Systems (PEDES), 2016

[10] . Yang, and F. Feng, “A novel resistance-based thermal model for lithium-ion batteries,” International Journal of Energy Research, vol. 42, 2018.

[11] Y. Inui, S. Hirayama, and T. Tanaka, “Detailed estimation method of heat generation during charge/discharge in lithium-ion battery using equivalent circuit,” Electronics and Communications in Japan, vol. 102, 2019

[12] A. Gunnarshaug, P. Vie, and S. Kjelstrup, “Review—reversible heat effects in cells relevant for lithium-ion batteries,” Journal of The Electrochemical Society, vol. 168

[13] P. Keil, K. Rumpf, and A. Jossen, “Thermal impedance spectroscopy for li-ion batteries with an ir temperature sensor system,” 2013 World Electric Vehicle Symposium and Exhibition (EVS27), 2013.

[14] H. Maleki, S. Al-Hallaj, J. Selman, R. Dinwiddie, and H. Wang, “Thermal properties of lithium-ion battery and components,” Journal of The Electrochemical Society, vol. 146, 1999.

[15] G. Yu, X. Zhang, C. Wang, W. Zhang, and C. Yang, “Experimental study on specifc heat capacity of lithium thionyl chloride batteries by a precise measurement method,” Journal of the Electrochemical Society, vol. 160, 2013.

[16] N. Nieto, L. Diaz, J. Gastelurrutia, I. Alava, F. Blanco, J. Ramos, and A. Rivas, “Thermal modelling of large format lithium-ion cells,” Journal of the Electrochemical Society, vol. 160, 2012.

[17] S. J. Bazinski and X. Wang, “Experimental study on the influence of temperature and state-of-charge on the thermophysical properties of an LFP pouch cell,” Journal of Power Sources, vol. 293, 2015.

[18] A. El-Sharkaw y and T. Crabtree, “Estimates of the convective heat-transfer coefficients for under-hood and underbody components,” 04 2019

8. Glossary

ANN: Artificial Neural Network

BEV: Battery Electric Vehicle

BMS: Battery Management System

GA: Genetic Algorithm

LIB: Lithium-Ion Battery

OCV: Open Circuit Voltage

SoC: State of Charge

SoH: State of Health

Tmax: Maximum cell temperature

Tmin: Minimum cell temperature

V2L: Vehicle-To-Load

WLTP: Worldwide Harmonised Light-Duty Vehicles Test Procedure